Development of Mineralised Gene-Activated Matrices for Osteochondral Tissue Regeneration

Daniel David White

Submitted in accordance with the requirements for the degree of

Doctor of Philosophy

The University Of Leeds

School of Mechanical Engineering

Institute of Medical and Biological Engineering

January 2024

I confirm that the work submitted is my own and that appropriate credit has been given where reference has been made to the work of others.

This copy has been supplied on the understanding that it is copyright material and that no quotation from the thesis may be published without proper acknowledgement.

University of Leeds

Abstract

School of Mechanical Engineering

Institute of Medical and Biological Engineering

Doctor of Philosophy

Development of Mineralised Gene-Activated Matrices for Osteochondral Tissue Regeneration

By Daniel David White

Abstract

Full thickness osteochondral defects cannot naturally heal if critically sized due to the acellular, avascular, and aneural tissue structures of articular cartilage and subchondral bone. Despite a range of autograft and allograft implantations available to medical professionals to replace damaged tissue, many rely on the availability of donor tissue and – in the case of allografts - require deceullarisation prior to implantation. As an alternative to using donor tissue, gene-activated matrices (GAMs) are synthetic, acellular scaffolds that combine mimicry of the native extracellular matrix (ECM) of the osteochondral - via a multi-layered or gradient structure - with embedded genetic payloads to help spatially control stem cell differentiation and ECM deposition *in-vivo*.

Our group has recently improved upon an existing method to synthesise particles carrying genetic payloads within the nanoconfining matrix of agarose gels. This method, termed: 'particle synthesis via agarose gel electrophoresis' (PS-AGE), utilises modified agarose gel apparatus to synthesise calcium phosphate (CaP) particles in small layers < 2mm thick. In the literature, PS-AGE has previously been utilised to encapsulate proteins within CaP layers but has not yet been exploited for GAM fabrication due to the non-biomimetic geometry of CaP layers and overall gel that are inherently non-uniform in PS-AGE. Furthermore, agarose lacks any cell attachment motifs that are necessary for use as an osteochondral GAM material. The use of PS-AGE for osteochondral GAM fabrication is also hampered by a lack of exploration in the relationship between CaP particle size and biomolecular loadings (such as pDNA) or even basic experimental parameters (such as salt and gel concentration, or voltage). Despite these shortcomings in the literature, it is theorised that – with several modifications - PS-AGE could be used to fabricate GAMs suitable for a critically-sized pre-clinical osteochondral model.

The research in this work first investigates the functionalisation of agarose gels with polydopamine to establish cell attachment motifs across the gel surface. Particle characterisation of cryogel groups found that separate additions of pDNA loadings and a polydopamine coating reduced the primary modal diameter of CaP particles compared to control groups. Further, the combination of a pDNA loading and a polydopamine coating were symbiotic in their reduction of primary modal diameters, which was theorised to result from multimodal nucleation pathways of pDNA-CaP particles. However, no conclusive indication of enhanced cell attachment – or transfection – were provided by cytotoxicity and transfection assays respectively.

An 'ideal' subset of experimental conditions were obtained by systematically investigating the influence of individual experimental parameters (salt concentration and type, agarose concentration and type, temperature, and applied potential) on particle diameters. These ideal conditions were utilised in a modified PS-AGE method termed: particle synthesis via cylindrical agarose gel electrophoresis (PS-CAGE), with the aim of synthesising pDNA/CaP and pDNA-loaded magnesium phosphate (pDNA/MgP) particles with diameters ≤ 100 nm. This culminated in the fabrication of PDA-coated, cylindrical monolayer GAMs encapsulating cylindrically shaped and uniform pDNA/CaP or pDNA/MgP layers. In the case of pDNA/CaP GAMs, particle layers were greater than 2 mm in thickness and reflected the overall geometry required for an osteogenic layer in a critically-sized osteochondral defect rabbit model.

GAMs incubated with C2C12 cells showed evidence of transfection *in-vitro* via fluorescence microscopy due to green fluorescent protein (GFP) production. However, the high agarose concentration of GAM groups – required to reduce particle diameters – is thought to have significantly inhibited cellular infiltration and hence limit cell exposure to pDNA/CaP and pDNA/MgP particles. The use of dynamic cell seeding, as opposed to static, is expected to improve cellular infiltration into these cryogels and potentially enhance luciferase enzyme escape from the cryogel into the surrounding cell media, thus improving transfection assay sensitivity.

Overall, the PS-CAGE system was able to synthesise ~100 nm diameter pDNA/CaP particles as a macroscopically thick mineralised layer embedded within a PDA-coated cryogel. With further optimisation of the PS-CAGE system to produce bi-layers of genetic payloads, and with further development of *in-vitro* testing, there is great potential for the PS-CAGE to produce complete, multi-layered or gradient osteochondral GAMs. One could also pursue the synthesis of pDNA/MgP particles as osteogenic layers if layer thickness could be significantly increased.

Acknowledgements

I'd like to thank my supervisory team. Firstly, to Georg Feichtinger: thank you for guiding me through the first stages of my PhD and setting a high standard for scientific work. Secondly to Neil Thomason: thank you for giving such excellent support over the past years and dragging me to the finish line.

Thank you to Sarah Myers and Nicola Conway for your support in my laboratory work and training. I am deeply grateful for your encouragement, help, and enthusiasm in my time at Leeds. Also, to Stuart Mickelthwaite and John Harrington at LEMAS, for your technical expertise and provision of a fantastic research facility through which I acquired much of my thesis data. A huge thank you to all the academics and staff who contributed to the CDT TERM.

Outside of my project, I also want to thank my friends at Leeds. To Rory and Trent, thank you for helping make the powerlifting and weightlifting club a reality (and continued success) and always making the time for a quick pint and catchup with a friend.

To the boys – James, Kern, Matt, Paddy, and Simon – I'm so grateful to have had such great mates during my PhD studies. Studying alongside each of you made me a better scientist. More importantly, you were great friends to me and I'm not sure I would have gotten through such challenging times without you. It is an encouraging thought to know that when my life turned upside down, my mates were ready with a cold one, and I'll never forget that.

Also a huge individual thank you to Matt. Our projects have run parallel for years and you've been unbelievably helpful. Thanks for the hour-long discussions about our projects and helping me countless times in the lab.

I also want to acknowledge the encouragement from my new colleagues at KCL. Thank you for for being so welcoming, for encouraging me everyday to finish my write-up over the past 18 months, and for sharing in my submission and viva celebrations.

To Edgar and Maria, thank you for giving me a place to stay and food to eat for 2.5 years. I am deeply grateful for your selflessness and help.

To Tania, who believed in me even when I couldn't. You have done more for me than I can write down, and this acknowledgement will not do justice to how much you have helped me. Thank you for putting up with me for 9-years, for laughing at my jokes, for making me a better person, for helping me everyday, for finding the humour in everything, for being unapologetically yourself, and for enjoying every sit-com show with me.

To my family who have read so many "I can't make it, I'm writing my thesis" messages from myself over the past 5 years. Thank you for being patient and always asking how I'm getting on. To my Pops, Keneth, and my late Grandma, Angela, thank you for your enthusiastic questioning of "when can we call you a doctor?" I can now confirm I am a doctor. This and all the other words of encouragement helped to keep me going.

Lastly, I acknowledge my late parents, Sandra and Alfred White. I will not get to share in this final graduation with you, but you will be with me in spirit as you have been during my PhD. I have stood on your shoulders for so long and continue to benefit from how good and loving you were as parents. I think of you everyday, and I miss you deeply.

Contents

1 Literature Review 1
1.1 Gene Therapy 1
1.1.1 Non-viral Gene Therapy 1
1.2 Calcium Phosphate Particles as nVVs 2
1.2.1 Introduction 2
1.2.2 Particle Size and Morphology 3
1.2.3 Crystal Structure 6
1.3 Synthesis of DNA/RNA-CaP-NPs 8
1.3.1 Crystallisation in Confinement 11
1.3.2 PS-DW-AGE for Gene Therapy 17
1.4 Summary 26
1.5 Global Aims and Objectives 27
1.5.1 Aims 27
1.5.2 Objectives 27
2 Development of Polydopamine-coated pDNA/CaP cryogels 29
2.1 Introduction 29
2.2 Research Aims and Objectives 31
2.2.1 Research Aims 31
2.2.2 Research Objectives 31
2.3 Materials and Methods 32
2.3.1 pDNA stock solution 32
2.3.2 Loading solutions 33
2.3.3 Buffer Solutions 33
2.3.4 Gel Slabs 33
2.3.5 Gel loading 34
2.3.6 pDNA mobility 36
2.3.7 pDNA Encapsulation Efficiency 37
2.3.8 Scanning Electron Microscopy (SEM) 39
2.3.9 X-ray Diffraction (XRD) 41
2.3.10 Cell Culture and Transfection 41
2.3.11 Data Analysis 46
2.4 Results 47
2.4.1 pDNA Mobility in Gels 47

2.4.2 Cryogel Appearance 49
2.4.3 XRD 53
2.4.4 SEM 54
2.4.5 pDNA Encapsulation Efficiency 77
2.4.6 Cytotoxicity Assays 80
2.4.7 Transfection Assays 81
2.4.8 SEM Analysis post In-vitro 83
2.5 Discussion 86
2.5.1 pDNA mobility 86
2.5.2 Cryogel appearance 87
2.5.3 XRD 88
2.5.4 SEM 89
2.5.5 pDNA Encapsulation Efficiency 93
2.5.6 Transfection 95
2.5.7 Cytotoxicity 97
2.5.8 Enhancing Transfection Efficacy 98
2.5.9 Enhancing the Pre-clinical Relevancy of Cryogels 101
2.6 Conclusion 103
3 Development and Testing of Particle Synthesis Apparatus 105
3.1 Introduction 105
3.1.1 Improving Transfection Efficacy 105
3.1.2 Improving Pre-Clinical Relevancy 106
3.1.3 Alternative Non-Viral Vectors 107
3.1.4 Controlling Primary Particle Size 109
3.1.5 Inter-parameter relationships 112
3.1.6 Mitigating Inter-parameter Influences 120
3.1.7 Improving Pre-Clinical Relevancy of Cryogels 126
3.1.8 New Apparatus 131
3.2 Research Aims and Objectives 134
3.2.1 Overview 134
3.2.2 Research Aims 134
3.2.3 Research Objectives 134
3.3 Materials and Methods 136
3.3.1 Computational Modelling 136
3.3.2 Design and Manufacture of New Apparatus 146
3.3.3 Apparatus testing 165

3.4 Results 170
3.4.1 Electrostatics models 170
3.4.2 Ion Transport Models 174
3.4.3 Apparatus testing 191
3.5 Discussion 205
3.5.1 Computational modelling 205
3.5.2 Precipitation test 207
3.5.3 PS-CAGE System 209
3.5.4 Temperature/pH Control Unit 211
3.5.5 Current Test 212
3.6 Conclusion 214
4 Particle Size Reduction and Final Cryogel Synthesis 216
4.1 Introduction 216
4.1.1 New Apparatus 216
4.1.2 pDNA/MgP particles and pDNA/PEI complexes 216
4.1.3 Layer Synthesis 217
4.1.4 Summary 218
4.2 Research Aims and Objectives 220
4.2.1 Research Aims 220
4.2.2 Research Objectives 220
4.3 Materials and Methods 221
4.3.1 CaP and MgP Particle Synthesis in the PS-SW-AGE System 221
4.3.2 Particle Synthesis in the PS-CAGE System 232
4.3.3 SEM Analysis 236
4.3.4 pDNA encapsulation 236
4.3.5 Cell Culture 237
4.3.6 In-vitro Testing 237
4.3.7 Data Analysis 239
4.4 Results 240
4.4.1 Particle Synthesis via Varied Salt Concentration 240
4.4.2 Particle Synthesis via Varied Agarose Concentration 256
4.4.3 Particle Diameter and Agarose Type 264
4.4.4 Particle Diameter and Applied Potential 268
4.4.5 Particle Diameter and Temperature 271
4.4.6 Particle Diameter and Combinative Parameters 281
4.4.7 pDNA/PEI Layer Synthesis 286

4.4.8 Particle Diameters in the PS-CAGE System....287
4.4.9 Summary of Particle Diameter Investigations....290
4.4.10 Particle Synthesis in the PS-CAGE System Using an Ideal Subset of Parameter Conditions 292
4.4.11 Hydrogel Appearance....295
4.4.12 Cryogel Appearance....296
4.4.13 Cytotoxicity Assays....299
4.4.14 pDNA-encapsulation Efficiency....301
4.4.15 Transfection Assays....303
4.4.16 Fluorescence Microscopy....304
4.4.17 SEM analysis post-cell culture....307
4.5 Discussion....309
4.5.1 PS-DW-AGE System....309
4.5.2 Final Cryogel Synthesis in the PS-CAGE System....310
4.6 Conclusion....313
5 Final Discussion....315
6 Appendix....320
Bibliography....342

List of Figures

Figure 1.1. Overview of the PS-SW-AGE approach loading regime.....19

Figure 1.2. Typical examples of pDNA/CaP layers (without FBN) produced via PS-SW-AGE.....20

Figure 1.3. SEM image of CaP particles embedded in the surface of a lyophilised GAM. 20

Figure 1.4. Luciferase activity for pDNA/CaP GAM groups produced via the PS-SW-AGE approach.....20

Figure 2.1. Gel tray layout with 4 comb inserts.....34

Figure 2.2. Bio-Rad Sub-cell GT horizontal gel electrophoresis system and a submerged gel slab with four well rows. 35

Figure 2.3. Distribution of groups in the gel slab and the approximate cutting lines for gels excised from the gel.....36

Figure 2.4. Determination of irregular particle diameter and width using feret diameters.....40

Figure 2.5. 48-well plate layout for (top) the transfection plate and (bottom) the cytotoxicity plate. White wells indicate unused wells. 43

Figure 2.6. Layout of the 96-well transfection plate.....44

Figure 2.7. pDNA bands in (left) uncoated and (right) PDA-coated agarose gel slabs. 47

Figure 2.8. Distances travelled by pDNA bands over time in uncoated agarose and PDA-agarose gel slabs. Errorbars indicate standard deviation. 48

Figure 2.9. Uncoated and PDA-coated agarose cryogel appearances. (A) Agarose cryogels after first lyophilisation and (B) after 70 % EtOH sterilisation and second lyophilisation. (C) PDA-coated agarose cryogels after first lyophilisation and (C) after 70% EtOH ster 49

Figure 2.10. Digital Microscope images of (A) Blank group cryogel and (B) PDA-blank group cryogel.....50

Figure 2.11. Internal porous structure of (A) blank group cryogel and (B) PDA-blank group cryogel. 51

Figure 2.12. High magnification digital microscope images of PDA-blank cryogel internal pore structure. 52

Figure 2.13. XRD spectra for blank (green), pDNA/CaP (blue), PDA-pDNA/CaP (red) and HAp powder (black) samples.....53

Figure 2.14. SEM images of intact blank and PDA-blank cryogel surfaces.....55

Figure 2.15. Lyophilised blank cryogel (intact). 56

Figure 2.16. Low magnification SE image of a powdered CaP group sample. 57

Figure 2.17. BSE image of a powdered blank cryogel, showing an absence of particles on the agarose surface. 58

Figure 2.18. BSE image of the CaP sample. 59

Figure 2.19. Agarose fragments displaying particles from the CaP cryogel sample. Particles highlighted in red demonstrate hexagonal-like morphologies. 61

Figure 2.20. High magnification images of particles from the CaP cryogel sample.....62

Figure 2.21. Histogram for particles from the CaP sample (n = 912). Data is non-uniformly distributed (95 % confidence intervals). 63

Figure 2.23. Particles from the pDNA/CaP cryogel sample. Particle highlighted in red square demonstrate a hexagonal-like morphology. 64

Figure 2.24. Histogram for particles from the pDNA/CaP sample (n = 1105). Data is non-uniformly distributed (95 % confidence intervals). 65

Figure 2.25. SE images of a PDA blank sample. (A) Low magnification image of a fragment and (B) a high magnification image of the rough surface highlighted in red square. 67

Figure 2.26. SE images of particles from PDA-CaP group of the same agarose fragment. Red circles indicate particles that present little attachment to the agarose surface. 68

Figure 2.27. SE image of particles from the PDA-CaP cryogel group. Red circles indicate large agglomerates. 69

Figure 2.28. SE image of particles from PDA-CaP cryogel sample. Red cicles indicate particles of hexagonal-like morphologies and blue circles indicate coalesced particles. 70

Figure 2.29. Histogram for particles from the PDA-CaP sample (n = 661). Data is non-uniformly distributed (95 % confidence intervals). 71

Figure 2.30. SE image of particles from the PDA-pDNA/CaP cryogel sample. Coalesced particles are highlighted in blue and evidence of beam flattening is highlighted in green. 72

Figure 2.31. SE images of particles from separate agarose fragments in PDA-pDNA/CaP cryogel sample. (A) Small, sub-150 nm particles and (B) large, 80 – 500 nm particles. Evidence of beam flattening is highlighted in green circles.....73

Figure 2.32. Histogram of particle diameters from the PDA-pDNA/CaP sample. 74

Figure 2.33. Modal bin centres for particle diameters from cryogel samples. 75

Figure 2.35. Mean particle diameters (± SD) for cryogel groups. Errors bars indicate standard deviation. * Indicates statistical difference (95 % confidence intervals). 76

Figure 2.37. Total pDNA release (μg) from uncoated and PDA-coated cryogel groups. Orange: unsterilised cryogels submerged in control buffer. Green: sterilised cryogels submerged in control buffer. Purple: sterilised cryogels submerged in decalcification buffer. ** Indicates statistical difference (99 % confidence intervals). 77

Figure 2.38. Cell viability of cryogel groups (± % of blank control) at 48-hours. No groups demonstrated any statistically significant differences to one another (including the blank control). Error bars indicate standard deviation. 80

Figure 2.39. Luciferase luminescence for cryogels as a +% of the negative control. 82

Figure 2.40. Particles on agarose fragments from the PDA-pDNA/CaP cryogel group after 24-hours in cell media. 83

Figure 2.49. Particles on agarose fragments from the pDNA/CaP cryogel group after 24-hours in cell media.....84

Figure 3.1. Schematic of inter-parameter relationships in the PS-SW-AGE approach. Green = fully-controlled parameters, and blue = semi-controlled parameters. Arrows indicate an inter-parameter influence.....112

Figure 3.3. Orientation of the x-, y-, and z-axis in the horizontal electrophoresis. 129

Figure 3.4. The process of punching and removing small cylinders encapsulating particle layers from large cylinders. 132

Figure 3.5. (A) Mini Trans-Blot cell with cooling pack (Bio-Rad Laboratories, Inc.); (B) TE62 Vertical Electrophoresis System (Hoefer Inc.); (C) SUB25C Maxi-Cooled Submarine Gel Electrophoresis Unit (Hoefer Inc.). 133

Figure 3.6. Position of electrodes for all models. 136

Figure 3.7. Geometry of the wells in the PS-SW-AGE and PS-DW-AGE models. 137

Figure 3.8. Geometry of gels in the PS-CAGE models. 138

Figure 3.9. Full geometry of PS-SW-AGE, PS-DW-AGE, and PS-CAGE models. 139

Figure 3.10. Segmentation of gel cylinders into 1 mm segments and calculation of chord length. 143

Figure 3.11. 3D model of the gel tray. 147

Figure 3.12. 3D model of the gel comb. 147

Figure 3.13. 3D-models of gel punch components: (A) punch; (B) piston and (C) cross-sectional view of the punch and piston assembly. 148

Figure 3.14. 3D-CAD model of the gel cutting mask. 149

Figure 3.15. 3D model of the comb riser (3 mm size). 149

Figure 3.16. Design of the cylindrical cast and base. 150

Figure 3.17. Exploded view of 10 mm gel casts. 151

Figure 3.18. Exploded assembly view of the cutting mask (five holes), mask holder, and gel cast. 152

Figure 3.19. 3D-CAD model of a raised electrode holder. 153

Figure 3.20. Overview of the heat exchanger. 155

Figure 3.21. 3D CAD model of the heat exchanger: (A) without housing and (B) with housing. 157

Figure 3.22. Overview of the electronic circuitry and components of the heat exchanger. 158

Figure 3.23. Rear view of the electronics circuitry shelf. 160

Figure 3.24. Pseudo code flowchart of coding for Arduino. 161

Figure 3.25. Layout of the bottom layer of the enclosure. 162

Figure 3.26. Layout of the top layer of the enclosure. 163

Figure 3.27. 3D-CAD model of the tubing platform with silicone tubing (green).....164

Figure 3.28. Agarose gel cast in a cylindrical gel mould. (Left) gel cylinders within the mould (lid removed); and (right) a gel cast removed from the mould and stood upright using nylon bolts. 167

Figure 3.29. (Top) Four small gel cylinders cut from a large gel cylinder; (bottom) five gel cylinders cut from a large gel cylinder. 168

Figure 3.30. Electrostatic models showing electric field strength (Vm-1). (A) PS-SW-AGE model; (B) PS-DW-AGE model. 170

Figure 3.31. Electrostatic model showing electric field strength (Vm^{-1}) for the PS-CAGE model. The left domain shows the 2M $CaCl_2$ gel, the central domain is the recipient gel, and the right domain is the 12 mM Na_2HPO_4 gel (see Figure 3.8 for model geometry). 171

Figure 3.32. Line graphs of electrostatic models showing electric field strength (Vm-1). (A) PS-SW-AGE model; (B) PS-DW-AGE model.....172

Figure 3.33. Line graph showing electric field strength in the PS-CAGE model. 173

Figure 3.34. Animation of Ca^{2+} ion transport in the PS-SW-AGE model. The external link for this Figure is provided as follows: Figures 175

Figure 3.35. Line graph animation of Ca^{2+} ion transport in the PS-SW-AGE model. The external link for this Figure is provided as follows: Figures 176

Figure 3.3.37. Animation of HPO_4^{2-} + $H_2PO_4^-$ ion transport in the PS-SW-AGE model. The external link for this Figure is provided as follows: 177

Figure 3.37. Animation of HPO_4^{2-} + $H_2PO_4^-$ ion transport in the PS-SW-AGE model. The external link for this Figure is provided as follows: Figures 177

Figure 3.38. Line graph animation of HPO_4^{2-} + $H_2PO_4^-$ ion transport in the PS-SW-AGE model. The external link for this Figure is provided as follows: Figures 177

Figure 3.39. Line graph animation for the mixing product, m, for the PS-SW-AGE model. The external link for this Figure is provided as follows: Figures 178

Figure 3.40. Animation of mixing product, m, for the PS-SW-AGE model. The external link for this Figure is provided as follows: Figures 178

Figure 3.41. Animation of Ca^{2+} ion transport in the PS-DW-AGE model. The external link for this Figure is provided as follows: Figures 179

Figure 3.42. Line graph animation of Ca^{2+} ion transport in the PS-DW-AGE model. The external link for this Figure is provided as follows: Figures 179

Figure 3.43. Animation of HPO_4^{2-} + $H_2PO_4^-$ ion transport in the PS-DW-AGE model at pH 7.4. The external link for this Figure is provided as follows: Figures 180

Figure 3.44. Animation of HPO_4^{2-} + $H_2PO_4^-$ ion transport in the PS-DW-AGE model at pH 8.0. The external link for this Figure is provided as follows: Figures 181

Figure 3.45. Line graph animation of HPO_4^{2-} + $H_2PO_4^-$ ion transport in the PS-DW-AGE model at pH 7.4. The external link for this Figure is provided as follows: Figures 181

Figure 3.46. Line graph animation of HPO_4^{2-} + $H_2PO_4^-$ ion transport in the PS-DW-AGE model at pH 8.0. The external link for this Figure is provided as follows: Figures 182

Figure 3.47. Animation of mixing product, m, for the PS-DW-AGE model at pH 7.4. The external link for this Figure is provided as follows: Figures 183

Figure 3.48. Animation of mixing product, m, for the PS-DW-AGE model at pH 8.0. The external link for this Figure is provided as follows: Figures 183

Figure 3.49. Line graph animation of mixing product, m, for the PS-DW-AGE model at pH 7.4. The external link for this Figure is provided as follows: Figures 184

Figure 3.50. Line graph animation of mixing product, m, for the PS-DW-AGE model at pH 8.0. The external link for this Figure is provided as follows: Figures 184

Figure 3.51. Animation of Ca2+ ion transport in the PS-CAGE model. The external link for this Figure is provided as follows: Figures 185

Figure 3.52. Line graph animation of Ca^{2+} ion transport in the PS-CAGE model. The external link for this Figure is provided as follows: Figures 186

Figure 3.53. Animation of HPO_4^{2-} + $H_2PO_4^-$ ion transport in the PS-CAGE model. The external link for this Figure is provided as follows: Figures 187

Figure 3.54. Line graph animation of HPO_4^{2-} + $H_2PO_4^-$ ion transport in the PS-CAGE model. The external link for this Figure is provided as follows: Figures 188

Figure 3.55. Animation of the mixing product in the PS-CAGE model. The external link for this Figure is provided as follows: Figures 189

Figure 3.56. Line graph animation of the mixing product in the PS-CAGE model. The external link for this Figure is provided as follows: Figures 190

Figure 3.57. Gel slices cut by the gel punch. (A) Sliced holes from the gel slab; (B) excised gels. 191

Figure 3.58. CaP particle layers produced in agarose gel slabs using the PS-DW-AGE system. (A) CaP layers produced in a 1 wt % agarose gel at 180 V; (B) CaP layers produced in a PDA-coated 1 wt % agarose gel at 180 V; (C) MgP layers produced in a 1 wt % agarose gel at 180 V; (D) MgP layers produced in a PDA-coated 1 wt % agarose gel at 180 V. 192

Figure 3.59. Recipient gel cylinders with CaP layers. (Left) shows the plan view of the recipient gel cylinder displaying the cylinder face that was positioned adjacent to the Na_2HPO_4 loading gel. (Middle and right) side view of two separate gel cylinders encapsulating a CaP layer. 194

Figure 3.60. CaP layers within smaller cylinders. 195

Figure 3.61. PDA-coated recipient gel cylinders with CaP layers. 196

Figure 3.62. A CaP layer within a small PDA-coated cylinder.....197

Figure 3.63. A selection of small PDA-coated cylinders.....197

Figure 3.64. CaCl2 and Na2HPO4 loading gels following adjacent loading.....198

Figure 3.65. (Top) Side-view of an Na_2HPO_4 loading gel encapsulating a CaP layer. (Bottom) a smaller gel cylinder cut from the loading gel, encapsulating a CaP layer. 199

Figure 3.66. PDA-coated CaCl2 loading gel with a CaP layer produced during adjacent loading. 200

Figure 3.67. Temperature measurements at the tank middle, adjacent to gel cylinders.....201

Figure 3.68. pH measurements at the anode, tank middle, and cathode. 202

Figure 3.69. Current measured through the electrophoresis tank for the control test. 203

Figure 3.70. Current measured through the electrophoresis tank for the experimental test. .203

Fi**gure 4.1.** Layout of loading solutions for all loading pairs.....225

Figure 4.2. Layout of loading solutions in a gel slab loaded with a Mg2+-doped CaCl2 solution. 226

Figure 4.3. Layout of loading solutions in a gel slab with agarose concentration of either 1, 2, 3, 4, or 5 wt % agarose. 227

Figure 4.4. Layout of loading solutions in a 1 wt % agarose gel slab using different applied potentials.....228

Figure 4.5. Layout of loading solutions in a 1 wt % agarose gel slab using different temperatures. 229

Figure 4.6. Layout of loading solutions in a 1 wt % agarose gel slab using different buffer types. 230

Figure 4.7. Layout of loading solutions in a 3 wt % agarose gel slab using buffer types. 231

Figure 4.8. CaP particles on the surface of separate agarose fragments from the 4.125 M $CaCl_2$ + 25 mM Na_2HPO_4 sample. (A) Fragment encapsulating a high density of particles; (B) fragment two encapsulating two distinct particle populations of contrasting size. Coloured circles indicate the following: red and blue = sub-surface particles; green = measured particle; yellow = large particle; purple = sub-100nm particles. 240

Figure 4.9. CaP particles on the surface of separate agarose fragments from the 2 M $CaCl_2$ + 12 mM Na_2HPO_4 sample. (A) Fragment one with moderately dispersed particles; (B) fragment two with clustered particles. 242

Figure 4.10. CaP particles on the surface of separate agarose fragments from the 1 M $CaCl_2$ + 12 mM Na_2HPO_4 sample. (A) Fragment one with moderately dispersed particles; (B) fragment two with clustered particles. Red circles indicate sub-surface particles, green circles indicate measured particles.....243

Figure 4.11. Histogram of CaP particle measurements from the 4.125 M, 2 M, and 1 M $CaCl_2$ samples. Arrows indicate primary and secondary modal peaks. 244

Figure 4.12. Primary and secondary peak CaP particle diameters for 1 M, 2 M and 4.125 M CaCl2 samples. 245

Figure 4.13. MgP particles from the 3.75 M MgCl2 + 25 mM Na2HPO4 sample. Red square indicates magnified area. 246

Figure 4.14. MgP particles from the 1.8 M MgCl2 sample. Red squares indicate magnified areas, blue circles indicate areas with sub-100 nm particles. 247

Figure 4.15. Agarose fragments with MgP particles from the 0.9 M MgCl2 sample. Blue circles indicate coalesced particles. 248

Figure 4.16. Histogram of MgP particle measurements from the 0.9 M, 1.8 M, and 3.75 M MgCl2 samples. Arrows indicate primary and secondary modal peaks. 249

Figure 4.17. Primary and secondary peak MgP particle diameters for 0.9 M, 1.8 M and 3.75 M MgCl2 samples. 250

Figure 4.18. Agarose fragments with Mg2+-doped CaP particles from the Mg2+-doped CaP sample. Red square indicates magnified area. 251

Figure 4.19. Histogram of particle measurements from the 4.125 M CaCl2, 3.75 M MgCl2, and 3.7125 M CaCl2 + 0.4125 M MgCl2 samples. Arrows indicate primary and secondary peaks of each sample. 252

Figure 4.20. Primary and secondary peak particle diameters for 4.125 M CaCl2, 3.75 M MgCl2, and 3.7125 M CaCl2 + 0.4125 MgCl2 samples. 253

Figure 4.21. Mean CaP and MgP particle diameters plotted against respective salt concentration. Error bars indicate standard deviation. 254

Figure 4.22. Typical images of CaP particles on agarose fragments at different agarose concentrations. (A) 1 wt % agarose; (B) 2 wt % agarose; (C) 3 wt % agarose; (D) 4 wt % agarose, and (E) 5 wt % agarose. *X* denotes the agarose wt % for the respective sample name. 257

Figure 4.23. Primary and secondary modal peak particle diameters for 1, 2, 3, 4, and 5 wt % agarose samples. 258

Figure 4.24. Histogram of CaP particle measurements from the 1, 2, 3, 4, and 5 wt % agarose samples. Arrows indicate the primary and secondary modal peaks for samples of the same colour. 258

Figure 4.25. Typical images of MgP particles on agarose fragments at different agarose concentrations. (A) 1 wt % agarose; (B) 2 wt % agarose; (C) 3 wt % agarose; (D) 4 wt % agarose, and (E) 5 wt % agarose. *X* denotes the agarose wt % for the respective sample name. 260

Figure 4.26. Histogram of MgP particle measurements from the 1, 2, 3, 4, and 5 wt % agarose samples. Arrows indicate the primary and secondary modal peak diameter for samples of the same colour. 261

Figure 4.27. Primary and secondary modal peak diameters for 1, 2, 3, 4, and 5 wt % agarose samples. 261

Figure 4.28. Mean (± SD) CaP and MgP particle diameters at agarose concentrations of 1 – 5 wt %. 262

Figure 4.29. Mean CaP and MgP particle diameters plotted against agarose pore diameters experimentally measured by Narayanan et al. (2006). Error bars indicate standard deviation. 263

Figure 4.30. Typical SEM images of CaP and MgP particles on agarose fragments synthesised using either NuSieveTM or SeaKem® agarose. 264

Figure 4.31. Histogram of CaP and MgP particle measurements from NuSieve™ and SeaKem® agarose samples. Arrows indicate the primary and secondary (if applicable) modal peaks for samples of the same colour. 265

Figure 4.32. Primary and secondary modal peak particle diameters for CaP and MgP particles synthesised in either NuSieveTM or SeaKem® agarose. 266

Figure 4.33. Mean (± SD) CaP and MgP particle diameters synthesised in either SeaKem® or NuSieveTM agarose. Error bars indicate standard deviation. 267

Figure 4.34. Typical SEM images of CaP particles synthesised using varied applied potentials. (A) CaP particles synthesised at 60 V; (B) CaP particles synthesised at 120 V; and (C) CaP particles synthesised at 180 V. 268

Figure 4.35. Histogram of CaP particle measurements from 60, 120, and 180 V samples. Arrows indicate the primary and secondary (if applicable) modal peaks for samples of the same colour. 269

Figure 4.36. Primary and secondary modal peak particle diameters for CaP particles synthesised at applied potentials of 60, 120, and 180 V. 270

Figure 4.37. Mean (± SD) values of CaP particle diameters synthesised with applied potentials of 60, 120, and 180 V. Error bars indicate standard deviation. 270

Figure 4.38. Typical SEM images of CaP particles synthesised at various temperatures. (A) CaP particles synthesised at 4 °C; (B) CaP particles synthesised at 21 °C; and (C) CaP particles synthesised at 42 °C. 271

Figure 4.39. High magnification SEM images of a CaP particle synthesised at 4 °C. 272

Figure 4.40. Histogram of CaP particle measurements from 4, 21 and 42 °C samples. Arrows indicate the primary and secondary (if applicable) modal peaks for samples of the same colour. 273

Figure 4.41. Typical SEM images of MgP particles synthesised at various temperatures. (A) and (B) MgP particles synthesised at 21 °C; (C) and (D) MgP particles synthesised at 42 °C. 274

Figure 4.42. Histogram of MgP particle measurements from 4, 21 and 42 °C samples. Arrows indicate the primary and secondary (if applicable) modal peaks for samples of the same colour. 275

Figure 4.43. Mean (± SD) values of CaP and MgP particle diameters synthesised at varied temperatures. 276

Figure 4.44. Typical SEM images of CaP particles synthesised using 25 mM HEPES (pH 8.0). (A) Low magnification image of CaP particles and (B) higher magnification image of CaP particles. Red square indicates magnified area. 277

Figure 4.45. Typical SEM images of CaP particles synthesised using 25 mM Tris-HCl (pH 8.0). (A) Low magnification image of CaP particles and (B) higher magnification image of CaP particles. Red square indicates magnified area. 278

Figure 4.46. Histogram of CaP particle measurements from CaP HEPES and CaP Tris samples. Arrows indicate the primary and secondary (if applicable) modal peaks for samples of the same colour. 279

Figure 4.47. Mean (± SD) values of CaP particle diameters synthesised using either HEPES or Tris buffer. 280

Figure 4.48. Mean (± SD) CaP and MgP particle diameters for unmodified, 2 M CaCl2, 1.8 M MgCl2, CaP 3 wt % agarose, MgP 3 wt %, and combinative samples. Error bars indicate standard deviation. 281

Figure 4.49. Typical SEM images of CaP and MgP particles produced using combinative parameter changes and different buffers. (A) CaP particles synthesised in 25 mM HEPES; (B) CaP particles synthesised in 25 mM Tris-HCl; (C) MgP particles synthesised in 25 mM HEPES; (D) MgP particles synthesised in 25 mM Tris-HCl. 283

Figure 4.50. Histogram of CaP and MgP particle size measurements comparing combinative parameter changes in different buffers. Arrows indicate the primary and secondary (if applicable) modal peaks for samples of the same colour. 284

Figure 4.51. Mean diameters for CaP and MgP particles synthesised using combinative parameter changes* in either HEPES or Tris-HCl. *2 M CaCl2 or 1.8 MgCl2 and 3 wt % agarose. 285

Figure 4.52. pDNA/PEI complexes formed in (A) the PS-DW-AGE system and (B) PS-CAGE system. 286

Figure 4.53. CaP and MgP particles synthesised via the PS-CAGE system. (A) and (B): CaP particles, (C) and (D) MgP particles. 287

Figure 4.54. Histogram of CaP and MgP particle size measurements for samples synthesised using either the PS-CAGE and PS-DW-AGE systems. 288

Figure 4.55. Mean particle diameters for CaP and MgP particles synthesised in the PS-DW-AGE and PS-CAGE systems. 289

Figure 4.56. Surface topographies of: (A) the PDA-pDNA/CaP sample; and (B) the PDA-pDNA/MgP sample. 294

Figure 4.57. Images of hydrogels and cryogels. (A) pDNA/CaP hydrogel; (B) pDNA/MgP hydrogel; (C) pDNA/CaP cryogel; and (D) pDNA/MgP cryogel. 295

Figure 4.58. Digital microscopy images of (A) blank; (B) pDNA/CaP; and (C) pDNA/MGP cryogels. 296

Figure 4.59. High magnification digital microscope image of a typical pDNA/MgP cryogel. Black clusters are approximately 2 - 10 µm in diameter. 297

Figure 4.60. Appearance of cryogels when submerged in cell media. (Top) pDNA/CaP cryogels and (bottom) pDNA/MgP cryogels 298

Figure 4.61. Cell viability as a percentage (%) of the blank cryogel control. 299

Figure 4.62. pDNA release from cryogel groups into decalcification buffer. Error bars indicate standard deviation. 301

Figure 4.63. Luminescence (± % of blank control) for cryogel groups as a measure of transfection efficacy. Error bars indicate standard deviation. 303

Figure 4.64. Fluorescence microscopy images of cryogel groups. 305

Figure 4.65. Fluorescence microscopy images of cryogel groups. 306

Figure 4.66. Typical SEM images of pDNA/CaP/PEI cryogels after a 24-hour incubation in cell media 307

Figure 4.67. Typical SEM images of pDNA/CaP/PEI cryogels after a 24-hour incubation in cell media.....308

Figure 6.1. EDS map of an agarose fragment surface from a CaP cryogel sample. (A) SE image of target area; (B) EDS layered map and (C) EDS summary spectrum of detected elements. 320

Figure 6.2. EDS map for pDNA/CaP cryogel sample. (A) SE image of target area; (B) EDS layered map and (C) EDS summary spectrum of detected elements.....322

Figure 6.3. Orthographic drawing of the gel tray for the PS-DW-AGE system.....333

Figure 6.4. Orthographic drawing of a comb for the PS-DW-AGE system. 334

Figure 6.5. Orthographic drawing of the gel punch.....335

Figure 6.6. Orthographic drawing of the piston. 336

Figure 6.7. Orthographic drawing of the comb riser for the PS-DW-AGE system. 337

Figure 6.8. Orthographic drawing of the cutting mask for the PS-DW-AGE system.....338

Figure 6.9. Orthographic drawing of the cylindrical gel cast for the PS-CAGE system. 339

Figure 6.10. pDNA velocities in various SeaKem® agarose concentration plotted against time. Blue = 1 wt %; orange = 2 wt %; grey = 3 wt %. 340

Figure 6.11. pDNA velocities in SeaKem® agarose at different applied potentials, plotted against time. Blue = 60 V; orange = 180 V; grey = 300 V.....340

List of Tables

Table 1.1. CaP particle properties from studies using the PS-DW-AGE approach 17

Table 2.1. Overview of loading solution formulations.....33

Table 2.2. Overview of cryogel group names and their new group name following submergence in buffer. 38

Table 3.1. Materials, their relative permittivity values, and their respective references. 141

Table 3.2. Ionic species used in the ion transport models. 144

Table 3.3. Percentages of HPO42- and H2PO4- at pH 7.4 and 8.0 as calculated using the Henderson-Hasselbalch equation. 144

Table 3.4. Concentrations and pH for each cylindrical gel type. 166

Table 4.1. Stock Salt Solution Constituents. 221

Table 4.2. Loading Solution Constituents. 222

Table 4.3. Group names and their respective loading solutions pairs and ionic ratios. 223

Table 4.4. Agarose mass and working buffer volume for each agarose concentration. 223

Table 4.5. Stock salt solution formulations. 232

Table 4.6. Salt loading and recipient gel concentrations and constituents. 234

Table 6.1. Gel tray design specifications. 323

Table 6.2. Gel comb design specifications. 324

Table 6.3. Gel punch design specifications for the individual punch and piston components. 325

Table 6.4. Cutting mask design specifications. 325

Table 6.5. Comb Riser Design Specifications. 325

Table 6.6. Specifications for the Gel Cylinder Cast. 326

Table 6.7. Specifications of the raised electrode holders. 327

Table 6.8. Heat exchanger and water loop specifications for the temperature/pH control unit. 328

Table 6.9. Design specifications for the electronic systems of the temperature/pH control unit. 330

Table 6.10. Design Specifications of the enclosure. 331

List of abbreviations

ACP	Amorphous calcium phosphate
AGDD	Agarose gel double-diffusion
AMgP	Amorphous magnesium phosphate
ATX-PSU	Advanced technologies extended power supply unit
BMSCs	Bone marrow stem cells
BSE	Backscattered electron
CAD	Computer-aided design
CaP	Calcium phosphate
CFD	Computational fluid dynamics
CI	Confidence intervals
DAPI	4’,6-diamidino-2-phenylindole
DCP	Dicalcium phosphate
D.H_2O	Deionised water
DLS	Dynamic light scattering
DMEM	Dulbecco’s Modified Eagle’s Medium
DNA	Deoxyribonucleic acid
DNA/RNA/CaP	DNA or RNA encapsulated calcium phosphate
DNA/RNA/CaP-NPs	DNA or RNA encapsulated calcium phosphate nanoparticles
E.Coli	Escherichia coli
EDL	Electrical double layer
EDS	Energy dispersive x-ray spectroscopy
EDTA	Ethylenediaminetetraacetic acid
EtOH	Ethanol

FBN	Fibronectin bovine protein
FBS	Foetal calf serum
GAM	Gene-activated matrix
LB	Lysogeny broth
LED	Light emitting diode
HAp	Hydroxyapatite
HEPES	4-(2-hydroxyethyl)-1-piperazineethanesulfonic acid
LDH	Lactate dehydrogenase
MFC	Medial femoral condyle
MgP	Magnesium phosphate
µPs	Microparticles
NBF	Neutral buffered formalin
NC	Normally closed
NO	Normally open
NPs	Nanoparticles
nVVs	non-viral vectors
OCP	Octacalcium phosphate
OD	Optical density
PBS	Phosphate buffered saline
pDNA	plasmid deoxyribonucleic acid
pDNA/CaP	pDNA-loaded calcium phosphate
pDNA/CaP-NPs	pDNA-loaded calcium phosphate nanoparticles
pDNA/CaP/PEI	pDNA-loaded calcium phosphate with PEI coating
pDNA/MgP	pDNA-loaded magnesium phosphate
pDNA/PEI	pDNA-loaded polyethylenimine

PLGA	poly(D,L-lactide-co-glycolide acid)
PDA	Polydopamine
PDA-pDNA/CaP	Polydopamine-coated pDNA-loaded calcium phosphate
PEI	Polyethylenimine
pGFP	plasmid encoding for the green fluorescent protein
pMetLuc	plasmid encoding for the luciferase enzyme
PS-CAGE	Particle synthesis via cylindrical agarose gel electrophoresis
PS-DW-AGE	Particle synthesis via double-well agarose gel electrophoresis
PS-SW-AGE	Particle synthesis via single-well agarose gel electrophoresis
RNA	Ribonucleic acid
SBF	Simulated body fluid
SD	Standard deviation
SE	Secondary electron
SEM	Scanning electron microscopy
siRNA	small interfering ribonucleic acid
SCP	Supercritical point
SOC	Super Optimal Broth media with catabolite repression
TDSPM	Transport of diluted species through porous media
TEM	Transmission electron microscope
TK-HDS	Tukey Kreamer honestly significant difference
Tri-MgP	$Mg_3(PO_4)_2$
Tris	Tris(hydroxymethyl)aminomethane
XRD	X-ray diffraction

Dedicated to Sandra and Alfie

1 Literature Review

1.1 Gene Therapy

In gene therapy, therapeutic genes are encoded into deoxyribonucleic acid (DNA) or ribonucleic acid (RNA) molecules for delivery to the cell nucleus or ribosome respectively. The DNA or RNA is then read and instructs the cell to upregulate a particular protein depending on the encoded gene. Viruses such as retroviruses, lentiviruses and adenoviruses are highly efficient in transferring genetic data to cells and as such are commonly used as viral vectors to deliver genes to target cells (Lundstrom, 2018). However, concerns over viral vector safety have led to a significant increase in the research of non-viral gene delivery (Ramamoorth and Narvekar, 2015).

1.1.1 Non-viral Gene Therapy

Non-viral gene therapy encompasses a wide range of techniques divided into physical or chemical methods. In physical methods, injection of a 'naked' DNA or RNA payload to achieve systemic or regional transfection is the simplest and safest way to deliver a genetic payload to cells (Herweijer and Wolff, 2003, Al-Dosari and Gao, 2009). However, the unprotected payload is subject to degradation by nucleases and clearing by phagocytes (Nam et al. (2009). Thus, unprotected payloads can lead to poor transfection efficacy. Naked DNA/RNA injection has therefore been combined with electroporation and hydroporation techniques that temporarily enhance cell membrane permeability, reducing the extracellular 'linger' time of DNA or RNA and consequently increasing transfection efficacy of naked genetic payloads (Tamura and Sakata, 2003, Newman and Bettinger, 2007).

Chemical methods primarily describe non-viral vectors (nVVs); particles in the micron and sub-micron range that encapsulate and condense nucleic acid payloads to enhance their survivability, specificity and transfection efficacy (Li and Huang, 2000). The use of cationic lipids and polymers, or inorganic nanoparticles, can protect nucleic acids from nuclease degradation and electrostatically shield them from the net-negative charge of the cell membrane. This facilitates cellular infiltration and transport of the nucleic acid to the nucleus or ribosome via the endocytic pathway. The transfection efficacy is of nVVs is generally lower than that of their viral counterparts, given the evolutionary advantage of viruses. However, in many cases, nVVs

have been shown to be less cytotoxic, immunotoxic, and can be manufactured at a lower cost than viral vectors (Ibraheem et al., 2014). For these reasons, nVVs have gained significant interest in the field of gene therapy over the past two decades (Rodriguez et al., 2013).

DNA or RNA payloads have been conjugated with a wide variety of nVVs. This includes heavy metallic, inorganic nanoparticles (NPs) such as gold NPs (Uchida et al., 2009) and silver NPs (Sarkar et al., 2015) for use in ballistic (gene-gun) DNA techniques. Meanwhile, iron oxide NPs have been employed in magnetofection techniques where magnetic fields are used to manipulate and concentrate NPs to a desired target location (Sosa-Acosta et al., 2020). In contrast to inorganic nVVs, organic molecule-based nVVs primarily include liposomal (Lee and Lee, 2012) and polymeric (Yang et al., 2012) conjugations.

1.2 Calcium Phosphate Particles as nVVs

1.2.1 Introduction

Calcium phosphate (CaP) particles are part of the inorganic realm of nVVs and have been researched extensively since their first use in the 1970s (Graham et al., 1973). Research has gone on to produce DNA or RNA encapsulated (or adsorbed) CaP (DNA/RNA-CaP) particles with a range of sizes, morphologies, crystal structures and core-shell architectures. Nowadays, DNA/RNA-CaP particle synthesis has become widely accessible via commercial kits such as ProFection™ (Promega Corporation, Wisconsin, USA) and CalPhos™ (Takara Bio Inc., Shiga, Japan), amongst others, that allow co-precipitation of DNA or RNA with CaP via pre-prepared salt solutions. Such commercial kits do not aim for specific physicochemical properties, but rather aim to minimise size and agglomeration, whilst maximising nucleic acid encapsulation and/or adsorption. However, several physicochemical properties of DNA/RNA-CaP particles are known to influence their transfection efficacy, such as size (Neuhaus et al., 2016), shape (Gratton et al., 2008) and chemical composition (Bose and Tarafder, 2012). Further, since crystal structure influences a given particle's surface charge, one can expect DNA or RNA adsorption to be dependent on crystal structure. It should therefore be critical to consider these properties during DNA/RNA-CaP particle synthesis to maximise their transfection efficacy potential.

1.2.2 Particle Size and Morphology

It is widely accepted in literature reviews and studies that DNA/RNA-CaP particles of diameters ≤ 100 nm e.g DNA/RNA-CaP nanoparticles (DNA/RNA-CaP-NPs) have much greater transfection efficacy than micro-particles (µPs) (diameters of 0.1 – 100 µm) (Welzel et al., 2004, Dorozhkin, 2010, Lin et al., 2014). Enhanced transfection efficacy with reducing CaP particle size arises for several reasons, including stronger cell membrane-particle interaction for NPs than µPs (Han et al., 2012), an inefficiency of µPs to penetrate cell membranes (Pedraza et al., 2008), and enhanced cell viability and proliferation evoked by NPs (Cai et al., 2007). Smaller CaP particles have even demonstrated greater osteogenic effects (Yang et al., 2018). Stronger cell membrane-particle interactions may arise primarily through increased charge density as particle size reduces. Meanwhile, enhanced cell viability or reduced cytotoxicity of CaP-NPs compared to CaP-µPs has been suggested to arise from a reduced intracellular Ca^{2+} concentration upon dissolution (Masouleh et al., 2017).

Reducing particle size has a knock-on effect on specific surface area and the total number of nVVs. Specific surface area, which correlates to nucleic acid absorption capacity, increases significantly with reducing particle size, hence solutions of smaller particles can theoretically carry a greater mass of nucleic acid payload per unit mass of particles. If we assume DNA/RNA-CaP-NPs are spherical, an increase in surface area per unit mass as particle size reduces can be explained by examination of the relationship between the surface area of a sphere, A, and its radius, r:

$$A = 4\pi r^2 \qquad 1.1$$

Let us consider two separate, homogeneous, DNA/RNA-CaP-NP suspensions, with spherical particles in suspension one measuring 50 nm in diameter, and spherical particles in suspension two measuring 100 nm in diameter. Using Equation 1.1, it is calculated that suspension one has four times greater specific surface area than that of suspension two due to the relationship between particle surface and its squared radius. We can therefore expect a commensurable increase in nucleic acid loading capacity, provided there is a linear relationship between nucleic acid loading capacity and surface area. Of course, this theorised relationship will diminish at very small particle sizes where nucleic acids might struggle to adsorb strongly. This assumption also relies on retention of crystallinity as particle size reduces, since nucleic acid adsorption occurs

on positively charged surface planes. For example, if both suspensions had DNA/RNA-CaP-NPs exhibiting fully crystalline hydroxyapatite (HAp) structures, nucleic acid adsorption would occur preferentially on (001) and (010) planes (Del Valle et al., 2014). One could also argue that since the ratio of adsorbed nucleic acids to surface ions increases as particle size reduces, greater stability is achieved *in-vitro*. This would arise through the protection of CaP-NP surfaces from unwanted growth or premature dissolution in extracellular environments.

As DNA/RNA-CaP-NP size is reduced, the total number of nVVs also increases, provided overall mass is maintained. This can be explained by comparing spherical particle volume, V, and radius, r, in Equation 1.2:

$$V = \frac{4}{3}\pi r^3 \qquad 1.2$$

From this, one can see that suspension one with 50 nm diameter particles has eight times more particles than in suspension two (100 nm diameter particles) for the same unit mass, given the cubic relationship between volume and radius. Simply reducing particle size by a factor of two therefore increases the total number of nVVs in solution by a factor of eight.

An important consideration for studies investigating the change in transfection efficacy with nVV size is the sedimentation effect of larger particles in monolayer studies that can theoretically produce artefacts in transfection efficacy data. A cell monolayer administered with a DNA/RNA-CaP-NP suspension will see larger particles or agglomerates travel to the cell monolayer quicker than smaller particles. This can be shown by examination of Stokes' law for terminal velocity, v, of a sphere falling in a fluid:

$$v = \frac{2}{9}(p_p - p_f)gR^2 \qquad 1.3$$

Where p_p is the mass density of the particle (kgm^{-3}), p_f is the mass density of the fluid (kgm^{-3}), g is gravitational field strength (ms^{-2}), and R is particle radius (m). Using this relationship, one can see that particles from suspension one will take four times as long to reach the monolayer than particles from suspension two. In practice, directly administering either suspension onto a monolayer would mix cell media and particle suspension, immediately exposing cells to the nVVs and averting the need to wait for sedimentation. Furthermore, replenishment of cell media and/or particle suspensions, or the use of dynamic cell culture, agitates particles in suspension

and helps to homogenise the number of particles in cell monolayers between experimental groups. However, short-term transfection studies that do not require cell media exchanges should take caution in comparing data between experimental groups of differently sized nVVs.

Similarly to particle size, particle morphology contributes to the specific surface area of DNA/RNA-CaP-NPs and therefore impacts DNA/RNA loading efficiency, as well as cell viability (Pujari-Palmer et al., 2017, Oberbek et al., 2018) and osteogenic effects (Kalia et al., 2014). But whilst several studies have measured the response of cells to CaP-NPs of different morphologies, an optimal shape has not been agreed upon in the literature. For example, Kalia et al. (2014) concluded that CaP-NPs of spherical morphology had a greater osteogenic effect than 'rice-shaped' CaP-NPs, whilst Wu et al. (2019) found 'needle-like' particles demonstrated nearly double the cell viability of 'granular' shaped particles. Such differences in cell viability between spherical, needle- or 'rod-like' CaP-NPs are prevalent in the literature, the persistence of which is assumed to be due to inconsistencies in particle concentrations and dissimilar crystal structures arising from varied synthesis routes.

Another consideration is the range of specific surface areas and total number of nVVs provided by the various morphologies of CaP particles. As previously mentioned, spherical CaP-NPs provide a four-fold increase in specific surface area and eight-fold increase in total particle number when particle diameter is halved. Using Equations 1.1 and 1.2, the surface area to volume ratio for a spherical particle is calculated as 3/r. In contrast, hexagonal prisms – a common morphology of HAp-NPs – exhibit a surface area to volume ratio of 16/r when base edge and height are equal. This ratio increases as the ratio of base edge to height increases i.e. as a platelet-like morphology is approached and decreases as base edge to height ratio increases i.e. as a rod-like morphology is approached.

From these simple calculations, one could say that platelet-like morphologies offer far more favourable surface area to volume ratios and therefore enhanced nucleic acid binding as compared to rod-like and spherical morphologies. However, specific surface area is not so easily correlated to nucleic binding capacity when considering the multiple planar surfaces of HAp-NPs. Though the hexagonal prism approaches an infinite surface area to volume ratio as its height decreases, the ratio of a(b)-plane to c-plane surface area also decreases, hence the nucleic acid binding capacity is reduced as a platelet shape is approached. The popularity of HAp-NPs with rod-like hexagonal prism morphologies in the literature can therefore be attributed to the vast majority of particle surface area being available for DNA- or RNA-adsorption.

1.2.3 Crystal Structure

It is apparent in the literature that the impact of DNA/RNA-CaP-NP crystal structure on transfection efficacy is less well studied than that of particle size and morphology. From one perspective, this lack of a defined relationship between DNA/RNA-CaP-NP crystal structure and transfection efficacy could be due to complexities in obtaining suitable particle samples for comparison. Synthesising particle samples with similar sizes and morphologies but with different crystal structures is inherently difficult given the interrelation of these properties, where crystal structure influences nucleation and growth rate (and therefore particle size), as well as morphology. Therefore, one cannot easily correlate crystal structure as the only physicochemical property impacting transfection efficacy.

Nucleic acid binding capacity describes the maximum number of nucleic acids that can be adsorbed onto a nVV, where a larger binding capacity means a larger nucleic acid payload mass per nVV. For surface-adsorption, nucleic acid binding capacity is assumed to change with particle crystal structure due to differences in surface charge. In the case of CaP-NPs of different crystallinity, surface charge will vary due to differing Ca^{2+}:$H_xPO_4^{x-3}$ ratios and the organisation of these ions in lattice planes. For example, HAp has the formula $Ca_5(PO_4)_3OH$, an ionic ratio of approximately 1.67, and has a hexagonal crystal system. Like all CaP species, HAp-NPs maintain electroneutrality and therefore have a net-neutral charge, but their crystal structures develop planes of non-zero net charge. HAp-NPs therefore boast surfaces with ionic constituents formed predominantly of either Ca^{2+} or PO_4^{3-} with net-positive or net-negative charges respectively that are electrically shielded in solution by an electrical double layer (EDL). The c-plane of HAp is negatively charged since there are more PO_4^{3-} than Ca^{2+} ions, and the a(b)-plane is positively charged since there are more Ca^{2+} than PO_4^{3-} ions. Nucleic acids can therefore be readily adsorbed onto the a(b)-plane of HAp-NPs (Bose and Tarafder, 2012), whilst nucleic adsorption on the negatively charged c-plane requires intermediary surface functionalisation, such as with arginine (Bakan et al., 2017).

The surface area of a(b)-planes of HAp particles can often greatly exceed that of the c-plane using specific synthesis parameters. For example, synthesising HAp in the presence of organic modifiers such as fatty acids can force growth to occur at the c-plane, resulting in rod- or needle-like morphologies; as shown by Lett et al. (2019). The combination of a high Ca^{2+} content, and the potential for a large a(b)-plane to c-plane surface area ratio, affords HAp particles with a large nucleic acid binding capacity, which further explains why HAp particles are the most popular CaP species in gene therapy research (Bakan, 2018).

CaP particle crystal structure, as with size, is closely linked to solubility and stability in extracellular and intracellular environments. For solution-based gene therapy, nVVs must be stable in extracellular environments. Specifically, nucleic acids must be protected against nuclease degradation, particles must not agglomerate or grow beyond a size where cellular infiltration is no longer possible, and particles must not dissolve extracellularly to prematurely release the nucleic acid payload. nVVs must also have a suitable intracellular degradation/dissolution profile within the endosome to grant endosomal escape of the nucleic acid cargo and subsequent delivery to the nucleus (or ribosome in the case of RNA). The crystal structure of the CaP particle must therefore contribute to a balance between extracellular and intracellular stability and solubility.

HAp particles are known to dissolve in the acidic conditions of the endosome (pH 4.5 – 6.5) (Zhang and Ryan (1999) but are also prone to unwanted growth in extracellular solution due to the extremely low enthalpy of formation and solubility of HAp (pKsp = 58.9) (Mcdowell et al., 1977). Theoretically, this is exacerbated by the availability of Ca^{2+} and $H_xPO_4^{x-3}$ ions in bodily fluids. HAp particles are therefore often prepared as multi-shelled nVVs (Bakan, 2018), with one or more shells of nucleic acids or biopolymers, one or more shells of HAp, and an outermost shell of nucleic acid or biopolymer. The nucleic acid or biopolymer outermost shell helps to prevent the accumulation of ions from solution that would lead to unwanted growth, whilst HAp shells act as both adsorption or loading sites for nucleic acids and protect inner nucleic acid shells from nuclease degradation.

Other CaP species such as amorphous CaP (ACP) (formula of $Ca_xH_y(PO_4)_z.nH_2O$), dicalcium phosphate (DCP) (formula of $CaHPO_4$), are each less stable than HAp with regards to solubility due to their lower pKsp values (Chow and Eanes, 2001). Only octacalcium phosphate (OCP) (formula of $Ca_8H_2(PO_4)_6.5H_2O$) has a pKsp greater than that of HAp, but this phase is metastable and hydrolyses to more stable CaP phases. The popularity of HAp-NPs in solution-based gene therapy is therefore also a consequence of the excellent resistance to dissolution in extracellular environments but ability to dissolve intracellularly. However, is sometimes the case that less stable CaP phases are sought in non-solution-based gene therapy, as is the case for surface mediated transfection where dissolution or transformation processes are required to release nucleic acid payloads (Oyane et al., 2012).

1.3 Synthesis of DNA/RNA-CaP-NPs

Commercial CaP transfection kits are useful in rapidly synthesising DNA/RNA-CaP-NPs with the user's chosen DNA/RNA, without the need for complex apparatus or equipment. These kits most often use the two-step co-precipitation method, whereby a chosen DNA/RNA is mixed with a $CaCl_2$ solution, then a $H_xPO_y^{x-3}$-containing salt is mixed into the $CaCl_2$-nucleic acid solution. The intention here is to adsorb Ca^{2+} ions onto the phosphate backbone of the DNA/RNA, with the resulting complexes acting as nucleation centres for CaP. Depending on the ratio between salt and DNA/RNA concentration, DNA/RNAs could also be adsorbed onto CaP surfaces either during or post-growth, resulting in a heterogeneous population of DNA/RNA-CaP-NPs with different shell architectures. For example, a high ratio of DNA to salt will theoretically result in the encapsulation and adsorption of DNA, whilst lower ratios of DNA to salt ultimately reduce the probability of adsorption on particle surfaces if DNA molecules are preferentially employed as nucleation centres.

Despite the simple preparation of DNA/RNA-CaP-NPs, transfection efficacies vary between studies using commercial CaP transfection kits and can require optimisation for a specific cell line (Guo et al., 2017). This is theorised to be due to the lack of consistency in experimental conditions between users and studies, such as slight differences in pH, temperature and mixing conditions, where mixing conditions refers to the rate of reactant mixing in different methods (titration, magnetic stirring, pipetting). Furthermore, impurities in the salt solutions can act as CaP nucleation centres, hence increasing the total number of nucleation centres and reducing the encapsulation efficiency of DNA or RNA. The compound effect of variation in these thermodynamic and kinetic conditions will result in different nucleation and growth rates between experiments, leading to the synthesis of CaP particles with different sizes, morphologies, and stability *in-vitro*, thereby producing a range of transfection efficacies. As an alternative to commercial kits, there is a wide range of synthesis routes that allow for greater control over several DNA/RNA-CaP-NP physicochemical properties (Sadat-Shojai et al., 2013) and many utilise standard laboratory equipment and consumables.

The precipitation method is closely related to the co-precipitation approach employed by commercial kits, but they are distinguished by the way in which DNA/RNA is coupled to the CaP particle. In the precipitation method, CaP-NPs are synthesised in the absence of RNA/DNA to form a suspension, to which a DNA/RNA solution is added to surface functionalise the particles with DNA/RNA. This method has the advantage of allowing the user to optimise CaP particle size independently of DNA/RNA; especially useful when a DNA/RNA sample is in short supply or if

experimental conditions would damage the DNA/RNA. As discussed earlier, the DNA/RNA shell offers a stabilising effect by inhibiting further growth or agglomeration of particles but makes DNA/RNA susceptible to nuclease degradation *in-vitro*. Multi-shell DNA/RNA-CaP-NPs negate this issue and are constructed by simply adding alternating solutions of salts and DNA/RNA to build up additional layers. Sokolova et al. (2006) utilised this approach to synthesise "single-shell", "double-shell" and "triple-shell" DNA-CaP-NPs, with outer shells of DNA, CaP and DNA respectively. Sokolova et al. (2006) found all these CaP-NPs species had greater transfection efficacy toward HeLa and human umbilical vein endothelial cells (HUVEC) than the standard calcium coprecipitation method, but lower transfection efficacy than Polyfect®; a commercially available dendrimer-based transfection agent/kit. Similarly, Kovtun et al. (2009) found triple-shell DNA-CaP particles had greater transfection efficacy than DNA-CaP particles synthesised using the co-precipitation method and similar efficacy to Polyfect® when transfecting HUVEC cells.

Besides precipitation and co-precipitation, there are a wide range of wet-chemical synthesis approaches for DNA/RNA-CaP-NPs that can either encapsulate nucleic acids, adsorb them onto surfaces, or use a combination of both. If encapsulating nucleic acids, reaction parameters must of course leave the nucleic acids intact and undamaged and must therefore be of suitable temperature, pH, pressure, and limit shear stresses during mixing. The microemulsion approach utilises water and oil phase separations that form micelles that act as nanoscale reactors or templates in which reactants are mixed under highly controlled nucleation and growth conditions and rarely grow larger than the micelle itself (López-Quintela et al., 2004). NPs are also provided with good steric stabilisation following synthesis via the microemulsion approach due to the physical separation of neighbouring particles (Malik et al., 2012). Cao et al. (2011) utilised the microemulsion approach to synthesise plasmid DNA (pDNA) -loaded CaP-NPs (pDNA-CaP-NPs) and successfully transfected Sprague-Dawley rat bone marrow stem cells (BMSCs). Transmission electron microscope (TEM) images from (Cao et al.) demonstrated their pDNA-CaP-NPs were considerably smaller than those produced using a commercial kit, in addition to having greater cellular uptake and transfection efficacy. Bisht et al. (2005) also synthesised pDNA-CaP-NPs via the microemulsion approach. Measuring between 30 – 40 nm in some samples, these particles were able to transfect HeLa cells with a transfection efficacy comparable to Polyfect®. Of course, the microemulsion approach can be used to simply fabricate CaP-NPs, which can then be extracted and mixed with nucleic acids for surface-adsorption - rather than encapsulation – of nucleic acids.

Arguably the most popular route for CaP-NP synthesis, besides precipitation, is the hydrothermal route. This route is popular for its highly controllable reaction parameters – including temperature and pressure profiles, precursor concentration and reaction time, thus allowing excellent governance of CaP-NP size, morphology and crystal structure (Chuprunov et al., 2020, Ebrahimi et al., 2021). However, the high temperatures and pressures involved prevent the incorporation of DNA/RNA into the reaction mixtures and therefore prevent their encapsulation, requiring post-synthesis mixing to adsorb DNA/RNAs onto CaP-NP surfaces. Flame-spray pyrolysis has also been used to synthesise CaP-NPs for use in tissue engineering or drug/gene delivery applications (Ataol et al., 2015, Tsikourkitoudi et al., 2020). But, similarly to hydrothermal synthesis, the high synthesis temperature far exceeds the stability temperature range of nucleic acids and as such requires post-synthesis surface functionalisation to load CaP-NP surfaces with DNA/RNA.

Electrochemical synthesis describes NP synthesis routes that use an electrical field to induce a change in supersaturation via the transport of ions. Fundamentally, this involves the use of an electrode pair in an electrolyte solution, where an applied potential across the electrodes induces the deposition of the desired species on the recipient electrode, commonly referred to as electrochemical deposition or electroplating. A common example is the use of a copper anode and substrate electrode that are submerged in $CuSO_4$. Here, the copper on the surface of the anode is oxidised, releasing copper ions (Cu^{2+}) into the electrolyte solution, whilst Cu^{2+} ions are reduced at the cathode where a layer of copper is deposited that is equal to the rate of oxidation. This results in a net-transfer of copper from the anode to cathode surfaces. By exchanging the electrolyte and working electrode for other chemical species, one can synthesise and deposit a variety of different materials that include nanoscale inorganic species. For example, 'nanostructured-CaP' was deposited onto titanium disks by Lu et al. (2020) using an aqueous electrolyte of $Ca(NO_3)_2$ and $NH_4H_2PO_4$. It should be noted that nanostructured CaP simply implies a CaP surface with nanotopography since the substrate electrode becomes saturated or 'soiled' with CaP, rather than individual particles.

To avoid soiling the working electrode, Daltin et al. (2019) used sonication-modified electrochemical synthesis (sono-electrochemical) whereby an aqueous electrolyte of $Ca(NO_3)_2$, $NH_4(H_2PO_4)$ and NaOH was used to deposit CaP-NPs onto a substrate electrode. In this case, sonication avoids the 'soiling' of the working electrode by kinetically ejecting CaP-NPs from the electrode surface into the electrolyte. Electrochemical synthesis of CaP-NPs is uncommon in the literature due to the soiling of the working electrode, hence most electrodeposition of CaP

focuses on the electrophoretic deposition of CaP-NPs post-synthesis onto implant materials to enhance their bioactivity *in-vivo* (Wei et al., 2005, Geuli et al., 2016).

The sol-gel approach is a form of template synthesis, in which precursors and solvents are first mixed, then processed to form a 'sol' of colloidal structures. A gel subsequently forms in the mixture and hence phase separation occurs between the sol and gel. The gel can then be processed via supercritical, thermal, or freeze drying to form an aerogel, xerogel, or cryogel respectively. Singh et al. (2014) utilised the sol-gel approach to synthesise CaP-based NPs that were subsequently surface functionalised with alendronate for bone tissue engineering applications. Meanwhile, Dordelmann et al. (2014) co-precipitated CaP with poly(D,L-lactide-co-glycolide acid) (PLGA) and either DNA or small interfering RNA (siRNA), forming DNA/RNA-encapsulated CaP/PLGA-NPs that successfully infiltrated HeLa cells.

1.3.1 Crystallisation in Confinement

A particularly unique inorganic branch of NP synthesis is crystallisation in confinement, where confinement – according to Meldrum and O'Shaughnessy (2020) - refers to an environment that changes the kinetics or thermodynamics of crystallisation by restricting the dimensions of a system in one, two or three dimensions. Mediums demonstrating different pore volumes, shapes and interconnectivities have been used for crystallisation in confinement, including droplets (Reiner et al., 2023), hydrogels (Liu et al., 2022) and porous glass (Cantaert et al., 2013). Microfluidic systems can also utilise crystallisation in confinement given reactant mixing takes place in volumes below the microscale. As described in detail by Meldrum and O'Shaughnessy (2020), crystallisation in the pores of these confining environments influence several crystal properties, including size and morphology. Furthermore, nucleation rates within confining environments are theorised to be drastically lower than that of bulk solutions due to a lack of impurities required for heterogeneous nucleation, as well as the rapid depletion of ions and supersaturation as crystallites grow within comparatively sized pores. And, as precipitates grow within pores, there is a rapid depletion of ions that subsequently reduces supersaturation. Confining volumes, especially in the micro- and nanoscale, therefore have the capacity to modulate nucleation and growth rate to influence crystallite and precipitate size. One could therefore use pore size as a template material to modulate the size and crystal structure of particles.

Cantaert et al. (2013) fabricated a U-tube shaped double-diffusion apparatus to demonstrate the effects of confinement on the crystallisation of CaP particles. In their work, a track-etched membrane with pore diameters of 50 and 200 nm was used to separate solutions of 4.5 mM $CaCl_2$ and 2.1 mM K_2HPO_4 solutions, each with 25 mM Tris-HCl and adjusted to pH 7.4. Analysis with TEM after 3- to 6-hours of diffusion at 37 °c showed rod-like CaP particles that were either partially or fully amorphous in structure with diameters reflective of their confining pore size. These CaP particles grew to micron-sized polycrystalline rods after 1-day. Pore-size and shape was therefore shown to dictate particle size and morphology respectively.

1.3.1.1 Hydrogels for Crystallisation in Confinement

Track-etched membranes offer great control over pore diameter and therefore particle size, but their 2D top-down fabrication prevents the formation of an interconnected porous network, which would be particularly interesting for bone tissue engineering applications. In contrast, hydrogels offer a highly interconnected 3D porous matrix with tuneable pore sizes in the micro- and nanoscale and modifiable surface chemistries (Annabi et al., 2010). This makes them excellent candidates for the synthesis of micro- or nanomaterials, such as CaP-NPs, via the crystallisation in confinement phenomena. Furthermore, hydrogels are highly sought-after materials in the field of tissue engineering given they can often mimic the extracellular matrix of a variety of tissue types and their surfaces can often be functionalised, such as for enhanced cell attachment (El-Sherbiny and Yacoub, 2013).

Though its primary use in research laboratories is for gel electrophoresis, agarose is a hydrogel that has been used in tissue engineering research for some time (Zarrintaj et al., 2018). And, since agarose fibres provide an abundance of surfaces and pores for precipitation to occur (Duffus et al., 2009, Li et al., 2009, Kwak et al., 2021), crystallisation in confinement effects could be utilised to morph agarose hydrogels into a bone tissue engineering materials and/or synthesise DNA/RNA-CaP-NPs.

1.3.1.2 Agarose for Crystallisation in Confinement

Three approaches have been used in the literature for the precipitation of inorganics nanomaterials within agarose matrices. The simplest approach is to prepare a single molten agarose and salt solution that spontaneously precipitates inorganic NPs on or around agarose

fibres when cooled below the gelation temperature (Tian et al., 2013, Wang et al., 2013, Tran, 2016, Shin et al., 2022a). This occurs due to the constant precursor concentration but with a supersaturation toward an inorganic species that increases with decreasing temperature, followed either by precipitation on agarose fibres as they spontaneously precipitate at the gelation temperature.

The second approach is alternate soaking that involves the sequential and repeated submergence of a buffered agarose gel in different solutions, such as in $CaCl_2$ and Na_2HPO_4 to precipitate HAp (Tabata et al., 2003, Tabata et al., 2005). Since the submergence time, number of repetitions and precursor concentrations determine the rate of diffusion of ions into the agarose matrix, these parameters can be modulated to control supersaturation. The alternate soaking approach is therefore distinct from the simulated body fluid (SBF) approach that induces HAp formation on hydrogel surfaces by submerging the material in a single SBF solution for longer periods of time (due to lower concentrations of Ca^{2+} and phosphate ions ($H_xPO_4^{x-3}$).

The third technique is the agarose gel double-diffusion (AGDD) approach, where ions diffuse from either side of an agarose hydrogel that separates opposing reservoirs of precursor salt solutions. Here, supersaturation is achieved following ion migration from both sides of the gel. Precipitation therefore occurs at a point in the gel where ion bands overlap and reach supersaturation conditions. This process is dependent on the relative diffusivity of ions, where rapidly diffusing ions theoretically reduce the time till precipitation and dissimilar counter-ion diffusion constants shift the zone of precipitation toward the inlet of the less mobile ion.

1.3.1.3 Agarose Membrane Double-Diffusion

Xue and Zhang (2019) performed the AGDD approach using a device manufactured in-house in which an agarose gel separated reservoirs of 0.5 M $MnSo_4$ and 0.6 M NaOH to synthesise porous Mn_3O_4 NPs. They found that NP diameter decreased with increasing agarose wt %, from 30 - 150 nm at 1 wt % agarose to 20 - 30 nm at 2.5 wt %, concluding that this size reduction owes to the smaller agarose pore size in the higher wt % gel. Xue and Zhang (2019) also theorise the crystallinity of their Mn_3O_4 NP samples diminish as agarose wt % increases, as indicated by broader, less defined x-ray diffraction (XRD) peaks. This may also be due to a dwindling crystallite size with diminished XRD peak intensity that fails to rise above the amorphous signals produced by agarose.

Only a small number of studies have exploited the AGDD approach to synthesise CaP particles. Previous to the study by Cantaert et al. (2013), Hunter and Goldberg (1993) grew HAp-NPs using a 2 wt % agarose gel consisting of 150 mM NaCl, 0.01 wt% NaN_3, and 10 mM Tris-HCl (pH 7.4) to separate $CaCl_2$ and Na_2HPO_4. Note that $CaCl_2$ and Na_2HPO_4 had equal concentrations of either 5.5 or 7.5 mM. These solutions were continually pumped along opposite ends of the gel without recycling to maintain constant concentrations either side of the agarose gel. They found a minimum 7.5 mM of $CaCl_2$ and Na_2HPO_4 was required to induce the precipitation of a CaP band over a period of 5-days, as indicated by no visual precipitation or change in ion concentration within the gel. Interestingly, CaP could be precipitated below this concentration threshold at 5.5 mM $CaCl_2$ and Na_2HPO_4 when bone sialoprotein was positioned in the agarose gel, indicating a protein-dependent nucleation and growth (biomineralisation) process occurs under these conditions. They also noted that powder XRD analysis showed that CaP precipitated at 7.5 mM $CaCl_2$ and Na_2HPO_4 was HAp. This differs from the ACP synthesised by Cantaert et al. (2013) after a reaction time of 3-6 hours. This difference in crystal structure likely arose from Hunter and Goldberg (1993) analysing samples 5-days after the reaction began, allowing metastable ACP to transform to HAp in solution. Furthermore, it is likely that the 3D agarose matrix exposes internalised particles to solution on all sides and hence accelerates transformation processes compared to particles in 2D pores of porous glass.

1.3.1.4 Agarose Gel Electrophoresis Approaches

The AGDD approach can be modified using electric fields to create the approach named in this work as ‘particle synthesis via double-well agarose gel electrophoresis approach’ or PS-DW-AGE, which - to this author’s knowledge – has been used to synthesise CaP particles by a relatively small number of researchers. Although similar in experimental setup to the AGDD approach, the PS-DW-AGE approach significantly enhances ion transport via an electric field that applies an electrophoretic driving force to all ions.

Watanabe and Akashi (2006) were the first group to demonstrate the utility of this technique. They cast a 3 wt % agarose gel to separate 40 mM $CaCl_2$ and 40mM Na_2HPO_4 solution reservoirs placed at opposing ends of a horizontal electrophoresis tank. The gel comprised of 10 mM Tris-HCl, pH 4.8, whilst the salt solutions were adjusted to pH 7.4 with Tris-HCl. After applying 100 V potential for 30-minutes, a 2 cm thick white band appeared in the gel. After submerging the gel in ultrapure water for an undisclosed time to remove excess ions, lyophilised gel samples were

imaged via scanning electron microscopy (SEM). They found 1 µm HAp particles had precipitated in the centre of the gel slab and attributed the zone of precipitation's central position between reservoirs to a pH gradient formed by the electrophoresis process. More specifically, they suggest precipitation occurred in the portion of the gel with neutral pH.

As with Cantaert et al. (2013), it is possible that Watanabe and Akashi (2006) initially synthesised ACP particles that transitioned to HAp when submerged in water. The same group later combined the PS-DW-AGE approach with the alternate soaking method, with the resulting HAp/agarose composite demonstrating potential for bone regeneration (Watanabe and Akashi, 2006, Watanabe et al., 2007). However, no investigation into the control of particle properties via the modulation of experimental parameters was attempted. Furthermore, CaP particles were not characterised prior to submersion in ultrapure water, hence their initial size, morphology, and crystal structure remain unknown.

Kamitakahara et al. (2007) modified the PS-DW-AGE approach by Watanabe and Akashi (2006) by using the conventional agarose gel slab for nucleic acid characterisation, adding small volumes of salt solutions to gel wells. The salt solution volume is reduced to the µL range, down from the estimated 100 mL range required by Watanabe and Akashi (2006) to fill reservoirs at either end of the electrophoresis tank. Kamitakahara et al. (2007) used a 1 wt % agarose gel with a 40 mM Tris buffer adjusted to pH 8 with acetic acid, along with 40 µL of 20 mM $CaCl_2$ and 12 mM Na_2HPO_4 loading solutions loaded into wells 48 mm apart.

A white precipitate appeared between the wells after 11-minutes of applying a 100 V potential, which grew in intensity after longer periods but disappeared after 45-minutes. Gel slices containing white precipitate were removed after 20-minutes and soaked in ultrapure water for 3-days. Following lyophilisation, Kamitakahara et al. (2007) used SEM analysis to find 500 nm spinous particles; the first characterisation of electrophoretically synthesised CaP particles without submersion in ultrapure water. XRD analysis of these particles showed poorly defined peaks, postulated to be either due to the amorphous agarose background, small HAp crystals, or a dominant ACP phase. After heat treatment of samples at 600 °c for 1-hour, peaks characteristic of HAp could be identified in XRD spectra. In a later study, the same group later reduced particle size ranging from 500 - 600 nm in a 1 wt % agarose gel, and to between 300 - 400 nm in a 3 wt % agarose gel (Kamitakahara et al., 2012). Furthermore, they established that precipitation occurs at an applied potential of 50 V when the run time is increased from 12- to 23-minutes. This demonstrates that there is a minimum volt-minute threshold for precipitation to occur; below which counterions are not transported sufficient distances to collide with one

another and diffuse to concentrations insufficient for supersaturation toward CaP to be achieved.

From the same group, Kimura et al. (2018) used the PS-DW-AGE approach to identify changes in CaP particle properties with reaction time. Spherical particles with diameters below 100 nm appeared after 3-minutes of an applied potential which increased in diameter with time: reaching between 200 – 400 nm after 12-minutes. XRD of samples at all time points, in addition to a selected area electron diffraction (SAED) pattern at 12-minutes indicated an amorphous structure. After being submerged in water, samples gradually demonstrated diffraction peaks indicative of HAp that increased in intensity with time up to the final time point of 3-days, suggesting a transformation from ACP to HAp. The apparent crystallographic change was upheld by significant particle morphological changes following submergence in water, where spherical particles transitioned to flowered, needle particles after 3-days and even demonstrated morphological changes after only 30-minutes.

As with Xue and Zhang (2019), Kimura et al. (2018) observed an inverse relationship between agarose wt % and particle diameter. Based on this author's estimates from their published figures, particles were reduced to between 100 – 300 nm for 6 wt % gels. Kimura et al. (2018) also found particle diameters decrease with increasing pH, measuring between 30 – 250 nm and 40 – 150 nm for pH 9 and 10 buffers respectively (based on estimates from their published figures). They also noted that the submersion of all samples resulted in the transformation of spherical ACP particles to spinous HAp particles, which they theorised to result from the dissolution of the metastable ACP phase that released sufficient ions into the surrounding solution to induce a supersaturation toward HAp.

Table 1.1 summarises the properties of CaP particles synthesised via the PS-DW-AGE approach. Results from these authors indicate that the PS-DW-AGE approach is capable of producing spherical ACP particles ranging from 30 – 400 nm, where greater agarose wt % or pH decrease the average particle diameter. All studies indicated that ACP spherical particles were metastable, transforming to spinous HAp particles with diameters between 300 – 1000 nm when submerged in ultrapure water. Detailed explanations for CaP particle crystallographic and morphological changes in agarose gels of different thicknesses and varied Ca^{2+} to $H_xPO_4^{x-3}$ ratios are available from double diffusion models (Shin et al., 2022b). However, the applicability of these crystallisation theories for the PS-DW-AGE approach is debatable since ion transport is dominated by migration under the electric field and not by diffusion.

Table 1.1. CaP particle properties from studies using the PS-DW-AGE approach.

Study Authors	Agarose (wt %)	pH	Voltage (V)	Time (minutes)	$CaCl_2$ (mM)	Na_2HPO_4 (mM)	CaP Particles	
							Phase	Diameter (nm)
Watanabe and Akashi (2006)	3	8	100	30	40	40	HAp **	~1000 **
Kamitakahara et al. (2007)	1	8	100	20	20	12	HAP #	500 **
Kamitakahara et al. (2012)	1	8	100	15	200	120	HAp **	500 - 600 **
		8	100	15	200	120	HAp **	500 - 600 **
	3	8	50	23	200	120	HAp **	300 - 400 **
Kimura et al. (2018)	1	8	100	12	200	120	ACP	200 – 400
							HAP **	~500 * **
		9					ACP	30 - 250 *
							HAP **	~500 * **
		10					ACP	40 - 150 *
							HAP **	~500 * **
	3	8					ACP	50 - 200 *
							HAP **	~500 * **
	6	8					ACP	100 - 300 *
							HAP **	~500 * **

** Estimated based on published figures*
*** After submersion in ultrapure water and freeze-drying*
 # After submersion in ultrapure water, freeze-drying and heat treatment

1.3.2 PS-DW-AGE for Gene Therapy

Based on the previously discussed studies using AGDD or PS-DW-AGE, there is great potential to direct the synthesis of CaP particles within agarose gels toward gene therapy applications. For example, using DNA or plasmid-DNA (pDNA) would allow for the encapsulation or adsorption of nucleic acids into/onto CaP surfaces within the agarose gel in a similar method to protein-dependent CaP precipitation demonstrated by Hunter and Goldberg (1993). This would allow for the encapsulation or adsorption of nucleic acids into/onto CaP within the agarose gel and form a gene-activated matrix (GAM). This could be modified further with an applied potential using a PS-DW-AGE approach, allowing GAM fabrication to occur more rapidly.

Particle size could be modulated through adjustment of several experimental parameters, including: agarose wt %, pH, temperature, and applied potential, to optimise particle properties for gene therapy applications. Given the generally preferred use of CaP-NPs i.e. sub-100 nm particles in gene therapy (Bakan, 2018), the ability to reduce particle size via numerous experimental parameters in the PS-DW-AGE approach is highly beneficial. GAMs fabricated via

the PS-DW-AGE approach would ultimately require lyophilisation to transform pore size from the nano- to microscale, thereby allowing cellular infiltration. This would prove favourable in stabilising ACP phases contained within the gel prior to *in-vitro* or *in-vivo* use.

It is interesting to consider the stability of ACP particles in gene therapy. They are not commonly used to deliver payloads to cells due to their metastability, so one would be forgiven in thinking their utility in gene therapy is lacking. However, metastable CaP phases are sought where surface-mediated transfection is desired. Hence GAMs containing DNA- or pDNA-loaded ACP particles could be remodelled *in-vitro* and therefore release ions and their nucleic acid payload into the surrounding microenvironment. Precipitation of DNA- or pDNA-loaded HAp may then occur in solution *in-vitro*; forming secondary particles. Secondary particles may precipitate with stable HAp phases given that the confining effects of the matrix would become much weaker in the microscale environment of the cryogel after agarose lyophilisation. Furthermore, these secondary particles would be mobile in solution – unlike primary ACP particles that would probably be dried onto agarose surfaces during lyophilisation – and therefore be available to infiltrate cells.

1.3.2.1 Particle Synthesis via Single-well Agarose Gel Electrophoresis

A modified approach of the PS-DW-AGE that uses a single-well in place of a double-well was previously developed by our group - Feichtinger et al. (2019) - and is herein termed the particle synthesis via single-well agarose gel electrophoresis (PS-SW-AGE) approach. This method was developed for the synthesis of pDNA-loaded CaP (pDNA/CaP) particles in agarose cryogels as potential osteogenic GAMs. The PS-SW-AGE approach utilises a gel slab in a conventional horizontal electrophoresis tank and is analogous to that of Kimura et al. (2018), but requires one well per precipitate layer instead of two since $H_xPO_4^{x-3}$ ions are contained within the buffer and gel. The pDNA/CaP GAMs produced via this approach have also been functionalised with fibronectin bovine protein (FBN) post-lyophilisation to enhance cellular attachment to the cryogel. Thus far, the transfection efficacy of these GAMs hint at their potential use as osteogenic GAMs for bone tissue engineering applications.

An overview of the loading protocol for the PS-SW-AGE approach is shown in Figure 1.1. In this previous work by Feichtinger et al. (2019), a 1 wt % agarose gel (NuSieve™, Lonza Group AG, Basel, Switzerland) containing 0.75 mM Na_2HPO_4 and 25 mM HEPES buffer with pH 7.4 was cast with separated rows of wells. pDNA is loaded into the gel as one of two solutions. Solution one

was a pDNA loading solution comprised of 5 µg reporter pDNA (plasmid encoded with the luciferase gene) and 5 wt % glycerol. Solution two contained the same components as solution one, but with the addition of 10 µg of FBN. After the pDNA solutions were loaded into separate wells for solutions 1 and 2, a 60 V potential was applied to load pDNA and FBN into the gel. After 6-minutes, the potential was removed and $CaCl_2$ loading solutions comprised of various $CaCl_2$ concentration and 5 wt % glycerol were added to the wells. Electric field polarity was then reversed, and a 60 V potential was applied for a further 6-minutes. After 2 - 3 minutes, white precipitates begin to appear adjacent to the wells. Generally, these precipitate layers appear more intense in the presence of pDNA, and even more intense in the presence of pDNA and FBN.

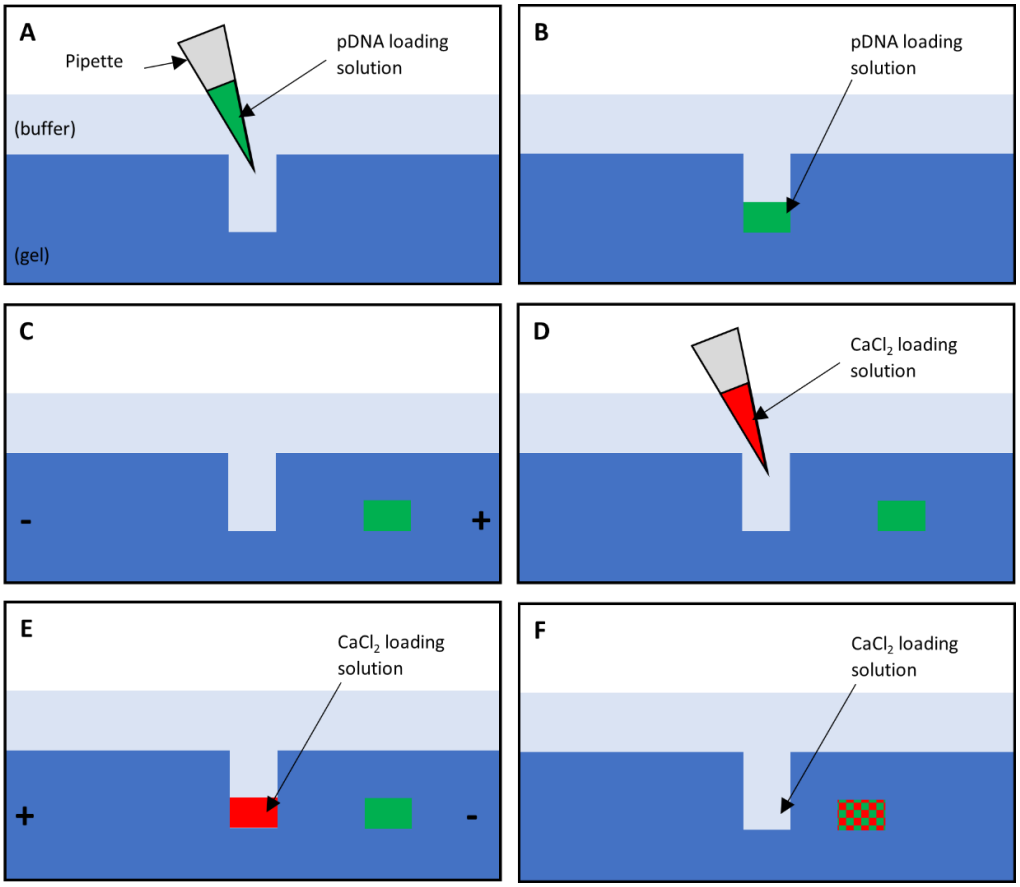


Figure 1.1. Overview of the PS-SW-AGE approach loading regime. (A) 25 µL of pDNA loading solution is pipetted into well; (B) pDNA loading solution settles at the bottom of the well; (C) a 60 V potential is applied to the gel for 6-minutes, (D) 25 µL of $CaCl_2$ loading solution is pipetted into the well; (E) $CaCl_2$ solution settles at the bottom of the well; (F) electric field polarity is reversed and a 60 V potential is applied for 6-minutes.

A typical example of pDNA/CaP layers (without FBN) are shown in Figure 1.2, where layers measure between 1.5 – 2 mm in thickness. Though the pDNA/CaP layer is relatively thin, the synthesis of discrete mineralised layers could prove useful in osteogenic tissue engineering applications where a layered scaffold architecture is required, such as for osteochondral tissue regeneration.

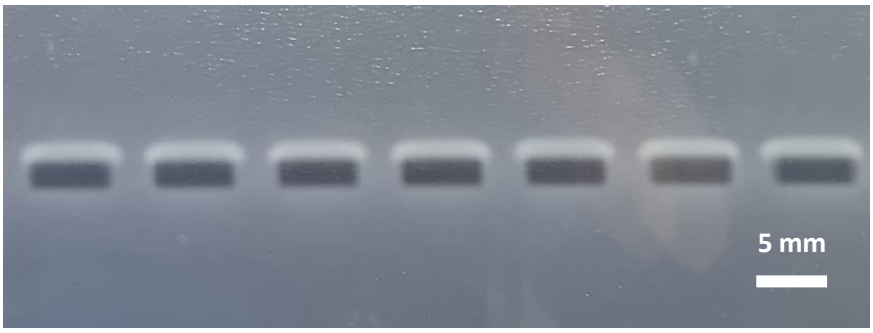


Figure 1.2. Typical examples of pDNA/CaP layers (without FBN) produced via PS-SW-AGE.

Gels containing CaP precipitate layers were extracted using a scalpel, then lyophilised, followed by sterilisation in 70 % ethanol (EtOH), and lyophilised again to produce a (sterilised) macroporous GAM. As shown in Figure 1.3, SEM analysis of the GAM revealed spherical particles ranging from 200 – 400 nm via backscattered electron (BSE) detection. However, detailed characterisation of particles was not conducted.

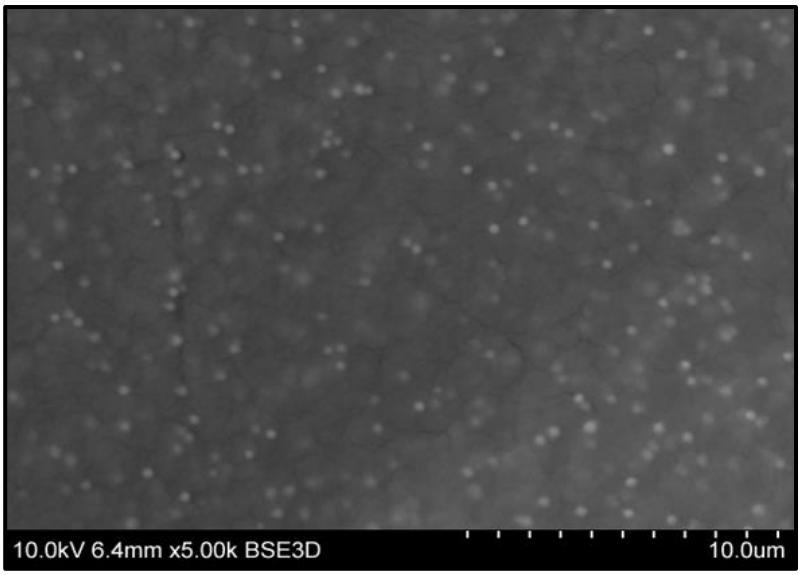


Figure 1.3. SEM image of CaP particles embedded in the surface of a lyophilised GAM.

A study was carried out to investigate the effect of FBN and various Ca^{2+}:H_xPO_4 ratios on the transfection efficacy of pDNA/CaP GAMs on C2C12 cells. Ca^{2+}:H_xPO_4 ratios of 0 (no $CaCl_2$), 83.3, 120.37, 157.41, and 166.67 were used, each with and without FBN to form a total of 10 groups. Following synthesis, extraction, lyophilisation, sterilisation, and further lyophilisation, 5 x 10^4 C2C12 cells were cultured on each GAM and luciferase luminescence assays were performed at 24-hour, 48-hour, 7-day and 4-week time points. Luminescence measurements for each group were calibrated against a negative control, hence all measurements are 'fold luminescence over negative control'. Note that the negative control refers to a pDNA-loaded cryogel.

As shown in Figure 1.4, the pDNA/CaP GAM with an ionic ratio of ~167 showed the greatest luciferase activity at 48-hours, whilst at 7-days the pDNA/CaP GAM with an ionic ratio of ~120 was greatest but showed a large standard error arising from widely distributed values (circled outlier excluded). All FBN-pDNA/CaP GAMs had lower luciferase activity at 48-hours compared to their non-FBN counterparts but exhibited either similar or larger values for all ionic ratios at 7-days. FBN-pDNA/CaP GAMs also demonstrated larger standard errors than pDNA/CaP GAM groups, but this is likely due to smaller group sizes. The FBN-pDNA/CaP GAMs synthesised using an ionic ratio of ~167 showed the greatest luciferase activity at 7-days of all groups in the study.

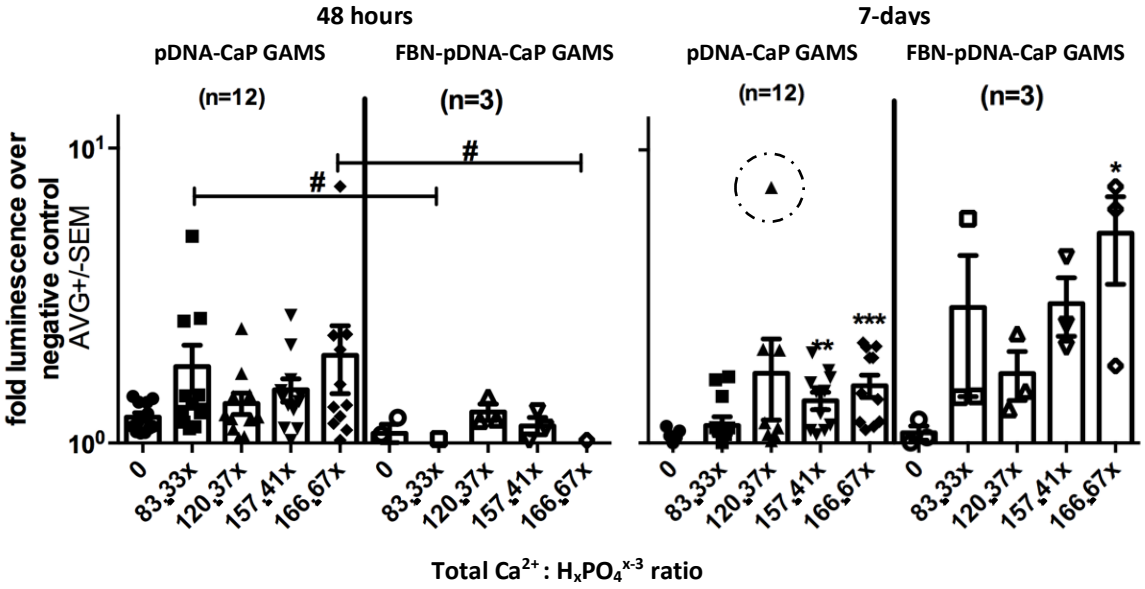


Figure 1.4. Luciferase activity for pDNA/CaP GAM groups produced via the PS-SW-AGE approach with varied Ca^{2+}:$H_xPO_4^{x-3}$ ratios and with or without FBN. Luciferase activity is measured as fold luminescence over negative control. Data given as mean (± standard error).

Dunn's multiple comparisons test (nonparametric). # or * $p \leq 0.05$, ** $p \leq 0.01$, *** $p \leq 0.001$. Compared to negative control in each group.

It should be noted that the Ca^{2+}:$H_xPO_4^{x-3}$ ionic ratios are calculated using the assumption that the precipitation layer occupies a 45 µL volume, from which the number of moles of $H_xPO_4^{x-3}$ ions is calculated. For the ionic ratio of ~167, then, 225 mM $CaCl_2$ is required. However, when considering the ionic ratio based purely on initial concentration of ions, this ionic ratio is 300.

Regardless of ionic ratio calculation, these results indicate that FBN-pDNA/CaP GAMs synthesised using 225 mM $CaCl_2$ (ionic ratio of ~167) boast the greatest luciferase activity of all groups at 7-days. This is theorised to be due to the enhanced cell attachment afforded by FBN, given that cell attachment in the pDNA/CaP GAMs will be poor given agarose itself boasts no cell attachment motifs and CaP surfaces will occupy a minority of the internal GAM surface. FBN may also modify the biomineralisation process during synthesis, since the mass of biomolecules in FBN groups is three times greater than those without FBN. This could have a complex influence on the nucleation and growth of pDNA/CaP particles since there are more biomolecules to act as nucleation centres. Particle sizes may therefore be reduced in FBN-pDNA/CaP GAMs which would accelerate dissolution/transformation processes that are beneficial for surface-mediated transfection.

Unfortunately, given that FBN is electrophoretically loaded into the gel, each gel slice will not exhibit a uniform distribution of FBN. Though this is also the case for pDNA/CaP particles, the primary function of FBN is to enhance cell attachment and should therefore coat all agarose surfaces such that cell infiltration and attachment can occur at all GAM surfaces.

1.3.2.2 Alternative Particle Species

Interestingly, the $CaCl_2$ salt used in the PS-SW-AGE approach could be exchanged for other chloride salts such as $CoCl_2$, $MnCl_2$ and $MgCl_2$ - to name but a few - to precipitate a wide variety of phosphate particles. Magnesium phosphate (MgP) could be added alongside CaP, given Mg^{2+} ions have been shown to stem CaP mineralisation through disruption of the crystal lattices during growth (Landi et al., 2008) and therefore aid in controlling secondary particle nucleation and growth. Ultimately, any nVV with charged constituents can be synthesised using the PS-SW-AGE approach, provided the isoelectric point of constituents are not 0 at the buffer pH and they are able to pass through the nanoscale agarose pore network.

1.3.2.3 Polydopamine to Enhance Cell Attachment

The ability of FBN to enhance cell attachment of cells has long been known (Kan et al., 1982), but its cost precludes substantial use in enhancing cell attachment for pDNA/CaP GAMs. Furthermore, the electrophoretic loading of FBN theoretically results in a non-homogenous coating of agarose due to the inert agarose surface that would prevent significant adsorption. As an alternative, Polydopamine (PDA) has been used in the literature to coat a variety of biomaterial surfaces for drug delivery and tissue engineering applications (Cheng et al., 2019). PDA is generally formed by placing a commercially available dopamine-HCl powder in alkaline solution for overnight polymerisation, then mixing the PDA solution with the desired material. The polymerisation process results in an abundance of catechol, amine and imine functional groups that can facilitate protein adhesion and cell attachment (Sarkari et al., 2022).

1.3.2.4 Polydopamine-coated Agarose

The polymerisation of dopamine and subsequent coating of PDA onto agarose hydrogel surfaces for enhanced cell adhesion could be achieved via one of three main processes: 1) molten mixing; 2) dip/diffusion mixing; or 3) electrophoretic loading. In molten mixing, alkaline dopamine mixtures are mixed directly with molten hydrogel solutions and polymerise onto agarose during gelation (Su et al., 2021), whilst dip/diffusion mixing is the submersion of a hydrogel in alkaline dopamine mixtures, allowing dopamine to diffuse into the hydrogel and polymerise on surfaces post-gelation (Lee et al., 2009, Dinh et al., 2018). Meanwhile, electrophoretic loading or electrochemical plating of PDA to coat hydrogels is unexplored in the literature but has the potential to be applied to agarose in the same way as FBN in the PS-SW-AGE approach. However, given that electrophoretic loading of PDA would likely be inefficient in coating internal and external surfaces due to its unidirectional transport and short dwell time, this process should be avoided.

1.3.2.5 Molten Mixing Process

Via the molten mixing process, Su et al. (2021) synthesised a PDA-coated 2 wt % agarose gel with PDA concentrations up to 0.2 mg mL^{-1}. They demonstrated increases in cell viability, attachment, proliferation, and migration as PDA concentration increased. Interestingly, increasing PDA

concentration increased the average cryogel pore sizes from ~33 µm for uncoated agarose to ~60 µm for 0.2 mg mL^{-1} PDA. Improved performance may therefore arise (at least in part) due to greater cell penetration afforded by these larger pores, rather than being entirely due to the PDA surface coating. The increased cryogel pore size could be due to a complex disruption of intra- and/or intermolecular hydrogen bonding of agarose molecules or nuclei by ions (Na^+, OH^-), or by PDA molecules themselves during the gelation process. Ultimately, though, is it not known whether PDA modifies agarose pore size during the gelation process, the lyophilisation process, or both. This is a crucial consideration, since the PS-SW-AGE approach takes advantage of the nanoconfining agarose hydrogel pore network to control pDNA/CaP particle size, so a PDA coating via molten mixing could increase hydrogel pore size and therefore increase particle size.

1.3.2.6 Dip/diffusion Process

Coating by the dip/diffusion process simply applies a coating on a fully formed coating on a hydrogel post-gelation. Agarose hydrogel pores would therefore be only marginally reduced, depending on the thickness of the PDA coating. The thickness of the coating depends primarily on PDA concentration and submersion time, with PDA coatings growing up to 50 nm on silicon substrates after 24-hours (Lee et al., 2007). Despite there being no data available within the literature regarding PDA coating thicknesses on agarose hydrogel or cryogel substrates, the tuneable thickness of PDA coatings via concentration and submersion times indicates the dip/diffusion process has a more controllable influence on agarose pore size than molten mixing. What the literature fails to reveal is changes in the swelling behaviour of agarose hydrogels following PDA coating, given the change in surface chemistry of the hydrogel. For instance, a 10 nm PDA coating of internal agarose surfaces could immediately reduce pore diameters from 100 nm to 80 nm. However, a consequence of the PDA coating would be the attraction of charge shielding ions at the surface to form an EDL. The attraction of salt ions into the hydrogel would therefore change its swelling behaviour and hence its pore size. The addition of a PDA coating via the dip/diffusion process therefore has an unknown impact on agarose pore size due to the competing effects of the PDA coating and agarose swelling behaviour.

Regardless of whether a PDA coating increases or reduces agarose hydrogel pore size, ion transport properties will be influenced, as will the supersaturation achievable within individual pores, hence nucleation rate and particle growth will also change. Secondly, PDA coatings are known to modify the CaP biomineralisation process of their substrates due to changes in surface

topography and hydrophilicity (Ku et al., 2010, Murari et al., 2020). Of course, whether PDA enhances or lessens the biomineralization potential of a material ultimately depends on the substrate material itself. In the case of agarose, there is insufficient data available to compare uncoated- and PDA-coated agarose surface topographies and hydrophilicities, but one can assume PDA-coated agarose surfaces are more hydrophilic given their PDA-surfaces comprise of charged functional groups and agarose surfaces are inert.

Besides biomineralisation, PDA coatings have been used to immobilise DNA under certain conditions, most notably at low pH where amine groups are protonated and can therefore bind to DNA phosphate groups (Wang et al., 2015). Besides using acidic conditions, DNA can also be immobilised on PDA surfaces via 'metal-ion bridging', where polyvalent metal ions such as Ca^{2+}, Mn^{2+}, and Ni^{2+} can be adsorbed onto PDA surfaces via non-covalent interactions with PDA quinone groups. Metal ions then subsequently bind to DNA phosphates, immobilising DNA on the PDA surfaces. Since the PS-SW-AGE approach uses a buffer of pH 7.4 with 0.75 mM Na_2HPO_4, a small number of protonated amine groups may be present. Hence the electrophoretic mobility of pDNA may be reduced within a PDA-coated agarose hydrogel. Furthermore, subsequent loading of Ca^{2+} into the gel would facilitate Ca^{2+}-quinone interactions and the formation of an EDL. pDNA molecules could therefore be rapidly adsorbed onto PDA surfaces when the Ca^{2+} ions begin to occupy the EDL on the surfaces of the PDA-coated gel.

pDNA adsorption onto PDA via Ca^{2+}-quinone interactions in the PS-SW-AGE will no doubt be complex and highly dynamic given the influence of the electric field during synthesis. But in any case, pDNAs – whether immobilised on surfaces or free in solution – can still serve as CaP nucleation centres. Of bigger concern is the potential for unbound PDA molecules that could 'mop up' pDNA molecules prior to encapsulation within CaP or their adsorption on to CaP surfaces. Long wash times, as used by Su et al. (2021), must therefore be utilised. But ultimately, any PDA molecules larger than the pore size would be encapsulated within the hydrogel.

1.3.2.7 Summary of Polydopamine-coating Agarose

Both methods of applying a PDA coating to agarose have distinct advantages and disadvantages. However, it is argued that the molten mixing process is the simplest, quickest, and most logical approach to use. Since PDA coating and gelation occur simultaneously, molten mixing theoretically provides the most efficient and uniform coating process. Although PDA is

potentially responsible for increases in agarose hydrogel pore diameters, greater agarose wt % can counter these effects.

1.4 Summary

GAMs containing DNA- or pDNA-loaded CaP particles as nVVs for gene therapy applications can be synthesized using a variety of single- or multi-step synthesis routes. But most methods produce particle dispersions suitable for the transfection of cell monolayers. For 3D tissue engineering scaffolds such as GAMs, synthesising nVVs within the scaffold itself allows one to coat specific areas of the scaffold with the desired nVV. AGDD was first used decades ago to synthesise CaP within agarose hydrogels and was used to co-precipitate CaP with protein molecules.

Since then, this method was modified to produce the PS-DW-AGE approach that electrophoretically transports ions to synthesise ACP particles. This results in a precipitation process that is far quicker than in AGDD. Introduced by Watanabe and Akashi (2006), the PS-DW-AGE approach allows the synthesis of discrete layers of ACP particles with tuneable diameters within an agarose hydrogel. This approach was adapted further for the synthesis of pDNA/CaP particles by our group, where the process was modified by removed one of the wells and using a gel slab containing $H_xPO_4^{x-3}$ ions; resulting in the PS-SW-AGE approach.

Though CaP synthesis is not pDNA-dependent, results demonstrate that pDNA is immobilised and encapsulated using this approach. Transfection efficacy of these GAMs – measured by luciferase activity - is enhanced via the electrophoretic incorporation of FBN, likely to due to increased cell attachment afforded by the extracellular matrix protein. However, the high cost of FBN and theorised non-uniform coating of agarose with FBN resulting from unidirectional loading warrants the use of a more suitable coating material. PDA, applied pre-particle synthesis via the molten mixing method, has the potential to enhance cell attachment *in-vitro*. The PDA-coating also has the potential to capture pDNA on surfaces during PS-SW-AGE and hence modify the nucleation and growth kinetics of CaP particles and may even enhance the encapsulation efficiency of pDNA.

Given that pDNA can be adsorbed onto PDA surfaces via Ca^{2+}-quinone interactions, it is assumed that pDNA-retention of GAMs will be enhanced, given CaP precipitation on agarose fibres now may also encapsulate pDNA molecules. And, any unbound pDNA in solution can still act as a nucleation centre for CaP. Furthermore, the increased hydrophilicity afforded by the PDA

surface is known to change CaP mineralisation kinetics, potentially enhancing the surface area of the CaP coating. It is therefore of interest to produce and develop PDA-coated pDNA/CaP (PDA-pDNA/CaP) particles embedded within cryogels as potential GAMs for osteogenic tissue engineering applications.

1.5 Global Aims and Objectives

Previous work by Feichtinger et al. (2019) has demonstrated that pDNA/CaP particles synthsised via PS-AGE and embedded within agarose cryogels have the capacity to transfect cells. Furthermore, PS-SW-AGE has an inherent capacity to produce GAMs with discrete mineralised layers. Therefore, it is of interest to explore the PS-AGE technology further to probe its potential in fabricating GAMs with optimised particle sizes in gels expressing appropriate size and shape for pre-clinical models.

1.5.1 Aims

Develop and optimise a PS-AGE approach to facilitate the production of GAMs with layered, optimally-sized, mineral-phosphate genetic payloads suitable for osteochondral tissue regeneration.

1.5.2 Objectives

1. Investigate the effect of a PDA coating on pDNA/CaP GAMs on pDNA/CaP particle synthesis and transfection
2. Develop, computationally model, and experimentally test a new PS-AGE system to facilitate the fabrication of cylindrical GAMs
3. Systematically vary individual experimental parameters and measure the subsequent change in particle diameters to obtain an ‘ideal’ subset of experimental conditions to synthesis pDNA-loaded particles with diameters of 100 nm orless.
4. Fabricate cylindrical monolayer GAMs embedded with < 100 nm diameter pDNA-loaded particles and measure particle size stability and transfection efficacy *in-vitro*.

2 Development of Polydopamine-coated pDNA/CaP cryogels

2.1 Introduction

The PS-SW-AGE approach is an electric field-assisted template method that facilitates the synthesis of pDNA/CaP particles within an agarose hydrogel, which can then be lyophilised to form a cryogel with potential use as an osteogenic GAM. Utilising loading solutions and an electric field, this approach allows the mixing of Ca^{2+} and $H_xPO_4^{x-3}$ ions with pDNAs within an agarose matrix, where nucleation and growth are subject to nanoconfining conditions that limit their growth potential. In unpublished data, transfection efficacies of pDNA/CaP cryogels were approximately 1.9-times greater than pDNA cryogel control groups at 7-days, whilst FBN-pDNA/CaP cryogels were approximately 6.7-times greater than FBN-pDNA cryogel control groups at 7-days (Figure 1.4). These results indicate the PS-SW-AGE approach has good potential in developing osteogenic GAMs for use in gene therapy applications. In particular, the synthesis of a discrete layer of pDNA/CaP – as was shown in Figure 1.2 – is of interest for the regeneration of multi-layered tissues using layered scaffold architectures, such as the osteochondral.

Though good transfection efficacy of FBN-pDNA/CaP cryogels produced via the PS-SW-AGE approach is reported in unpublished data, there has been no further development of these cryogel GAMs. As previously discussed, there is potential to use PDA in place of FBN to provide uniform coating of the internal agarose surface. As a secondary effect, PDA may also provide more favourable mineralisation of hydrogel surfaces that could decrease pDNA/CaP particle diameters. pDNA/CaP particles would therefore have an increased specific surface area and hence an enhanced rate of dissolution/transformation, which is necessary to form secondary pDNA/CaP particles *in-vitro*. One could even reduce the size and increase the surface area of pDNA/CaP particles further by modulating experimental parameters such as salt and agarose concentration.

Going forward, the first modification to pDNA/CaP cryogels should be the introduction of PDA as a surface coating. Subsequent characterisation of pDNA/CaP particle size can then be conducted to determine the influence of both pDNA and PDA on pDNA/CaP size. Crystal structure should also be investigated to determine the crystallinity of such particles. ACP, being

metastable, would be more advantageous for cryogels in this work if particles are immobilised on surfaces. Therefore, cryogels would rely on surface-mediated transfection given ACP can more easily dissolve. In contrast, HAp would be more advantageous if particles are mobile *in-vitro* as this phase of CaP is more stable. However, it is assumed that the lyophilisation process immobilises particles on cryogel surfaces, hence ACP particles are favoured in this work. It would also be valuable to quantitatively analyse pDNA encapsulation to provide a better understanding of how efficiently pDNA is incorporated into cryogels and CaP particles.

Incorporating PDA into the hydrogels prior to synthesis is ultimately expected to yield smaller pDNA/CaP particle diameters, enhance pDNA encapsulation, and therefore enhance transfection efficacy compared to uncoated cryogels. An in-depth characterisation of particle diameter and morphology will be conducted using SEM, whilst crystal structure analysis will be performed with XRD. Changes in the crystal structure of pDNA/CaP particles between uncoated and PDA-coated groups are not expected given that the nano-confining effects of agarose are expected to stabilise ACP in both groups. Transfection efficacies of cryogel groups will be quantified via luciferase activity assays, as used previously by our group, to allow for some comparison against the previous (unpublished) data. Cytotoxicity assays will also be performed to investigate potential changes in cell viability in the presence of PDA and CaP.

2.2 Research Aims and Objectives

The PS-SW-AGE approach has demonstrated the capacity to produce agarose cryogels encapsulating pDNA/CaP for potential use as osteogenic GAMs. The use of PDA as a surface coating to form PDA-pDNA/CaP cryogels is expected to uniformly coat internal agarose hydrogel surfaces and therefore enhance the cell viability of PDA-pDNA/CaP groups compared to pDNA/CaP groups. PDA-pDNA/CaP cryogel groups are also theorised to have reduced primary pDNA/CaP particle diameters, enhanced pDNA-encapsulation, and greater transfection efficacy compared to pDNA/CaP groups. It is also expected that PDA-pDNA/CaP and pDNA/CaP groups will share amorphous XRD spectra due to nanoconfining effects stabilising ACP in both groups.,

2.2.1 Research Aims

(1) Establish whether polydopamine can enhance cellular attachment and reduce pDNA/CaP particle diameters.

2.2.2 Research Objectives

(1) Fabricate uncoated and PDA-coated cryogel groups via the PS-SW-AGE approach, with and without pDNA loadings.
(2) Characterise the diameter, morphology, and crystal structure of particles within cryogels.
(3) Determine the pDNA-encapsulation efficiency of cryogel groups.
(4) Compare the transfection efficacy and cytotoxicity of cryogel groups.

2.3 Materials and Methods

2.3.1 pDNA stock solution

Competent Escherichia coli (E. coli) TOP10 cells were inoculated with a pDNA encoding for the luciferase enzyme, herein termed 'pMetLuc', which was then isolated from the cells and purified using commercially available kits in preparation of pDNA loading in the PS-SW-AGE approach. Briefly, E. coli TOP10 cells in 5 mL of lysogeny broth (LB) media with 50 μg μL^{-1} ampicillin were cultured overnight at 37 °C on a shaker at 250 rpm. The culture was then added to 100 mL of LB media (with 50 μg μL^{-1} ampicillin) and cultured overnight at 37 °C on a shaker at 250 rpm. The resulting culture was transferred to sterile 50 mL tubes and centrifuged at 4000 rpm at 4 °C for 10-minutes. The supernatant was removed, and the pelleted cells were resuspended in a 30 mL solution of 80 mM $MgCl_2$, 20 mM $CaCl_2$ and deionised water ($D.H_2O$), then centrifuged again at 4000 rpm, 4 °C, for 10-minutes. The cell pellet was resuspended in a 2 mL, 4 °C solution of 100 mM $CaCl_2$, 10 vol % glycerol and $D.H_2O$, then separated into 100 μL aliquots and stored at -70 °C to form pMetLuc glycerol stocks.

5 μL of pMetLuc glycerol stock was mixed with 30 μL of competent E. coli TOP10 and incubated on ice for 30-minutes, then heat shocked at 42 °C for 45-seconds and cooled on ice for two minutes. 50 μL of Super Optimal Broth media with catabolite repression (SOC) was added to the cells and incubated for 45-minutes at 37 °C on a shaking incubator at 250 rpm. Meanwhile, a mixture of agar (1.5 wt %) and LB media was autoclaved. The mixture was allowed to cool to 50 °C before ampicillin was added at a concentration of 50 μg uL^{-1}. Once homogenised, the mixture was cast in a petri dish to from LB-agar plates.

25 μL of cells were plated on an LB-agar plate and incubated overnight. Single colonies were identified, collected, and resuspended in 5 mL LB-media containing 50 μg μL^{-1} ampicillin. The colonies were then incubated at 37 °C on a shaker at 250 rpm. A Minipreparation kit (Qiagen, N.V., Venlo, Netherlands) was then used to isolate and purify small quantities of pMetLuc from the cell culture, following the manufacturer's protocol. Next, an Endofree Plasmid Maxipreparation kit (Qiagen) was used to clone larger quantities of pMetLuc. The resulting pMetLuc pellet was suspended in molecular biology grade water, as per the manufacturer's protocol, to produce pMetLuc stock solutions. Finally, the concentration of pMetLuc was measured using a NanoDrop™ One/One^C Microvolume UV-VIS Spectrophotometer (Thermo Fisher Scientific, Massachusetts, USA).

2.3.2 Loading solutions

Loading solutions for cryogel fabrication were prepared; their concentrations are listed in Table 2.1. Briefly, 2000 µL of pMetLuc (herein referred to as pDNA) loading solution was prepared by diluting the pDNA stock solution with glycerol and $D.H_2O$ to give a final pDNA concentration of 0.1 ug μL^{-1} and 5 vol % glycerol. A $CaCl_2$ loading solution was prepared by diluting 180 µL of 2.5 M $CaCl_2$ in glycerol and $D.H_2O$ to give a final concentration of 225 mM $CaCl_2$ and 5 vol % glycerol. A blank loading solution comprised only of glycerol and $D.H_2O$.

Table 2.1. Overview of loading solution formulations

Loading Solution	**pDNA stock (3.13 µg μL^{-1}) (µL)**	**2.5 M $CaCl_2$ (µL)**	**Glycerol (µL)**	**$D.H_2O$ (µL)**	**Total (µL)**
'Blank'	0	0	100	1900	2000
pDNA (0.1 µg μL^{-1})	63.9	0	100	1836.1	2000
225 mM $CaCl_2$	0	180	100	1720	2000

2.3.3 Buffer Solutions

A concentrated buffer solutionn of 500 mM HEPES + 15 mM Na_2HPO_4 was prepared by adding 238.3 g of HEPES powder and 7.1 g of Na_2HPO_4 to 800 mL of $D.H_2O$. The solution was brought to pH 7.4 using 6 M NaOH and made up to a final volume of 1000 mL with $D.H_2O$. 90 mL of the concentrated solution was diluted with $D.H_2O$ at a ratio of 1:19 to a final volume of 1.8 L of working/running buffer solution. The running buffer concentration was therefore 25 mM HEPES and 0.75 mM Na_2HPO_4 (pH 7.4).

2.3.4 Gel Slabs

For the PDA-coated agarose gel slabs, the protocol described by Su et al. (2021) was adapted for use in this work. Briefly, 128.7 mL of working buffer was mixed with 26 mg of dopamine hydrochloride (Sigma-Aldrich, Massachusetts, USA) to give a dopamine hydrochloride concentration of 0.2 mg mL^{-1}. This solution was incubated at room temperature (shielded from

light) for 24-hours, then mixed with 1.3 g of agarose powder (SeaKem® LE Agarose, Lonza, Basel, Switzerland). The mixture was heated until the agarose completely melted, then allowed to cool to 60 °C and poured onto a 15 x 15 cm gel tray with 4 comb inserts (Figure 2.1). After 60-minutes at room temperature, the agarose had gelled completely and the combs were removed. To remove excess PDA, the gel slab was washed in 1000 mL of running buffer solution on an orbital shaker for 4-days where buffer solution was refreshed every 24-hours.

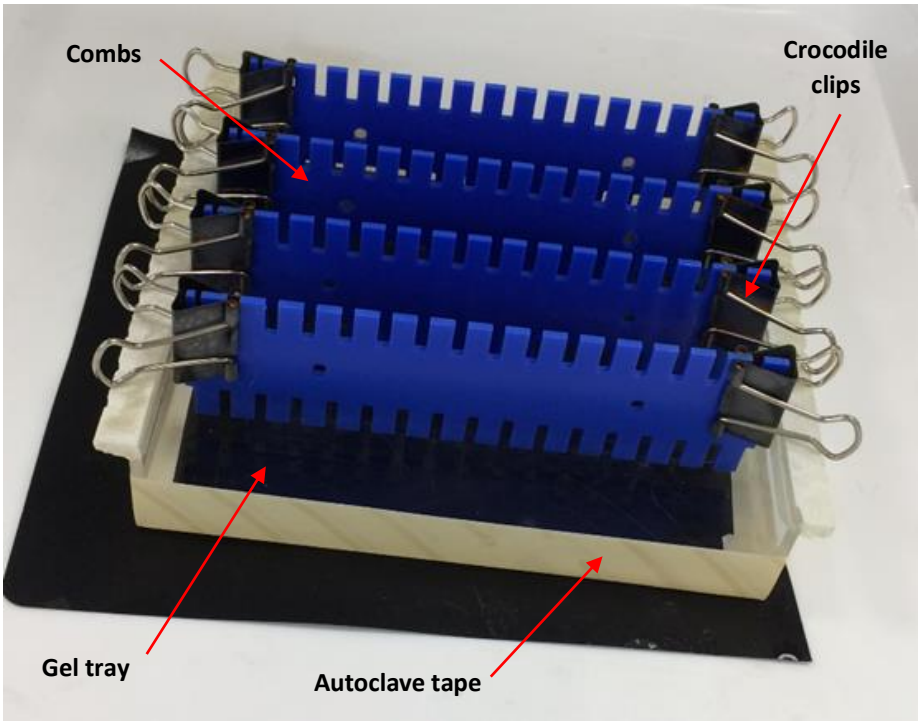


Figure 2.1. Gel tray layout with 4 comb inserts.

For the blank agarose gel slabs, the same processes to produce PDA-coated gel slabs was used, but was done using 128.7 mL of working buffer without PDA.

2.3.5 Gel loading

Uncoated and PDA-coated gel slabs were prepared separately by placing a gel slab into the electrophoresis tank (Sub-Cell GT, Bio-Rad, Massachusetts, USA) using the following process. Gel slabs were positioned in the tank centre and approximately 1670 mL of remaining running buffer was added to the tank (Figure 2.2) to submerge the gel slabs. As shown in Figure 2.2 and Figure

2.3, each row of 16 wells in the gel slabs were used for separate experimental groups, giving a total of 32 gels per group e.g. 32 of each of the following uncoated groups: blank (unloaded), pDNA, CaP, pDNA/CaP, PDA-blank (unloaded), PDA-pDNA, PDA-CaP, and PDA-pDNA/CaP.

The first row of each gel slab was used as a blank control set with no loadings; the second row was used for gels encapsulating pDNA; the third for gels encapsulating pDNA/CaP particles; and the fourth for gels encapsulating CaP particles only (Figure 2.3). 25 µL of the pDNA loading solution was pipetted into each well in rows one and two, then a 60 V potential was immediately applied across the gel for 6-minutes. pDNA molecules were directed toward the positively charged electrode due to their overall negative zeta potential and hence were 'loaded' into the agarose gel.

After 6-minutes, gel slices adjacent to rows one and two (on the side closer to the positive electrode) were cut into cuboidal shapes using a scalpel, producing gels measuring approximately 4 mm (length) x 6 mm (width) x 5mm (depth). The red dotted line in Figure 2.3 displays the approximate cutting line made by the scalpel to excise gels. Once cut, these small gels were removed from the gel slab with forceps and placed in 24-well plates in groups of four and immediately frozen at -70 °C. $CaCl_2$ loading solution was then pipetted into the wells of rows three and four, followed by reversal of the electric field polarity and immediate application of a 60 V potential for another 6-minutes.

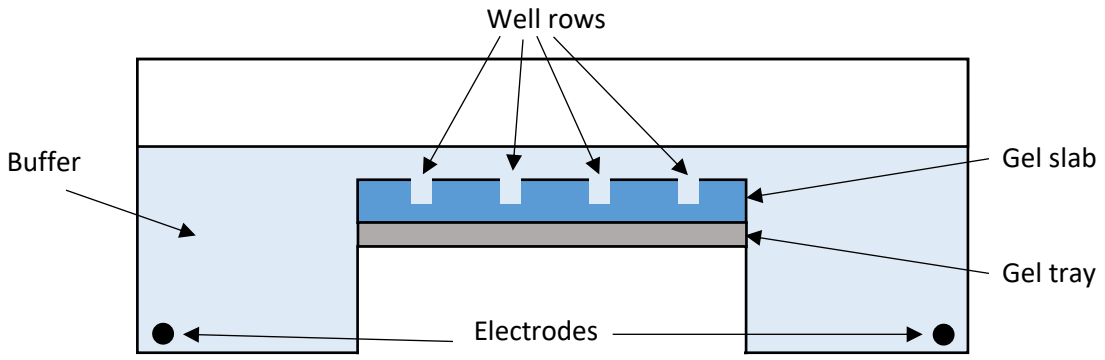


Figure 2.2. Bio-Rad Sub-cell GT horizontal gel electrophoresis system and a submerged gel slab with four well rows.

As with rows one and two, small gels were excised from areas adjacent to the wells of rows three and four, placed in 24-well plates (four gels per well) and immediately frozen at -70 °C. All excised gels were then lyophilised for 24-hours.

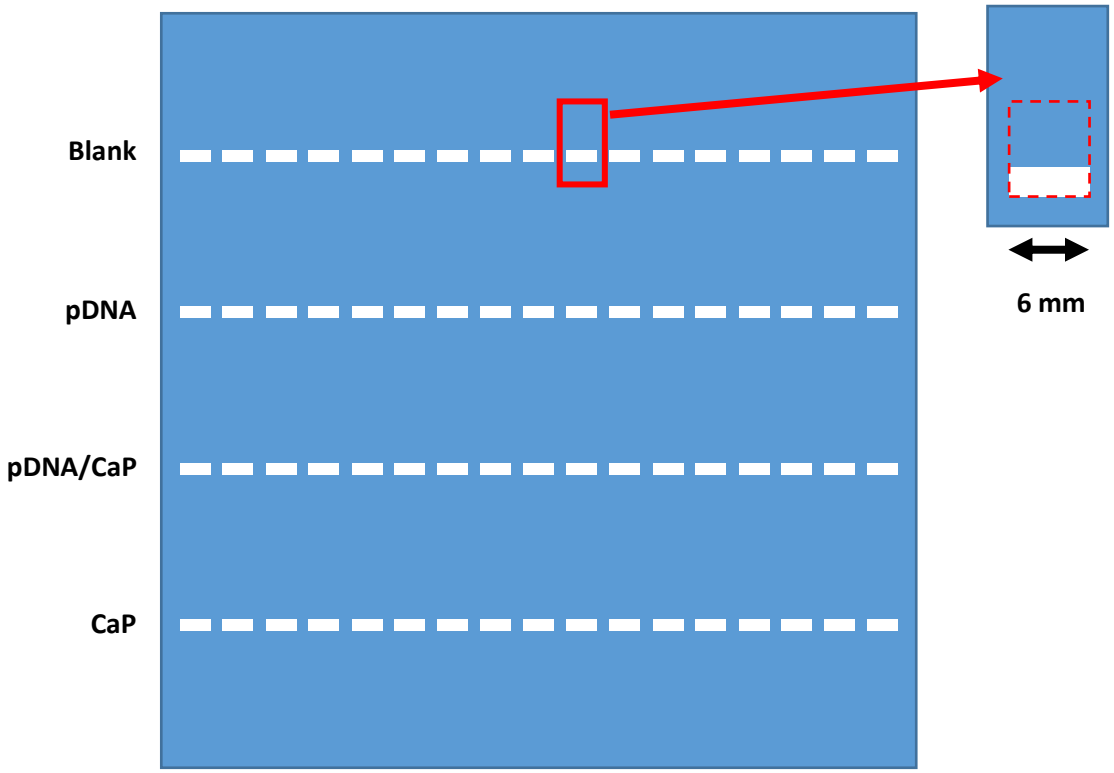


Figure 2.3. Distribution of groups in the gel slab and the approximate cutting lines for gels excised from the gel.

After lyophilisation, the 24-well plates containing the resulting cryogels were sterilised by adding 2 mL of 70 % EtOH to each well in the well plate and incubating the cryogels for 10-minutes. The 70 % EtOH was then removed and the cryogels were placed at -70 °C for two hours and lyophilised again.

2.3.6 pDNA mobility

Agarose and PDA-agarose gel slabs were prepared according to the protocols in 2.3.4, but with a single row of 16 wells, and were placed in the horizontal electrophoresis tank and submerged in a buffer of 25 mM HEPES, 0.75 mM Na_2HPO_4, pH 7.4. pDNA loading solution at a concentration of 0.1 µg μL^{-1} (as prepared in 2.3.2) was loaded into all 16 wells of each gel. A 60 V potential was applied for 6-minutes, followed by excision of a gel encapsulating the first 4 wells and 15 mm of surrounding gel. The excised gel was rinsed and submerged in a 1:10,000 dilution of SYBR™ Safe DNA Stain (Thermo Fisher Scientific) for 30-minutes. Meanwhile, a 60 V potential was applied across the gel slab for another 6-minutes, followed by excision of the next four wells and submersion of these gels in SYBR™ Safe. This process was repeated until the 60 V potential had

been applied for a total of 24-minutes and four gel slices (each with four wells) had been removed from the gel slab at 6-, 12-, 18-, and 24-minute time points.

After 30-minutes of submersion in the stain solution, excised gels were imaged with a UV gel imager (UVP Gel DoC-it, Analyytikjena, Jena, Germany). Images were analysed in ImageJ to measure the distances travelled by the pDNA loadings using the line tool. A transparent, UV responsive plastic ruler was placed alongside excised gels during imaging for calibration. pDNA travel distances were measured from the back of each well to the front of the pDNA band. From this distance, 2 mm was subtracted to account for the thickness of the well, giving the maximum distance travelled by the pDNA band. A mean distance (± SD) was calculated for each time-point (n = 4 for each time-point).

2.3.7 pDNA Encapsulation Efficiency

To determine encapsulation efficiency of pDNA within cryogel groups, three cryogels from each group were submerged in one of two buffers – control or decalcification buffer - to measure the amount of pDNA released from cryogels into each solution. The control buffer comprised of $D.H_2O$ with 40 mM Tris (pH 8.0), whilst the decalcification buffer comprised of $D.H_2O$, 40 mM Tris, and 150 mM EDTA (pH 8.0). For each cryogel group, three microcentrifuge tubes were allocated to a control set and another three were allocated to a decalcification set. 500 µL of appropriate buffer was added to each, followed by addition of cryogels to their respective tubes and incubation for 48-hours at 37 °C.

To determine the amount of pDNA leaching from cryogels into 70 % EtOH during the sterilisation step, a third set of microcentrifuge tubes was allocated to each cryogel group (n = 3). 500 µL of control buffer was added to each tube followed by addition of unsterilised cryogels to their respective tubes. An overview of cryogel group names for this experiment are listed in Table 2.2.

After 48-hours, the microcentrifuge tubes were centrifuged at 18,000 g for 15-minutes to force the cryogels and any agarose fragments to the bottom of the tubes. 250 µL of supernatant from each tube was extracted and diluted with 2250 µL of the same buffer (1:9 dilution) in a new tube. Of the total 2500 µL of dilute sample solution, 50 µL of each sample was placed in triplicate in a black flat-bottom 96-well plate in preparation for fluorescence measurements.

Table 2.2. Overview of cryogel group names and their new group name following submergence in buffer.

Cryogel Group	**Test Group Name**		
	Control buffer (unsterilised)	**Control buffer**	**Decalcification buffer**
Blank	Blank (unsterilised)	Blank (control)	Blank (Decal)
pDNA	pDNA (unsterilised)	pDNA (control)	pDNA (Decal)
CaP	CaP (unsterilised)	CaP (control)	CaP (Decal)
pDNA/CaP	pDNA/CaP (unsterilised)	pDNA/CaP (control)	pDNA/CaP (Decal)
PDA-blank	PDA-blank (unsterilised)	PDA-blank (control)	PDA-blank (Decal)
PDA-pDNA	PDA-pDNA (unsterilised)	PDA-pDNA (control)	PDA-pDNA (Decal)
PDA-CaP	PDA-CaP (unsterilised)	PDA-CaP (control)	PDA-CaP (Decal)
PDA-pDNA/CaP	PDA-pDNA/CaP (unsterilised)	PDA-pDNA/CaP (control)	PDA-pDNA/CaP (Decal)

For the quantitative measurement of pDNA, a Quant-iT^{TM} PicoGreen^{TM} dsDNA assay kit (Thermo Fisher Scientific) was used. Two sets of pDNA standards in the range of 125 – pg μL^{-1} to 0.25 ng μL^{-1} were prepared using the same pDNA stock used to prepare cryogel groups. Standards for the unsterilised and control sets were prepared with control buffer, whilst standards for the decalcification set were prepared with the decalcification buffer. All standards were added in triplicate, 50 µL volumes, along with 50 µL of buffer-only controls (also in triplicate).

50 µL of dsDNA reagent solution was added to all standard, buffer-only and sample wells, mixed well, and incubated for 5-minutes. A spectrophotometric microplate reader (Plate Chameleon^{TM}, Hidex Oy, Turku, Finland) was used to measure absorbance with excitation and emission wavelengths of 502 and 523 nm respectively (as per assay manufacturer's instruction). Each well was measured in triplicate and a mean value was taken for each. All fluorescence measurements for standards and samples were calibrated against their respective buffer-only controls. A standard curve was plotting for each of the control and decalcification standards.

For any given cryogel sample, Equation 2.1 was used to calculate the mass of pDNA released into the 500 µL volume of control or decalcification buffer using

$$pDNA\ release\ (\mu g)\ = \left(\left(\frac{y - c}{m} \right) \times DF \times 500\ \mu L \right) \quad 2.1$$

Where y is sample absorbance (arbitrary units), c is the y-intercept of the standard curve, m is the x-coefficient of the standard curve, and DF is the dilution factor (in this case, 10).

The mean (± SD) mass of pDNA released from cryogel groups (n = 3) was then calculated for the three different sets: unsterilised, control, and decalcification. Equation 2.2 was then used to determine the encapsulation efficiency (%) for any given cryogel group:

$$pDNA\ encapsulation\ efficiency\ (\%) = \left(1 - \left(\frac{pDNA\ release\ (\mu g)_{S,C}}{pDNA\ release(\mu g)_{D}} \right) \right) \times 100 \quad 2.2$$

Where $pDNA\ release(\mu g)_{S,C}$ is the mean mass of pDNA released from a sterilised cryogel group into control buffer and $pDNA\ release(\mu g)_{D}$ is the mean mass of pDNA released from a cryogel group into decalcification buffer.

2.3.8 Scanning Electron Microscopy (SEM)

For each cryogel group, a set (n = 8) of cryogels were placed in a tea strainer, submerged in liquid nitrogen for 15-seconds and immediately ground to a powder using a pestle and mortar. Powdered samples were stored in microcentrifuge tubes in a dry environment to prevent absorption of moisture. A cryogel from each of the blank and PDA-blank groups were kept intact for SEM imaging.

For each cryogel group, a 12 mm aluminium SEM stub (Agar Scientific, Essex, UK) was covered with a carbon sticker and a small quantity of homogenised, powdered sample was sprinkled onto the stub. Each sample was pressed onto the carbon sticker via a rolling action with a sterile glass pipette. For the intact cryogel samples, the cryogels were placed on carbon stickers and carbon paint was coated around the bottom and sides of the cryogels to enhance their conductivity. All samples were then coated with a 5 nm thick coating of Iridium using a Cressington 208 HRD Iridium Sputter Coater (Cressington Scientific, Watford, UK).

A Hitachi SU8230 high performance cold field emission SEM (Hitachi, Tokyo, Japan) with Oxford Instruments Aztec Energy Dispersive x-ray Spectroscopy (EDS) system with 80 mm X-MAX SDD detector (Oxford Instruments, Abingdon, Oxfordshire) was used to image cryogel samples. Secondary electron (SE) images were captured at 2 kV accelerating voltage (low probe current), BSE images were captured at 10 kV (low probe current), and energy dispersive x-ray (EDX) analysis maps were captured at 15 kV (high probe current). For SE and BSE imaging, a 5 mm working distance was used and a 15 mm working distance was used for EDX mapping.

SE imaging was preferentially used due to the high sensitivity of samples to the electron beam. BSE imaging was only possible in a small number of sample locations, hence BSE images were excluded from particle size measurements. Only particles above agarose surfaces were included in particle size measurements since those beneath the surface had poorly resolved edges. From each sample, a minimum of six agarose fragments with embedded particles were imaged. For each fragment, three images were acquired at different locations. All particles above the surface in these images were measured. Where particles were high in packing density, particles were only included in measurements if their circumferential edge could be completely resolved.

ImageJ was used to measure particle sizes using the line tool, where largest feret diameter ($feret_x$) and corresponding perpendicular feret diameter ($feret_y$) was obtained for each particle, as shown in Figure 2.4. Aspect ratios for each particle were then calculated using Equation2.3:

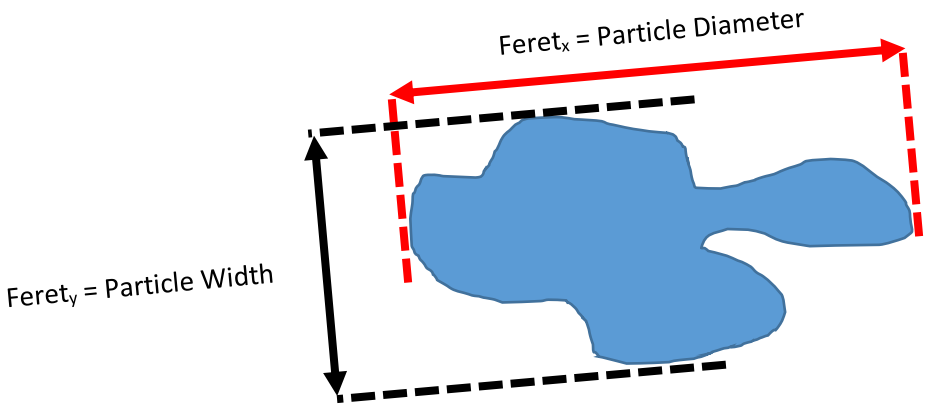


Figure 2.4. Determination of irregular particle diameter and width using feret diameters.

$$\text{Aspect ratio} = \frac{feret_x}{feret_y} \qquad 2.3$$

Due to the large range in grey scale values and background artefacts, images could not be reliably converted to a binary format that would allow for automated particle sizing in ImageJ. Such conversion resulted in a significant loss of particle data and artefacts in test images. Particles were therefore manually measured with minimal manipulation of image contrast and brightness.

Sample particle measurements were collected and transformed to histograms using a bin width (w) calculated via Equation 2.4:

$$w = \frac{range}{\sqrt{n}} \qquad 2.4$$

Where range is the difference between the smallest and largest particle diameters (with no excluded measurements), and n is the total number of particles measured for a given dataset. The lower boundary of the smallest bin is equal to the smallest measurement rounded down to the nearest integer. For each bin, frequency was used to calculate the 'percentage of total'.

2.3.9 X-ray Diffraction (XRD)

Crystal structure analysis was performed for powdered cryogel samples and a commercially available HAp powder (Sigma-Aldrich) control using a Bruker D8 Diffractometer (Bruker Corporation, Massachusetts, USA). Samples were analysed at room temperature, using a 2θ range of 20 – 60 °, a step-size of 0.016 °, and a Cu K-α x-ray source.

2.3.10 Cell Culture and Transfection

2.3.10.1 Resurrection of Cryo-Preserved Cells

A cryo-tube of C2C12 cells was taken from liquid nitrogen storage, placed at -70 °C storage and allowed to gradually increase in temperature. The cells were then rapidly thawed in a 37 °C water bath and reconstituted in 1.5 mL of cell media consisting of Dulbecco's Modified Eagle's Medium (DMEM) (Sigma-Aldrich) with 2mM l-glutamine, 2.5 vol % Penicillin-Streptomycin solution and 5 vol % foetal calf serum (FBS). The cells were then transferred to a T175 cell flask (Thermo Fisher Scientific) and incubated overnight at 37 °C with 5 % CO_2. The following morning,

cell media was aspirated, and the cells were washed in 2 x 10 mL of phosphate buffered saline (PBS) (Sigma-Aldrich), which was finally replaced by 20 mL of cell media.

2.3.10.2 Cell Passage

Confluency and morphology of cells in the T175 flask were checked daily using light microscopy. After 2-days, cells showed approximately 70 % confluency and a pH change indicated by phenol red, indicating suitability for passage. Cell media was aspirated, and the cells were washed in 2 x 10 mL of PBS. 5 mL of trypsin was added to the cells which were then incubated for 5-minutes at 37 °C. Following incubation, cells were checked for detachment/mobility under a light microscope. 6 mL of cell media was then added to the cells to inactivate trypsin and the resulting cell suspension was transferred to a 50 mL centrifuge tube and centrifuged at 150 g for 5-minutes. The cell pellet was resuspended in 10 mL of cell media; 2.5 mL of this cell suspension was added to two T175 flasks, along with 20 mL of fresh cell media in each flask.

2.3.10.3 Cell Counting

Once 70 % confluency was again achieved in the two T175 flasks, cells were pelleted and reconstituted in cell media to form a single, concentrated cell suspension in 10 mL cell media. 50 µL of concentrated cell suspension was mixed with 50 µL of 0.4% Trypan Blue solution and added to the glass side of a haemocytometer and placed in the cassette of Countess™ 3 Automated Cell Counter (Thermo Fisher Scientific). Upon acquisition of cell concentration, a total cell number was calculated based on the now 9.950 mL total volume of cell media. The concentrated cell suspension was centrifuged at 150 g for 5-minutes and resuspended in fresh cell media to give a cell suspension with a working cell concentration of 10×10^6 cells mL^{-1}.

2.3.10.4 Cryogel Cell Seeding

A high concentration agarose gel is required to coat the base of wells to prevent cells attaching to the base of well plates. This gel was prepared using SeaKem™ agarose with $D.H_2O$ and autoclaving the solution at 121 °C for 15-minutes. 250 µL of the molten solution was pipetted into the wells of three 48-well plates. Once cooled, cryogels from each group were placed individually in wells on top of the agarose gel using sterile forceps. One 48-well plate was

assigned to luciferase assays (transfection plate) and contained an n = 4 for each cryogel group and cell media controls. Another 48-well plate was assigned as the cytotoxicity plate. Cryogels from each cryogel group (n = 6) were placed in the cytotoxicity plate; three as positive controls (to be lysed) and three as experimental samples. The layout for each well plate is illustrated in Figure 2.5. Note that an additional plate was used for PDA-coated groups.

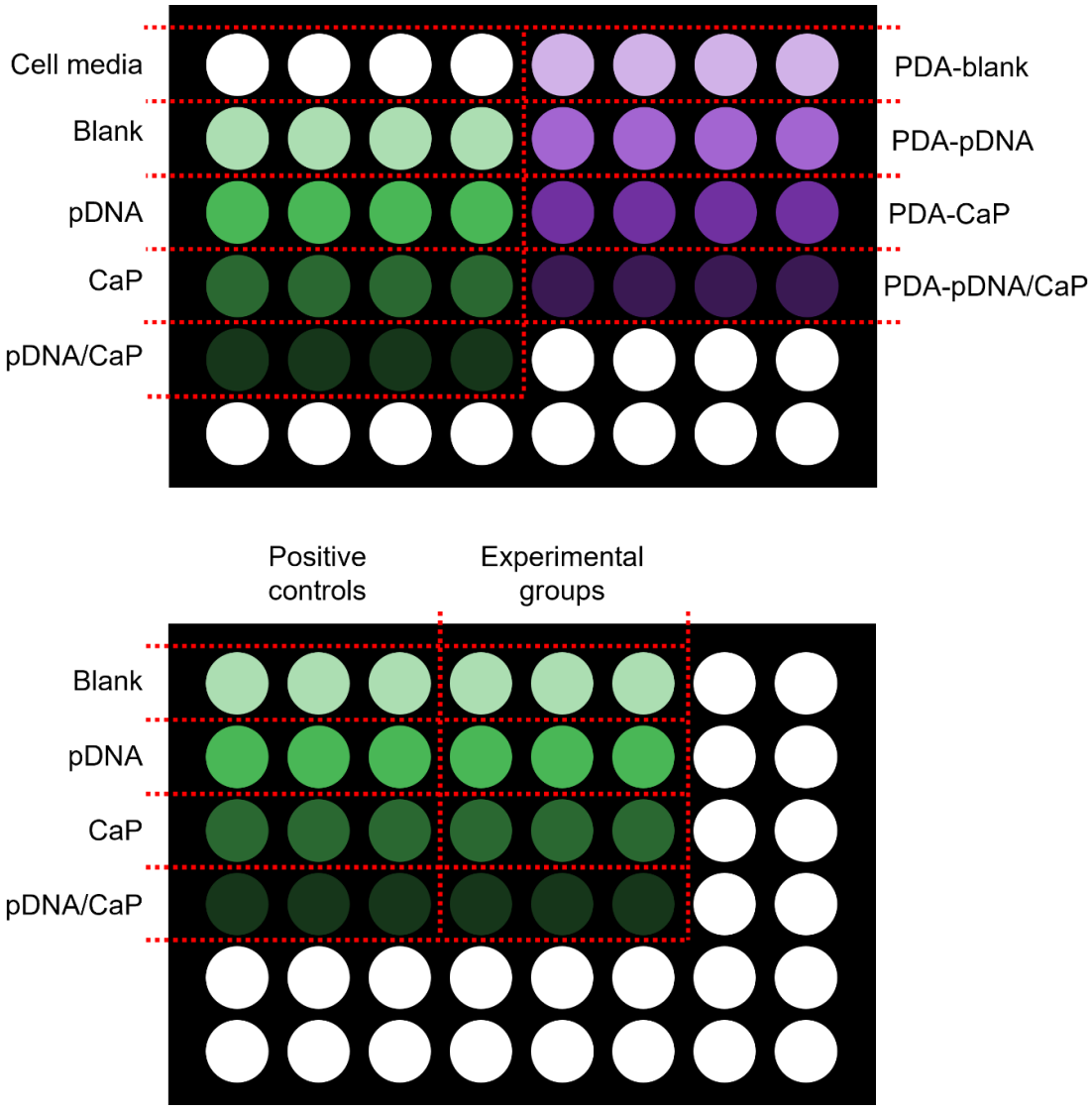


Figure 2.5. 48-well plate layout for (top) the transfection plate and (bottom) the cytotoxicity plate. White wells indicate unused wells.

50 µL of cell suspension (2.5 x 10^5 cells) was then pipetted slowly onto the top of each cryogel. Any excess cell suspension that did not soak into the cryogel was re-pipetted on top of the cryogel until the cryogel swelled and soaked up most of the cell suspension. The cryogels were then incubated at 37 °C for 3-hours to allow cells to attach to the cryogels. After incubation, 800

µL of cell media (without cells) was gently added to each well. Care was given not to pipette media directly onto cryogels which would potentially dislodge cells. The cryogel well plates were then placed back into incubation overnight.

After 14-hours of incubation, cryogels were transferred to three fresh separate 96-well plates that did not contain an agarose gel base coating. The transfer of cryogels to fresh 96-well plates was done primarily to increase the concentration of luciferase enzyme produced by transfected cells and thereby increase the sensitivity of luciferase assays. This also prevents luciferase enzyme loss into the agarose hydrogel. Secondary to assay sensitivity, the transfer to fresh 96-well plates mitigates any reduction in cell media nutrient concentration that may occur as nutrients diffuse into the sterile agarose gel coating the bottom of the 48-well plates. Briefly, 180 µL of cell media from all wells of the 48-well plates was transferred to 96-well plates, replicating the same layout as in Figure 2.5. Cryogels were then transferred to their respective wells in the 96-well plates using sterile forceps and placed back into incubation until time-points.

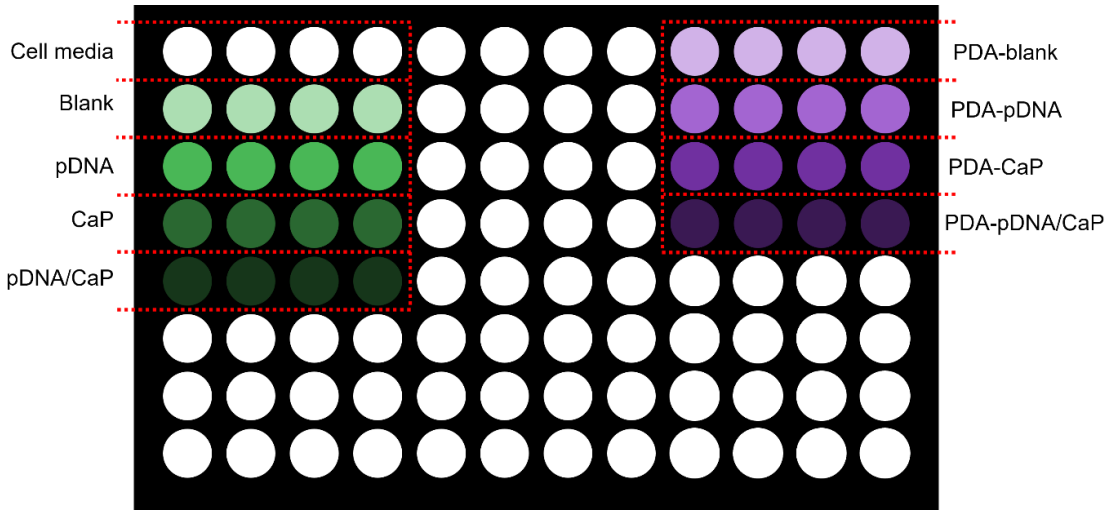


Figure 2.6. Layout of the 96-well transfection plate.

2.3.10.5 Transfection Quantification

At 24-, 48-, 72-hour, and 7-day time points, all cell media from the transfection plate was transferred to another 96-well plate, where each sample was homogenised via pipetting. 50 µL of the homogenised cell media was then transferred to a white 96-well plate. A concentrated coelenterazine solution was first prepared by reconstituted 250 µg of coelenterazine powder (ProMega, Wisconsin, USA) in 50 µL of acidified methanol. 1.4 µL of concentrate solution was then diluted in 698.6 µL of PBS to give a working solution concentration of 0.2 vol % coelenterazine (or 0.4 ng μL^{-1}). 10 µL of the coelenterazine working solution was then added to the homogenised 50 µL cell media samples, gently mixed via pipetting and incubated protected from light for 30-minutes. The well plate was then placed in a spectrophotometric plate reader (Plate Chameleon™, Hidex Oy, Turku, Finland) measuring for luminescence. Luminescence measurements for uncoated coated cryogel groups were baselined against the blank group, whilst PDA-coated groups were baselined against the PDA-blank group.

2.3.10.6 Cytotoxicity

16-hours prior to the 48-hour time point, systematic controls (cell-only) for cytotoxicity assays were established by seeding three wells of a separate 96-well plate with 9000 cells in 100 µL of cell media. After 16-hours of incubation at 37 °C and 5 % CO_2, this well plate was removed alongside the 48-hour cytotoxicity plate. All cryogels from the 48-hour cytotoxicity well plate (and cell media controls) were removed and transferred to the same 96-well plate, along with with 180 µL of fresh cell media. The 96-well plate was then incubated for a further 24-hours.

After 24-hours, 28 µL of 10X lysis solution was added to positive control cryogels (10 µL per 100 µL of cell media) and thoroughly mixed. In total, 28 µL of 10X lysis solution was added to each cryogel sample (rather than the recommended 18 µL) to account for the estimated additional 100 µL of cell media adsorbed into cryogels. For cell media controls, 5 µL of 10X lysis solution was added to wells. The 96-well plate now contains the systematic control (cell only), and cryogel groups divided into lysed (n = 3 for each group) and experimental sets (n = 3). This well plate was incubated for a further 45-minutes to lyse cells.

During incubation, the assay buffer was thawed at room temperature and protected from light. After 45-minutes of incubation, the 96-well plate was removed from incubation and 50 µL of

CytoTox® Reagent (ProMega) was added to each sample well. The well plate was then incubated at room temperature and protected from light for 30-minutes.

After incubation, 50 µL of stop solution was added to each lysed well. The absorbance at 490 nm was then measured for all wells. All absorbance measurements were first calibrated against the cell media control, followed by calculated of mean values for lysed and non-lysed cryogels. Percentage cytotoxicity for a given cryogel group was then calculated using Equation 2.5:

$$Cell\ viability\ (cryogel)\ (\%) = \left(\frac{Unlysed\ cryogels\ (OD_{490\ nm})}{Lysed\ cryogels\ (OD_{490\ nm})}\right) \quad 2.5$$

Using Equation 2.6, cell viability (± %) was calculated by comparing the cell viability of a given cryogel group to that of the blank cryogel group:

$$Cell\ viability\ (\pm\ \%\ of\ blank) = Cell\ viability\ (Blank) - Cell\ viability(cryogel) \quad 2.6$$

The percentage cytotoxicity for each cryogel group was then calibrated against the blank group. Normally the LDH assay protocol requires baselining cytotoxicity against cell only controls. However, the same number of cells in these cryogels cannot be seeded onto well plates due to excessive cells per unit area. Hence the blank cryogel group was instead used in-place of a cell-only control.

2.3.11 Data Analysis

Unless specified, mean values are provided with SD as follows: mean ± SD. The Shapiro-Wilk test was used to test datasets for normality. Where data was non-parametric, the Tukey Kreamer Honestly Significant Difference (TK-HDS) test was performed for multiple comparison statistical analysis. All statistical tests were carried out using 95 % confidence intervals (CI).

2.4 Results

2.4.1 pDNA Mobility in Gels

The distance travelled by pDNA in agarose and PDA-agarose gel slabs was measured to determine changes in pDNA mobility as a result of the PDA coating. Figure 2.7 shows images of stained uncoated agarose and PDA-agarose gels loaded with pDNA, excised from the electrophoresis tank at different time points.

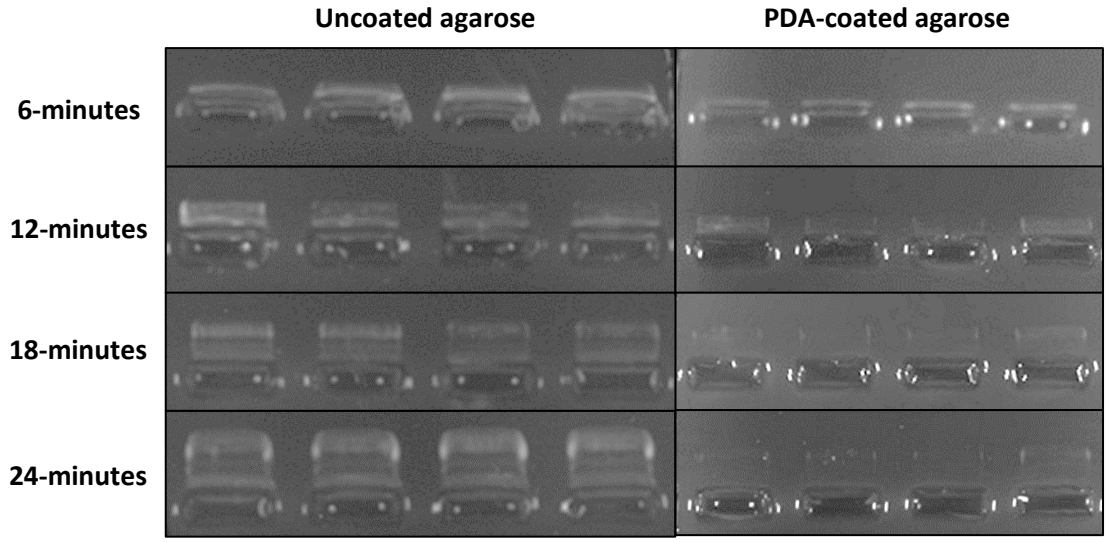


Figure 2.7. pDNA bands in (left) uncoated and (right) PDA-coated agarose gel slabs.

The pDNA bands are more clearly observed in the uncoated agarose gel at all time points, whilst the bands in the PDA-agarose are comparatively fainter and reduce in visibility with time, with leading edges that become fainter. By 24-minutes, only the sides of the pDNA bands remain visible in the PDA-agarose slab. This reduced visibility of pDNA in the PDA-coated gel could arise from the increased opacity of the gel and therefore reduced transmission of excitation and emission wavelengths through the gel required for the DNA stain to perform appropriately, but this would not explain why the sides of bands remain visible.

Bands in both gels stretch over time, which could stem from an incomplete loading of pDNA from wells into the gel slab after 6-minutes. In this hypothesis, the majority of pDNA is loaded after 6-minutes but a minority remains within the well. Upon removal of the 6-minute gel slice

any pDNA in the well is ejected during washing. Meanwhile, pDNA remains in the wells of the gel slab and diffuses back away from the well-gel interface. Upon reapplication of the applied potential, the pDNA band in the gel continues to progress through the gel but there is a time delay before the residual pDNA in the well is loaded into the gel. This cycle repeats, creating a 'ladder' of pDNA in the 24-minute gel slice (from the uncoated gel slab) with each new step diminishing in intensity relative to the previous step. If this ladder effect is prevalent in the PDA-coated gel slab, it may explain (to some extent) why pDNA intensity diminishes with time.

Due to their reduction in intensity with time, pDNA bands in the PDA-coated agarose become difficult to measure accurately. Adjustments to the brightness and contrast in ImageJ were required to enhance the visibility of these bands and make more reliable measurements.

The mean distances (± SD) travelled by pDNA bands at each time point for uncoated agarose and PDA-agarose gel slabs were calculated and plotted as a function of time in Figure 2.8. Linear fits applied to both datasets give an $R^2 = 0.97$ for the uncoated agarose gel and $R^2 = 0.99$ for the PDA-agarose gel. The gradients of the slopes are similar, having comparable x-coefficients of 0.159 and 0.149 for the agarose PDA-agarose respectively, indicating a similar mobility between the gels between 6- and 24-minutes. However, their y-intercepts are evidently different, having values of 0.99 and 0.49 for uncoated agarose and PDA-agarose respectively. This indicates an

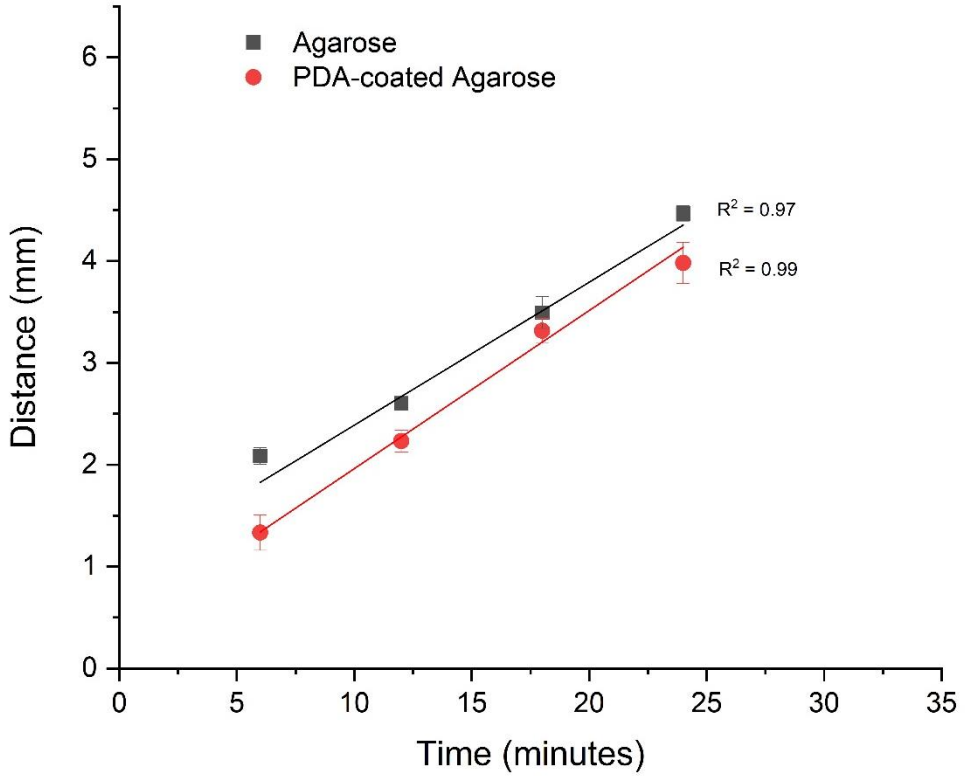


Figure 2.8. Distances travelled by pDNA bands over time in uncoated agarose and PDA-agarose gel slabs. Errorbars indicate standard deviation.

initial reduced mobility of pDNA in the PDA-coated agarose. This could arise through adsorption of pDNA on PDA surfaces or conjugation of pDNA with excess PDA molecules.

2.4.2 Cryogel Appearance

Following the first lyophilisation, cryogels had a uniform shape that appeared to reduce only slightly from their original hydrogel size after the first lyophilisation step. However, as shown in Figure 2.9 (B), the second lyophilisation reduces the uniformity and size of both agarose and PDA-coated agarose samples. The change in appearance between the two lyophilisation steps is likely due to the contrasting properties of buffer solution (containing salts) present during the first lyophilisation step and 70 % EtOH present in the second lyophilisation step. The 'frosted' appearance in Figure 2.9 (C) is therefore likely to be crystallised residual salts from the buffer or loading solutions. The reduced visibility of salts between Figure 2.9 (C) and (D) suggests that the 70 % EtOH wash is removing much of the salts from the cryogels.

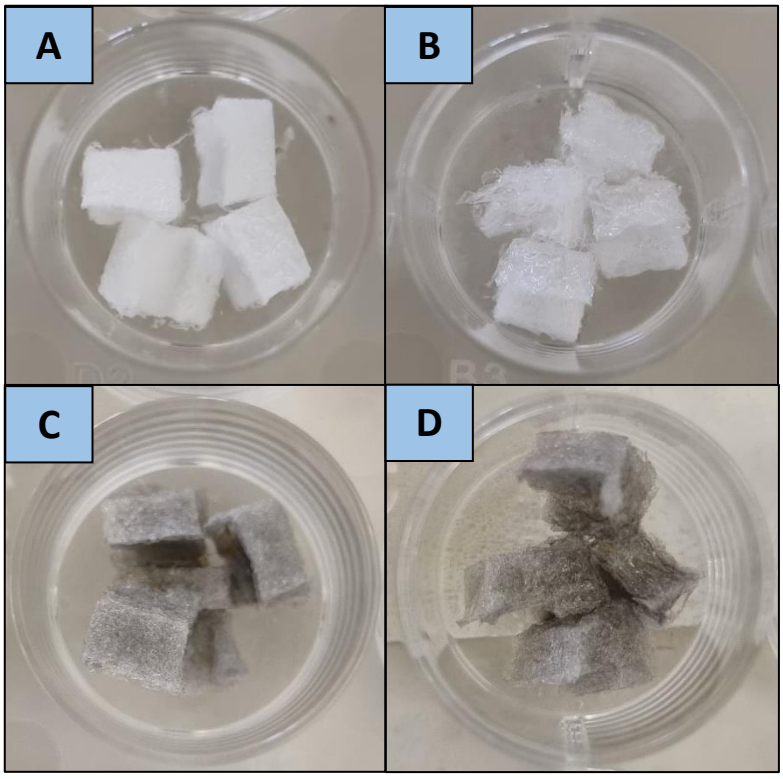


Figure 2.9. Uncoated and PDA-coated agarose cryogel appearances. (A) Agarose cryogels after first lyophilisation and (B) after 70 % EtOH sterilisation and second lyophilisation. (C) PDA-coated agarose cryogels after first lyophilisation and (C) after 70% EtOH ster

Digital images of blank and PDA-blank cryogels post-sterilisation and lyophilisation reveal a rough surface topography, but with little evidence of a porous surface in both cryogels Figure 2.10. The colour of the PDA-blank cryogel is darker than that of the blank cryogel due to the PDA coating, but there are also black spots distributed throughout the cryogel surface that are assumed to be PDA clusters. These cryogels were sliced in half using a scalpel to observe the internal porous structure.

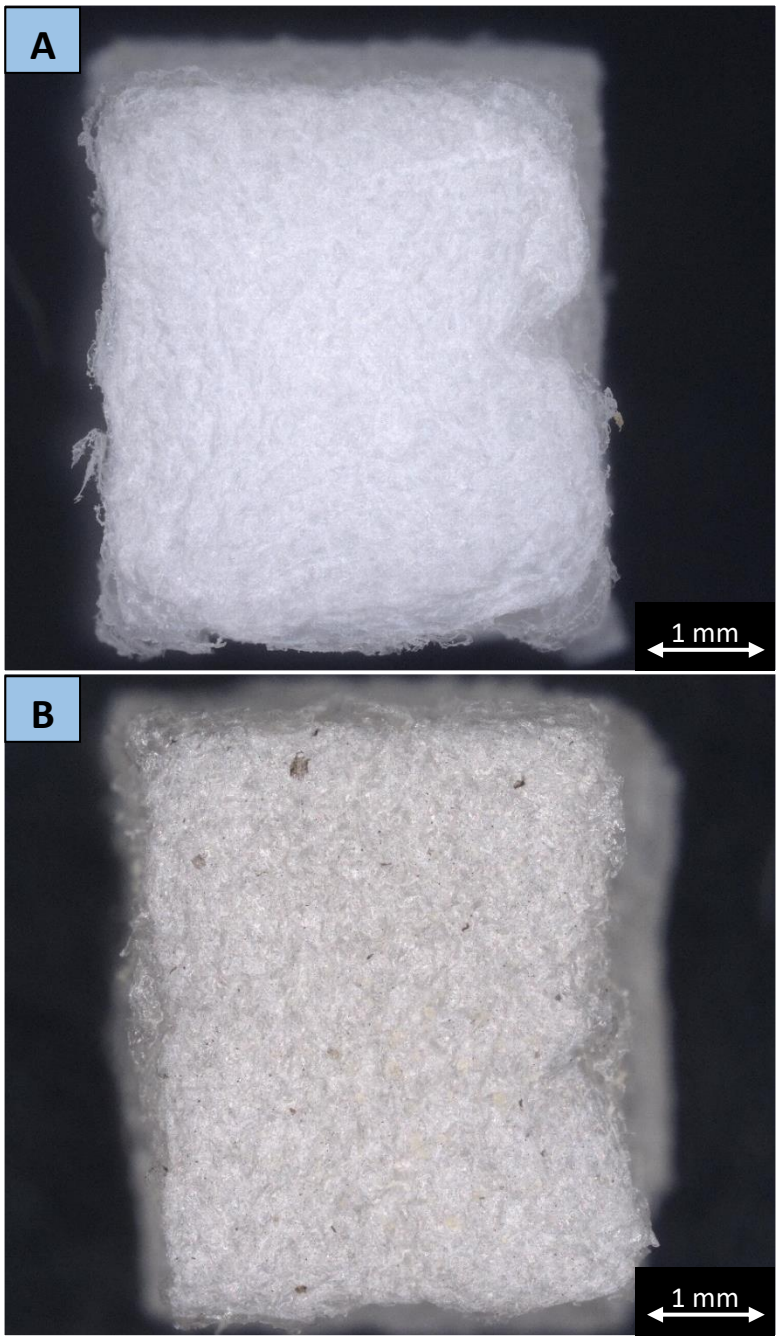


Figure 2.10. Digital Microscope images of (A) Blank group cryogel and (B) PDA-blank group cryogel.

As shown in Figure 2.11, the blank cryogel has a highly porous internal structure with pore sizes ranging from 50 – 200 µm. In contrast, the porous structure of the PDA-blank is less easily identified. Pale voids, which could be the pores themselves since PDA clusters are vacant in these areas, can be seen through the PDA-blank which measure between 30 – 150 µm.

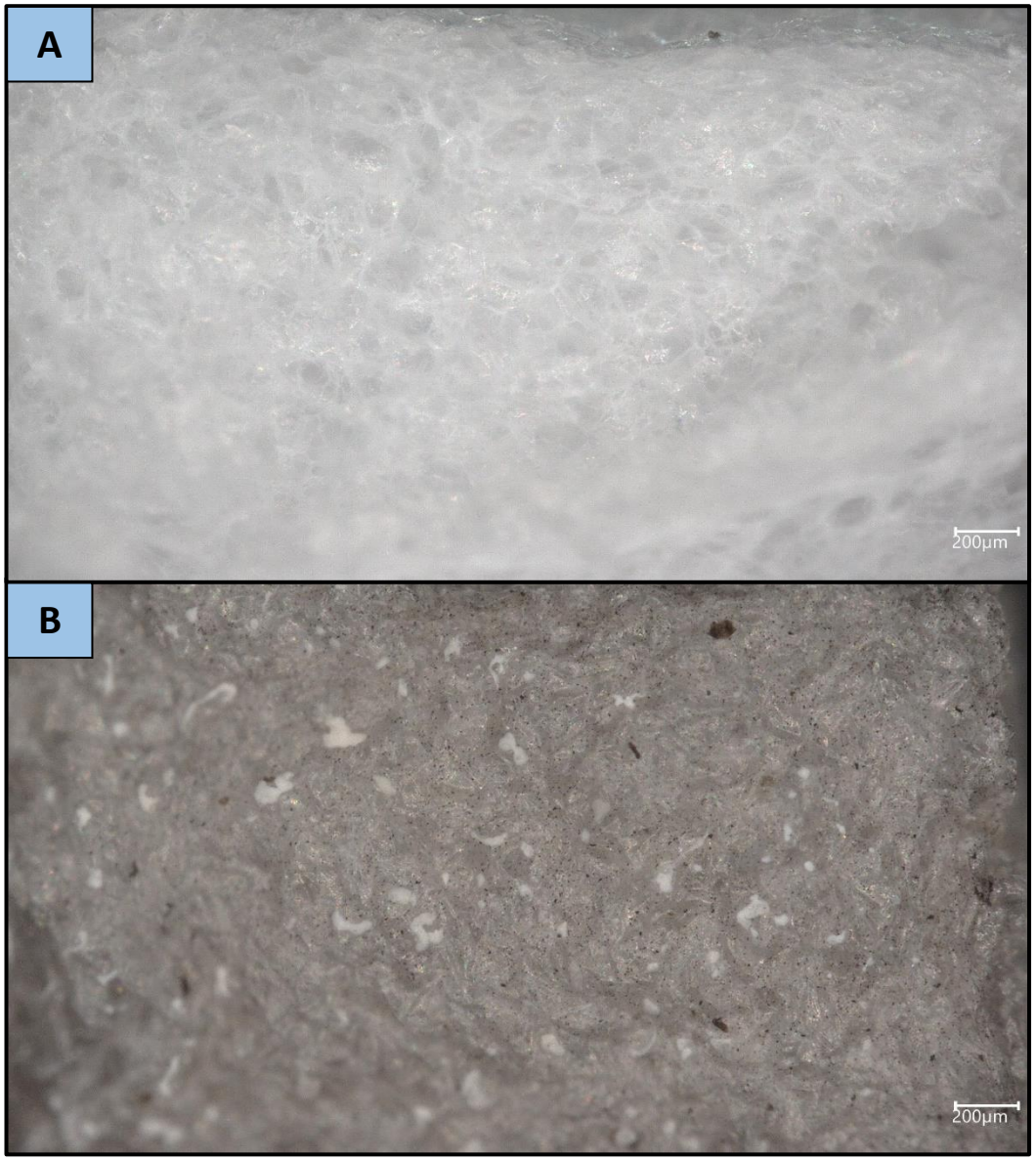


Figure 2.11. Internal porous structure of (A) blank group cryogel and (B) PDA-blank group cryogel.

At greater magnification, the PDA clusters become clearer and are all below 10 µm in diameter, as shown in Figure 2.12. The pale voids are difficult to interpret; they could be pores based on the absence of PDA clusters in this focal plane, but the blurred foreground of these images could indicate these images are taken through pores themselves. Agarose fibres or ridges can be seen in Figure 2.12 (B) but based on the presence of PDA clusters between neighbouring fibres/ridges these are likely not the circumferential edges of pores.

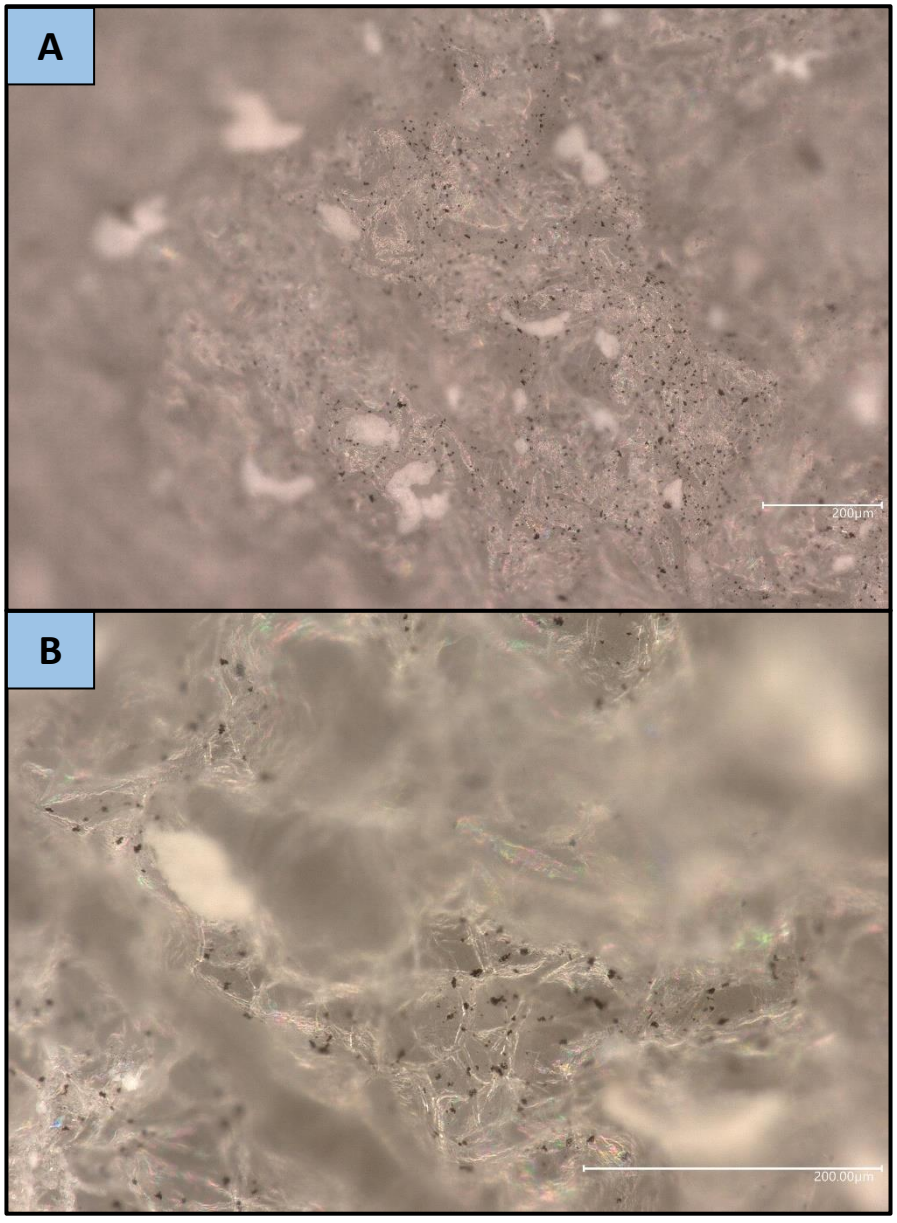


Figure 2.12. High magnification digital microscope images of PDA-blank cryogel internal pore structure.

2.4.3 XRD

XRD spectra for samples from blank, pDNA/CaP, and PDA-pDNA/CaP groups, as well as a HAp powder control, are shown in Figure 2.13. The blank agarose sample has a broad, shallow peak between 2θ of 32 – 39° which indicates an amorphous structure. In comparison, the pDNA/CaP and PDA-pDNA/CaP groups have almost identical broad peaks between 2θ of 31 - 35° that coincide with the region of intense characteristic peaks of HAp for the (211), (112), (300) and (202) crystal planes.

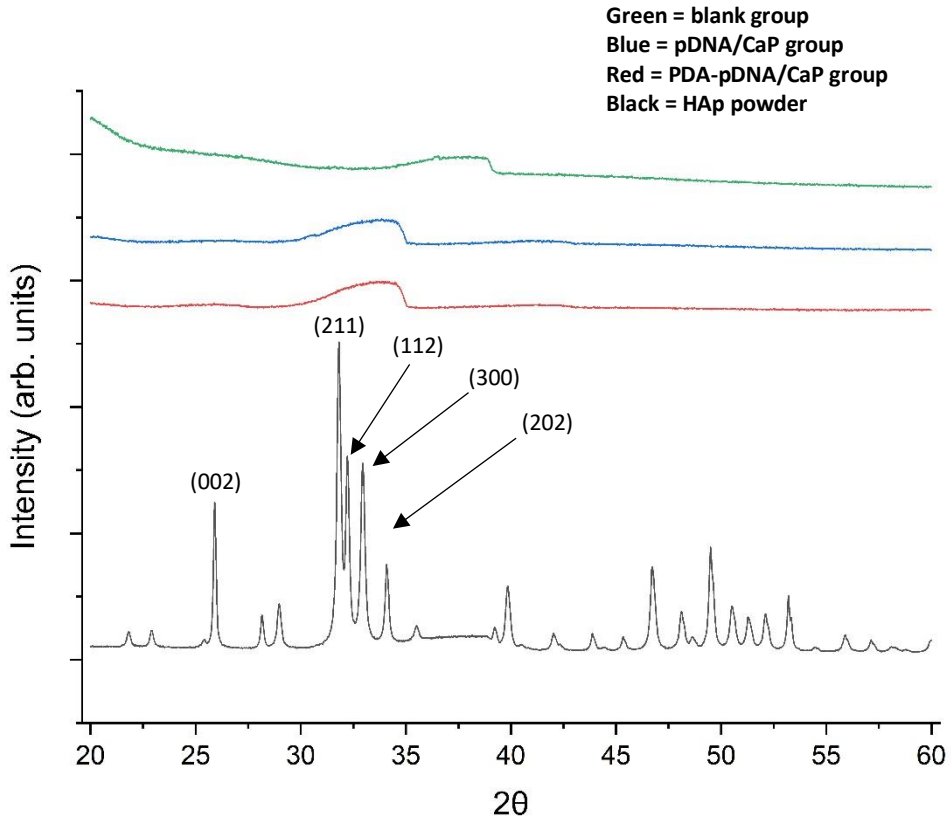


Figure 2.13. XRD spectra for blank (green), pDNA/CaP (blue), PDA-pDNA/CaP (red) and HAp powder (black) samples.

The broad peaks in the pDNA/CaP and PDA-pDNA/CaP samples either indicate an amorphous structure (i.e. ACP) or that crystal size is low and/or of low crystallinity. The presence of HAp in these two samples can therefore not be ruled out based on this data.

2.4.4 SEM

2.4.4.1 Intact Cryogels

A cryogel from each of the blank and PDA-blank group were kept intact to identify the surface properties of the cryogels, these images are shown in Figure 2.14. At low magnification (Figure 2.14 (A) and (B)) the cryogels are similar; both presenting a surface that is mostly smooth with regions toward the edges that boast much rougher textures. A typical image of the smooth surface areas of the blank group are shown in Figure 2.14 (E), whilst the smooth surface areas of the PDA-blank typically resemble platelets at higher magnification (Figure 2.14 (F)) and evidence of a 60 µm pore at toward the centre of the image. The rougher areas of the blank and PDA-blank cryogels are shown in Figure 2.14 (C) and (D) respectively. These areas may be ruffles of agarose pore boundaries or ridges in which the PDA-blank cryogel presents more densely packed boundaries than the blank cryogel.

A blank cryogel was sliced in half and imaged via SEM to observe the internal porous structure generated by the lyophilisation process. As shown in Figure 2.15, the blank cryogel has pore sizes ranging from approximately 50 – 200 µm, which is within the same size range as pores identified via digital microscopy earlier. The external and internal porosity appear highly different, however, under hydrated conditions the surface porosity may be induced by the hydration of surface agarose sheets.

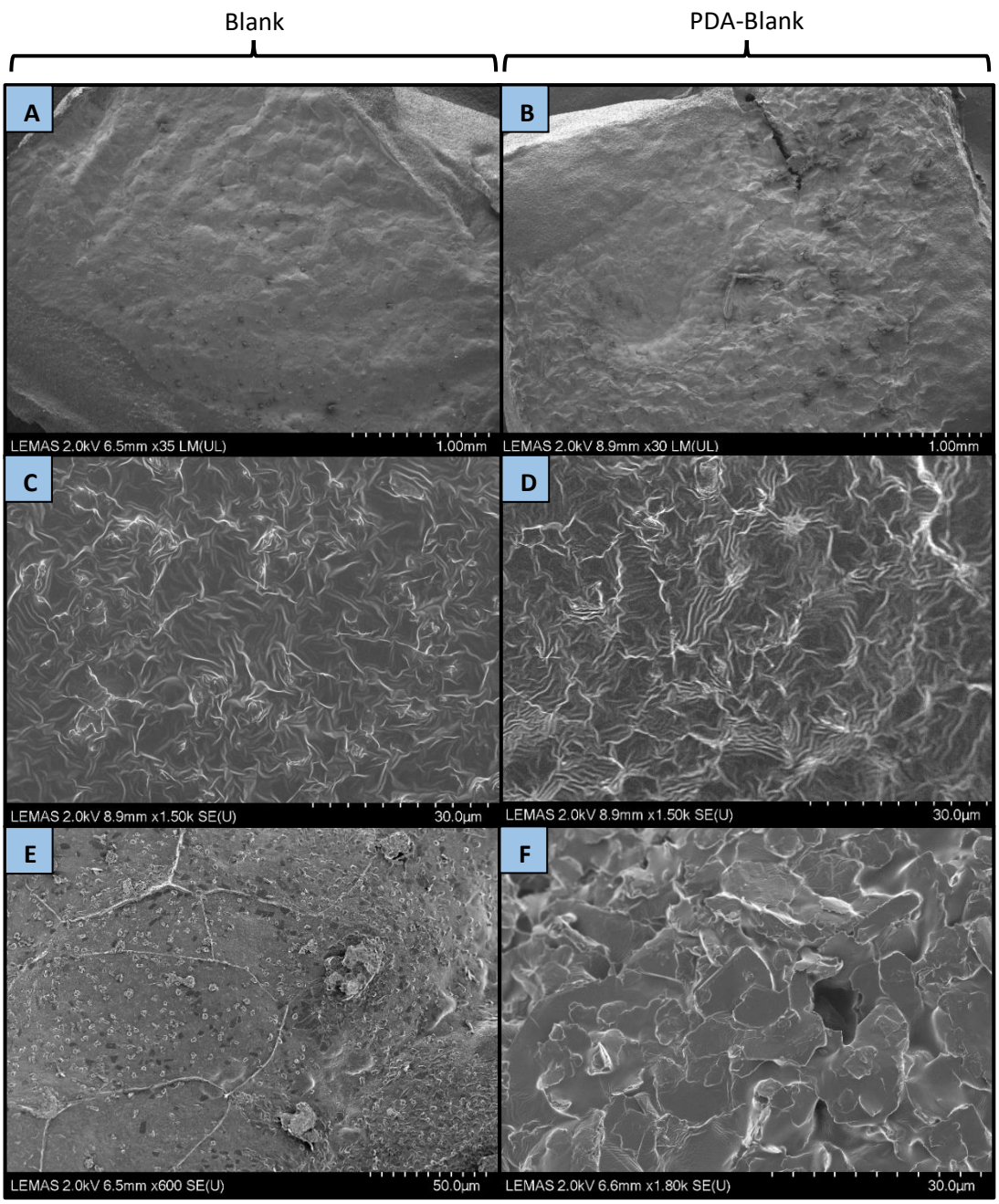


Figure 2.14. SEM images of intact blank and PDA-blank cryogel surfaces.

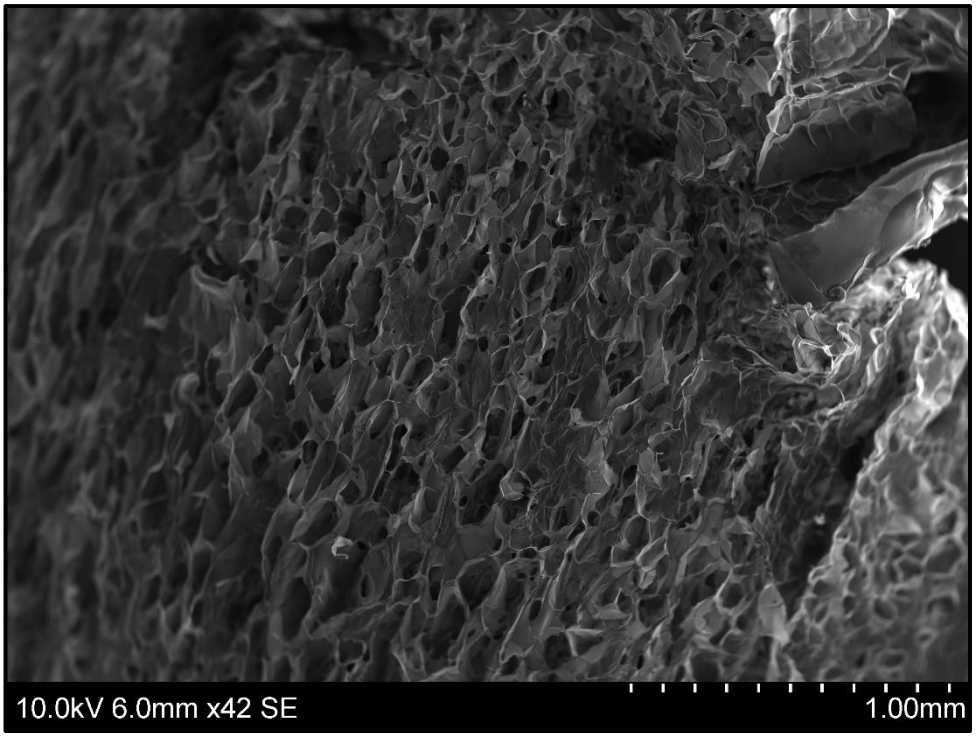


Figure 2.15. Lyophilised blank cryogel (intact).

2.4.4.2 Powdered Samples

Particles embedded within powdered cryogel samples were analysed using SEM to obtain particle diameters and aspect ratios. A low magnification image of a CaP group sample is shown in Figure 2.16 as a typical example of agarose fragmentation on the SEM stubs, with fragments ranging from 5 μm to 1 mm. Charging effects – indicated by white fragments – are an effect of fragment stacking on the carbon sticker that reduces conductivity in these areas, hence producing contrast in SE imaging. Such fragments were avoided for particle analysis since charging disrupts normal electron pathways and therefore distorts images. Typically, lone fragments away from stacked clusters were ideal for imaging giving their close residency to the carbon sticker itself.

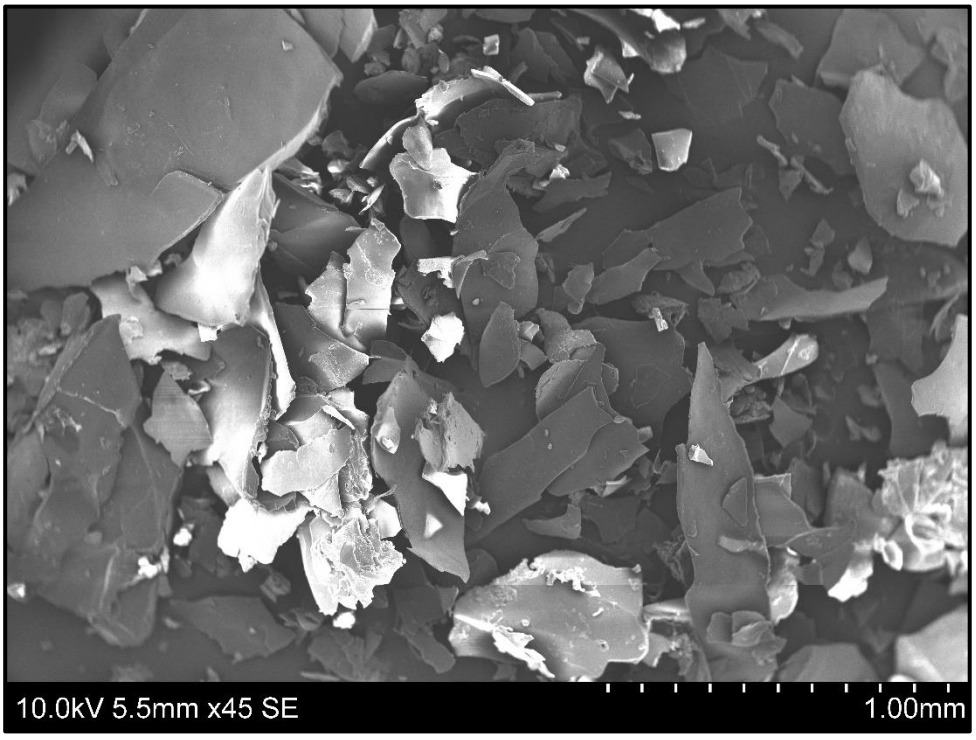


Figure 2.16. Low magnification SE image of a powdered CaP group sample.

The agarose demonstrated a high degree of sensitivity toward the electron beam at accelerating voltages of > 10 kV. To avoid 'burning' of the sample during BSE and SE imaging, focus and contrast adjustments were made near to target areas, followed by translation of the beam to the target area. Imaging generally needed to be performed at magnifications of x 20 k or lower to avoid burning, but occasional higher magnification was possible for single-particle imaging in stable areas. Particles presented good beam stability with no apparent changes to their

appearance in SE imaging. In contrast, much larger salt crystals were easily identified by their rapid 'beam flattening' upon exposure to the electron beam for short durations.

2.4.4.3 Blank and pDNA Groups

Agarose fragments from the blank group demonstrated a generally homogeneous appearance with few surface features. Agarose fibres could occasionally be observed but each fragment generally resembled flat sheets, as shown in Figure 2.17. The absence of pores may simply be due to the destruction of nanoscale pores during lyophilisation, whilst microscale pores created during lyophilisation were erased by the powderisation process. pDNA samples were identical in appearance to agarose controls since the added DNA molecules are unobservable using typical SEM imaging; hence images of pDNA samples are not provided.

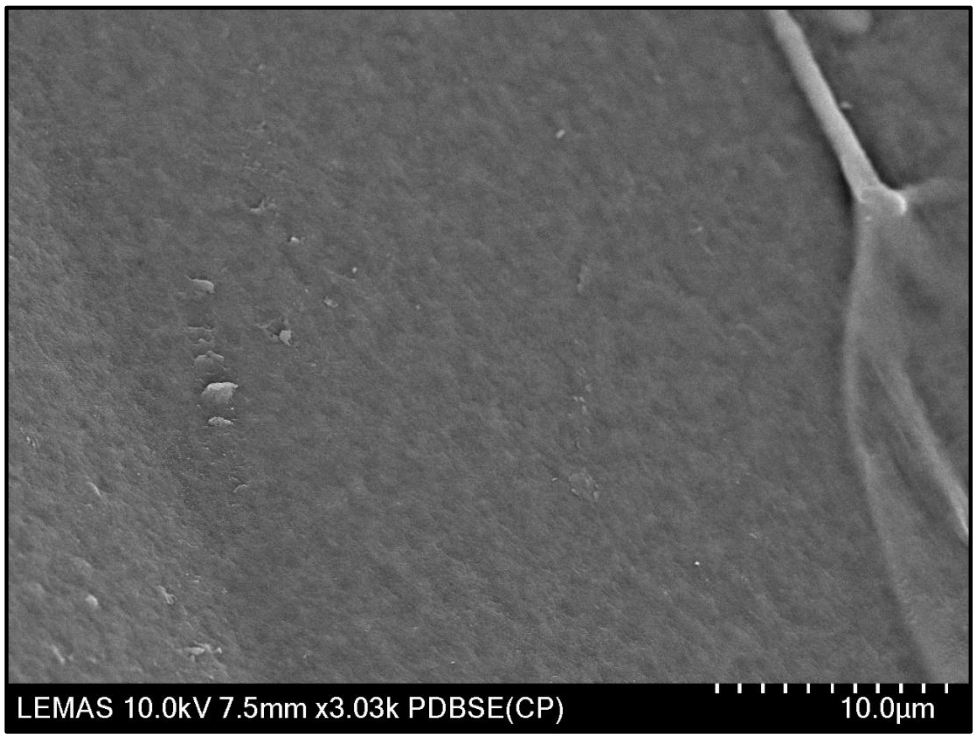


Figure 2.17. BSE image of a powdered blank cryogel, showing an absence of particles on the agarose surface.

2.4.4.4 CaP Cryogel Group

Powdered CaP cryogel samples showed agarose fragments embedded with particles (Figure 2.18) clearly visible against the background agarose under BSE imaging. Such contrast in BSE imaging indicates the particles are comprised of elements with heavier atomic mass than that of the agarose. The particles appeared either on or close to the agarose surface with clearly defined edges or embedded deeper in the agarose fragment with comparatively lower brightness and poorly defined edges. Particles with poor contrast and/or poorly defined edges were ignored for particle sizing. Generally, SE imaging (at an accelerating voltage of 2 kV) was found to give better images for particle sizing since SE signals originate from shallower sample depths and produce more highly resolved data for surface particles. Comparatively, BSE imaging allowed observation of particles embedded below the agarose surface. However, the high sensitivity of agarose to the electron beam, especially at the higher accelerating voltages needed for BSE imaging, frequently resulted in extensive damage to the local sample area. And even in BSE imaging, only surface particles have the defined resolution required for particle sizing.

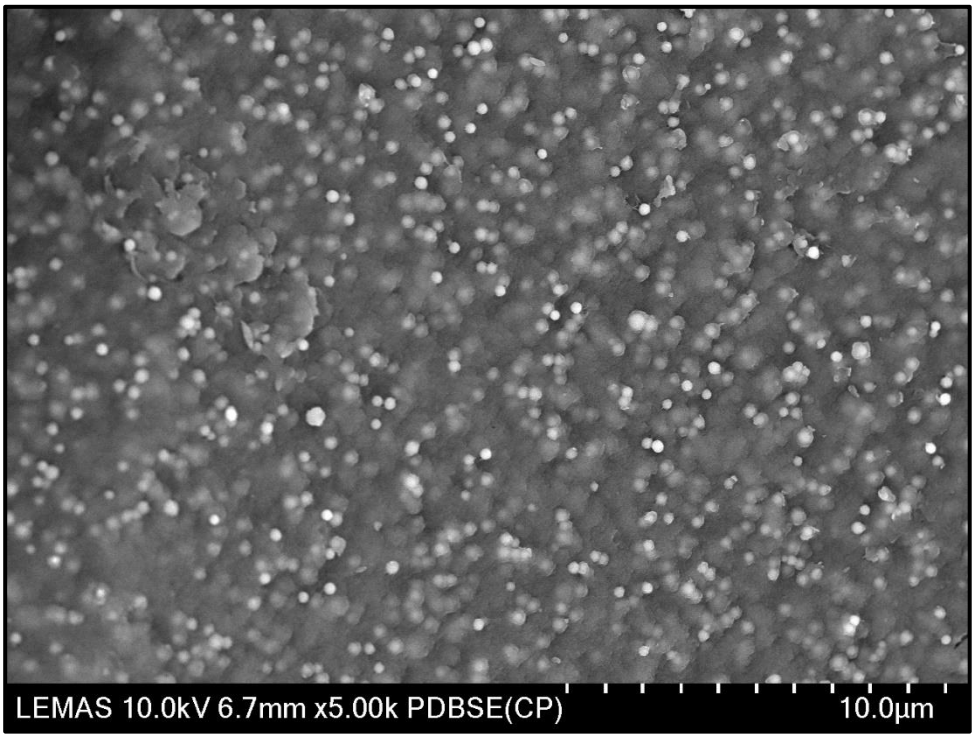


Figure 2.18. BSE image of the CaP sample.

As shown in Figure 2.19, the agarose fragments show a variation in particle packing density, particle morphology, and particle sizes. Figure 2.19 (A) shows particles ranging in sizes from approximately 150 – 500 nm. These particles appear multimodal in their size distribution, as highlighted by the (red) circled particles, where most particles are of their order of 150 nm or 300 nm in diameter. Most particles are spherical or have round edges, with some exhibiting irregular morphologies or faceted edges. A small number of particles exhibit hexagonal-like morphologies, such as the example magnified in the red square.

Figure 2.19 (A) also displays some agglomeration, as particles are mostly in close proximity to larger clusters. Neighbouring particles could have nucleated and grew here together or agglomerated in solution during synthesis. In contrast to the packing density of particles in Figure 2.19 (A), the fragment in (B) presents more uniform, monodisperse particles with fewer clusters. The particles in Figure 2.19 (B) are also much smaller than those in (A), ranging from 50 – 200 nm, with a mix of spherical and irregular morphologies. Together, the images in Figure 2.19 demonstrate the heterogeneity of particle size, morphology, and packing density that can be obtained within the CaP sample that is theorised to result from non-uniform supersaturation across the zone of precipitation.

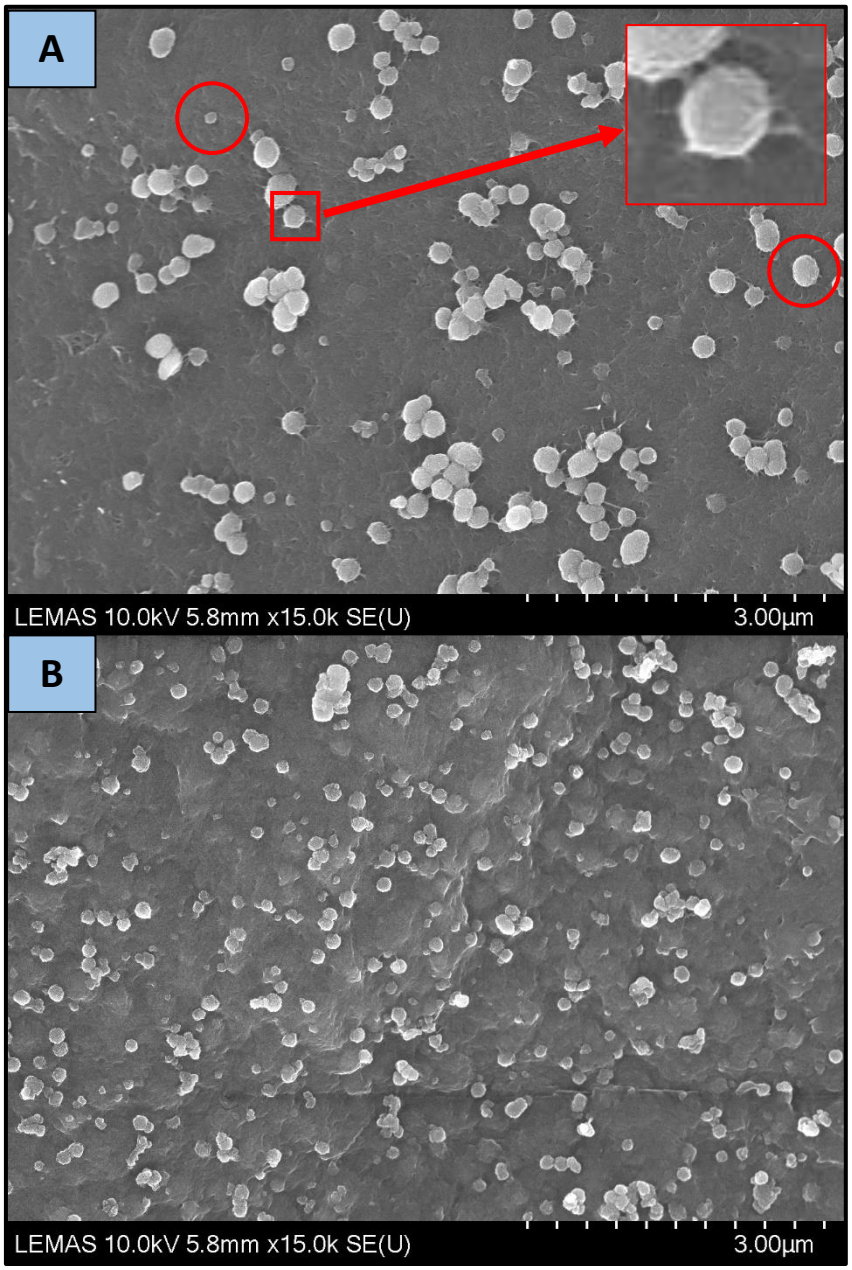


Figure 2.19. Agarose fragments displaying particles from the CaP cryogel sample. Particles highlighted in red demonstrate hexagonal-like morphologies.

Using greater magnification, the nanotopography of particles was visualised. As shown in Figure 2.20, the surface of CaP particles demonstrated a high surface roughness, which – combined with spherical and irregular particle morphology - is an indicator of low particle crystallinity. Though one must consider the effect of the 5 nm iridium coating at this magnification, the utility of iridium in ultra-high resolution SEM imaging is due to its very fine grain size and should therefore not be resolvable at this magnification.

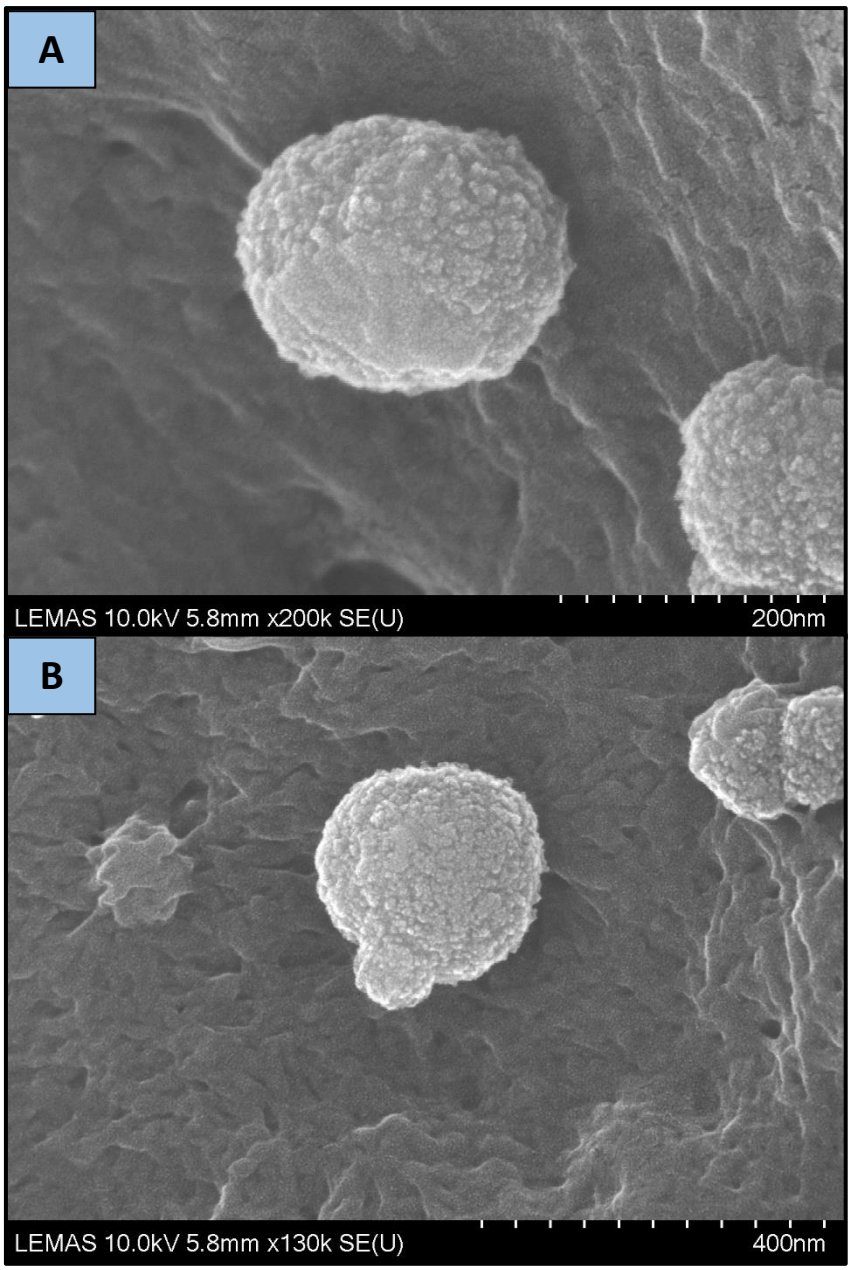


Figure 2.20. High magnification images of particles from the CaP cryogel sample.

Interestingly, the particle in Figure 2.20 (B) appears to be comprised of one large and one small particle that could have coalesced during growth or via their collision during transport by the electric field. Particles with such morphologies are commonplace in the CaP cryogel sample and will therefore have made some contribution toward increasing the mean particle diameter.

The mean diameter and aspect ratio of particles embedded in the CaP group sample was 211 ± 59 nm and 1.15 ± 0.12 respectively (n = 912). This mean particle diameter is similar to the 191 nm pore diameter of Seakem® LE agarose calculated by Narayanan et al. (2006) (value extrapolated from graphical data). A histogram representing the diameters of particles from CaP samples is shown in Figure 2.21. The histogram demonstrates unimodality with a slight negative skew given that 47 % of particles are smaller than the modal bin (modal bin has a centre of 216 nm) and 41 % are larger than the modal bin. Note that the median diameter is 203 nm. The particle diameter dataset for the CaP sample is non-uniformly distributed (95 % confidence intervals).

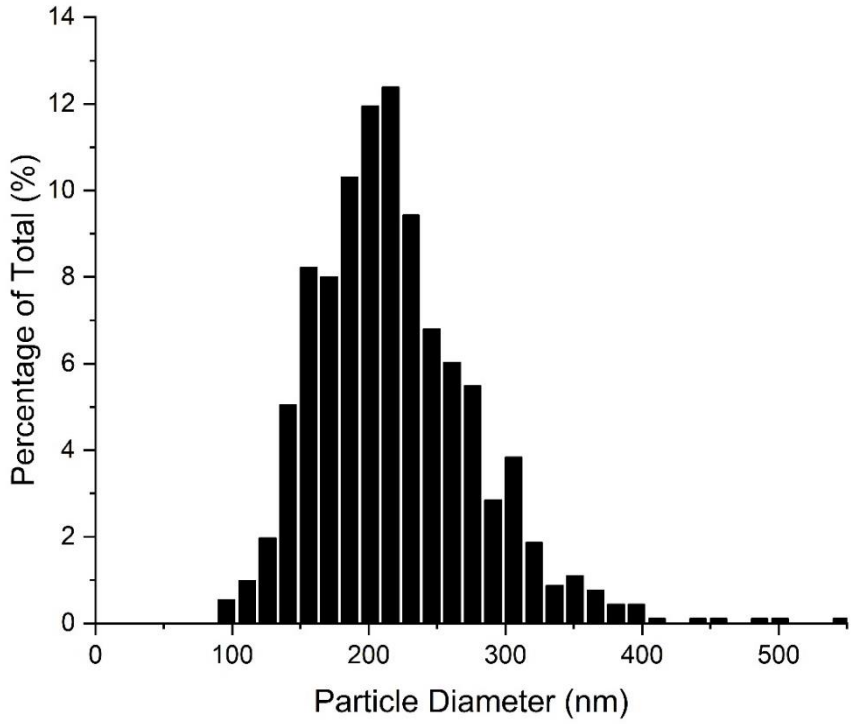


Figure 2.21. Histogram for particles from the CaP sample (n = 912). Data is non-uniformly distributed (95 % confidence intervals).

EDS data was also acquired during SEM imaging for each sample. However, the agarose surface was very sensitive to the high accelerating voltage and beam current required to produce X-rays of a sufficient count rate for reliable EDS data collection. Since low magnification had to be used to prevent rupturing the agarose surface, little elemental resolution of particles could be obtained. For these reasons, EDS analysis was abandoned. EDS maps are therefore omitted here but are provided in the Appendix Figure 6.1 and Figure 6.2 for CaP and pDNA/CaP groups respectively.

2.4.4.5 pDNA/CaP Cryogel Group

Particles from the pDNA/CaP sample were comparable to those of the CaP sample with regards to packing density, morphology, and diameter. Between different agarose fragments, packing densities and diameters clearly vary, as with the CaP sample. For example, the particles in (A) range approximately between 250 – 450 nm, whilst those in Figure 2.23 (B) range between 150 – 350 nm. Though the particle diameter range is greater for the fragment in (A), these particles appear more consistent in their size. Overall, the mean particle diameter and aspect ratio was 226 ± 92 nm and 1.14 ± 0.11 respectively (n = 1105).

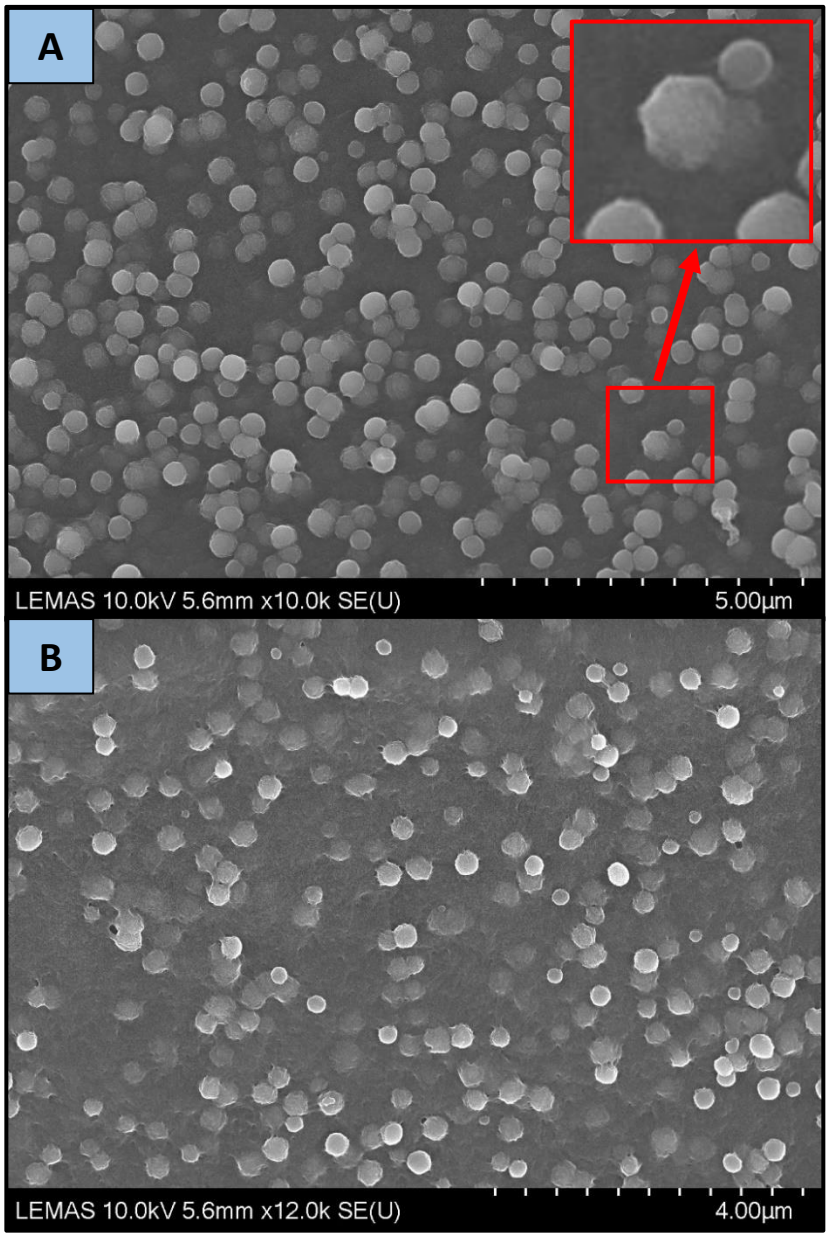


Figure 2.23. Particles from the pDNA/CaP cryogel sample. Particle highlighted in red square demonstrate a hexagonal-like morphology.

Particles in Figure 2.23 (A) appear more uniform in their sphericity and have fewer particles with faceted edges, though a small number of particles – such as the example highlighted in red - have hexagonal-like morphologies. Overall, more irregular morphologies are observed in Figure 2.23 (B). For both CaP and pDNA/CaP cryogel samples, smaller particles consistently demonstrate fewer uniform morphologies which hints at reducing crystallinity with reducing particle diameter.

The histogram for pDNA/CaP particle diameters is shown in Figure 2.24. The data shows bimodality since primary and secondary modal bins (peaks) are observed. The primary modal bin has a centre of 219 nm and represents 11.7 % of particles in this sample, whilst the secondary modal bin has a centre of 105 nm and represents 4.5 % of particles. Since almost 57 % of particles are greater than the primary modal bin, the histogram has a slight positive skew. The median particle diameter is 236 nm and the mean particle diameter is 226 nm ± 92 (n = 1105).

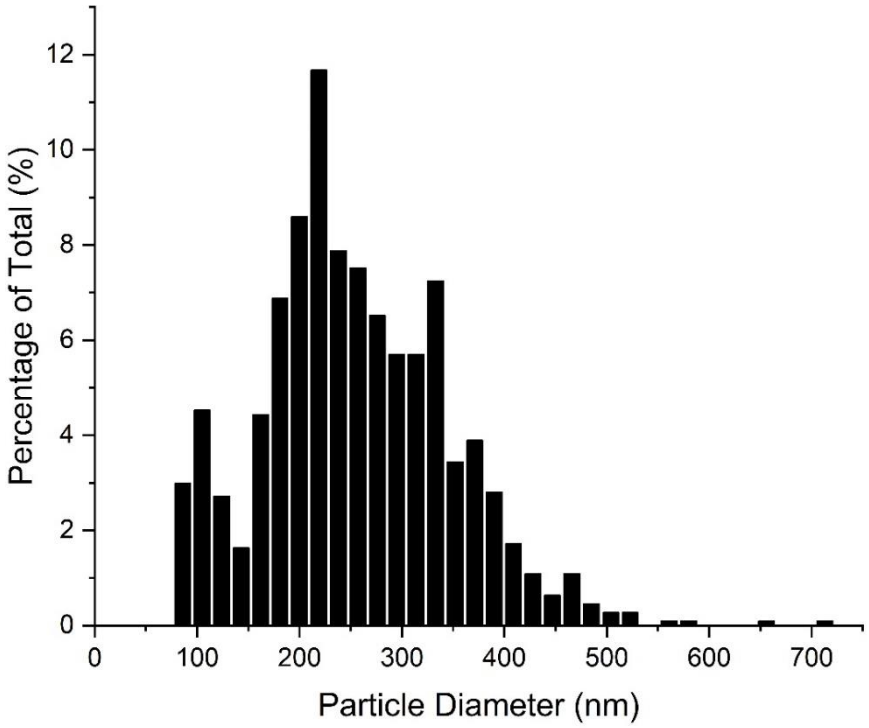


Figure 2.24. Histogram for particles from the pDNA/CaP sample (n = 1105). Data is non-uniformly distributed (95 % confidence intervals).

There appears to be a transition of unimodality to multimodality from the CaP to pDNA/CaP sample due to the addition of pDNA. The primary modal bin remains approximately the same, shifting from 216 nm for the CaP sample to 219 nm for the pDNA/CaP sample, but with the addition of a secondary modal bin centre at 105 nm for the pDNA/CaP sample.

The proposed mechanism through which this occurs is that pDNA molecules interfere with nucleation and growth of particles and act as nucleation centres. As nucleation centres, the addition of pDNA will increase the number of nuclei within the gel per unit volume during synthesis, thereby reducing free ions and particle growth potential. If pDNA also act as capping agents, pDNA would kinetically limit the growth of particles, but this is unlikely given the affinity of Ca^{2+} ions to pDNA. Hence pDNA molecules on CaP surfaces may not prevent more CaP nucleating on their phosphate backbone.

2.4.4.6 PDA-blank and PDA-pDNA Cryogel Groups

PDA-blank and PDA-pDNA samples were identical in appearance given that pDNA was not observed in both samples. The PDA-blank and PDA-pDNA samples appeared similar to blank and pDNA samples at low magnification, but at higher magnifications a rough surface topography is revealed (Figure 2.25 (B)) which is likely a result of the PDA coating. This rough surface topography is not observed in any uncoated sample when imaged under the same conditions (SE, 2.0 kV, ≥ x10 k magnification).

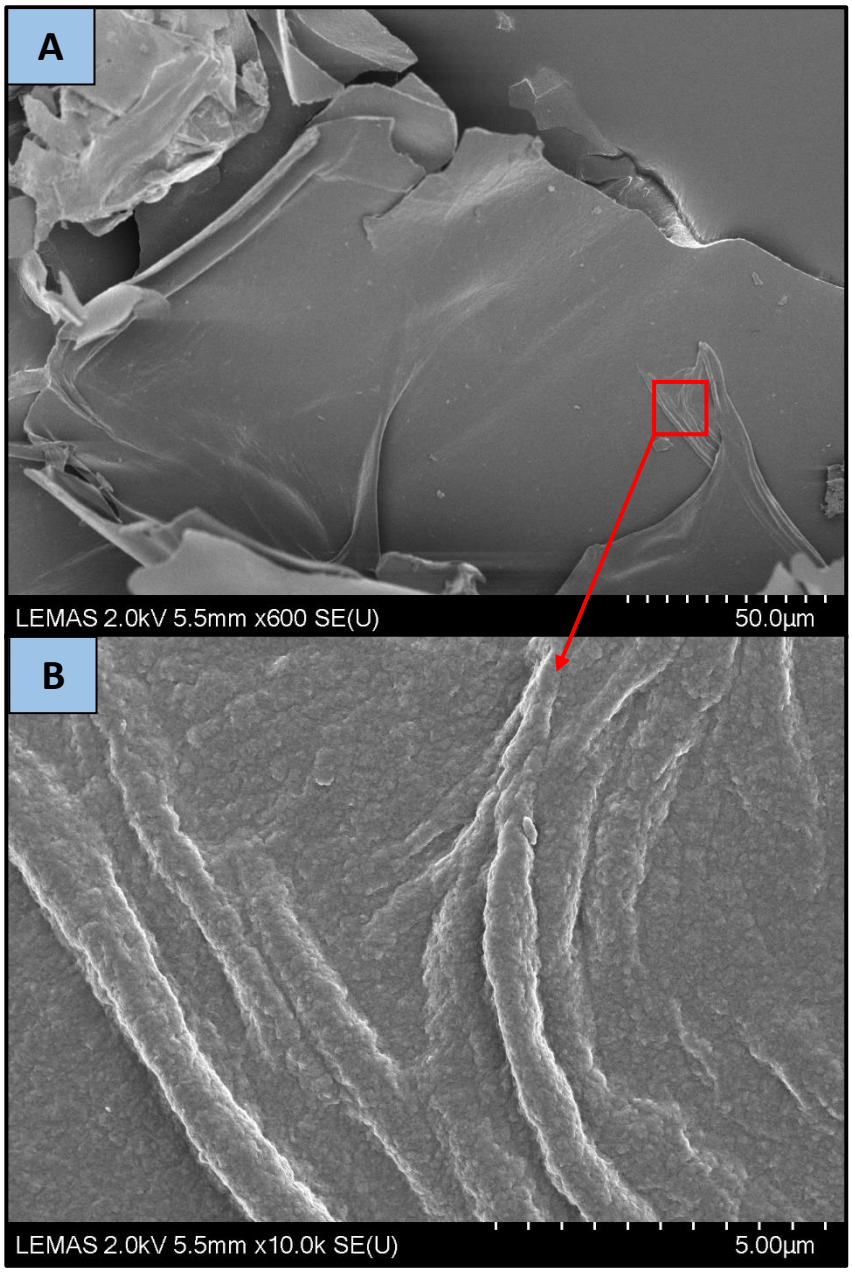


Figure 2.25. SE images of a PDA blank sample. (A) Low magnification image of a fragment and (B) a high magnification image of the rough surface highlighted in red square.

2.4.4.7 PDA-CaP Cryogel Group

Particles from the PDA-CaP group demonstrated several similarities to those in CaP and pDNA/CaP groups, in that particles varied in size, morphology and packing density between agarose fragments. Figure 2.26 (A) shows particles from the same agarose fragment at different magnifications, ranging from 50 - 300 nm, boasting regular, spherical morphologies. The packing density of particles in Figure 2.26 (A) is non-uniform, with most particles appearing above the agarose surface.

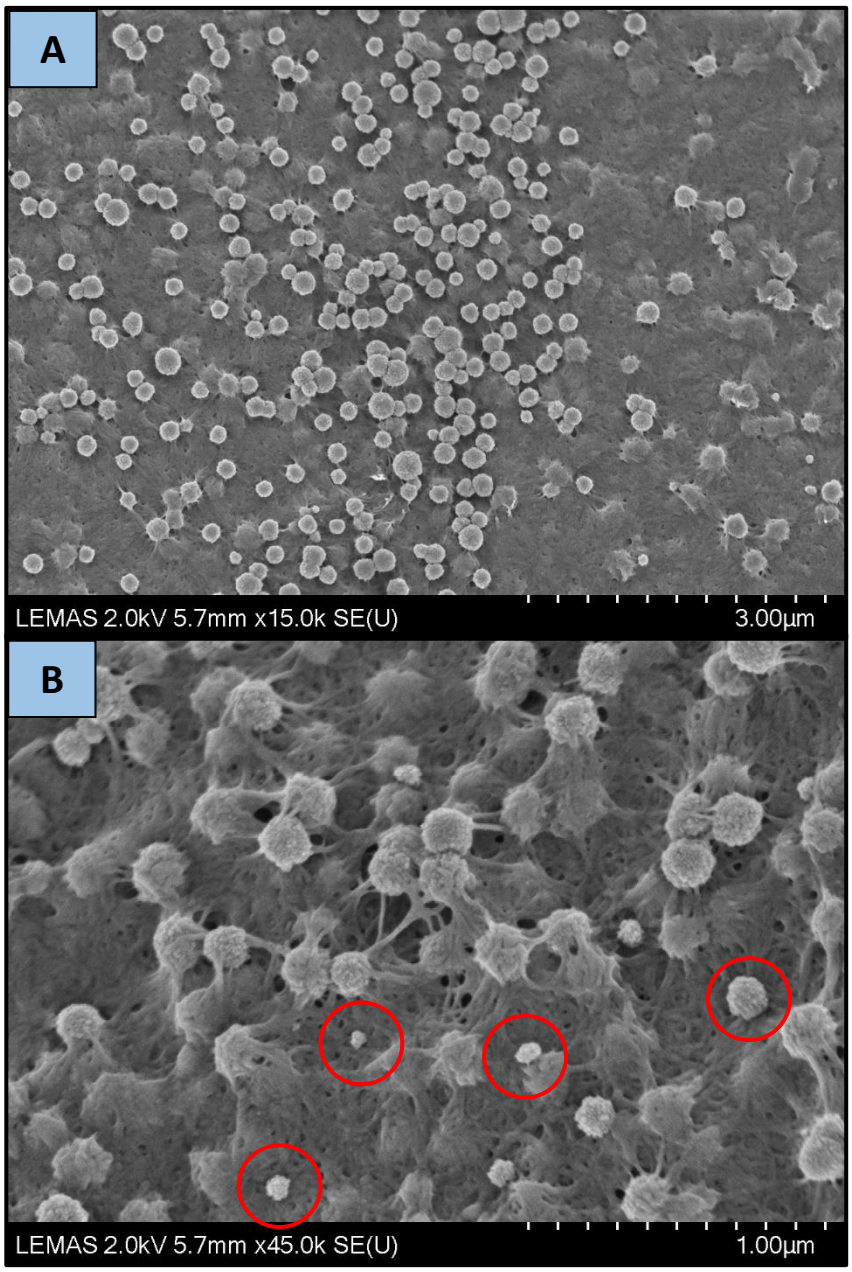


Figure 2.26. SE images of particles from PDA-CaP group of the same agarose fragment. Red circles indicate particles that present little attachment to the agarose surface.

Upon closer inspection of the same agarose fragment (Figure 2.26 (B)), a rough particle topography is revealed where particles resemble clustered nodules. Agarose fibres appear to anchor to surface particles, whilst others appear to envelop particles completely and make them appear sub-surface. Some fibres close to particles appear to be thickened by a coating, which is possibly CaP since greater density to surrounding agarose would explain their more intense appearance than other fibres. For some particles, there is an absence of agarose fibre attachment, indicated by red circles. The two distinct particle types therefore present are: (1) particles anchored to fibres (fibrous); and (2) particles with no fibrous attachments (unbound). This author suggests that fibrous particles remain at their nucleation site during synthesis and coat neighbouring fibres whilst unbound particles are transported (either electrophoretically or during lyophilisation/sterilisation) to their final locations in these images.

As with the CaP and pDNA/CaP samples, the PDA-CaP sample displays variation in particle size, morphology and packing density between agarose fragments. Figure 2.27 shows an agarose fragment with much smaller particle sizes than those observed in Figure 2.26, ranging from approximately 40 – 200 nm with some larger agglomerates, with most particles appearing slightly embedded into the surface. The morphologies of these particles are far less regular than in Figure 2.26 (A), since faceted and straight edges are commonplace with particles throughout the fragment. Localised agglomerates can be seen, as indicated by red circles, which comprise of much larger particles measuring up to 200 nm in diameter.

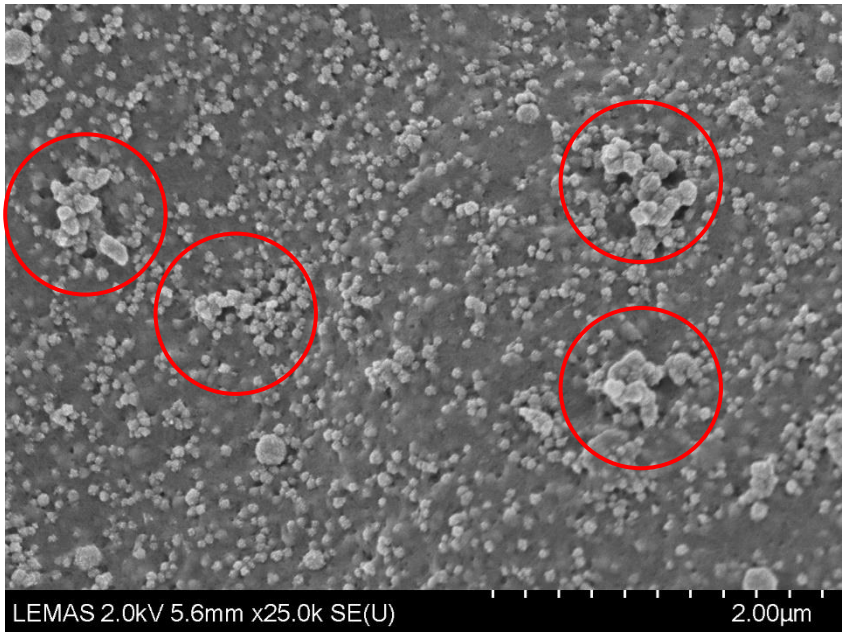


Figure 2.27. SE image of particles from the PDA-CaP cryogel group. Red circles indicate large agglomerates.

Some agarose fragments from the PDA-CaP sample revealed much larger particles, such as in Figure 2.28 below. Here, particles have a wide size distribution from 100 – 500 nm and a high packing density that appears to stack particles on top of each other in some areas. There is also some tessellation occurring between particles, as indicated by red circles, which can emphasise the almost hexagonal morphologies of some mid-sized to larger particles.

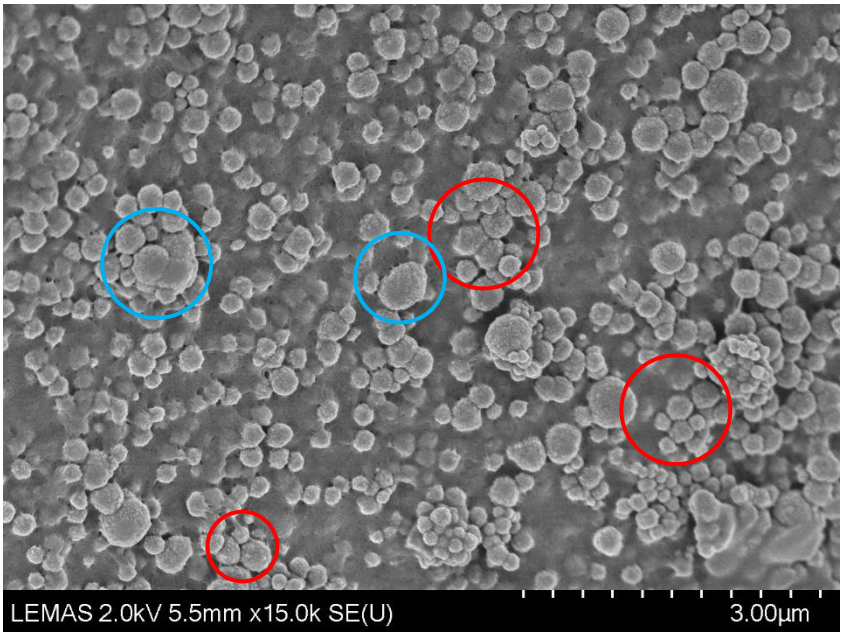


Figure 2.28. SE image of particles from PDA-CaP cryogel sample. Red cicles indicate particles of hexagonal-like morphologies and blue circles indicate coalesced particles.

There is also some evidence of particle coalescence, as indicated by particles highlighted in blue circles. Faint lines down the centre of these larger particles suggest the coalescence of two smaller particles. This is frequently observed in samples with larger agarose particles and has previously been demonstrated in Figure 2.20 (B).

Figure 2.29 shows the histogram for particle diameters from the PDA-CaP sample (n = 661). The data shows bimodality, with a primary modal bin centre at 198 nm representing 15.4 % of all particles and a secondary modal bin centre at 93 nm representing 5.7 % of all particles. Since 52.7 % of particles are smaller than the primary modal bin, the data demonstrates a positive skew. The median diameter is 173 nm and the mean diameter is 172 ± 73 nm.

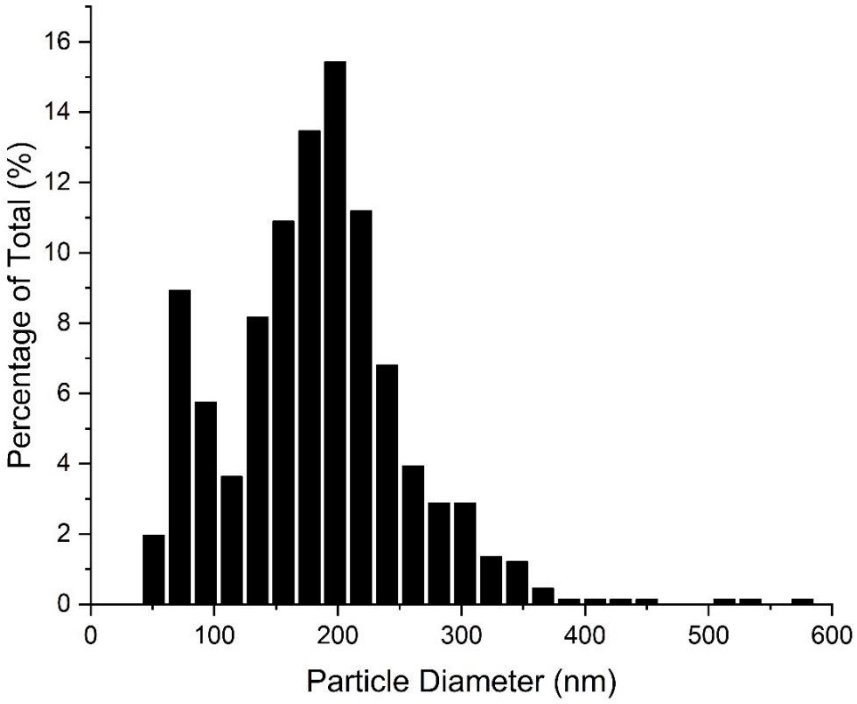


Figure 2.29. Histogram for particles from the PDA-CaP sample (n = 661). Data is non-uniformly distributed (95 % confidence intervals).

2.4.4.8 PDA-pDNA/CaP Cryogel Group

Particles from an agarose fragment belonging to the PDA-pDNA/CaP sample are shown in Figure 2.30. Here, particles are highly agglomerated, non-surface bound by anchoring fibres, and have a large size distribution from 100 – 700 nm. At this magnification, the rough surface topography of particles is clearly observed. Interestingly, some particles present beam flattening, as indicated by green circles. Such effects may result from charging effects due to poor conductive, possibly arising from a non-uniform surface coating. Beam flattened particles are unlikely to be a different particulate species more sensitive to the electron beam given their size and morphology are highly similar to neighbouring particles.

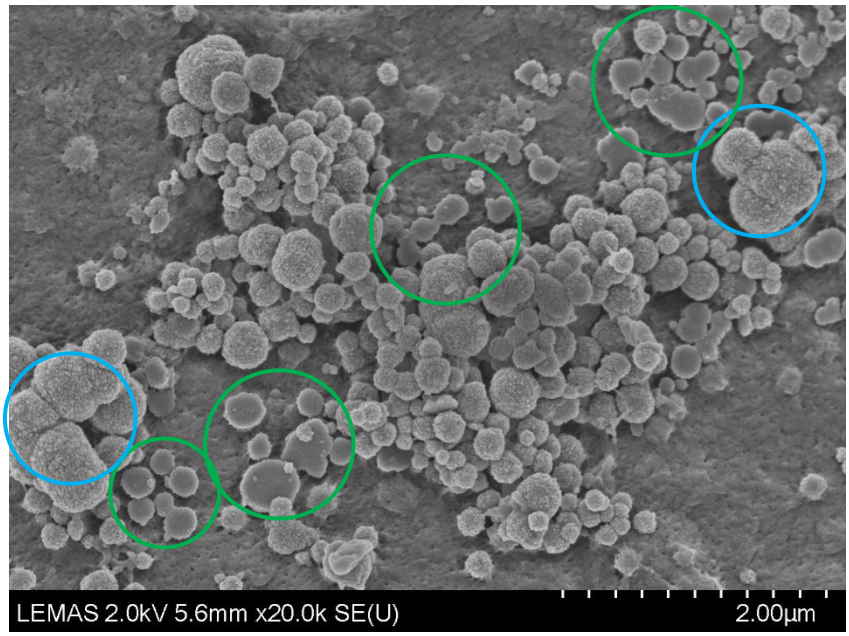


Figure 2.30. SE image of particles from the PDA-pDNA/CaP cryogel sample. Coalesced particles are highlighted in blue and evidence of beam flattening is highlighted in green.

Elsewhere in the agglomerate, evidence of coalescence is observed (blue circles) involving larger particles, similar to those in Figure 2.28. The stacking and agglomeration of particles in this agarose fragment could further the claim that some particles are mobilised from their original nucleation location and transported elsewhere either during synthesis or lyophilisation/sterilisation.

Particles from two separate agarose fragments are shown in Figure 2.31. Those in Figure 2.31 (A) range between approximately 40 – 140 nm and have irregular morphologies, whilst those in

Figure 2.31 (B) range from 80 – 500 nm and have highly spherical morphologies. More beam flattening effects are observed in Figure 2.31 (A), highlighted by the green circle.

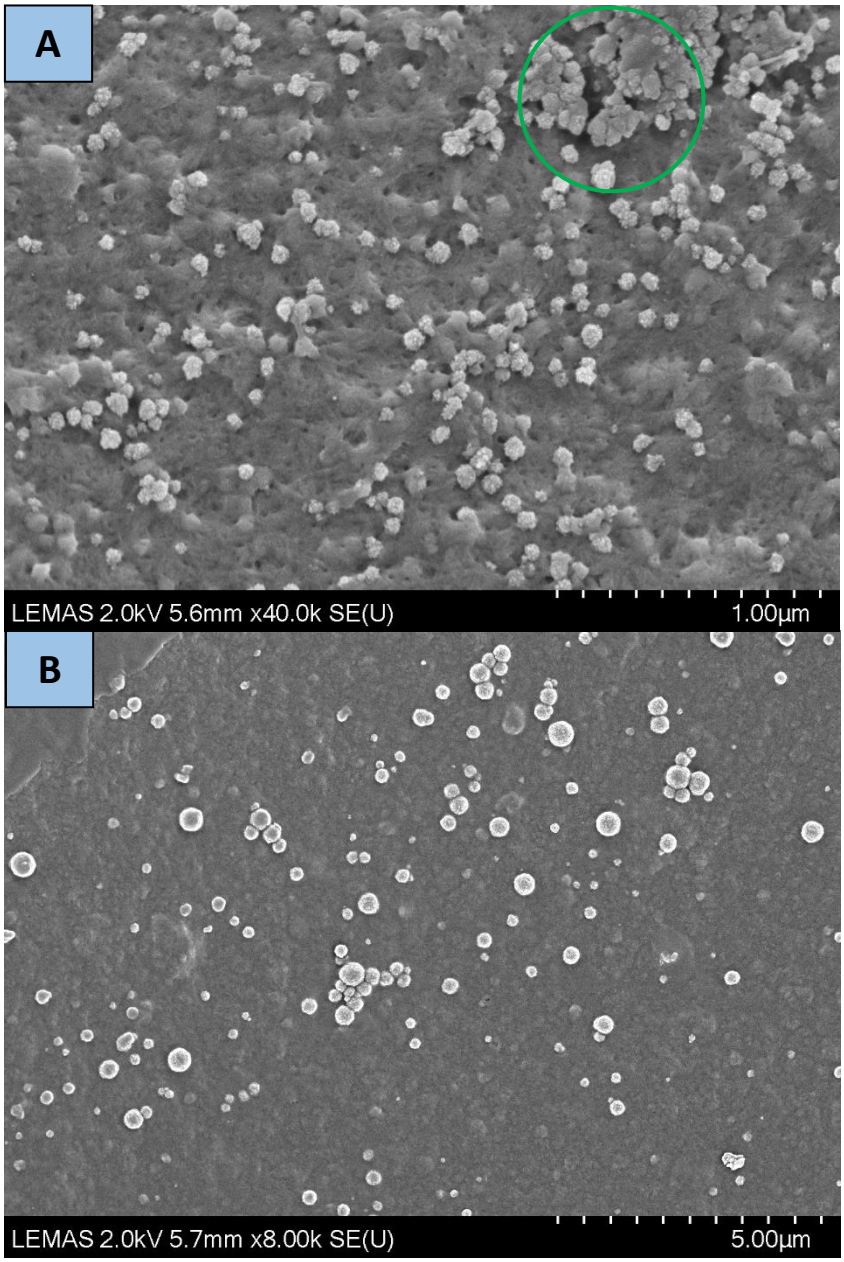


Figure 2.31. SE images of particles from separate agarose fragments in PDA-pDNA/CaP cryogel sample. (A) Small, sub-150 nm particles and (B) large, 80 – 500 nm particles. Evidence of beam flattening is highlighted in green circles.

The particle packing density between these two agarose fragments are quite contrasting. Those in Figure 2.31 (B) are mostly more than 1 µm from their nearest neighbour, compared to those in Figure 2.31 (A) that are generally within 100 nm of their closest neighbouring particle.

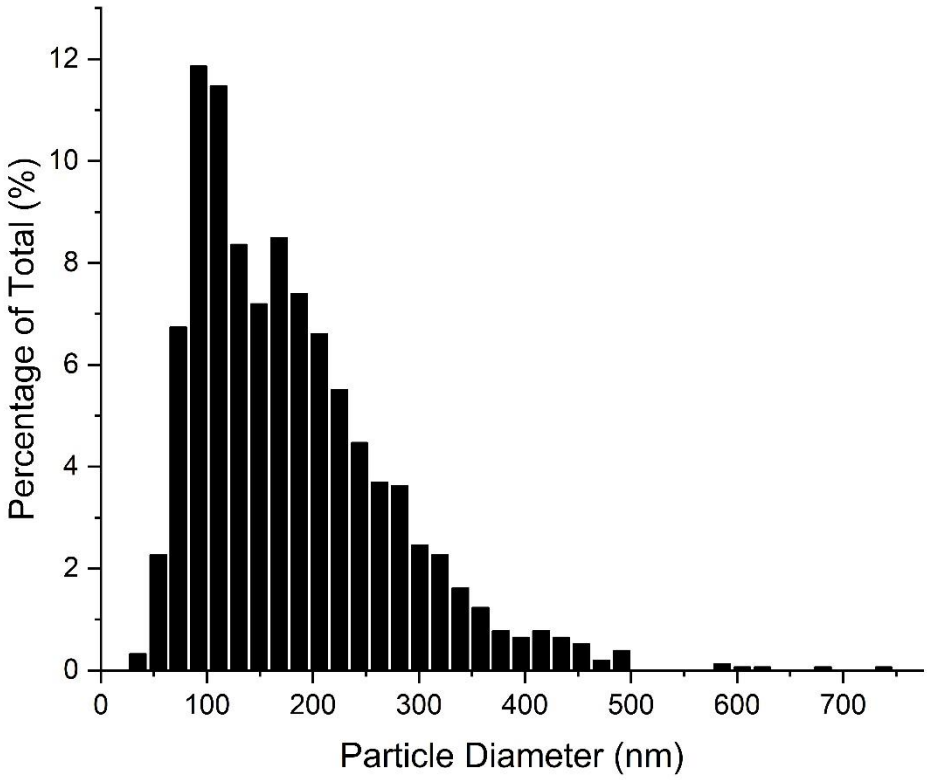


Figure 2.32. Histogram of particle diameters from the PDA-pDNA/CaP sample.

Figure 2.32 shows the histogram for particle diameters from the PDA-pDNA/CaP sample. Unlike the histogram for the PDA-CaP sample (Figure 2.29), particle diameter data for the PDA-pDNA/CaP sample is unimodal with the modal bin centre at 92 nm. The histogram has a positive skew given 79 % of particles are larger than the modal bin. The median particle diameter is 152 nm and the mean particle diameter is 171 nm ± 94 nm.

There appears to be a shift from the bimodality of the PDA-CaP sample to the unimodality of the PDA-pDNA/CaP sample. However, it is theorised that the addition of pDNA and PDA result in multi-pathway nucleation and growth and hence a particle size distribution that is so multimodal it appears unimodal. This suggests that the introduction of pDNA is again affecting the nucleation and growth of particles. As with the pDNA/CaP sample, it is theorised that pDNA molecules within the PDA-pDNA/CaP cryogel group act as additional nucleating surfaces that increase the total nuclei per unit volume during synthesis and therefore limit the overall growth potential of particles.

2.4.4.9 Summary of SEM Data

The centres of primary and secondary modal bins have been taken from the histograms of CaP, pDNA/CaP, PDA-CaP, and PDA-pDNA/CaP samples and plotted in Figure 2.33 below. Primary modal bins are taken simply as the largest bin, whilst secondary modal bins are taken as the largest modal bin from the secondary peak. In the case of the unimodal data produced for the CaP sample, or for the unimodal-resembling data of the PDA-pDNA/CaP samples, only primary modal bins are extracted.

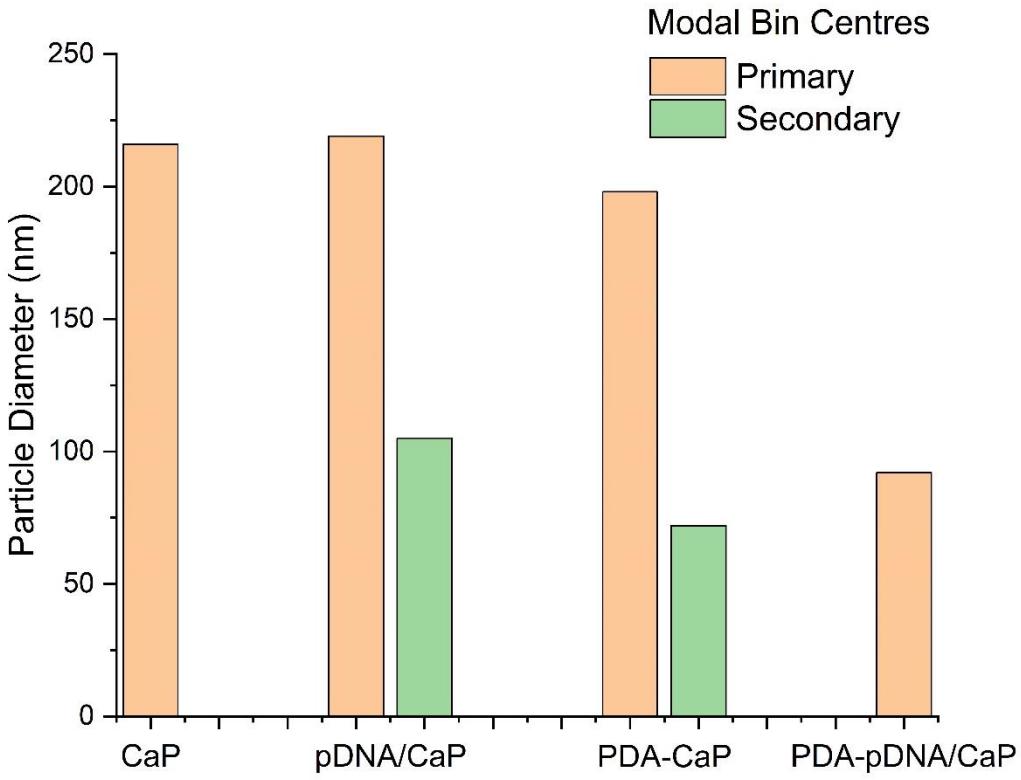


Figure 2.33. Modal bin centres for particle diameters from cryogel samples.

The pDNA/CaP sample has a slightly larger primary modal bin centre of 219 nm compared to that of the CaP sample (216 nm), but with the addition of a smaller, secondary modal bin centre at 105 nm. The addition of pDNA to CaP therefore shifts the particle size distribution from unimodal to bimodal with the introduction of a smaller particle population. This is theorised to result from pDNA acting as additional nucleation centres for CaP that consequently reduce the growth potential of CaP particles. The PDA-CaP sample presents similar (but slightly smaller) primary and secondary modal bin centres (198 nm and 72 nm respectively) to the pDNA/CaP sample. This suggests that the addition of the PDA coating reduces the primary and secondary

modal diameters of the CaP sample more significantly than the addition of pDNA. PDA therefore has a more substantial effect on particle nucleation than pDNA.

The effects of the combinative additions of pDNA and PDA are seen when comparing CaP and PDA-pDNA/CaP samples. The particle size distribution remains unimodal but becomes negatively skewed where the primary modal bin centre reduces from 216 nm to 92 nm. This is assumed to be a multi-pathway effect, where pDNA molecules are both mobile and bound to PDA surfaces, hence pDNAs could operate as nucleation centres on surfaces and in solution. Since it is theorised that a compound effect of pDNA and PDA of nucleation and growth of CaP particles is taking place, it would make sense that secondary and tertiary peaks could be hidden behind the strong primary peak. Hence the PDA-pDNA/CaP sample is theorised to be multimodal.

The mean particle diameters (± SD) for all samples are displayed in Figure 2.35. The CaP sample boasts a smaller mean particle diameter (212 ± 59 nm) than the pDNA/CaP sample (226 ± 92 nm), whilst the PDA-CaP and PDA-pDNA/CaP samples are highly similar (172 ± 73 nm and 171 ± 94 nm respectively). Whilst these mean values allow for a general comparison of each dataset, they are less descriptive of CaP particle diameters, given the presence of uni- and multimodality within datasets, as well as non-uniform distributions.

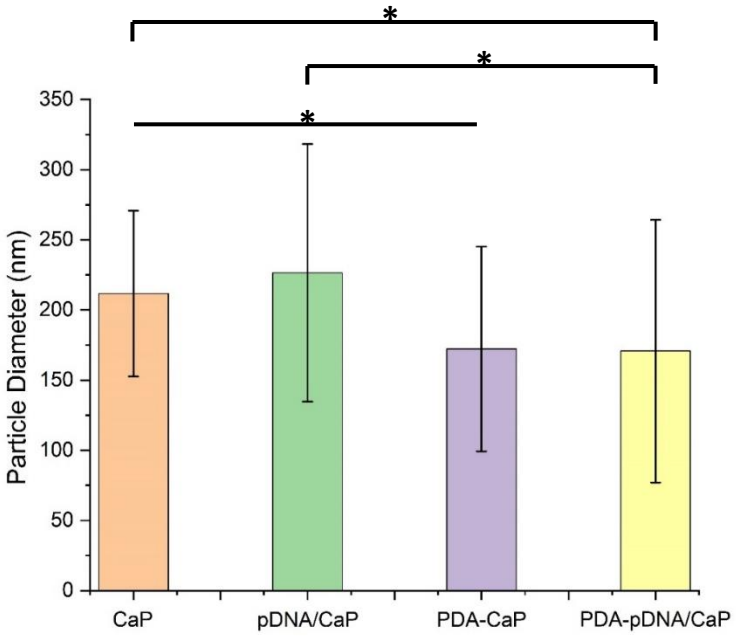


Figure 2.35. Mean particle diameters (± SD) for cryogel groups. Errors bars indicate standard deviation. * Indicates statistical difference (95 % confidence intervals).

2.4.5 pDNA Encapsulation Efficiency

Encapsulation efficiency of pDNA in different cryogel groups was determined by measuring and comparing the pDNA release from cryogels into different separate buffers using a PicoGreen™ dsDNA assay kit. Figure 2.37 shows the release of pDNA (µg) from pDNA, pDNA/CaP, PDA-pDNA, and PDA-pDNA/CaP cryogel groups. For both sets of standards (prepared with either control or decalcification buffer), the linear fit of the standard curves had $R^2 > 0.999$.

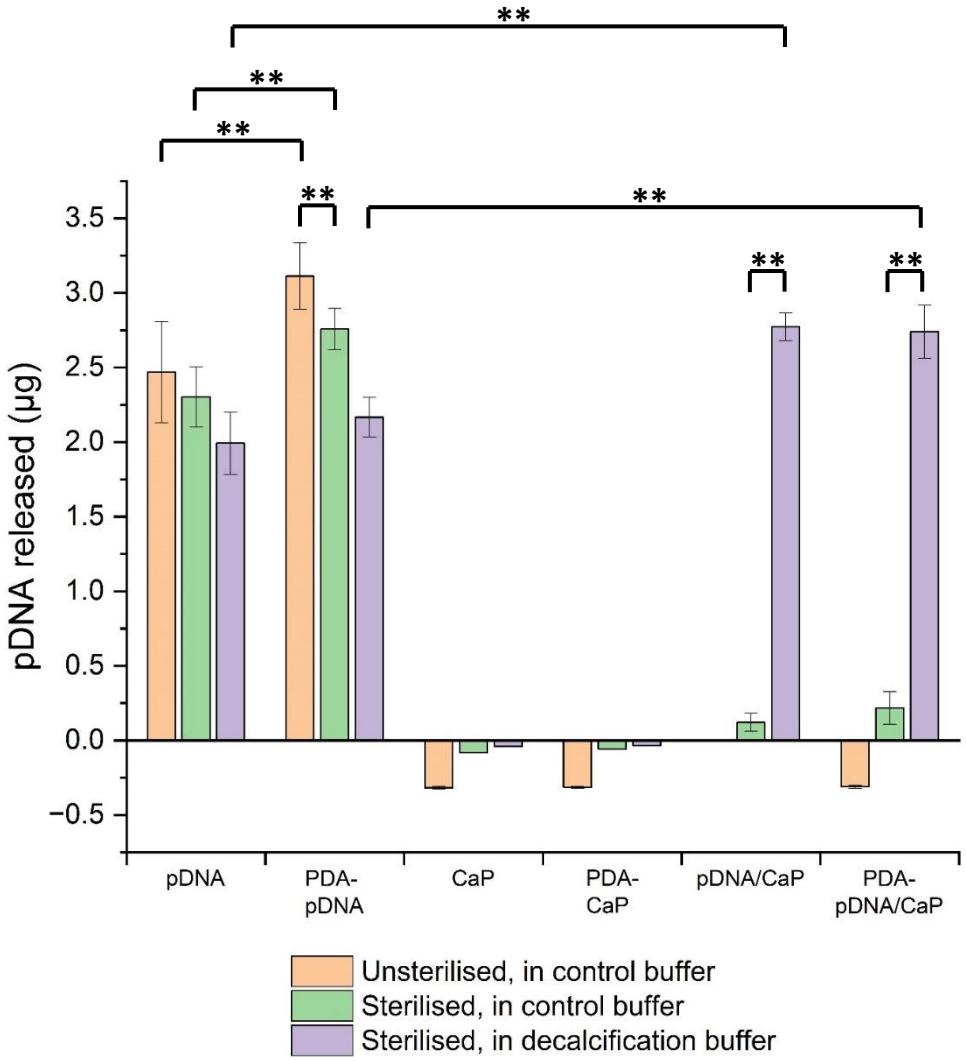


Figure 2.37. Total pDNA release (µg) from uncoated and PDA-coated cryogel groups. Orange: unsterilised cryogels submerged in control buffer. Green: sterilised cryogels submerged in control buffer. Purple: sterilised cryogels submerged in decalcification buffer. ** Indicates statistical difference (99 % confidence intervals).

pDNA release for pDNA and pDNA/CaP cryogel groups are calibrated against the blank cryogel group, whilst PDA-pDNA and PDA-pDNA/CaP cryogel groups are calibrated against the PDA-blank group. pDNA groups released between 2 – 2.5 µg of pDNA, where the most pDNA was

released from the unsterilised cryogels into control buffer (2.7 μg), followed by sterilised cryogels into control buffer and sterilised cryogels into decalcification buffer. A similar observation is seen for the PDA-blank group, with the most pDNA released from unsterilised cryogels into control buffer (3.1 μg), followed by 2.8 μg released by sterilised cryogels into control buffer and 2.2 μg released into decalcification buffer.

It is interesting that the PDA-pDNA cryogel appears to release more pDNA than the 2.5 μg pDNA initially loaded into the gel. This is not due to an imbalanced calibration toward blank and PDA-blank groups, given negligible pDNA release was measured for both controls (data not shown). It is possible that the interaction of pDNA and mobile PDA fragments caused some amplification of the fluorescent signal to artificially enhance the mass of pDNA released.

The stepwise reduction of pDNA release from the unsterilised, control, and decalcification cryogels in the pDNA and PDA-groups is similar, where the least pDNA is released into decalcification buffer. Given that the standards for control and decalcification cryogels were prepared with the appropriate buffers, it is unlikely that the reduced pDNA release in decalcification buffer is due to the PicoGreen™ assay being desensitised to pDNA in the presence of EDTA. Instead, this author suggests that the decalcification buffer reduces the diffusion of pDNA from pDNA and PDA-pDNA cryogels due to higher viscosity.

Assuming that the pDNA release for the unsterilised cryogels from pDNA and PDA-pDNA groups is 100 % of the pDNA encapsulated within the hydrogel, there is a loss of 0.17 ± 0.2 μg and 0.36 ± 0.14 μg of pDNA from these groups respectively due to the sterilisation process. These values represent a 6.7 % and 11.4 % loss of pDNA from the pDNA and PDA-blank groups respectively.

As expected, there is negligible release of pDNA from CaP and PDA-CaP cryogel groups. The greater negative values observed for unsterilised cryogels for both groups may simply be due to these cryogels containing more salts (Na_2HPO_4, $CaCl_2$, NaOH) that have not been washed out due to the sterilisation process. Despite these salts not being listed in the PicoGreen™ protocol as influencing fluorescence signal, their presence could reduce the sensitivity of the assay toward pDNA.

The pDNA/CaP and PDA-pDNA/CaP groups demonstrate the greatest release in the decalcification buffer, measuring 2.77 ± 0.09 μg and 2.74 ± 0.18 μg respectively. In contrast, the pDNA release into control buffer for the pDNA/CaP group is 0.12 ± 0.06 μg, whilst 0.22 ± 0.11 μg is released by the PDA-pDNA/CaP group. There is negligible release from the unsterilised

pDNA/CaP cryogel group, and the PDA-pDNA/CaP displays a small negative value (-0.311 μg) almost identical to that of the PDA-CaP group (- 0.315 μg).

The stark difference between the amount released into control and decalcification buffer indicates the presence of EDTA is required to decalcify the cryogel and release the encapsulated pDNA, and therefore that CaP is either encapsulating or strongly adsorbing pDNA. The limited release of pDNA from pDNA/CaP and PDA-pDNA/CaP cryogel groups into control buffer also suggest that the majority of pDNA is either encapsulated or prevented from diffusing out of the cryogel due to remineralisation of released pDNAs. Together, the pattern of pDNA release from the pDNA/CaP and PDA-pDNA/CaP groups into control and decalcification buffers provide evidence the pDNA is strongly associated with CaP. Furthermore, the greater release of pDNA from the pDNA/CaP cryogel group compared to the pDNA cryogel group, and the greater release of pDNA from the PDA-pDNA/CaP group compared to the PDA-pDNA cryogel group, together demonstrate the loading of $CaCl_2$ and resulting precipitation of CaP encapsulate a greater mass of pDNA with these CaP-containing cryogels.

The simplest method to calculate encapsulation efficiency of pDNA for pDNA/CaP and PDA-pDNA/CaP cryogel groups is the comparison of pDNA released into control and decalcification buffers using Equation 2.7 below:

$$Encapsulation\ efficiency(\%) = \left[1 - \left(\frac{pDNA\ release\ into\ control\ buffer}{pDNA\ release\ into\ decalcification\ buffer}\right)\right] \times 100\% \quad 2.7$$

Where $pDNA\ release\ into\ control\ buffer$ is assumed to measure the release of unabsorbed or un-encapsulated pDNA within the cryogel, and $pDNA\ release\ into\ decalcification\ buffer$ is assumed to be the release of all pDNA within the cryogel. Hence, Equation 2.7 provides the encapsulation efficiency (%) of pDNA. This equation was used to calculate the encapsulation efficiency of the pDNA/CaP and PDA-pDNA/CaP cryogel groups.

pDNA/CaP and PDA-pDNA/CaP have similar encapsulation efficiencies of 95.7 ± 3.2 % and 92.1 ± 6.0 % respectively. The lower encapsulation efficiency calculated for the PDA-pDNA/CaP cryogel group mostly stems from the slightly larger pDNA release into control buffer than that of the pDNA/CaP group.

2.4.6 Cytotoxicity Assays

LDH assays were used to measure LDH activity - an indicator for cytotoxicity – at a 48-hour time point. Raw data measurements were first calibrated against the cell media control, followed by calculation of cell viability for each cryogel group by comparing lysed and none-lysed sets. The cell viability for the blank control was measured to be 72.5 ± 2.4 %, which is the value all cryogel groups were baselined against. Cell viability for cryogel groups are plotted in Figure 2.38 below.

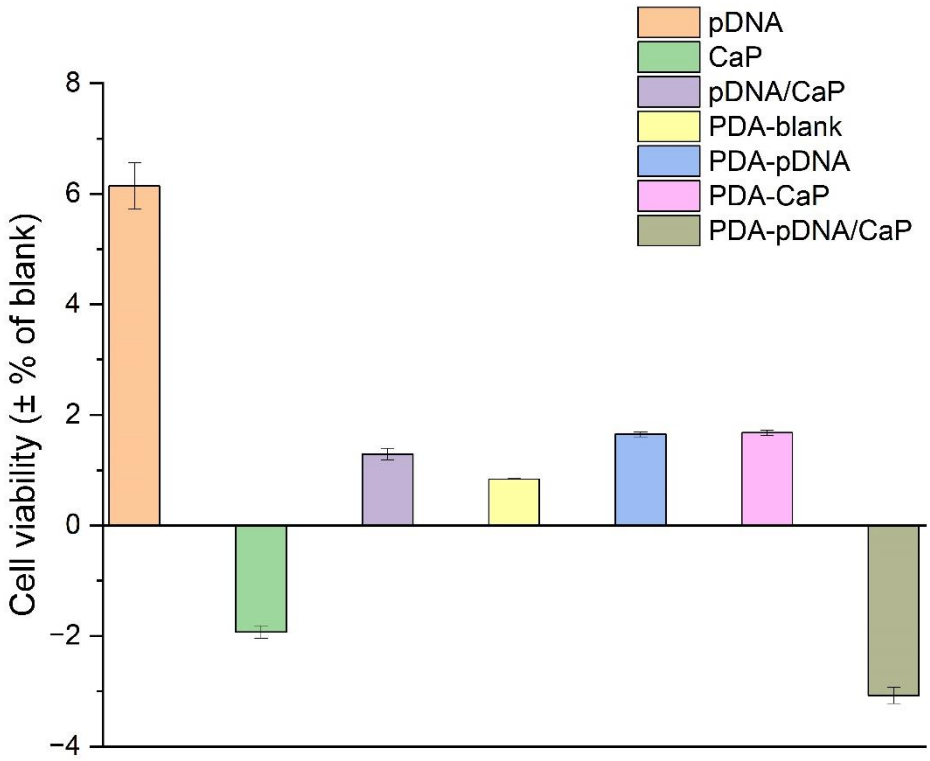


Figure 2.38. Cell viability of cryogel groups (± % of blank control) at 48-hours. No groups demonstrated any statistically significant differences to one another (including the blank control). Error bars indicate standard deviation.

All cell viabilities are within approximately + 6 % to -3 % of the blank control cryogel at this 48-hour time point, which makes comparisons between groups difficult. The pDNA group displays a cell viability of 6.14 ± 0.42 %, the largest cell viability of any group. The PDA-blank has comparatively lower cell viability of 0.83 ± 0.01 %. PDA-pDNA and PDA-CaP cryogel groups display comparable cell viabilities of 1.65 ± 0.05 % and 1.68 ± 0.05 ± respectively. Only the CaP and PDA-pDNA/CaP groups display negative cell viabilities of -1.93 ± 0.11 and -3.1 ± 0.15 % respectively.

Whilst it is somewhat possible to say that the PDA coating enhances cell viability compared to the blank control, no comparisons within this dataset are significant. Such similarities in cell viability may arise if cells are not able to infiltrate into cryogels prior to this time point and be exposed to the particulate contents within.

2.4.7 Transfection Assays

Transfection of cells within cryogels was determined by measuring luciferase activity at different time points. A mean value of luminescence for each cryogel group was first calculated (n = 4). Mean luminescence for pDNA, CaP, and pDNA/CaP groups was then baselined against the blank group, whilst the mean luminescence for the PDA-pDNA, PDA-CaP, and PDA-pDNA/CaP group were baselined against the PDA-blank group. Luminescence for each experimental group is therefore plotted as ± % luminescence of control in Figure 2.39 below.For both CaP and PDA-CaP cryogel groups, luminescence remains below 4% across all time points. pDNA and PDA-pDNA cryogel groups exhibit the greatest luciferase activity of all 6 groups, peaking at approximately 7 % (48-hours) and 8.5% (24-hours) respectively. Interestingly, both the pDNA/CaP and PDA-pDNA/CaP cryogel groups exhibit lower luminescence than the pDNA and PDA-pDNA groups respectively, which could indicate that luciferase activity is greater in the absence of CaP. As with cytotoxicity data, these results reveal relatively low changes in luciferase activity. This could be due to a combination of effects that will require discussion.

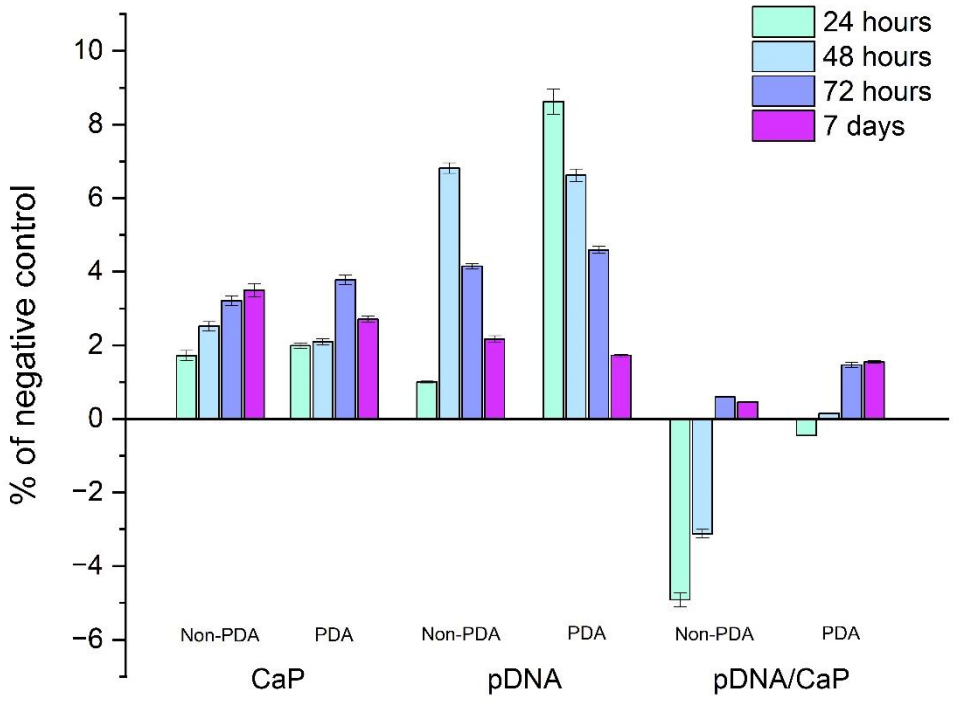


Figure 2.39. *Luciferase luminescence for cryogels as a +% of the negative control.*

2.4.8 SEM Analysis post In-vitro

pDNA/CaP and PDA-pDNA/CaP cryogels removed after 24-hours of being submerged in cell media were washed in 70 % EtOH and prepared for SEM analysis via powderisation. Figure 2.40 and Figure 2.49 below reveal particles from the PDA-pDNA/CaP and pDNA/CaP cryogels respectively following their incubation within cell media.

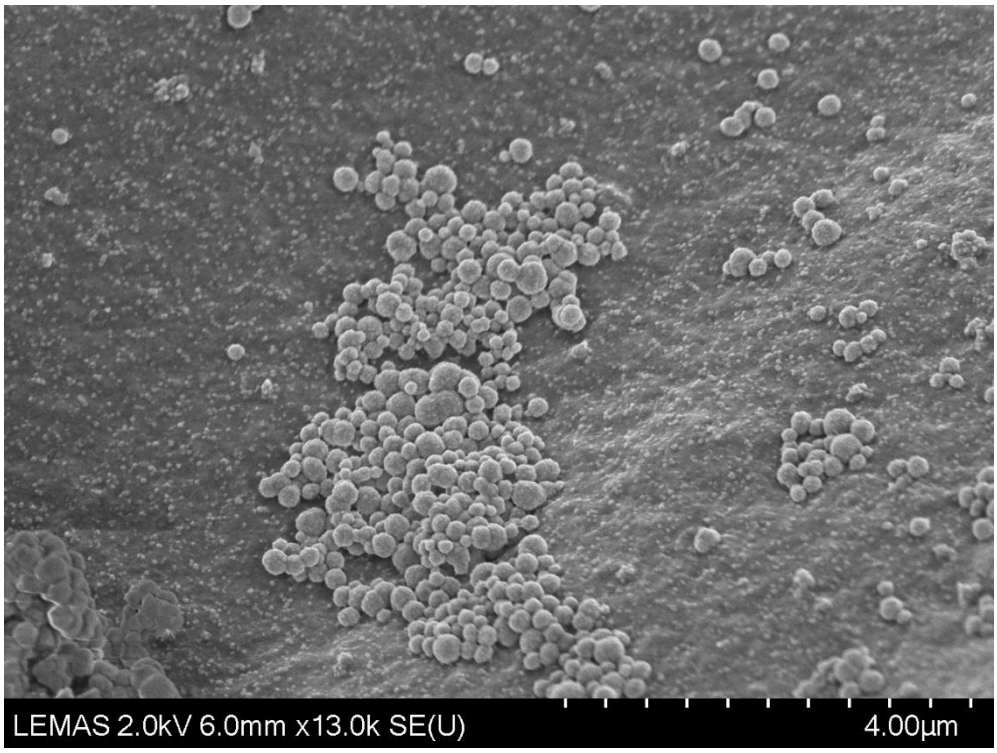


Figure 2.40. Particles on agarose fragments from the PDA-pDNA/CaP cryogel group after 24-hours in cell media.

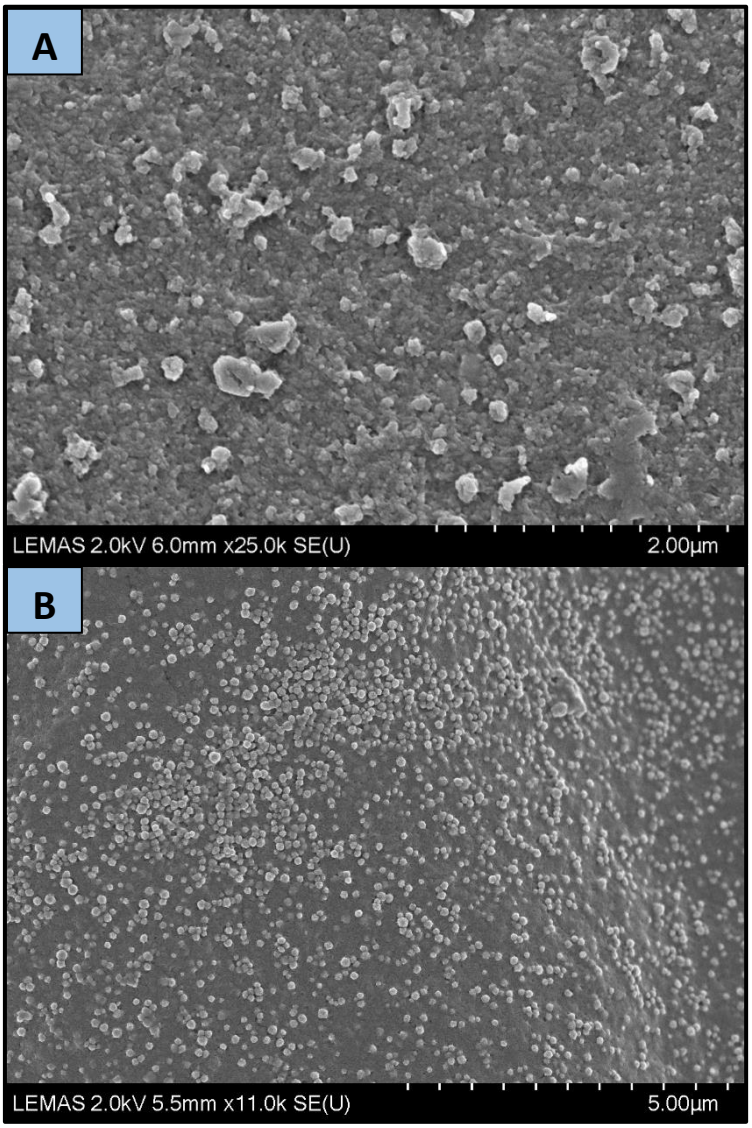


Figure 2.49. Particles on agarose fragments from the pDNA/CaP cryogel group after 24-hours in cell media

For the pDNA/CaP sample there appears to be partial transformation of particles from their initial spherical morphology, with new larger particles forming and a subset of smaller particles amongst the agarose fragment (Figure 2.49(A)). Meanwhile in Figure 2.49 (B) there appears to be retention of primary particle size and morphology, suggesting these particles may not have been exposed to cell media and perhaps embedded below the agarose cryogel surface. Figure 2.40 shows a similar pattern, where particles with the same size and morphology of primary particles can be seen, but with a large amount of sub-100 nm particles scattered across the agarose fragment. Based of these images, it seems that a dissolution/transformation of particles is occurring, as evidenced by large numbers of sub-100 nm particles not seen previously in SEM

analysis. However, it appears that a good portion of primary particles remain untransformed, which could mean they are shielded from cell media and hence cannot dissolve or transform.

2.5 Discussion

The PS-SW-AGE approach has been used as a novel synthesis route for pDNA/CaP particles embedded within PDA-coated agarose cryogels. The PS-SW-AGE approach utilises the effects of crystallisation in confinement and electric field-regulated ion transport; the combination of which effectively categorises the PS-SW-AGE approach as an electric field-assisted template synthesis route. This approach has been combined with a PDA-coating technique to surface-functionalise agarose hydrogels to encourage cell attachment as an alternative to FBN previously utilised by our group. PDA-pDNA/CaP agarose gels were subsequently lyophilised to form cryogels as potential osteogenic GAMs. These cryogels were characterised using SEM and XRD, as well as appropriate assays to determine pDNA encapsulation efficiency, cytotoxicity, and transfection efficacy toward C2C12 cells.

2.5.1 pDNA mobility

pDNA mobility was determined using post-staining with SYBR™ Safe DNA gel stain. At 6-minutes, pDNA bands in PDA-coated samples are easily visible, but beyond this time the bands become increasingly difficult to observe and hence distance measurements become unreliable. The reduced visibility of the pDNA bands in the PDA-agarose could arise due to an increased opacity of the gel (brought on by the PDA coating). Another proposed mechanism is that the complexation the pDNA with loose PDA fragments and adsorption of pDNA onto PDA surfaces reduce the effective concentration of pDNA with time, thus diminishing band intensity.

DNA is known to adsorb onto PDA surfaces via amine-phosphate interactions under acidic conditions that protonate amine groups, or via Ca^{2+}-bridges where Ca^{2+} ions act as an intermediary between an amine and phosphate pair. Given the buffer pH is 7.4 and is comprised of HEPES molecules, Na^{2+}, $H_xPO_4^{x-3}$, and OH^- ions, these are not 'ideal' conditions for pDNA adsorption, but protonated amine groups are likely still present given the buffer pH is close to neutral. Meanwhile, unabsorbed/residual PDA molecules and fragments that were not removed during the washing step could be forming complexes with pDNA molecules. Such complexes will reduce the sensitivity of the SYBRSafe™ stain to pDNA. This is well documented in the literature where pDNA band mobility is not only retarded at higher nitrogen-to-phosphate ratios but diminishes in intensity (Li et al., 2011, Hu et al., 2012, Yao et al., 2015, Chen et al., 2022).

The multi-banded appearance, which is more visible for the blank gel, is likely to be residual pDNA in the wells after each 6-minute interval. Given that the 60 V potential and large electrode

separation will result in small transport distances for the pDNA molecules, it is assumed that not all pDNA molecules will be loaded from the well into the gel. Hence, every 6-minutes a diminishing concentration of pDNA diffuses away from the well-gel interface and back toward the well bulk. The ladder appearance therefore results from the pDNA concentration in the well that reduces further every 6-minutes. Although this experiment produced an unusual pDNA band pattern, a slight contrast in pDNA mobility between uncoated and PDA-coated agarose gels over the first 6-minutes was determined. Despite the commensurable rate of pDNA transport in both gel types between 6- to 24-minutes, the y-axis offset shown in Figure 2.8 suggests that pDNA is transported a smaller distance into the gel when synthesising PDA-coated cryogel groups.

2.5.2 Cryogel appearance

The reduction in cryogel uniformity and overall size between lyophilisation steps probably results from the poor sublimation efficiency of 70 % EtOH used in the sterilisation step. 70 % EtOH has a eutectic point close to -50 °C, so the transit of sterilised cryogels from the -70 °C freezer to the freeze dryer could warm the cryogels such that the eutectic point of 70 % EtOH is surpassed. In this case, evaporation occurs upon application of the vacuum, rather than sublimation. Though the cryogel has already been lyophilised following synthesis, the evaporation of 70 % EtOH would cause shrinkage of the cryogel. This also has the unfavourable consequences of reducing internal free space, pore size, and can even reduce the ability of cells to penetration into the cryogel. The sterilisation process could be made two-stage, consisting of an initial 70 % EtOH sterilisation followed by washing in autoclaved D.H_2O to prevent shrinkage during lyophilisation. However, the submergence of CaP particles (with suspected ACP crystal structure) in D.H_2O has been shown to induce transformation in as little as 30-minutes (Kimura et al., 2018), hence the use of D.H_2O would be unsuitable.

Unfortunately, there are no other known sterilisation methods appropriate for the agarose cryogels. Supercritical point (SCP) drying with CO_2 is argued to be unsuitable, since this method provides a frictionless surface which could eject CaP particles loosely bound to surfaces from the cryogels. Even with EtOH sterilisation, pDNA loss from pDNA and PDA-pDNA cryogels is evident (Figure 2.37), though the loss of pDNA/CaP particles due to 70 % EtOH sterilisation would require the comparison of unsterilised and sterilised cryogels, both submerged in decalcification buffer, which was not produced in this work. Regardless, one could reasonably assume that SCP would increase the loss of pDNA through removal of pDNA/CaP particles from

cryogels. Thermal treatments and ionising radiation are of course unsuitable given their inherent ability to denature and/or destroy pDNAs.

Where CaP and pDNA/CaP particles are present within agarose hydrogels, the local volume of buffer in the pore is reduced, hence the expansion of the pore during ice crystallisation will be more restricted than empty pores. By extension, the free internal space provided by the lyophilisation step and cell penetration will be more restricted in the localities of sufficiently concentrated CaP particles. But given the microscale environment of these cryogels, a surface coating of sub-micron sized particles would have little effect on overall pore volume. Despite an expected constriction of CaP-embedded cryogels, there is no noticeable difference in appearance between blank and CaP cryogel groups. A lack of changes in morphology or size could simply be because CaP occupies a small fraction of total cryogel volume, whilst also being toward the centre of the cryogel. If CaP particles are present nearer to cryogel surfaces, these areas may present more obvious signs of constriction.

The suspected fragments of PDA evidence in Figure 2.12 are less than 10 μm in diameter and appear to be at a relatively high density on agarose fibres. These fragments could contribute to the reduction of pDNA band visibility observed in Figure 2.7 by forming complexes with incoming pDNA molecules, though their presence is not suspected to reduce cell viability given PDA-blanks present similar cell viability to blank control groups (Figure 2.39).

2.5.3 XRD

XRD analysis of HAp powder, blank, pDNA/CaP, PDA-pDNA/CaP cryogels was performed to determine the crystal structure of synthesised particles. The blank control demonstrated an amorphous structure with a broad, shallow peak between 32 – 39 °, whilst the pDNA/CaP and PDA-pDNA/CaP groups present nearly identical spectra with a broad, shallow peak between 2θ of 31 - 35°. The broad peak for the pDNA/CaP and PDA-pDNA/CaP cryogels is within the same region as strong HAp that indicate the (211), (112), (300), and (202) crystal planes. This suggests that the CaP phases within these cryogels have low crystallinity, either being comprised of small crystallites or being amorphous. The nodular morphology and topography of CaP particles in all CaP-containing cryogel groups agree with this, where nodules could be small HAp crystallites.

These results agree with those from Kamitakahara et al. (2012) and Kimura et al. (2018), who confirmed that CaP particles synthesised using the PS-DW-AGE approach were amorphous, as confirmed by TEM electron diffraction and XRD. Another study by Kamitakahara et al. (2007)

may have initially synthesised ACP. However, their subsequent thermal treatment of samples at 600 °C to decompose agarose and eliminate its background signal for XRD likely led to a crystallographic transition from amorphous to HAp-like CaP. This is made possible by the relatively low-thermal transition temperature of ACP at 600 °C (Sinusaite et al., 2021). Hence the thermal treatment of cryogel samples to purge the amorphous agarose signal from XRD spectra was not utilised in this work to avoid thermally-induced crystal transformation of ACP.

2.5.4 SEM

2.5.4.1 Agarose macrostructure

SEM of intact blank and PDA-blank cryogels demonstrated contrasting surface topographies. At low magnification these cryogel groups were highly similar in that no pores were observed on the top surface, but ripples of agarose fibres could be seen close to the edges of the cryogels. Higher magnification of the flat surface of cryogels revealed contrasting surface topographies. The blank cryogel was mostly flat with salt crystals and ridges of agarose fibres, whilst the PDA-blank was coated in a platelet surface which could be the PDA-coating, which is perhaps 'broken' upon lyophilisation where vapour penetrates through the surface beneath.

The top surfaces of both cryogels did not display any visible porosity, which is in stark contrast to the internal pore structure of a blank cryogel. It could be that these cryogel surfaces were in contact with the base of wells in well plates during lyophilisation, hence an ice cap could be formed around the base of the cryogel that inhibits sublimation and pore formation on these surfaces. It could also be that, when hydrated in cell media, these cryogel surfaces become porous during swelling. However, without the use of an SEM with an environmental stage, identifying changes in microscale porosity on cryogel surfaces during hydration would be very difficult. Given that the cryogels rapidly changed colour to red when submerged in cell media, the cryogels should be hydrophilic and porous enough to also allow cell infiltration. However, if surface porosities on a cryogel are not consistent due to anisotropic lyophilisation, cell seeding would need to be done on the most porous surface available.

2.5.4.2 The Impact of pDNA on CaP Nucleation

Despite variation between agarose fragments, overall, CaP and pDNA/CaP cryogels displayed highly similar morphologies, agglomerations and packing densities of CaP particles. However, significant dissimilarities arise between their histogram distributions, with the CaP and pDNA/CaP groups demonstrating unimodality and multimodality respectively (Figure 2.21 and Figure 2.24). The CaP and pDNA/CaP groups display primary modal bin centres of 216 nm and 219 nm respectively, whilst the pDNA/CaP group also has a secondary modal bin centre of 105 nm. This transition from unimodal to multimodal distribution is theorised to arise from the presence of pDNA molecules acting either as nucleation centres.

As nucleation centres, pDNA molecules offer a competing surface area to that of agarose fibres on which CaP can nucleate on. This could theoretically increase the nucleation rate, increase the number of nuclei, reduce the ions available for subsequent growth, and therefore reduce the mean particle diameter. Hunter and Goldberg (1993) demonstrated a similar outcome, whereby CaP precipitation was dependent on the presence of BSP, hence CaP was theorised to be nucleating on BSP. However, one must consider both the magnitude of the nucleation energy barrier reduction afforded by each surface, as well as the total surface area available for nucleation to occur.

It is difficult to compare the contribution of agarose and pDNA surface toward nucleation. However, the inert and uncharged surface of the agarose will not provide a more significant reduction in nucleation energy (per unit mass) than pDNA molecules which boast a negatively charged phosphate backbone of the pDNA. Given that the CaP and pDNA/CaP groups shared highly similar primary modal bin centres, it appears that nucleation and growth on agarose surfaces is responsible for particles within this size range. By extension, the pDNA would be responsible for the secondary modal bin centre of 105 nm in the pDNA/CaP centre. However, the nucleation and growth of CaP particles within the agarose matrix in the presence of pDNA is likely to be highly heterogeneous and occurring via multiple mechanisms. For example, CaP could nucleate on pDNA, then pDNA could adsorb onto CaP, and so on. It is therefore assumed that the nucleation of CaP in the presence of pDNA is multimodal: nucleating on agarose fibres, mobile pDNA molecules, and adsorbed pDNA molecules.

As discussed, pDNA offers a favourable surface for CaP nucleation to take place, hence the adsorption of pDNA onto pDNA/CaP particles during synthesis is assumed to offer additional nucleation sites to CaP. Consequently, inter-particle stabilisation of pDNA/CaP particles due to

a pDNA shell is unlikely, since it would require all Ca^{2+} or $H_xPO_4^{x-3}$ ions to have been consumed in CaP precipitation elsewhere. However, it remains possible that pDNA/CaP particles could have internalised pDNA by adsorbing pDNA onto CaP surfaces, either instead of or in addition to nucleating on pDNA. There is therefore potential for the PS-SW-AGE approach to produce multiple particle species. Firstly, CaP particles produced by nucleation of CaP on agarose surfaces and not adsorbing pDNA. Secondly, pDNA/CaP particles produced by nucleation of CaP on mobile pDNA molecules. Thirdly, pDNA/CaP particles produced by adsorption of pDNA onto CaP particles. Finally, compound pDNA/CaP particles, produced by multiple instances of CaP nucleation on pDNA or pDNA adsorption on CaP.

2.5.4.3 The Impact of PDA on CaP Nucleation

A PDA coating was added to agarose cryogels prior to CaP or pDNA/CaP particle synthesis to enhance cell attachment and proliferation. As a secondary effect, PDA modified the heterogeneous nucleation and growth of CaP particles due to the interaction of Ca^{2+} and $H_xPO_4^{x-3}$ ions with catechol and amine groups respectively. In the literature, PDA has been shown to shift the CaP nucleation mode of hydrophobic materials (such as agarose) from the Volhmer-Weber (islanding) growth mode to the Stranski-Krastanov (islanding and planar) growth mode (Murari et al., 2020). The observed effect of a PDA coating in this work is that the CaP particle size distributions transition from unimodal to bimodal for CaP and PDA-CaP groups respectively, with a reduction in mean CaP particle size. Though CaP particles remain spherical within both groups, SEM analysis demonstrated that particles spread out along agarose fibres in the PDA-CaP group. So, whilst an overall reduction in CaP particle size results from the PDA coating, further reductions in CaP particle size on PDA surfaces may eventually result in a CaP surface coating rather than individual particles.

Interestingly, PDA may increase agarose hydrogel pore size when interacting with agarose molecules and fibres during gelation or increase cryogel pore size during lyophilisation (Su et al., 2021). If the former is true, the nanoscale confinement effects of the agarose matrix are reduced given the larger mean pore size of a PDA-agarose gel. Despite this, particle diameters transition from a unimodal to bimodal histogram distribution for CaP and PDA-CaP samples respectively, and a reduction in primary modal bin diameter and mean diameter is observed. Therefore, changes in surface chemistry afforded by PDA overcome any potential reduction in nanoscale confinement effects, leading to a significant reduction in mean particle diameter.

For gene therapy applications, there is no 'ideal' size of pDNA/CaP particles, but studies mostly favour pDNA/CaP particles below 100 nm due to their generally greater transfection efficacy than larger pDNA/CaP particles (Bakan, 2018). As cryogels in this research are intended as surface-mediated transfection materials, smaller particles theoretically offer a greater surface area and therefore more rapid dissolution and transformation processes *in-vitro*, which is accelerated further by the proposed metastability of the ACP phase of the pDNA/CaP particles.

2.5.4.4 The Compound Effects of pDNA and PDA on CaP Nucleation

When comparing the PDA-CaP and PDA-pDNA/CaP groups, the incorporation of pDNA appears to have little impact on the mean particle diameter. However, there is a shift from bimodality to multimodality in the particle diameter histogram distributions for PDA-CaP and PDA-pDNA/CaP groups respectively. As with the CaP and pDNA/CaP samples, it is theorised that pDNA will act as an additional nucleation surface. The difference here is that pDNA is incorporated into a PDA-coated agarose hydrogel, rather than uncoated agarose, hence pDNAs will either be adsorbed onto PDA surfaces or remain free in solution prior to the loading of Ca^{2+}, both of which offer sources of nucleation to CaP. Hence multipath nucleation of CaP is theorised to take place in the PDA-pDNA/CaP group.

The proposed multipath nucleation of CaP is described as follows. Prior to the loading of $CaCl_2$ solution, pDNAs are either adsorbed onto PDA surfaces or free in the bulk solution, where adsorption is facilitated by the protonation of amine groups. Upon loading of $CaCl_2$, Ca^{2+} ions are transported into the gel, some of which electrostatically interact with catechol groups on the PDA surface and coat the PDA surface in Ca^{2+}. With Ca^{2+}, $H_xPO_4^{x-3}$ ions present within the agarose hydrogel above the supersaturation threshold, CaP first nucleates on either mobile pDNAs, pDNAs anchored to the PDA surfaces, or the PDA surface itself. Where CaP nucleates onto pDNAs, the resultant pDNA/CaP particles either remain mobile, remain anchored, become mobile, or become anchored. The change from mobile to anchored or anchored to mobile is made possible by the electric field which electrophoretically transports all charged species, facilitating collisions. Secondary CaP nucleation can then occur on mobile or anchored pDNA/CaP particles. The result is a highly heterogeneous pDNA/CaP particle population that share a similar growth potential due to the confinement of the agarose matrix but are mineralised with CaP via a multipath nucleation mechanism. These pDNA/CaP particles can then collide and coalesce if transported by the electric field, producing larger particles.

As has been discussed, the PS-SW-AGE approach cannot compete with highly controllable synthesis routes such as microemulsion synthesis with regards to producing a highly uniform particle species. Microemulsions can comprise of micelles in the sub-100 nm range (Malik et al., 2012) and hence can exhibit greater confinement effects than the agarose network in this work. With the PS-SW-AGE approach, precursor ions and molecules are mixed via electrophoretic convergence of ion and pDNA bands, which inherently results in a non-uniform supersaturation toward CaP that is spatiotemporal-dependent. In contrast, supersaturation in microemulsions are near-homogeneous throughout the solution, as well as being highly controllable through the titration of precursors. It is no surprise then that, from SEM data, particles from all groups in this work have a relatively wide size distribution and can each be described as heterogeneous with regards to their diameter and morphology. However, the utility of the PS-SW-AGE approach is in the simplicity of the method: the ability to synthesise a coated or uncoated cryogel embedded with pDNA-loaded particles in a single step and the discretion of the pDNA/CaP particle band that could be used to mimic layered or gradient tissue architectures.

2.5.5 pDNA Encapsulation Efficiency

The pDNA encapsulation efficiency of CaP particles in uncoated and PDA-coated cryogel groups was tested using a comparison of two sets of samples; one submerged in a control buffer (40 mM Tris, pH 8) and one submerged in a decalcification buffer (40 mM Tris, 150 mM EDTA, pH 8). The control buffer was used to measure the normal release of pDNA from cryogels without accelerating CaP dissolution, whilst the decalcification buffer was used to release the maximum amount of pDNA from cryogels by completely dissolving CaP and chelating dissociated Ca^{2+} ions to prevent any re-precipitation of CaP. pDNA concentrations in control and decalcification buffers from pDNA/CaP and PDA-pDAN/CaP groups were then used to calculate an encapsulation efficiency of the 2.5 µg loaded into each gel.

Firstly, there was little pDNA loss due to sterilisation of pDNA and PDA-pDNA cryogels in 70 % EtOH, evidenced by only a 6.7 % and 11.4 % increase in pDNA release respecitvely from unsterilised cryogels of these groups. For sterilised cryogels, pDNA release was greater in PDA-pDNA groups rather than pDNA groups, which is theorised to be due to a greater retention of pDNA in PDA-coated cryogels during synthesis because of lower pDNA mobility. As shown in 2.4.1, pDNA mobility is slightly reduced when loaded into the PDA-coated gel, theorised to result from adsorption onto PDA surfaces or complexation with unbound PDA molecules/fragments,

or a combination of both. Prior to incubation in control or decalcification buffers, PDA-blank cryogels would therefore be encapsulating a greater mass of pDNA compared to the pDNA cryogels.

The reduced amount of pDNA released into decalcification buffer for the pDNA and PDA-pDNA groups is thought to result from a reduced diffusivity of pDNA molecules in the decalcification buffer. Incubation was conducted under agitated (shaken) conditions to try and mitigate such disparities in diffusivity, but any greater viscosity of the decalcification buffer compared to the control buffer would still reduce pDNA diffusivity. Reduced detection of pDNA in supernatant samples from pDNA and PDA-blank cryogels is therefore theorised to result from the reduced diffusivity of pDNA in the decalcification buffer.

Both the pDNA/CaP and PDA-pDNA/CaP groups release a greater pDNA mass than the pDNA and PDA-pDNA groups respectively, signifying that CaP is enhancing encapsulation efficiency of pDNA within cryogels. The proposed mechanism through which this occurs is that CaP precipitates on surface-bound and mobile pDNA molecules, which are then dried onto cryogel surfaces during lyophilisation. Submergence of pDNA/CaP and PDA-pDNA/CaP cryogels then results in negligible pDNA release since it is mostly encapsulated within CaP. Though CaP itself is subject to dissolution and transformation processes in solution within the 48-hour time frame of this experiment, pDNA released during these processes is likely to be encapsulated again. This will occur either through pDNA acting as nucleation centres for secondary CaP particle nucleation, or from pDNA adsorbing strongly onto secondary CaP particle surfaces.

Encapsulation efficiency of pDNA for the pDNA/CaP and PDA-pDNA/CaP groups was calculated using Equation 2.7, where the mass of pDNA released into control buffer is divided by the mass of pDNA released into decalcification buffer and converted to a a percentage. The resulting encapsulation efficiencies for the pDNA/CaP and PDA-pDNA/CaP groups were 95.7 ± 3.2 % and 92.1 ± 6.0 % respectively (no statistically significant difference).

One limitation in using this method to calculate pDNA encapsulation efficiency strongly adsorbed is that secondary pDNA/CaP particles could be released from pDNA/CaP and PDA-pDNA/CaP cryogels into control buffer. If sufficiently stable, these secondary particles would not dissolve sufficiently to release the pDNA encapsulated within. pDNA would therefore be released from the cryogel via pDNA/CaP particles and remain undetected due to their shielding from the PicoGreen™ nucleic acid stain by CaP. The amount of pDNA release into control buffer could therefore be higher than what was measured by the PicoGreen™ assays. In contrast, the decalcification buffer would prevent any dissolution/transformation processes from occurring

and therefore prevent pDNA escaping from the cryogel in a CaP particle. Despite the limitations in determining accurate pDNA encapsulation efficiencies, one must acknowledge that pDNA mobilisation in secondary pDNA/CaP particles is an integral part of surface-mediated transfection in these cryogels.

Alternative methods to determine pDNA encapsulation (or adsorption) are available in the literature. For example**,** Bhakta et al. (2005) prepared magnesium phosphate (MgP) and manganous phosphate particles then solubilised both particulate species in acidic buffer (pH 3.0) and measured pDNA release by measuring optical density (OD) spectrophotometrically at a λ = 260 nm. Encapsulation efficiency was then calculated by divided pDNA release with the total amount of pDNA loaded into the synthesis mixture. However, measuring pDNA in acidic conditions and with non-chelated ions is non-ideal given the interference of low pH and ionic strength with spectrophotometric measurements of nucleic acid concentration. In contrast, the use of a decalcification buffer has the advantage of using EDTA to chelate Ca^{2+} ions and a more neutral pH. In a semi-quantitative method, Son and Kim (2010) prepared PLGA- and PEI-based particles encapsulating pDNA and calculated how well pDNAs are protected from DNase using a 'DNase protection assay', where unprotected pDNA is digested and and the resulting mixtures are analysed via gel electrophoresis. For pDNA/CaP particles, this would reveal the adsorption of pDNA onto CaP, but not encapsulation.

2.5.6 Transfection

Luciferase assays were performed to quantify the amount of luciferase enzyme produced by cells cultured on each cryogel group, used as a direct measurement for transfection efficacy. Using the blank and PDA-blank cryogels as negative controls for uncoated and PDA-coated groups respectively, luminescence values for experimental groups were translated to '± % of blank control'. All groups, at all time points, demonstrated less than +9 % of the negative control. CaP and PDA-CaP cryogel groups reached nearly 4 %, which could indicate that the presence of CaP or dissolved ionic components may marginally boost enzyme activity and therefore luminescence. In comparison, peak measurements of 7 % and 8.5 % were recorded for pDNA (48-hours) and PDA-pDNA (24-hours) groups respectively, both of which gradually declined toward the 7-day timepoint. pDNA/CaP and PDA-pDNA/CaP cryogels demonstrated the lowest luminescence, reaching approximately 0.5 % and 1.5 % respectively.

The measurements for pDNA/CaP and PDA-pDNA/CaP cryogels can be compared to data produced by our group in an earlier (unpublished) study. Using the data in Figure 1.4, cryogel groups loaded with the same Ca:$H_xPO_4^{x-3}$ ratio as in this work (166.66) reached peak values of 211.6 % at 48-hours for the pDNA/CaP group (compared against pDNA cryogel control), whilst FBN-pDNA/CaP cryogels reached -21 % (compared against FBN-pDNA cryogel control). For the cryogels in this work at 48-hours, the pDNA/CaP cryogel group was measured as -9.9 % of the pDNA group, whilst the PDA-pDNA/CaP cryogel group was measured as -6.4 % of the PDA-pDNA group. However, at 7-days the performance of pDNA/CaP and FBN-pDNA/CaP cryogels in previous work by Feichtinger et al. (2019) reach very high values; 190 % and 670 % respectively when compared against their respective pDNA control groups. This far exceeds the pDNA/CaP and PDA-pDNA/CaP groups in this work, where the pDNA/CaP group has a value of -1.7 % compared to the pDNA group, whilst the PDA-pDNA/CaP group has a value of -0.18 % compared to the PDA-pDNA group at the 7-day time-point.

These results are despite many synthesis parameters – besides the use of FBN or PDA - between the two studies remaining the same, including: buffer strength and pH, Na_2HPO_4 concentration, pDNA concentration and mass, voltage, time, $CaCl_2$ concentration, and the lyophilisation and sterilisation process.

One parameter that did change was the agarose powder type. Previously, NuSieve™ (Lonza) was used, which is a low strength gel – where strength is defined as the force in g cm^{-2} required to fracture the gel - for characterisation of low molecular weight DNA fragments. In this study, SeaKem™ (Lonza) was used, which is a much higher strength gel used for the characterisation of larger molecular weight DNA fragments. This change in agarose gel type was made given how mechanically weak NuSieve™ is, which can easily be crushed in hydrogel or cryogel form at 1 wt %. In comparison, SeaKem™, is much more mechanically robust; having a gel strength at 1 wt % of 1200 g cm^{-2}, which is comparable to a 4 wt % NuSieve™ gel (1400 g cm^{-2}).

Though pore size characterisations in the literature are only available for SeaKem™, the lower gel strength and ability to resolve smaller DNA fragments implies that NuSieve™ has a much smaller mean pore diameter. Naturally, then, SeaKem™ will have weaker nanoscale confinement effects on CaP nucleation and growth compared to NuSieve™ and will consequently facilitate the synthesis of a CaP particle population with a larger mean diameter. Though a shift in mean particle diameter is theorised to result from a change in pore size, the lack of an in-depth particle analysis from the NuSieve™ study prevents any reliable comparison of the two studies. Despite this, one can reasonably assume that pDNA/CaP particles synthesised

using NuSieve™ are smaller than those in the SeaKem® gel due to the smaller hydrogel pore size. Furthermore, the surface of NuSieve™ gel may be more porous due to smaller agarose fibres, thereby facilitating greater cellular infiltration than in SeaKem®.

Another parameter that was changed was the number of cells per scaffold, which increased by a factor of 5 from 5 x 10^4 per cryogel for the NuSieve™ study to 2.5 x 10^5 per cryogel for the current study. This change was brought about by the optimisation experiments performed by our group (unpublished), which looked at cell adhesion, proliferation, and cytotoxicity, to optimise cell density. No severe change in the cell media colour was observed for this current study between daily changes of cell media, which would otherwise indicate excessive cells numbers by exhaustion of cell media nutrients. But it is perhaps possible that a significant number of cells were dying if poorly attached; hence the lack of nutrient absorption.

The NuSieve™ study also seeded cells onto cryogels with the standard technique of an unmodified 48-well plate. This contrasts with the agarose-coating of wells in 48-well plates used in this study, which aims to provide the highest cryogel attachment potential for cells by removing their access to the more favourable cell culture plastic. One must therefore question whether the comparatively higher transfection efficacy of cryogels in the previous work by Feichtinger et al. (2019) using NuSieve™ arose due to the attachment of cells to the cell culture plastic that will enhance cell viability. This may also provide cells with a foundation on which they can infiltrate into cryogels where transfection can take place.

2.5.7 Cytotoxicity

Cytotoxicity was measured using an LDH assay with the protocol adjusted for 3D cell culture. LDH is an enzyme released from cells with ruptured cell membranes, thus allowing the LDH concentration to be used as quantitative indicator of cell viability. Experimental groups each had a lysed and non-lysed set to calculate cell viability. These values were then baselined against the blank cryogel group as a control, allowing for direct comparison of uncoated and PDA-coated cryogel groups. The length of incubation required to lyse all cells from cryogel groups was stipulated as 1-hour for cell monolayers in the protocol. However, a 4-hour lyse buffer incubation was arbitrarily chosen for the positive controls, with agitation every 30-minutes, which was assumed to provide a near-maximum cell death without encroaching too close toward the 9-hour half-life of LDH.

The blank control had a cell viability of 72.5 ± 2.4 % at the 48-hour time point, showing most cells survived without a PDA-coating. Other groups showed cell viabilities that were within + 6 to -3 % of the blank control. Whilst no statistically significant differences exist within the dataset, this data can be used to indicate that cell viability of cryogel groups is comparable to that of the control. It would perhaps be useful to incorporate cell proliferation assays in future work to determine whether the initial cell population is able to attach to- and proliferate on cryogel surfaces.

Whilst the pDNA group showed enhanced cell viability, it is interesting that the PDA-pDNA group had 4 % lower cell viability than the PDA-blank group. Perhaps the adsorption of pDNA onto PDA surfaces in the PDA-pDNA group reduces the number of cell attachment sites available on the PDA surface. The PDA-CaP group had 3.75 % less cell viability than the PDA-blank group, which could also be due to the obstruction of the PDA surface with CaP particles. Meanwhile, the PDA-pDNA/CaP group had 20.4 % less cell viability than the PDA-blank. This could simply arise due to the formation of a multimodal particle size distribution where smaller particles provide greater surface coverage of the PDA-surface and hence reduce the number of cell attachment sites. Localised spikes in Ca^{2+} concentration would theoretically be greatest in the PDA-pDNA/CaP group due to greater surface area to volume of the embedded particle population which will exhibit the most rapid dissolution rate.

2.5.8 Enhancing Transfection Efficacy

The transfection efficacy of PDA-pDNA/CaP cryogels has the potential to improved using several pathways: (1) increasing the uniformity of pDNA concentration; (2) reducing pDNA/CaP particle diameter; and (3) improving secondary particle stability. It is also proposed that the transfection efficacy of these cryogels should be measured using multiple plasmid types and multiple experimental routes i.e. through spectrophotometric assays and fluorescence microsopy. It would be interesting to investigate the potential of extracting CaP and pDNA/CaP particles from cryogels for their characterisation independent of cryogels for more accurate suspension-based characterisation of: (1) size; (2) pDNA encapsulation efficiency; and (3) transfection efficacy. However, this is beyond the scope of this work.

2.5.8.1 Increase pDNA presence throughout agarose gel

Encapsulation efficiency of pDNA in cryogels synthesised via the PS-SW-AGE approach reached 96 % and 92 % for pDNA/CaP and PDA-pDNA/CaP cryogels respectively. This is despite suboptimal synthesis conditions, where CaP precipitation needs to precipitate on the pDNA band for encapsulation or adsorption to take place. It would be simpler to have pDNA occupy the entire zone of precipitation and surrounding region, meaning that the transport of pDNAs results in a net-zero change in pDNA concentration at the zone of precipitation. This would ultimately result in a much lower encapsulation efficiency given much of the pDNA would not be encapsulated or adsorb onto CaP, but the pDNA/CaP layer itself would not rely on the bidirectional transport of Ca^{2+} ions and pDNAs. Furthermore, the pDNA/CaP layer would likely have a greater ratio of encapsulated pDNAs compared to adsorbed pDNAs, where encapsulated is preferred to protect pDNAs from degradation by DNase.

2.5.8.2 Reduce pDNA/CaP Size

A contributing factor to poor transfection efficacy of this method may be that the PS-SW-AGE synthesis approach produces pDNA/CaP particles that are too large for surface-mediated transfection to occur rapidly enough to achieve high supersaturations *in-vitro* required for small secondary pDNA/CaP particle sizes. Despite the encouraging primary modal bin of particles in the PDA-pDNA/CaP group reducing below 100 nm due to the use of pDNA and PDA, a mean particle size of 171 ± 94 nm remained, which is far larger than the sub-100 nm pDNA/CaP particles frequently used in gene therapy research (Bose and Tarafder, 2012, Bakan, 2018).

Though some pDNA/CaP particles within pDNA/CaP and PDA-pDNA/CaP groups may be mobilised and be responsible for transfecting cells, SEM analysis has shown that both primary and secondary particles are present in pDNA/CaP and PDA-pDNA/CaP groups after cell culture. From this, one can deduce that both primary and secondary pDNA/CaP particles could take part in transfection and hence allow pDNA/CaP and PDA-pDNA/CaP cryogels to transfect cells via two modalities. Alternatively, primary pDNA/CaP particles may remain immobilised on agarose surfaces and be protected from cell culture and dissolution *in-vitro* by agarose collapsed around particles during lyophilisation, in which case surface-mediated transfection would be the only modality of transfection.

Since it is not possible to know whether single- or multi-modal transfection routes take place, reducing pDNA/CaP particle size below 100 nm will reduce primary particle size into a more favourable transfection range and significantly increase the surface area of particles. Increases in surface area will enhance single-modal transfection by reducing particle stability, increasing dissolution rate, and provide a higher concentration of ions for secondary pDNA/CaP formation *in-vitro*. Hence a greater concentration of ions can be produced during dissolution to increase supersaturation and nucleation rate, thereby reducing secondary pDNA/CaP particle diameters.

As with most particle synthesis routes, reducing pDNA/CaP particle diameters typically requires adjustment of supersaturation, temperature, mixing rate, reaction time, or a mixture of these. Here, supersaturation could be adjusted by changing salt concentration and buffer pH, whilst mixing rate would be adjusted by changing the applied potential (electric field strength). As found by Kimura et al. (2018), increasing agarose wt % decreases particle size, offering another parameter to modulate pDNA/CaP particle size.

One complexity that must be managed in reducing CaP particle diameters using the PS-SW-AGE approach is the dependence of parameters on one another. For example, it is well known that greater applied potentials in gel electrophoresis yield greater gel slab temperatures through the joule heating effect, so the use of higher voltages must therefore be combined with a means of temperature control. Temperature increases through joule heating effects will be also exaggerated using longer reaction times, more conductive buffers, and loading salt concentrations. Such co-dependencies will need to be discussed if an accurate correlation between individual experimental parameters and particle size is to be identified.

2.5.8.3 Improving particle stability

If we assume that pDNA is released during the dissolution and transformation processes of primary pDNA/CaP particles *in-vitro*, pDNA could either be encapsulated by or adsorb onto secondary CaP particles, with adsorption being less ideal given the exposure of pDNAs to degrading DNase. It would therefore be advantageous to utilise an additional coating to protect pDNA from degradation *in-vitro*, but also enhance interparticle stabilisation. Polymers with positively charged groups – such as polyethylenimine (PEI) – have long been used to form complexes with nucleic acids for transfection applications (Baker et al., 1997). The addition of a positively charged polymeric shell would result in PEI-coated pDNA/CaP (pDNA/CaP/PEI) particles with stronger interaction strengths between particle surfaces and cell membranes. This

has the potential to increase the number of particles internalised by cells and therefore overall transfection efficacy. Adding such polymers to cryogels containing pDNA/CaP particles could be done either electrophoretically, or by simple soaking in a PEI solution.

2.5.8.4 Improve transfection measurements

Besides improving transfection efficacy of cryogels, one must also consider the way in which transfection efficacy is measured. Thus far, an assay-based method to quantify luciferase enzyme activity has been the only method to measure transfection efficacy. However, a visual method should be employed in parallel to mitigate any issues that arise with the assay route. For example, the use of a plasmid encoding for the green fluorescent protein (GFP) (pGFP) would facilitate semi-quantitative analysis of transfection using fluorescence microscopy. Rather than adjust the concentration or mass or pDNA loaded into agarose gels to accommodate both plasmids, it would be best to produce cryogels boasting single plasmid types to maintain a greater sensitivity in both the assay and microscopy characterisation routes. Provided these plasmids are of similar mass, there will be negligible impact on their electrophoretic mobility over short loading times and therefore minimum impact on pDNA/CaP nucleation and growth.

2.5.9 Enhancing the Pre-clinical Relevancy of Cryogels

2.5.9.1 Particle Layer Shape and Thickness

An important consideration for PDA-pDNA/CaP cryogels in this work is their potential application for osteochondral tissue regeneration, provided several modifications are made. The precipitate zone of CaP particles embedded within the agarose gel is, in its current form, not suitable to be used as the mineralised or osteogenic layer of an osteochondral GAM. For one, the precipitate shape and thickness is non-uniform due to the non-uniform electric field profile during synthesis. An osteogenic layer that mimics the native architecture of the mineralised osteochondral tissue to facilitate lateral and inferior osteointegration and overall restoration of native biomechanics. The first step in enhancing pre-clinical relevancy of the PDA-pDNA/CaP should therefore be to synthesise a layer of pDNA/CaP that is the same thickness as the mineralised layer in a relevant pre-clinical model.

2.5.9.2 Cylindrical Cryogel Shape

Since debridement of lesion tissue is performed to leave cavities in the osteochondral that can be filled with either cylindrically-shaped or tapered osteochondral plugs and scaffolds (Chen et al., 2023), the overall shape of the PDA-pDNA/CaP should be that of a cylinder. The pDNA/CaP layer is currently an irregular shape, which resides within an irregular cuboid shape cryogel. The irregular shape, small size and thickness or the pDNA/CaP layer prevent the gel from being cut to a cylinder shape. One could try using the current gel slab format to produce a pDNA/CaP layer with a larger cross-sectional area, where a cylinder 'punch' could be used to cut out a gel with an appropriately shaped pDNA/CaP layer. However, the gel slab thickness is currently only 7 mm and the width of the well – which dictates precipitate width – is only 6 mm. The current gel slab format is therefore unsuitable for producing pDNA/CaP precipitates with larger surface areas.

A new synthesis approach that differs significantly to the gel slab format is needed to allow the fabrication of uniformly shaped precipitate layers of pDNA/CaP particles, whilst also allowing gels to be easily cut into cylindrical shapes. Ideally, this approach would allow for the synthesis of cylindrically shaped layers of pDNA/CaP particles within a cylindrically shaped gel. This would facilitate the fabrication of several small gels, each cut from a larger gel. Besides a new gel cast to form gel cylinders, a means of holding the gel cylinder in the tank and a loading solution against the gel cylinder surface would both be required.

The relatively thin gel slab is purposely used in the horizontal gel electrophoresis tank since its electric field strength varies only slightly through the 7 mm thickness of the gel slab, hence the use of gel cylinders would require modification of electrode layouts to maintain a uniform electric field profile through the gel cylinders. This uniform electric field profile is critical to allow ions to mix evenly throughout the gel cylinder cross section, potentially reducing the size of the pDNA/CaP particle size distribution through homogenised supersaturation over the cylinder cross-section.

2.6 Conclusion

The PS-SW-AGE approach has been used to synthesise pDNA/CaP particles in uncoated and PDA-coated agarose hydrogels. The addition of a PDA coating pre-synthesis and the electrophoretic addition of pDNA each caused a reduction in CaP particle diameters which – when combined for the PDA-pDNA/CaP group – reduced both mean and primary modal particle diameters. The combination of pDNA and PDA is theorised to reduce pDNA/CaP particle size through a complex multimodal mechanism involving nucleation of CaP onto (1) pDNA molecules free in solution; (2) pDNAs adsorbed onto the PDA coating; and (3) the PDA coating. For all groups, the small size of particles, spherical and irregular morphologies with nodular topographies indicate their crystal structure comprises of ACP. The amorphous XRD spectra of pDNA/CaP and PDA-pDNA/CaP cryogels provide further evidence of ACP in these groups, which agrees with that produced in similar research by Kimura et al. (2018).

Cell viabilities were comparable to that of the blank control for all groups, with the blank control itself exhibiting over 72 % cell viability at 48-hours. Such marginal differences in cell viabilities may be due to poor cellular infiltration into cryogels (due to low surface porosity) and thus minimal exposure to particles within. This would also contribute to poor transfection efficacies, where transfection efficacies of the pDNA/CaP and PDA-pDNA/CaP groups were poor. In particular, the PDA-pDNA/CaP group did not exceed 2 % more than the PDA-blank control. However, surface porosities may increase under hydrated conditions, which would be difficult to image given the translucency of these cryogels.

SEM analysis of cryogels that were incubated in cell media for 24-hours revealed evidence that there is an inefficient solubilisation of primary pDNA/CaP particles *in-vitro*, hinting that not all primary pDNA/CaP particles can take part in surface-mediated transfection. This is assumed to be due to encapsulation of particles within cryogel surfaces.

Increasing the uniformity of pDNA distribution at the zone of precipitation, reducing pDNA/CaP particle diameters, and enhancing the stability of secondary pDNA/CaP particles *in-vitro* are each proposed to improve the transfection efficacy of cryogels produced by the PS-SW-AGE approach in the future. There are also several routes to improve the pre-clinical relevancy of cryogels produced via the PS-SW-AGE approach. Such routes centre around the need to produce a cylindrical pDNA/CaP layer with a thickness representative of a pre-clinical model, all within a cylindrical gel shape.

3 Development and Testing of Particle Synthesis Apparatus

3.1 Introduction

A PDA coating has been used to change the surface chemistry of an agarose gel slab used in the PS-SW-AGE approach to primarily improve cell attachment. A secondary consequence of this coating was the synthesis of pDNA/CaP particles with a multimodal size distribution exhibiting a smaller primary modal diameter than that of pDNA/CaP cryogels, all the while maintaining high pDNA encapsulation efficiency exceeding 90 %. Despite encapsulating smaller primary particles, PDA-pDNA/CaP cryogels demonstrated poor transfection efficacy when compared to a blank cryogel control. It was theorised that the primary contributors to poor transfection efficacy of PDA-pDNA/CaP cryogels stemmed from a combination of insufficiently small particle diameters, limited availability of particles at agarose surfaces, poor secondary particle stability, and a localised/non-uniform concentration of pDNA throughout the cryogel.

3.1.1 Improving Transfection Efficacy

The PDA-pDNA/CaP cryogel encapsulates pDNA/CaP particles and is theorised to rely on surface-mediated transfection as the primary transfection route. Particle surface area (and therefore particle size) is therefore a crucial property given this will largely dictate particle stability and solubility. This author theorises that smaller particles boasting an overall greater surface area to volume ratio will encourage more rapid dissolution of pDNA/CaP particles and release Ca^{2+} ions, $H_xPO_4^{x-3}$ ions, and pDNA molecules at a high concentration. Thus, high supersaturation toward CaP will result, encouraging nucleation-dominant synthesis of secondary pDNA/CaP particles *in-vitro*. The first proposed change to improve overall transfection efficacy, then, is to reduce primary pDNA/CaP particle size to a < 100 nm diameter. The additional benefit of reducing pDNA/CaP particles into this size range is that if a minority of primary pDNA/CaP particles remain stable *in-vitro* and can be mobilised by cell culture media, they would be within the preferred size range for transfection (Bakan, 2018).

Similar to this first proposed change of reducing particle size, the second proposed change is to reduce the primary particle size distribution width to allow for more uniform dissolution

throughout the PDA-pDNA/CAP cryogel. The third proposed change is to increase the stability of secondary pDNA/CaP particles to increase the longevity of pDNA-carrying vectors both extra- and intra-cellularly. The fourth and final proposed change is to increase the uniformity of pDNA concentration throughout the volume of the gel during pDNA/CaP synthesis to produce a pDNA/CaP particle layer that exhibits a high and uniform pDNA encapsulation efficiency.

3.1.2 Improving Pre-Clinical Relevancy

In addition to improving the overall transfection efficacy of PDA-pDNA/CaP cryogels, the pre-clinical relevancy of cryogels fabricated by the PS-SW-AGE approach require substantial improvement, hence several changes have been recommended. With regards to cryogel shape and size, the cryogel must be made cylindrical in shape given that current synthetic osteochondral scaffolds – such as TruFit® and MaioRgen - are cylindrically shaped to fit into cylindrically debrided lesions (Boffa et al., 2021). Cryogel diameter is dependent on the desired pre-clinical model as the critical size of defects varies significantly between models, ranging from 0.75 – 3 mm in rats, 2 – 4 mm in rabbits and from 6 to 7 mm in sheep (Cook et al., 2014).

Further to diameter, cryogel depth is also dependent on the chosen model and the depth of the debrided lesion. It should be noted that there is no standardised depth of debridement in full thickness osteochondral defect models, given the depth of debridement into the subchondral and cortical bone is ultimately dependent on the scaffold architecture and the subsequent degree of osteointegration required for the implant material/geometry. Additionally, there may be a preference over displacement force; given that deeper plugs require greater forces to displace them from cavities given they exploit greater frictional forces at the plug-tissue interface (Kock et al., 2006).

In humans, 8 – 10 mm deep osteochondral plugs have been used (Vellios et al., 2021), which is similar to 10 mm deep plugs in a sheep model (Nosewicz et al., 2012). Rabbit models, where 3 mm deep defects are commonly used (Wei and Messner, 1999) are a more suitable pre-clinical model for the cryogels in this work given the resulting cryogel volumes would be more practical for *in-vitro* work. The critically sized defect in rabbit – the minimum diameter for a defect that cannot heal naturally – is debated to be either 3 or 4 mm (Ahern et al., 2009). Cryogels in this work should therefore be at least 3 mm in depth and at least 4 mm in dimeter.

pDNA/CaP layer thickness should also reflect that of the native rabbit osteochondral tissue. Cartilage in the rabbit medial femoral condyle (MFC) measures 0.3 mm (Räsänen and Messner, 1996), hence the osteogenic pDNA/CaP layer should extend from the base of the cryogel up to 0.3 mm from the top surface. Importantly, the utility of the PS-SW-AGE approach to produce a layer of chondrogenic vectors has not yet been investigated, so it is not known whether a complete osteochondral GAM synthesised via PS-SW-AGE in this work could be synthesised monolithically. This is due to the potential co-dependency of osteogenic and chondrogenic layers synthesised under the influence of an electric field, hence these layers may need to be synthesised separately and then amalgamated to form a single osteochondral GAM. Regardless, the osteogenic layer should be at least 2.7 mm thick.

3.1.3 Alternative Non-Viral Vectors

The PS-SW-AGE approach has thus far only demonstrated the capacity to synthesise pDNA/CaP particles. However, there is great potential to explore the synthesis of other pDNA-encapsulating inorganic particle species given any charged constituents can be electrophoretically transported for co-location. MgP is a particularly interesting option given its great potential in bone tissue engineering applications (Laurenti et al., 2016, Golafshan et al., 2020, Kazakova et al., 2021, Bavya Devi et al., 2022). Further, the particulate form of MgP (when crystalline) has been used to encapsulate pDNAs and successfully transfect cell monolayers using particle suspensions (Bhakta et al., 2005, Bhakta et al., 2009). Meanwhile, amorphous MgP (AMgP) particles have been shown to enhance cell proliferation and boost osteoblastic gene expression when compared to HAp particles (Nabiyouni et al., 2015). Magnesium-substituted calcium phosphates have also gathered interest in bone tissue engineering since Mg^{2+} ions can sufficiently disrupt the lattice structure to stem and control HAp crystal growth (Omema et al., 2020).

Regarding particle synthesis, the far greater solubility of MgP species such as $Mg_3(PO_4)_2$ (tri-MgP) compared to HAp (Racz and Soper, 1968, Chow and Eanes, 2001) should theoretically provide more manageable nucleation and growth rates during synthesis. Though this is arguably advantageous in conventional wet-chemical synthesis routes to limit particle size, the PS-SW-AGE approach requires a greater threshold supersaturation than in bulk wet-chemical synthesis because of nanoconfinement. Consequently, it is difficult to predict what species of MgP (tri-MgP, AMgP, or other) will precipitate, whether these species will precipitate in the presence of pDNA to form pDNA-loaded MgP (pDNA/MgP) particles, or if any MgP species can even

precipitate within an agarose hydrogel. Even if precipitation does occur, it is possible that the lower supersaturation toward MgP (compared to CaP) will produce a pDNA/MgP particle layer of inadequate thickness for an osteogenic GAM layer. Despite this, the numerous benefits of MgP in gene therapy and bone tissue engineering applications are difficult to ignore. Therefore, the synthesis of pDNA/MgP particles via the PS-SW-AGE approach to produce an osteogenic layer will be investigated alongside pDNA/CaP particles.

PEI has also been used extensively in gene therapy to form complexes with nucleic acids that can transfect different cell types (Baker et al., 1997, Oskuee et al., 2009, Sabin et al., 2022). The lack of mineral content in such complexes and their ease of preparation - as described by Longo et al. (2013) – establishes their suitability as vectors for the chondrogenic layer of the osteochondral GAM. Furthermore, both PEI and pDNA can be electrophoretically transported for co-location due to their charge, hence pDNA-loaded PEI (pDNA/PEI) complexes have potential to be synthesised via the PS-SW-AGE approach.

As with pDNA/MgP particles, pDNA/PEI layer thickness is difficult to predict given the literature presents no similar synthesis approach and it is not known how significantly the nanoconfinement effects of the agarose matrix will impact the nucleation and growth of pDNA/PEI complexes. The most comparable pDNA/PEI synthesis route was that used by Koh et al. (2009) who used a microfluidic route (which utilises microconfinement) where pDNA/PEI complex size was significantly reduced compared to complexes produced in bulk solution. If precipitation can occur in agarose, then, PS-SW-AGE may yield even smaller pDNA/PEI complexes. The synthesis of pDNA/PEI complexes for use as non-viral vectors in the chondrogenic layer of the osteochondral GAM will therefore be investigated. As previously discussed, separate osteogenic (pDNA/CaP or pDNA/MgP) and chondrogenic (pDNA/PEI) cryogel GAMs should be prepared, since it is likely that osteogenic and chondrogenic vectors share dissimilar synthesis parameters. As such, their parallel or sequential synthesis may produce non-ideal conditions for one of both vector types. Cryogels encapsulating pDNA/CaP or pDNA/MgP are herein referred to as osteogenic cryogels, whilst cryogels encapsulating pDNA/PEI are herein referred to as chondrogenic cryogels.

3.1.4 Controlling Primary Particle Size

As previously discussed, reducing pDNA/CaP primary particle size to sub-100 nm diameters within the osteogenic cryogel is expected to give improved transfection efficacies in the osteogenic layer of the osteochondral GAM. For pDNA/MgP particles, research by (Bhakta et al., 2005) and (Bhakta et al., 2009) found that sub-100 nm diameter particles were able to successfully transfect cell monolayers. Beyond these studies there is little research that would allow one to identify any trend between pDNA/MgP particle diameter and transfection efficacy. Both pDNA/CaP and pDNA/MgP particles should therefore aimed to be synthesised with sub-100 nm diameters to maximise their surface-area-to-volume ratio, thereby encouraging dissolution/transformation processes required for surface-media transfection. The same principles in controlling particle size for pDNA/CaP and pDNA/MgP particles applies to pDNA/PEI complexes, but their size requirements are less stringent. pDNA/PEI particle sizes between approximately 500 nm and 2000 nm have successfully transfected cells, where transfection efficacy peaks for particles approximately 800 nm in diameter (Sang et al., 2015). Additionally, Ogris et al. (1998) found that smaller pDNA/PEI complexes with 40 nm diameters had poorer transfection efficacy compared to larger complexes. pDNA/PEI complexes will therefore not be reduced below 100 nm. Besides, it will ultimately be difficult to measure pDNA/PEI complex size, given pDNA cannot be identified in conventional SEM.

3.1.4.1 Conventional Synthesis

In conventional wet-chemical synthesis routes, reducing pDNA-mineral particle size is done by controlling supersaturation, s, and temperature, T, according to Equation 3.1 which defines the critical radii of a particle, r_{crit}, according to classical nucleation:

$$r_{crit} = \frac{2\gamma v}{k_B T\ ln(s)} \tag{3.1}$$

Where k_B is the Boltzmann constant, and γ and v are surface energy (Jm^{-2}) and molar volume (m^3) of the precipitating species. The first (and arguably the simplest) way of reducing r_{crit} in conventional wet-chemical synthesis routes is by increasing the supersaturation toward the desired species. In the simplest terms, this sways the precipitation reaction to being nucleation-

dominant where a high number of nuclei spontaneously form, consuming precursor and therefore limiting subsequent growth and thus reducing particle size. Increasing supersaturation toward the desired species can be achieved by increasing the initial reactant concentrations, adjusting reactant mixing rates, or through adjusting the temperature and pH of the reacting mixture. Pressure can also be adjusted to change supersaturation in synthesis routes such as hydrothermal synthesis, but such a route is not commonly used for nucleic acid-containing particles. Note that surface energy and molar volume are properties of the precipitating species itself and therefore cannot be 'adjusted' experimentally, but depend on supersaturation, temperature, and the ionic species present in the salt solutions.

Supersaturation can be argued to be a more crucial determinant of nucleation rate when compared to temperature, given that an increase in supersaturation from two to four can increase the nucleation rate by a factor of 10^{70} but an increase in temperature from 250 K to 300 K increases nucleation rate only by a factor of 10^{10} (Kwon and Hyeon, 2011). Increasing the initial concentration of salts and pDNA is therefore the simplest way of increasing supersaturation toward the desired species. But the rate of mixing and the method by which salt and pDNA solutions are mixed is as important as their initial concentration. Rapid mixing will provide a high supersaturation but often with non-uniform concentrations. In comparison, slowly titrating one solution into another solution that is continuously stirred can utilise high supersaturation but under more uniform mixing conditions. Titration under stirred conditions can therefore produce narrower particle size distributions; hence the approach's popularity in pDNA/CaP synthesis (Liu et al., 2011, Khan et al., 2016).

Whilst temperature itself is a determinant of r_{crit}, it is also a factor in determining supersaturation. This is due to the temperature-dependent solubility of even highly insoluble species - such as HAp – where an increase in temperature leads to an increase in the apparent solubility of HAp (Prakash et al., 2006). So reducing temperature reduces supersaturation, but temperature is inversely proportional to r_{crit}. Due to these competing effects, the relationship between temperature and particle or complex size will depend on the severity of the change in solubility with temperature. Of course, then, a stable temperature is most desirable to maintain a constant supersaturation. In conventional CaP particle synthesis, the temperature of the reacting mixture is modulated by measuring the temperature and then providing/extracting thermal energy to/from the mixture depending on the desired temperature and whether the reaction is exothermic or endothermic (Qiu et al., 2022). Critically, the temperature of the

reacting mixture for pDNA-loaded particles must not exceed the temperature at which the pDNA thermally denatures

pH can also be adjusted to control supersaturation toward the desired species, given mineral species such as HAp have pH-dependent solubilities (Larsen and Jensen, 1989). pH also changes the protonation/hydroxylation of chemical species, such as $H_xPO_4^{x-3}$, and the concentration of OH^- ions, both of which are constituents of HAp and therefore influence supersaturation. Like temperature, pH can be adjusted by continuously monitoring the reacting solution and adjusting the pH accordingly through the addition of an acid or base. For example, the synthesis of HAp has been shown to decrease simulated body fluid solution pH through consumption and production of OH^- and H^+ ions respectively (Minouei et al., 2012). OH^- ions can therefore be added in the form of NaOH to maintain the desired reacting solution pH (and OH^- concentration).

3.1.4.2 PS-SW-AGE

Modulating supersaturation or temperature independently of one another provides the most precise control over particle physicochemical properties, thus providing the ideal reaction conditions in which to tune pDNA/CaP and pDNA/MgP particle size. For example, increasing the supersaturation of the solution by increasing the concentration of all reactants, whilst maintaining temperature by extracting the thermal energy produced by the reacting solution (in the case of an exothermic reaction). Alternatively, one can increase the temperature of the reacting solution whilst adjusting the pH to compensate for the temperature-dependence of pH to maintain the desired supersaturation at a given temperature.

In the PS-SW-AGE approach, however, adjusting supersaturation or temperature independent of one another is complex given the lack of control over some experimental parameters. Furthermore, ion mixing is primarily driven by the applied potential as opposed to stirring or titration, which brings about complex inter-parameter relationships. Consequently, modulating any single parameter will impact another, resulting in co-dependent parameters. The relationship between particle size and any single experimental parameter is therefore less consequential such that one cannot provide a meaningful combination of parameter conditions that serve as an ideal subset to synthesise sub-100 nm pDNA/CaP and pDNA/MgP particles.

As some inter-parameter relationships will be less substantial than others, it will be useful to first discuss the significance of these relationships. Methods of control over experimental

parameters can then be considered to mitigate the most significant inter-parameter relationships. Then, once measures of control are established, experimental parameters (salt concentration and species, agarose concentration, buffer temperature, applied potential, pH) can be controlled/modulated independently to establish their relationship with particle size. This will allow the selection of an ideal subset of experimental parameters that provide the desired particle size.

3.1.5 Inter-parameter relationships

In the PS-SW-AGE approach, salt concentration and species, agarose concentration, buffer temperature, applied potential, and buffer pH, can be classified as either controlled or semi-controlled parameters depending on whether their initial value changes during synthesis. Each of these parameters complexly influence supersaturation and temperature which govern the nucleation and growth of particles. Of concern is the variation of these parameters in (and within the locality of) the zone of precipitation of particles.

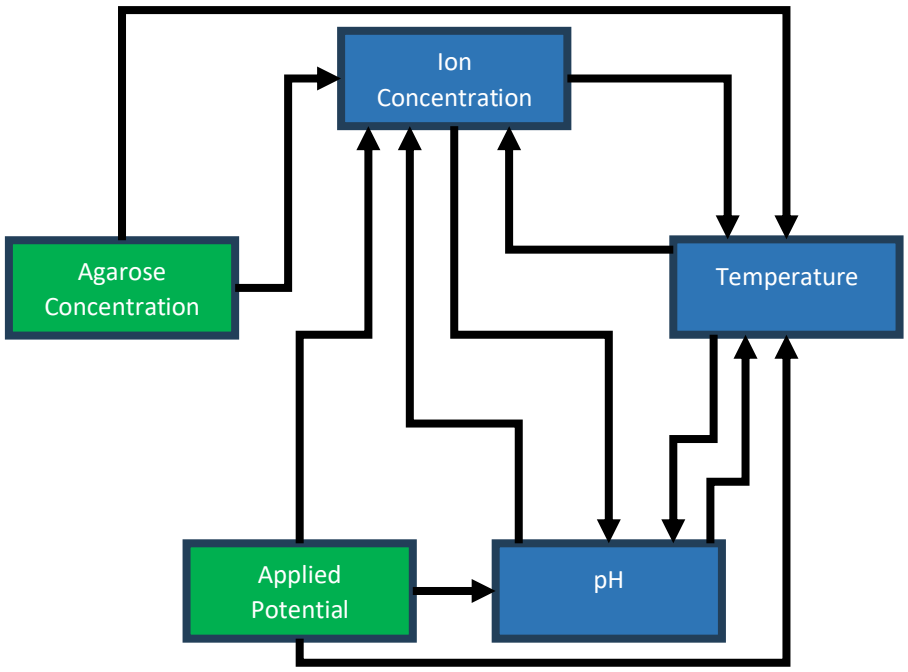


Figure 3.1. Schematic of inter-parameter relationships in the PS-SW-AGE approach. Green = fully-controlled parameters, and blue = semi-controlled parameters. Arrows indicate an inter-parameter influence.

A change in the magnitude in any single parameter influences at least two other parameters, as shown in the map of inter-parameter relationships in Figure 3.1. Since agarose concentration does not change from its initial value and the initial applied potential is maintained by the power

pack, both are considered fully controlled parameters uninfluenced by any other parameter and assumed not to change during PS-SW-AGE. In contrast, ion concentration, temperature and pH are semi-controlled, given their initial values are controlled but subject to change during PS-SW-AGE.

As previously argued, it is critical to discuss the effect of these parameters on one another in order to: (1) predict the magnitude and locality of their co-dependence (local to zone of precipitation or global); (2) develop and implement a means of modulating the desired parameter(s) to eliminate or significantly reduce inter-parameter influences; (3) independently modulate single parameters to produce an ideal subset of conditions to synthesise sub-100 nm pDNA/CaP and pDNA/MgP particles.

3.1.5.1 Agarose Concentration and Ion Concentration

Agarose concentration has several influences on other parameters; the first being that of ion concentration. Pore size is known to be inversely proportional to agarose concentration (Pernodet et al., 1997, Narayanan et al., 2006). In this discussion, tortuosity of agarose is assumed to be proportional to agarose concentration, assuming one considers agarose pores as spheres. By increasing agarose concentration, then, pore size reduces and tortuosity increases, both of which will reduce the mean free path of ions travelling through the gel and thus reduce their effective electrophoretic velocity since ions have a longer effective distance to travel between two points.

The relative permittivity of agarose gel has been shown to diminish with an increasing agarose concentration, which (from a macroscopic viewpoint) would enhance the electric field strength through the gel and increase ion electrophoretic velocity and modulate ion concentration gradients. However, a model by Hsu et al. (2012) showed that an increased agarose concentration increases the relative permittivity of the liquid component of gels. Since the liquid component is the transport medium for ions, ions will actually be subjected to greater frictional forces and thus reduced electrophoretic velocity.

Increasing agarose concentration is therefore expected to reduce the electrophoretic driving force of ions in the PS-SW-AGE approach and therefore decrease the effective velocity of ions. Local ion concentration would subsequently increase if ion bands are compressed during transport. But changes to ion concentration would only be evident at medium boundaries – such as the well-gel interface - where a disparity in porosity/tortuosity and liquid relative permittivity will cause ion bands to compress or stretch depending on the direction of transport. This is simply due to the non-zero thickness of ion bands where ions at the leading and trailing edges accelerate/decelerate at different rates due to the time delay in transitioning between mediums. So, when an ion band is transported from a medium of low agarose concentration (large pores and low liquid relative permittivity) to a medium of high agarose concentration (small pores and high liquid relative permittivity), the ion band will compress. When transitioning from a lower to higher agarose concentrations the opposite will be true and an ion band will stretch.

In high concentration agarose gels, there is of course a lower total liquid content that is segmented into a large number of small pore volumes, in contrast to a low concentration

agarose gels with a higher total liquid content divided into a smaller number of larger pores. An interesting consideration then is that ions electrophoretically transported from a low concentration gel to a high concentration gel would increase in concentration due to the lower liquid content. Though this increase in concentration is expected to be marginal, given that an increase in agarose gel concentration from 1 wt % to 3 wt % only reduces the liquid content by 2 wt %. Furthermore, this is a simplistic assumption that ignores the increase in diffusion flux arising from the greater ion concentration gradient, hence any increase in ion concentration between agarose gels of comparable agarose wt % would be negligible.

While ion concentration is influenced by agarose concentration, there is a more complex relationship between agarose concentration and supersaturation due to the nanoconfinement effects of the agarose network. Take a high concentration agarose gel for instance with a very small pore size. An ion band transported from a medium of larger pore size and greater relative permittivity will be stretched. So if two ion bands of opposite charge travelling toward each other are both stretched to the same extent, the supersaturation ratio upon their mixing at the zone of precipitation is lower than if the ion bands were not stretched. But given that pore size is reduced, the nanoconfinement effect imposes a greater supersaturation threshold within the pore given the ratio of ion to precipitate volume has decreased (Meldrum and O'Shaughnessy, 2020). Furthermore, supersaturation is dependent on the species precipitating. So nanoconfinement effects will have less of an impact on the supersaturation threshold of more insoluble species.

3.1.5.2 Agarose Concentration and Temperature

As discussed, agarose concentration dictates gel pore size, tortuosity, and liquid relative permittivity, and – by extension – ion mobility and concentration. Since ions are the charge carriers during electrophoresis, the concentration of ions will determine local conductivity and the magnitude of heat generated via joule heating. Therefore, agarose concentration could have an impact on temperature. For direct current, the heat generated (P) is proportional to current squared (I^2) and the applied potential (V). Theoretically then, agarose concentration should be inversely proportional to heat generated. However, it was previously discussed that ion concentration will only slightly increase with agarose concentrations due a negligible loss of water content from, say, a 1 wt % gel to a 2 wt % gel. Therefore, increasing agarose concentration will produce a negligible increase in joule heating due to changes in ion concentration.

Interestingly, a positive feedback loop exists between temperature and electrical conductivity that is intrinsic to agarose gel electrophoresis. Heat generated by joule heating will increase the conductivity of the gel, which increases current through the gel, which increases the heat generated by joule heating, and so on. A temperature increase in the gel with time may therefore be inevitable but could be mitigated to some extent with higher concentration agarose gels.

3.1.5.3 Applied Potential and Ion Concentration

The applied potential is the only other fully controlled parameter, alongside agarose concentration, given its initial value is maintained by the power pack through adjustment of the current. The applied potential has an impact on ion concentration and supersaturation, temperature, and pH, and is therefore the most influential parameter in PS-SW-AGE. Ion concentration at any time during transport in PS-SW-AGE is dependent on the initial loading solution concentration and the electric field profile along the ion transport path. As previously discussed, changes in relative permittivity can induce ion band compression or stretching.

The applied potential can (to some extent) be considered as the amplitude of the electric field profile, since electric field strength for constant fields is proportional to the applied potential, and ion drift velocity is proportional to the electric field strength. Thus, ion drift velocity is proportional to the applied potential. Changing the applied potential will therefore exacerbate ion band compression or stretching, where compression or stretching depends on the direction of transport (and ion charge) between two mediums of contrasting relative permittivity.

3.1.5.4 Applied Potential and Temperature

Heat generated by the joule heating effect, H, is related to current, I, and applied potential, V, through Equations 3.2 and 3.3:

$$H = I^2 \times R \times t \tag{3.2}$$

Equation

$$H = V \times I \times t \tag{3.3}$$

Where R is the resistance (Ω) of the medium across which the potential is applied and the current passes through, and t is the time (s) that the potential is applied for. Given that H is proportional to V, one can expect an increase in the applied potential to proportionally increase the heat generated via joule heating. Furthermore, an increase in the temperature of the buffer and gel will lead to a decrease in resistance in both mediums and therefore allow for greater current, further intensifying the heat generated and creating a positive feedback loop between temperature and current.

The buffer and gel temperature does not continue to rise indefinitely. Eventually an equilibrium between the thermal input of joule heating and thermal transfer to the surrounding air is achieved. Even so, over long periods or at high potentials, temperatures can become hot enough to denature pDNA and even melt agarose gels. This is a well-known effect in gel electrophoresis which is significant enough to prompt the development of numerous cooled electrophoresis tanks to mitigate the effects of joule heating.

3.1.5.5 Applied potential and pH

A greater applied potential will escalate the rate of oxidation and reduction reactions at the anode and cathode respectively. During this electrolysis of H_2O, H_2(g) and O_2(g) are produced alongside OH^- and H^+ ions at either end of the tank. Whilst the gases bubble to the surface and escape the tank, ions introduced into the localities of the electrodes create a pH gradient across the tank. The build-up of pH gradients can be prevented by simply recirculating buffer between electrodes i.e. pumping buffer from the anode to the cathode and vice versa.

3.1.5.6 pH and Temperature

The electrolysis of water that is intrinsic to the PS-SW-AGE approach introduces H^+ and OH^- ions at either end of the tank, so one can expect an increase in the conductivity of the buffer and hence an increase in the current flowing through the tank. As previously discussed, heat generated by joule heating, H, is proportional to current, I. The heat generated by joule heating will therefore increase as the pH gradient becomes more severe with time due to the greater number of charge-carrying ions in the buffer. It was also previously mentioned that a positive feedback loop exists between temperature and conductivity; so by extension this applies to temperature and pH provided oxidation and reduction reactions continue to provide H^+ and OH^- ions to the buffer.

A pH change from 7.4 to 8.0 would provide more optimal conditions for the synthesis of HAp (or ACP) according to the pH-dependent stability of the mineral (Johnsson and Nancollas, 1992). It is interesting to note that this will have a knock-on effect to the conductivity and temperature of the buffer. The greater amount of NaOH added to the buffer to increase the pH will lead to a higher concentration of charge-carrying Na^+ and OH^- ions and hence boost buffer conductivity. A buffer of pH 8.0 can therefore be expected to generate more heat via joule heating due to the increased current flowing through the buffer.

3.1.5.7 pH and Ion Concentration

If we assume that CaP particles precipitating during PS-SW-AGE are stoichiometrically equivalent to HAp, then the following reactions proceed:

$$10Ca^{2+} + 6HPO_4^{2-} \xrightarrow{2OH^-} Ca_{10}(PO_4)_6(OH)_2 + 6H^+ \quad 3.4$$

$$10Ca^{2+} + 6H_2PO_4^- \xrightarrow{2OH^-} Ca_{10}(PO_4)_6(OH)_2 + 12H^+ \quad 3.5$$

Where reaction in Equation 3.4 proceeds when Ca^{2+} and HPO_4^{2-} ions mix and the reaction in Equation 3.5 proceeds when Ca^{2+} and $H_2PO_4^-$ ions mix. The ratio of incidence between these two reactions depends primarily on the pH of the buffer where molar fractions of $H_xPO_4^{x-3}$ species at pH 7.4 and 8.0 differ.

Twice the amount of H^+ is produced when H_2PO_4 is the reactant so this reaction would produce a more acidic local environment post-precipitation. In conventional wet chemical synthesis these reactions occur in bulk solutions that are stirred to provide uniform concentrations of reactants, hence H^+ concentration can be considered close to constant throughout the reacting solution and can be adjusted almost immediately via continuous pH monitoring and additions of NaOH if necessary. In contrast, these reactions in PS-SW-AGE occur under nanoconfinement. H^+ ions close to the edges of the zone of precipitation may be electrophoretically transported and exchanged for OH^- ions travelling in contraflow, but particles themselves will restrict the diffusion of H^+ and OH^- ions from/to the zone of precipitation. Furthermore, continuous monitoring and adjustment of pH within the agarose matrix is not practical using a pH probe

since the probe will distort the electric field and ion concentrations. Ultimately, one can expect the local pH at the zone of precipitation to become more acidic as a result of HAp-like CaP precipitation with no practical intervention available to maintain a pH of 8.0.

3.1.5.8 Temperature and Ion Concentration

Roebuck and Goldblith (1975) found the relative permittivity of a 0.98 wt % agarose gel decrease from 76.6 to 71.4 at 25 °C and 45 °C respectively. So, as relative permittivity of agarose gels is temperature dependent, ion transport velocity in the PS-SW-AGE approach is also temperature dependent. As previously discussed, the effect on ion concentration in ion bands is due to the disparity between ion velocities at the leading and trailing edges that either stretches or compresses the ion bands. Temperature would have a similar effect at a medium interface (such as the well-gel interface) where joule heating may establish a temperature gradient. One possibility here is that the relative permittivities of the loading solution and agarose gel are amplified to different extents, which would amplify the stretching or compression of the ion band as it is transported from one medium to the other.

Temperature is also intrinsically related to the solubility of a precipitating species, where even highly insoluble species such as HAp have been shown to have an apparent temperature-dependent solubility over an arguably small temperature range (Prakash et al., 2006). Temperature therefore influences the supersaturation ratio of a given species in the PS-SW-AGE approach. This is an interesting concept for HAp synthesis in the PS-SW-AGE approach since the wet-chemical synthesis of HAp is itself exothermic. In conventional wet-chemical synthesis routes, the absorption of thermal energy into the reacting solution can be considered near-homogeneous under stirred conditions and can be dealt with simply by closely monitoring the temperature and extracting the thermal energy via cooling. But the PS-SW-AGE approach is a non-stirred approach and is not currently cooled. Supersaturation will therefore vary through the zone of precipitation due to the unmanaged exothermic reaction. Thus far, pDNA/CaP layers are so thin that temperature gradients due to exothermic reactions can be considered negligible, but this will become more severe when synthesising thicker pDNA/CaP layers.

Ion concentration will also impact the temperature at the zone of precipitation. This is simply down to the relationship between ion concentration and conductivity. Specifically, the conductivity of salt solution increases with concentration; this is true for $CaCl_2$ at low concentrations and peaks around 2.75 M, after which conductivity decreases until the solubility

limit is reached (Sun and Newman, 1970). Where the $CaCl_2$ concentration provides a greater conductivity, more current flows through the $CaCl_2$ loading solution and through the dissociated Ca^{2+} ion band. The same can be assumed for the $H_xPO_4^{x-3}$ band. More current inherently means more joule heating, but given ion bands are not static, a trail of thermal energy can be expected in the wake of any ion band transported through the agarose gel. This thermal energy will be absorbed by the buffer and agarose matrix and can therefore influence the critical radii at the zone of precipitation through changes to both temperature and the temperature-dependent supersaturation.

3.1.6 Mitigating Inter-parameter Influences

Each parameter in the PS-AGE approach influences at least two other parameters. Whilst agarose concentration and applied potential are fully controlled, the remaining parameters deviate from their initial values and are therefore semi-controlled. Ultimately, this leads to poor control over supersaturation and temperature at the zone of precipitation and therefore difficulties in regulating the nucleation and growth of particles in the PS-SW-AGE approach.

3.1.6.1 pH

Arguably, pH is the simplest parameter for which a method of control can be devised. By controlling pH, one can eliminate the positive feedback loop between temperature and pH that occurs due to both parameters increasing buffer conductivity with time. Whilst pH control in wet chemical synthesis requires monitoring and adjustment, the PS-SW-AGE approach simply requires circulation of the buffer to prevent a pH build-up that is inherent in agarose gel electrophoresis. This can be accomplished using a pair of peristaltic pumps that pump buffer from one electrode to another in a circular motion, forming a simple pH control unit. Monitoring and adjustment of the pH will not be required given the ratio of buffer to particle volume is very high, thus precipitation reactions are not expected to influence the global pH of the PS-SW-AGE system. However, there is little that can be done to mitigate pH changes at the zone of precipitation due to the production of H^+ following HAp precipitation. This is an unavoidable consequence of using nanoconfinement to control particle synthesis since fluids are almost static.

3.1.6.2 Temperature

Temperature at the zone of precipitation, though impossible to measure without influencing precipitation reactions, will increase under an applied potential due to joule heating and exothermic reactions. Temperature therefore varies spatiotemporally in the agarose gel matrix which is highly unfavourable when trying to control temperature-dependent supersaturation and increase the homogeneity of the particle size distribution. It is theorised that temperature increases at the zone of precipitation can be eased significantly by cooling the buffer surrounding the gel which would enhance thermal transfer from the gel to the buffer. By continuously monitoring buffer temperature close to the gel, the desired temperature could be reached using a temperature control unit consisting primarily of a heat exchanger that begins to extract thermal energy only when the desired temperature is approached or surpassed. More homogeneous buffer temperatures would be obtained when combined with buffer circulation pumps to prevent a pH gradient build-up. Hence a temperature/pH control unit should be devised.

The use of a temperature/pH control unit will only go so far in maintaining a homogeneous reaction temperature at the zone of precipitation. It could certainly stabilise global buffer temperature in the tank and thus nearly eliminate joule heating of the buffer and therefore prevent thermal energy from being transferred to the agarose gel. However, it will not be possible to eradicate temperature fluctuations that originate from the agarose gel itself given the gel's liquid component cannot be circulated. One must accept that some inter-parameter influences are intrinsic to the PS-SW-AGE approach and will – to some extent – increase the heterogeneity of pDNA/CaP and pDNA/MgP particle size distributions.

3.1.6.3 Ion Concentration

Ion concentration has the greatest influence on supersaturation but is also the most difficult parameter to control in the PS-SW-AGE approach. This is due to ion concentration being influenced by all other parameters, having dependence on the initial loading solution concentration and the electric field profile along the ion band transport path. Note also that the electric field profile is a consequence of the agarose concentration, applied potential, temperature and pH.

The non-uniform electric field profile due to the cuboidal shape of the well in the PS-SW-AGE approach will theoretically produce an ion concentration with a bell curve distribution. This will force ions into a C-shape upon transportation into the gel and therefore produce a non-uniform supersaturation at the zone of precipitation. A solution to providing uniform electric field profiles is to change the initial loading shape of ions from cuboidal to cylindrical. This is because the electric field strength between two point charges reduces radially, hence a cylindrically shaped loading solution will exhibit a highly symmetrical electric field profile in contrast to the lower symmetry of a cuboidal loading solution.

A change in ion concentration at medium boundaries is predicted to be most substantial at the well-gel interface. To avoid this, the experimental layout of the PS-SW-AGE approach should transition to a gel-based loading system, whereby salt and pDNA solutions are mixed with agarose to create 'loading gel' mixtures. These loading gels would need to be set and assembled adjacent to the desired 'recipient gel' in a dry environment prior to submersion. The loading gel and recipient gel could be cast cylindrically, thus providing the desired symmetrical electric field profile to better control ion concentration and enhance gel pre-clinical relevancy by producing a cylindrical particle layer within a cylindrical gel. Gel-gel interfaces will of course still present some disparity in porosity and relative permittivity because of the effect salts have on agarose gelation, but less-so than at the well-gel interfaces. The use of cylindrical loading gels would also eliminate the unwanted diffusion of ions prior to applying the potential and eliminate turbulent flow in the well during pipetting that would otherwise reduce the uniformity of ion concentration in the well.

As ion concentration is dependent on the electric field profile along the ion transport path and therefore the relative permittivity of the transport medium, the zone of precipitation should ideally be moved away from medium boundaries. An argument can therefore be made to employ the PS-DW-AGE approach utilised by Kimura et al. (2018) as opposed to the PS-SW-AGE approach utilised so far in this research. The use of opposing wells in the PS-DW-AGE approach would shift the zone of precipitation into the bulk of the agarose gel and allow ions to mix in an absence of medium boundaries where electric field profiles are less turbulent. If combined with the aforementioned cylindrical loading gels, one could sandwich a $CaCl_2$ loading gel and an Na_2HPO_4 loading gel around a recipient gel, thus combining several beneficial changes to better control ion transport, concentration, and mixing.

3.1.6.4 Agarose Concentration

The effect of agarose concentration on ion concentration and supersaturation is thought to be highly advantageous for the synthesis of pDNA/CaP and pDNA/MgP particles, despite the complex relationship. This is due to the high insolubility of mineral species such as HAp that lead to rapid growth in conventional wet-chemical synthesis and can make controlling particle size difficult. The nanoconfinement effects of the agarose gel combat this rapid growth by raising the supersaturation threshold toward mineral species within pores. Efforts should therefore be made to produce agarose gels with a small pore size distribution by controlling cooling temperature and rate to deliver a uniform supersaturation threshold throughout the gel and therefore a narrow particle size distribution.

3.1.6.5 Applied Potential

Ideally for the PS-DW-AGE approach, the applied potential would only influence ion concentration and rate at which ions bands mix. A range of applied potentials could then be applied to compress or stretch ions bands to achieve the desired mixing rate and supersaturation. If temperature and pH are managed adequately, applied potential could be varied independently to determine its relationship with particle size.

An interesting consideration is that the magnitude of the applied potential will also determine the post-synthesis transport of particles. Upon their nucleation, particles will be electrophoretically transported from their initial location if: (1) the particles are small enough to pass through the agarose network; (2) they are not strongly adhered to the agarose surface, and (3) they have a non-zero zeta potential at the pH of the surrounding buffer. Consequently, excised gels for particle size characterisation produced using a range of applied potentials may contain an incomplete particle population whose size distribution is positively skewed towards larger particle sizes through the loss of smaller particles. Such an effect must be considered when trying to identify a relationship between applied potential and particle size.

3.1.6.6 Improving Secondary Particle Stability

In most pDNA/CaP particle transfection systems, particle size is often regarded as the most critical particle property in CaP-based transfection (Orrantia and Chang, 1990, Guo et al., 2017). Particle stability is arguably as important as particle size, given that poor inter-particle stability

can lead to agglomeration which increases the effective size of particles and therefore reduce transfection efficacy. This can arise from a lack of electrostatic or steric repulsion between particles. Cationic biopolymer shells are a useful addition to pDNA/CaP particles that can boost zeta potential magnitudes and hence improve the stability of particle suspensions (Qiu et al., 2022). Furthermore, the positive surface charge of particles is thought to enhance particle-cell membrane interaction (Arvizo et al., 2010).

The proposed metastability of primary pDNA/CaP particles *in-vitro* facilitates primary particle dissolution/transformation processes that facilitate secondary pDNA/CaP particle nucleation and growth. Good intracellular stability of secondary pDNA/CaP particles is necessary to prevent premature or rapid dissolution within the acidic endosomal and lysosomal compartments of the cell prior to the optimal pDNA release point. Further to improving inter-particle repulsion, biopolymer shells can serve as a kinetic barrier between surface ions and water molecules to prevent such premature dissolution.

Conventional synthesis of pDNA/CaP particles are solution-based and therefore require inter-particle stability to prevent agglomeration and dissolution of particles. Such stability is required from synthesis to administration on cell monolayers, since no secondary pDNA/CaP particles are sought. In contrast, PDA-pDNA/CaP cryogels produced via the PS-SW-AGE approach are theorised to rely on the metastability of embedded pDNA/CaP particles so that dissolution/transformation can take place. Hence, the metastability of primary pDNA/CaP particles here is a valuable asset. It is secondary pDNA/CaP particles that would benefit from enhanced stabilisation *in-vitro*, given these particles are responsible for nucleic acid delivery to the cell nuclei. Interestingly, secondary pDNA/CaP particles will not be restricted to the same nanoconfinement during nucleation and growth given their formation occurs in a cryogel environment and their nucleation or growth will not be restricted to a 6-minute window under an applied potential. Crystalline phases such as HAp may then nucleate and grow on released pDNAs to form secondary pDNA/CaP particles, with the HAp crystal structure providing increased resistance to dissolution *in-vitro* (compared to ACP crystal structure of primary pDNA/CaP particles).

Though secondary pDNA/CaP particles could indeed be formed of HAp, they would still be susceptible to pDNA payload loss if pDNA is adsorbed to the outer surface of the particle rather than encapsulated. Stabilising biopolymer shells would therefore prove beneficial for secondary

pDNA/CaPs too. But the biopolymer would likely need to be added post synthesis to avoid interference with the already complex nucleation and growth dynamics of primary pDNA/CaP particles.

One concern of introducing a biopolymer to stabilise secondary particles is the potential effect on primary particle stability. The biopolymer must not stabilise primary particles to significantly hinder their dissolution, thereby preventing the release of ions and pDNAs necessary for secondary particle nucleation and growth. This would easily be accomplished if all pDNAs were encapsulated by CaP particles and not adsorbed onto their surfaces. In this scenario, a cationic biopolymer could be incorporated into the cryogel post-synthesis and would not adsorb onto primary particle surfaces due to the net-positive surface charge of pDNA/CaP particles. However, given pDNA adsorption onto CaP surfaces is difficult to measure and is assumed to be non-zero, the addition of a biopolymer post-synthesis may prevent a portion of primary particles from dissolving *in-vitro*.

PEI is a cationic polymer of particular interest in this work since its overall positive charge at neutral pH facilitates complexation with pDNA. In the literature, these complexes exhibit good transfection efficacies (Fischer et al., 1999, Sabin et al., 2022) and can exceed that of commercially available polymeric transfection agents (Zaric et al., 2004). The positive charge of PEI means it can be transported via electrophoresis so it could be conveniently incorporated to the PS-DW-AGE approach after pDNA/CaP or pDNA/MgP particle synthesis. But penetration of PEI into the agarose hydrogel would be almost unidirectional, hence any blockages encountered due to the pDNA/CaP or pDNA/MgP particle layer would prevent uniform distribution of PEI within the gel. Furthermore, sustained application of the applied potential risks transporting already formed small particles away from particle layers. Simply bathing cryogels with embedded particles in a PEI solution would provide a much more uniform coverage of PEI throughout the agarose matrix since PEI would diffuse into the cryogel from all directions.

If bathing hydrogels, one must keep in mind that prolonged submersion periods in any neutral pH solution will eventually induce the dissolution and/or transformation of primary particles (Kimura et al., 2018). This could be exacerbated if submerging cryogels since the diffusion of ions would not be restricted by a nanoconfining hydrogel matrix. Submersion times would vary considerably between cryogels and hydrogels due to contrasting porosity/permeability, where hydrogels would significantly diminish the effective diffusivity of PEI molecules and require a

much longer submersion time. The most sensible option would therefore be to submerse cryogels for shorter periods.

An interesting secondary advantage to using PEI to coat pDNA/CaP particles is that PEI could essentially 'mop up' residual pDNA molecules that have not complexed with or adsorbed onto CaP or MgP particles. pDNA/PEI complexes would nucleate and grow within the nanoconfining agarose matrix where growth potential is lower than in bulk solution. Even under microconfinement, pDNA/PEI complexes have been significantly reduced in diameter due to the substantial reduction in supersaturation that limits the growth potential of complexes (Koh et al., 2009). Though the 'mopping up' of unbound pDNAs could boost transfection efficacy, the primary goal should be to synthesise primary pDNA/CaP and pDNA/MgP particles that completely encapsulate pDNA in a layer of mineral particles. PEI would then ideally be loosely adsorbed onto cryogel surfaces following lyophilisation. PEI could then be mobilised from surfaces upon hydration of the cryogel in cell media, loitering in the now microscale pore network ready to coat newly formed secondary pDNA/CaP and pDNA/MgP particles.

3.1.7 Improving Pre-Clinical Relevancy of Cryogels

3.1.7.1 Forming a cylindrical Cryogel and Particle Layer

As discussed previously, the cryogel itself must be suitable for use in a full-thickness rabbit osteochondral model. The cryogel is therefore required to be 4 mm in diameter (for a critically sized defect) and be at least 3 mm in thickness, where the osteogenic layer is 2.7 mm thick. The cryogel must be cylindrical in shape to fill a debrided osteochondral cavity, whilst the particle layer must have a cylindrical cross-section and extend to the circumference of the cryogel for lateral osteointegration with the native mineralised tissue.

Numerous issues associated with creating a cylindrical cryogel of these dimensions with a cylindrical particle layer using the PS-DW-AGE or PS-SW-AGE approaches have been considered earlier. Most significant of these issues is the inability to electrophoretically transport ions as cylindrical bands to form the desired cylindrical shape, and the format/orientation of the gel slab that prevents a cylindrical gel shape from ultimately being extracted. As previously discussed, the use of cylindrically shaped loading gels is touted to provide more uniform ion concentrations by: 1) reducing the disparity in relative permittivity and porosity between the loading gels and the recipient gel; and 2) providing an initial ion band shape that echoes the

radial shape and symmetry of the electric field between two point charges. Using a pair of cylindrical loading gels sandwiched around a recipient gel will resemble the PS-DW-AGE approach introduced by (Kimura et al., 2018) and thus take advantage of the more consistent and stable electric field profile in the gel bulk. Besides better control over particle size, the use of cylindrical loading gels and recipient gel will naturally facilitate the formation of cylindrical particle layers within the recipient gel.

Another benefit of using a cylindrical loading gel format is that the recipient gel, if cylindrical, would simply be removed from the tank and cut using a gel punch to extract multiple gels for lyophilisation, each containing a particle layer across their cross section. If cylindrical loading and recipient gels are physically contained within a cast during use, this would increase the unidirectionality of ion flow and mitigate unwanted lateral diffusion of ions that can occur in the PS-DW-AGE and PS-SW-AGE approaches. The cylindrical gels could be assembled prior to submersion to maximise this benefit, thus making ion diffusion from gels into surrounding buffer negligible. And, if an appropriate cast design is manufactured, a row of loading gel and recipient gels could be sandwiched together to produce a whole row of gels that each encapsulate a particle layer.

One disadvantage to using sandwiched casts of cylindrical loading and recipient gels is that ions adjacent to the wall of the cast will be subjected to lower electrophoretic forces and thus lead to a degree of parabolic ion flow. This is simply a consequence of the stern layer and is more commonly observed in an electro-osmotically-driven microfluidic system (Tarn and Pamme, 2014). Punching smaller cylindrical gels from the larger gel should therefore be done away from the circumferential surface of the recipient gels to avoid producing gels encapsulating severely angled or incomplete particle layers. An interesting consequence of parabolic ion flow using cylindrical gels is the formation of concavely shaped particle layers which would coincidently more accurately mimic the native concave shape of the osteochondral at the MFC.

The PS-DW-AGE and PS-SW-AGE approaches use a gel slab format within a horizontal gel electrophoresis tank where electrodes are positioned at the bottom of the reservoirs and the gel slab sits on a much higher shelf in the z-axis (axis are shown in Figure 3.3). This large z-axis separation is highly favourable when characterising nucleic acids in conventional agarose gel electrophoresis as electric field strength along the z-axis will vary only slightly. Hence, identical pDNAs positioned either at the top or bottom of a 2 mm deep well will not separate significantly

due to their relative position in the z-axis. However, a loading and recipient gel sandwich, positioned centrally within the tank, will be much larger in size than a 2 mm thick loading solution. Electric field strengths will then vary along the z-axis of gel cylinders, being greatest at the bottom. Ion velocities at the bottom of the cylinder would therefore be greater and lead to non-uniform ion band mixing and potentially non-uniformly shaped particle layers as a result. New electrodes should therefore be designed to be in line with the centre of gel cylinders.

3.1.6.2. Layer thickness and location

The PS-SW-AGE approach produced pDNA/CaP layers that were visually observed to be approximately 1.5 mm thick, which is less than adequate for a rabbit osteochondral GAM. Assuming a 3 mm thick osteochondral GAM requires only a 0.3 – 0.5 mm thick chondrogenic layer, a 2.5 – 2.7 mm thick osteogenic layer is needed. One could try to use greater salt concentrations in loading gels to increase supersaturation toward the desired mineral in the hope of increase particle layer thickness. However, this could instead increase the particle layer intensity (whiteness) due to an increased particle number and/or packing density. In this author's opinion, the relationship between experimental parameters and particle layer thickness is more difficult to predict in the PS-SW-AGE approach than in the PS-DW-AGE approach due to the zone of precipitation being at the gel-well and hence the presence of a non-uniform electric field profile.

The thickness of CaP layers produced by Kimura et al. (2018) provide the only insight into particle layer thickness predictions in the PS-DW-AGE approach. Though they observed particle size to be dependent on agarose concentration, pH, and time, the thickness of the particle layer in response to these parameters was beyond the scope of their research. Interestingly, Kamitakahara et al. (2012) noted a disappearance of the CaP particle layer with time, which they theorised to result from dissolution of the particles under an applied potential. However, this author suggests that the disappearance of particle layers is due to a combination of re-dissolution and electrophoretic transport of particles away from the zone of precipitation. On the one hand this could indicate that high potentials with long run times should be avoided, but if particle transport does occur then this could be a method of stretching particle layers to the desired size.

Loading gels could be cast to the desired thickness to increase or decrease the volume of each salt without changing salt concentration. In the PS-DW-AGE approach, this would be equivalent to increasing the width of the wells and adding proportionally more loading solution in the PS-SW-AGE approach. This would conveniently allow several loading cylinders of different salt concentrations and total salt amount within the same mould to test a range of supersaturations in the same run.

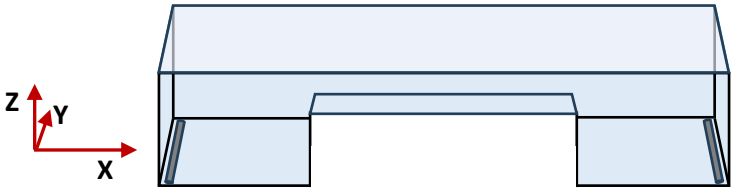


Figure 3.3. Orientation of the x-, y-, and z-axis in the horizontal electrophoresis.

The PS-DW-AGE approach boasts a much greater sample throughput compared to the proposed cylindrical PS-AGE, herein termed particle synthesis via cylindrical agarose gel electrophoresis (PS-CAGE). For example, a standard 150 x 150 mm gel slab could allow up 64 well-pairs to produce 64 individual samples. In contrast, if gel cylinders are (for example) 20 mm in diameter, only six gels could fit in parallel across the width of the tank. Furthermore, only a single row of gel cylinders could be used given they are required to be equidistance from each electrode. The PS-DW-AGE approach in a modified gel slab therefore presents an opportunity to optimise particle size using high throughput synthesis. An ideal subset of parameters obtained using a PS-DW-AGE system can then be used in a PS-CAGE system. PS-DW-AGE experimentation with a modified gel slab would of course be paired with the control measures described earlier to govern temperature, pH and ion concentration, so that these controlled conditions can later be applied to the PS-CAGE system.

3.1.7.2 Summary of Improving Cryogel Transfection Efficacy and Pre-Clinical Relevancy

Several improvements have been suggested to improve the transfection efficacy and pre-clinical relevancy of cryogels produced in this work. Several modifications to the electrophoresis tank itself have been proposed to enhance control over particle synthesis and cryogel fabrication. Firstly, using a cylindrical loading and recipient gel sandwich will prevent premature and lateral ion diffusion, employ more uniform electric field profiles at the zone of precipitation and transport uniform, cylindrical ion bands. Each of these will provide greater control over ion concentration and therefore particle nucleation and growth. Using cylindrical loading and

recipient gels will allow cylindrical particle layers to be formed with large cross-sections from which several smaller gels can be cut to suitable sizes for pre-clinical models. Casts could be designed to hold several loading or recipient gels in parallel, thus allowing multiple gel sets to be fabricated in one instance.

To limit the temperature increase of the buffer and gel due to joule heating effects, a heat exchanger will be devised to extract thermal energy from the buffer. Cooled buffer will then itself act as a heat exchanger in the tank to cool the gel(s). Peristaltic pumps will be used to avoid the build-up of a pH gradient which will conveniently serve to homogenise buffer temperature. A temperature/pH control unit would thus diminish several inter-parameter dependencies that prevent temperature and pH from being maintained at the zone of precipitation.

An important consideration is how pDNA can be incorporated into a recipient gel prior to synthesis to provide a uniform concentration of pDNA for particle synthesis. pDNA could either be electrophoretically loaded into the recipient gel or mixed with the molten agarose mixture and cast to form a pDNA-incorporated agarose gel cylinder. However, the molten agarose mixture includes PDA which would form complexes with pDNA. Instead, pDNA could be mixed with a molten gel mixture to form an uncoated cylindrical pDNA loading gel which can then be used to electrophoretically load the PDA-coated recipient gel (which will have been washed of excess PDA prior to loading).

The addition of PEI has the potential to enhance the overall transfection efficacy of cryogels with osteogenic particle layers by increasing the stability of secondary particles. Adsorption of PEI onto secondary particle surfaces would provide electrosteric repulsion and thus limit particle agglomeration. A PEI coating on secondary particles would also serve as a kinetic barrier between surface ions and water molecules to provide resistance against both extracellular and intracellular dissolution. Furthermore, PEI has capacity to instil a positive particle zeta potential and thus increase the interaction strength between particles and cell membranes, which would lead to greater cellular uptake. Submerging osteogenic cryogels in PEI solution after particle synthesis should provide a uniform diffusion of PEI, whilst limiting primary particle transformation/dissolution if submersion times are kept short.

The use of the PS-CAGE approach will significantly reduce the number of samples that can be prepared in one instance. It would therefore be convenient to develop a PS-DW-AGE system –

based on that used by Kimura et al. (2018) - to facilitate high throughput sample production. This would allow the ideal set of experimental parameter conditions to obtain sub-100 nm diameter particles for use in the PS-CAGE approach more rapidly. The existing components used to form the agarose gel slab however provide an inadequate well number and combs cannot be accurately or repeatedly positioned, and commercially available sets are not fit for purpose. Furthermore, a means of cutting out uniform particle layers in a highly repeatable manner is also required. A bespoke gel tray, comb, and gel punch system must therefore be designed and manufactured to perform this high throughput testing of experimental parameters and provide an ideal subset of parameter conditions for final cryogel production via the PS-CAGE approach.

3.1.8 New Apparatus

3.1.8.1 PS-DW-AGE System

The PS-DW-Age system will consist of a gel tray, combs, gel punch, cutting mask, and comb riser. The main function of this system is to facilitate the production of a gel slab with pairs of well rows compatible with an 8-channel multi-pipette i.e. 16 wells per row, with row pairs spaced 7 mm apart. The system must immobilise combs using grooves in the tray walls which can simultaneously be used to position a cutting mask which itself is used to position a gel punch. The gel punch will negate the need for scalpels and tweezers during cutting, whilst the mask will allow gels to be excised repeatedly with regards to their size and shape. A set of comb risers that allow the z-axis position of well bases to be raised from 1 mm to 3 mm is also required so that the minimum z-axis position required to avoid well base tears can be obtained.

3.1.8.2 PS-CAGE System

The PS-CAGE system will consist of moulds, each comprised of a cast, base, and lid, to cast rows of cylindrical gels. Upon removal from the mould, gel cylinders will remain attached within casts. A set of casts can then be aligned in the electrophoresis tank to form a gel cast sandwich of two loading gels and a recipient gel. A new pair of electrodes are required to raise the electrode z-position to be in line with the centre of these gel cylinders. As with the PS-DW-AGE system, a gel punch and mask are required to excise gels in a repeatable manner. Since gels are cast cylindrically, the mask should allow gels to be removed with each gel equidistance from the centre (Figure 3.4).

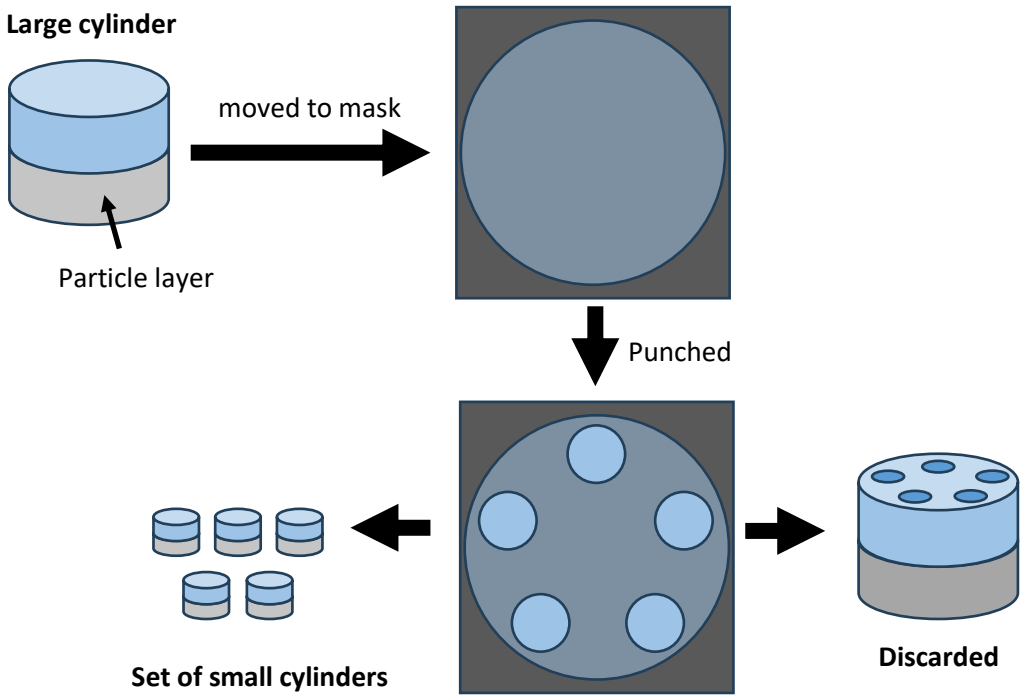


Figure 3.4. The process of punching and removing small cylinders encapsulating particle layers from large cylinders.

3.1.8.3 Temperature/pH Control Unit

Commercially available cooling systems for electrophoresis systems employ either direct or indirect cooling. In direct cooling, buffer would be circulated from the ports at the base of the electrophoresis tank and pumped through a heat exchanger using peristaltic pumps. Such a system would simultaneously cool and prevent a pH gradient build-up. However, circulation of an electrically 'live' solution is highly hazardous.

In contrast, indirect cooling places a heat exchanging surface such as a cold pack or water tank in contact with the buffer without the need for buffer circulation. Indirect cooling systems are widely available, such as the SUB25C Maxi-Cooled Submarine Gel Electrophoresis Unit (Hoefer Inc., Massachusetts, USA) shown in (C), and utilise a small water block beneath from the main tank that can be connected to a water supply. Some vertical systems, such as the TE62 (Hoefer Inc) shown in Figure 3.5 (B) use a similar approach to the SUB25C but opt for a ceramic heat exchanger at the base for use with water recirculation. Simpler vertical systems like the Mini Trans-Blot Cell (BioRad Laboratories, Inc., as shown in Figure 3.5 (A) employ a pre-frozen cool pack in contact with the buffer solution. In each of these systems, one can expect non-uniform buffer temperatures since the buffer itself is not circulated.

Of the systems mentioned, the ceramic heat exchanger surface of the TE62 will have the greatest thermal conductivity but has a relatively small thermal exchange surface when compared to the SUB25C. The Mini Trans-Blot Cell system has the greatest surface area to buffer volume since the entire cooling pack is submerged in buffer, but its cooling capacity diminishes with time as it absorbs thermal energy. The heat exchanging surfaces are positioned more optimally in the SUB25C and Mini Trans-Blot Cell systems given they are directly adjacent to the gel.

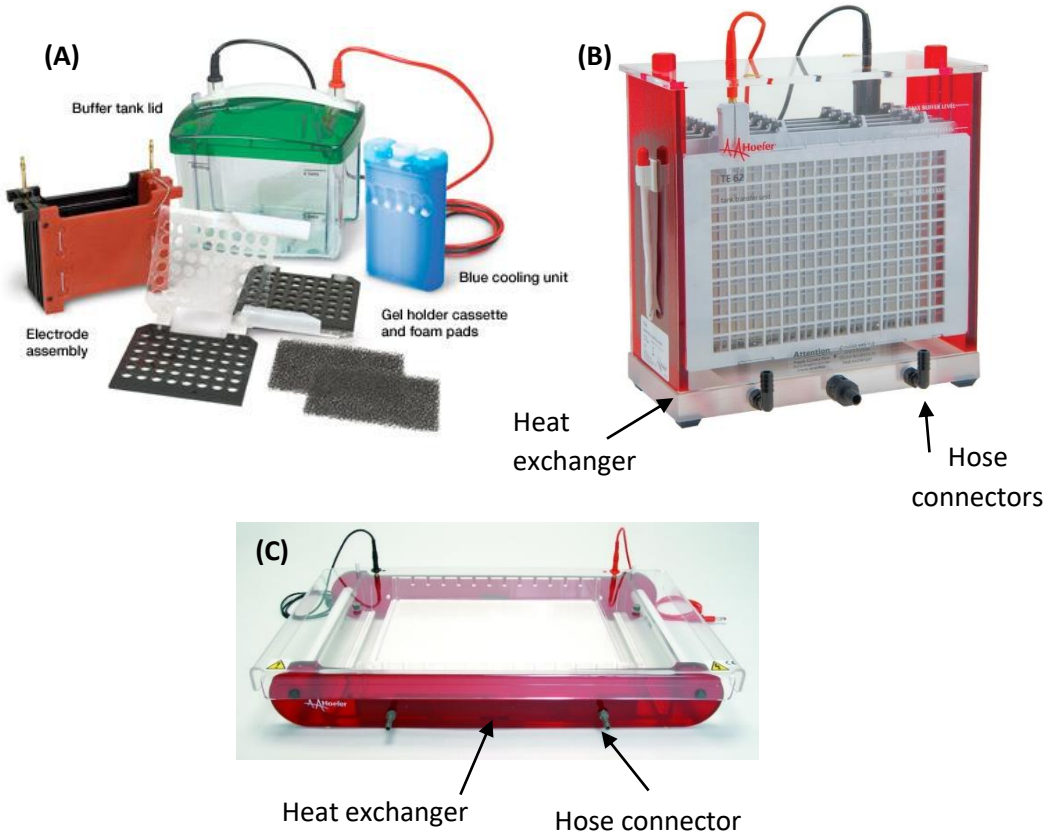


Figure 3.5. (A) Mini Trans-Blot cell with cooling pack (Bio-Rad Laboratories, Inc.); (B) TE62 Vertical Electrophoresis System (Hoefer Inc.); *(C)* SUB25C Maxi-Cooled Submarine Gel Electrophoresis Unit (Hoefer Inc.).

Combining an indirect cooling solution with a means of buffer circulation would provide more design freedom over the shape and position of the heat exchanging surface. The heat exchanging surface could be designed from tubing that is submersible to provide a larger surface area than just using the tank surfaces. Peltier modules could be used to form the main heat exchanger that is located external to the tank, allowing the coolant running through tubing to reach sub-ambient temperatures. A control system would be required for this proposed cooling method to maintain consistent buffer temperatures in the tank.

3.2 Research Aims and Objectives

3.2.1 Overview

A new gel tray system is needed for high throughput testing via a PS-DW-AGE approach where experimental parameters can be modulated to obtain an ideal subset of conditions to synthesise pDNA/CaP and pDNA/MgP particles with sub-100 nm diameters. A cylindrical gel casting system is required to utilise this ideal subset of parameters found and enable the production of cylindrical PDA-pDNA/CaP and PDA-pDNA/MgP cryogels using a PS-CAGE system. Both systems must be designed to function in the existing horizontal electrophoresis tank. The experimental layout of these systems (specifically gel shape and electrode position) should be computationally modelled to demonstrate the theorised improvements in electric field profile uniformity and ion transport in areas proximal to the zone of precipitation.

The PS-DW-AGE system should consist of a tray and combs, a square shaped gel punch and cutting mask, whilst the PS-CAGE system should consist of cylindrical gel casts, a cylindrical gel punch and cutting mask. A temperature/pH control unit is required to mitigate the temperature and pH changes at the zone of precipitation in both PS-DW-AGE and PS-CAGE systems. The temperature/pH control unit should consist of peristaltic pumps for buffer circulation and a heat exchanger with a control system capable of maintaining consistent buffer temperature whilst a large potential is applied across the tank.

3.2.2 Research Aims

(1) Develop computational models to test PS-AGE systems and fabricate a PS-CAGE system based on computational results

3.2.3 Research Objectives

(1) Computationally model the electric field profiles and ion transport around the zones of precipitation in the PS-SW-AGE, PS-DW-AGE, and PS-CAGE systems to validate the claim that electric field profiles at the zone of precipitation and ion transport/mixing are more uniform in the PS-DW-AGE and PS-CAGE systems than in the PS-SW-AGE system.
(2) Design the apparatus for the PS-DW-AGE and PS-CAGE systems.
(3) Fabricate the apparatus for the PS-DW-AGE and PS-CAGE systems.

(4) Design and fabricate a temperature/pH control unit compatible with both the PS-DW-AGE and PS-CAGE systems.

(5) Experimentally validate the functionality of PS-DW-AGE and PS-CAGE systems.

(6) Experimentally validate the functionality of the temperature/ pH control unit.

3.3 Materials and Methods

3.3.1 Computational Modelling

3.3.1.1 Measurements

COMSOL Multiphysics (COMSOL Inc., Stockholm, Sweden) was used to computationally model the electric field strength profiles and ion transport/mixing in areas local to the zone of precipitation. Measurements were taken of the internal portion of the empty horizontal electrophoresis tank, including the platinum wire electrodes length and thickness. The tank was then filled with 1.8 L of d.H_2O and a 130 mL agarose gel (and gel tray) with 4 rows of wells was placed on the tank shelf. The depth of the buffer and gel were then measured, along with well dimensions (depth, width, length).

The position of the platinum wire electrodes relative to the base and rear wall of the tank were measured. For the PS-CAGE model, the raised electrode positions maintained the same separation as the original electrodes in the PS-SW-AGE model and the PS-DW-AGE model, as shown in Figure 3.6.

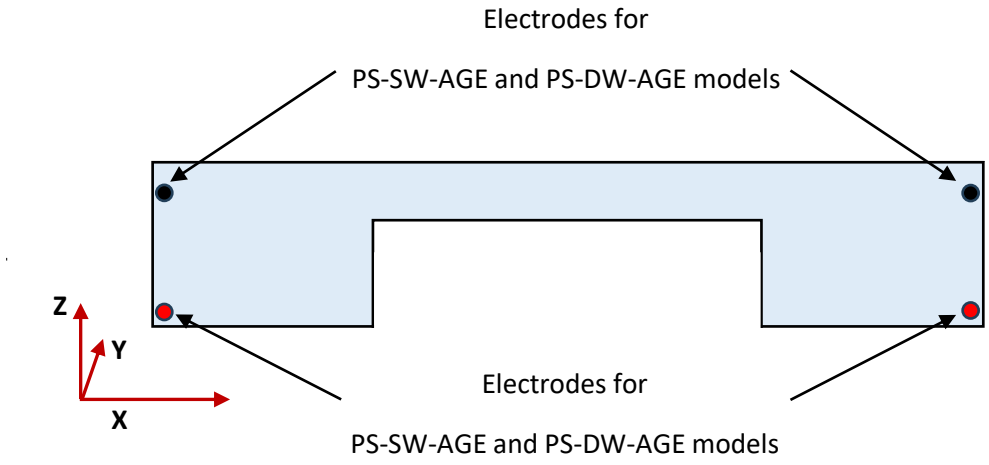


Figure 3.6. Position of electrodes for all models.

3.3.1.2 Assumptions

The wells in the gel slab of the PS-SW-AGE model hold approximately 48 µL each, totalling 3.1 mL of buffer across the 64 wells (4 rows of 16). The PS-DW-AGE model will hold approximately 6.1 mL of buffer across 128 wells (8 rows of 16). The 3 mL difference in volume between these

gel slabs was assumed to have negligible impact on the height of buffer in the tank, hence the same buffer height was used for both the PS-SW-AGE and PS-DW-AGE models.

25 µL $CaCl_2$ loading solution was assumed to be settled uniformly at the bottom of the well in the PS-SW-AGE model. Similarly, both of 25 µL $CaCl_2$ and Na_2HPO_4 loading solutions were assumed to settle uniformly in the PS-DW-AGE model. The top of the loading solutions is calculated to be 2.08 mm from the well base for a 2 mm x 6 mm well. Platinum wires were assumed to be completely straight. All material domains were set to 293.15 K. For the PS-CAGE model, the gel cast was not included given the material does not accommodate ion transport. A void domain was positioned around the gel cylinders in place of the cast.

3.3.1.3 Geometry

A 2D-model in the plane normal to the y-axis was constructed for each model using the aforementioned measurements and assumptions. Each model used the same overall tank geometry. For the PS-SW-AGE and PS-DW-AGE models, the same gel height and well dimensions were used, where the only geometrical difference between the models was the addition of a second well for the PS-DW-AGE model spaced 7 mm apart (edge-to-edge) (see Figure 3.7). The well in the PS-SW-AGE model was positioned 3.5 mm to the left of the centre of the electrodes to keep a consistent starting position for Ca^{2+} ions between the PS-SW-AGE and PS-DW-AGE models. In both models the wells were 2 mm thick (x-axis) and 4 mm deep (z-axis).

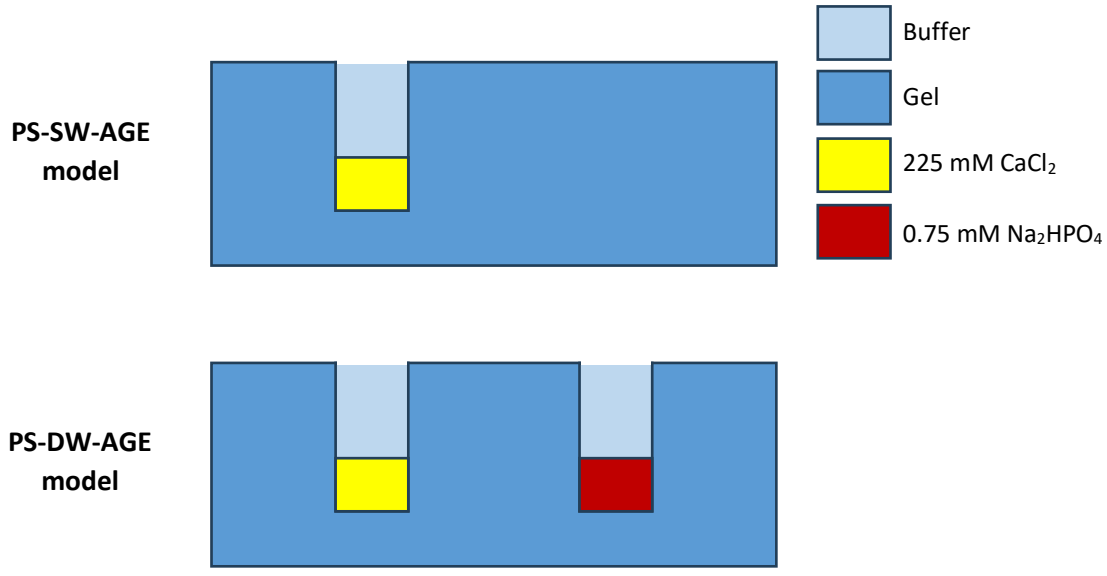


Figure 3.7. Geometry of the wells in the PS-SW-AGE and PS-DW-AGE models.

The loading and recipient gels in the PS-CAGE model were each 22 mm in diameter and 4 mm thick (Figure 3.8). The electrode position (not shown in Figure 3.8) was raised in the z-axis for the PS-CAGE model to be in line with the centre of the gel cylinders (see Figure 3.6). The plane of the 2D-models travelled through the centre of wells in the PS-SW-AGE and PS-DW-AGE models, and through the centre of the gel cylinders in the PS-CAGE model. Though models span the entire width and height of the tank, only domains close to the zone of precipitation were visualised to reduce computation time. Full model geometries for all models are shown in Figure 3.9.

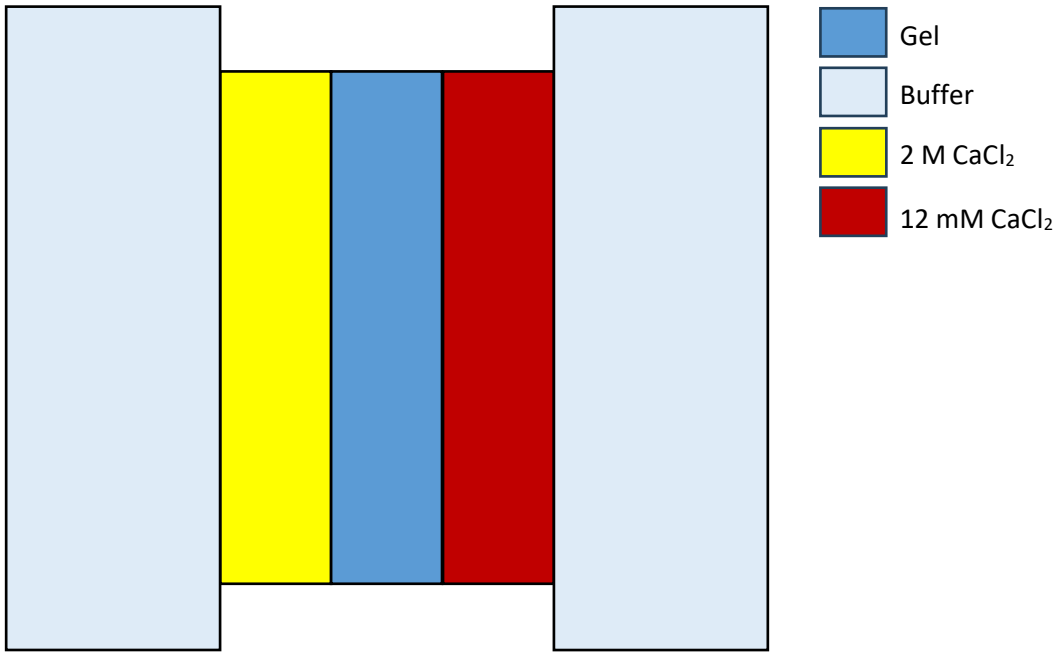


Figure 3.8. Geometry of gels in the PS-CAGE models.

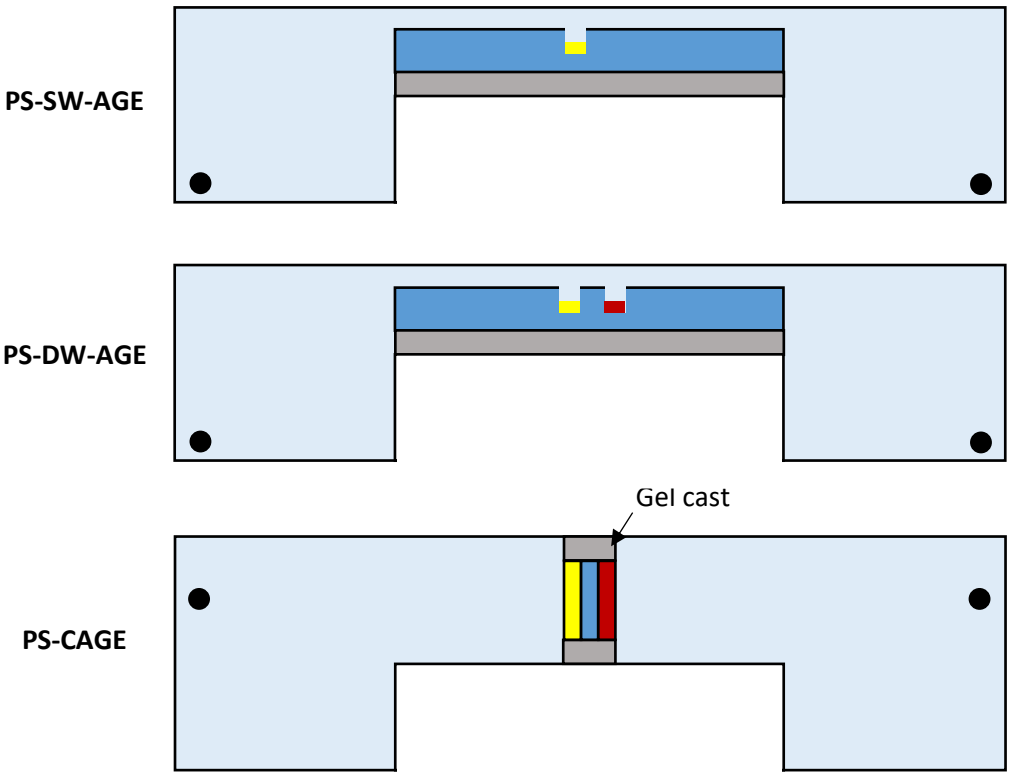


Figure 3.9. Full geometry of PS-SW-AGE, PS-DW-AGE, and PS-CAGE models.

3.3.1.4 Electrostatics Models

The electrostatics module in COMSOL allows electric field strengths to be calculated independent of time using a stationary model, hence electric field strengths are calculated only for t = 0 s and so do not take into account changes in relative permittivity or conductivity resulting from ion transport. Each domain within the model is assigned a material, for which a fixed relative permittivity is specified. The relative permittivity of materials could not be experimentally determined in-house, therefore relative permittivity values for similar materials were extracted from literature and are displayed in Table 3.1.

In all cases, sources did not determine the relative permittivity of the exact material required for the model. This is because the material formulations used here are either uncommon (such as 0.75 mM Na_2HPO_4 + 5 vol % glycerol) or sources provide relative permittivity values for slightly different formulations. For instance, the relative permittivity source for the material: 1 wt % Agarose gel, 25 mM HEPES + 0.75 mM Na_2HPO_4, pH 7.4, used a concentration of 0.98 wt % rather than 1 wt %, as well as $D.H_2O$ for liquid content and a different brand of agarose to SeaKem™ (Roebuck and Goldblith, 1975). Similarly, Navarkhele et al. (1998) provide a relative permittivity of $CaCl_2$ at a concentration of 200 mM rather than 225 mM but do so with no glycerol component.

Table 3.1. Materials, their relative permittivity values, and their respective references. Materials are assigned to domains from specific models, as indicated in the rightmost column.

** Denotes data taken from reference: (Roebuck and Goldblith, 1975)*

** Denotes data taken from reference: (Archer and Wang, 1990)

*** Denotes data taken from reference: (Navarkhele et al., 1998)

***** Denotes data taken from reference: (Mollerup and Breil, 2015)*

Material	Relative Permittivity	Substituted Material	Domain (and model)
1 wt % Agarose gel, 25 mM HEPES + 0.75 mM Na_2HPO_4, pH 7.4	76.6 *	0.98 wt % agarose ($D.H_2O$ liquid component)	Gel slab (PS-SW-AGE)
25 mM HEPES + 0.75 mM Na_2HPO_4, pH 7.4	80.2 **	$D.H_2O$	Buffer (PS-SW-AGE)
225 mM $CaCl_2$, 5 vol % glycerol	80.7 ***	200 mM $CaCl_2$ ($D.H_2O$ liquid component)	$CaCl_2$ Loading solution (PS-SW-AGE)
2 M $CaCl_2$, 5 vol % glycerol	48.0 ****	2 M CaCl2 ($D.H_2O$ liquid component)	$CaCl_2$ Loading solution (PS-DW-AGE)
1 wt % agarose gel, 25 mM HEPES, pH 7.4	76.6 *	0.98 wt % agarose ($D.H_2O$ liquid component)	Gel slab (PS-DW-AGE)
1 wt % agarose gel, 25 mM HEPES, pH 8	76.6 *	0.98 wt % agarose ($D.H_2O$ liquid component)	Gel slab (PS-DW-AGE) Recipient gel (PS-CAGE)
0.75 mM Na_2HPO_4, 5 vol % glycerol	80.2 **	$D.H_2O$	Na_2HPO_4 loading solution (PS-DW-AGE)
25 mM HEPES, pH 7.4	80.2 **	$D.H_2O$	Buffer (PS-DW-AGE)
25 mM HEPES, pH 8.0	80.2 **	$D.H_2O$	Buffer (PS-DW-AGE, PS-CAGE)
1 wt % agarose gel, 2 M $CaCl_2$	48.0 ****	2 M CaCl2 ($D.H_2O$ liquid component)	$CaCl_2$ loading gel (PS-CAGE)
1 wt % agarose gel, 12 mM Na_2HPO_4	76.6 *	0.98 wt % agarose ($D.H_2O$ liquid component)	Na_2HPO_4 loading gel (PS-CAGE)

To this author's knowledge, there are no experimental or theoretical calculations of the relative permittivity of $CaCl_2$ or Na_2HPO_4 solutions mixed with any amount of glycerol, or indeed a value for low concentration HEPES solutions. Therefore, the 0.75 mM Na_2HPO_4 + 5 vol % glycerol solution and 25 mM HEPES, pH 7.4 solution were both assigned the same relative permittivity as $D.H_2O$. This is at least a reasonable assumption given the low concentration of salts in both solutions. Furthermore, the relative permittivity of $D.H_2O$ is predicted to reduce only negligibly when 5 vol % glycerol is present, based on a trend identified by Angulo-Sherman and Mercado-Uribe (2014).

In all models a void in the buffer with the same cross-sectional dimensions at the platinum electrode was used, hence there was no need to include a platinum material in the model. A 180 V potential was applied to the circumferential surface of the left-hand electrode, whilst a 0 V potential was applied to the right-hand electrode. All other domains were assigned an initial potential of 0 V.

The primary out-of-plane thickness for all models was 150 mm (width of the tank). For the PS-SW-AGE and PS-DW-AGE models, wells were assigned an out-of-plane thickness of 6 mm. Out-of-plane thickness for the gels in the gel cylinder model was varied along the z-axis by segmenting cylinder domains into 1 mm thick segments along the z-axis and assigning an average thickness equal to the chord length, C, running through the centre of the segment (Figure 3.10). Chord length was calculated using Equation 3.6:

$$C = 2\sqrt{2Rh - h^2} \qquad 3.6$$

Where R is the radius of the cylinder (22 mm) and h is the distance from the chord to the cylinder centre. For example, the lowest segment has a chord length (out-of-plane-thickness) of 6.24 mm, whilst the second lowest segment has a thickness of 8.71 mm. This calculation was repeated for each segment in the bottom half of the cylinder, from which values were applied symmetrically in the top half.

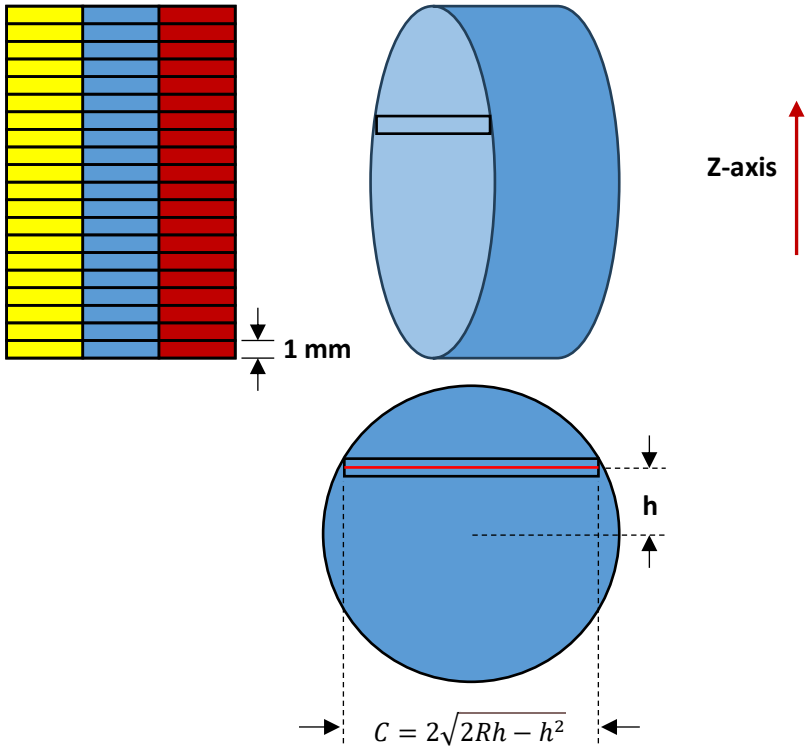


Figure 3.10.Segmentation of gel cylinders into 1 mm segments and calculation of chord length.

3.3.1.5 Ion Transport Models

Ion transport was modelled in the PS-SW-AGE, PS-DW-AGE and PS-CAGE models using the 'transport of diluted species through porous media' (TDSPM) module within COMSOL Multiphysics. A single test at pH 7.4 was performed for the PS-SW-AGE model as a control, whilst separate tests at pH 7.4 and 8.0 were conducted for the PS-DW-AGE model to investigate the impact of pH change on phosphate ion speciation and transport. A single test at pH 8.0 was conducted for the PS-CAGE model. Geometries, material constants, and applied potentials remained constant between electrostatic and ion transport models.

A porosity of 0.99 was assigned to all agarose gel components which assumed proportional changes in porosity with agarose wt %. The porosity of other non-porous materials were kept as 1 by definition. Ion species (at time = 0 s) were assigned to their respective material domains within each model. For instance, Ca^{2+} and Cl^- ions were assigned to the $CaCl_2$ domains within each model whilst HPO_4^{2-}, $H_2PO_4^-$, and Na^+ ions were assigned to the Na_2HPO_4 domains. The concentration, electric charge, and diffusion constant of these ions (and their respective references) are shown in Table 3.2.

Table 3.2. Ionic species used in the ion transport models. Concentrations and electric charge are listed for each ion. Diffusion constants were taken from the reference: (Parkhurst and Appelo, 2013).

Ion	Concentration	Electric Charge	Diffusion Constant
Ca^{2+}	2 M	+2	7.93×10^{-10}
Cl^-	4 M	-1	2.00×10^{-9}
Na^+	1.5 mM	+1	1.33×10^{-9}
HPO_4^{2-}	0.4605 mM (pH 7.4) 0.648 mM (pH 8)	-2	6.90×10^{-9}
H_2PO4^-	0.2895 mM (pH 7.4) 0.102 mM (pH 8)	-1	8.46×10^{-9}

The relative concentrations of HPO_4^{2-} and $H_2PO_4^{2-}$ at pH 7.4 and 8.0 were calculated using the Henderson-Hasselbalch equation, shown in Equation 3.7:

$$pH = pK_{a2} + log_{10}\left(\frac{[A^-]}{[HA]}\right) \quad 3.7$$

Where $[HA]$ is the acid concentration, $[A]$ is the conjugate base concentration and pK_{a2} (equal to 7.2) is the negative logarithm of the acid dissociation constant for the equilibrium:

$$H_2PO_4^- \leftrightarrow HPO_4^{2-} + H^+ \quad 3.8$$

Substituting $[HPO_4^{2-}]$ for $[A]$ and $[H_2PO_4^-]$ for $[HA]$, the percentage of each species was calculated and displayed in Table 3.3 below.

Table 3.3. Percentages of HPO42- and H2PO4- at pH 7.4 and 8.0 as calculated using the Henderson-Hasselbalch equation.

$\boldsymbol{pH}$	$\boldsymbol{pK_a}$	$\boldsymbol{[HPO_4^{2-}]}$ **(%)**	$\boldsymbol{[H_2PO_4^-]}$ **(%)**
7.4	7.2	61.4	38.6
8.0	7.2	86.4	13.6

HEPES molecules were ignored in this model since a specific electric charge could not be obtained for HEPES within the pH range 7.4 to 8.0. HEPES theoretically has a negative charge ranging from 0.99 to 0.01 between pH 9.5 to 5.5 (Al-Ghobashy, 2014) and a diffusion constant for HEPES of 4.4 x 10^{-10} m^2s^{-1} has been determined experimentally (Chen et al., 2019). The electric charge of HEPES will be significantly less than 0.99 at pH 8.0 and 7.4 and the diffusion constant is of the order of 10-times smaller than that of Ca^2. Therefore, the flux of HEPES - even across steep concentration gradients – is assumed to be negligible. H_2O molecules were included in the model for electroneutrality, where H_2O concentration was domain-dependent based on the concentration of other components and the assumption that all domains had a density of 1 gcm^{-3}.

Ion transport for all models was determined up until 600-seconds at intervals of 0.1-seconds. Note that 600-seconds is longer than the 360-second loading time used experimentally for the PS-SW-AGE approach. This longer experimental time was used since the PS-DW-AGE and PS-CAGE models are expected to have longer reaction times.

To determine the zone of precipitation in each model, a 'mixing product', m, was plotted according to Equation 3.9:

$$m = [Ca^{2+}] \times [HPO_4^{2-} + H_2PO_4^{-}] \qquad 3.9$$

Whilst a ratio of Ca^{2+} to $H_xPO_4^{x-3}$ ions would ideally be plotted, the existence of zero values for both ion types in some domains results in calculation errors. Calculating a mixing product using multiplication rather than division avoids these errors and provides a good estimation of spatiotemporal ion mixing.

3.3.1.6 Computational Data

Electric field strengths from electrostatic models were plotted as colour maps, where blue indicates an electric field strength of 0 Vm^{-1} and red indicates the maximum field strength for a given map. Ion concentrations were plotted as colour maps at intervals of 0.025 s and compiled to create animations of ion transport over a 600 s period. In any frame, blue indicates a concentration of 0 M, whilst red indicates the maximum concentration for a given animation.

Line graphs of electric field strength were plotted for models using an arc parallel to the x-axis. For the PS-SW-AGE and PS-DW-AGE models, these arcs passed through the centre of wells, whilst for the PS-CAGE model this arc passed through the centre of gel cylinders.

3.3.2 Design and Manufacture of New Apparatus

3.3.2.1 Design Specifications

Design specifications were produced for all components of the proposed PS-DW-AGE and PS-CAGE systems, including the temperature/pH control unit. Specifications primarily include summary descriptions of parts and sub-parts, primary and secondary functions, material selections and manufacturing processes.

For the PS-DW-AGE system, design specifications for individual parts are listed in the Appendix: gel tray in Table 6.1; combs in Table 6.2; gel punch in Table 6.3, cutting mask in Table 6.4; and comb riser in Table 6.5. For the PS-CAGE system, design specifications are segmented into: (1) gel cylinder cast, and (2) the raised electrode holders, which are listed in the Appendix in Table 6.6 and Table 6.7 respectively. The design specifications for the temperature/pH control unit are segmented into: (1) heat exchanger and water loop; (2) the electronics systems, and (3) the enclosure, listed in the Appendix in Table 6.8, Table 6.9, and Table 6.10 respectively.

All CAD designs (3D-models and orthographic drawings) were created using Solidworks (Dassault Systèmes, Vélizy-Villacoublay, France).

3.3.2.2 PS-DW-AGE System

A gel tray was designed to be formed by three parts: two walls glued to a base (Figure 3.11). Slits measuring 2.1 mm wide, spaced 9 mm apart (centre to centre) for comb positioning. The orthographic drawing for the gel tray is shown in the Appendix (Figure 6.3). A low tolerance of ± 0.05 mm for the repeating pitch of the slits was used to limit compounding error during manufacture. The gel tray was manufactured by Barkston Plastics Engineering Ltd (Barkston Plastics, West Yorkshire, UK).

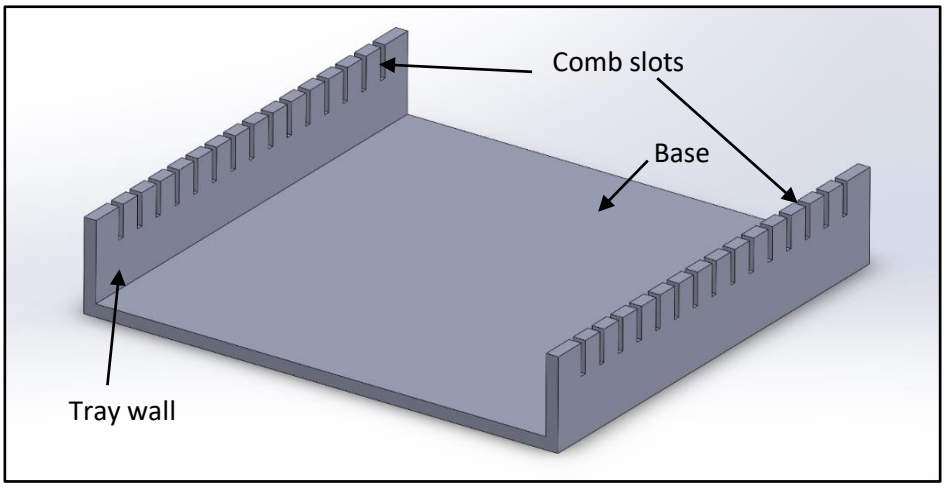


Figure 3.11. 3D model of the gel tray.

The CAD design of the comb is shown in Figure 3.12 and its orthographic drawing is displayed in the Appendix (Figure 6.4). The comb was designed to be 2 mm thick and has 16 teeth, spaced 3 mm apart (edge to edge), each with a cross-section measuring 6 mm x 2 mm. At either end of the comb a step was added to prevent downward travel in the gel tray slits. Grips protrude upward at both ends so that the comb can be leveraged easily from a set gel. As with the gel tray slits, the repeating pitch of the teeth is ± 0.05 mm. Combs were manufactured by Barkston Plastics Engineering Ltd.

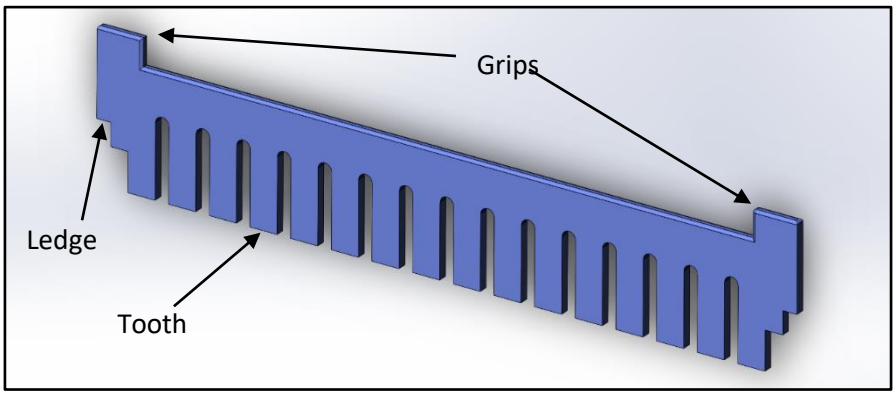


Figure 3.12. 3D model of the gel comb.

A gel punch was designed to allow simple and quick extraction of cuboid shaped gels from the gel slab. The two components for the gel punch; a punch and a plunger, are shown in Figure 3.13. The orthographic drawings for the punch and plunger are shown in the Appendix in Figure 6.5 and Figure 6.6 respectively. The external measurements of the cutting edge are 6 mm x 7 mm with a 0.5 mm thick edge for cutting 5 mm (along the y-axis) x 6 mm (along the x-axis) gel cuboids. The barrel of the punch widens at the top where a spring can sit, on top of which the plunger is positioned. A hole in the larger chamber will allow buffer to escape if withdrawn up the barrel.

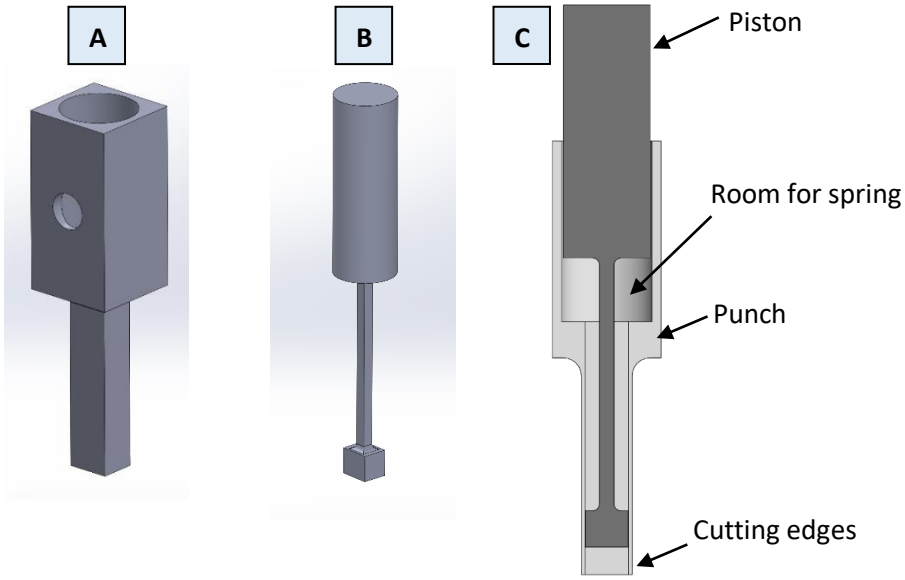


Figure 3.13. 3D-models of gel punch components: (A) punch; (B) piston and (C) cross-sectional view of the punch and piston assembly.

The plunger is designed to slide down the shaft of the punch with minimal air gaps to utilise capillary action to force buffer to occupy air gaps and hence create a slight vacuum effect to help draw in sliced gels. The piston is longer than the punch so it can fully eject gels from the barrel of the punch. The gel punch and piston were manufactured in-house, each from 316-stainless steel.

Three pairs of comb risers were designed to be manufactured via 3D-printing. As shown in the 3D-CAD model in Figure 3.15 and the orthographic drawing in Appendix Figure 6.7, the riser has teeth spaced 9 mm apart to match that of the slits in the gel tray wall. Each pair of comb risers have teeth measuring either 1, 2, or 3 mm in height, 5 mm in length and 2 mm in width. Comb risers were manufactured with an Objet1000 3D printer (Stratasys, Minnesota, USA).

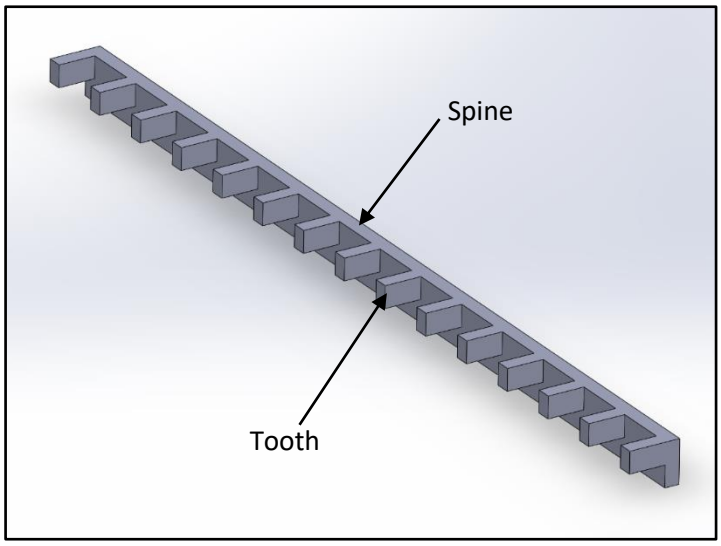


Figure 3.15. *3D model of the comb riser (3 mm size).*

The cutting mask was designed to position the gel punch directly over gel areas between well pairs containing particle layers, using the slits in the gel tray walls as a guide. This would allow the mask to be moved from row to row for highly repeatable extraction of gels with embedded particles. The 3D-CAD model (Figure 3.14) and orthographic drawing (Appendix Figure 6.8) show the gel cutting mask contains 16 square cut-outs slightly larger than the cutting edges of the gel punch to prevent any significant lateral movement. A pair of ledges at either end of the mask are spaced 9 mm apart (centre to centre) to allow the mask to sit on the slits of the gel tray wall.

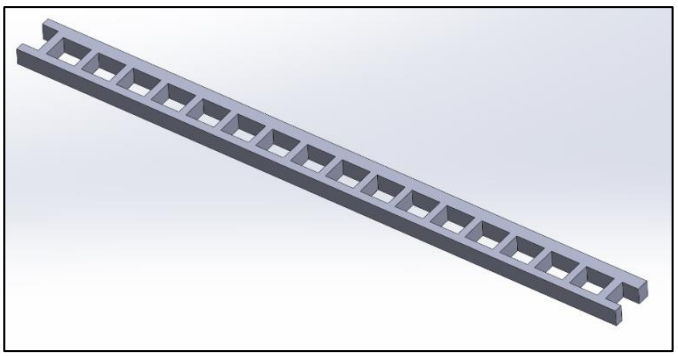


Figure 3.14. 3D-CAD model of the gel cutting mask.

3.3.2.3 PS-CAGE System

The gel mould was designed to comprise of three separate components: a cast, base, and lid. Separate sets of these were designed for the two loading gels and the recipient gels so that a sandwich of three gel casts can be utilised in the tank at the same time. The width of each cast could not exceed a width of 158 mm (maximum width of electrophoresis tank) and height of 24 mm (maximum buffer depth at the electrophoresis tank shelf). Hence, the cast was designed to be 157.5 mm in width, 23 mm in height, and produce six cylindrical gels measuring 22 mm in diameter (Figure 3.16). The orthographic drawing for the cast component is displayed in the Appendix (Figure 6.9).

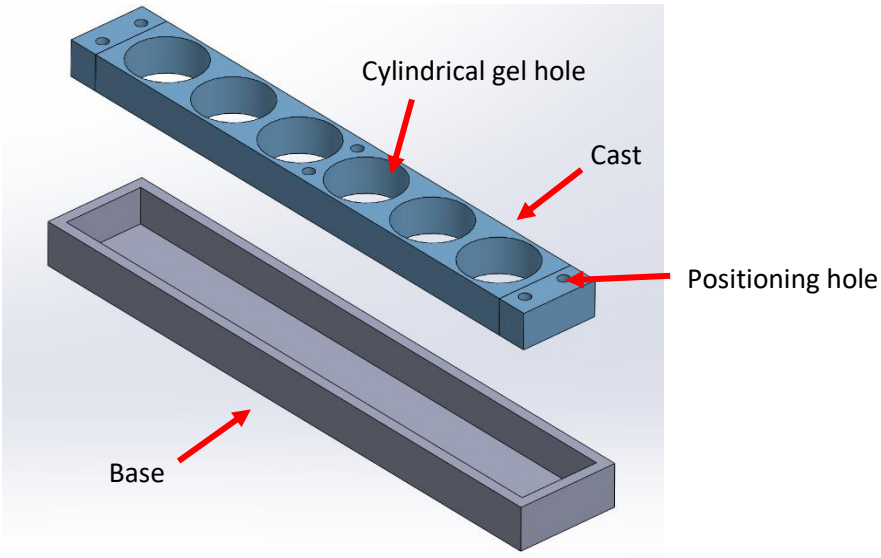


Figure 3.16. Design of the cylindrical cast and base.

Several casts of different thicknesses were designed for both the loading and recipient gels, measuring: 2 mm, 4 mm, 7 mm, or 10 mm in thickness. A range of thicknesses were used for the casts as it is not yet known what minimum thickness is required to physically retain gels within the mould during disassembly of the cast or submersion of the mould. For the recipient gel mould, six cylindrical holes each measuring 22 mm in diameter were spaced 23 mm apart (centre to centre). In contrast, 20 mm diameter cylindrical holes spaced 23 mm apart were used for the loading gel moulds. The smaller diameter used for the loading gels was to limit ion 'slip' around the edges of recipient gels during electrophoresis.

Six smaller holes measuring 3.2 mm in diameter are positioned at the same location in all moulds to allow moulds to be bolted together with 3 mm nylon bolts. An exploded assembly view of three 10 mm thick casts is shown in Figure 3.17 (without nylon bolts).

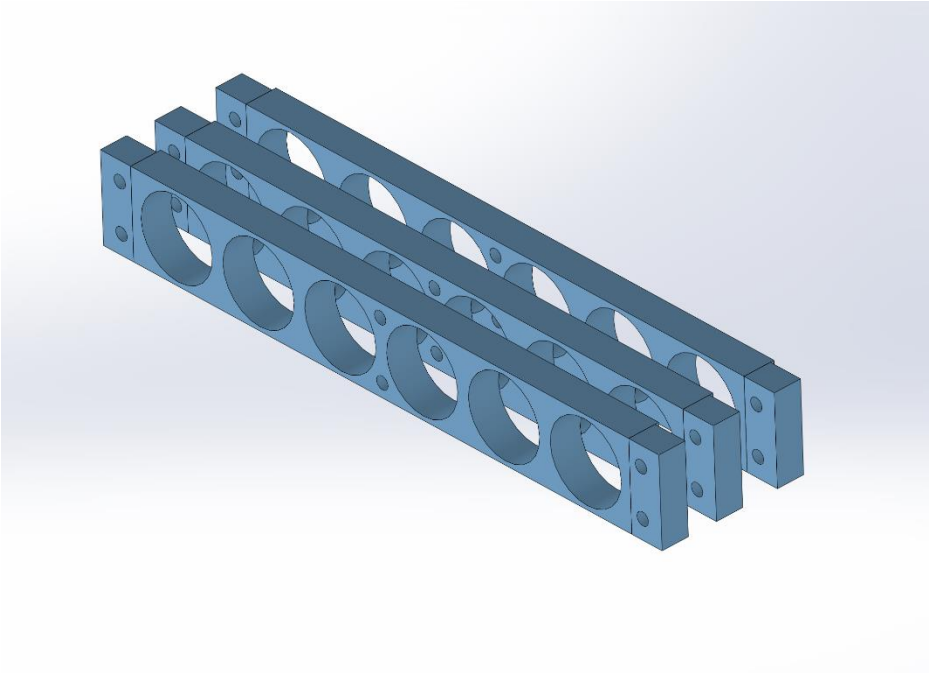


Figure 3.17. Exploded view of 10 mm gel casts.

Bases of the moulds are simply hollow cuboids with a depth equal to that of their respective mould to allow complete submersion of moulds when placed in the base. A lid (plastic sheet) can then be positioned atop of the mould/base pair and held down with weights to expel excess agarose and air bubbles. Disassembly of the mould is then as simple as removing the lid and pulling out the cast.

The gel mould components (cast and base) were 3D-printed in-house using an Objet 1000 Multi-Material 3D printer (Stratasys) using VeroWhite 3D printing material (Stratasys). The lid was a 2 mm thick acrylic sheet cut to size in-house to fit over the mould assembly.

A cutting mask is required to ensure small gel cylinders are removed in equidistance from the gel centre in a radial pattern. The cutting mask will therefore consist of two parts. The first part will be a mask that can be positioned above the cast, with either four holes measuring 7 mm in diameter or five holes measuring 6 mm in diameter, both distributed in a radial pattern (Figure 3.18). The final number of holes in the mask will be decided upon their testing and their ability to cut uniform cylinders. 7 mm holes will allow a 6.5 mm outer diameter tube (with 0.25 mm

thick walls) to slide through the hole and cut out 6 mm diameter gels, whilst 6 mm holes will allow a 5.5 mm outer diameter tube to cut out 5 mm diameter gels.

The second part of the cutting mask is a mask holder that is fixed in place above the gel cast and immobilises the smaller mask above each gel cylinder (also shown in Figure 3.18). The mask holder is similar to the gel cast but with notches cut across each cylindrical hole to prevent the mask rotating during cutting. Likewise, the mask holder is designed to be bolted to a gel cast to prevent the cast from moving. The exploded assembly view of the cutting mask, mask holder, and gel cast shown in Figure 3.18 shows how these components align.

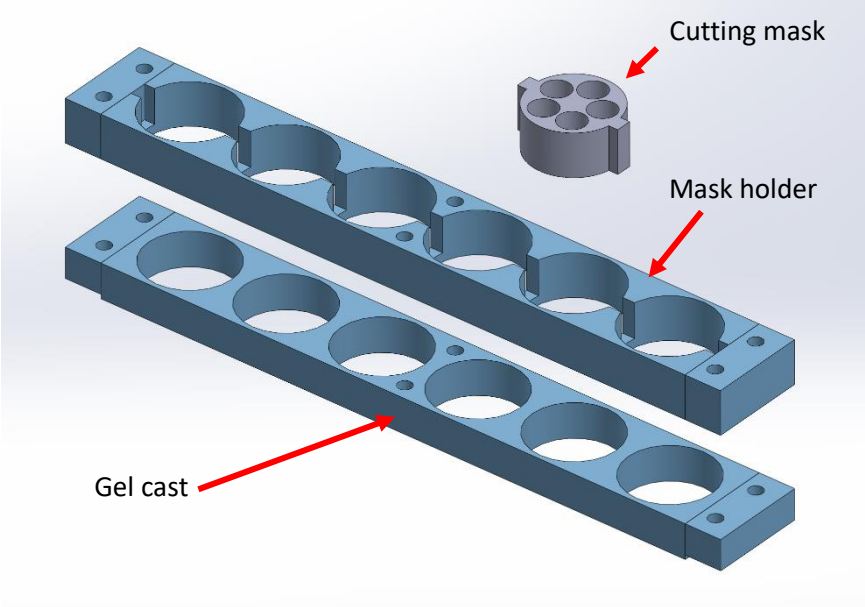


Figure 3.18. Exploded assembly view of the cutting mask (five holes), mask holder, and gel cast.

The cutting mask and mask holder were printed using an Objet 1000 Multi-Material 3D printer (Stratasys) using VeroWhite 3D printing material (Stratasys).

The raised electrode holders were designed to hook onto opposing ends of the electrophoresis tank and suspend a platinum wire below the buffer surface to be in-line with the centre axis of gel cylinders sitting within the gel mould (same z-position). As per the design specifications (Appendix Table 6.6) the raised electrode holders are to be made primarily from acrylic since it is non-conductive and can be chemically joined together. As shown in Figure 3.19, a thin acrylic sheet is used to connect the two acrylic blocks, allowing space for the tank lid above. Banana plugs are to be accommodated in the holes either side of the acrylic block. Whilst only one

banana plug is needed per electrode wire to complete the DC circuit, the banana plug itself is a convenient anchorage for the platinum wire; hence two are used.

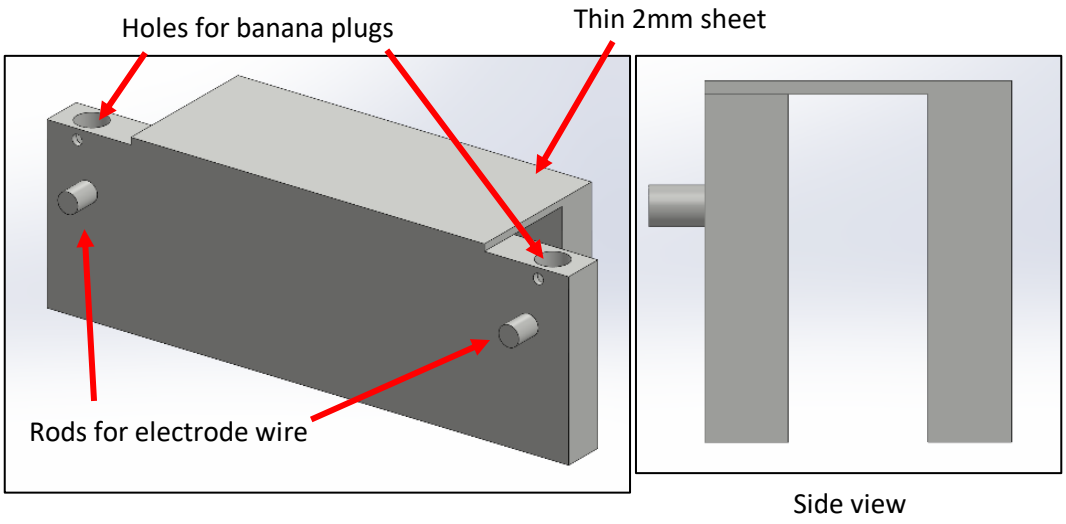


Figure 3.19. 3D-CAD model of a raised electrode holder.

The raised electrode holders were constructed from three pieces of acrylic sheet which were cut and drilled in-house and chemically bonded fixed together. 0.25 mm diameter platinum wire was wrapped around banana plugs on either side of the assembly and glued in place under tension.

3.3.2.4 Temperature/pH Control Unit

Four peristaltic pumps will be used to circulate buffer, positioned in the corners of the tank with tubes submerged to the same depth as the raised electrodes. The pumps will need to be bolted onto a platform that raises the platform and have silicone tubing attached to their inlets/outlets. Manual control of the pumps will be facilitated by the on/off switch of a buck converter power supply.

The heat exchanger will be primarily comprised of a Peltier module array (see design specifications in Appendix Table 6.8) that utilises the thermoelectric effect to convert an electric potential into a temperature gradient into an electrical potential (or vice-versa). Two water loops will be thermally coupled to either side of the Peltier array where water flow is controlled by an aquarium pump in each loop. The application of an electric potential to the Peltier module array will reduce the temperature on one surface whilst increasing the temperature on the other, thus allowing thermal energy to be extracted from one loop; herein termed the 'cold loop', whilst donating thermal energy to the other loop; herein termed the 'hot loop'. The cold loop tubing will be submerged in the buffer of the electrophoresis tank to extract thermal energy produced by joule heating.

A control system will provide real-time monitoring of water loop, buffer, and ambient air temperatures, and directly control the on/off function of individual Peltier modules using a programmable microprocessor to closely regulate buffer temperatures. An overview of component interconnectivity within the heat exchanger unit is shown in Figure 3.20.

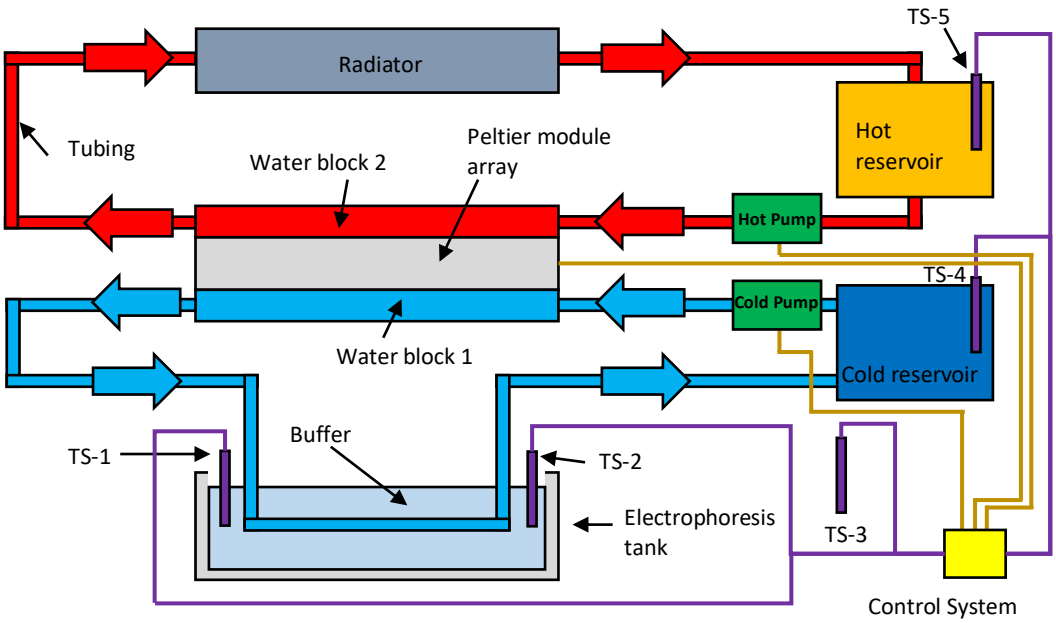


Figure 3.20. Overview of the heat exchanger.

Red indicates the hot loop, blue indicates the cold loop, and arrows within the water loops indicate the direction of flow. Each loop has a reservoir from which water is pumped and temperatures are monitored. A radiator is included in the hot loop to lower water temperature to maintain a sufficient temperature difference across the Peltier module array. Temperature sensors are denoted by 'TS' followed by their number identifier.

The ability of the heat exchanger to maintain a constant buffer temperature when a potential is applied to the buffer depends on the difference between the cooling wattage of the Peltier modules and the total effect of joule heating. In a completely insulated system, a buffer temperature increase can be calculated from Equation 3.3 discussed earlier:

$$H = V \times I \times t \qquad 3.3$$

Where H is heat (J), V is the applied voltage (V), I is current (A), and t is time (s). From preliminary testing, it was observed that applying a 180 V potential for 600-seconds results in a current sustained above 0.2 A for the test duration. Consequently, the minimum heat produced under these conditions is 21,600 J, which is equivalent to 36 W over 600-seconds.

4186 J is required to raise the temperature of 1 L of H_2O by 1 °C in a completely insulated system, hence 21,600 J can raise the temperature of 2 L of buffer by 5 °C in 10-minutes under thermally insulated conditions. Given that the power of Peltier modules is most often 60 W, one could assume that a single module is sufficient to counter the effects of joule heating, especially given that thermal energy of the buffer/tank can by naturally transferred to the surrounding air.

However, it cannot be assumed that the Peltier modules will be 100 % efficient, therefore, four Peltier modules will be used to provide redundancy in the event that modules are highly inefficient or if greater applied potentials are applied across the buffer. Conveniently, commonly used 120 mm water blocks are the same length as four Peltier modules, so 100 % of Peltier surfaces can be thermally coupled to water block surfaces.

The design for the Peltier Module array, shown in Figure 3.21(A) shows the arrangement of the four Peltier modules (green) with the cold loop water block below, the hot loop water block above, and fanned heat sinks atop the hot loop block. A small high-speed fan sits atop the heat sinks and is positioned to push air downward and along the fanned heat sinks for more efficient cooling than that by ambient air.

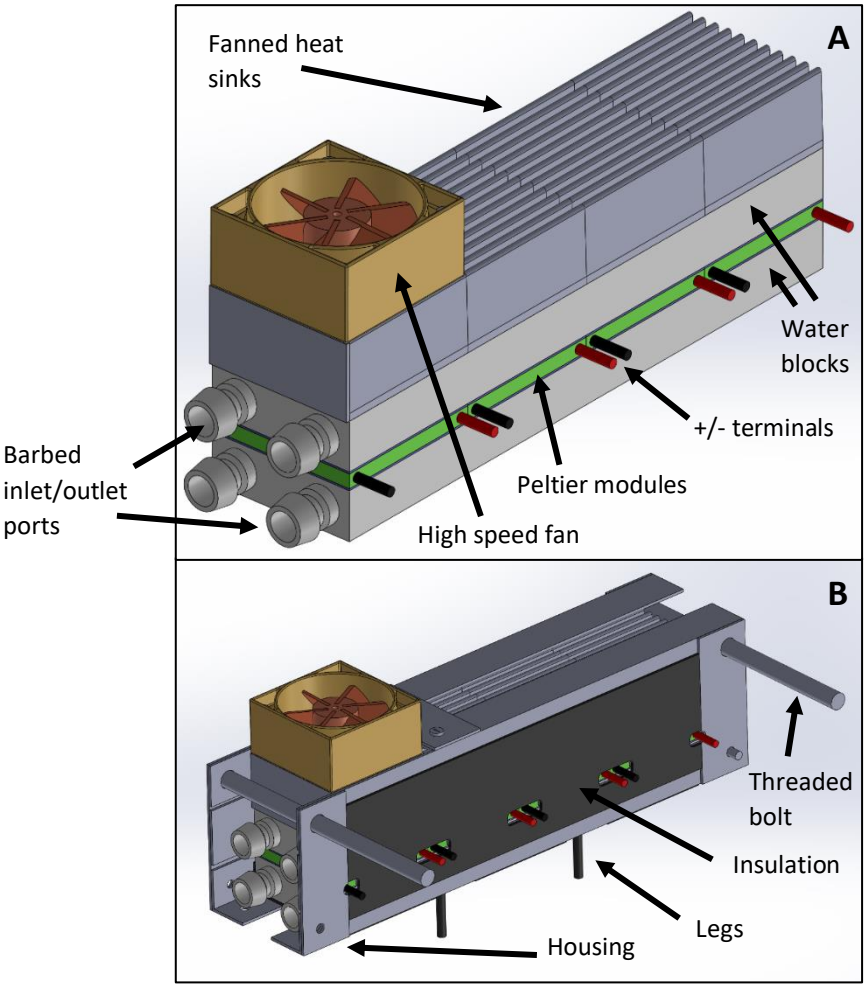


Figure 3.21. 3D CAD model of the heat exchanger: (A) without housing and (B) with housing.

The housing around the top of the Peltier module array will further encourage air flow to be directed from the fan through the fins of all four heat sinks. Thermal insulation is provided on either side to prevent the cold side of the Peltier modules absorbing heat from the air but still provides space for the Peltier module terminals. Threaded bolts are to be used to connect the heat exchanger to the enclosure.

The Peltier module array was manufactured using 60 W Peltier modules, fanned aluminium heat sinks, aluminium angle bar for the housing, 8 mm threaded stainless steel nuts, nylon nuts and bolts for the legs, and soft foam thermal insulation. Arctic MX-4 thermal paste (Arctic GmbH, Braunschweig, Germany) was used to thermally couple Peltier modules to 120 mm aluminium water blocks. The fan used was a 40 mm NF-A4x10 FLX 3-pin fan (Noctua, Vienna, Austria).

The electronic circuitry is responsible for reading temperature data via temperature probes and turning the Peltier modules on or off depending on the measured temperature and the target temperature (input). It will also facilitate operation of the pumps and fans via a user interface. An Arduino (Arduino, Turin, Italy) microprocessor will be used to manage the input/output functions of the electronics and is the central component within the electronic circuitry (see design specifications in Appendix Table 6.9).

The circuit overview of the temperature/pH control unit shown in Figure 3.22 illustrates how components are powered and controlled. The Advanced Technologies extended power supply unit (ATX-PSU) provides 5 V to an amber light emitting diode (LED) indicating standby mode. Closing of switch P1 turns a green 'On' LED and activates a 12 V supply by automatically closing switch P2. Switches R1, R2, R3 and R4 control the voltage delivery to the relay via the common contact connection. For each relay, a wire from the 'normally closed' (NC) connection provides voltage to a green LED, in parallel with a Peltier module. Each Peltier module has a combined voltmeter/ammeter with an LCD screen run in parallel to monitor the voltage across and current through the module. A wire is also connected to the 'normally open' (NO) connection of each relay, leading to a red LED to indicate 'off'. All LEDs in the system are in parallel with a 220 Ω resistor.

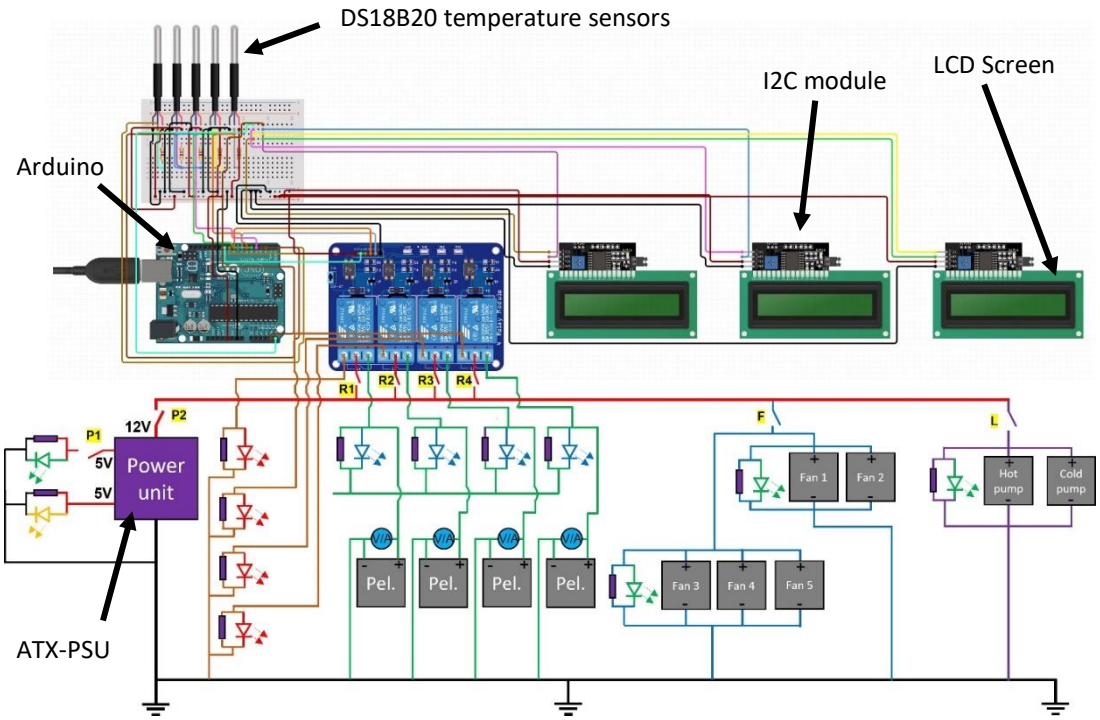


Figure 3.22. Overview of the electronic circuitry and components of the heat exchanger.

The 12 V line from the ATX-PSU provides power to two sets of fans and a pair of pumps, each with an individual green LED to indicate 'on'. Both pumps are switched on by a single switch so that both water loops are operated simultaneously. Similarly, all fans are switched on by a single switch but are divided into two circuit loops where each has a green LED; fans one and two draw air into the enclosure, whilst fans three and four are for the radiator and fan five is for the Peltier module array.

From Figure 3.22, one can see five DS18B20 temperature sensors that are powered by the 5 V potential of the Arduino. These sensors provide temperature readings to the Arduino via their central data wire which is communicated to the Arduino via a digital port. The Arduino can then display these temperature readings onto separate lines of multiple 16 x 2 digital LCD displays. An I2C module is used as an interface between the Arduino and display which has an inbuilt PCF8574 chip that converts I2C serial data to parallel data, substantially reducing wiring complexity.

Sensors one and two provide buffer temperature, from which the Arduino calculates an average to provide a single buffer temperature. Sensors three, four and five provide ambient, cold reservoir and hot reservoir temperature readings respectively. The Arduino calculates the buffer temperature average and sends signals to the relay module to move individual relays from the NC or NO position, or vice versa, depending on the current temperature and target temperature. For steady temperature control, each Peltier module will have a different activation/deactivation temperature. For example, Peltier module 1 will switch off when the measured temperature is within 1 °C of the target temperature, whilst Peltier module 2 will switch off when the measured temperature is within 0.5 °C of the target temperature.

The electronics were assembled on an acrylic shelf designed to be lifted in and out of the enclosure (Figure 3.23). A polycarbonate panel (machined in-house) was connected to the acrylic shelf to position the various components for the user interface (switches, LEDs, LCD screens, voltmeter/ammeters, buck convertor). Only 12 V supply lines from the ATX-PSU were used - except for the 5 V supply to the primary 'on' switch - so wires supplying other voltages were safely capped off using shrink wraps. A PCB board was used to create most of the circuitry for the user interface components.

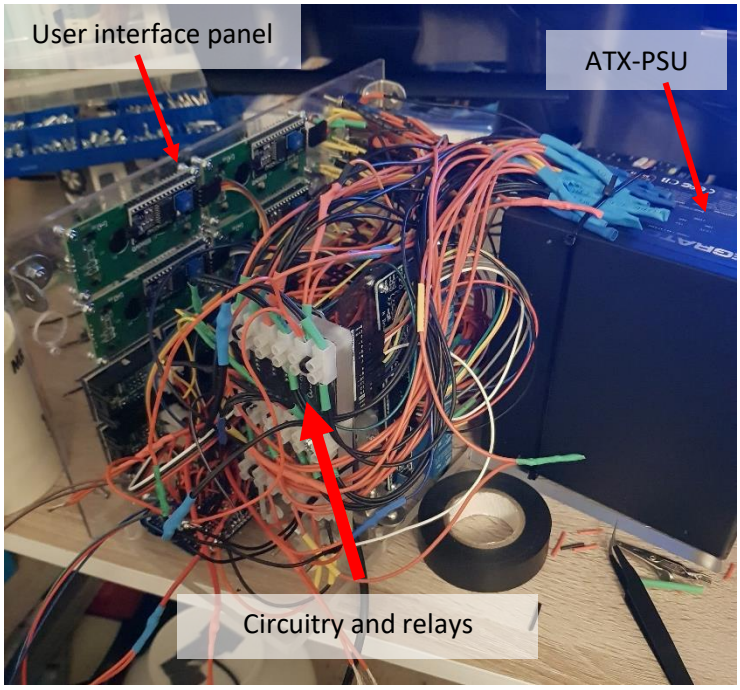


Figure 3.23. Rear view of the electronics circuitry shelf.

The coding for the Arduino performs two primary functions: 1) the switching of relays based on measured buffer temperature (T_A) within proximity to a target temperature (T_T); and 2) the display of all measured temperatures on LCD screens. A pseudo code flowchart is shown in Figure 3.24 that illustrates the input/output functions of the Arduino coding.

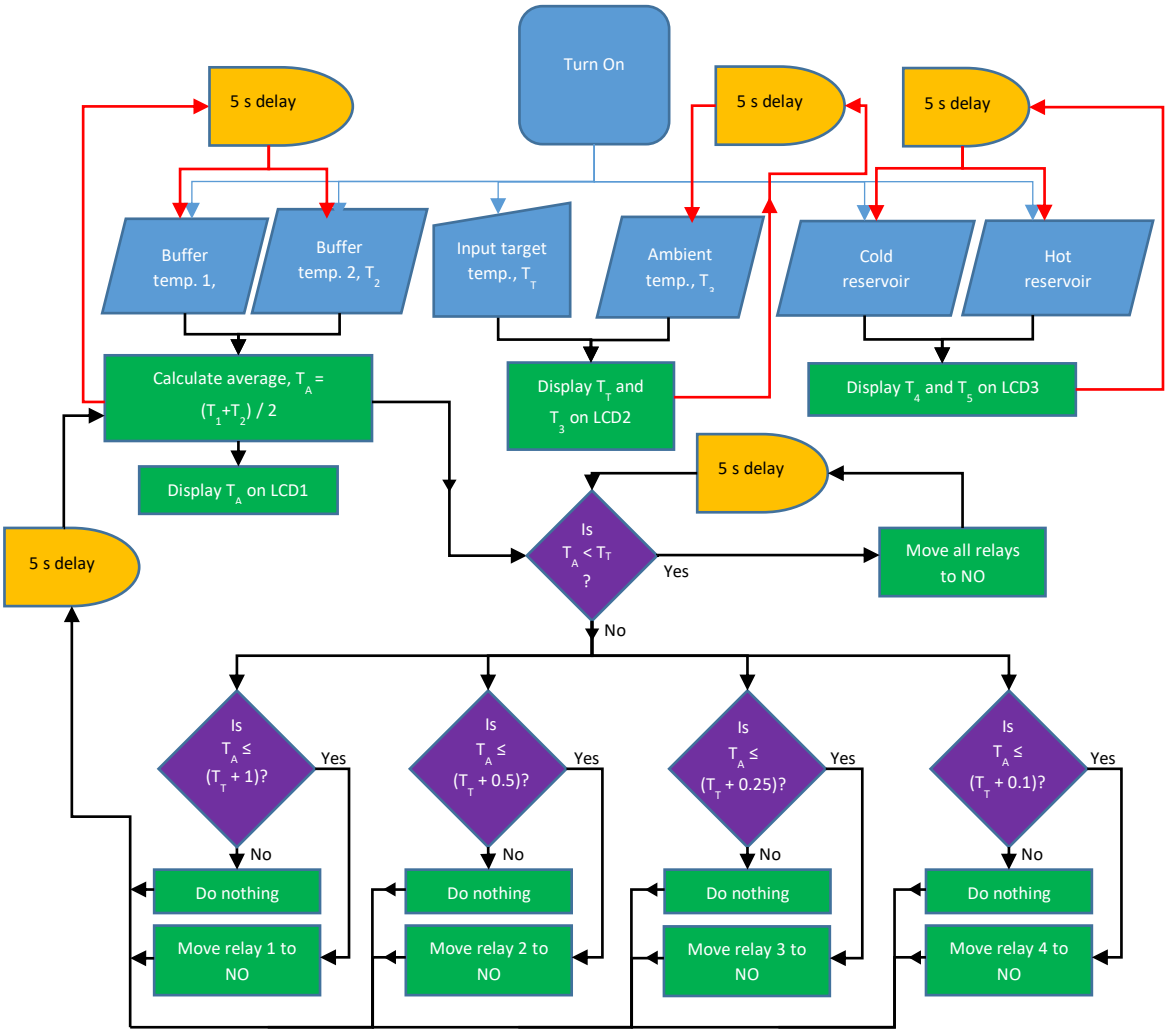


Figure 3.24. Pseudo code flowchart of coding for Arduino.

T_T is required as an input in the code itself, whilst $T_{1\text{-}5}$ are data provided by temperature sensors and refreshed every five seconds. The average of T_1 and T_2 are first calculated to give T_A, then T_A and $T_{3\text{-}5}$ are all displayed on separate lines on LCD1, LCD2 and LCD3 respectively. A primary decision is then made: is $T_A < T_T$?. If yes, then the buffer temperature is too low and all relays are moved to NO to switch off all Peltier modules, then checked again after a five second delay. If $T_T \leq T_A$, then further secondary decisions are made that will determine individual relay positions to control temperatures as T_A approaches T_T. As T_T is approached, the secondary decisions turn off Peltier modules to reduce the rate of temperature decrease with the aim of

maintaining T_T to within 0.25 °C. (i.e. using only two Peltier modules) to prevent any substantial over-cooling.

An enclosure is needed to encapsulate most of the heat exchanger unit, which includes the Peltier module array and the electronic circuitry (ATX-PSU, Arduino, user interface). The cold loop reservoir and pump, and the radiator for the hot loop, also need to be positioned within the enclosure. The hot reservoir and submerged pump will remain outside of the enclosure due to the reservoir's large size, as will the submersible section of the cold loop tubing.

Since water loop components are to be enclosed alongside electronic components, the enclosure is to be divided into a section for the water loops and another section for the electronic components (except for the Peltier module array). This will ensure the majority of electronics are not exposed to water in the event of a leak.

A two-layer enclosure is to be constructed; a plan-view of the bottom layer is shown in Figure 3.25 and houses the heat exchanger, cold loop pump, radiator, and fans one and two. The fans are positioned to draw air into the enclosure to help keep the cold loop pump cool and to provide an air supply to the fans of the heat exchanger and radiator. Exhaust air is directed out the back of the enclosure.

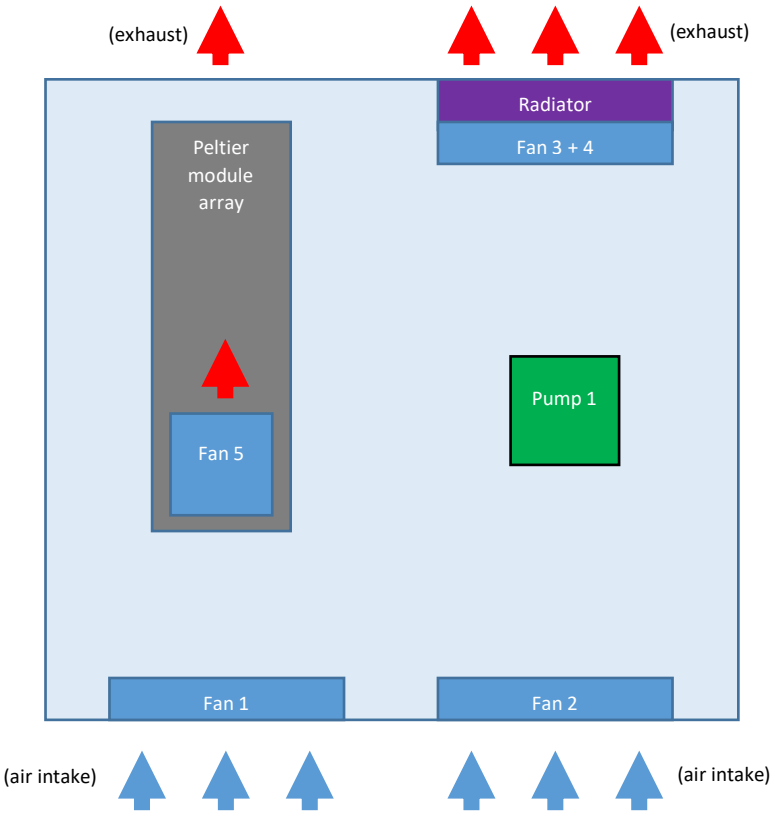


Figure 3.25. Layout of the bottom layer of the enclosure.

The plan-view of the upper layer of the enclosure is displayed in Figure 3.26. The upper layer shape is determined by the need to position the cold loop reservoir at the highest point possible for drainage and filling purposes, whilst the radiator's height means it occupies the full height of the enclosure. The ATX-PSU Arduino and electronics rest on a weight-bearing shelf, whilst the user interface panel (switches, LEDs, LCD screens, voltmeter/ammeters, USB-port) forms the front panel of the enclosure. A wall separates the bottom layer from the top layer with a port for wires from the heat exchanger and fans to pass through. Reservoir 1 will be supported by the wall, allowing it to be positioned directly above pump 1, which is ideal for removing air from the cold loop. The ATX-PSU will be positioned on its side so that its air intake will come from the side of the enclosure and exhausted out the rear.

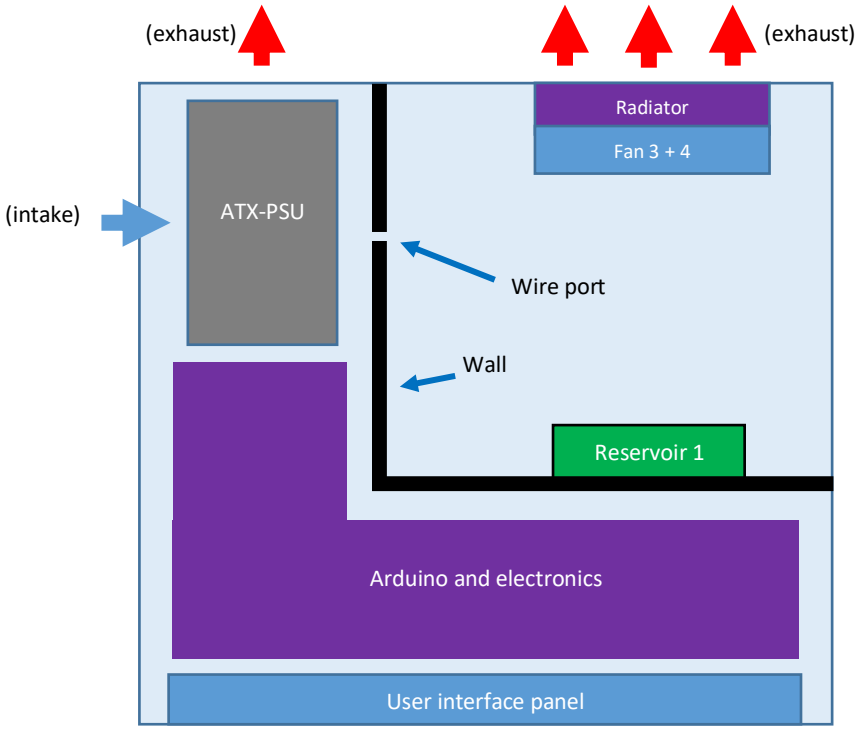


Figure 3.26. Layout of the top layer of the enclosure.

The enclosure was constructed primarily from polycarbonate sheet and assembled in-house. The Peltier module array, cold loop reservoir, pump 1 and radiator were bolted into their positions on the lower layer of the enclosure. Silicone tubing was used to join the following connections in the hot loop: the outlet of the hot loop pump to the Peltier module array inlet, the Peltier module array outlet to the radiator inlet, the radiator outlet to the hot reservoir. Silicone tubing was used to join the following connections in the cold loop: the cold reservoir

outlet to the pump inlet, the pump outlet to the Peltier module array inlet, the Peltier module array outlet was the submersible tubing, and the submersible tubing to the reservoir inlet.

Submersible tubing is to be used within the electrophoresis tank as the heat exchanging surface that is submerged within the buffer. Ideally, one would use a material of high thermal conductivity for the tubing such as copper or aluminium, but these are electrically conductive. Meanwhile, hard-line tubing materials such as glass require extensive fittings to connect one piece to another and as such overly complicate the cold loop with a large number of potential leak sites. Silicone tubing, whilst low in thermal conductivity, is already used elsewhere in the cold loop due to its flexibility. Using simple tube splitters to increase the number of tubes submerged within the buffer, the heat exchanging surface area of silicone tubing can be increased to offset the low thermal transfer efficiency that is inherent of the material.

Two tubing platforms are required to keep the silicone tubing submersed within the buffer at either end of the tank and in the correct shape. The design for a submersible tubing platform is shown in Figure 3.27 below. The platform has a capacity for four separate 12 mm diameter silicone tubes, guided into a U-shape, and can be lifted in and out of the tank as required. The shape and position of the tubing platform prevents silicone tubing from disrupting the electric field within the centre of the tank. Acrylic was cut and chemically bonded together to form the platform and four separate 12 mm silicone tubes were fed through each platform.

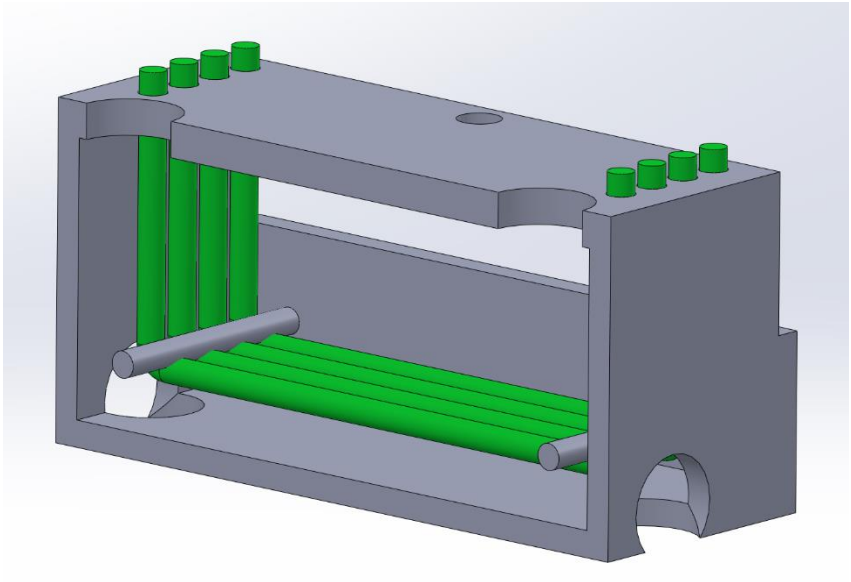


Figure 3.27. 3D-CAD model of the tubing platform with silicone tubing (green).

3.3.3 Apparatus testing

3.3.3.1 PS-DW-AGE system

The gel tray, combs, comb risers, gel punch and cutting mask were first tested with regard to their ability to cast a gel slab with uniformly shaped wells in parallel rows that retained well bases, followed by the ability of the gel punch to repeatedly cut uniformly shaped gels from the gel slab. The gel tray and combs were assembled to form 8 well rows (4 well row pairs), then 130 mL of a molten 1 wt % agarose solution was poured into the gel tray and allowed to cool for 45-minutes. After submersion in the tank, combs were removed from the gel to inspect the integrity of well bases. This process was repeated to form and test for well base tears using gel slabs produced with the 1 mm, 2 mm, and 3 mm thick comb risers. The test showed the 2 mm comb risers are required to prevent well base tearing.

The gel punch and cutting mask were tested by slicing and removing gels from the gel slab produced with the 2 mm thick comb riser. The cutting mask was positioned between a pair of well rows and the gel punch was used to slice and remove six gels. The gels were collected and measured using a digital micrometer to determine their size.

A gel slab produced using 2 mm thick comb risers was used to determine how thick particle layers appeared in the PS-DW-AGE system. Briefly, loading solutions of either 2 M $CaCl_2$ + 5 vol % glycerol or 1.8 M $MgCl_2$ + 5 vol % glycerol were loaded into one row of wells whilst loading solutions of 12 mM Na_2HPO_4 + 5 vol % glycerol were loaded into the opposite row of wells. A 180 V potential was applied across the electrophoresis tank for 600-seconds, during which the time for particle layers to appear was measured. The thickness of particle layers was measured visually using calibrated images in ImageJ using the line tool. The same test was performed in a PDA-coated gel slab, prepared according to the protocol described in 2.3.4.

3.3.3.2 PS-CAGE system

The ability of casts to retain cylindrical gels was first tested. Three separate gel moulds with gel casts measuring either 2 mm, 4mm, and 7 mm in thickness were paired with their respective base. A 100 mL mixture of 1 wt % agarose with 25 mM HEPES buffer was then prepared and the molten solution was allowed to cool to 80 °C before being poured into each mould until it overflowed with mixture. An acrylic lid was lowered onto each mould at an angle to remove

bubbles and was weighted down to squeeze out excess solution and ensure a flat face is formed on top of the cylinders. After 45-minutes the lids were removed, after which the casts were pried from their respective bases.

Once removed, excess gel was cleaned from all sides of the cast and from the small bolt holes. The 2 mm, 4 mm, and 7 mm thick moulds were submerged briefly in water to see whether they could hold onto the gel cylinders. The 4 mm thick cast was identified as the minimum thickness of cast that can retain gel cylinders when submerged.

A second test was performed to test whether precipitation occurs when casts of $CaCl_2$ and Na_2HPO_4 loading gels are sandwiched around a recipient gel cast. Solutions for each of the $CaCl_2$, Na_2HPO_4 and recipient gels were prepared; these are listed in Table 3.4. All solutions were adjusted to pH 8 using either 6 M HCl or 6M NaOH and made up to a final volume of 500 mL.

Table 3.4. Concentrations and pH for each cylindrical gel type.

Cylindrical gel type	**HEPES concentration [mM]**	**$CaCl_2$ (mM)**	**Na_2HPO_4 (mM)**	**pH**	**Final volume (mL)**
$CaCl_2$ loading gel	25	2000	0	8	500
Na_2HPO_4 loading gel	25	0	12	8	500
Recipient gel	25	0	0	8	500

30 mL of each solution was added to separate conical flasks, to which 0.3 g of SeaKem™ was added. Each mixture was heated until agarose fully dissolved and was then allowed to cool to 80 °C. The cooled $CaCl_2$ loading gel, Na_2HPO_4 loading gel, and recipient gel mixtures were each poured into moulds with 4 mm thick casts. Lids were placed on each mould, weighed down, and the gels were allowed to gel for 60-minutes. The increased cooling time from 45-minutes used for the gel slab to the 60-minutes used here is to compensate for $CaCl_2$ salts that will increase the gelation temperature of agarose (Piculell and Nilsson, 1989).

The casts were removed from their bases (see Figure 3.28) and prepared for submersion by removing excess agarose. The casts were then loosely bolted together with a 1 mm gap between casts. This separation is to ensure that air is not trapped between adjacent gel cylinder faces when submerged in buffer, as well as preventing premature diffusion of ions between touching gels. The raised electrode holders were hooked over opposing ends of the electrophoresis tank and connected to a DC power supply. The tank was then filled with 2 L of 25 mM HEPES buffer (pH 8). The loading and recipient gel casts were submerged, and nuts were quickly tightened to form the gel cast 'sandwich'.

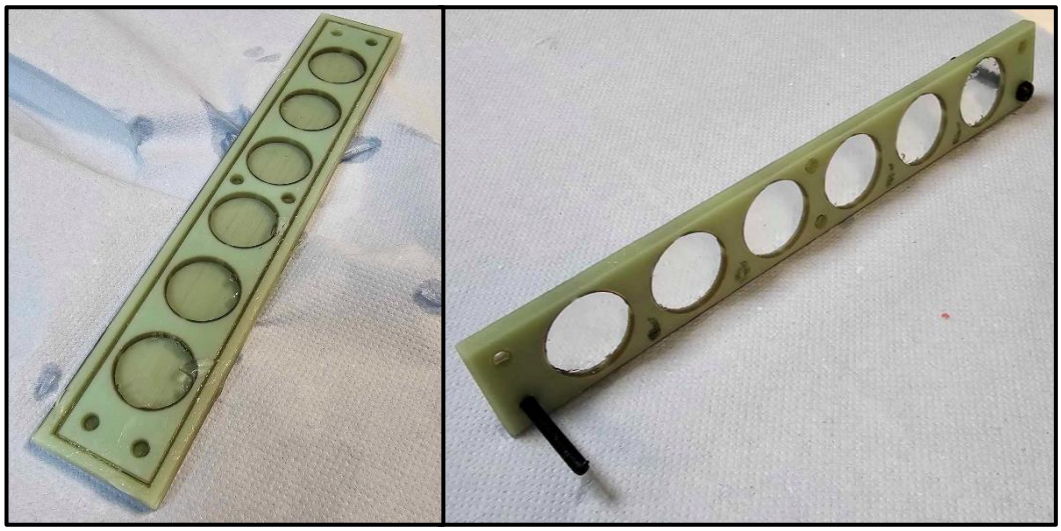


Figure 3.28. Agarose gel cast in a cylindrical gel mould. (Left) gel cylinders within the mould (lid removed); and (right) a gel cast removed from the mould and stood upright using nylon bolts.

A 180 V potential was applied across the tank for 600-seconds and the corresponding current was recorded throughout the test. The greater potential and duration compared used here compared to the previously used 60 V for 360-seconds for the PS-SW-AGE system is due to the difference in maximum ion travel distance. In the PS-SW-AGE approach, Ca^{2+} ions travelled a maximum of 3.5 mm; from the farthest well edge to farthest precipitate edge. In the PS-CAGE system, this distance is estimated to be approximately 6 mm, from the farthest loading gel face to the centre of the recipient gel. Although a larger potential is used here, a longer duration will allow for observation of the particle layer post-synthesis to see if any changes occur regarding layer size or shape post-precipitation. This test was repeated using a PDA-coated recipient gel, prepared by polymerising PDA according to the protocol described in 2.3.4 and pouring the resulting mixture into a 4 mm thick cylindrical gel mould.

After 600-seconds the applied potential was removed, the gel cast sandwich was withdrawn from the tank and disassembled to reveal the recipient gels. Four of the cylindrical recipient gels were extracted from their mould and re-submerged in buffer for good contrast during imaging. Images were taken of the front, rear, and side faces of the cylindrical gels. Two gels were kept in the mould and used to test the gel cutter by bolting the mask holder onto the mould. The four-hole mask was positioned above one gel cylinder and the five-hole mask was positioned above the remaining cylinder. 6 mm and 5 mm diameter cylindrical gels were then sliced using the four-hole and five-hole mask respectively. Images in Figure 3.29 below show the gels cut using both masks.

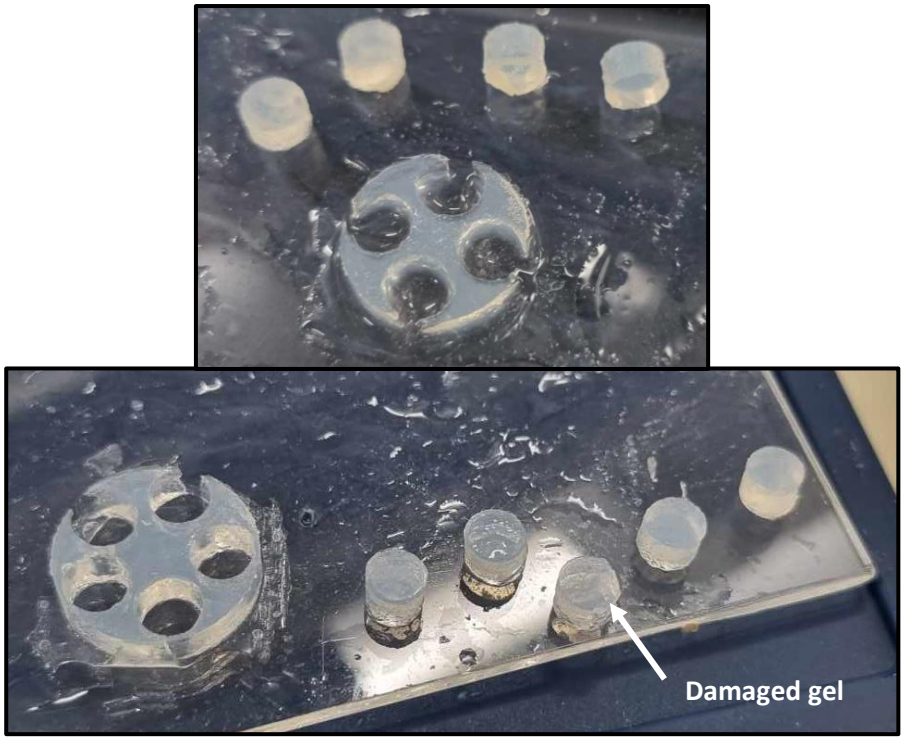


Figure 3.29. (Top) Four small gel cylinders cut from a large gel cylinder; (bottom) five gel cylinders cut from a large gel cylinder.

Though each mask generally produced uniformly shaped gel cylinders, the closer spacing of the five-hole mask resulted in one gel being damaged during cutting. Therefore, the four-hole mask was used in future experiments.

3.3.3.3 Temperature/pH control Unit

The functionality of the temperature/pH control unit was tested at room temperature. First, the electrophoresis tank was fitted with the raised electrodes and filled with 2 L of 25 mM HEPES buffer solution (pH 8). The submersible tubing platforms were placed at the base of either end of the tank and the tubing for the peristaltic pumps were positioned near the electrodes. The initial buffer temperature was measured using two temperature probes in the centre of the tank.

Following the same protocol described for testing gel casting in the PS-CAGE system, a gel cast sandwich of loading and recipient gels were prepared and submerged in the tank immediately prior to the application of the applied field. The Arduino was then programmed to hold a buffer temperature of 21 °C and a 180 V potential was applied across the tank for 600-seconds. Current through the buffer was measured and recorded throughout the test. Following removal of the applied potential, temperature probes were immediately placed either side of the cast sandwich to record the buffer temperature. 5 mL samples of buffer were immediately extracted from each end of the tank and adjacent to the gel cast sandwich for pH measurement.

3.4 Results

3.4.1 Electrostatics models

An electrostatics model for each of the PS-SW-AGE, PS-DW-AGE, and PS-CAGE systems was constructed using COMSOL Multiphysics to measure the local electric field strengths around zones of precipitation. Rainbow colour maps plotted in a plane perpendicular to the y-axis in each model are shown in Figure 3.30 for the PS-SW-AGE and PS-DW-AGE models, and the PS-CAGE model is shown in Figure 3.31. In all electrostatic models, red and blue indicate the highest and lowest electric field strength respectively. Note that scale bars are absolute, where each model has its own scale.

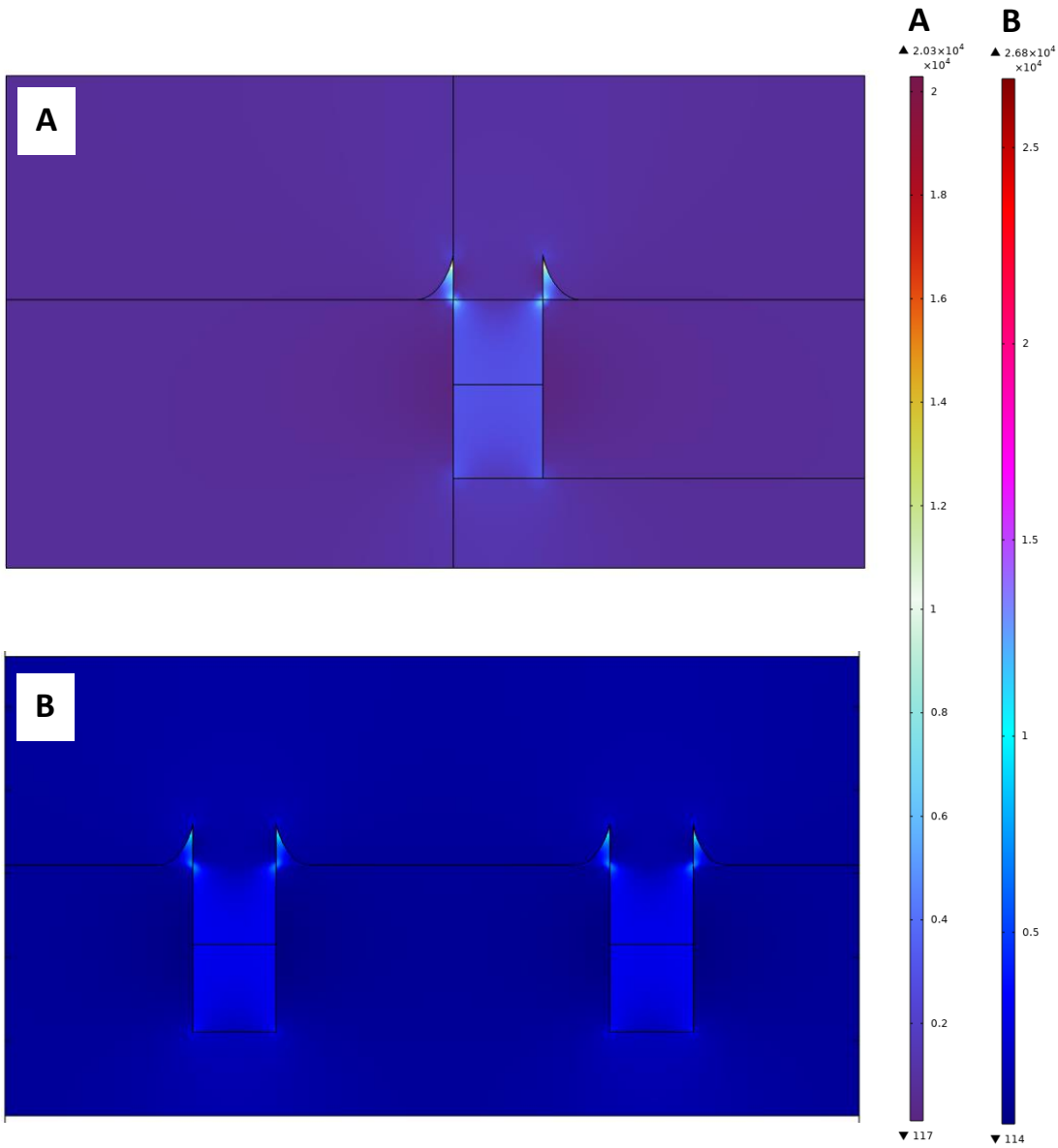


Figure 3.30. Electrostatic models showing electric field strength (Vm-1). (A) PS-SW-AGE model; (B) PS-DW-AGE model.

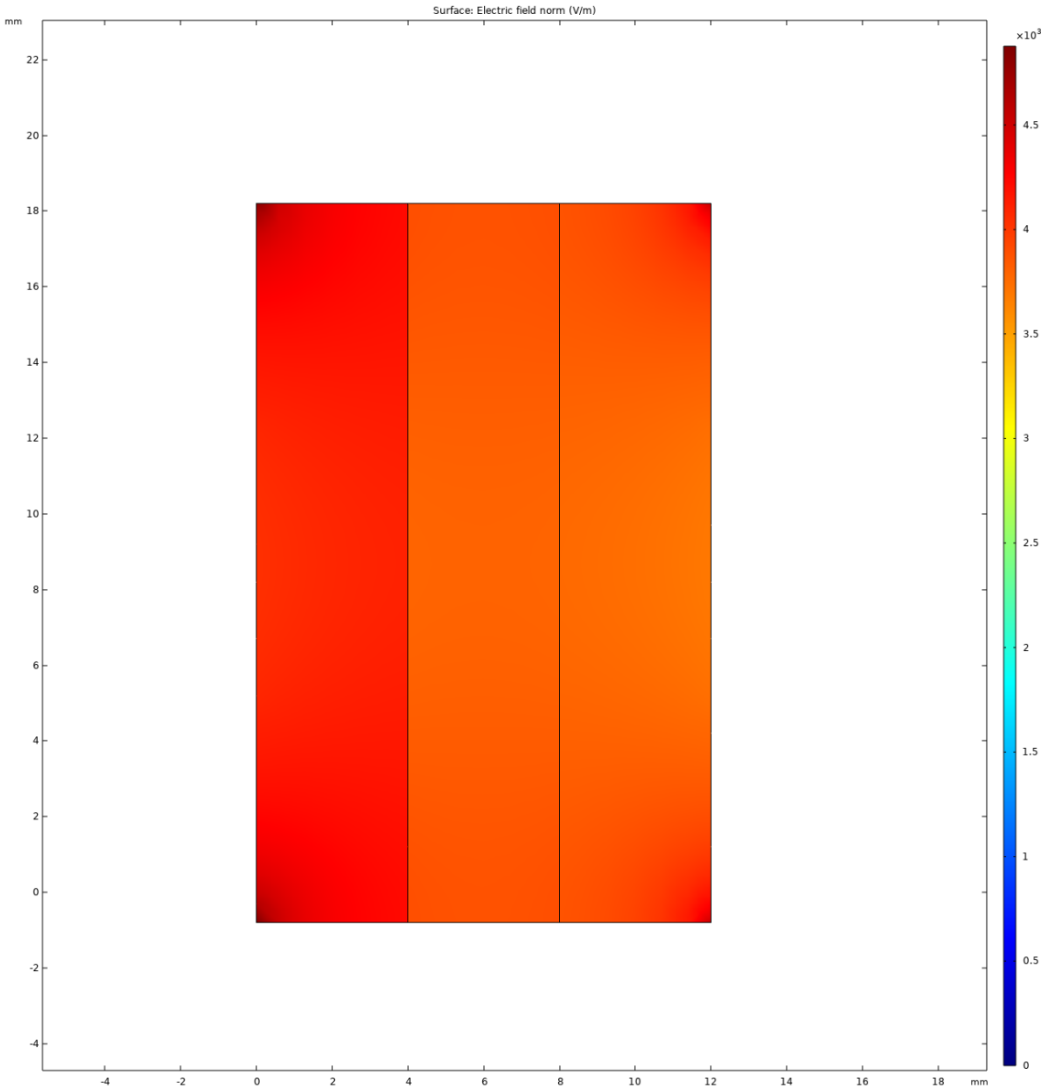


Figure 3.31. Electrostatic model showing electric field strength (Vm^{-1}) for the PS-CAGE model. The left domain shows the 2M $CaCl_2$ gel, the central domain is the recipient gel, and the right domain is the 12 mM Na_2HPO_4 gel (see *Figure 3.8* for model geometry).

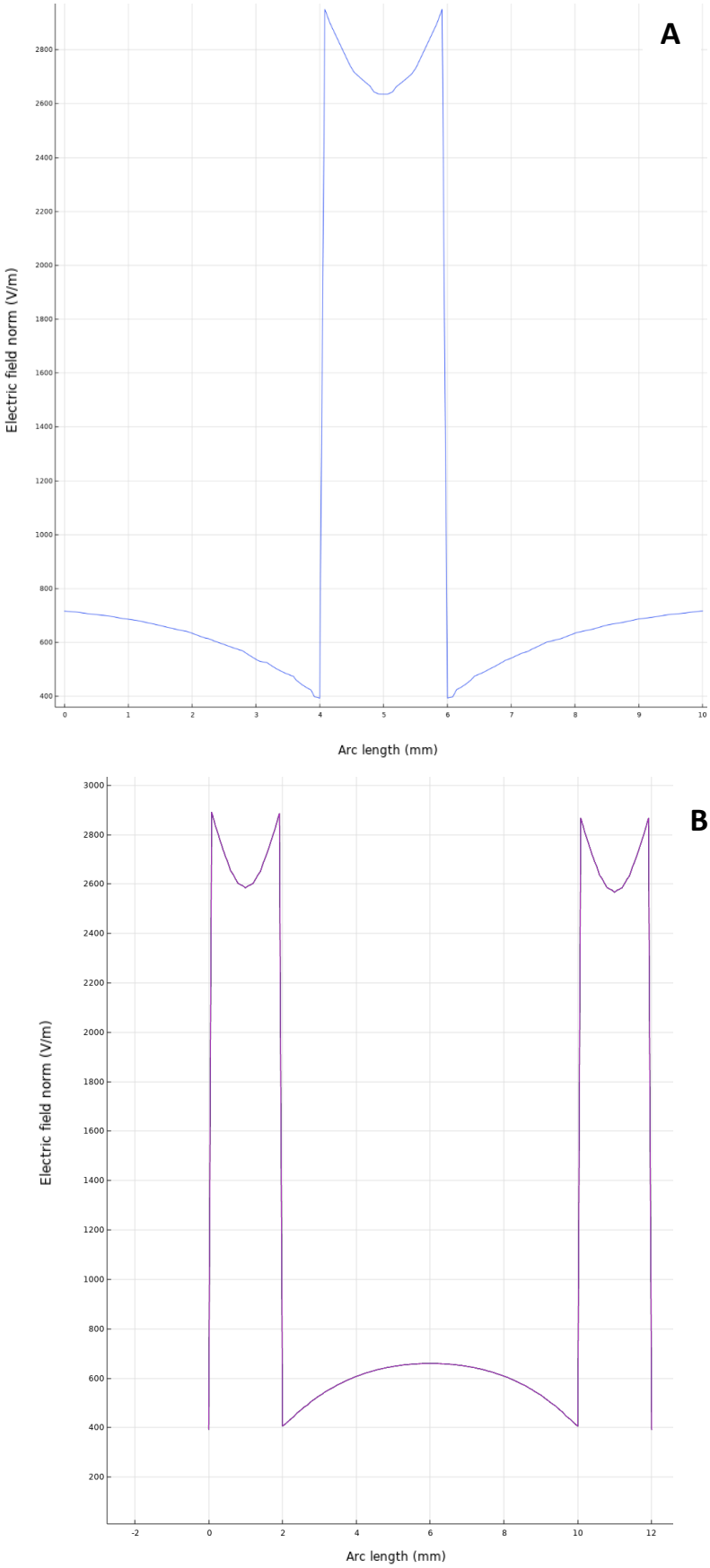


Figure 3.32. Line graphs of electrostatic models showing electric field strength (Vm-1). (A) PS-SW-AGE model; (B) PS-DW-AGE model.

From Figure 3.30, one can see that electric field strengths within the PS-SW-AGE and PS-DW-AGE models are greatest at the meniscus at the top of the well and in the area immediately adjacent to the wells. Electric field strength in both well models diminishes significantly toward the bulk of the gel slabs. In contrast, the PS-CAGE model (Figure 3.32) has a more consistent field strength across the central recipient gel domain and right hand Na_2HPO_4 loading gel domain but greater field strengths in the $CaCl_2$ loading gel. The PS-CAGE model presents symmetrical field strengths between the lower and upper halves of the cylinders due to its symmetrical 3D shape.

The line graph data for the PS-SW-AGE and PS-DW-AGE models are shown in Figure 3.32. These graphs demonstrate a reduction in electric field strength between well edges and the gel bulk. For the PS-SW-AGE model, field strength varied by over 200 Vm^{-1} non-linearly through the zone of precipitation (between 2 – 4 mm). Assuming the zone of precipitation occurs somewhere between 4 – 8 mm in the PS-DW-AGE, electric field strength varies by less than 100 Vm^{-1} in the PS-DW-AGE model. Assuming the zone of precipitation also occurs between 4 – 8 mm for PS-

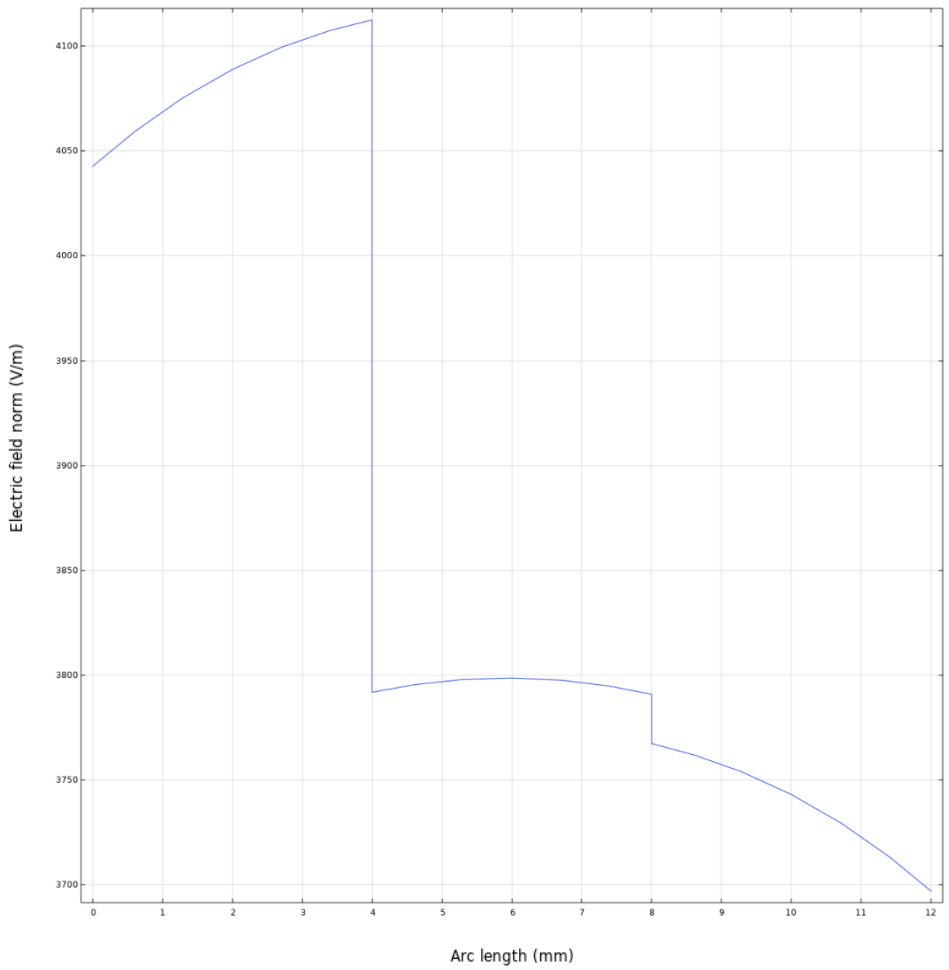


Figure 3.33. Line graph showing electric field strength in the PS-CAGE model.

CAGE model too, however, the electric field strength varies by only approximately 10 Vm^{-1}, as shown in Figure 3.33.

3.4.2 Ion Transport Models

3.4.2.1 PS-SW-AGE Ion Transport

Ca^{2+} ion transport in the PS-SW-AGE model was modelled using the expression: $C = [Ca^{2+}]$, where C is concentration and $[Ca^{2+}]$ is Ca^{2+} concentration at time t. Figure 3.34 and Figure 3.35 display the animated colour map and animated line graph for Ca^{2+} ion transport respectively. At t = 0 s, Ca^{2+} is fully contained within the well and by approximately t = 70 s has been completely injected into the agarose gel. As expected, ion concentration increases substantially at the well-gel interface where the ion band appears to compress. The line graph animation (Figure 3.35) shows that this concentration peaks at over 14 M Ca^{2+}. The $Ca2^{+}$ ion band in Figure 3.34 appears to move in an ellipsoidal manner that stretches in the x-axis with time and stabilises at around 0.5 M Ca^{2+}.

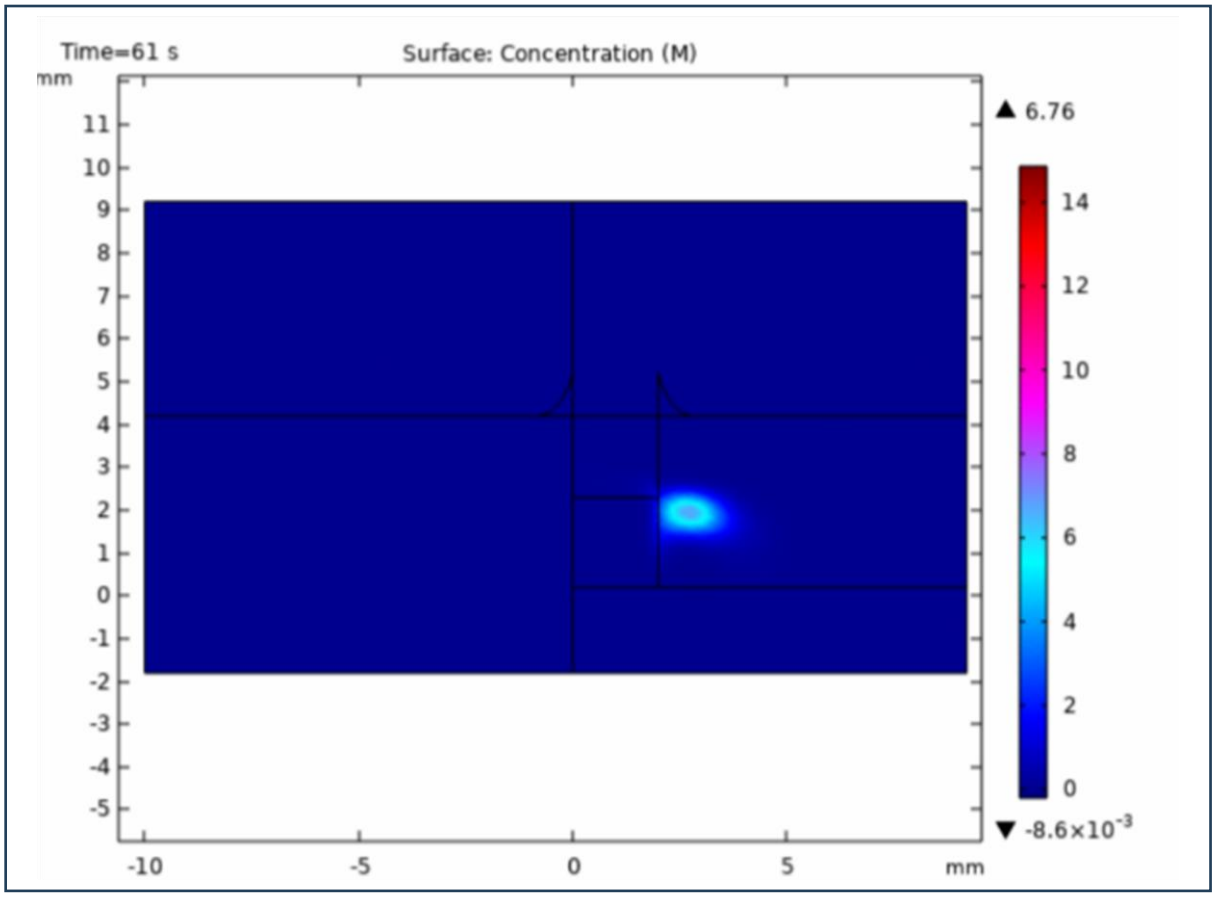


Figure 3.34. Animation of Ca^{2+} ion transport in the PS-SW-AGE model. The animated figure can be found in the supplementary materials.

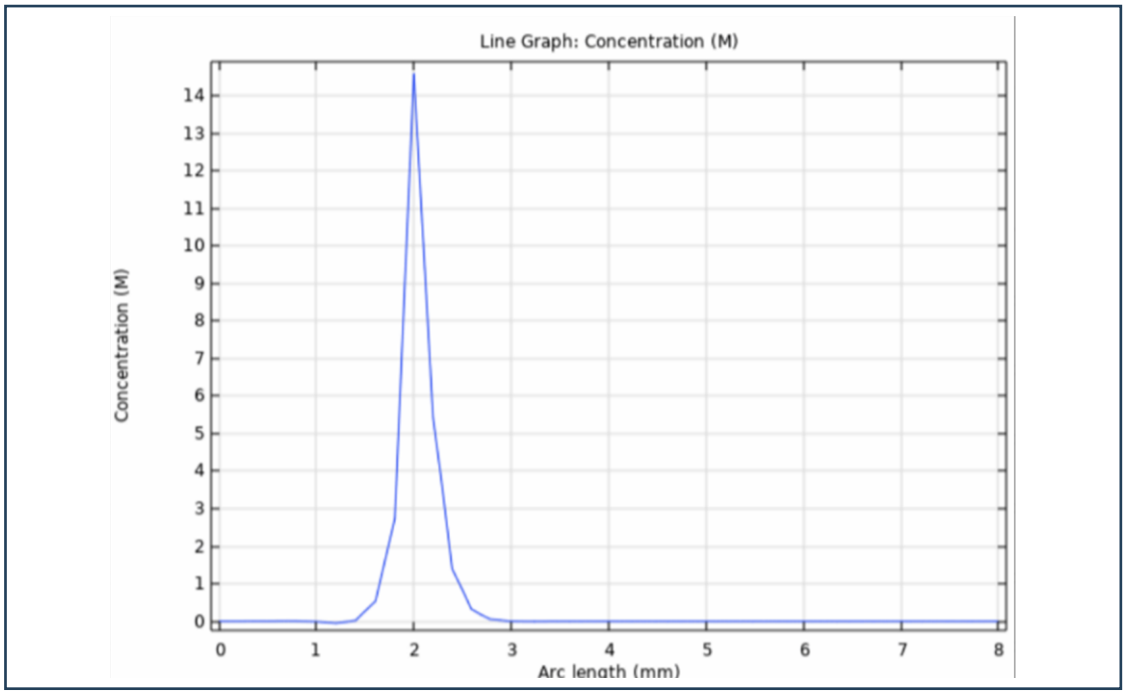


Figure 3.35. Line graph animation of Ca^{2+} ion transport in the PS-SW-AGE model. The animated figure can be found in the supplementary materials.

HPO_4^{2-} and $H_2PO_4^-$ ion transport in the PS-SW-AGE model is very different to that of Ca^{2+} due to its presence throughout the agarose gel and buffer. displays how HPO_4^{2-} and $H_2PO_4^-$ ion concentration increases on the left of the well but appears stable on the right of the well. The line graph animation in Figure 3.38 demonstrates this further, where HPO_4^{2-} + $H_2PO_4^-$ concentration is gradated between arc length 2 – 2.5 mm. Besides this gradient, the remainder of the model sustains a HPO_4^{2-} + $H_2PO_4^-$ concentration of 12 mM.

Figure 3.40 and Figure 3.39 show the concentration colour map and line graph animations for the mixing product, m, in the PS-SW-AGE model. Note that the mixing product was described in Equation 3.9 earlier and highlights the expected zone of precipitation. The greatest mixing product is found close to 2.25 mm from the well-gel interface in the first 20-seconds which is the same location and time which Ca^{2+} concentration peaks. This is simply because the colour map animation for m essentially mirrors that of Ca^{2+} concentration. It is important to keep in mind that this model ignores precipitation reactions and therefore assumes no loss of ions due to the formation of CaP particles.

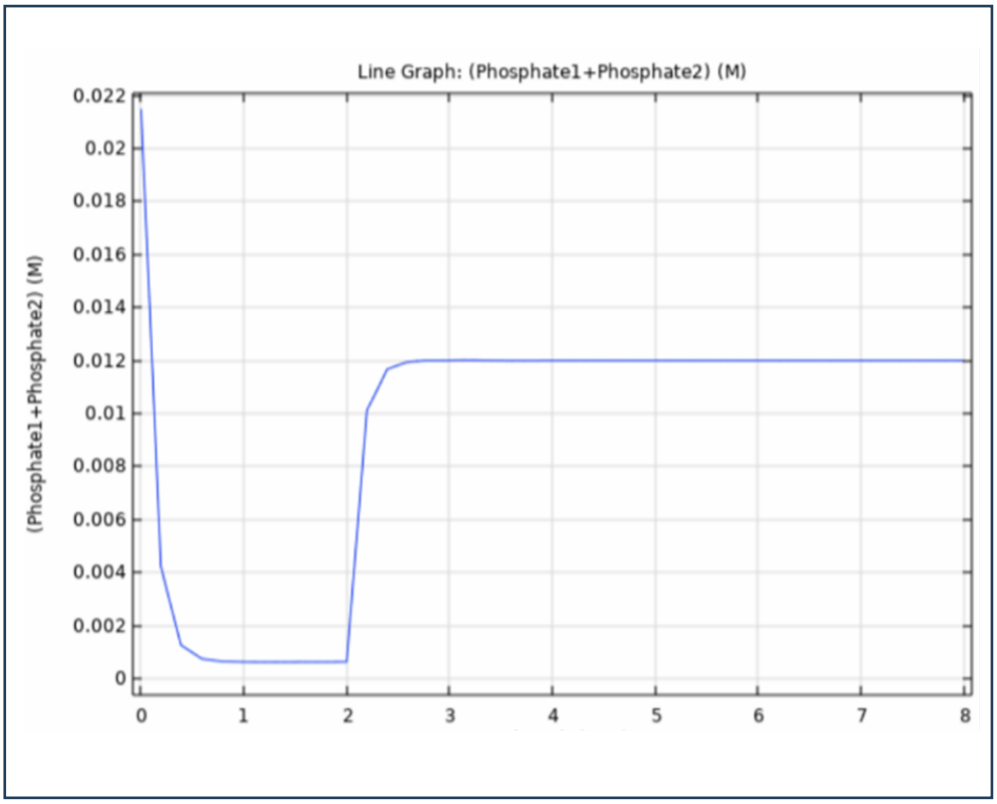


Figure 3.37. Animation of HPO_4^{2-} + $H_2PO_4^-$ ion transport in the PS-SW-AGE model. The animated figure can be found in the supplementary materials.

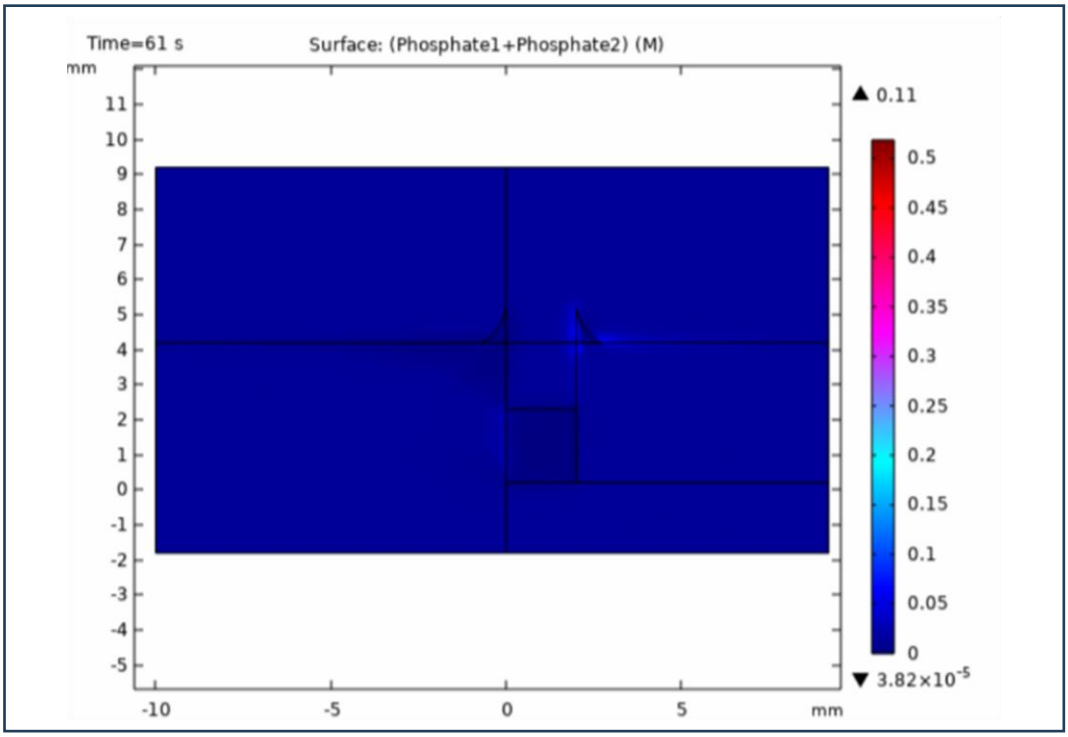


Figure 3.38. Line graph animation of HPO_4^{2-} + $H_2PO_4^-$ ion transport in the PS-SW-AGE model. The animated figure can be found in the supplementary materials.

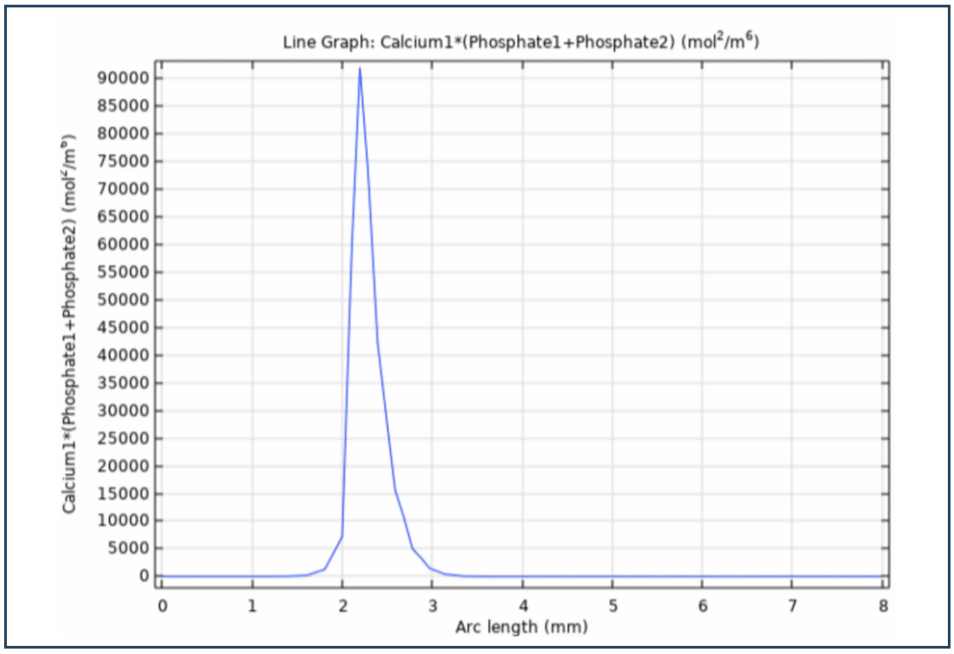


Figure 3.39. Line graph animation for the mixing product, m, for the PS-SW-AGE model. The animated figure can be found in the supplementary materials.

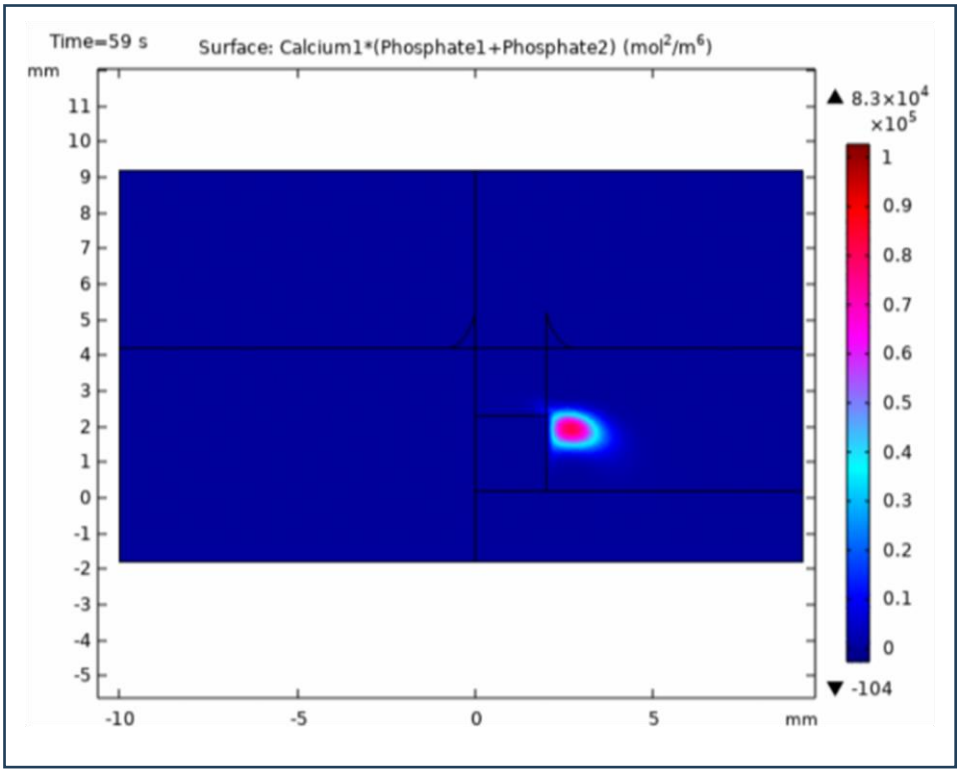


Figure 3.40. Animation of mixing product, m, for the PS-SW-AGE model. The animated figure can be found in the supplementary materials.

PS-DW-AGE Ion Transport

Separate ion transport models at pH 7.4 and 8 were produced for the PS-DW-AGE system. Ca^{2+} transport is consistent at both pH 7.4 and 8 (since relative permittivities for domains were kept constant regardless of pH). Figure 3.41 and Figure 3.42 display the colour map and line graph animation respectively of Ca^{2+} transport in the PS-DW-AGE model at pH 7.4 and 8.0.

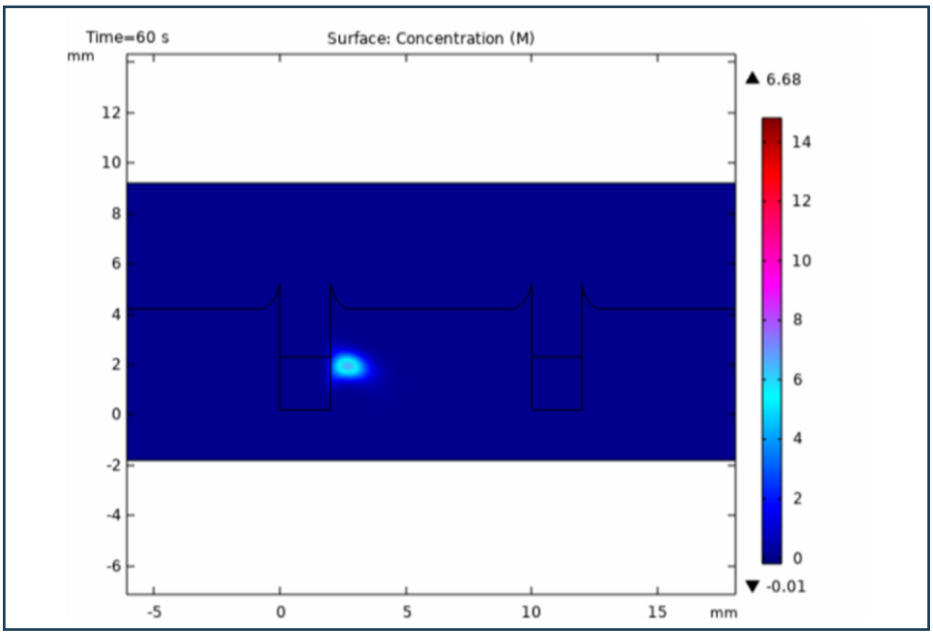


Figure 3.41. Animation of Ca^{2+} ion transport in the PS-DW-AGE model. The animated figure can be found in the supplementary materials.

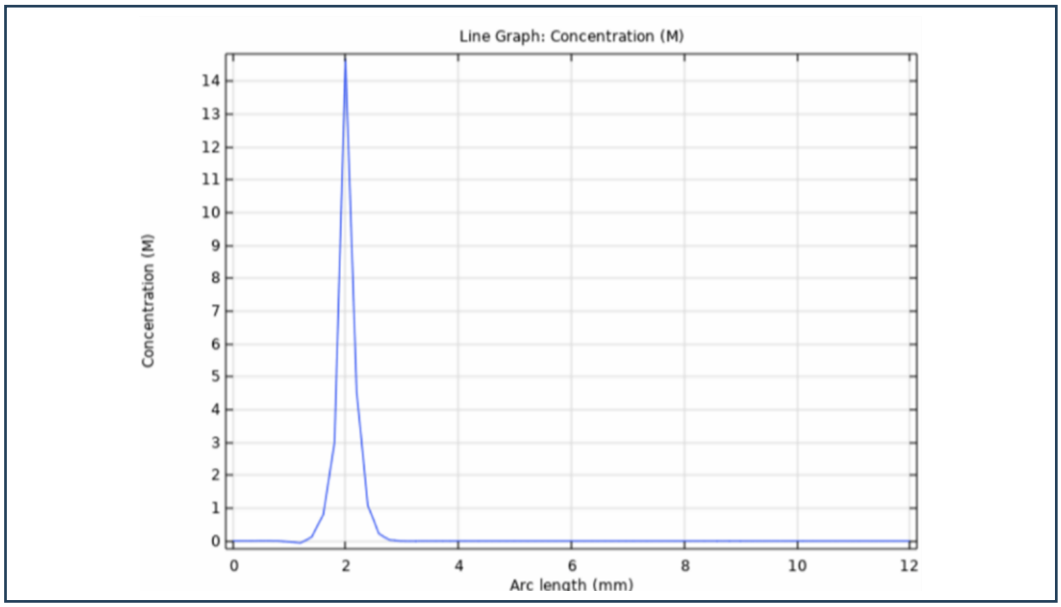


Figure 3.42. Line graph animation of Ca^{2+} ion transport in the PS-DW-AGE model. The animated figure can be found in the supplementary materials.

Transport of Ca^{2+} ions is identical between the PS-SW-AGE and PS-DW-AGE models prior to collision of Ca^{2+} ions with the opposite well. However, the transport of HPO_4^{2-} and $H_2PO_4^-$ ions are fundamentally different between the PS-SW-AGE and PS-DW-AGE due to their presence in the gel/buffer and well respectively. Figure 3.43 and shows the colour map for the concentration of HPO_4^{2-} + $H_2PO_4^-$ ions at pH 7.4.

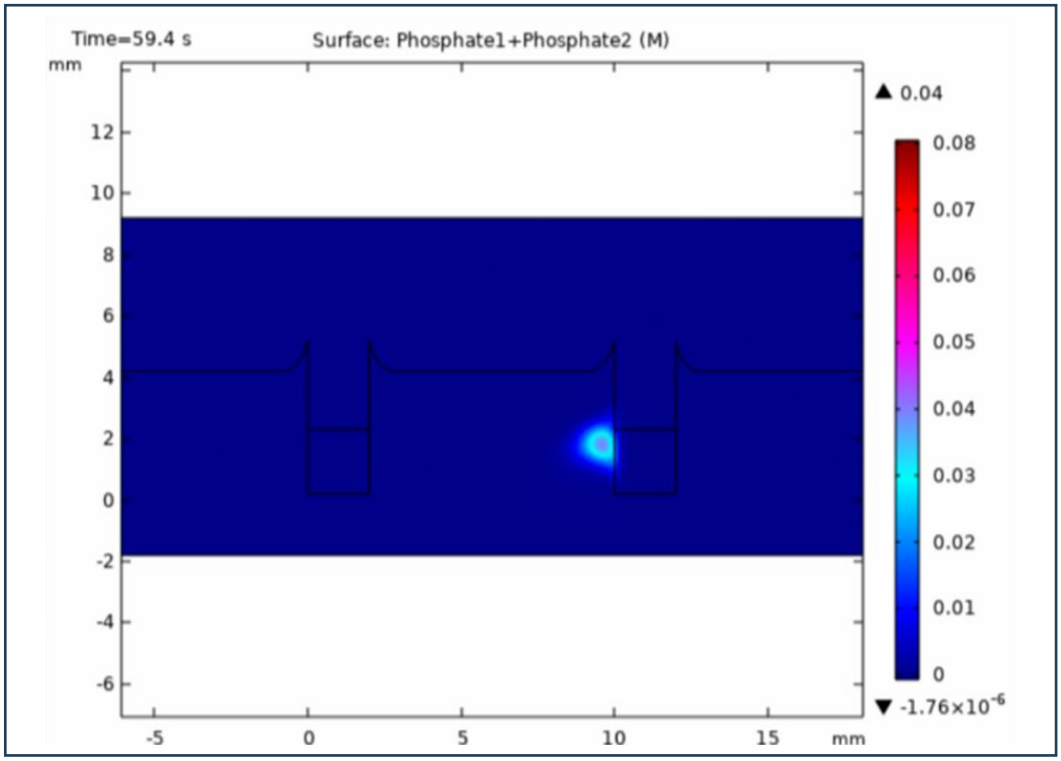


Figure 3.43. Animation of HPO_4^{2-} + $H_2PO_4^-$ ion transport in the PS-DW-AGE model at pH 7.4. The animated figure can be found in the supplementary materials.

At both pH 7.4 and 8.0, HPO_4^{2-} and $H_2PO_4^-$ ions are rapidly injected into the gel and a stacking effect occurs at the well-gel interface where the ion bands are compressed and concentration peaks, as with Ca^{2+} ions. The ions then reduce in concentration as they extend along the x-axis in an ellipsoidal pattern. The pH-dependent speciation of $H_xPO_4^{x-3}$ ions changes the ratio of HPO_4^{2-} and $H_2PO_4^-$ ions between pH 7.4 and 8.0, being subtle and not obvious without further inspection. After 250-seconds at pH 7.4, a separation of HPO_4^{2-} and $H_2PO_4^-$ ions becomes apparent. This separation can also be seen in the line graph animation of HPO_4^{2-} and $H_2PO_4^-$ ion transport at pH 8.0 in the PS-DW-AGE model (Figure 3.44).

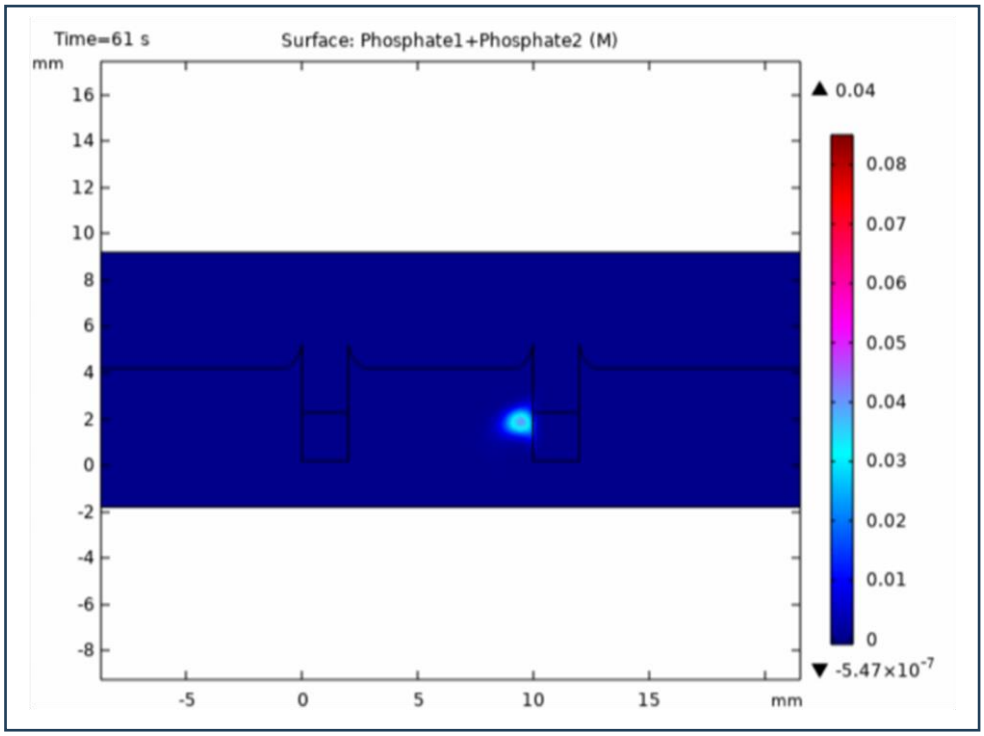


Figure 3.44. *A*nimation of HPO_4^{2-} + $H_2PO_4^-$ ion transport in the PS-DW-AGE model at pH 8.0. The animated figure can be found in the supplementary materials.

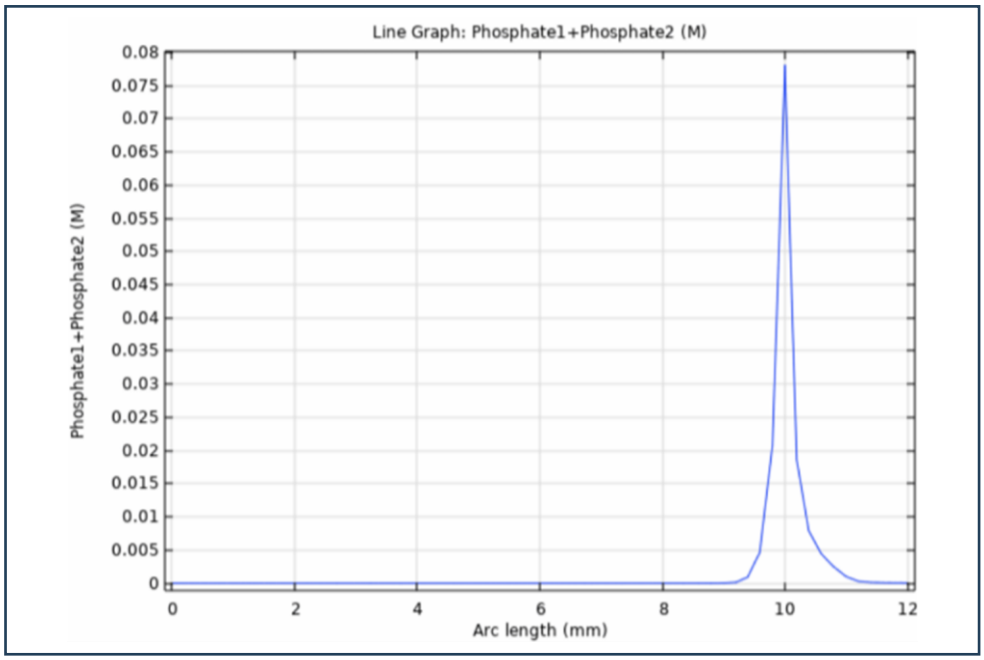


Figure 3.45. Line graph animation of HPO_4^{2-} + $H_2PO_4^-$ ion transport in the PS-DW-AGE model at pH 7.4. The animated figure can be found in the supplementary materials.

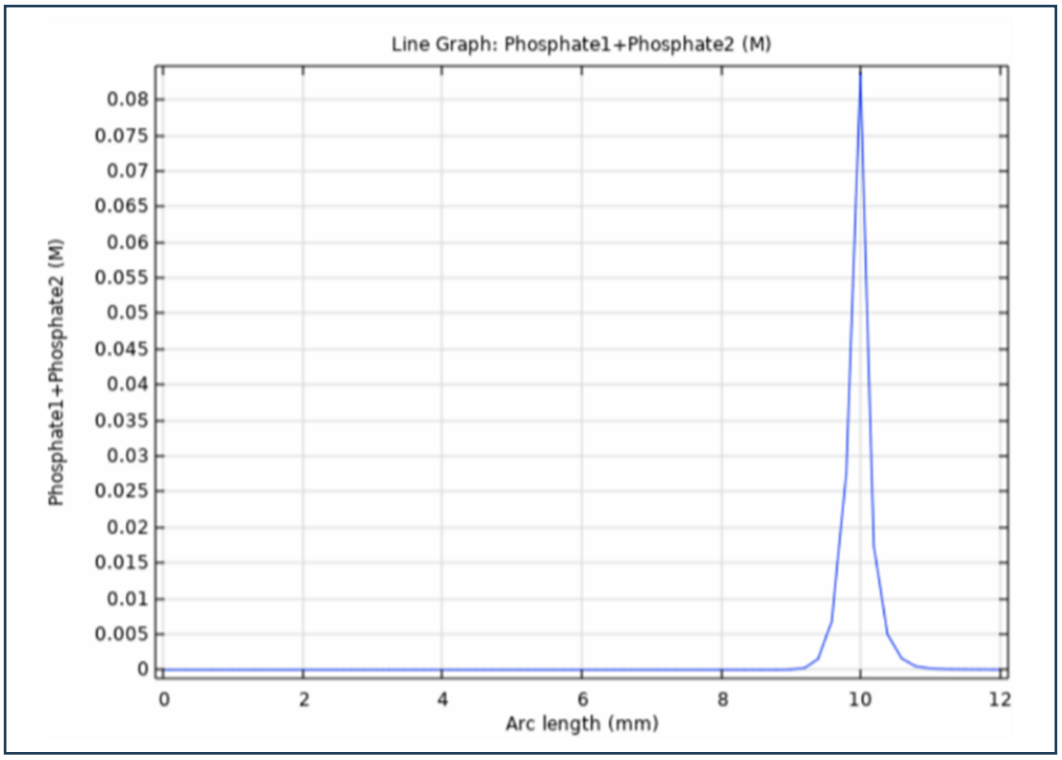


Figure 3.46. Line graph animation of HPO_4^{2-} + $H_2PO_4^-$ ion transport in the PS-DW-AGE model at pH 8.0. The animated figure can be found in the supplementary materials.

Figure 3.44 and Figure 3.46 show the colour map and line graph animation respectively for HPO_4^{2-} + $H_2PO_4^-$ ion transport in the PS-DW-AGE model at pH 8.0. Separation of HPO_4^{2-} and $H_2PO_4^-$ ions is far less noticeable at pH 8.0 due to a much lower concentration of $H_2PO_4^-$ ions. At both pH 7.4 and 8.0, the rolling peak of HPO_4^{2-} + $H_2PO_4^-$ concentration reduces to less than 2 mM.

A mixing product was calculated for each of the pH 7.4 and 8.0 PS-DW-AGE models. The colour map and line graph animations in Figure 3.47 and Figure 3.49 display the mixing product for the PS-DW-AGE model at pH 7.4. Mixing starts to take place at around 115-seconds in an ellipsoidal shape that skews toward the right due to the greater electrical mobility of Ca^{2+} ions. Figure 3.48 and Figure 3.50 display the colour map and line graph animations for the PS-DW-AGE model at pH 8.0. Similar to the model at pH 7.4, mixing takes place from 115-seconds in an ellipsoidal shape. Interestingly, the mixing product in the pH 7.4 model peaks initially between 450 – 500 at 6.5 mm but then rolls to the right and reaches a peak of over 650 at 7.5 mm. In comparison, the mixing product peaks at a single value of over 600 at 6.5 mm before diminishing and rolling to the right in the pH 8.0 model.

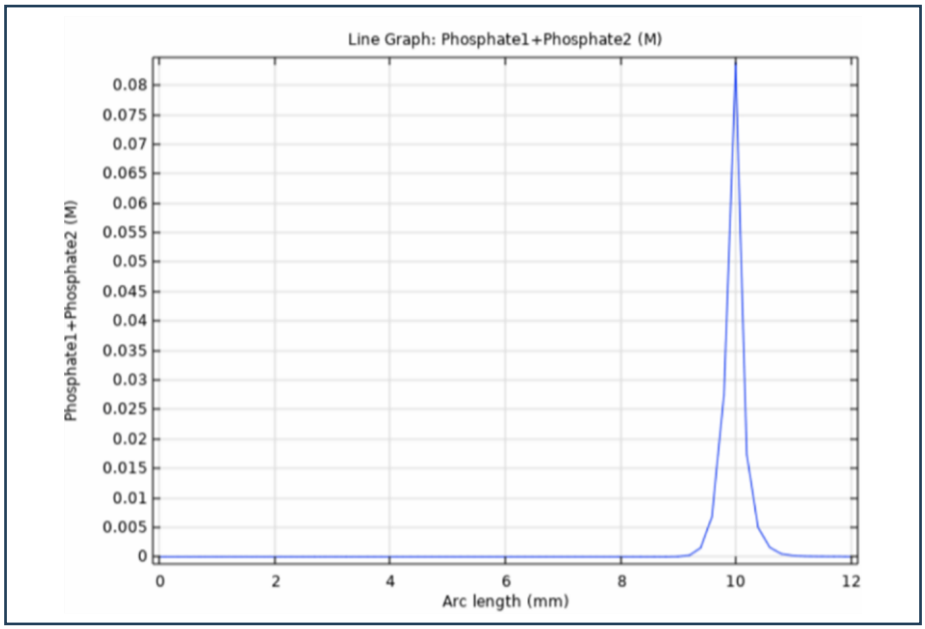


Figure 3.47. Animation of mixing product, m, for the *PS-DW-AGE* model at pH 7.4. The animated figure can be found in the supplementary materials.

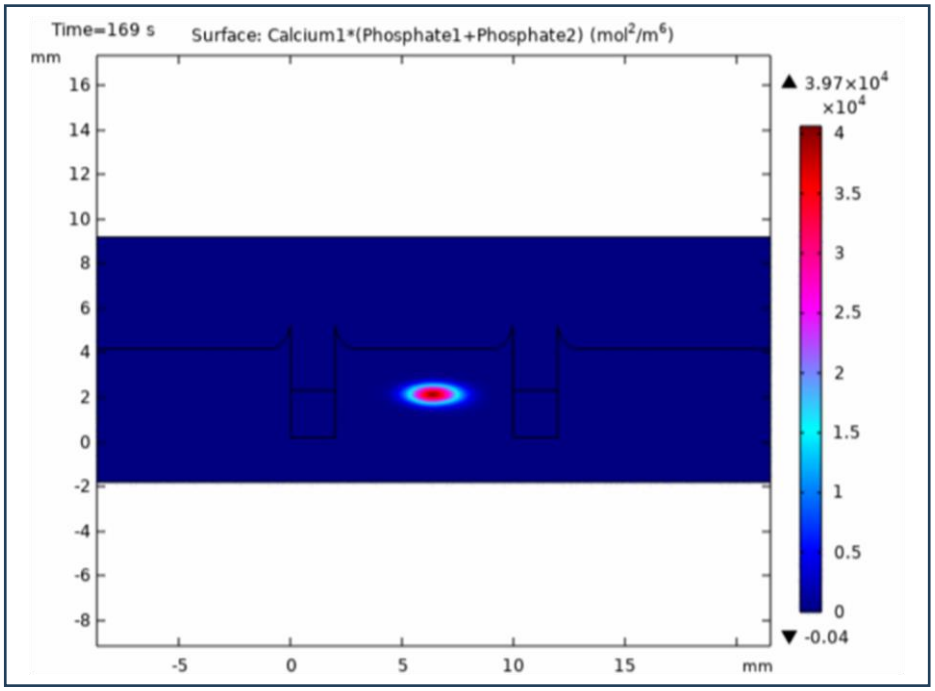


Figure 3.48. Animation of mixing product, m, for the PS-DW-AGE model at pH 8.0. The animated figure can be found in the supplementary materials.

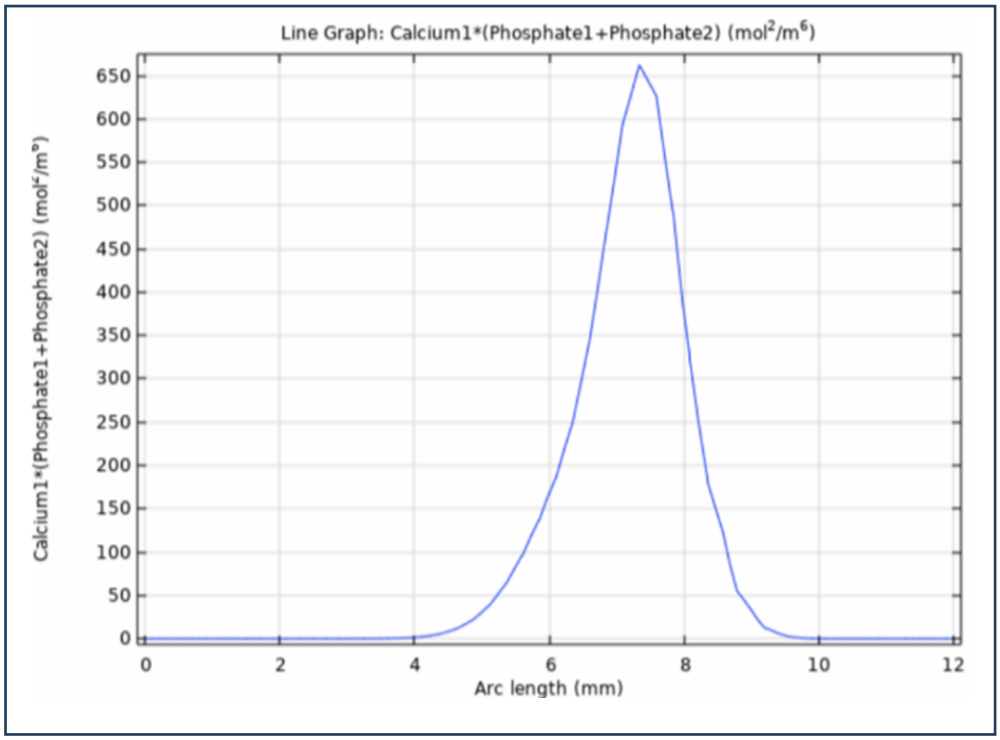


Figure 3.49. Line graph animation of mixing product, m, for the *PS-DW-AGE* model at pH 7.4. The animated figure can be found in the supplementary materials.

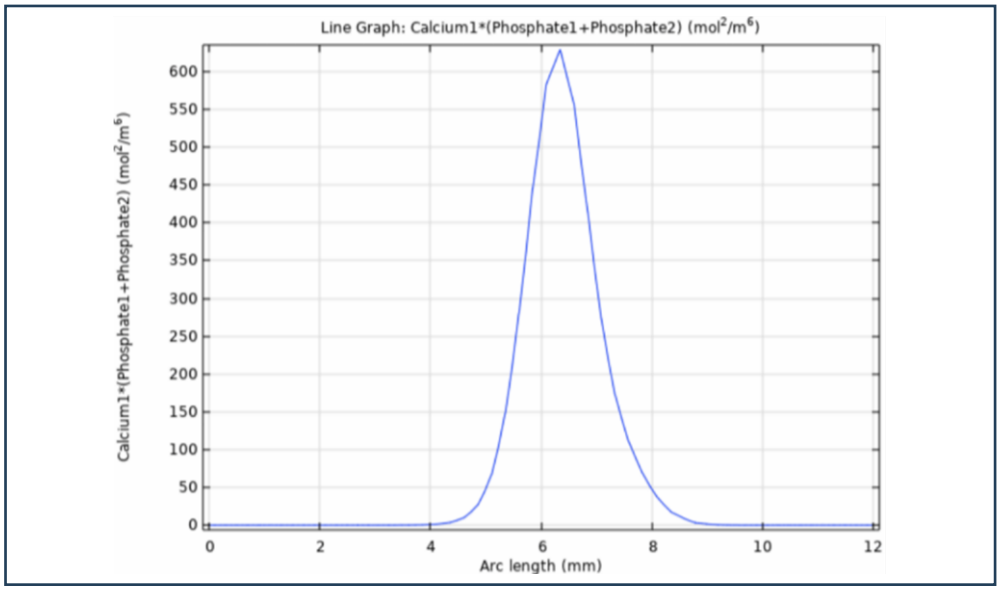


Figure 3.50. Line graph animation of mixing product, m, for the *PS-DW-AGE* model at pH 8.0. The animated figure can be found in the supplementary materials.

3.4.2.3 PS-CAGE Ion Transport

A model was created for ion transport in the PS-CAGE model at pH 8.0. A colour map and line graph animation of Ca^{2+} ion transport are shown in Figure 3.51 and Figure 3.52 respectively.

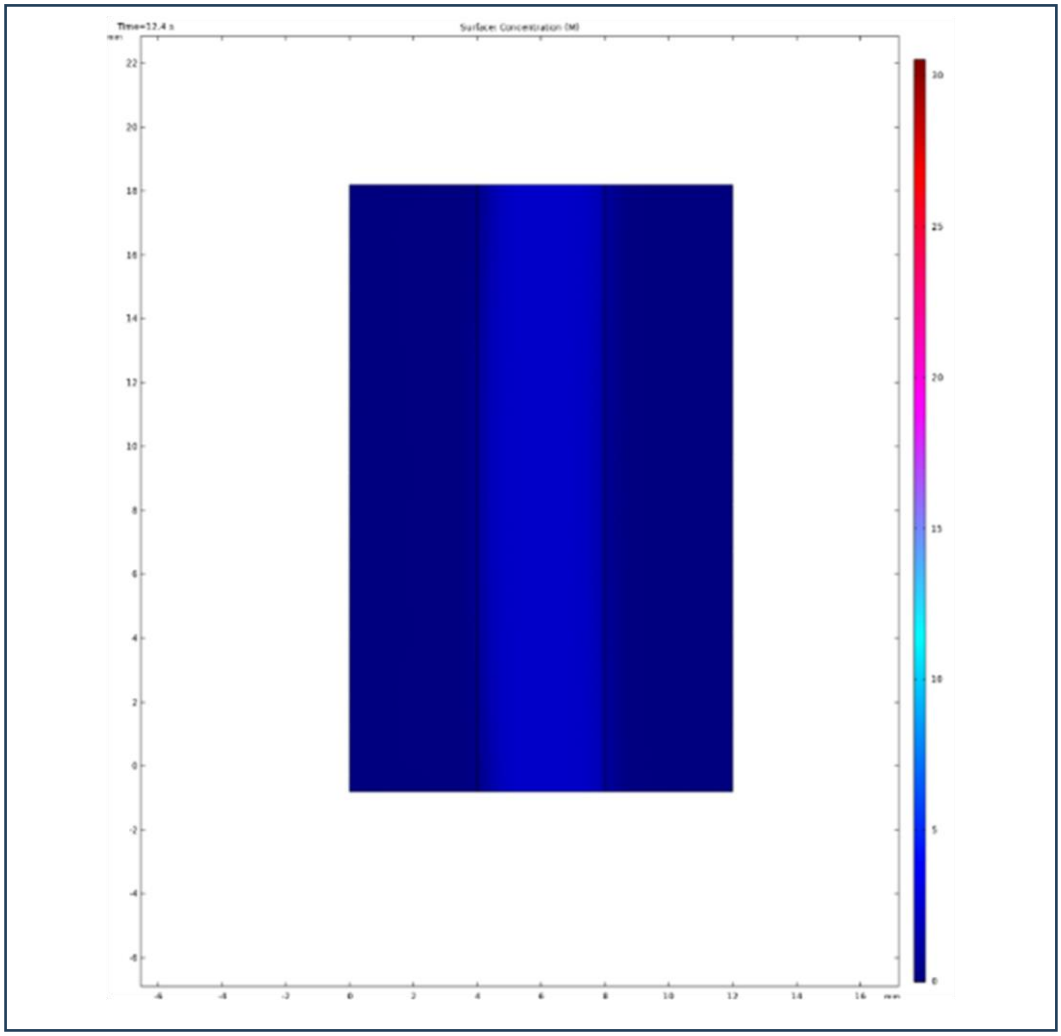


Figure 3.51. Animation of Ca2+ ion transport in the PS-CAGE model. The animated figure can be found in the supplementary materials.

The colour map shows how Ca^{2+} ions are ejected from the $CaCl_2$ loading gel in a uniform manner, changing from the initial cuboid to a slightly parabolic shape as the ion band travels through the recipient gel. The line graph animation illustrates how the rolling peak concentration of the Ca^{2+} band remains close to 2 M whilst moving through the gels. The width of the rolling peak extends slightly with time.

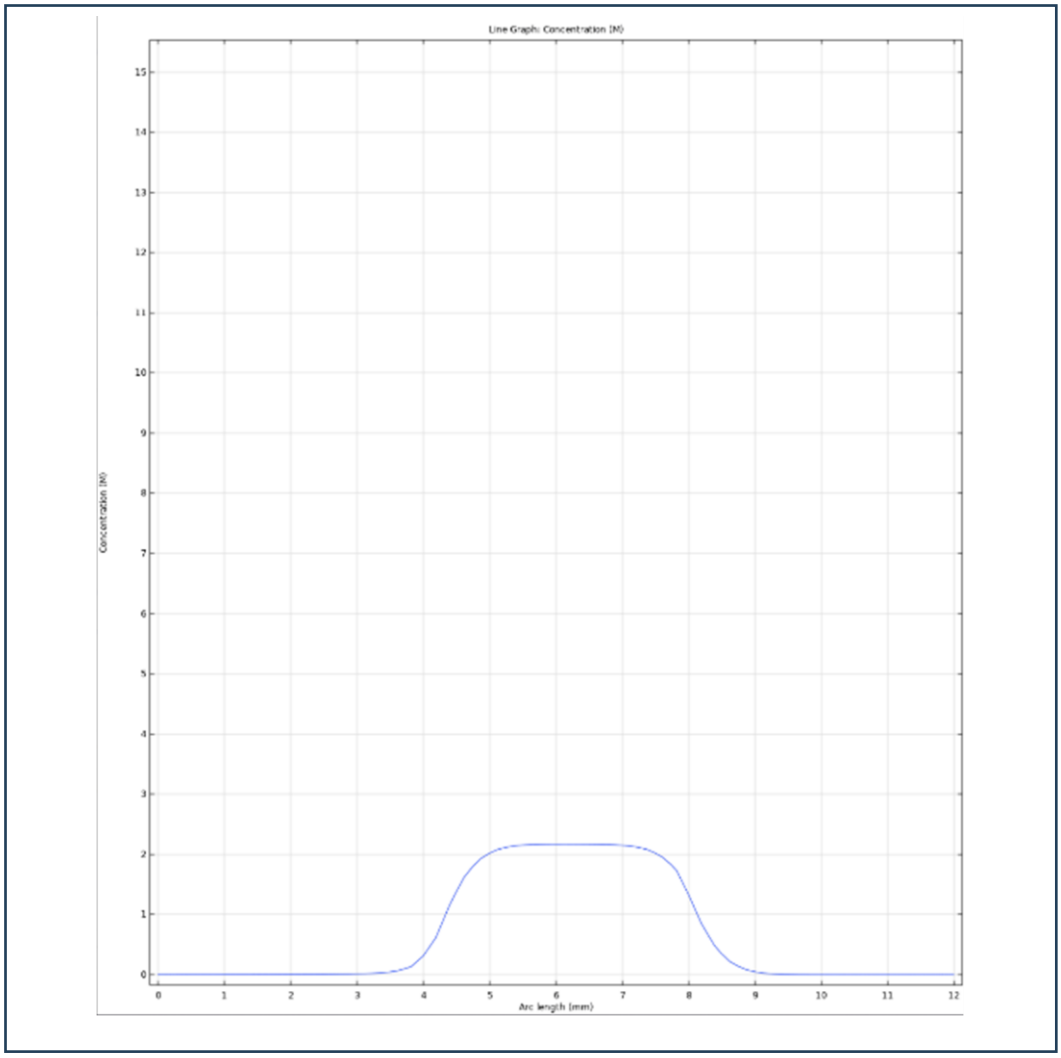


Figure 3.52. Line graph animation of Ca^{2+} ion transport in the PS-CAGE model. The animated figure can be found in the supplementary materials.

Colour map and line graph animations for the transport of HPO_4^{2-} + $H_2PO_4^-$ ions are shown in Figure 3.53 and Figure 3.54 respectively. As with the PS-DW-AGE model at pH 8.0, there is no clear separation of the ion band since most $H_xPO_4^{x-3}$ ions are HPO_4^{2-}. The initial 12 mM concentration of $H_xPO_4^{x-3}$ is therefore well maintained through the ion band's transport through the recipient gel.

As shown in Figure 3.55 (colour map) and Figure 3.56 (line graph), the mixing product for the PS-CAGE model peaks at a value of approximately 24,000 at 6.5 mm, which occurs at around 15-seconds. The much faster transport of ions in this model can be explained by the substantially greater electric field strengths in the cylindrical model compared to the single- and PS-DW-AGE models. The far greater mixing product in the PS-CAGE model results primarily from the uniform transport of all ion species through the recipient gel.

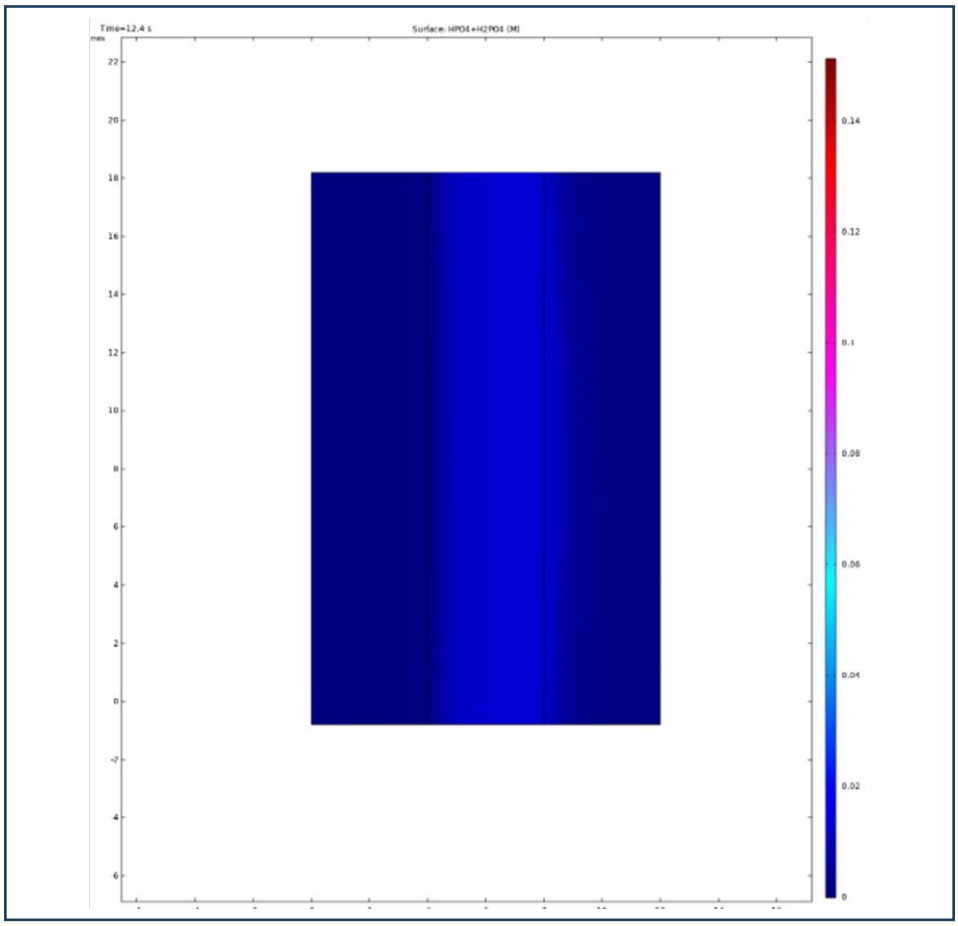


Figure 3.53. Animation of HPO_4^{2-} + $H_2PO_4^-$ ion transport in the PS-CAGE model. The animated figure can be found in the supplementary materials.

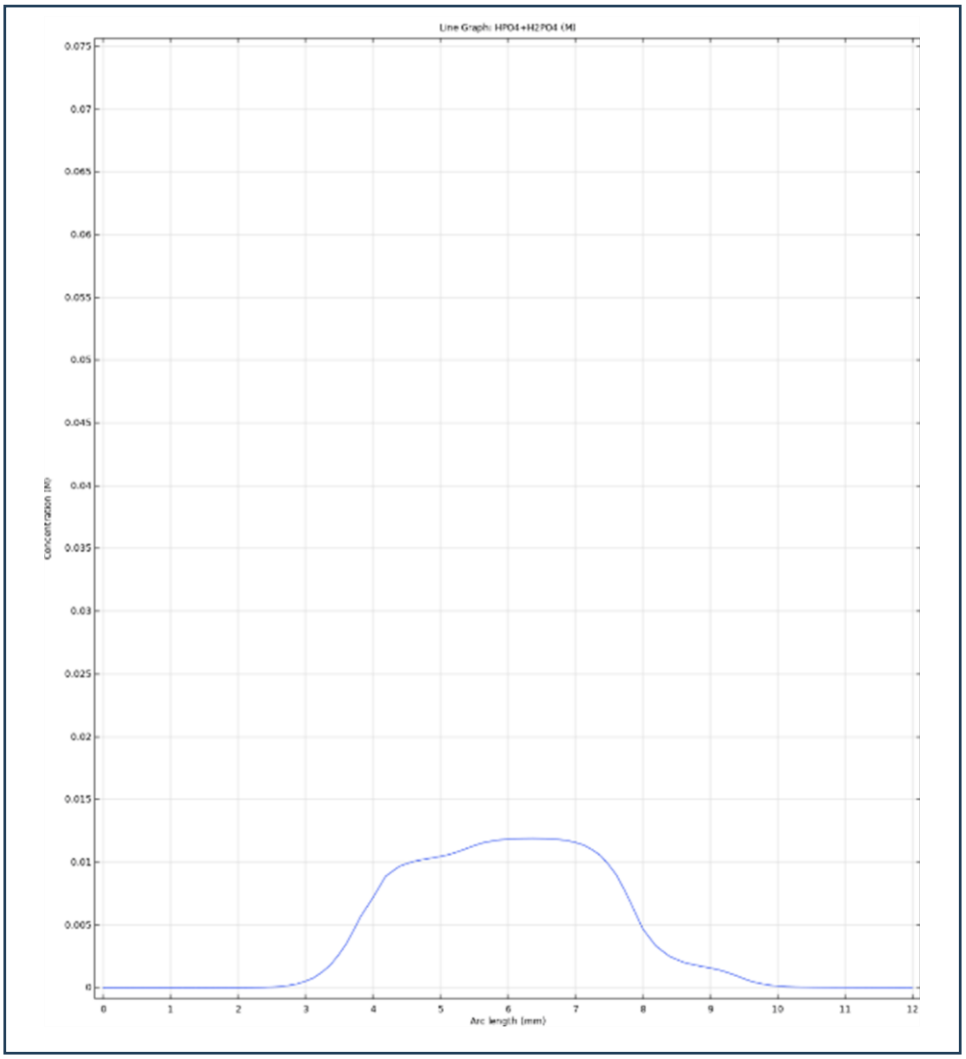


Figure 3.54. Line graph animation of HPO_4^{2-} + $H_2PO_4^-$ ion transport in the PS-CAGE model. The animated figure can be found in the supplementary materials.

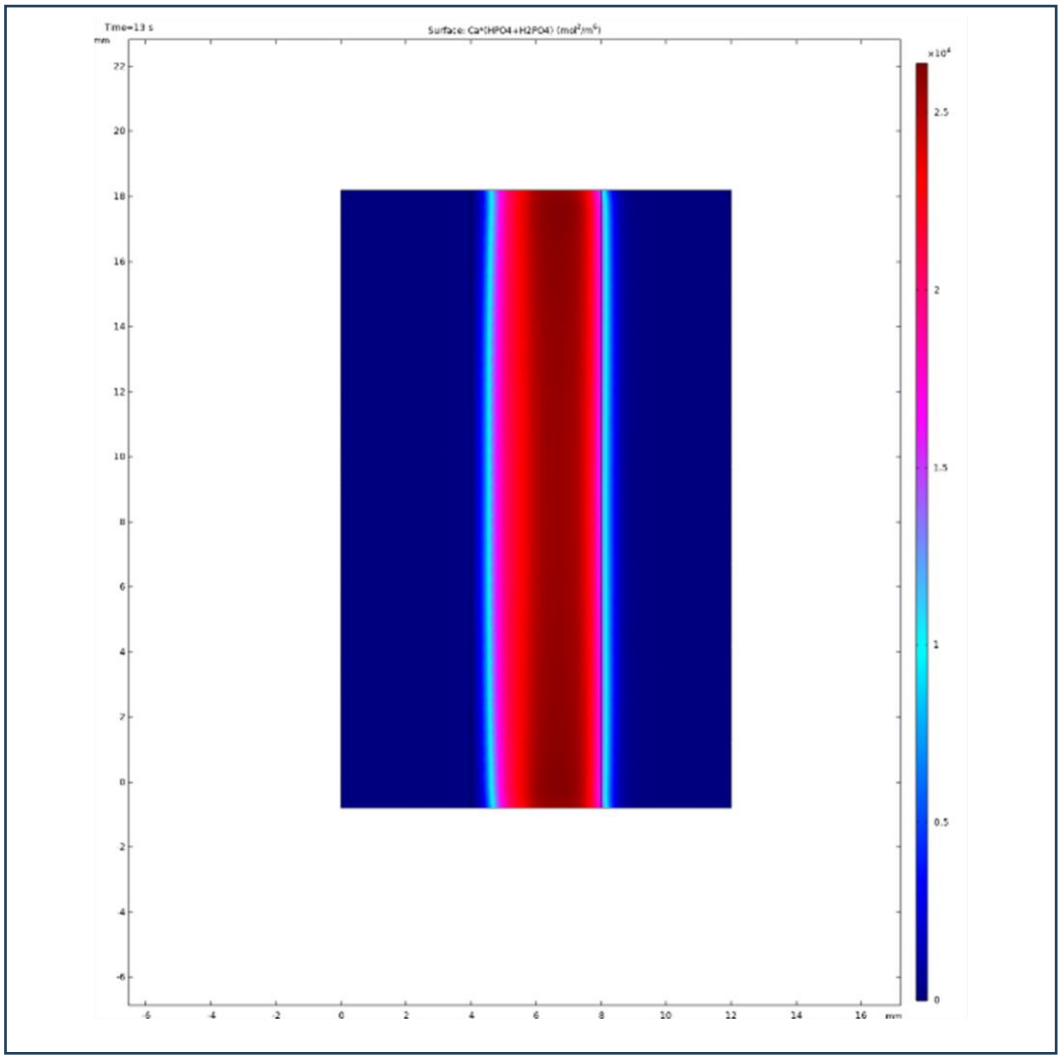


Figure 3.55. Animation of the mixing product in the PS-CAGE model. The animated figure can be found in the supplementary materials.

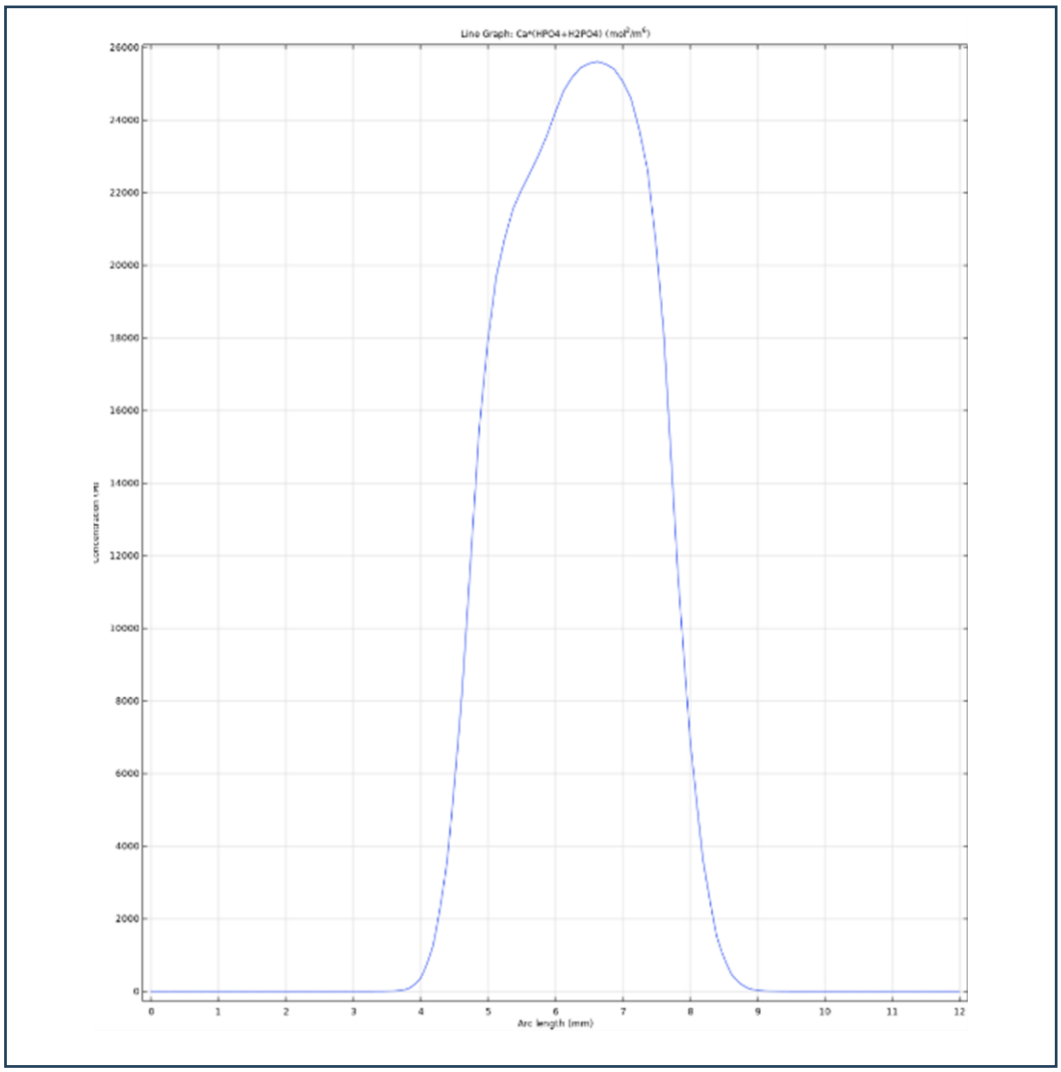


Figure 3.56. Line graph animation of the mixing product in the PS-CAGE model. The animated figure can be found in the supplementary materials.

3.4.3 Apparatus testing

3.4.3.1 PS-DW-AGE System

A 1 wt % agarose gel slab was prepared using the newly manufactured gel tray and a 2 mm thick comb riser for testing of the gel punch and cutting mask. Whilst in the electrophoresis tank and submerged in d.H_2O, the mask was positioned across a pair of well rows to guide the gel punch. Extraction of gel cuboids using the gel punch proved intermittently successful, as some gels remained in the gel slab and some were withdrawn into the gel punch shaft as intended. Nevertheless, the sliced gels that remain in the gel slab could be removed using tweezers with no visible damage to the gel cuboid. Six cuboidal gels removed from the gel slab were measured using a digital micrometer; these are shown in Figure 3.57. The excised cuboidal gels presented no visible tears and had average dimensions of 6 mm x 5 mm x 5 mm (average volume of 140 µL).

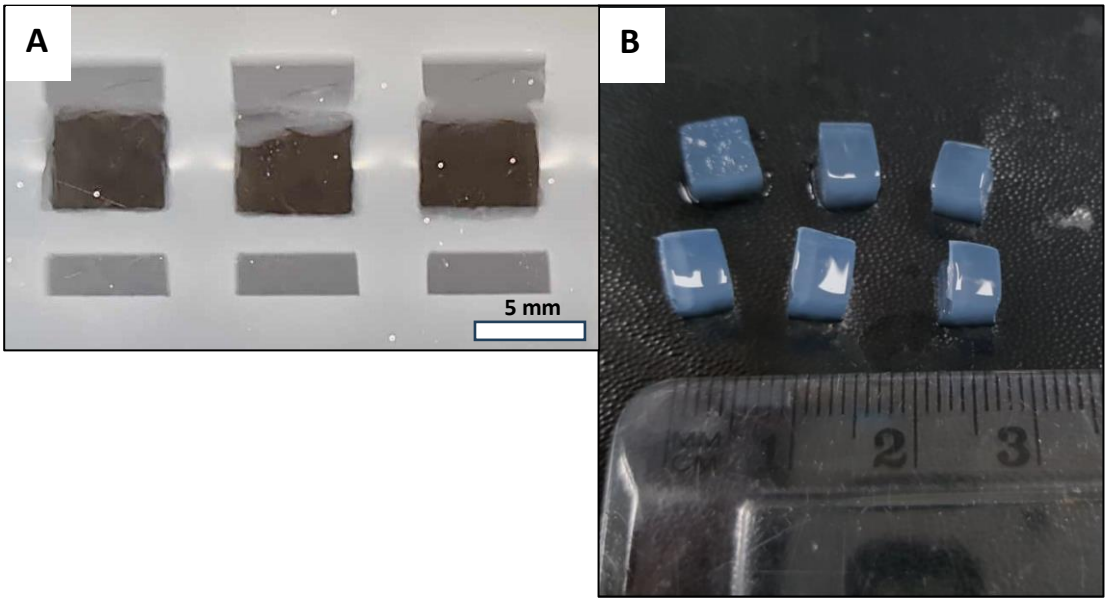


Figure 3.57. Gel slices cut by the gel punch. (A) Sliced holes from the gel slab; (B) excised gels.

A precipitation test was performed in the same gel slab. Figure 3.58 shows the precipitate layers produced after 600-seconds of a 180 V applied potential using well pairs loaded with either 2 M $CaCl_2$ or 1.8 M $MgCl_2$ in one well, and 12 mM Na_2HPO_4 in the opposite well. Figure 3.58 (A) and (B) show CaP and MgP particle layers formed in an uncoated 1 wt % agarose gel respectively whilst Figure 3.58 (C) and (D) show CaP and MgP particle layers formed in PDA-coated 1 wt % agarose gel respectively.

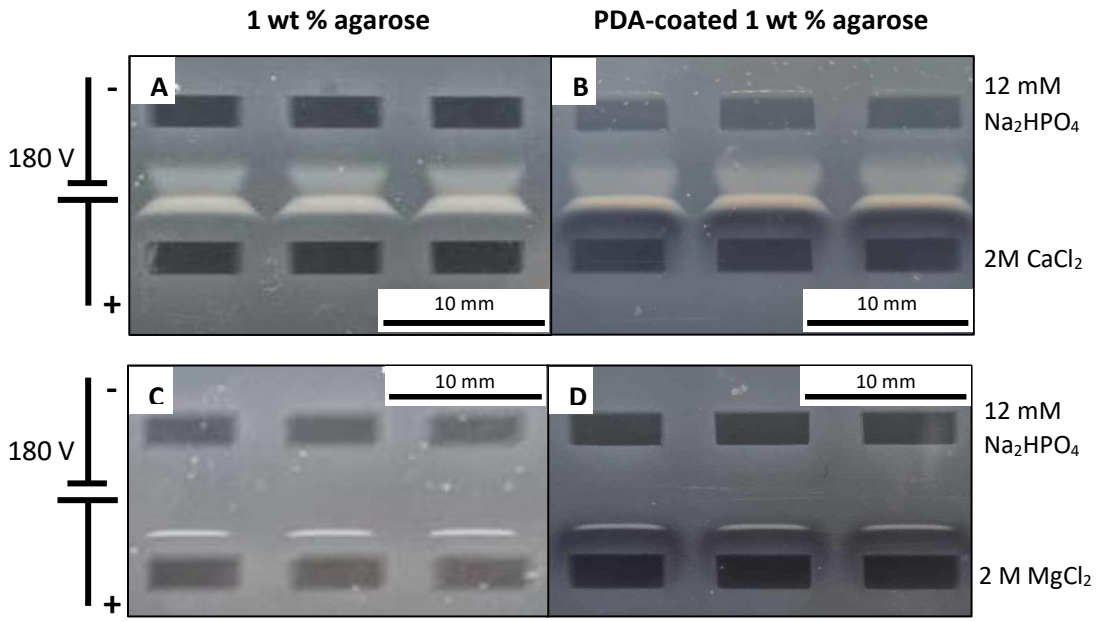


Figure 3.58. CaP particle layers produced in agarose gel slabs using the PS-DW-AGE system. (A) CaP layers produced in a 1 wt % agarose gel at 180 V; (B) CaP layers produced in a PDA-coated 1 wt % agarose gel at 180 V; (C) MgP layers produced in a 1 wt % agarose gel at 180 V; (D) MgP layers produced in a PDA-coated 1 wt % agarose gel at 180 V.

There is a stark contrast between these precipitate layers in terms of thickness, location, and general appearance. For the uncoated gel, a single layer was formed from $MgCl_2$ loadings which measured only 0.51 ± 0.04 mm (n = 6) in thickness and precipitated 1.90 ± 0.15 mm (n = 6) from the $MgCl_2$ well edge, whilst two layers were formed from $CaCl_2$; both of which were significantly thicker than that formed by $MgCl_2$. The primary layer – the faintest and closest layer to the Na_2HPO_4 well – measured 2.24 ± 0.21 mm (n = 6), whilst the secondary layer closer to the $CaCl_2$ well measured 1.03 ± 0.02 mm (n = 6) thick. The leading edge of the primary layer was measured to be 5.80 ± 0.07 mm (n = 6) from the $CaCl_2$ well. There was also a stark difference between their precipitation times. The primary layer formed by $CaCl_2$ became visible by 30-seconds, whilst the layer formed by $MgCl_2$ appeared after approximately 215-seconds.

Overall, the CaP layers between the uncoated and PDA-coated gels are broadly very similar in shape. There is however a dark mass below the primary precipitate layer which could be unbound positively charged PDA fragments moving alongside Ca^{2+} ions that increase in concentration at areas with relatively steep electric field gradients or blockages due to particles. For the PDA-coated gel, the primary CaP layer thickness measured 2.08 ± 0.10 mm (n = 6) and the secondary CaP layer thickness measured 1.35 ± 0.08 mm (n = 6) thick, with the primary CaP layer leading edge measuring 5.38 ± 0.18 mm (n = 6) from the $CaCl_2$ well, The layers formed by 1.8 M $MgCl_2$ and 12 mM Na_2HPO_4 well pairs in the PDA-coated gel appear similar to those

produced in the uncoated agarose gel. The MgP precipitate layer thickness in the PDA-coated gel was measured as 0.42 ± 0.02 mm (n = 6) and the precipitate leading edge was measured to be a distance of 1.96 ± 0.03 mm (n = 6) from the $MgCl_2$ well. The leading edge of the MgP layer was measured to be 1.98 ± 0.04 mm (n = 6) from the $MgCl_2$ well.

3.4.3.2 PS-CAGE System

The gel cast sandwich precipitation test was first conducted, which utilised 4 mm thick $CaCl_2$ (2 M) and Na_2HPO_4 (12 mM) gel cylinders sandwiched around a 4 mm thick recipient gel. After 180 V had been applied for 600-seconds, the sandwich was disassembled, and four recipient gel cylinders were removed and submerged in water for imaging; a selection of these are shown in Figure 3.59 showing recipient gels with CaP layers.

From a plan view, the CaP layer appears to be uniform in intensity but from the side view the layer appears thickest at the centre compared to at the edges. The layer within the gel in Figure 3.59 (B) is measured 1.57 mm in thickness at the centre, reducing to 0.9 mm at the outermost edge. The layers formed approximately 2.9 mm from the $CaCl_2$ loading gel surface (from the CaP layer centre). Figure 3.59 (C) shows the cylinders collect a scattered white coating on their circumferential surface; possibly resulting from Ca^{2+} and $H_xPO_4^{x-3}$ ions escaping around the edge of the cylinder and precipitating on this outer limit.

A cylinder kept in place within the cast was cut into four smaller cylinders using the cutting mask. Measurements of the four smaller gel cylinders showed a mean diameter of 5.71 ± 0.16 mm (n = 4). Taking layer thickness across the centre of small cylinders, layer thickness measured 1.20 ± 0.29 mm (n = 4). Care was taken to keep the small cylinders in their original orientation so that layer thickness relative to distance from the large cylinder centre could be measured.

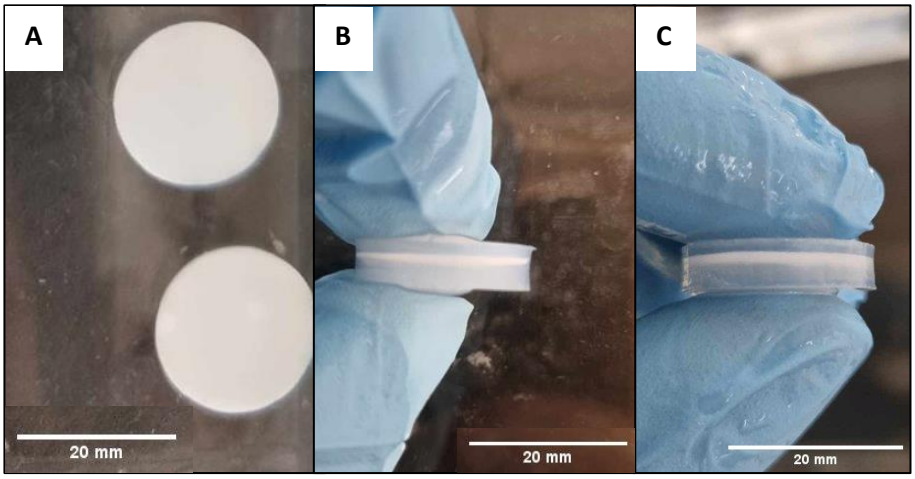


Figure 3.59. Recipient gel cylinders with CaP layers. (Left) shows the plan view of the recipient gel cylinder displaying the cylinder face that was positioned adjacent to the Na_2HPO_4 loading gel. (Middle and right) side view of two separate gel cylinders encapsulating a CaP layer.



Figure 3.60. CaP layers within smaller cylinders.

PDA-coated gel cylinders presented CaP layers that were more difficult to measure with regard to their thickness simply due to poor contrast between the precipitate layer and the surrounding gel. Despite that, the precipitate layer in Figure 3.61 (B) was measured to be approximately 1.6 mm thick – similar to that of the uncoated cylinders in Figure 3.60 – and measured approximately 2.6 mm from the $CaCl_2$ loading gel surface. One must acknowledge, however, that CaP precipitation on the circumferential surface of the cylinder may appear to increase the thickness of the precipitate layer. It appears to precipitation occurs preferentially toward one half of the cylinder, would could indicate that CaP particles precipitating at the edge of cylinders are being electrophoretically transported along the cylinders side.

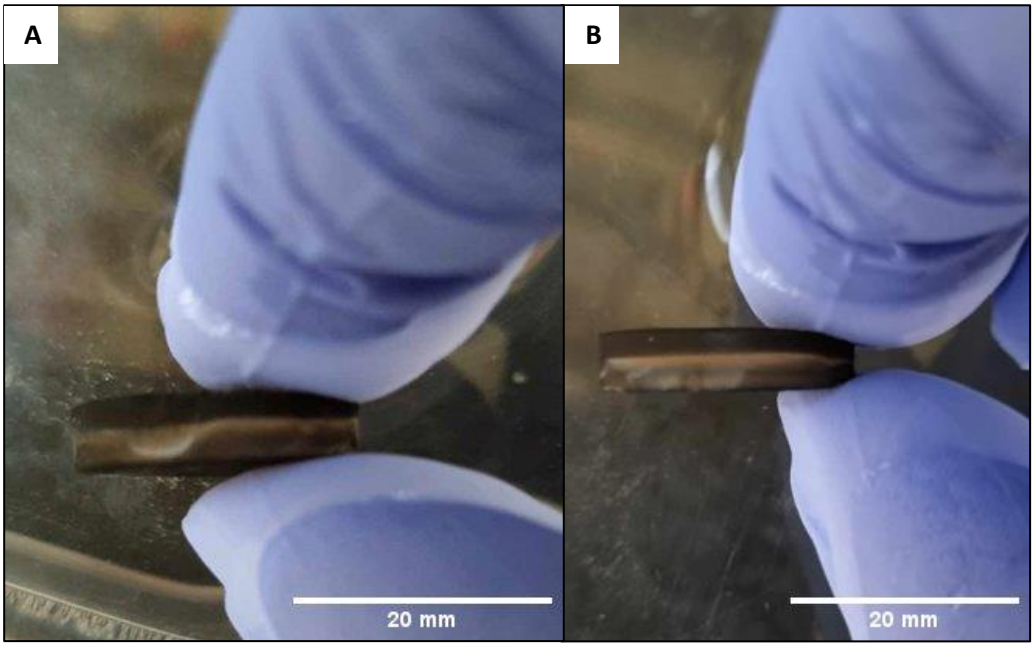


Figure 3.61. PDA-coated recipient gel cylinders with CaP layers.

Figure 3.62 shows a small PDA-coated cylinder after extraction with a precipitate layer measuring between 0.6 – 0.8 mm thick. However, poor contrast prevents a mean thickness from being calculated for these smaller cylinders.

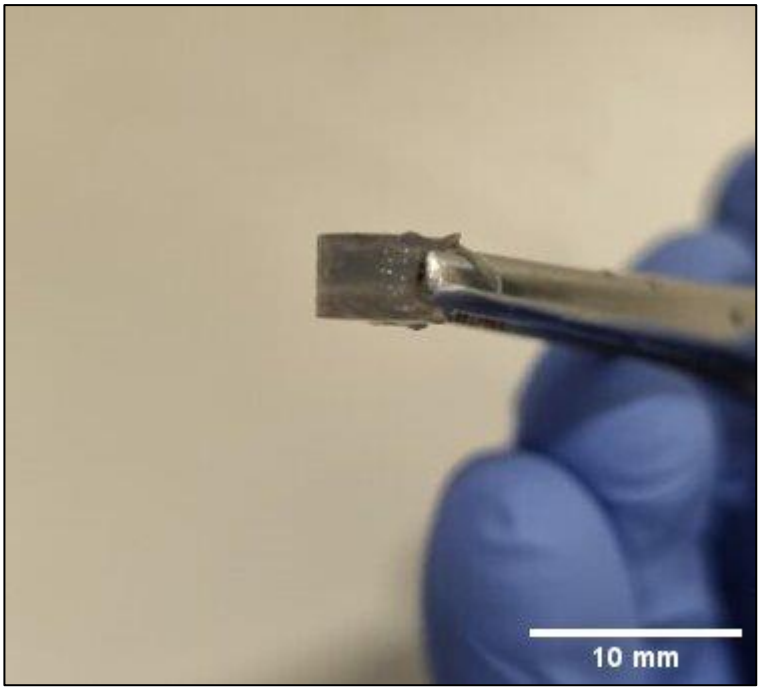


Figure 3.62. A CaP layer within a small PDA-coated cylinder.

Figure 3.63 displays a selection of small PDA-coated cylinders. These gels measured 6.09 ± 0.12 mm (n = 12) in diameter.

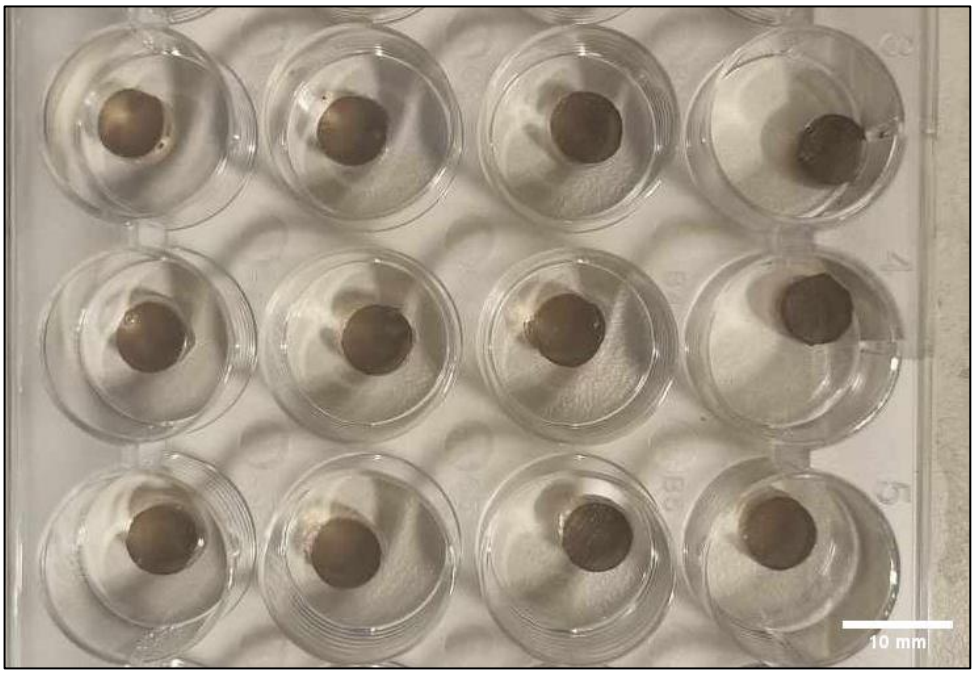


Figure 3.63. A selection of small PDA-coated cylinders.

Next was the adjacent loading tests, whereby the gel cylinder cast sandwich did not include a central recipient gel. Instead, gel pairs consisted either of 2 M $CaCl_2$ gel cylinders and uncoated 12 mM Na_2HPO_4 gel cylinders, or 2 M $CaCl_2$ gel cylinders and PDA-coated 12 mM Na_2HPO_4 gel cylinders. After a 180 V potential was applied for 600-seconds, gel cylinders were removed and imaged when submerged in buffer.

Figure 3.64 shows the faces of the loading gels that were adjacent to each other when the potential was applied. The $CaCl_2$ gel retained its pre-test appearance, but the Na_2HPO_4 gel – which was identical in colour to that of the $CaCl_2$ gel – turned completely white from this viewpoint. There are only trace amounts of white along the circumference of the $CaCl_2$ gel.

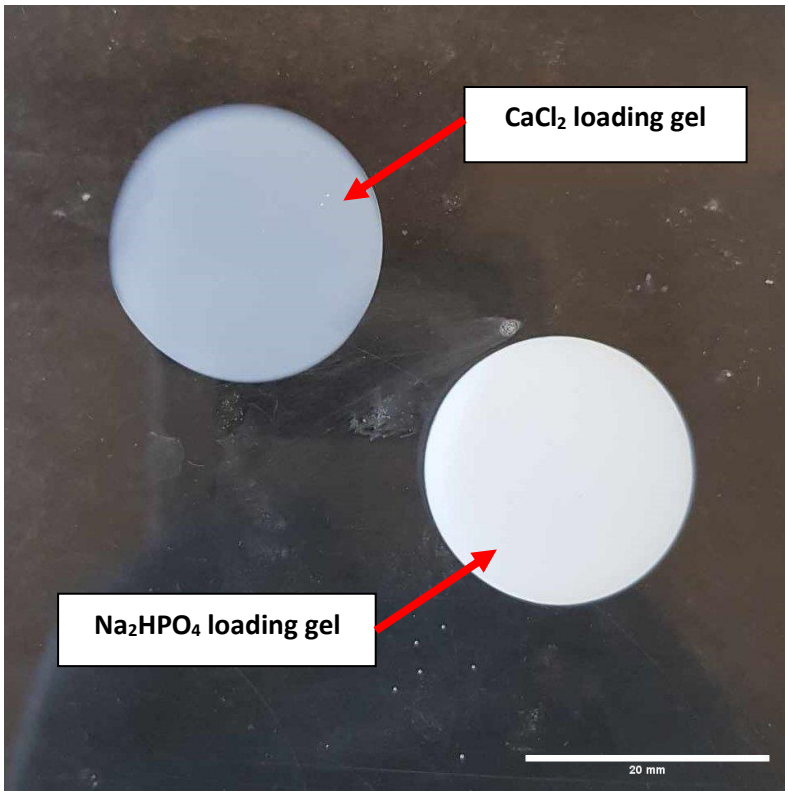


Figure 3.64. CaCl2 and Na2HPO4 loading gels following adjacent loading.

A side-view of the Na_2HPO_4 gel is shown in Figure 3.65. A CaP layer measuring 2.4 ± 0.02 mm (n = 6) in thickness at the centre is present within the gel. This layer starts immediately adjacent to the cylinder surface that was pressed against the face of the $CaCl_2$ loading gel. Layer thickness decreases to approximately 1.6 mm immediately adjacent to the circumferential edge of the gel cylinder which gives the CaP layer a doming shape. A typical example of a small cylinder cut from

the larger gel cylinder is also shown in Figure 3.65. The CaP layer for smaller cylinders was measured to be 2.04 ± 0.05 mm (n = 6).

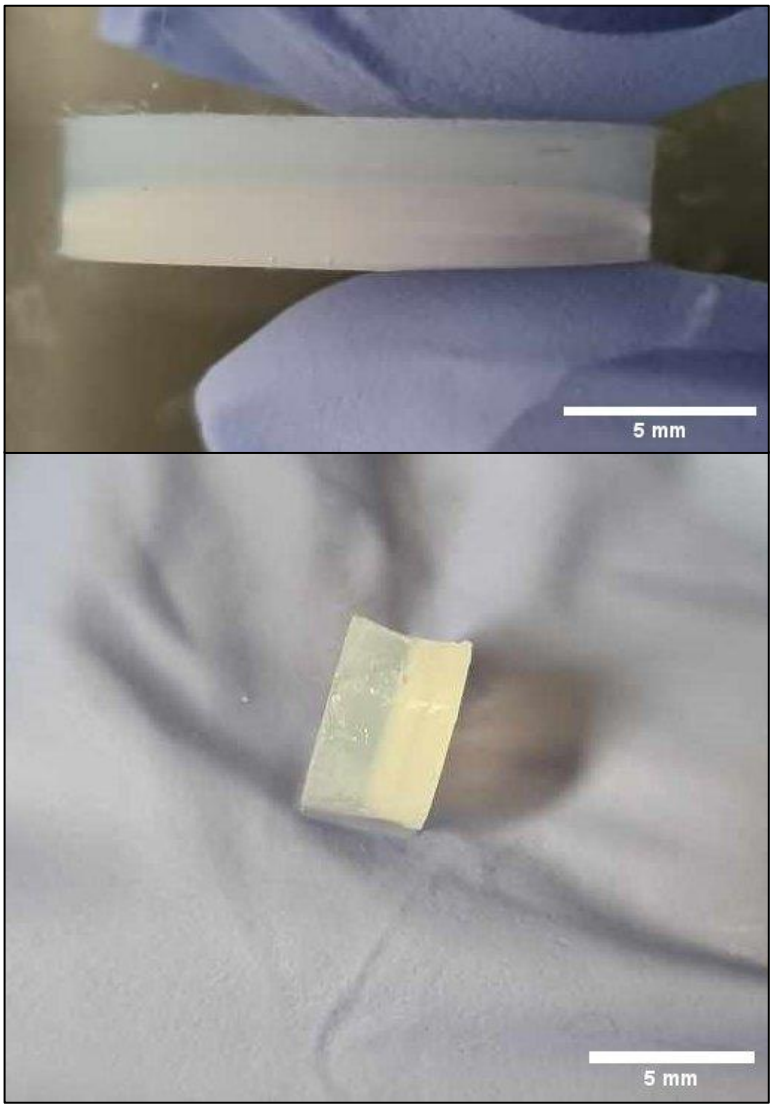


Figure 3.65. *(Top)* Side-view of an Na_2HPO_4 loading gel encapsulating a CaP layer. (Bottom) a smaller gel cylinder cut from the loading gel, encapsulating a CaP layer.

Precipitation of CaP using the adjacent loading format was also tested using PDA-coated gel cylinders prepared with 12 mM Na_2HPO_4 pressed against a 2 M $CaCl_2$ gel cylinder cast. After a 180 V potential was applied for 600-seconds, the PDA-coated gels were removed. Figure 3.66 shows a side-view of a PDA-coated Na_2HPO_4 gel that presents a CaP layer. Like the CaP layer in, Figure 3.65, the precipitate layer measures 2.38 ± 0.03 mm (n = 6) and has a domed shape with layer thickness reducing to approximately 1 mm adjacent to the circumferential edge of the cylinder. As in the uncoated gel cylinder, the CaP persists from the cylinder face pressed against

the $CaCl_2$ cylinder face. Interestingly, there is some brown discolouration around the leading edge of the CaP layer which contrasts with the much darker discolouration around the trailing edge of precipitates produced in the PDA-coated gel slab in Figure 3.58 (C). Smaller gel cylinders (not pictured) cut from these larger PDA-coated cylinders had precipitate layers measuring 1.98 ± 0.09 mm (n = 6), which is comparable to that of layers in uncoated small cylinders. Note that measurements of CaP layer thickness in PDA-coated gel cylinders extend from the gel face to farthest edge of the brown discolouration, as the brown area is assumed to comprise of CaP.



Figure 3.66. PDA-coated CaCl2 loading gel with a CaP layer produced during adjacent loading.

3.4.3.3 Temperature/pH Control Unit

The ability of the temperature/pH control unit to maintain a consistent buffer temperature and pH during electrophoresis was investigated. The first control test utilised a cast sandwich comprising of 2 M $CaCl_2$ gels, recipient gels, and 12 mM Na_2HPO_4 gels, each formulated using 1 wt % and cast to a 4 mm thickness. Initial temperatures were taken at the anode, cathode, and middle, whilst pH was assumed to remain unchanged from the initial pH 8.0 of the buffer.

A control test was first performed to obtain temperature and pH changes in the absence of temperature/pH control. After a 180 V potential was applied for 600-seconds, temperature and pH measurements were immediately taken. Temperature at the tank middle increased from 19.1 °C to 27.1 °C; a total increase of 8 °C (Figure 3.67). pH measurements at the anode, cathode, and tank middle were 8.02, 7.93, and 7.84 respectively (Figure 3.68). Thus, a pH gradient forms with a magnitude of 0.18 between the electrodes.

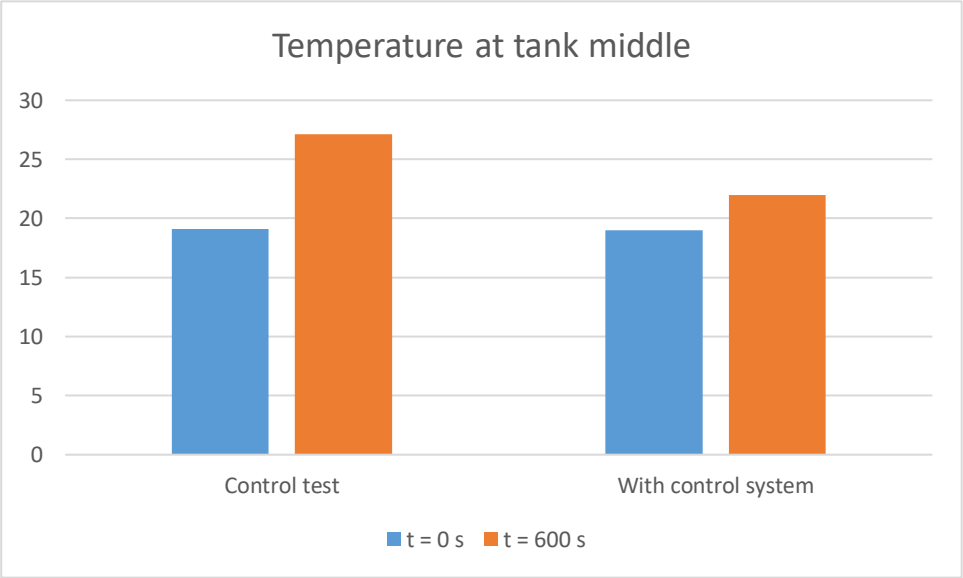


Figure 3.67. Temperature measurements at the tank middle, adjacent to gel cylinders.

The same conditions were used for the experimental test, but with the use of the temperature/pH control unit. An initial buffer temperature of 19.0 °C was recorded prior to applying a potential so a target temperature (T_T) of 19.0 °C was programmed into the Arduino. A 180 V potential was applied across the tank followed by immediate activation of the temperature/pH control unit.

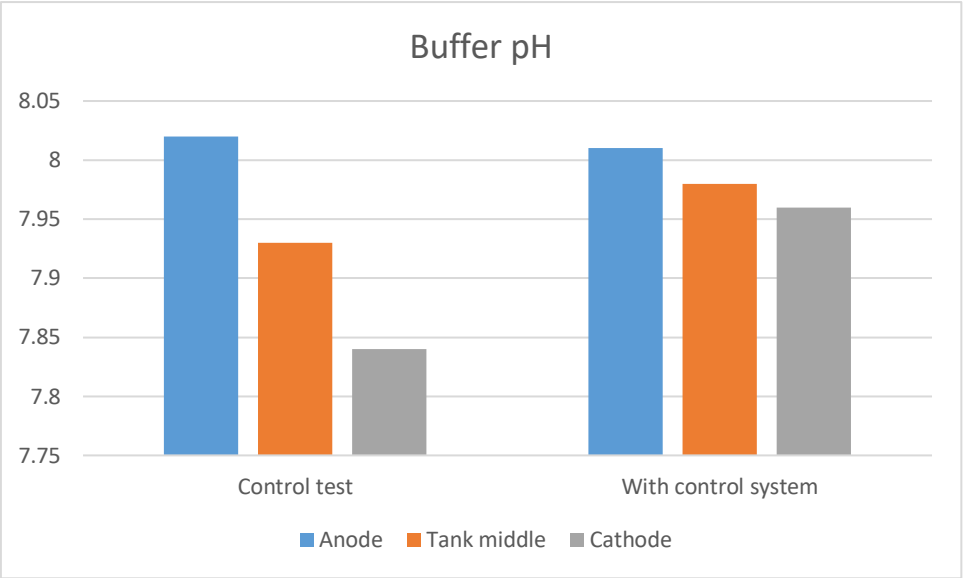


Figure 3.68. pH measurements at the anode, tank middle, and cathode.

After 600-seconds, temperature at the tank middle measured 22 °C; an increase of 3 °C from the initial temperature. pH measured at the anode, cathode, and tank middle, had values of 8.01, 7.99, and 7.98 respectively, resulting in a pH gradient of 0.03 between the electrodes. Therefore, the temperature/pH control unit reduced the temperature increase from 8 °C to 3°C at the tank middle, and reduce the magnitude of the pH gradient between the electrodes from 0.18 to 0.03.

3.4.3.4 Current test

Current was measured through the electrophoresis tank to determine the influence of salts present in gel cylinders on conductivity, which may indicate the consumption of $H_xPO_4^{x-3}$ ions (and a small fraction of Ca^{2+} ions) in precipitation reactions. A control test was first performed using a cylindrical gel cast sandwich containing no loading salts. Current through the tank was measured during the test by recording the current displayed on the electrophoresis power pack for the 600-second duration. Current (mA) is plotted against time (s) in Figure 3.69. Note that current was recorded when its value changed, rather than at timed intervals.

With no salts in the gel cylinders, current increased from 113 mA to 119 mA over 600-seconds; a near-linear regression with a gradient of 0.011 mAs^{-1} (R^2 = 0.98). This modest (~5 %) increase in current is to be expected given that temperature and pH changes will modify the resistivity of the buffer and gel over time.

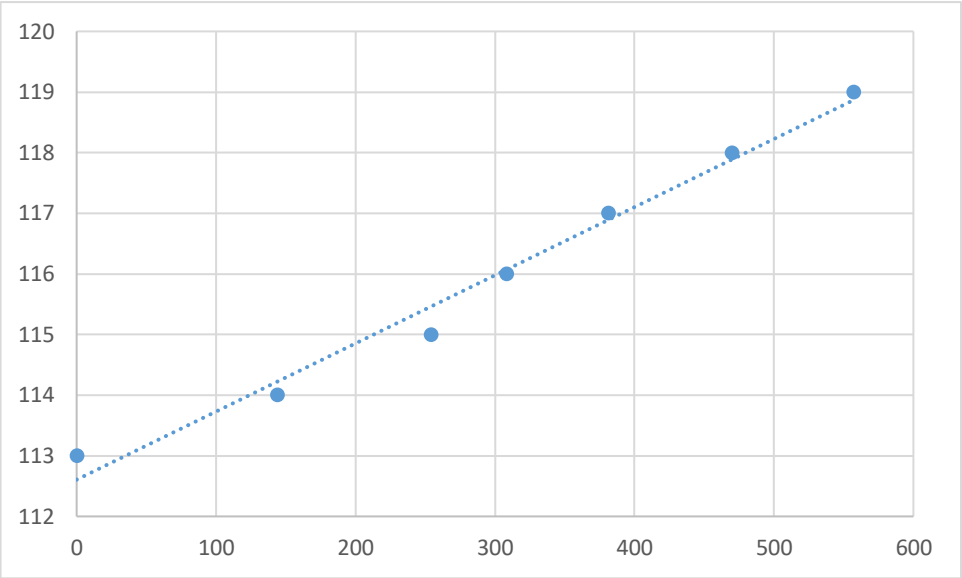


Figure 3.69. Current measured through the electrophoresis tank for the control test.

For the experimental test, a 2 M $CaCl_2$, recipient gel, and 12 mM Na_2PO_4 gel cast were used to form a gel cast sandwich. The current measured through the tank in the presence of salts increased from 175 mA to 206 mA over 600-seconds, as shown in Figure 3.70. The larger initial current is thought to result from the transport of charge-carrying salt ions that occupy the central cross-section of the electrophoresis tank.

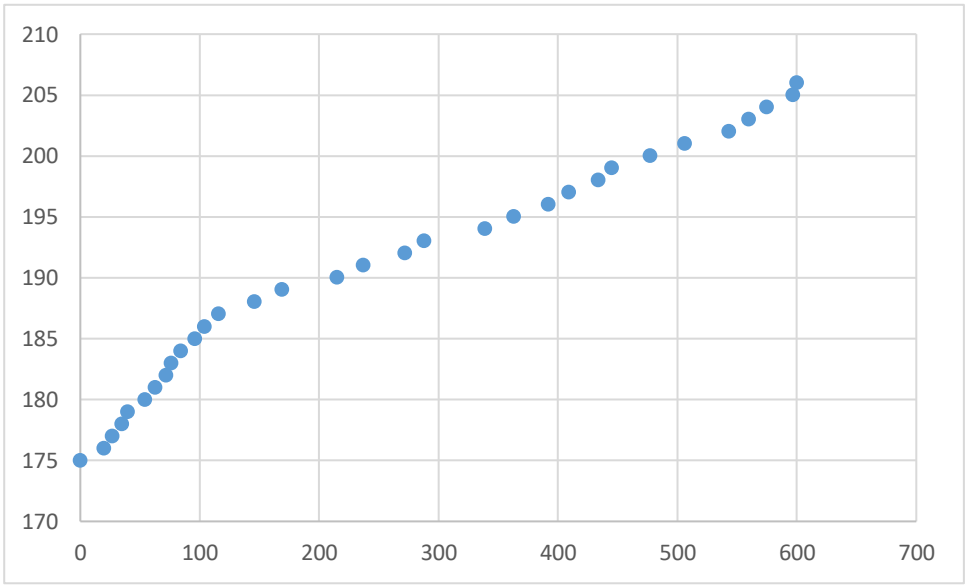


Figure 3.70. Current measured through the electrophoresis tank for the experimental test.

Interestingly for the experimental test, the first 100-seconds demonstrate a near-linear increase in current, with a gradient of 0.11 mAs^{-1} (R^2 = 0.99), which decreases to 0.038 mAs^{-1} (R^2 = 0.99) (linear regressions not shown) between 100- to 600-seconds. It is theorised that the presence of these two trends indicate a rapid increase in resistivity of the gels due to the consumption of charge-carrying ions in precipitation reactions. By extension, this implies that most precipitation of CaP occurs by 100-seconds (for a 180V applied potential).

3.5 Discussion

New PS-DW-AGE and PS-CAGE systems have been designed and fabricated in the pursuit of improving the transfection efficacy and pre-clinical relevancy of cryogels synthesised via the PS-SW-AGE approach for osteochondral tissue regeneration. The PS-DW-AGE system – in conjunction with the temperature/pH control unit - will be used to modulate experimental parameters such as salt type and concentration, agarose concentration and brand, applied potential, and buffer temperature, and determine the relationship of these parameters with pDNA/CaP and pDNA/MgP particle diameters. An 'ideal subset' of these experimental parameters can then be selected for the synthesis of sub-100 nm pDNA/CaP and pDNA/MgP particles in the PS-CAGE system.

The PS-CAGE system has been designed and fabricated with the intention of synthesising uniform, cylindrical particle layers (using the ideal subset of parameters) within a large gel that can be cut to form smaller gel cylinders with a clinically relevant size and shape.

Finally, a temperature/pH control unit has been designed and fabricated for use with both the PS-DW-AGE and PS-CAGE systems to provide a means of controlling the buffer temperature and pH to mitigate temperature and pH changes within the tank and gel. The use of the temperature/pH control unit should theoretically provide superior control over nucleation and growth of particles due to the enhanced control over temperature and pH, supersaturation is dependent on both of these conditions.

3.5.1 Computational modelling

Computational modelling was used to investigate various theorised advantages of the PS-DW-AGE and PS-CAGE systems compared to the PS-SW-AGE system. For the PS-DW-AGE system, this included more uniform electric field profile at the zone of precipitation and more uniform ion mixing than the PS-SW-AGE system. For the PS-CAGE system, advantages included a bell-curve-like transport of narrow ion bands and uniform ion mixing over a large cross-sectional area compared to both the PS-SW-AGE and PS-DW-AGE systems.

Firstly, electrostatics models demonstrated the reduced variation in electric field strength at the zone of precipitation for the PS-DW-AGE model. At the zone of precipitation (between 4 – 8 mm), electric field strength varied by less than 100 Vm^{-1} in the PS-DW-Age model, whilst for the PS-SW-AGE model this varied by over 200 Vm^{-1} between 6 – 8 mm (precipitation zone adjacent

to the well). The variation in electric field strength was lowest in the PS-CAGE model, varying by less than 10 Vm^{-1} between 4 – 8 mm. Though these models are independent of time and reflect system states at t = 0 s, they demonstrate how significant changes to geometry can make electric field profiles more uniform.

Ca^{2+} and HPO_4^{2-} + $H_2PO_4^-$ ion transport models demonstrated the flow of ions around contrasting geometries. For the PS-SW-AGE, HPO_4^{2-} + $H_2PO_4^-$ ion concentrations varied only slightly at the zone of precipitation due to their continuous presence throughout the gel and buffer. This contrasts to Ca^{2+} ion transport in the PS-SW-AGE and PS-DW-AGE models where the Ca^{2+} band moved as an irregular ellipsoidal shape that stretched over time. A similar transport of HPO_4^{2-} + $H_2PO_4^-$ ions occurred in the PS-DW-AGE model, where pH-dependent $H_xPO_4^{x-3}$ speciation could be observed in the two PS-DW-AGE models at pH 7.4 and pH 8.0. The PS-CAGE model produced much more uniform transport of all ion species, with each ion moving as a discrete band with a slight bell-curve shape that diffused only slightly at leading and trailing edges.

Mixing product; used as an indicator for the rate at which Ca^{2+} and $H_xPO_4^{x-3}$ ions mix, varied significantly between models in magnitude and shape. For the PS-SW-AGE model, the mixing product peaked at over 90,000 immediately adjacent to the well and reflected the shape of the transported Ca^{2+} band. For the PS-DW-AGE model at pH 7.4, the mixing product resembled a uniform ellipsoidal shape which peaked at over 650 but did so in two steps due to the separation of HPO_4^{2-} and $H_2PO_4^-$ waves. For the PS-DW-AGE model at pH 8.0, the same uniform ellipsoidal shape can be seen but peaks at a lower value of 600. However, given the vast majority of $H_xPO_4^{x-3}$ species in this model are HPO_4^{2-}, the $H_xPO_4^{x-3}$ ions travel almost as a single wave and hence produce a much more uniform spike in mixing product. The mixing product for the PS-CAGE model peaks at over 26,000, spiking as a highly uniform ellipsoidal shape after a much shorter period (< 30-seconds) than in the PS-DW-AGE model (> 140 seconds).

Though this computational data does not use in-house measured relative permittivities for material domains, the common use of relevant relative permittivities across models allows models to be compared to a good extent. More uniform ion mixing within a steady electric field profile was demonstrated in the PS-DW-AGE model compared to the PS-DW-AGE model, but at a greatly reduced mixing rate due to the diffusion of ion bands with time. In the PS-CAGE model, the use of symmetrical cylindrical gel geometries and opting for loading gels rather than loading solutions resulting in highly uniform ion transport and mixing, as well as a highly stable electric field profile at the zone of precipitation.

3.5.2 Precipitation test

Precipitation tests were conducted using either 2 M $CaCl_2$ or 1.8 M $MgCl_2$ (+ 5 vol % glycerol), each paired with wells loaded with a 12 mM Na_2HPO_4 loading solution. These tests were performed to observe CaP layer size and shape development over time which may prove useful in developing pre-clinically relevant layer shape and thicknesses. Observations over the 600-second period showed the CaP layer initially formed a small band close to the Na_2HPO_4 well which increased in thickness throughout the test. Shortly after the formation of the primary band, a secondary curved band closer to the $CaCl_2$ well formed that appeared to wrap around the well. In contrast, the MgP layer forms only a single, thin layer with a similar proximity to the $MgCl_2$ well as the secondary CaP layer.

It is theorised that the formation of the first CaP layer arises from the initial mixing of Ca^{2+} and $H_xPO_4^{x-3}$ ions under electrophoresis. CaP particles within this primary layer are then electrophoretically transported through the agarose matrix toward the $CaCl_2$ well due to their negative zeta potential. In close proximity to the $CaCl_2$ well the particles reduce in velocity due to the reduced local electric field strength. Large particles reducing in velocity close to the $CaCl_2$ well collide with smaller particles which are travelling at a comparatively greater velocity. This increased collision frequency around the well causes blockages in the agarose matrix, thus preventing the transport of further incoming particles and slowly increasing the curved layer thickness and density, eventually making the layer visible. Electric field profiles will change in response to the presence of this secondary CaP layer and encourage particles to divert around (including above/below in the z-axis) the layer.

MgP layer precipitation occurs after a significantly longer period, over 6-times longer than the first CaP layer and appears much closer to the $MgCl_2$ well. This suggests that one of two layer formation mechanisms are occurring. The first is that Mg^{2+} ions are travelling at a much slower velocity than Ca^{2+} ions, whilst the second is that MgP layer precipitation is analogous to CaP but primary and secondary bands cannot be distinguished given the lower particle number/mass formed.

Slow Mg^{2+} ions is an interesting prospect, especially given the diffusion constants of Ca^{2+} and Mg^{2+} ions are 7.93×10^{-10} m^2s^{-1} and $7.05\ 10^{-10}$ m^2s^{-1} respectively. These are relatively similar, and therefore the two ions have comparable electrical mobility (according to the Einstein-Smoluchowski equation). However, such constants are calculated for single ions in an infinitely dilute solution and so the high concentration of ions within the well will change the electrical

mobilities of Ca^{2+} and Mg^{2+} ions. Although, there is no literature that measures or calculates mobilities at these specific concentrations or any that do so in the presence of glycerol.

Disparities in electrical conductivity and relative permittivity of 2 M $CaCl_2$ and 1.8 $MgCl_2$ solutions should also be considered. Interestingly, Mollerup and Breil (2015) modelled the relative permittivities of $CaCl_2$ and $MgCl_2$ solutions and found that $MgCl_2$ has a lower relative permittivity than $CaCl_2$ at the same concentration. Hence the $MgCl_2$ domain should boast a greater electric field strength than the $CaCl_2$ domain. Initially then, a greater electric driving force should act on Mg^{2+} ions than Ca^{2+} ions when driven into the gel.

When considering escape from the well, one must also consider the interaction strength between the counter ions of each loading solution. Weng and Elliott (2014) calculated an electrostatic potential for the Mg^{2+}-CL^{-} interaction in an electrolyte/glycerol mixture to be approximately 290 kcal mol^{-1}, whilst for the Ca^{2+}-Cl^{-} interaction it was approximately 245 kcal mol^{-1}. This implies that Mg^{2+} ions are more strongly attracted to Cl^{-} ions and therefore take longer to escape the well.

The second mechanism that may explain the apparent delayed precipitation of the MgP layer revolves around the far greater solubility of MgP species, such as tri-MgP (pKsp = 5.83) (Racz and Soper, 1968), compared to HAp (pKsp = 58.9) (Mcdowell et al., 1977) or even CaP (pKsp = 28.9) (Gregory et al., 1974). Of course, this work has already established that CaP particles are likely ACP, hence AMgP may also be forming. In this mechanism, Mg^{2+} and $H_xPO_4^{x-3}$ ions collide in a similar region to where Ca^{2+} and $H_xPO_4^{x-3}$ ions collide, but precipitation does not become visible due to the lower nucleation and growth rate that imparts a greater limit on the number of particles that precipitate and their growth potential. This would ultimately mean MgP particles do not occupy a sufficient density within the agarose matrix to be visually observed. However, MgP particles that have precipitated would form and invisible primary layer can now be electrophoretically transported.

If MgP particles obtain a negative zeta potential with similar magnitude to CaP particles, they can begin to return toward the $MgCl_2$ under electrophoretic transport. The lower molar volume of MgP and the reduced supersaturation toward MgP will reduce the critical radii of MgP particles and lead to a slower growth rate (ignoring surface energies). If true, MgP particles would be smaller in diameter than CaP particles and therefore obtain a greater mean velocity than CaP particles of the same zeta potential.

The secondary MgP particle layer then becomes visible as particles from the primary layer are fed toward the $MgCl_2$ well, where a stacking effect occurs in areas where a relatively steep electric field gradient is present. Given the similar position of the secondary MgP layer and the secondary CaP layer, it is plausible that the local electric field gradient is organising particles to travel around wells and trapping particles in front of the well as they collide, causing coalescence and agglomeration that blocks the agarose matrix.

Precipitate layers formed in the PDA-coated agarose gel were almost identical in shape and thickness to those produced in the uncoated gel. One distinction, however, is the presence of a dark band below the MgP layer and the secondary CaP layer. This is thought to be unabsorbed PDA molecules or fragments that remained free in the agarose pore network, despite an extensive washing of the gel slab that included four separate 24-hour washes in buffer. The diffusion of PDA through the agarose matrix may therefore be too slow to remove unabsorbed PDA by a washing process in a suitable time frame.

3.5.3 PS-CAGE System

3.5.3.1 Casting test

The PS-CAGE system was fashioned for the synthesis of cylindrical and uniform CaP and MgP particles layers in a gel that can be cut to form cylindrical gels encapsulating a uniform cylindrical particle layer. Given casts can be made to the desired thicknesses and diameter, this system has the potential to produce a range of cryogel sizes with little adjustment to the experimental setup. Based on the increase in thickness of CaP particle layers produced in the PS-CAGE system compared to the PS-SW-AGE system, it appears that particle layer thickness can also be modulated. However, the theorised co-dependency of particle size and layer thickness may prevent fine tuning of both.

3.5.3.2 Gel Cast Sandwich

The gel cast sandwich tests demonstrated that a CaP precipitate layer can be produced using loading gels rather than salt solutions. The CaP layer within recipient gel cylinders appeared uniform in thickness and location, and had a similar thickness to that of the secondary CaP layers produced in Figure 3.58 using the PS-DW-AGE system. The main difference in CaP layer

appearance between the PS-CAGE and PS-DW-AGE systems is the presence of only one CaP layer in the cylindrical gels, which remains true for smaller cylinders excised from the large cylinders.

The formation of only a single CaP layer is thought to result from several factors. Firstly, the PS-CAGE system encourages the transport of more discrete ion bands than in the PS-DW-AGE system. This was confirmed in the ion transport models for the PS-CAGE model where ion bands are transported with a slight bell curve shape. In contrast, ion bands are far more diffuse and present as an irregular ellipsoidal shape in the PS-DW-AGE approach. Since the PS-CAGE system maintains greater ion band concentrations, a higher supersaturation toward CaP will result that provides a greater nucleation rate and leads to the formation of smaller particles when compared to the PS-DW-AGE system.

It is expected that the CaP layer produced via the PS-CAGE system consists of densely packed CaP particles that reduces the free space within the agarose matrix, create blockages, and inhibit electrophoretic transport of particles. Though this is similar to the PS-DW-AGE system, the difference here is that the CaP layer occupies the entire cross section of the recipient gel cylinder, hence a uniform CaP particle layer shape is retained.

The distance of the leading edge of the CaP layer to the $CaCl_2$ loading gel in the PS-CAGE system was similar to the distance between the leading edge of the primary CaP layer and the $CaCl_2$ well in the PS-DW-AGE system. Such a comparison is made by converting these distances into a percentage of total distance between loading gels or loading wells. For the PS-CAGE system, CaP layers were 2.9 mm from the $CaCl_2$ gel which corresponds to precipitation occurring at a position 73 % through the recipient gel thickness. In contrast for the PS-DW-AGE system, the primary CaP layer was 5.8 mm from the $CaCl_2$ well which corresponds to 83 % of the 7 mm well separation.

PDA-coated gel cylinders produced CaP layers that precipitated in a similar location to that of uncoated gels. However, accurate measurements of CaP layer thickness proved difficult due to the drastically lower contrast between CaP and the gel. Despite this, a single gel cylinder was clear enough to measure a thickness of between 0.6 – 08 mm and located 2.6 mm from the $CaCl_2$ loading gel. This layer was far thinner than the CaP layer in the PDA-coated gel slab that measured 2.08 ± 0.10 mm (n = 6) and was located 5.4 ± 0.18 mm (n = 6) from the $CaCl_2$ well. The CaP layer in the PDA-coated gel cylinder therefore precipitated at a position equivalent to 65 % through the gel thickness which contrasts to the primary CaP layer in the PDA-gel slab of the PS-DW-AGE system which was 5.4 mm from the $CaCl_2$ well which corresponds to 77 % of the 7 mm well separation. The PDA-coating therefore appears to shift the position of the CaP layer closer

toward to $CaCl_2$ source. Furthermore, CaP layers in the PS-CAGE system are also shifted toward the $CaCl_2$ source when compared to those produced in the PS-DW-AGE system.

3.5.3.3 Adjacent loading

The adjacent loading test demonstrated the precipitation of a CaP layer in the absence of a recipient gel. As shown in Figure 3.64 and Figure 3.65, the entire CaP layer precipitated in the Na_2HPO_4 loading gel to a thickness of 2.4 mm as measured in the main cylinder and 2.04 mm as measured in the smaller cylinders. The precipitation in the Na_2HPO_4 gel is thought to occur due to the greater electrical mobility of Ca^{2+} ions compared with Na_2HPO_4 ions that induces precipitation in the direction of Ca^{2+} ion travel. Neither gel presented any evidence of secondary CaP layers, therefore, the PS-CAGE system is able to produce a single, macroscopically unbroken CaP layer which is of course desirable for the osteogenic layer of an osteochondral GAM.

PDA-coated gel cylinders presented CaP layers with a similar shape and thickness to that of non-coated cylinders, though with the same brown discolouration observed during opposite loading. Smaller cylinders cut from the large cylinder have CaP layer thickness that is similar to those cut from non-coated cylinders. Unlike CaP layers produced in PDA-coated gels using a gel sandwich layout, CaP layers could be measured here due to better contrast and shared highly similar layer thicknesses to uncoated gels.

The increased thickness of the CaP layer using adjacent loading is thought to be due to the reduced distance between Ca^{2+} and $H_xPO_4^{x-3}$ ion starting positions, hence reduced time till collision and nucleation, such that high ion concentrations can be maintained. This is analogous to the PS-SW-AGE approach that utilised 225 mM $CaCl_2$ (nearly 10-times less $CaCl_2$ than in these experiments) but was still able to produce a CaP layer over 1.5 mm in thickness, which is comparable to CaP layers formed in the PS-DW-AGE system.

3.5.4 Temperature/pH Control Unit

The temperature/pH control unit demonstrated a good capacity of reducing a temperature and pH gradient increase during a 10-minute application of a 180 V potential. Temperature increase was reduced from 8 °C to 3 °C, whilst the pH gradient between electrodes was reduced from 0.18 to 0.03.

A buffer temperature increase could not be eliminated, despite the theoretically sufficient cooling capacity of the heat exchanger, which perhaps arises due to some inefficiencies in the temperature/pH control unit. Though the tubing and reservoir can be covered in thermal insulating material, the pump generates a significant amount of heat that is absorbed by the circulating water in the cold loop. This raises the minimum temperature that water in the cold loop can achieve, thus reducing the cooling capacity of the system. Peristaltic pumps are an alternative to the aquarium pump used, but these pump at a substantially smaller capacity and as such would not provide sufficient transfer of thermal energy.

3.5.5 Current Test

Current through the electrophoresis tank during the application of a 180 V potential was measured in two separate tests; (1) a control test using a gel sandwich produced using no loading salts and (2) an experimental test using a gel sandwich comprised of 2 M $CaCl_2$, 12 mM Na_2HPO_4 gels, and centrally positioned recipient gels. The starting currents for the control and experimental tests were 113 mA and 175 mA respectively. This disparity in initial current is simply due to the presence of salts in the experimental test that provides a larger overall conductivity. The control test current increased linearly to 119 mA at a mean rate of 0.011 mAs^{-1}, which is thought to result primarily from an increasing buffer temperature (due to joule heating) that increases the conductivity of the buffer. Additionally, the pH gradient build-up introduces a potential difference across the tank, so the DC power supply may also be increasing the current draw to maintain the applied 180 V potential difference, but this would be mostly eliminated in the experimental test.

The experimental test has a more complex change in current over 600-seconds. A linear current increase of 0.11 mAs^{-1} in current occurs up until 100-seconds, which is 10-times greater than in the control test. It is plausible that a greater buffer temperature increase is occurring here than in the control test due to the greater conductivity afforded by salt ions in the loading gels. Thus, a greater positive feedback loop occurs where the joule heating effect increases conductivity of the buffer, which increases joule heating, and so on. At 100-seconds, the linear increase in current reduces and a second linear trend of 0.038 mAs^{-1} takes over. This shift could signal the consumption of charge carrying ions in CaP precipitation reactions, causing the rate that conductivity is increasing to reduce. Note that only $H_xPO_4^{x-3}$ ions and a small portion of Ca^{2+} ions will have precipitated as CaP due to the large excess of Ca^{2+} ions, but Cl^- ions will remain from

the $CaCl_2$ loading gel to carry charge to the positive electrode. Such a large shift in conductivity may therefore result from these effects.

The introduction of electrically insulating CaP layers in the gel cylinders will effectively create resistors between the electrodes, thus reducing conductivity, so it is not clear whether the transition from one trend to another results predominantly from ion loss, CaP layers acting as resistors, or a combination of both. In any case, if ion consumption in precipitation reactions is sufficiently responsible for these changes in conductivity then it could be used to indicate that CaP precipitation reactions are mostly concluded by 100-seconds.

3.6 Conclusion

New PS-DW-AGE and PS-CAGE systems have been developed to ultimately improve the transfection efficacy and pre-clinical relevancy of PDA-coated cryogels encapsulating pDNA-mineral particles. A PS-DW-AGE system has computationally demonstrated more uniform electric field profiles at the zone of precipitation when compared to the previous PS-SW-AGE system, as well as more uniform ion transport and mixing. Precipitation tests using the PS-DW-AGE system demonstrated a capacity to produce both CaP and MgP layers in both uncoated and PDA-coated agarose gel slabs. Though CaP forms as two distinct layers, this thought to arise simply through particle transport. The PS-DW-AGE system will therefore be highly useful for throughput sample production to modulate particle size by varying several experimental parameters with the aim of obtaining an 'ideal' subset of parameters to use in the PS-CAGE system.

Computationally, the PS-CAGE system presents even more uniform electric field profiles, as well as more uniform ion transport and mixing than both the PS-SW-AGE and PS-DW-AGE models. Experimentally, the PS-CAGE system has been shown to produce uniformly shaped CaP layers in both PDA-coated and non-coated agarose gel cylinders. Whilst the use of two loading gels in the PS-CAGE system allows a discrete CaP layer to precipitate within the recipient gel bulk, the more promising loading layout is adjacent loading. Here, a much thicker CaP layer was formed within the Na_2HPO_4 gel that proceeded up to the gels surface. The thickness of this layer is similar to the thickness needed for an osteogenic layer for osteochondral regeneration in a pre-clinical rabbit model. Furthermore, the proximity of the CaP layer up to the flat gel surface, along with the fact that the CaP covers the entire cross-section of smaller 6 mm gels, suggests these gels have the desired mineral coverage for osteointegration *in-vivo*.

The temperature/pH control used proved successful in reducing a temperature and pH build up when using the PS-CAGE system, meaning the PS-DW-AGE and PS-CAGE systems will benefit from controlled temperature and pH conditions to better control nucleation and growth of particles during synthesis.

Overall, the PS-DW-AGE and PS-CAGE systems each functioned as intended, both computationally and experimentally. Going forward, an 'ideal subset' of experimental parameters is sought to produce pDNA-encapsulating particles that demonstrate sub-100 nm diameters and sufficient particle layer thickness to be clinically relevant, all within cylindrically shaped PDA-coated agarose gel cylinders.

4 Particle Size Reduction and Final Cryogel Synthesis

4.1 Introduction

4.1.1 New Apparatus

Apparatus for the PS-DW-AGE and PS-CAGE systems has been designed, fabricated, and tested to demonstrate these systems can synthesise particle layers. In the PS-DW-AGE system, it has been shown that both CaP and MgP particle layers can be formed within uncoated and PDA-coated gel slabs. In the PS-CAGE system, it has been established that CaP layers can be precipitated at the thickness required for osteogenic layers of osteochondral GAMs in a pre-clinical rabbit model. Gels produced by the PS-CAGE system can also be cut to the size required for pre-clinical models of critically sized defects. A temperature/pH control unit has also been devised to provide more stable conditions for particle synthesis in both systems. It is now possible to independently vary a range of experimental parameters to modulate particle diameters within the PS-DW-AGE system to identify an 'ideal subset' of parameters for use in final cryogel synthesis in the PS-CAGE system with more stable buffer temperature and pH.

4.1.2 pDNA/MgP particles and pDNA/PEI complexes

Since MgP precipitation has been demonstrated in the PS-DW-AGE system, MgP particles can now be considered alongside CaP particles as the mineral component of the osteogenic cryogel layer. For the chondrogenic layer, the synthesis of pDNA/PEI complexes in a PS-AGE system has previously been established as theoretically possible and should therefore be considered as the vector for the chondrogenic cryogel layer. It would likely be possible to synthesise either pDNA/CaP or pDNA/MgP particles with pDNA/PEI complexes in a monolithic gel using a sequential loading regime and optimised timings of loadings. However, one must consider the relevance of such an approach with regard to replicating native osteochondral tissue architecture and biomechanical properties. For example, it would be more relevant to produce each layer separately so that material properties of the supporting material (such as pore size) could be tuned independently.

4.1.3 Layer Synthesis

The articular cartilage and calcified layers of the osteochondral have contrasting mechanical properties and porosities. In humans, articular cartilage has a compressive moduli of the order of 10 MPa (Kabir et al., 2021) and pore diameters between 11 - 14 nm (Majda et al., 2017). Meanwhile, the subchondral plate demonstrates pore diameters of the order of 40 nm (Pouran et al., 2021) and cortical bone has pores reaching the microscale (Milovanovic et al., 2017). Furthermore, direct comparisons of bone and cartilage reveal contrasting storage and stiffness moduli (Fell et al., 2019). Therefore, using a single, monolithic agarose gel in the PS-CAGE system to produce a GAM encapsulating both osteogenic and chondrogenic layers will produce suboptimal properties in one or both layers. Researchers therefore frequently deploy biphasic, triphasic, multiphasic, or gradient scaffolds for osteochondral tissue regeneration (Chen et al., 2023).

The cryogels produced in this research would ideally be integrated into a triphasic structure, where the osteogenic and chondrogenic layers are synthesised in separate gels of the desired mechanical properties and porosity, where a third intermediate layer bonds the cryogel layers together. The intermediate layer would therefore reflect the functionality of the ZCC. Interestingly, the supposed surface-mediated transfection process employed by the osteogenic layer in this work would in fact rely heavily on a nearly impervious intermediate layer. This is due to the dissolution of primary pDNA/mineral particles in the osteogenic layer that would release ions into the surrounding agarose matrix; hence an intermediate layer would be required to prevent mineralisation of the chondrogenic layer *in-situ.*

Development of osteogenic and chondrogenic layers can therefore be conducted separately given they will ultimately be bonded together. This presents numerous advantages with regards to the simplicity of *in-vitro* testing of these layers, most significant of these being the need to only incubate cells on a single surface. Dual surface culturing would be required if one is to simulate cellular infiltration into the chondrogenic layer from the synovial fluid and cellular infiltration from microfracture holes beneath. Though pDNA/PEI complexes can be synthesised via pDNA characterisation using AGE (Kurosaki et al., 2009), complexes synthesised by such a route have not been utilised in gene therapy applications (to this author's knowledge). pDNA/PEI complexes produced via the PS-CAGE system would ultimately require extraction from agarose and suspension in solution to investigate and characterise their size and zeta potential. This is because pDNA/PEI characterisation via SEM would be troublesome given the inability of SEM to detect nucleic acids without heavy metal stains.

The individual synthesis of osteogenic- and chondrogenic-simulating layers via the PS-CAGE approach will ultimately require these layers to be amalgamated to form a triphasic cryogel. The intermediate layer could simply be a high concentration agarose gel and PDA mixture used as a glue and then freeze dried. Of course, other materials could be used for this intermediate layer since it will not interfere with synthesis processes in the PS-CAGE system. Alternatively, osteogenic- and chondrogenic-simulating layers could be synthesised and – as hydrogels – have their surfaces heated, melting local agarose to facilitate their 'welding' together. In either route, there would need to be optimisation of this layer with regard to several properties of the triphasic cryogel. For example, the intermediate layer must mechanically integrate the osteogenic and chondrogenic layer sufficiently to prevent delamination. The intermediate layer must also demonstrate an ability to prevent cell migration from one layer to another but facilitate nutrient diffusion, thus allowing the triphasic cryogel to simultaneously segregate cell phenotypes without restricting nutrient supply. Therefore, this research will focus only on the *in-vitro* testing of osteogenic and chondrogenic cryogel layers, and their integration via an intermediate layer will be pursued in future work.

4.1.4 Summary

The PS-DW-AGE system, complete with a temperature/pH control unit, is now available to accurately determine parameter relationships with particle size to build an ideal subset of parameter conditions to inform pDNA/CaP and pDNA/MgP particle synthesis in the PS-CAGE system. Since investigations in Chapter 2 have already demonstrated the multimodal influence of pDNA and PDA on particle synthesis, the PS-DW-AGE system will be used in the absence of pDNA loadings or PDA coatings. Though final cryogels synthesised via the PS-CAGE system will utilise both pDNA and PDA in their synthesis, it is necessary to simplify the internal agarose environment to more accurately plot parameter-particle relationships that may be de-sensitised with the addition of pDNA and PDA. Hence PDA will not be used in PS-DW-AGE experiments.

The PS-CAGE system, complete with the temperature/pH control unit, will utilise the ideal subset of parameter conditions identified in the PS-DW-AGE system. The intention is to then produce PDA-coated cryogels of cylindrical shape and (minimum) 4 mm diameter in-line with the requirements for use in a pre-clinical rabbit osteochondral defect model. These cryogels will encapsulate osteogenic-simulating layers of either pDNA/CaP or pDNA/MgP or a chondrogenic-simulating layer of pDNA/PEI. The 'simulating' terminology used here is due to the use of

plasmids with reporter genes. PEI will also be added to osteogenic-simulating cryogels to determine whether the addition of such biomolecules can enhance secondary particle stability and improve transfection.

4.2 Research Aims and Objectives

4.2.1 Research Aims

(1) Fabricate cylindrical GAMs embedded with sub-100 nm particles suitable for a pre-clinical osteochondral model.

4.2.2 Research Objectives

(1) Using the PS-DW-AGE system, establish:
    a. The relationship between CaP and MgP size with individual experimental parameters to obtain an ideal subset of parameter conditions for final cryogel synthesis
    b. That a pDNA/PEI complexe layer can be synthesised using pDNA and PEI loading solutions
(2) Using the PS-CAGE system, produce PDA-coated osteogenic cryogels containing a layer of either pDNA/CaP or pDNA/MgP particles synthesised using ideal subsets of parameter conditions, with out without the addition of PEI
(3) Using the PS-CAGE system, produce chondrogenic cryogels containing a layer of pDNA/PEI complexes
(4) Evaluate the *in-vitro* performance of PDA-coated cryogels synthesised in Research Aims 2. And 3.

4.3 Materials and Methods

4.3.1 CaP and MgP Particle Synthesis in the PS-SW-AGE System

4.3.1.1 Preparation of Stock Salt and Loading Solutions

A stock HEPES buffer solution was prepared by adding 238.3 g of HEPES powder to 1600 mL of $D.H_2O$ under stirred conditions, which was brought to pH 8.0 using 6 M NaOH. The solution was then added to a 2 L volumetric flask and made up a final volume of 2 L with $D.H_2O$ to give a final concentration of 1 M HEPES.

A stock Tris-HCl buffer solution was prepared by adding 30.29 g of Tris powder to 400 mL of $D.H_2O$ in a beaker under stirred conditions, which was then brought to a pH of 8.0 using 6 M HCl. The solution was added to a 500 mL volumetric flask and brought to a final volume of 500 mL using $D.H_2O$ to give a concentration of 500 mM Tris.

1 L stock solutions of 5 M $CaCl_2$, 5 M $MgCl_2$, and 100 mM Na_2HPO_4 were prepared according to the constituents of each stock solution are shown in Table 4.1.

Table 4.1. Stock Salt Solution Constituents.

Stock solution	**Salt**	**Final Solution Volume (L)**
5 M $CaCl_2$	735.05 g of $CaCl_2.2H_2O$	1
5 M $MgCl_2$	1016.55 g of $MgCl_2.6H_2O$	1
100 mM Na_2HPO_4	13.20 g of Na_2HPO_4	1

Briefly, 200 mL of $D.H_2O$ was added to each of three beakers and each salt was added to one beaker under constant stirring. For the $CaCl_2$ and $MgCl_2$ stock solutions, $D.H_2O$ was added incrementally to the beakers once no more salt could be dissolved. Once dissolved, the solutions were poured into volumetric flasks and made up to a final volume of 1 L with $D.H_2O$.

Next, a 250 mL stock glycerol solution was prepared by adding 119.05 g of glycerol (density of 1.26 gcm^{-3}) to a beaker, to which 80 mL of $D.H_2O$ was added and mixed until the mixture appeared homogenous. The mixture was then added to a 250 mL volumetric flask and made up to 250 mL with $D.H_2O$ to produce a 60 vol % glycerol stock solution.

50 mL of stock loading solutions were next prepared in falcon tubes using stock salt and glycerol solutions. The constituents for each loading solution are listed in Table 4.2. Note that each stock loading solution had 5 vol % of glycerol. A Mg^{2+}-doped $CaCl_2$ solution was formulated using a $CaCl_2$:$MgCl_2$ ratio of 9, which consisted of 3.7125 $CaCl_2$ + 0.4125 $MgCl_2$.

Table 4.2. Loading Solution Constituents.

Loading Solution	**Salt solution stock (mL)**	**Glycerol stock solution (60 vol %) (mL)**	**D.H_2O (mL)**
1 M $CaCl_2$	10	4.17	35.83
2 M $CaCl_2$	20	4.17	25.83
4.175 M $CaCl_2$	41.75	4.17	4.08
0.9 M $MgCl_2$	9	4.17	36.83
1.8 M $MgCl_2$	18	4.17	27.83
Mg^{2+}-doped $CaCl_2$	37.125 mL $CaCl_2$ + 4.125 mL $MgCl_2$	4.17	4.08
3.75 M $MgCl_2$	37.5	4.17	8.33
6 mM Na_2HPO4	3	4.17	42.83
12 mM Na_2HPO4	6	4.17	39.83
25 mM Na_2HPO4	12.5	4.17	33.33

The three Na_2HPO_4 loading solutions (6, 12, and 25 mM) are for pairing with $CaCl_2$ and $MgCl_2$ solutions to maintain specific ionic ratios. For CaP particles, a Ca^{2+}:$H_xPO_4^{x-3}$ ratio of 167 is maintained for $CaCl_2$ and Na_2HPO_4 well pairings to use a 100-times stoichiometric ratio for HAp (as used in Chapter 2 and 3). For MgP particles, a Mg^{2+}:$H_xPO_4^{x-3}$ ratio of 150 is maintained (as used in Chapter 3) to use a 100-times stoichiometric ratio for tri-MgP. Well pairings are listed in Table 4.3 below.

Table 4.3. Group names and their respective loading solutions pairs and ionic ratios.

Group Name	Loading Solution 1	Loading Solution 2	Ionic Ratio
CaP (1 M $CaCl2_2$)	1 M $CaCl_2$	6 mM Na_2HPO4	Ca^{2+}:$H_xPO_4^{x-3}$ = 167
CaP (2M $CaCl2_2$)	2 M $CaCl_2$	12 mM Na_2HPO4	Ca^{2+}:$H_xPO_4^{x-3}$ = 167
CaP (4.125 M $CaCl2_2$)	4.175 M $CaCl_2$	25 mM Na_2HPO4	Ca^{2+}:$H_xPO_4^{x-3}$ = 167
MgP (0.9 M $MgCl_2$)	0.9 M $MgCl_2$	6 mM Na_2HPO4	Mg^{2+}:$H_xPO_4^{x-3}$ = 150
MgP (1.8 M $MgCl_2$)	1.8 M $MgCl_2$	12 mM Na_2HPO4	Mg^{2+}:$H_xPO_4^{x-3}$ = 150
MgP (3.75 M $MgCl_2$)	3.75 M $MgCl_2$	25 mM Na_2HPO4	Mg^{2+}:$H_xPO_4^{x-3}$ = 150

Prior to synthesis of CaP and MgP particles, loading solution stocks were added to 96-well plates in the same layout as that required in the gel slab.

4.3.1.2 Preparation of Gel Slabs

Gel slabs for the PS-DW-AGE approach were prepared according to the same protocol described in 2.3.4. For HEPES buffers, 1.8 L of working buffer solution of 25 mM HEPES was prepared by adding 45 mL of stock HEPES solution to 1755 mL of $D.H_2O$. For Tris buffers, 1.8 L of working buffer solution of 25 mM Tris-HCl was prepared by adding 90 mL of stock Tris-HCl buffer to 1710 mL of $D.H_2O$. Agarose mixtures were prepared according to their required concentration; these are listed in Table 4.4.

Table 4.4. Agarose mass and working buffer volume for each agarose concentration.

Concentration of Agarose (wt %)	Mass of Agarose (g)	Working Buffer Volume (mL)
1	1.3	128.7
2	2.6	127.4
3	3.9	126.1
4	5.2	124.8
5	6.5	123.5

Each mixture was prepared in a conical flask covered with cling film and heated until agarose completely dissolved. The mixtures were allowed to cool until 65 °C before pouring. Components of the PS-DW-AGE system were assembled to produce 4 well pairs per gel slab with well pairs spaced 7 mm apart. A plan-view of well pair arrangements is provided for each parameter test. Once cooled, agarose mixture was poured into the gel tray and allowed to set for 45-minutes. Meanwhile, 1670 mL of buffer was poured into the horizontal electrophoresis tank. After 45-minutes, the tray was submerged in the tank and combs were removed.

4.3.1.3 Gel Cutting, Lyophilisation, and Powderisation

The gel punch and mask were used to excise all particle layers from the gel slab (the intended cut-out section is shown by the red dotted line in Figure 4.1. Cryogels were then prepared for SEM analysis using the protocol described in 2.3.8. Briefly, each cryogel group was collected, placed in a tea strainer, and submerged in liquid nitrogen for 30-seconds, then immediately crushed to a fine powder using a mortar and pestle. This process was repeated for each group to produce powdered group samples which were stored in a dry environment until analysed.

4.3.1.4 Particle Synthesis via Varied Salt Concentration

Two 1 wt % agarose gel slabs were prepared according to the protocol described in 4.3.1.2 using a 25 mM HEPES buffer (pH 8.0). The loading solution pairs listed in Table 4.3 were used to produce CaP and MgP particles. Each loading solution was added to 20 wells, with five well pairs per row, giving n = 20 for each group, as shown in Figure 4.1. Five well pairs were placed in each row of wells to account for any differences that may arise due to the distance between CaP and MgP layers with either electrode. Once loading solutions had been added to a gel slab, a 180 V potential was immediately applied for 600-seconds. Gels were then excised and powdered according to the protocol described in 2.3.8.

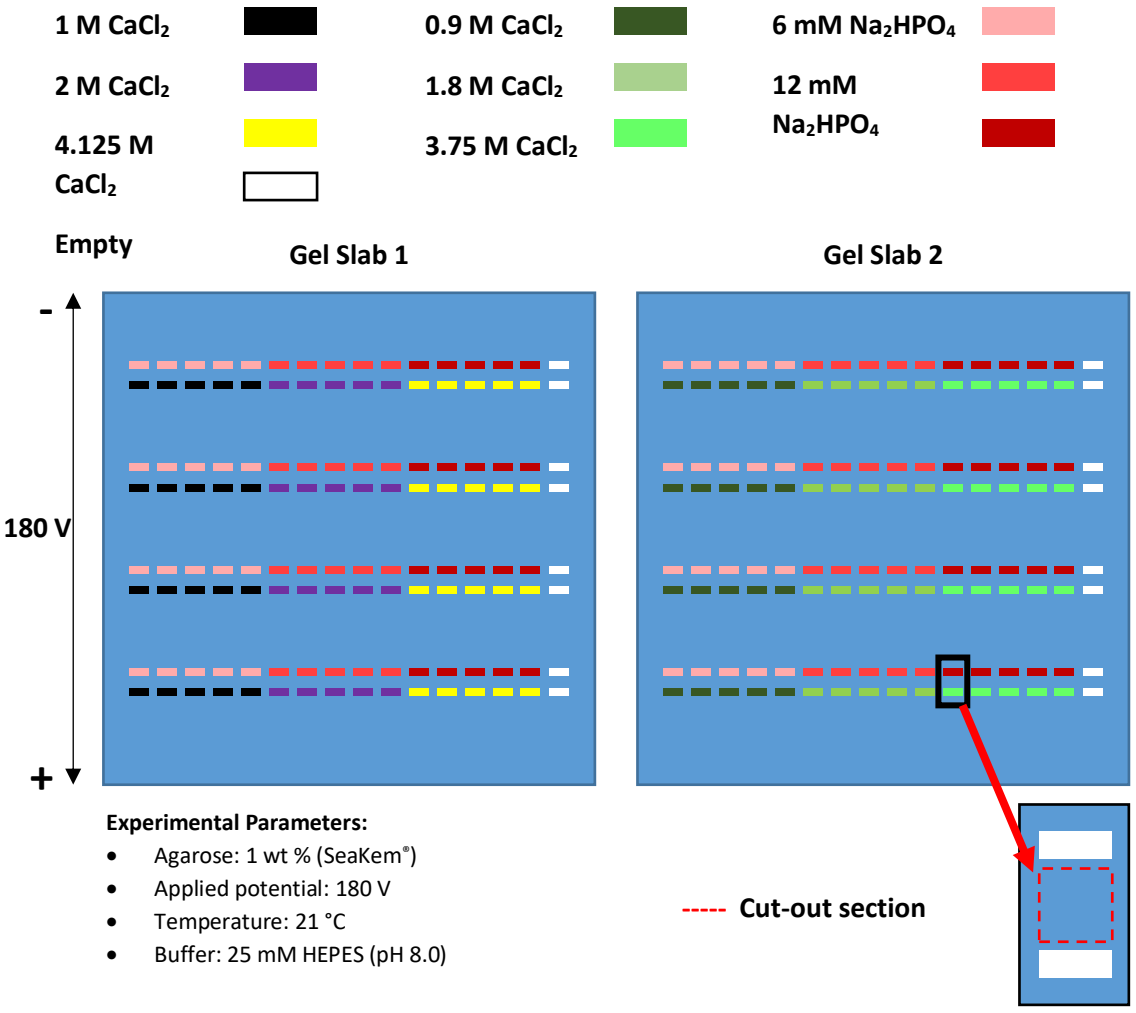


Figure 4.1. Layout of loading solutions for all loading pairs.

Note that the temperature/pH control unit was operated within the tank during the synthesis of all groups. This included maintaining room temperature and stabilising buffer pH.

4.3.1.5 Particle Synthesis via Salt Doping

A 1 wt % agarose gel slab (Seakem®) was prepared, as described in Table 4.4, using 25 mM HEPES (pH 8.0). This gel slab was loaded with a Mg^{2+}-doped $CaCl_2$ loading solution (described in Table 4.2) and the layout for these loading solutions is shown in Figure 4.2 below. After loading solutions were added, a 180 V potential was applied across the electrophoresis tank for 600-seconds. Gels were then excised and powdered according to the protocol described in 2.3.8.

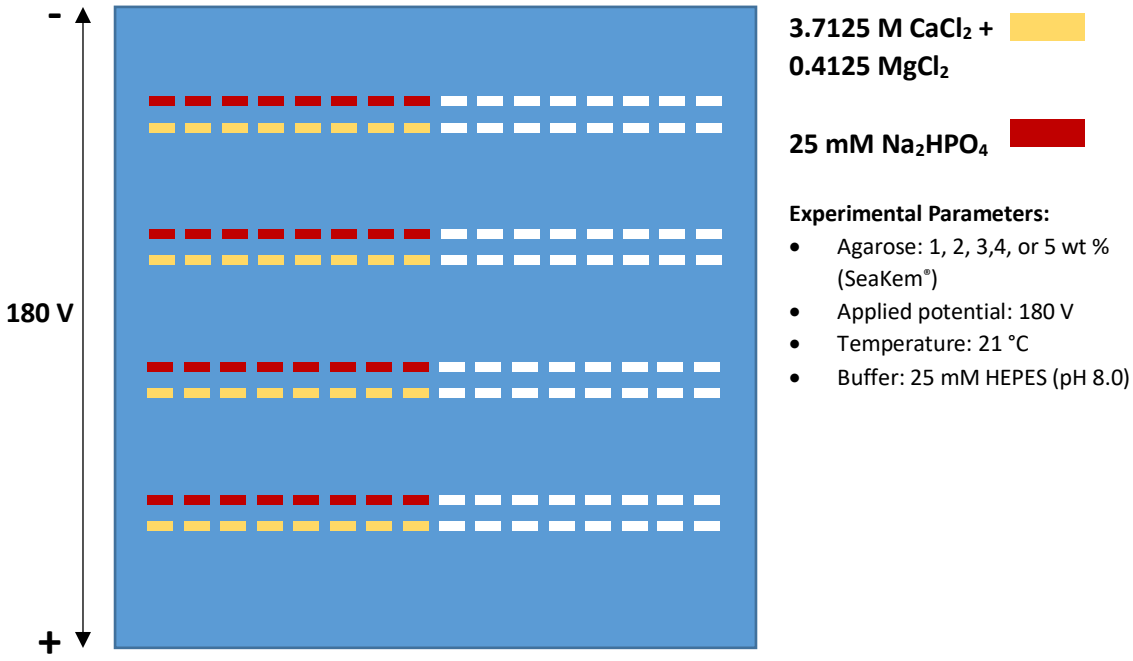


Figure 4.2. Layout of loading solutions in a gel slab loaded with a Mg2+-doped CaCl2 solution.

4.3.1.6 Particle Synthesis via Varied Agarose Concentration and Type

Agarose gel slabs were prepared at concentrations of 1, 2, 3, 4, and 5 wt % Seakem® agarose, as described in Table 4.4, using 25 mM HEPES (pH 8.0). Gel slabs were then loaded with loading solution pairs of 4.125 M $CaCl_2$ or 3.75 M $MgCl_2$, each with 25 mM Na_2HPO_4, as shown in Figure 4.3 below. Loading solution was applied to all wells, giving n = 32 for each group. Once loading solutions had been added to a gel slab, a 180 V potential was immediately applied for 600-seconds. Gels were then excised and powdered according to the protocol described in 2.3.8.

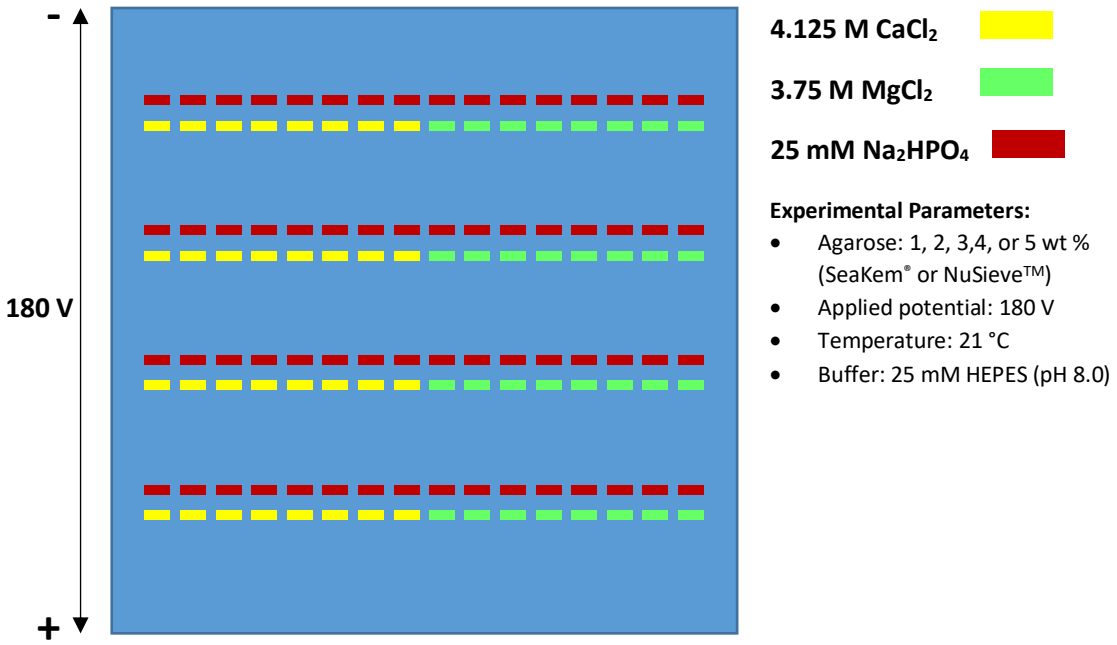


Figure 4.3. Layout of loading solutions in a gel slab with agarose concentration of either 1, 2, 3, 4, or 5 wt % agarose.

Another 1 wt % gel slab was prepared using the same composition described in Table 4.4, but with 1.3 g of NuSieve™ agarose. The NuSieve™ gel slab was loaded with the same loading solution and layout as Figure 4.3. All CaP and MgP particles were excised from the gel slab (giving n = 32 per group), followed by preparation of gels for SEM analysis using the protocol described in 2.3.8.

4.3.1.7 Particle Synthesis via Varied Applied Potential

1 wt % agarose gel slabs were prepared using the constituents listed in Table 4.4, using 25 mM HEPES (pH 8.0), and submerged in buffer in the electrophoresis tank. Each gel was loaded with the layout described in Figure 4.4, using 4.125 M $CaCl_2$ loading solutions paired with 25 mM Na_2HPO_4. A different applied potential was used for each gel slab for 600-seconds; either 60 V, 120 V, or 300 V. Gels were then excised and powdered according to the protocol described in 2.3.8.

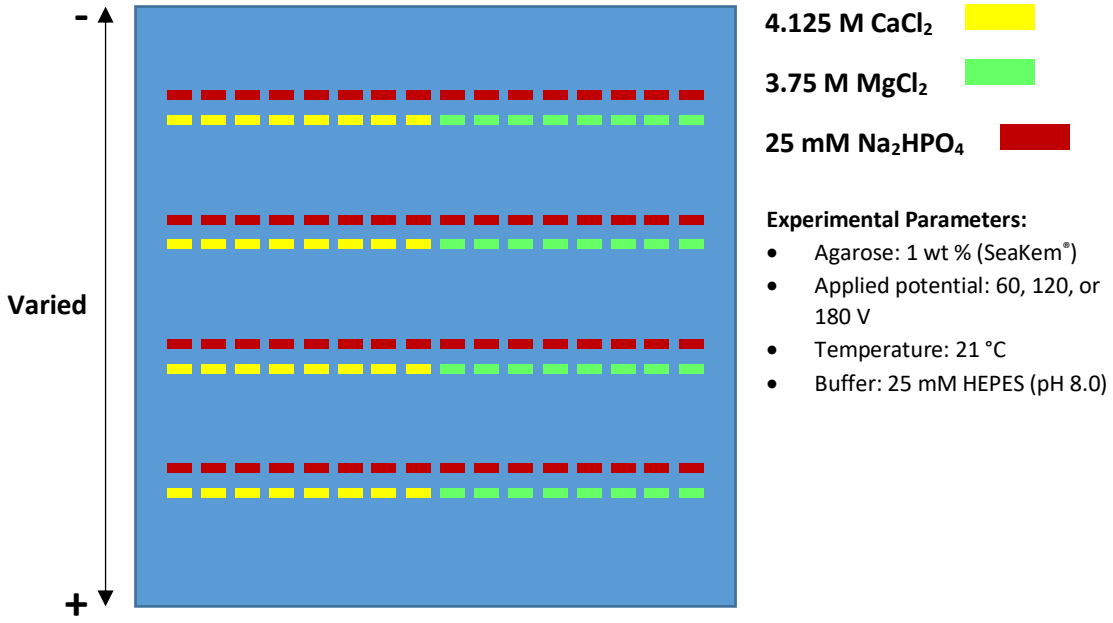


Figure 4.4. Layout of loading solutions in a 1 wt % agarose gel slab using different applied potentials.

4.3.1.8 Particle Synthesis via Varied Temperature

1 wt % agarose gel slabs were prepared using the constituents listed in Table 4.4, using 25 mM HEPES (pH 8.0), and submerged in buffer in the electrophoresis tank. Each gel slab was loaded with a loading solution layout shown in Figure 4.5 below. A 180 V potential was applied for 600-seconds, after which gels were excised and powdered according to the protocol described in 2.3.8.

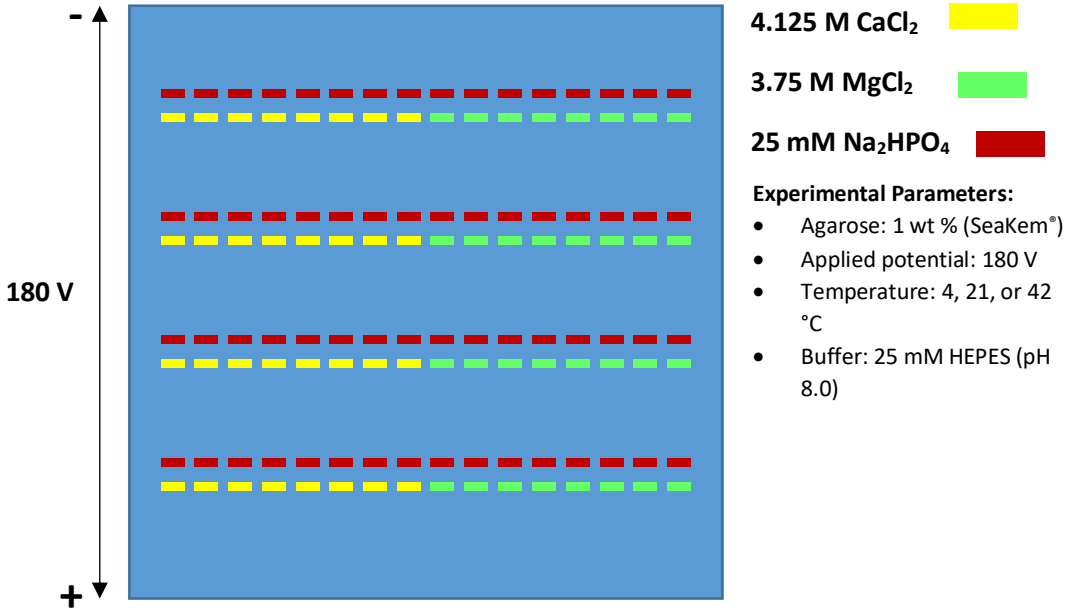


Figure 4.5. Layout of loading solutions in a 1 wt % agarose gel slab using different temperatures.

4.3.1.9 Particle Synthesis via Varied Buffer Type

1 wt % agarose gel slabs were prepared using the constituents listed in Table 4.4 using either a 25 mM HEPES (pH 8.0) or 25 mM Tris-HCl (pH 8.0) buffer. Gel slabs were submerged in buffer in the electrophoresis tank where loading solutions were added according to the layout shown in Figure 4.6. A 180 V potential was then applied for 600-seconds followed by immediate excision of gels which were powdered according to the protocol described in 2.3.8.

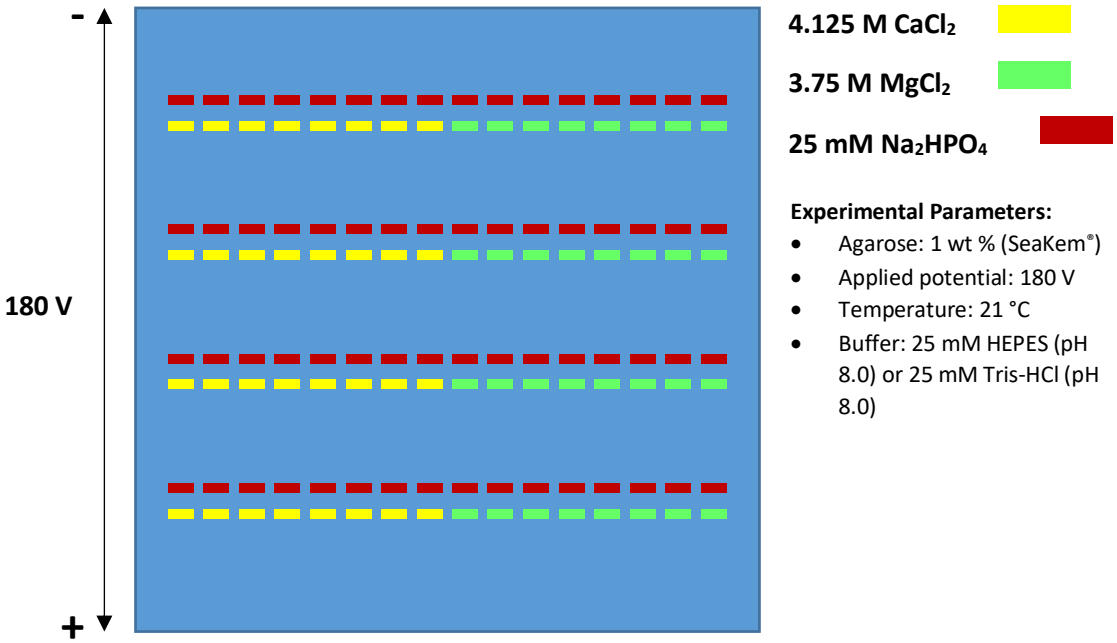


Figure 4.6. Layout of loading solutions in a 1 wt % agarose gel slab using different buffer types.

4.3.1.10 Particle Synthesis via Multiple Parameter Changes

A 3 wt % agarose gel slab was prepared according to the constituents listed in Table 4.4 using a 25 mM HEPES buffer solution (pH 8.0) and submerged in the electrophoresis tank. The loading solution layout shown in Figure 4.7 was applied to the gel slab and a 180 V potential was applied across the tank for 600-seconds. Here, a mid-range agarose wt % was used in combination with a mid-range salt concentration to inspect the effect of multiple parameter changes on CaP and MgP particle size. Gels were then excised immediately once the applied potential was removed and powdered according to the protocol described in 2.3.8.

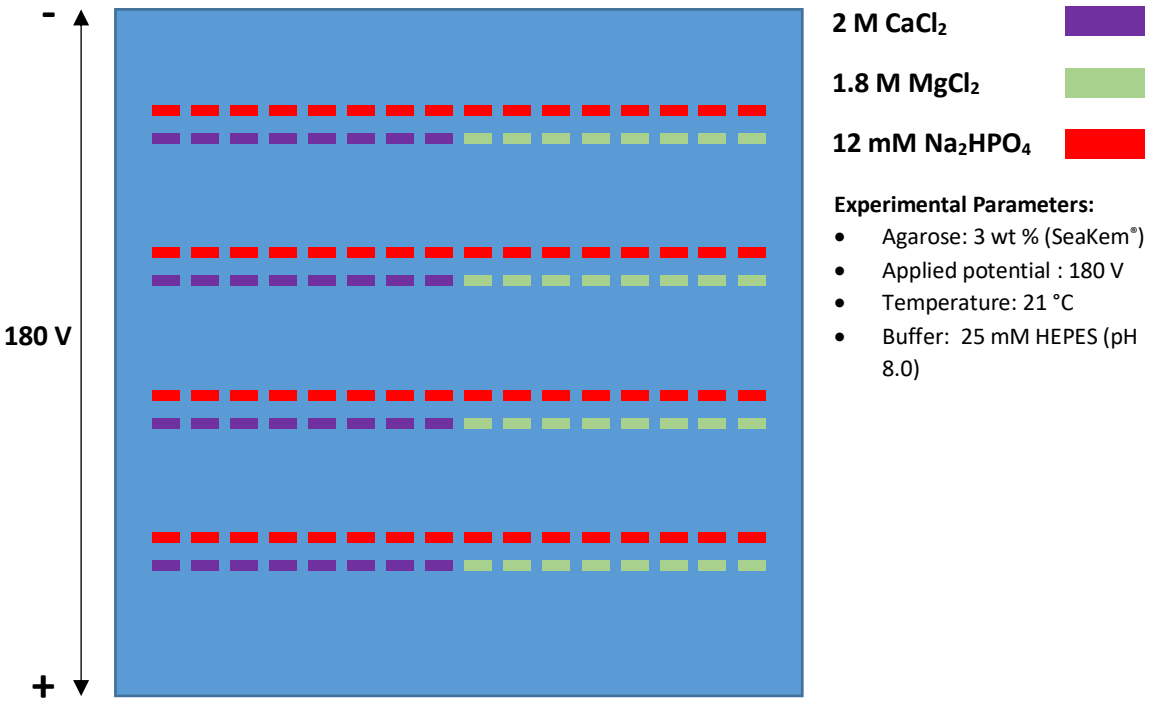


Figure 4.7. Layout of loading solutions in a 3 wt % agarose gel slab using buffer types.

4.3.2 Particle Synthesis in the PS-CAGE System

4.3.2.1 Stock Solution Preparation

Cylindrical agarose loading and recipient gels require stock salt solutions adjusted to pH 8.0 prior to mixing with agarose. Stock salt solutions for loading gels were prepared at higher concentrations than final loading gel solution concentrations to account for the addition of either 1 wt % agarose gel (for $CaCl_2$ and $MgCl_2$ loading gels) and 4 wt % agarose gel (for Na_2HPO_4 recipient gel).

Firstly, a 1 M HEPES solution was prepared by adding 59.58 g of HEPES powder to 400 mL of $D.H_2O$ under stirred conditions and making the volume up to 500 mL with $D.H_2O$ using a volumetric flask to give a final concentration of 500 mM HEPES. Next, stock salt solutions were prepared in separate beakers. 300 mL of $D.H_2O$ was added to each beaker and salt was added to each beaker under stirred conditions, followed by the addition of 25 mL of 500 mM HEPES stock solution and an adjustment to pH 8.0 using 6 M NaOH. The mixtures were added to separate volumetric flasks and made to 500 mL with $D.H_2O$, giving final concentrations listed in Table 4.5.

Table 4.5. Stock salt solution formulations.

Stock Salt Solution	Salt	500 mM HEPES (mL)	Final Volume (mL)
2.02 M $CaCl_2$ (pH 8.0)	74.24 g of $CaCl_2.2(H_2O)$	25	500
1.818 $MgCl_2$ (pH 8.0)	205.34 g of $MgCl_2.6(H_2O)$	25	500
12.48 mM Na_2HPO_4	17.72 g of Na_2HPO_4	25	500

The adjustment of loading gel solutions here to pH 8.0 are to account for the reduced diffusion of OH^- and H^+ ions in agarose gels in compared to in loading solutions for the PS-DW-AGE system which required no pH adjustment due to immediate mixing with the pH 8.0 buffer upon pipetting.

4.3.2.2 Stock pDNA Preparation

Two pDNA stocks were prepared: (1) pMetLuc which encodes for the luminescent luciferase enzyme; and (2) green fluorescent protein plasmid (pGFP) which encodes for the green fluorescent protein. The same protocol described in 2.3.1 was followed, this time with the use of Qiagen® Plasmid Giga Kits (instead of Mega Kits) for larger quantities of pDNA. The resulting pDNA pellets were resuspended in molecular biology grade water, and the concentration of each plasmid suspension was measured using a NanoDrop™ One/One^{C} Microvolume UV-VIS Spectrophotometer (Thermo Fisher Scientific, Massachusetts, USA).

4.3.2.3 Calculating pDNA and PEI concentrations

Separate pDNA and PEI loading gels are required for use in the PS-CAGE system. pDNA loading gels are required to electrophoretically load pDNA into all PDA-coated Na_2HPO_4 recipient gels, whilst PEI loading gels are only required to electrophoretically load PEI into pDNA/PEI gels. The same concentration of pDNA is required for use in the PS-CAGE system as was used previously in the PS-SW-AGE system, which was 0.1 µg uL^{-1}. Assuming this concentration remains unchanged when loaded into any gel type, a 4 mm thick, 20 mm diameter gel cylinder (1257 µL volume) will require a total of 126 µg of pDNA. Hence, to cast a row of six pDNA loading gel cylinders using a 25 mL agarose mixture, a total of 2500 µg of pDNA is required.

4.3.2.4 Preparation of pDNA Loading Gels

The pDNA loading gel solution was formulated according to the 0.1 µg uL^{-1} concentration. Briefly, 24.75 mL of HEPES solution (pH 8.0) and 0.25 g of SeaKem® agarose was added to a conical flask and heated until agarose completely melted. The mixture was then allowed to cool in a 65 °C water bath. Once cooled, the mixture was homogenised using a magnetic stirrer plate and gently heated to maintain a temperature above 60 °C. Meanwhile, a stock pDNA solution (10 µg uL^{-1}) was gently heated to 60 °C in a water bath. Once heated, 250 µL of pDNA stock solution was added to the agarose mixture and stirred for a further 10-minutes. The resulting mixture was then poured onto a 4 mm thick gel cylinder mould, to which a lid was added and weighed down to remove air bubbles. The gel cylinders were then left to cool for 6-minutes. Note that pGFP

was used to produce pDNA loading gels for groups intended for analysis via fluorescent microscopy, whilst pMetLuc was used for all other pDNA loading gels and analyses.

4.3.2.5 Preparation of Salt Loading and Recipient Gels

Salt loading gels comprised of 1 wt % agarose and either 2 M $CaCl_2$ or 1.8 M $MgCl_2$, whilst salt recipient gels were 4 wt % with 12 mM Na_2HPO_4. Each of these gels used their respective stock salt solution listed in Table 4.5 and was formulated according to the constituents listed in Table 4.6. Note that the final volume of mixture was sufficient to prepare a single row of six cylinders.

Table 4.6. Salt loading and recipient gel concentrations and constituents.

Gel Cylinder	**Stock Salt Solution (mL)**	**SeaKem® Agarose (g)**	**Final Volume (mL)**
1 wt %, 2 M $CaCl_2$	24.75	0.25	25
1 wt %, 1.8 M $MgCl_2$	24.75	0.25	25
PDA-coated 1 wt %, 12 mM Na_2HPO_4	24.75	1.0	25

Salt loading gels and PDA-coated recipient gels were prepared according to the protocol described in 3.3.3.

4.3.2.6 Preparation of PEI solution

PEI loading gels were prepared to provide a nitrogen : phosphate (N:P) atomic ratio of 10 i.e. using a PEI mass concentration 1.41-times greater than that of pDNA. Briefly, 1 wt % gel cylinders were prepared according to the protocol described in 3.3.4.4. Gel cylinders were removed from their casts and placed in individual wells of a 6-well plate. For the PEI solution, 1.49 g of HEPES powder was added to 200 mL of $D.H_2O$ and adjusted to pH 7.4 with 6 M NaOH. 20.25 g of PEI (molecular weight 10,000) (Thermo Fisher Scientific) was then added to the solution and dissolved fully under stirred conditions. The solution was then made up to 250 mL using $D.H_2O$ to give a final PEI concentration of 0.081 µg $µL^{-1}$. This concentration is required such that when a 4 mm thick pDNA cylinder is placed in a 6-well plate, adding 8743 µL of PEI solution results in

a total 10 mL volume of gel and solution in the well. Assuming PEI then diffuses into the gel and becomes uniform in concentration throughout the well over time, PEI will reduce in concentration by approximately 14 % to 0.071 μg μL^{-1}, which is the concentration required to provide an N:P ratio of 10 under these conditions. This same solution will be used to soak osteogenic-simulating cryogels encapsulating either pDNA/CaP or pDNA/MgP given they contain the same pDNA concentration.

4.3.2.7 Fabrication of Cryogel Groups

All cryogel groups were synthesised using a PDA-coated Na_2HPO_4 recipient gel, hence the PDA prefix is herein ignored for cryogel group names for the sake of brevity. Cryogel groups were named as follows: blank, pDNA, CaP, MgP, pDNA/PEI, pDNA/CaP, pDNA/MgP, pDNA/CaP/PEI, and pDNA/MgP/PEI.

For synthesised groups containing pDNA, the following protocol was followed. Briefly, pDNA loading gels were prepared according to the protocol described in 4.3.2.4, followed by preparation of PDA-coated 12 mM Na_2HPO_4 recipient gels according to the protocol described in 3.3.3. pDNA and recipient gel casts were then positioned in the electrophoresis tank according to conduct adjacent loading (as was done in 3.3.3). Note that temperature/pH control unit was activated for the synthesis of all groups to maintain room temperature and stable pH. A 180 V potential was then applied for 24-minutes to load the pDNA into the recipient gel. Data for distance travelled by pDNAs in different agarose concentrations or under different applied potentials was collected and is available in Appendix Figure 6.10 and Figure 6.11 respectively. After 24-minutes, the pDNA loading gels were removed and lyophilised for measurement of remaining pDNA later. The pDNA-loaded recipient gels were then either used as pDNA group gels or processed further to produce particle or complex layers. As discussed, pMetLuc was used to produce all pDNA loading gels except where pGFP was required to produce samples in preparation for fluorescence microscopy.

For the pDNA/CaP, pDNA/MgP, pDNA/CaP/PEI, and pDNA/MgP/PEI, the 2 M $CaCl_2$ or 1.8 M $MgCl_2$ loading gel was positioned adjacent to the pDNA-loaded recipient gel, followed by application of a 180 V potential for 600-seconds, producing pDNA/CaP or pDNA/MgP gels. To produce the pDNA/PEI group gels, PEI loading gels were placed adjacent to the pDNA-loaded recipient gels followed by application of a 180 V potential for 600-seconds.

For the CaP and MgP groups, 2 M $CaCl_2$ or 1.8 M $MgCl_2$ loading gels were positioned adjacent to PDA-coated 12 mM Na_2HPO_4 recipients (without pDNA), where a 180 V potential was applied for 600-seconds. For blank group gels, recipient gels were placed in the electrophoresis tank where a 180 V potential was applied for 600-seconds, followed by removal of gels.

For all groups, small gel cylinders were excised from the large gel cylinders and immediately frozen at – 70 °C for 2-hours and lyophilisation overnight. All groups, except for the pDNA/CaP/PEI and pDNA/MgP/PEI groups were then sterilised in 70 % EtOH for 10-minutes, frozen again and lyophilised overnight. For the pDNA/CaP/PEI and pDNA/MgP/PEI groups, gels from this group were first submerged in PEI solution for 5-minutes, rinsed briefly in $D.H_2O$, then sterilised in 70 % EtOH for 10-minutes before being frozen again and lyophilised overnight.

4.3.3 SEM Analysis

SEM analysis was conducted using the same sample preparation protocols, microscope, imaging, and measurement conditions as described in 2.3.8.

4.3.4 pDNA encapsulation

pDNA encapsulation efficiency within cryogel groups was determined according to the protocol described in 2.3.7. Briefly, cryogel groups were placed either into microcentrifuge tubes containing decalcification buffer (40 mM Tris, 150 mM EDTA, pH 8.0) (n = 3 per group). The tubes were incubated for 48-hours at room temperature, after which the tubes were centrifuged at 18,000 g for 15 minutes. 250 µL of supernatant was extracted from each tube and diluted at a ratio of 1:9 with decalcification buffer. 50 µL of the resulting sample was placed in triplicate in a black flat-bottom 96-well plate. pDNA standards in the range 125 – pg μL^{-1} to 0.25 ng μL^{-1} were prepared using decalcification buffer and added to the same well plate. 50 µL of dsDNA reagent solution (Quant-iT™ PicoGreen™ dsDNA assay kit, (Thermo Fisher Scientific) was added to each well, mixed via pipetting, followed by incubation of the plate for 5-minutes and fluorescence measurement at excitation and emission wavelengths of 502 nm and 523 nm respectively using a spectrophotometric microplate reader (Plate Chameleon™).

Mean values were calculated for each group, followed by use of Equation 2.2 to calculate the release of pDNA from each cryogel group.

4.3.5 Cell Culture

C2C12 cells were prepared according to the protocol described in 2.3.10 to produce cell suspensions with a concentration of either 5 x 10^6 cells mL^{-1} or 1.25 x 10^5 cells mL^{-1}. 250 µL of 3 wt % agarose was used to coat the well bases of 24-well plates according to the protocol described in 2.3.10 to prevent cells attaching to the plate. Cryogels for each group were divided into their respective groups and placed in separate 48-well plates with n-numbers dependent on the test set. The 48-well plates were assigned to one of the following test sets: (1) extract cytotoxicity; (2) proliferation assays; (3) transfection assays; and (4) fluorescence microscopy. For the extract cytotoxicity, and confocal microscopy test sets, an n = 3 for each group was used. For the proliferation assay and transfection assay test sets, an n = 4 was used.

For the contact cytotoxicity test set, two 24-well plates were established for the nine experimental groups and the following control groups: cell-only, steri strip, and superglue. Cryogels were placed in their respective wells and secured to the well base using steri strips, whilst a pair of crossed steri strips were secured to the base of the steri strip control wells and a dot of superglue was applied to the bottom of the superglue group wells. 2 mL of the 1.25 x 10^5 cells mL^{-1} cell suspension was then gently added to all wells. The 24-wells plates for the contact cytotoxicity test were then placed into incubation.

As per the protocol described in 2.3.10, 50 µL of cell suspension (2.5 x 10^5 cells) was applied to each cryogel followed by incubation of cryogels for 3-hours at 37 °C (5 % CO_2). 800 µL of cell media was then added to each well, being careful not to disturb cells on the cryogels. After 14-hours of incubation, cryogels were moved to 96-well plates to which 180 µL of fresh cell media was added. Every 24-hours, 180 µL cell media was removed and either used for assays or discarded, then replenished with 180 µL of fresh cell media.

4.3.6 In-vitro Testing

4.3.6.1 Contact Cytotoxicity

For the contact cytotoxicity test set, cell media was exchanged for fresh cell media at 24-hours. At 48-hours, cell media was removed, and the cells were washed twice in PBS (containing calcium and magnesium). After the removal of PBS, 2 mL of neutral buffered formalin (NBF) was added to each well for 10-minutes to fix the cells. Giemsa stain was then added until the cell

monolayer and cryogel in each well were completely covered. After 5-minutes, all Giemsa stain was removed and wells, washed with tap water, and finally left to dry overnight. Groups were then imaged using brightfield microscopy.

4.3.6.2 Extract Cytotoxicity

The same protocol as described in 2.3.10.6 was followed for LDH assays here. Briefly, after 48-hours of incubation, 28 µL of 10X lysis solution was added to control sets (n = 3) for each group and incubated for a further 45-minutes to lyse cells. Assay buffer was then mixed with CytoTox® Reagent, where 50 µL of the reagent mixture was then added to each well and incubated protected from light. 50 µL of stop solution was then added to each lysed well. Absorbance at 490 nm was measured for all wells. Measurements were first calibrated against a cell media control and then transformed to Cytotoxicity (%) via Equation 2.5.

4.3.6.3 Transfection Assays

Transfection efficacy for test groups was determined using luciferase assays according to the protocol described in 2.3.10.5. Briefly, at 24-, 48, and 72-hour time points, cell media was homogenised via pipetting, removed from the well, from which 50 µL of homogenised cell media was transferred to a white 96-well plate. 180 µL of fresh cell media was then added to the cryogel wells and the plate was returned to incubation until the next time point. 10 µL of 0.2 vol % coelenterazine (in acidified methanol) was added to each 50 µL sample and gently mixed via pipetting. Well plates were then incubated protected from light for 30-minutes, then measured for luminescence in a spectrophotometric plate reader (Plate Chameleon™).

4.3.6.4 Fluorescence Microscopy

The fluorescence microscopy well plates were removed from incubation at 72-hours, rinsed twice in PBS, then fixed in 10 % NBF. After 1-hour in NBF, the cryogels were washed again in PBS. A 4',6-diamidino-2-phenylindole (DAPI) solution was diluted in PBS at a working concentration of 0.5 µg mL^{-1}, of which 180 µL was added to each cryogel and incubated shielded from light at 1-hour. Cryogels were then washed in PBS and moved to a glass slide ready for fluorescence

microscopy. A scanning laser confocal microscopy (Leica DM6 CS, Lecia, Wetzlar, Germany) was then used to image samples with dual filter imaging via the LAS X Lecia (Leica) software. The DAPI excitation and emission filters were adjusted to 358 nm and 461 nm respectively, whilst the GPF excitation and emission filters were adjusted to 488 nm and 509 nm respectively.

4.3.7 Data Analysis

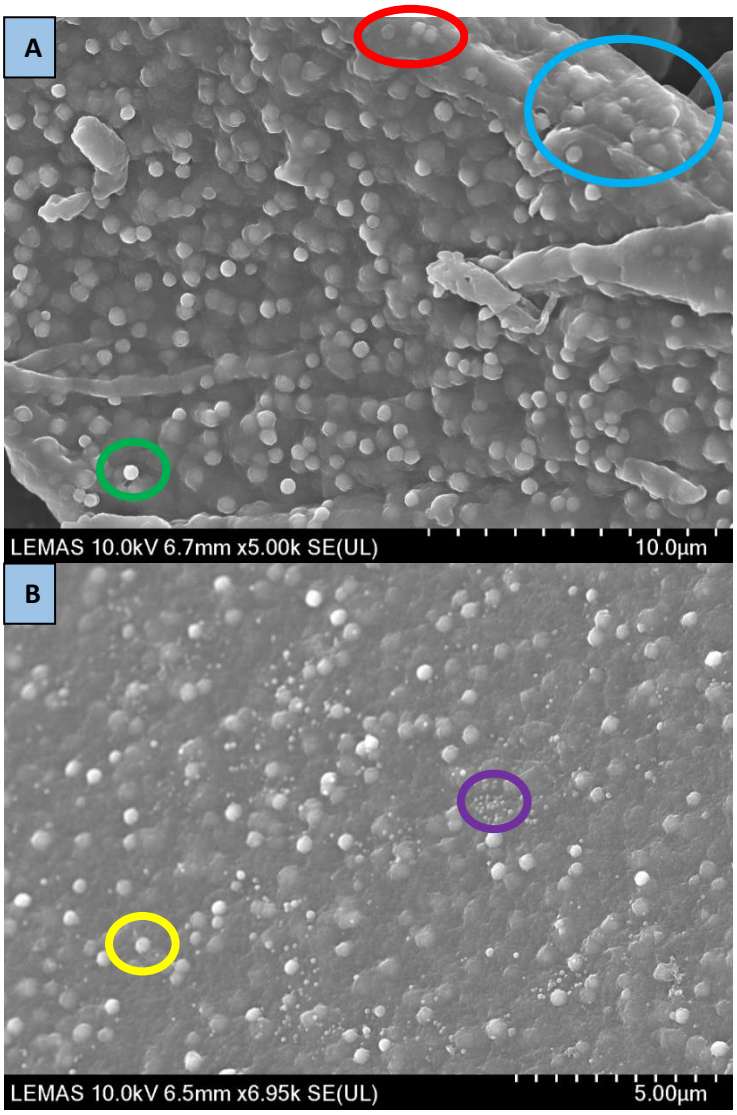
Unless specified, mean values are provided with standard deviation (SD) as follows: mean ± SD.

The Shapiro-Wilk test was used to test datasets for normality. Where data was non-parametric, the Tukey Kreamer Honestly Significant Difference (TK-HDS) test was performed to for multiple comparison statistical analysis. Unless indicated otherwise, statistical tests were carried out using 95 % confidence intervals (CI).

4.4 Results

4.4.1 Particle Synthesis via Varied Salt Concentration

CaP and MgP particles were synthesised using the salt pairings listed in Table 4.3, which are: 1 M $CaCl_2$ + 6 mM Na_2HPO_4, 2M $CaCl_2$ + 12 mM Na_2HPO_4, and 4.125 M $CaCl_2$ + 25 mM Na_2HPO_4. SEM images of typical CaP particles from the 4.125 M $CaCl_2$ sample are shown in Figure 4.8 , where Figure 4.8 (A) and Figure 4.8 (B) are of separate agarose fragments.



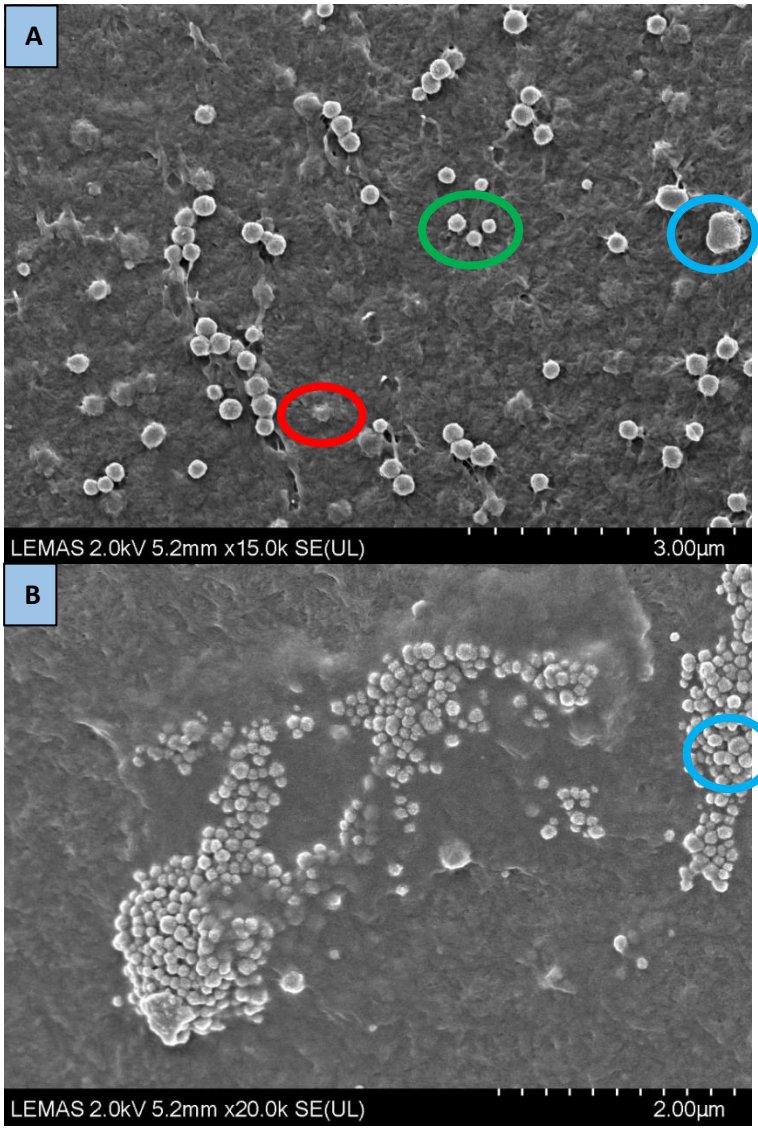
Sample Name:
- 4.125 M $CaCl_2$

Experimental Parameters:
- System: PS-DW-AGE
- Salt 1: 4.125 M $CaCl_2$
- Salt 2: 25 mM Na_2HPO_4
- Agarose: 1 wt % (SeaKem®)
- Applied potential = 180 V
- Temperature = 21 °C
- Buffer = 25 mM HEPES (pH 8.0)

Figure 4.8. CaP particles on the surface of separate agarose fragments from the 4.125 M $CaCl_2$ + 25 mM Na_2HPO_4 sample. (A) Fragment encapsulating a high density of particles; (B) fragment two encapsulating two distinct particle populations of contrasting size. Coloured circles indicate the following: red and blue = sub-surface particles; green = measured particle; yellow = large particle; purple = sub-100nm particles.

The high concentration of CaP particles in Figure 4.8 (A) are mostly spherical in morphology with a small number of particles exhibiting faceted edges and generally range between 400 – 500 nm in diameter. Particles appear to be buried throughout the agarose fragment given they are visible beneath the surface along the fragment side (circled in blue). A typical surface-bound particle i.e. suitable for size measurement is circled in green, and an example of a sub-surface particle not included in measurements is circled in red. CaP particles in Figure 4.8 (B) present bimodality with respect to their size, with large particles ranging between 400 – 500 nm (circled in yellow) and smaller particles with diameters ranging between 100 – 250 nm.

SEM images of CaP particles belonging to two separate agarose fragments from the 2 M $CaCl_2$ sample are displayed in Figure 4.9. A sub-surface particle is circled in red, and examples of superficial particles included in measurements are circled in green. Most particle diameters in Figure 4.9 (A) are of the order of 300 nm but there is a small number with sub-150 nm diameters, whilst those in Figure 4.9 (B) are closer to 200 nm and are significantly more tightly packed together. Both agarose fragments show particles that appear to have coalesced (circled in blue), and particles from both fragments appear to have rough surfaces comprised of small nodules. Most particles from both fragments present a spherical-like morphology where a small fraction can be considered irregular.



Sample Name:

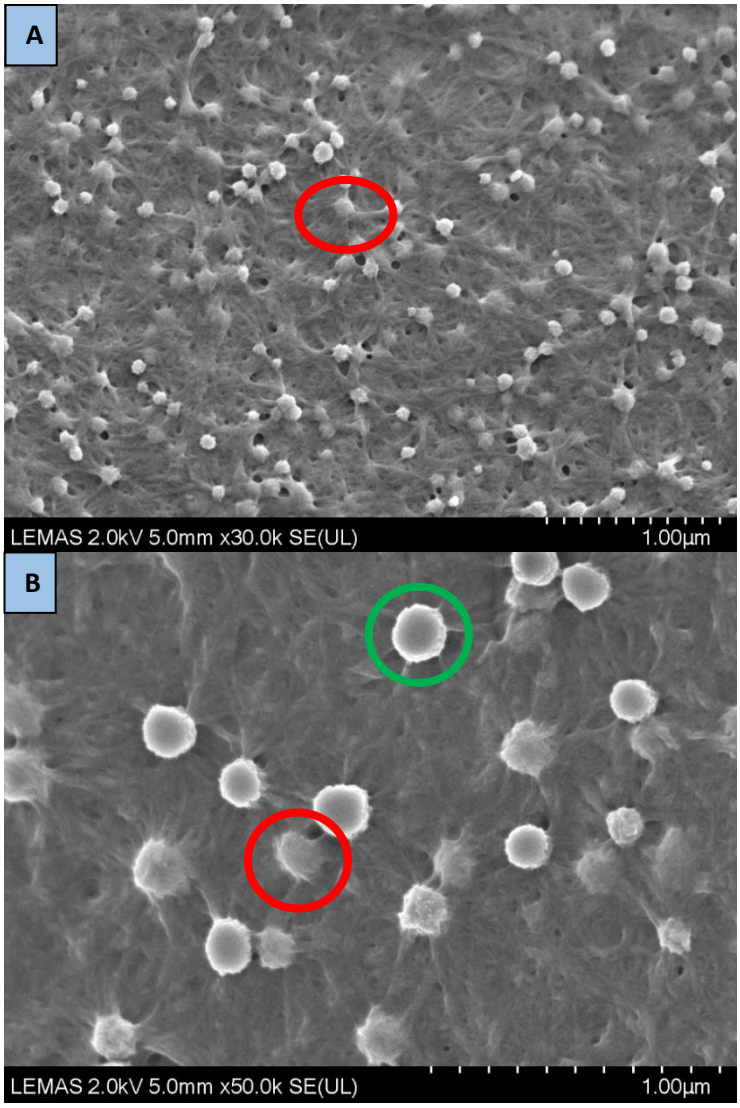
- 2 M $CaCl_2$

Experimental Parameters:

- System: PS-DW-AGE
- Salt 1: 2 M $CaCl_2$
- Salt 2: 12 mM Na_2HPO_4
- Agarose: 1 wt % (SeaKem®)
- Applied potential: 180 V
- Temperature: 21 °C
- Buffer: 25 mM HEPES (pH 8.0)

Figure 4.9. CaP particles on the surface of separate agarose fragments from the 2 M $CaCl_2$ + 12 mM Na_2HPO_4 sample. (A) Fragment one with moderately dispersed particles; (B) fragment two with clustered particles.

Typical particles from two separate agarose fragments from the 1 M $CaCl_2$ sample are shown in Figure 4.10. The first fragment (Figure 4.10 (A)) shows mostly regular shaped particles with most diameters of the order of 100 nm and a small number closer to 150 nm. Many agarose fibres envelope superficial particle edges (highlighted in red) and prevent their inclusion in measurements. Figure 4.10 (B) shows particles from the second agarose fragment where sub-surface particles (circled in red) and superficial particles (circled in green) can be seen. As with the first fragment, the superficial particles in the second fragment are mostly regular, but particles in the second fragment appear smoother.



Sample Name:

- 1 M $CaCl_2$

Experimental Parameters:

- System: PS-DW-AGE
- Salt 1: 1 M $CaCl_2$
- Salt 2: 6 mM Na_2HPO_4
- Agarose: 1 wt % (SeaKem®)
- Applied potential: 180 V
- Temperature: 21 °C
- Buffer: 25 mM HEPES (pH 8.0)

Figure 4.10. CaP particles on the surface of separate agarose fragments from the 1 M $CaCl_2$ + 12 mM Na_2HPO_4 sample. (A) Fragment one with moderately dispersed particles; (B) fragment two with clustered particles. Red circles indicate sub-surface particles, green circles indicate measured particles.

Generally, particles appear less uniform in shape as $CaCl_2$ concentration decreased; being highly spherical at 4.125 M $CaCl_2$ and becoming much more irregular at 1 M $CaCl_2$. Particle surface roughness also appears to increase with decreasing $CaCl_2$ concentration, but it must be acknowledged that image magnification increases with decreasing $CaCl_2$ concentration to compensate for measuring smaller particles. Therefore, particle surface roughness may simply become more resolved at greater magnification.

Histograms for the 4.125 M, 2 M, and 1 M $CaCl_2$ samples are plotted in Figure 4.11 below. The 4.125 M $CaCl_2$ sample boasts the widest diameter range (> 500 nm), whilst the 2 M $CaCl_2$ and 1 M $CaCl_2$ samples have ranges of approximately 400 nm and 350 nm respectively.

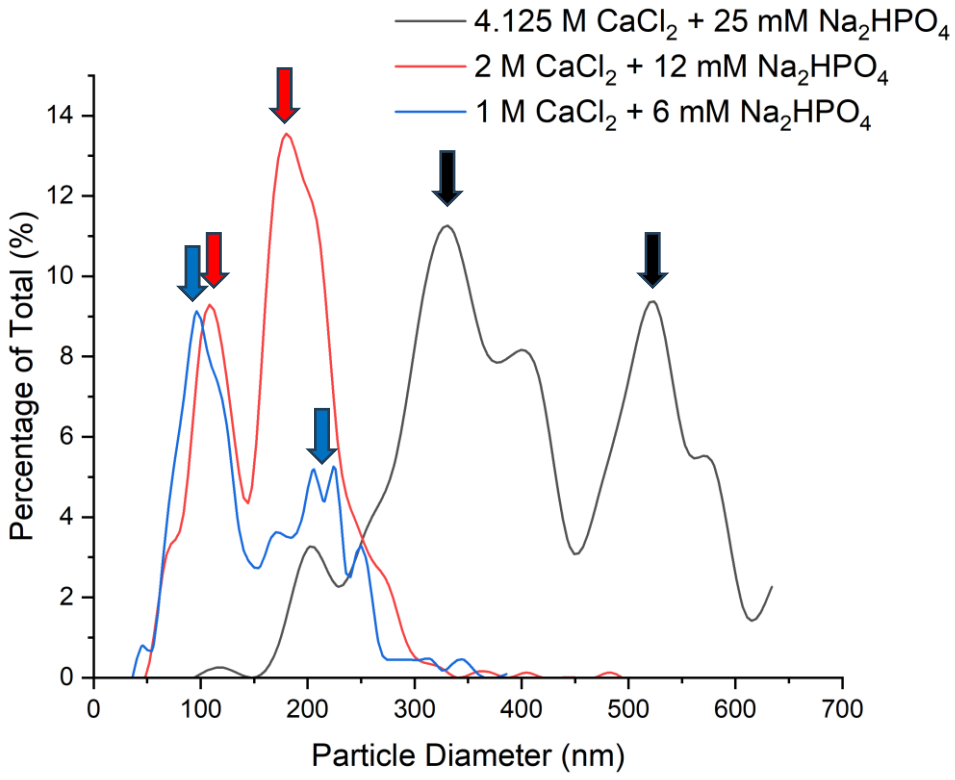


Figure 4.11. Histogram of CaP particle measurements from the 4.125 M, 2 M, and 1 M $CaCl_2$ samples. Arrows indicate primary and secondary modal peaks.

All three samples demonstrate bimodality with each having a primary and secondary peak; the values of which have been extracted and plotted in Figure 4.12. Primary peak diameter reduces with $CaCl_2$ concentration, from 331 nm for 4.125 M $CaCl_2$, to 181 nm for 2 M $CaCl_2$, and 96 nm for 1 M $CaCl_2$. Though secondary peaks reduce from 552 nm to 110 nm from the 4.125 M $CaCl_2$ to the 2 M $CaCl_2$ samples respectively, the secondary peak for the 1 M $CaCl_2$ sample is 217 nm.

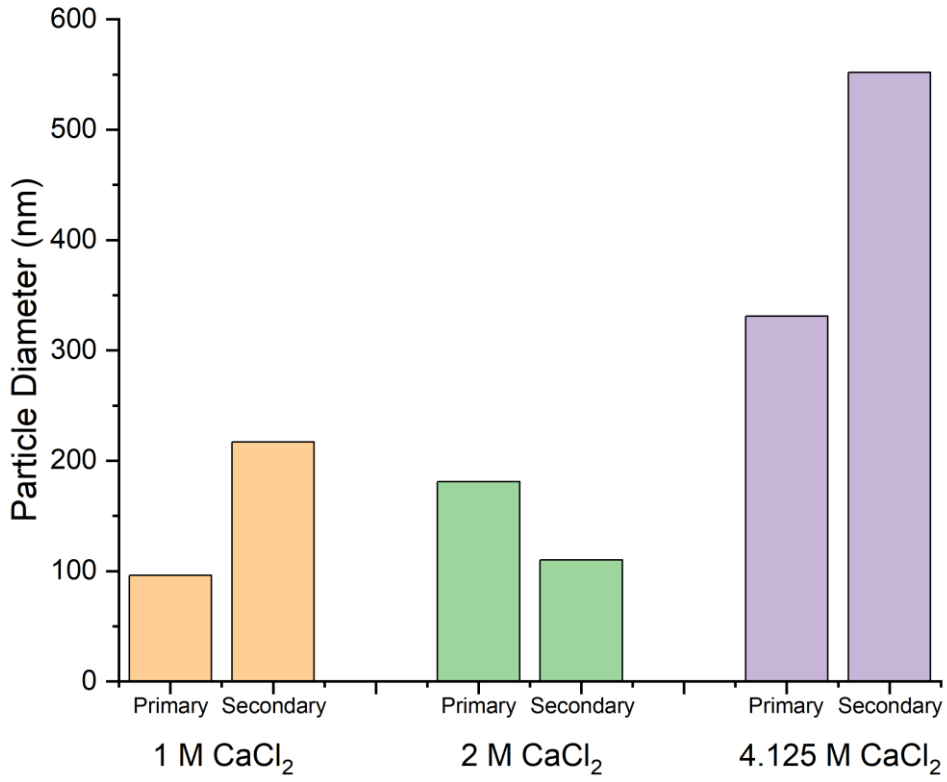
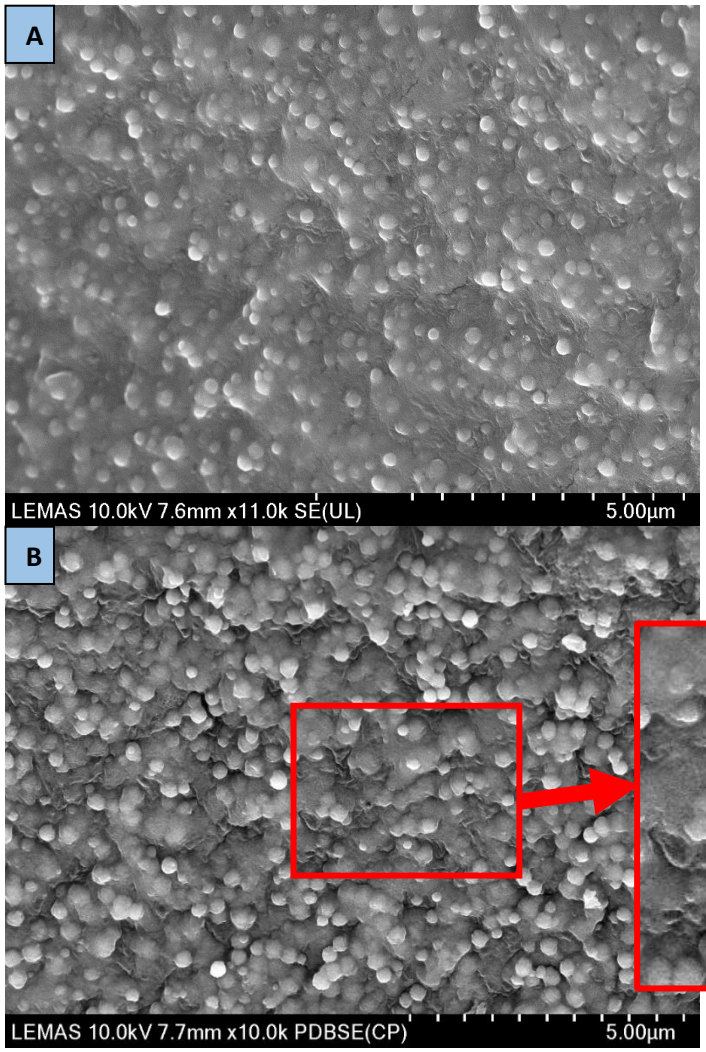


Figure 4.12. Primary and secondary peak CaP particle diameters for 1 M, 2 M and 4.125 M CaCl2 samples.

SEM images of agarose fragments with MgP particles from the 3.75 M $CaCl_2$ + 25 mM Na_2HPO_4 sample are shown in Figure 4.13 below. Both fragments demonstrate high particle densities where particles in both fragments range between 150 – 350 nm and are mostly spherical in morphology with little surface texture. Particles in Figure 4.13 (B) appear more superficial and clearer than those in Figure 4.13 (A) given BSE detection was successful in this particular region. An expanded region in Figure 4.13 (B) shows that many particles cannot be included in measurements as they appear sub-surface.



Sample Name:

- 3.75 M $MgCl_2$

Experimental Parameters:

- System: PS-DW-AGE
- Salt 1: 3.75 M $MgCl_2$
- Salt 2: 25 mM Na_2HPO_4
- Agarose: 1 wt % (SeaKem®)
- Applied potential: 180 V
- Temperature: 21 °C
- Buffer: 25 mM HEPES (pH 8.0)

Figure 4.13. MgP particles from the 3.75 M MgCl2 + 25 mM Na2HPO4 sample. Red square indicates magnified area.

MgP particles from the 1.8 M $MgCl_2$ sample are displayed in Figure 4.14. It is immediately obvious that particles from both agarose fragments in Figure 4.14 (A and B) have irregular morphologies and appear to have rough surfaces indicative of a nodular particle structure. Magnified areas from both fragments reveal show this more clearly. Areas circled in blue appear to feature a sub-100 nm particulate population which could be the building blocks of the larger particles.

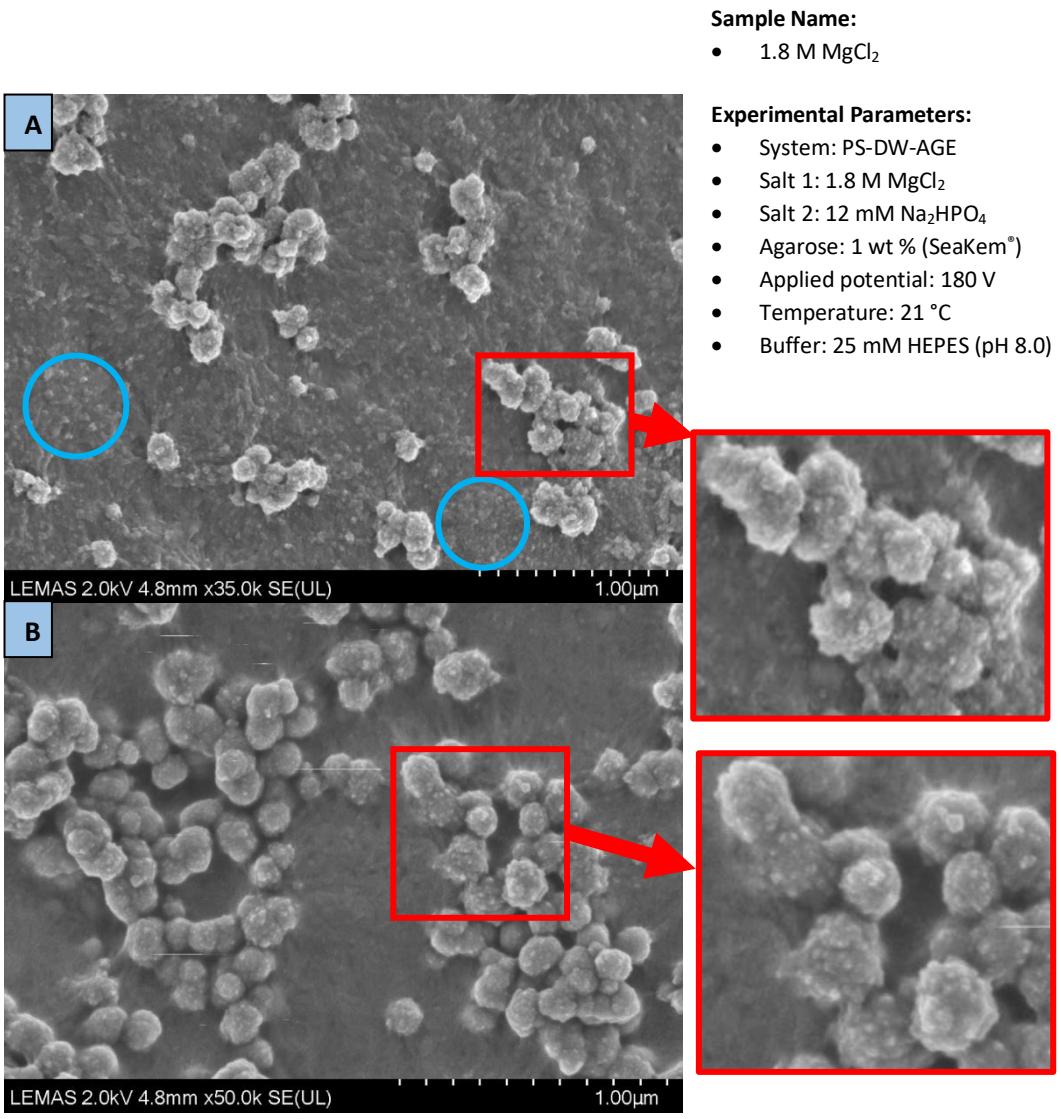
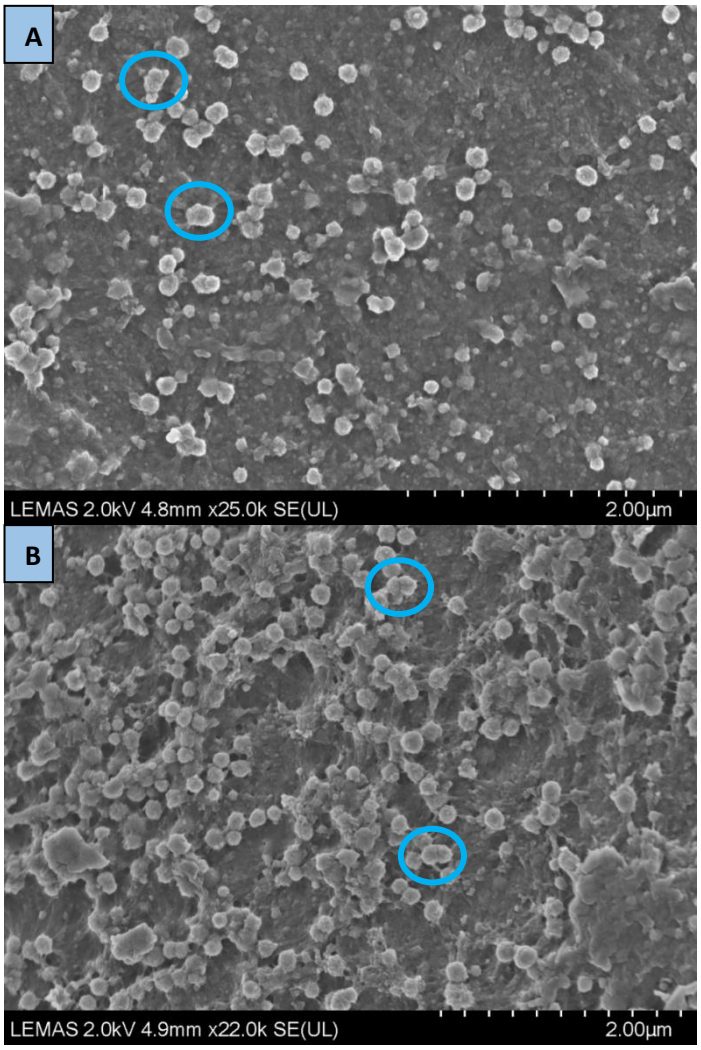


Figure 4.14. MgP particles from the 1.8 M MgCl2 sample. Red squares indicate magnified areas, blue circles indicate areas with sub-100 nm particles.

Figure 4.15 shows MgP particles from two agarose fragments belonging to the 0.9 M $MgCl_2$ sample. There is a contrast between these fragments in terms of particle density, but both demonstrate indications of bimodal particle size distribution with some particles exceeding 200 nm and many below 100 nm in diameter. Both fragments display some instances of coalescence, as circled in blue.



Sample Name:

- 0.9 M $MgCl_2$

Experimental Parameters:

- System: PS-DW-AGE
- Salt 1: 0.9 M $MgCl_2$
- Salt 2: 6 mM Na_2HPO_4
- Agarose: 1 wt % (SeaKem®)
- Applied potential: 180 V
- Temperature: 21 °C
- Buffer: 25 mM HEPES (pH 8.0)

Figure 4.15. Agarose fragments with MgP particles from the 0.9 M MgCl2 sample. Blue circles indicate coalesced particles.

Similarly to CaP particles, MgP particles appear to decrease in uniformity as $MgCl_2$ concentration decreases, where MgP particles from the 3.75 M $MgCl_2$ sample are highly spherical but those from the 1.8 M and 0.9 M $MgCl_2$ samples are much more irregular and display particles with rough surfaces that indicate a nodular composition of smaller particles. The bimodality of particle diameters was much more evident in the 1.8 M and 0.9 M $MgCl_2$ samples, where sub-100 nm particles can easily be seen at the agarose fragment surface.

MgP particle diameter histograms for the 3.75 M, 1.8 M, and 0.9 M $MgCl_2$ samples are plotted in Figure 4.16 below. The 0.9 M $MgCl_2$ sample demonstrates a clear bimodality of MgP particle diameters, but the 1.8 M and 3.75 M $MgCl_2$ samples exhibit a broad primary peak that may engulf any secondary peaks present. Therefore, it has been assumed that the peaks indicated by arrows are the respective primary and secondary peaks for samples of the same colour.

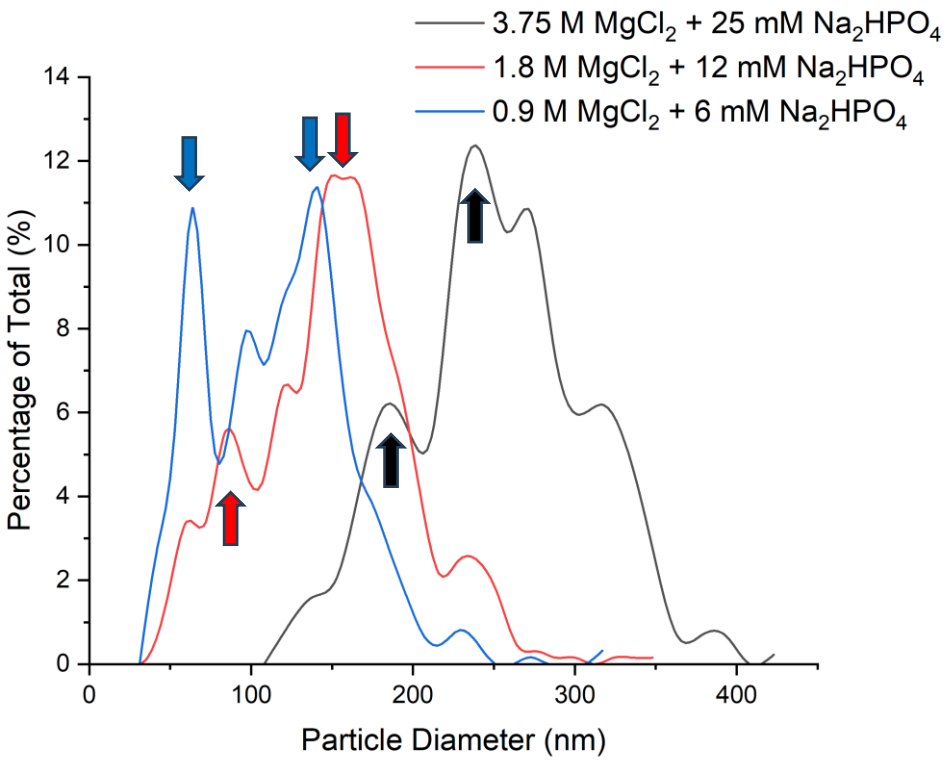


Figure 4.16. Histogram of MgP particle measurements from the 0.9 M, 1.8 M, and 3.75 M MgCl2 samples. Arrows indicate primary and secondary modal peaks.

From Figure 4.17, one can see a decrease in both primary and secondary peaks with decreasing $MgCl_2$ concentration, though for each sample the primary peak boasts a greater particle diameter than the secondary peak. This contrasts with two of the $CaCl_2$ samples in Figure 4.12 which presented primary peaks greater than secondary peaks.

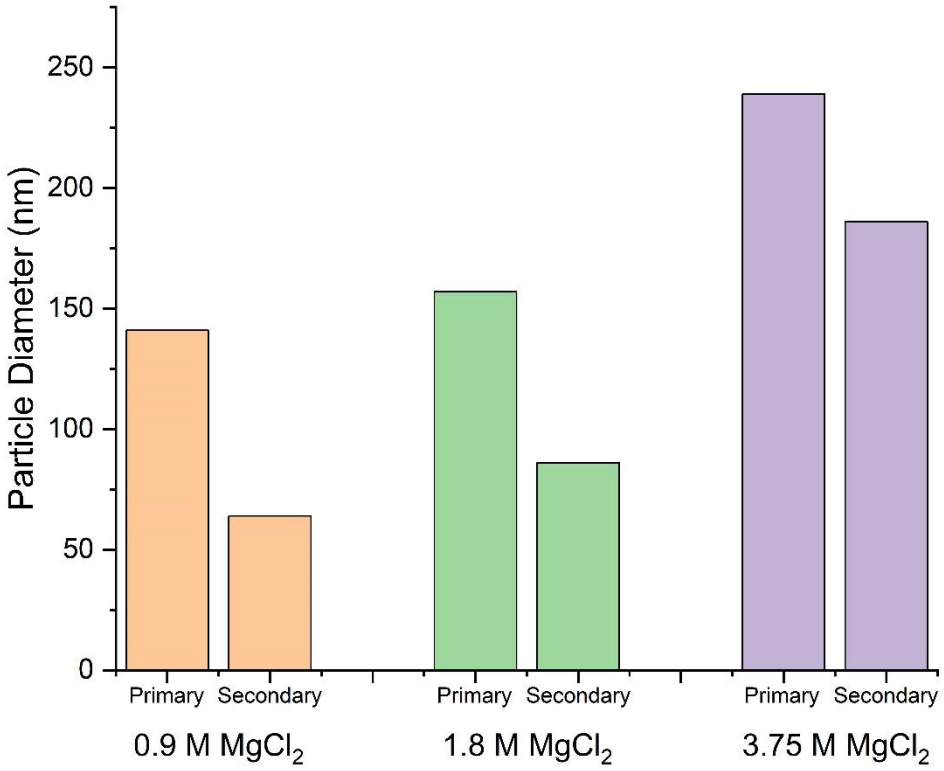


Figure 4.17. Primary and secondary peak MgP particle diameters for 0.9 M, 1.8 M and 3.75 M MgCl2 samples.

The 4.125 M $CaCl_2$ + 0.4125 M $MgCl_2$ sample was prepared using a loading solution of 3.7125 M $CaCl_2$ and 0.4125 M $MgCl_2$ to give a $CaCl_2$:$MgCl_2$ ratio of 9:1. Particles from two agarose fragments are displayed in Figure 4.18. As highlighted in red, the fragment in Figure 4.18 (A) reveals the majority of particles are encased in agarose just below the fragment surface, with a single particle available for measurement. Meanwhile, the second fragment Figure 4.18 (B) boasts more superficial particles. Superficial particles in both fragments range between 200 – 300 nm in diameter, have a mix of regular and irregular morphologies, and present a nodular surface topography. The mean particle diameter for 4.125 M $CaCl_2$ + 0.4125 M $MgCl_2$ sample was 261 nm ± 94 nm.

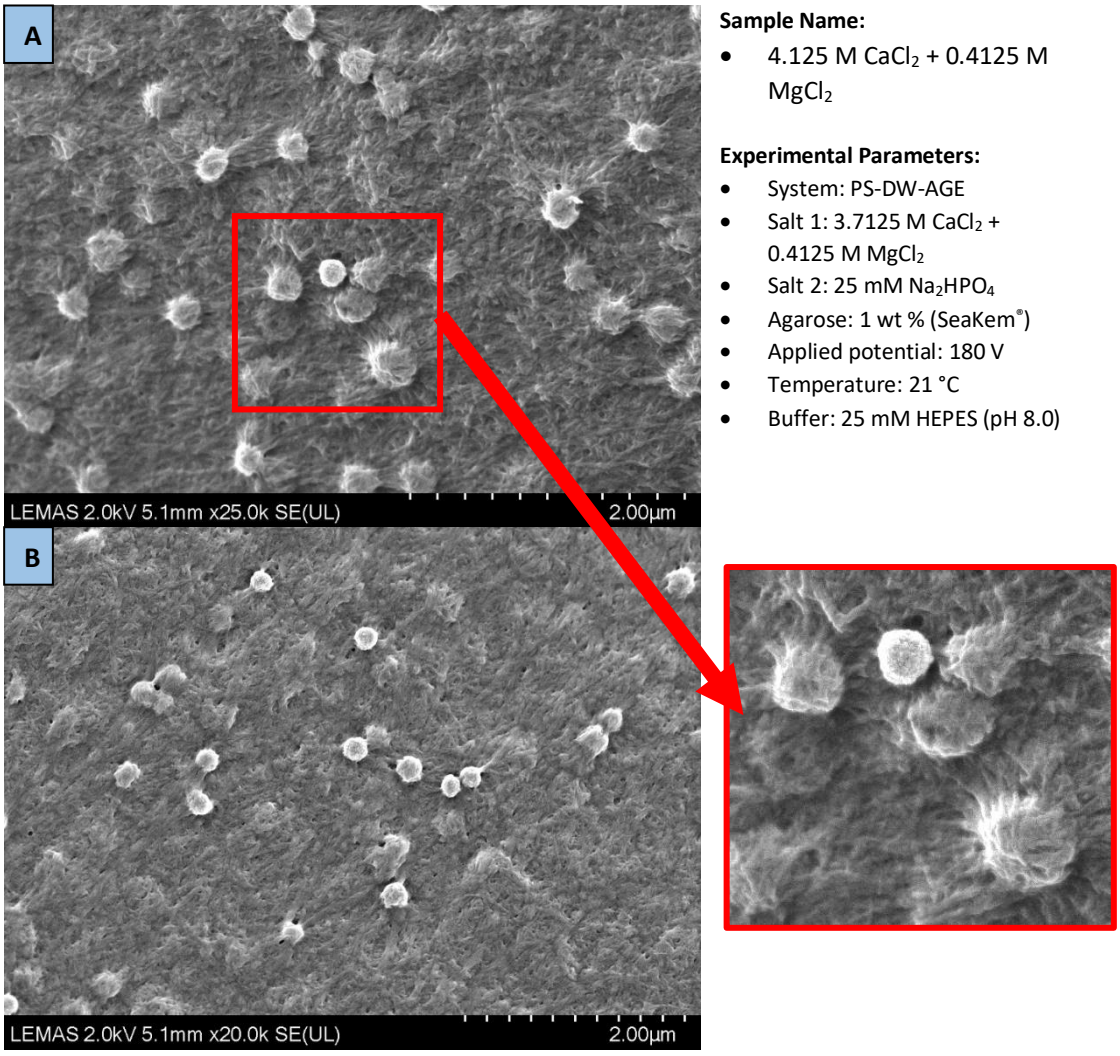


Figure 4.18. Agarose fragments with Mg2+-doped CaP particles from the Mg2+-doped CaP sample. Red square indicates magnified area.

The particle diameter histograms for the 4.125 M $CaCl_2$ and 3.75 M $MgCl_2$ samples (as shown in Figure 4.8 and Figure 4.13 respectively were plotted alongside that of the 3.7125 M $CaCl_2$ + 0.4125 M $MgCl_2$ sample in Figure 4.19 below. MgP particles in the 3.75 M $MgCl_2$ sample show far smaller primary and secondary peaks than CaP particles in the 4.125 M $CaCl_2$ sample. Particles from the 3.7125 M $CaCl_2$ + 0.4125 M $MgCl_2$ have a similar primary peak to the 3.75 $MgCl_2$ sample.

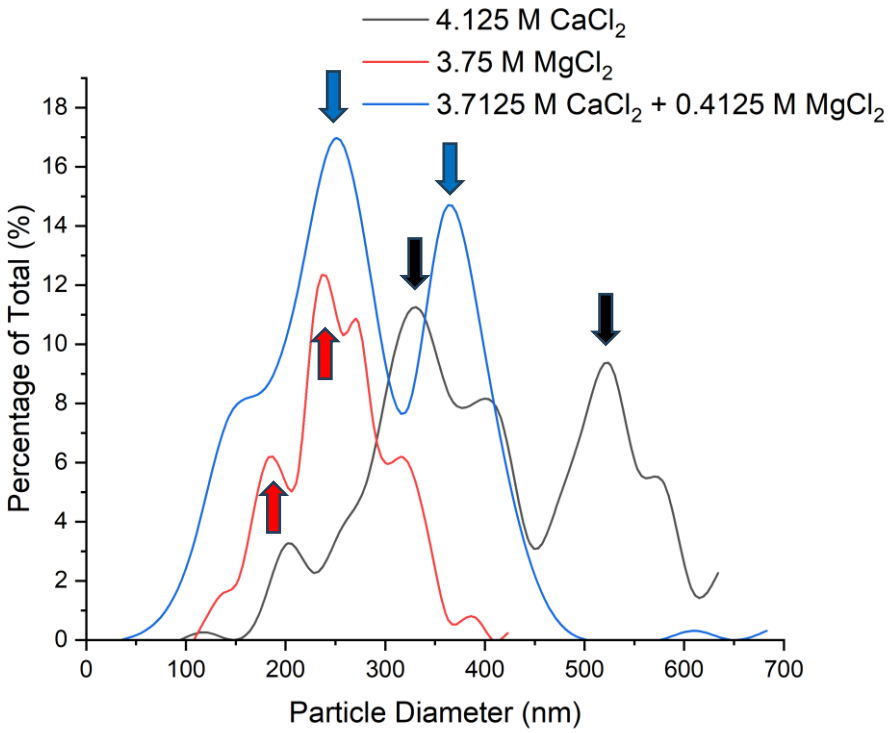


Figure 4.19. Histogram of particle measurements from the 4.125 M CaCl2, 3.75 M MgCl2, and 3.7125 M CaCl2 + 0.4125 M MgCl2 samples. Arrows indicate primary and secondary peaks of each sample.

Peak particle diameters extracted from Figure Figure 4.19 are displayed in Figure 4.20 below. The use of $MgCl_2$ to dope the $CaCl_2$ loading salt reduces the primary and secondary peaks of the 3.7125 M $CaCl_2$ + 0.4125 M $MgCl_2$ far below that of the 4.125 M $CaCl_2$ sample. Specifically, the primary peak is reduced by 75 nm and the secondary peak is reduced by 175 nm. This could either result from Mg^{2+} ions disrupting the lattice of CaP particles and subsequently restraining their growth, or that both CaP and MgP particle species precipitate and thus particle size measurements take both into account.

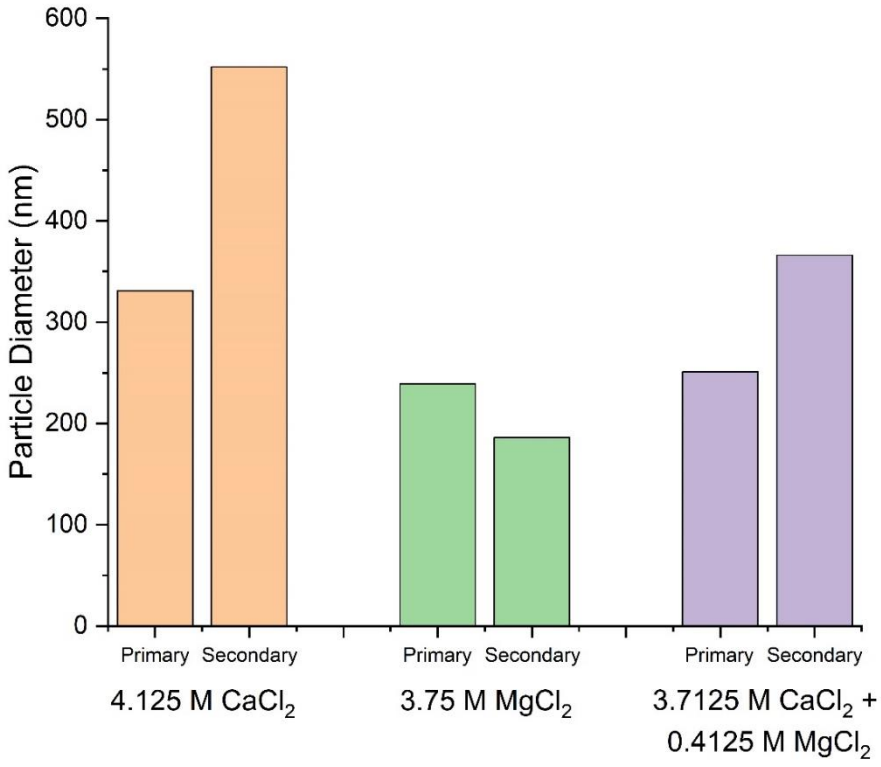


Figure 4.20. Primary and secondary peak particle diameters for 4.125 M CaCl2, 3.75 M MgCl2, and 3.7125 M CaCl2 + 0.4125 MgCl2 samples.

To summarise the effect of salt concentration and doping on particle diameters, particle diameters are linearly proportional to salt concentration within Na_2HPO_4 concentration range used. CaP particle diameters are more sensitive to changes in $CaCl_2$ concentration than MgP particle diameters are to changes in $MgCl_2$ concentrations. The use of $MgCl_2$ as a dopant for $CaCl_2$ appears to reduce both primary and secondary modal peaks.

Mean particle diameters of CaP and MgP particles from $CaCl_2$ and $MgCl_2$ samples respectively at different salt concentrations are plotted in Figure 4.21 below. For both CaP and MgP particles, there is an exponential trend between particle diameter and salt concentration, where trend lines have an $R^2 \geq 0.99$. Trendlines for both CaP and MgP particles were fit using Equation 4.1:

$$y = Ae^{\frac{x}{t}} + y_0 \quad 4.1$$

Where A is 1.65 and 96.7 for CaP and MgP particles respectively, whilst t is 0.82 and 3.86 for CaP and MgP particles respectively.

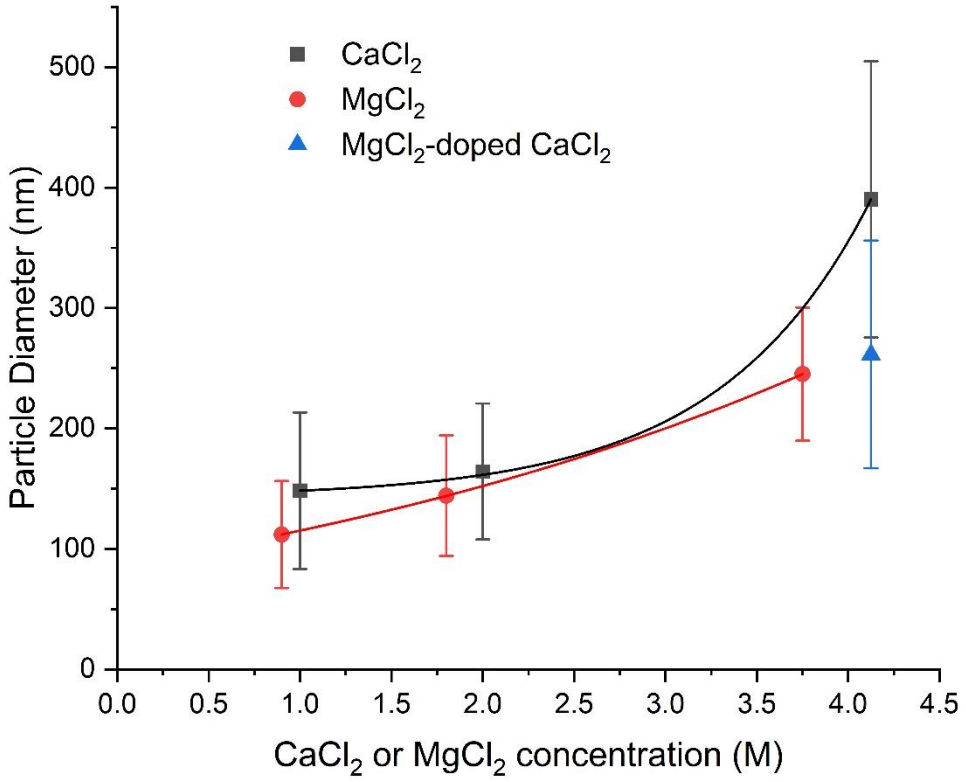


Figure 4.21. Mean CaP and MgP particle diameters plotted against respective salt concentration. Error bars indicate standard deviation.

Due to the exponential relationship between CaP particle diameters and $CaCl_2$ concentration, CaP particles are much more sensitive to changes in $CaCl_2$ concentration above 2 M. In contrast, the exponential relationship between MgP particles and $MgCl_2$ diameter is more linear in the $MgCl_2$ concentration range used. This difference between CaP and MgP particle sensitivity to salt concentration is thought to result from the far lower solubility of CaP species and therefore

the greater supersaturation toward CaP than MgP at the same salt concentration. In a homogenous system this would lead to a greater nucleation rate, but since this is a heterogeneous system in which growth rate also increases with supersaturation; hence increasing particle size with salt concentration. For both CaP and MgP particle diameters, the standard deviation of datasets decreases with salt concentration, indicating that particle size distributions are more tightly packed at lower salt concentrations.

The Mg^{2+}-doped $CaCl_2$ sample demonstrates a mean particle size of 261 nm ± 94 nm; far lower than that of the 4.125 M $CaCl_2$ sample (390 ± 115 nm). As previously discussed, this could result from either the interference of Mg^{2+} ions with the growth of CaP particles or the presence of both CaP and MgP particles in the sample. Regardless, the use of Mg^{2+}-doped $CaCl_2$ shifts the mean particle size that fits well with the exponential relationship between $MgCl_2$ concentration and particle size.

4.4.2 Particle Synthesis via Varied Agarose Concentration

CaP and MgP particles were synthesised using the PS-DW-AGE system at agarose concentrations between 1 – 5 wt %. Figure 4.22 shows typical images of CaP particles at 1, 2, 3, 4 and 5 wt % agarose. For this sample set, the 1 wt % agarose sample is the same as the 4.125 M $CaCl_2$ sample used in Figure 4.8. CaP particles are highly spherical at 1 wt % agarose but reduce in regularity toward greater agarose concentrations. Though Figure 4.22 (A) and (B) show lower magnification images for 1 and 2 wt % agarose samples respectively, CaP particles in these samples appeared smooth compared to the much rougher and often nodular surface of particles in the 4 and 5 wt % agarose samples in Figure 4.22 (D) and (E). Particles were more densely packed together at lower agarose concentrations.

Histograms for CaP particle diameters at agarose concentrations between 1 – 5 wt % are plotted in Figure 4.24. Particle diameters generally appear to reduce with an increasing agarose concentration and their size distributions also tend to narrow with increasing agarose concentration. All samples do demonstrate a clear multimodality, whilst the 4 wt % sample is nearly unimodal but has a small secondary peak close to 200 – 250 nm. Primary and secondary peaks for each sample are indicated by arrows of the same colour. The values for primary and secondary peaks have been plotted in Figure 4.23, where one can observe a reduction in primary modal peak of CaP particle diameter as agarose concentration increases from 1 to 5 wt %, and secondary peaks continue to decrease up to 4 wt % agarose.

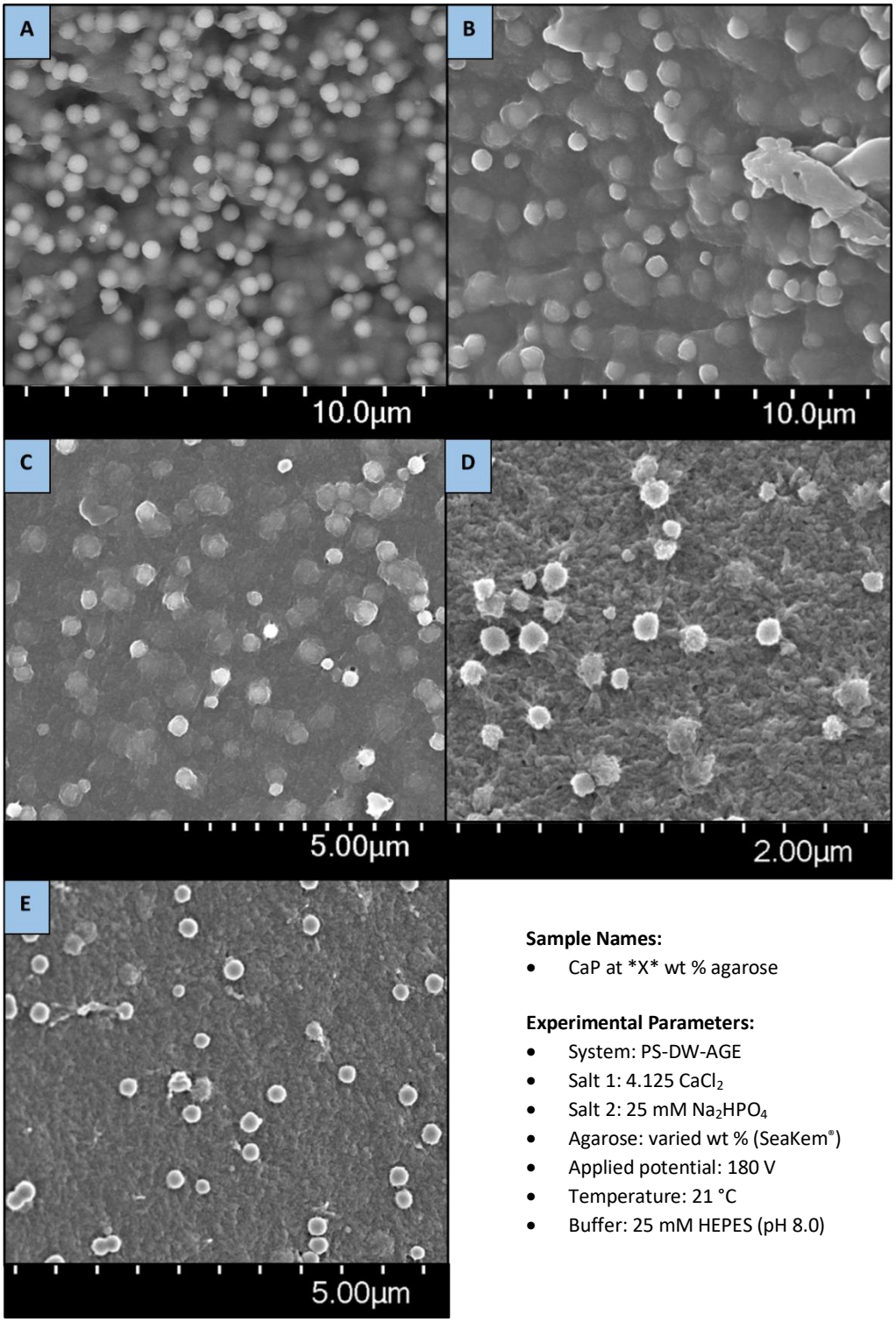


Figure 4.22. Typical images of CaP particles on agarose fragments at different agarose concentrations. (A) 1 wt % agarose; (B) 2 wt % agarose; (C) 3 wt % agarose; (D) 4 wt % agarose, and (E) 5 wt % agarose. *X* denotes the agarose wt % for the respective sample name.

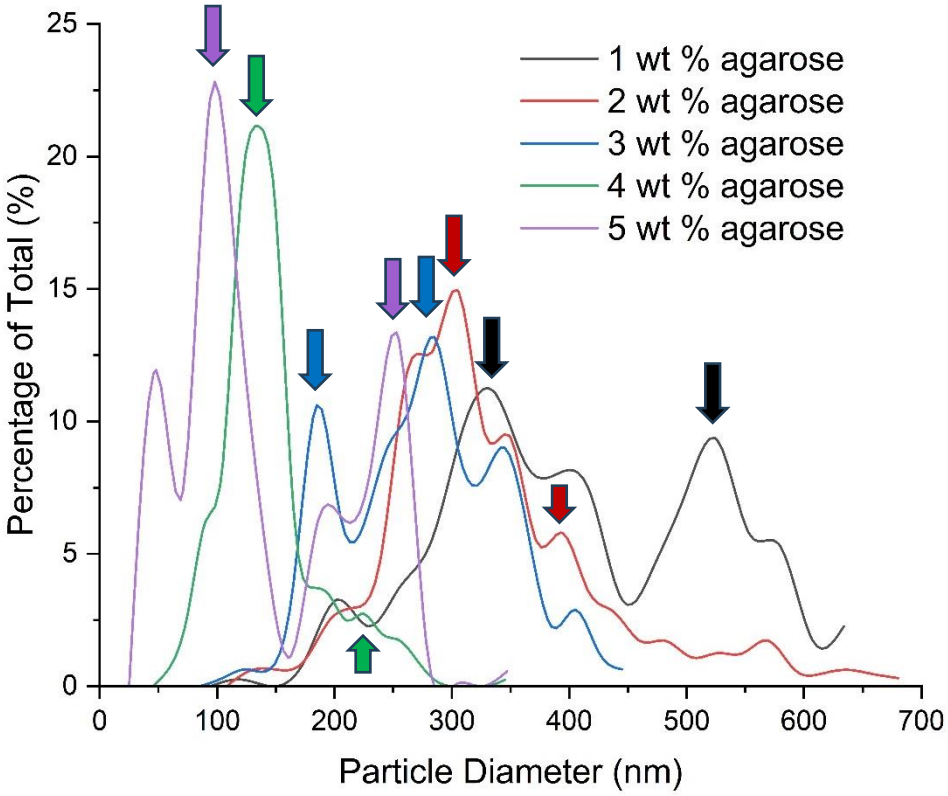


Figure 4.24. Histogram of CaP particle measurements from the 1, 2, 3, 4, and 5 wt % agarose samples. Arrows indicate the primary and secondary modal peaks for samples of the same colour.

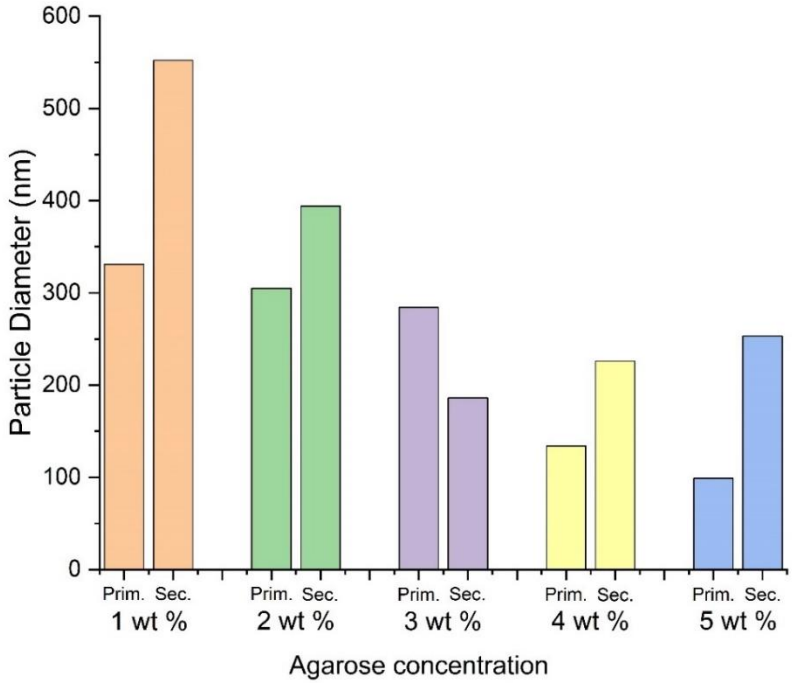


Figure 4.23. Primary and secondary modal peak particle diameters for 1, 2, 3, 4, and 5 wt % agarose samples.

Figure 4.25 shows typical images of MgP particles at 1, 2, 3, 4 and 5 wt % agarose. For this sample set, 1 wt % agarose samples are the same as the 3.75 M $MgCl_2$ sample (Figure 4.13). As with CaP particles, MgP particles reduce in regularity as agarose concentration increases, with MgP particles appearing mostly spherical at 1 wt % agarose and being more irregular at 4 and 5 wt % agarose. MgP particle packing density also reduces with an increasing agarose concentration. Particles appear to decrease in overall size with increasing agarose concentration, but – unlike CaP samples – individual samples present particles of similar sizes and therefore appear to be more unimodal.

Histograms of MgP particle diameters between 1 – 5 wt % agarose are plotted in Figure 4.26 where arrows indicate the positions of primary and secondary modal peaks for samples of the same colour. As with CaP particles, particle size distributions generally reduce in width with increasing agarose concentration. At a glance, these distributions shift from multimodal to bimodal and unimodal, but there remain both primary and secondary peaks in all samples. The values for these were extracted and plotted in Figure 4.27. Both primary and secondary modal peak diameters continue to decrease with an increasing agarose concentration, but the reduction in primary peak diameter slows as agarose concentration increases.

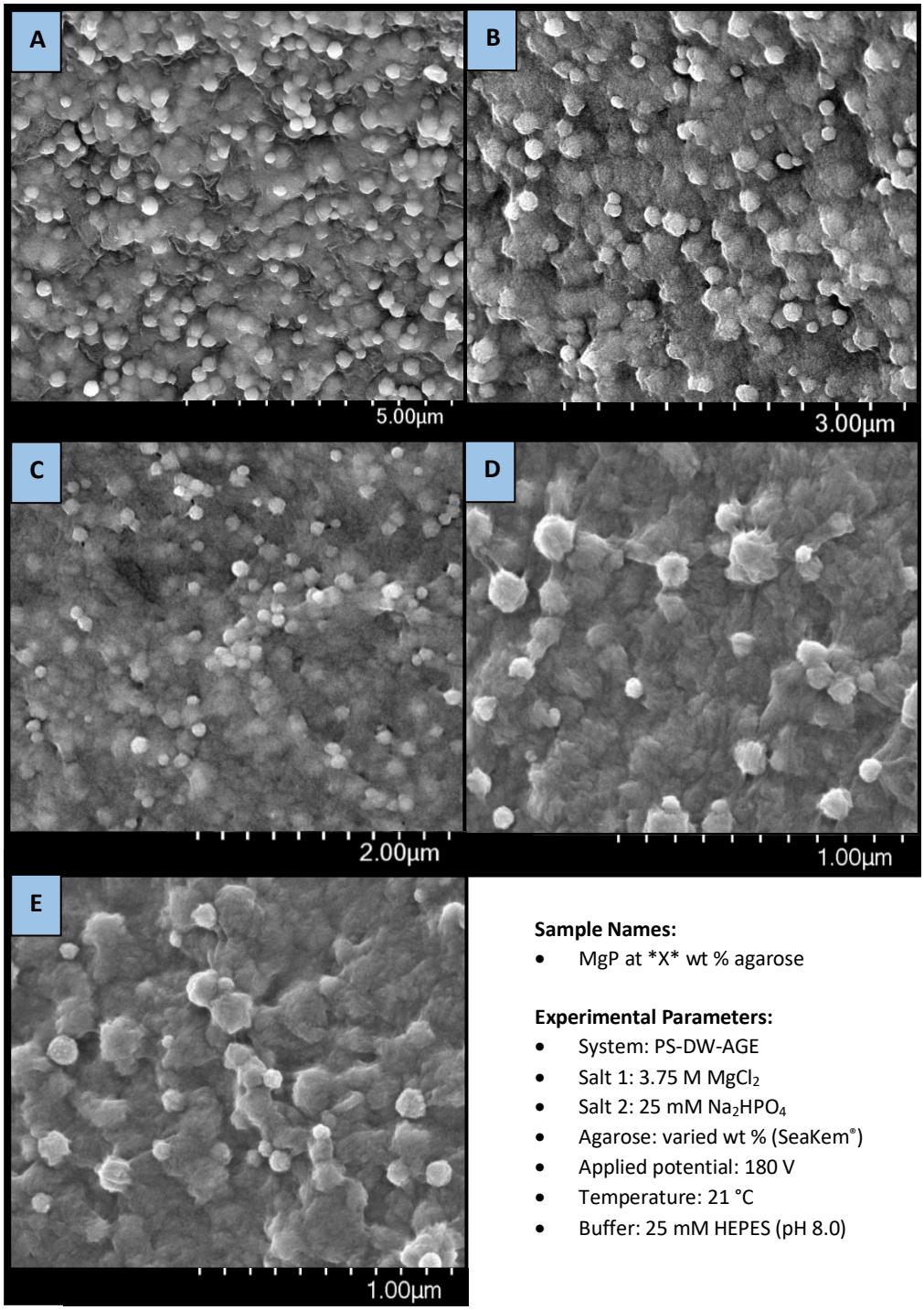


Figure 4.25. Typical images of MgP particles on agarose fragments at different agarose concentrations. (A) 1 wt % agarose; (B) 2 wt % agarose; (C) 3 wt % agarose; (D) 4 wt % agarose, and (E) 5 wt % agarose. *X* denotes the agarose wt % for the respective sample name.

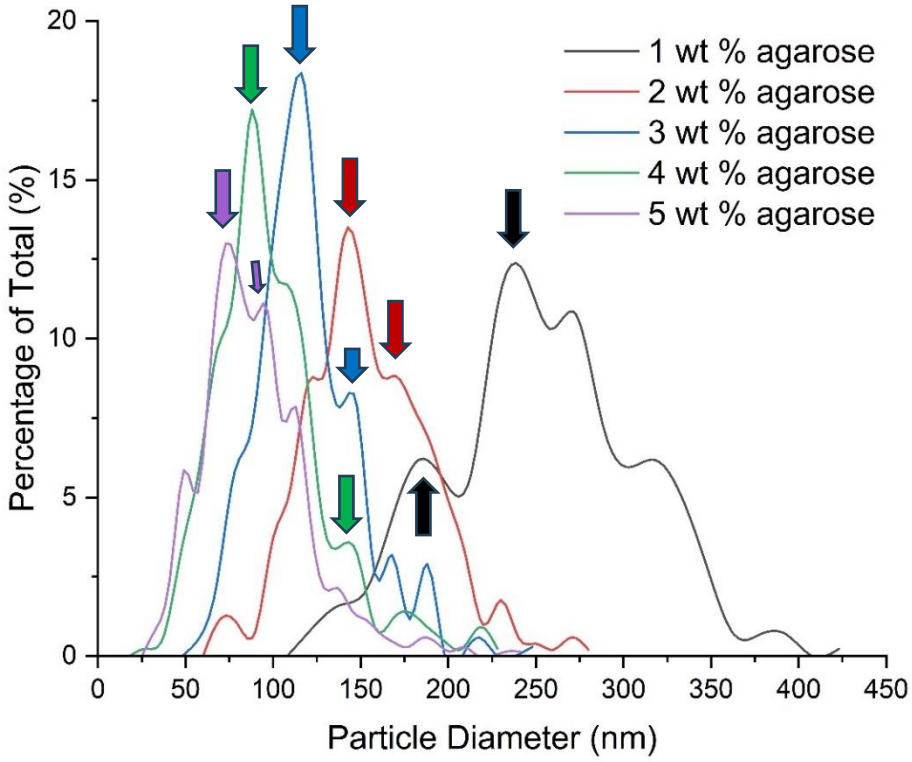


Figure 4.26. Histogram of MgP particle measurements from the 1, 2, 3, 4, and 5 wt % agarose samples. Arrows indicate the primary and secondary modal peak diameter for samples of the same colour.

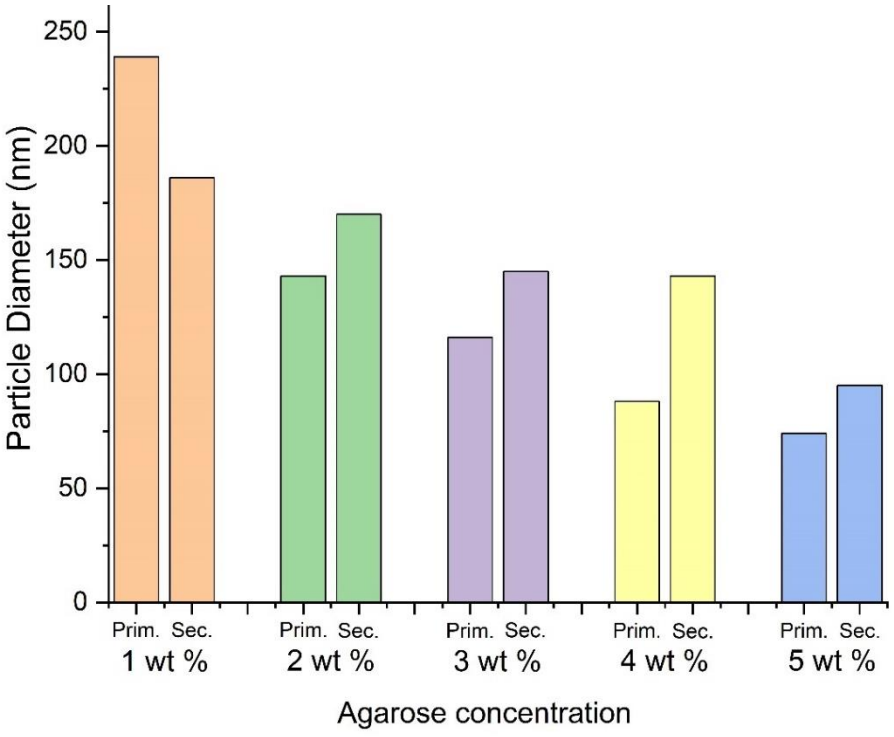


Figure 4.27. Primary and secondary modal peak diameters for 1, 2, 3, 4, and 5 wt % agarose samples.

Mean CaP and MgP particle diameters synthesised at agarose concentrations between 1 – 5 wt % are plotted in Figure 4.28 below. Both particle species decrease in mean diameter with increasing agarose concentration, where mean CaP particle diameters decrease by nearly 350 nm compared to nearly 150 nm for MgP particles across the agarose concentration range. Interestingly, it appears as though MgP particles diameter may be subject to an exponential decay with agarose concentration. This would make sense given that agarose pore size also exponentially decays with agarose concentration (Narayanan et al., 2006). In contrast, the CaP sample set sharply decreases in mean particle diameter from 3 to 4 wt % agarose, the absence of which would have given the CaP sample set a well fitted linear trend. Given the more rapid growth of CaP than MgP due to its greater supersaturation, it could be that CaP particles are able to grow beyond pore sizes and compress the agarose matrix around them.

For both CaP and MgP sample sets, SD values generally decrease with increasing agarose concentration which indicates narrower particle size distributions; as shown in their respective histograms in Figure 4.23 and Figure 4.26.

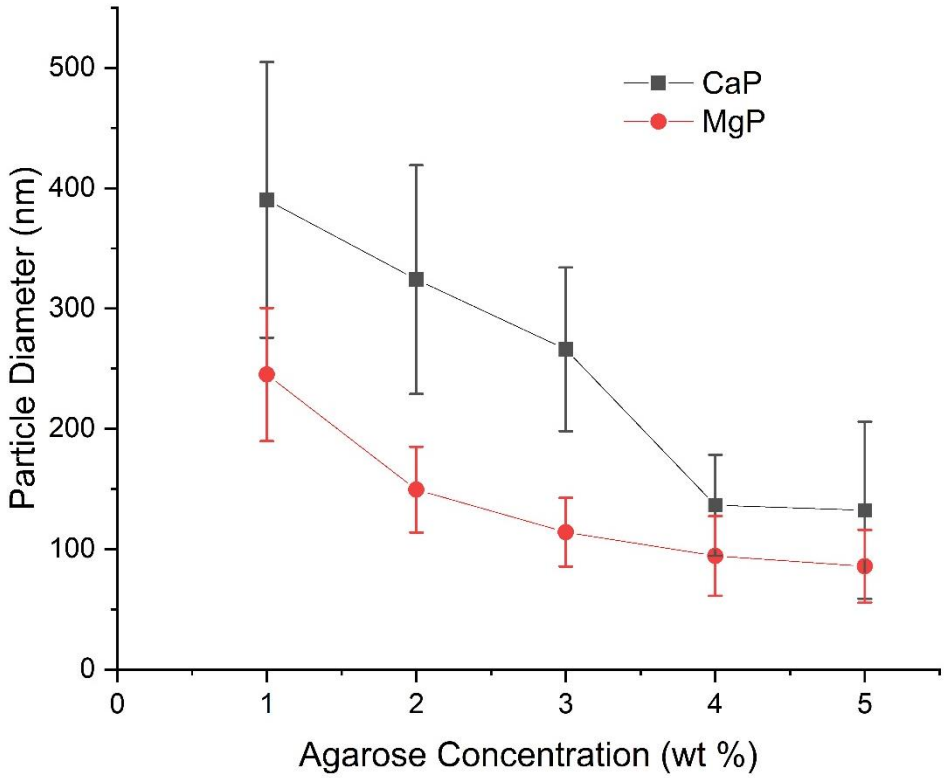


Figure 4.28. Mean (± SD) CaP and MgP particle diameters at agarose concentrations of 1 – 5 wt %.

Plotting mean CaP and MgP particle diameters obtained at 1, 2, and 3 wt % agarose against agarose pore diameters obtained experimentally by Narayanan et al. (2006) results in a linear relationship between particle diameter and agarose concentration, as shown in Figure 4.29 below. Given that Narayanan et al. (2006) determined pore sizes only between 1 – 3 wt % agarose, particle diameters obtained at 4 and 5 wt% are excluded from Figure 4.29. The linear trend line for the CaP and MgP sample sets have $R^2 = 0.96$ and $R^2 = 0.99$ respectively.

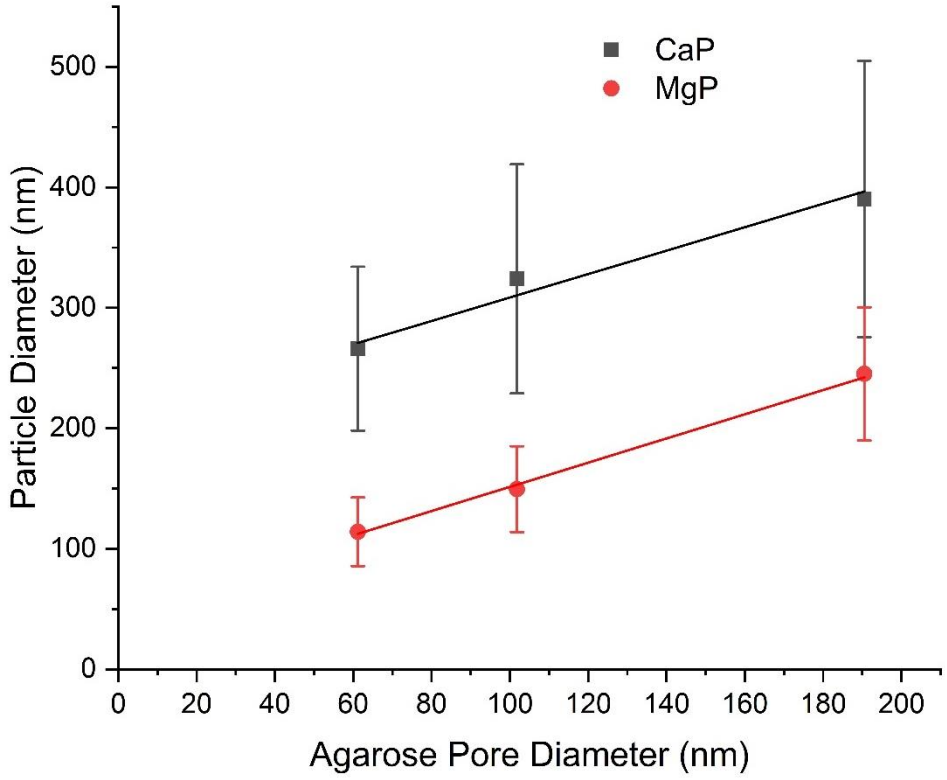


Figure 4.29. Mean CaP and MgP particle diameters plotted against agarose pore diameters experimentally measured by Narayanan et al. (2006). Error bars indicate standard deviation.

4.4.3 Particle Diameter and Agarose Type

CaP and MgP particles were synthesised in SeaKem® and NuSieve™ agarose gel slabs and analysed via SEM. Typical SEM images for both SeaKem® and NuSieve™ samples are shown in Figure 4.30. Both CaP and MgP particles appear smaller in the NuSieve™ samples compared to SeaKem® samples.

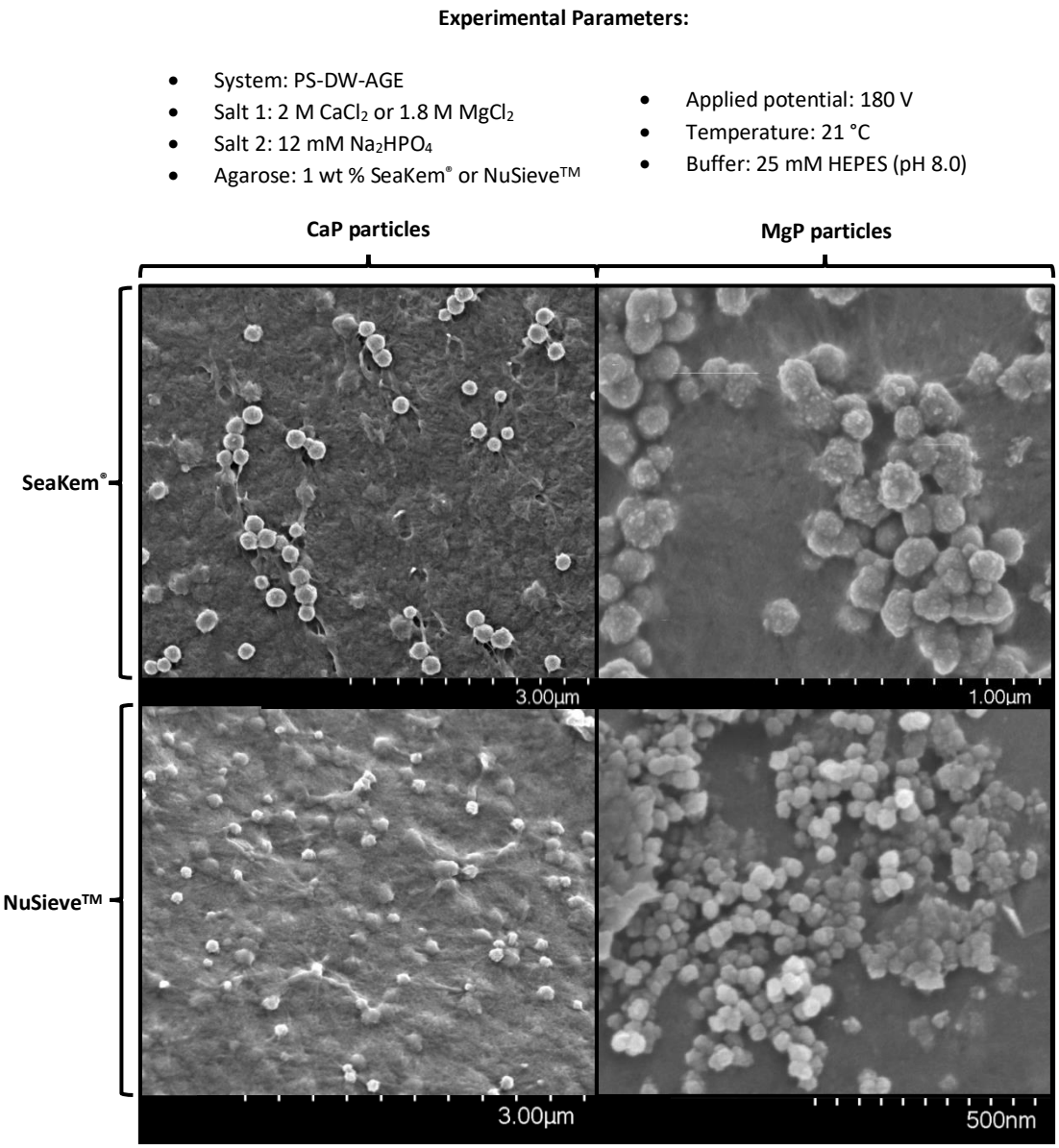


Figure 4.30. Typical SEM images of CaP and MgP particles on agarose fragments synthesised using either NuSieveTM or SeaKem® agarose.

CaP particles are more irregular in the NuSieve™ sample but MgP particles – though much smaller – are far more spherical in the NuSieve™ sample than in the SeaKem® sample. This is

interesting given that smaller particle sizes (regardless of particle species) have thus far been more irregular than larger particles. Besides size, the MgP particles in the SeaKem® sample are nodular in their appearance, which contrasts to NuSieve™ MgP particles that appear monolithic in their structure.

Particle size histograms for all four samples are plotted in Figure 4.31 below. Both CaP and MgP NuSieve™ particle samples present a unimodal size distribution with single modal peaks, which contrasts to CaP and MgP SeaKem® samples which both have primary and secondary modal peaks and relatively wide size distributions. Particle diameters clearly shift toward smaller values for NuSieve™ samples compared to SeaKem® samples of the same particle species.

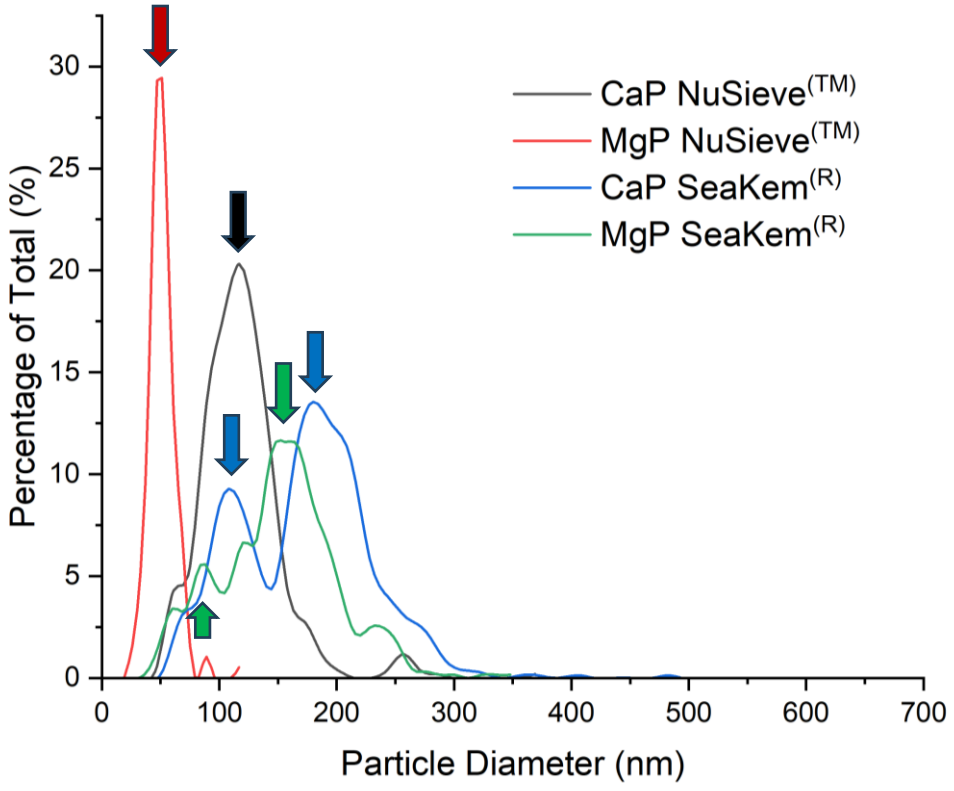


Figure 4.31. Histogram of CaP and MgP particle measurements from NuSieve™ and SeaKem® agarose samples. Arrows indicate the primary and secondary (if applicable) modal peaks for samples of the same colour.

Primary and secondary (if available) modal peaks were extracted from Figure 4.31 and are plotted in Figure 4.32. The primary modal peak diameter of CaP NuSieve™ is approximately 60 nm smaller than that of CaP SeaKem®, whilst the primary modal peak diameter of MgP NuSieve™ is nearly 110 nm smaller than that of MgP SeaKem®.

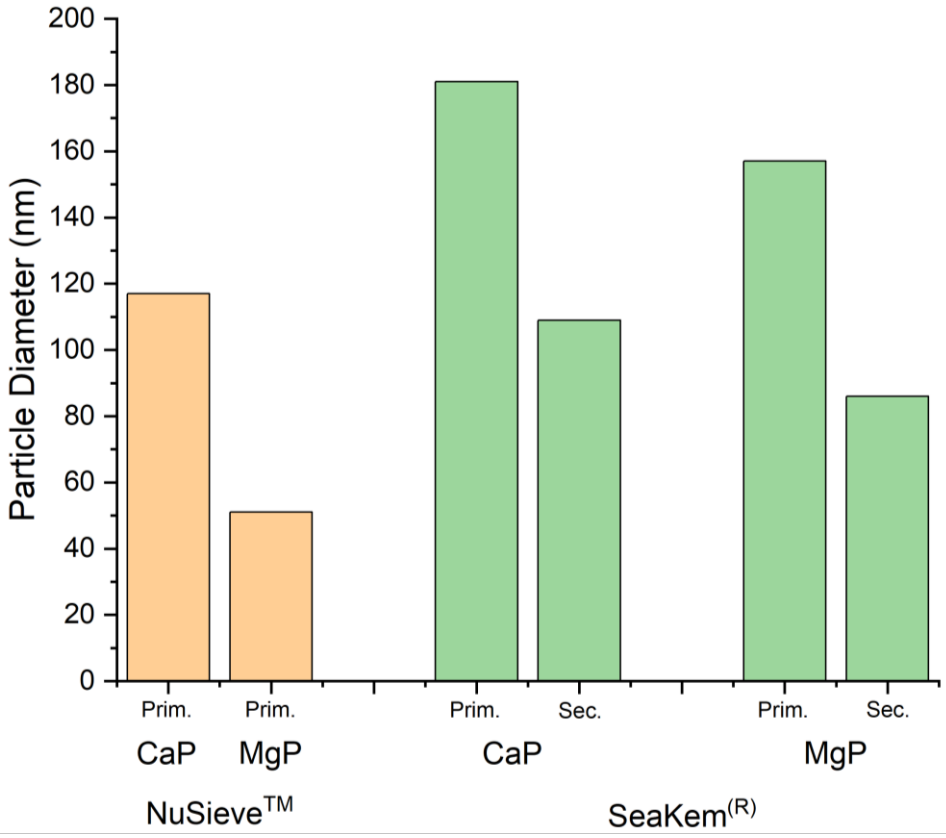


Figure 4.32. Primary and secondary modal peak particle diameters for CaP and MgP particles synthesised in either NuSieveTM or SeaKem® agarose.

Mean (± SD) diameters for CaP and MgP particles from NuSieve™ and SeaKem® samples are plotted in Figure 4.33. The particle diameter reducing effect of NuSieve™ is most evident for MgP samples, where the mean particle diameter of MgP NuSieve™ is approximately 90 nm smaller than that of MgP SeaKem™, whilst the difference between CaP NuSieve™ and CaP SeaKem® is only 50 nm. NuSieve™ samples also present considerably smaller SD values compared to their SeaKem® counterparts, which echoes the tighter particle size distributions observed in Figure 4.31.

This direct comparison of CaP and MgP particle diameters synthesised in either SeaKem® or NuSieve™ demonstrates that the nanoconfinement effects of the NuSieve™ gel are such that mean particle sizes and modal peaks are substantially reduced in size. This contributes to the argument that pDNA/CaP and FBN-pDNA/CaP cryogels produced via the PS-SW-AGE system had better transfection efficacies due (in part) to smaller particles facilitated by the highly confining NuSieve™ agarose.

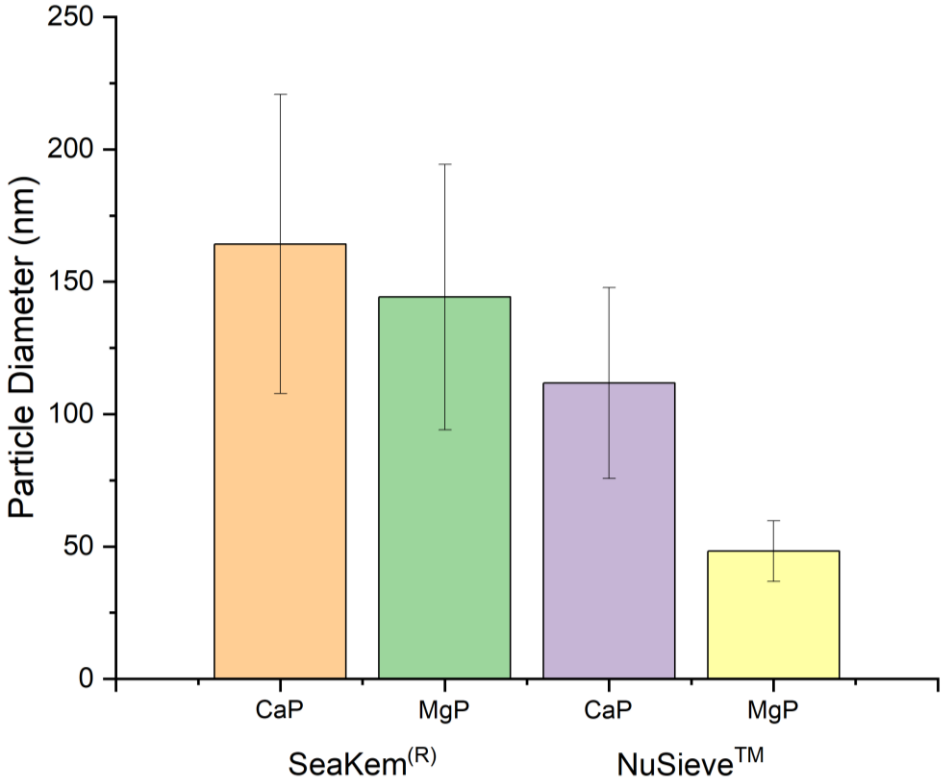


Figure 4.33. Mean (± SD) CaP and MgP particle diameters synthesised in either SeaKem® or NuSieveTM agarose. Error bars indicate standard deviation.

4.4.4 Particle Diameter and Applied Potential

CaP particles were synthesised in separate gel slabs at either 60, 120, or 180 V, to investigate the relationship between particle diameter and applied potential. Figure 4.34 shows typical SEM images of CaP particles synthesised at 60, 120, and 180 V. No differences in morphology or size could be identified between samples, as all three samples featured mostly irregularly shaped particles. The vast majority of particles in each sample appeared to range between 100 – 250 nm.

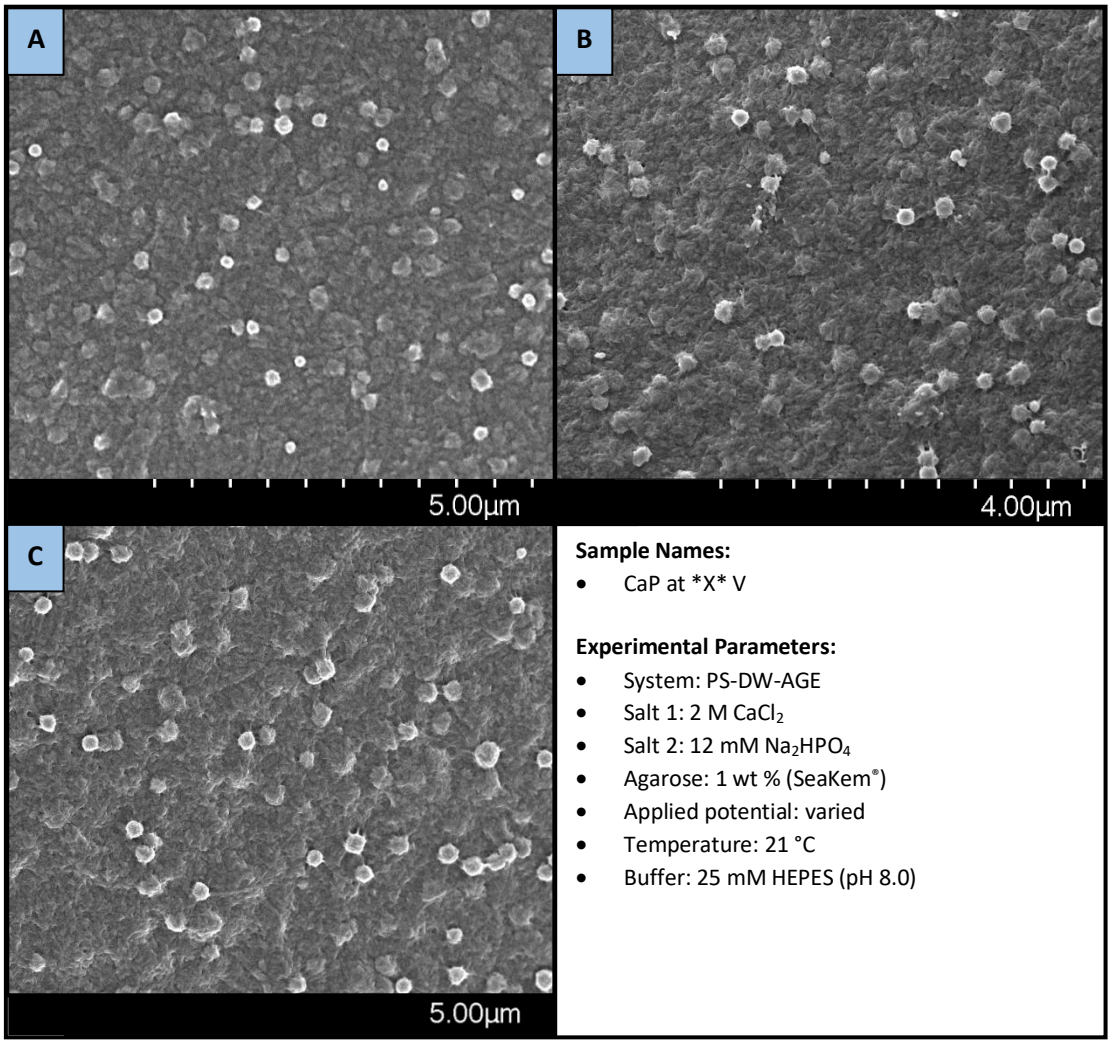


Figure 4.34. Typical SEM images of CaP particles synthesised using varied applied potentials. (A) CaP particles synthesised at 60 V; (B) CaP particles synthesised at 120 V; and (C) CaP particles synthesised at 180 V.

CaP particle diameters were measured and are plotted as histograms in Figure 4.35 below. It is immediately obvious that there is a large degree of overlap between the three samples and peak modal diameters are highly similar. The primary modal peaks of the 120 V and 180 V samples and the secondary modal peak of the 60 V sample are within approximately 10 nm of each other. Further, the primary and secondary modal peaks of the 60 V and 180 V samples respectively are also within (approximately) 10 nm of each other. Notably, the 120 V sample has a far less obvious secondary peak compared to that of the 60 V and 180 V samples.

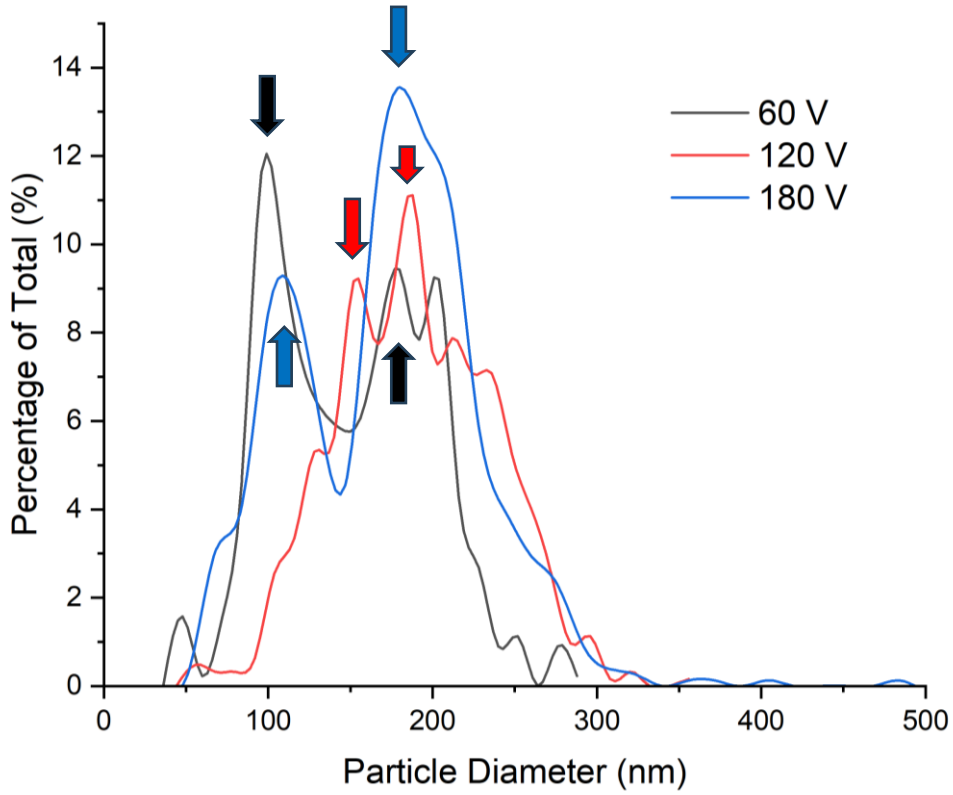


Figure 4.35. Histogram of CaP particle measurements from 60, 120, and 180 V samples. Arrows indicate the primary and secondary (if applicable) modal peaks for samples of the same colour.

Primary and secondary modal peaks for the 60, 120, and 180 V samples were extracted from Figure 4.35 and plotted in Figure 4.36. In addition to morphology, there appears to be no relationship between either primary or secondary modal peak diameter and applied potential. This is reflected in where mean (± SD) CaP particle diameters for the 60, 120, and 180 V samples, which are plotted in Figure 4.37. The largest difference in mean diameters is only 40 nm - between the 60 V and 120 V samples - which boast mean particle diameters of 145 nm ± 48 nm and 183 nm ± 48 nm respectively.

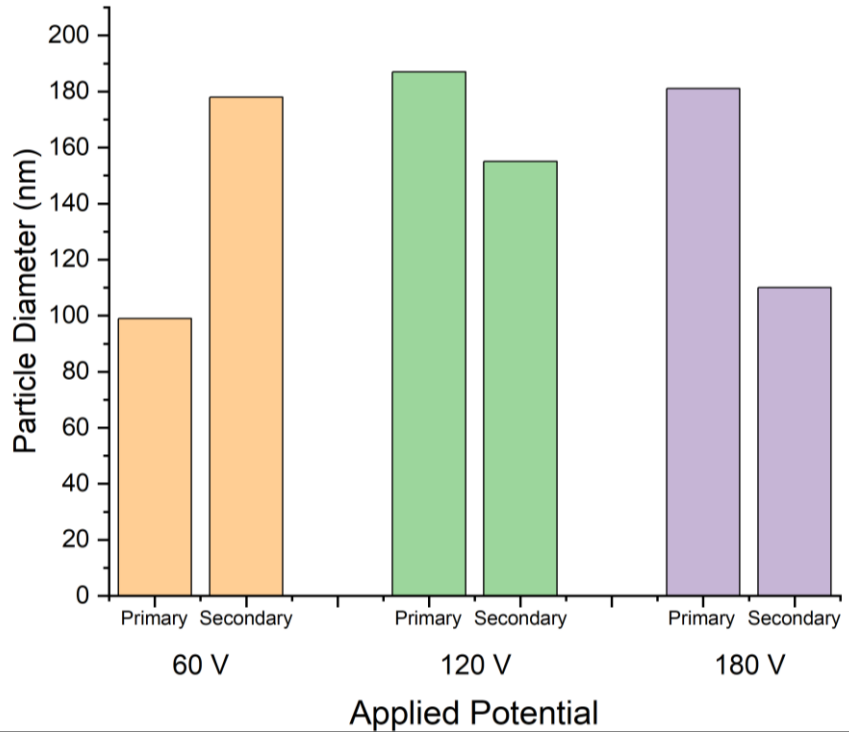


Figure 4.36. Primary and secondary modal peak particle diameters for CaP particles synthesised at applied potentials of 60, 120, and 180 V.

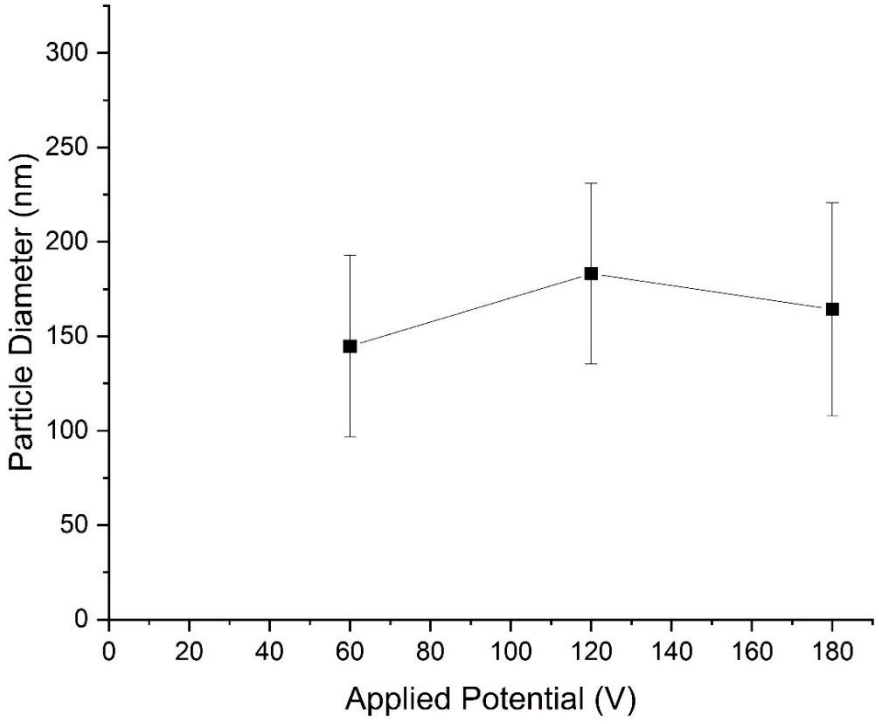


Figure 4.37. Mean (± SD) values of CaP particle diameters synthesised with applied potentials of 60, 120, and 180 V. Error bars indicate standard deviation.

4.4.5 Particle Diameter and Temperature

CaP and MgP particles were synthesised at temperatures of 4, 21, or 42 °C and prepared for SEM analysis. Note that the 2 M $CaCl_2$ and 1.8 $MgCl_2$ samples from Figure 4.9 and Figure 4.14 respectively were used for 21 °C samples in this sample set. Figure 4.38 shows typical SEM images of CaP particles synthesised at each of these temperatures. It is immediately obvious there are morphological differences of CaP particles between these samples. Firstly, the CaP 4 °C sample in Figure 4.38 (A) has a mixture of large (> 300 nm) and small (< 150 nm) particles, which present a nodular surface topography regardless of size. CaP particles synthesised at 21 °C, shown in Figure 4.38 (B), are more irregular and of the order of 200 nm in diameter.

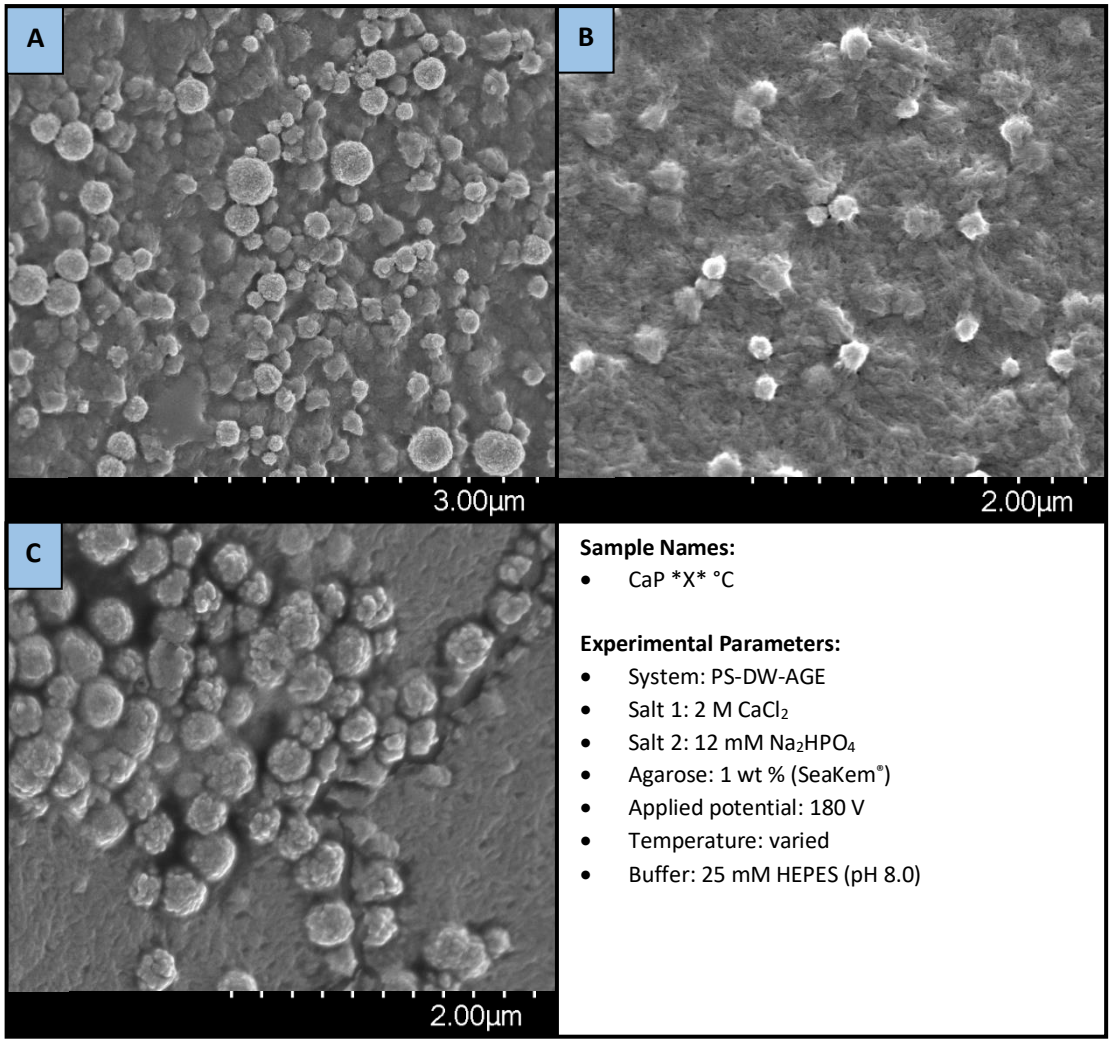


Figure 4.38. Typical SEM images of CaP particles synthesised at various temperatures. (A) CaP particles synthesised at 4 °C; (B) CaP particles synthesised at 21 °C; and (C) CaP particles synthesised at 42 °C.

Meanwhile, particles in the CaP 42 °C sample, shown in Figure 4.38 (C), are closer to 300 nm and display particles with surfaces comprising of 50 nm clusters, which are far larger than the nodules that particles in the CaP 4 °C sample are made of. The CaP 4 °C sample showed good stability at high magnification; hence a high magnification image of a CaP particle was acquired (Figure 4.39) to more clearly resolve the nodular surface of a typical particle. Nodules are less than 10 nm in diameter and appear only on particle surfaces, not on the neighbouring fragment, indicating they are not simply a product of the fine-grained iridium coating.

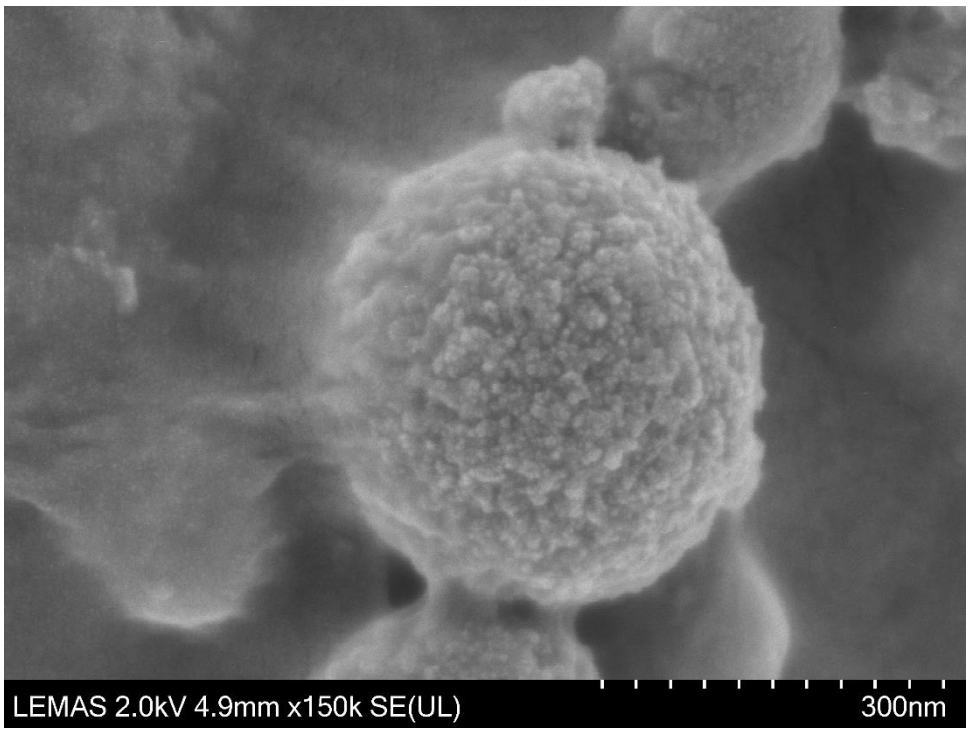


Figure 4.39. High magnification SEM images of a CaP particle synthesised at 4 °C.

CaP particle diameters were measured for each sample and have been plotted as histograms in Figure 4.40. The three samples display a size distribution mostly between 50 nm and 500 nm but exhibit different modalities. The CaP 4 °C sample size distribution is contained almost entirely under one primary peak at 215 nm, whilst the CaP 21 °C sample is more obviously bimodal with a primary and secondary peak at 181 nm and 110 nm respectively. CaP 42 °C presents a trimodal distribution with primary, secondary and tertiary peaks at 267, 93, and 156 nm respectively. Therefore, there is a tendency of samples to increase in modality as temperature increases.

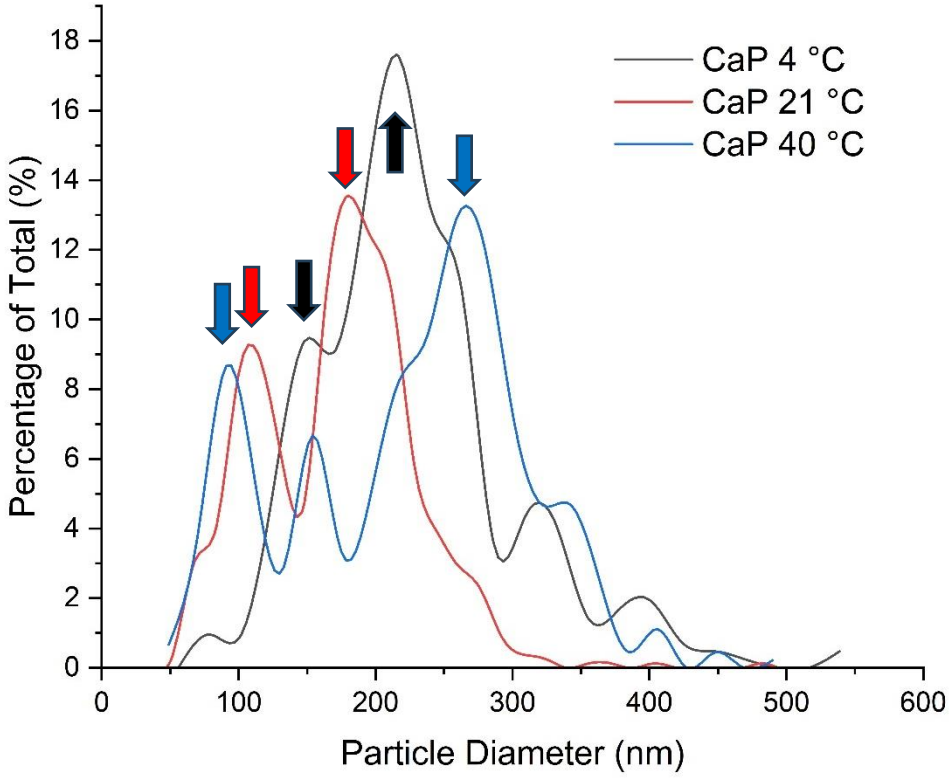


Figure 4.40. Histogram of CaP particle measurements from 4, 21 and 42 °C samples. Arrows indicate the primary and secondary (if applicable) modal peaks for samples of the same colour.

MgP particles were also synthesised at 4, 21, and 42 °C, but no MgP particles were observed in the 4 °C sample. Consequently, only particles from the MgP 21 °C and MgP 42 °C were imaged and measured. Figure 4.41 shows typical SEM images of MgP particles from these two samples. As shown was previously shown in Figure 4.14, the MgP 21 °C sample has a nodular appearance and boasts two particle populations of the order of 100 nm and 200 nm diameters (Figure 4.41 (A) and (B)). The MgP 42 °C sample displays a similar bimodal particle population and nodular appearance, as displayed in (Figure 4.41 (C) and (D)).

MgP particles for both samples were measured and are plotted in Figure 4.42 as histograms. The MgP 42 °C sample is stretched over an approximate 400 nm range whilst the MgP 21 °C has a more conservative range of approximately 300 nm. The primary modal peak for the MgP 21 °C sample overlaps the secondary peak of the MgP 42 °C sample at 160 nm, whilst the secondary modal peak for the MgP 21 °C sample overlaps the primary peak of the MgP 42 °C sample between 90 nm – 100 nm.

Experimental Parameters:

- System: PS-DW-AGE
- Salt 1: 1.8 M $MgCl_2$
- Salt 2: 12 mM Na_2HPO_4
- Agarose: 1 wt % SeaKem®
- Applied potential: 180 V
- Temperature: varied
- Buffer: 25 mM HEPES (pH 8.0)

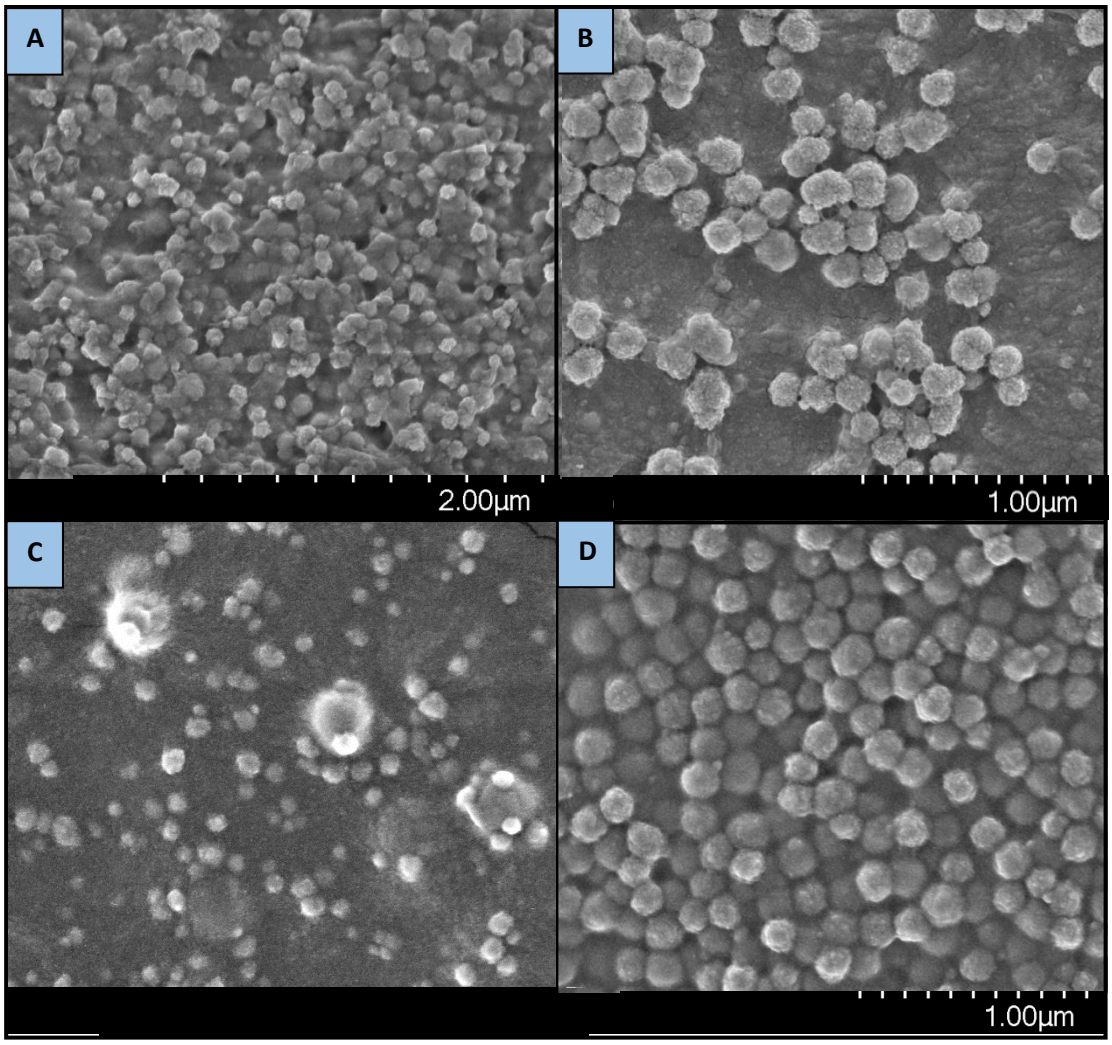


Figure 4.41. Typical SEM images of MgP particles synthesised at various temperatures. (A) and (B) MgP particles synthesised at 21 °C; (C) and (D) MgP particles synthesised at 42 °C.

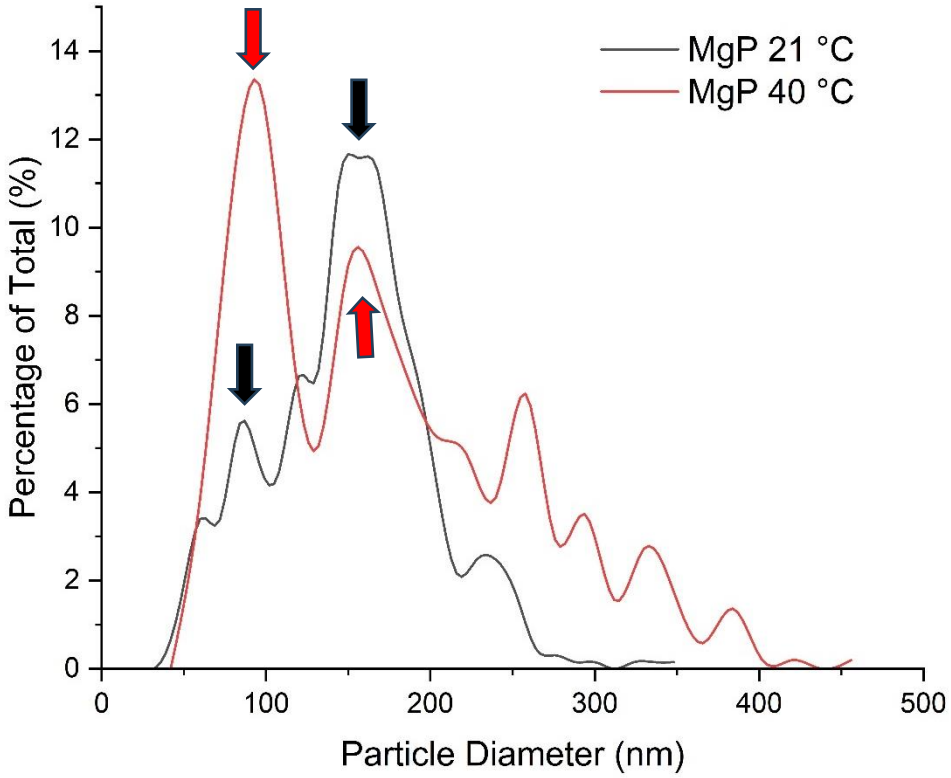


Figure 4.42. Histogram of MgP particle measurements from 4, 21 and 42 °C samples. Arrows indicate the primary and secondary (if applicable) modal peaks for samples of the same colour.

Mean diameters of CaP and MgP particles synthesised at varied temperatures were calculated and are plotted in Figure 4.43 below. Regardless of particle type, all samples display large SD values; a consequence of their wide particle size distributions and multimodal nature. Neither CaP or MgP sample sets demonstrate any discernible relationship between particle diameters and temperature. A larger sample set would need to be used to determine a relationship more accurately between particle size and temperature, spread across a wider temperature range. Interestingly, both CaP 21 °C and MgP 21 °C samples have the smallest mean particle diameters within their respective sets, which suggests that maintaining room temperature conditions is more beneficial to reducing particle size than maintaining other temperatures. Furthermore, the absence of a MgP 4 °C sample limit one from making any useful conclusion from this data regarding an optimal temperature to reduce CaP or MgP particle size.

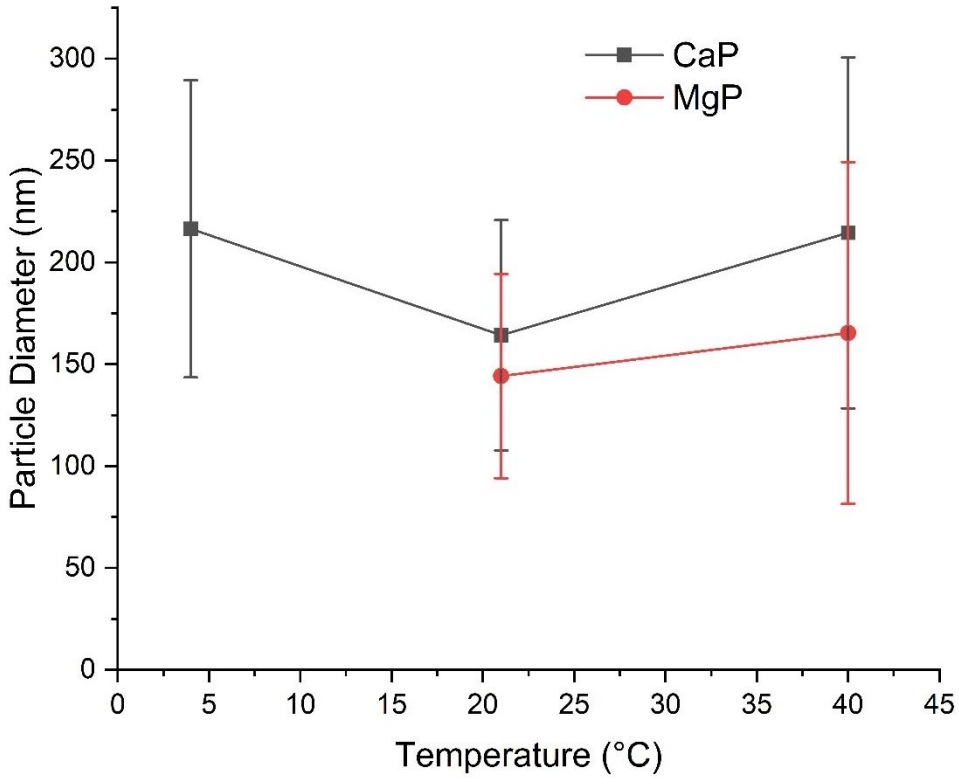
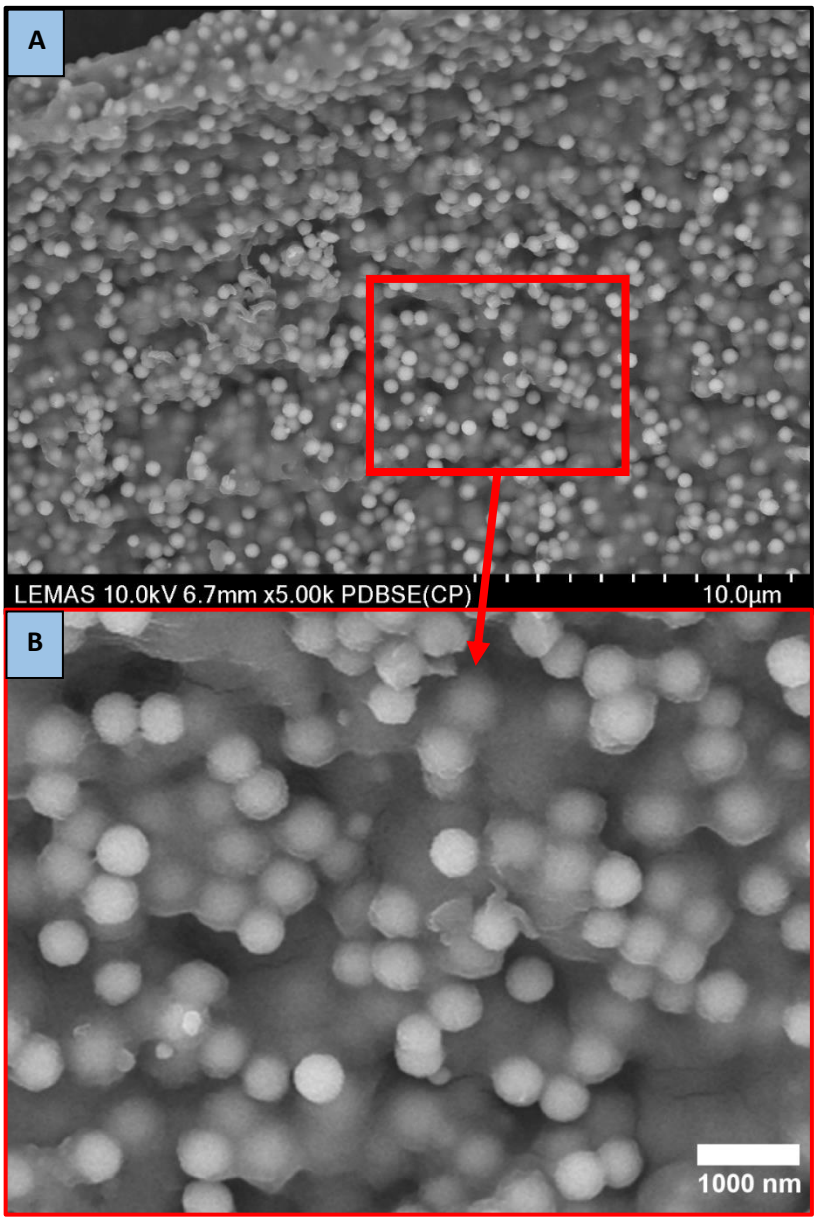


Figure 4.43. Mean (± SD) values of CaP and MgP particle diameters synthesised at varied temperatures.

4.1.1. Particle Diameter and Buffer Type

CaP and MgP particles were synthesised in buffers of either 25 mM HEPES (pH 8.0) or 25 mM Tris-HCl (pH 8.0) to establish what effect the buffer type has on particle size and morphology. Note that CaP HEPES and MgP HEPES samples were previously used for the 4.125 M $CaCl_2$ sample (Figure 4.8) and the CaP 1 wt % sample in Figure 4.22 (A). Figure 4.44 displays CaP particles synthesised using 25 mM HEPES buffer (pH 8.0), where highly spherical CaP particles are observed, ranging mostly between 300 – 500 nm with a small number of sub-300 nm particles.



Sample Name:

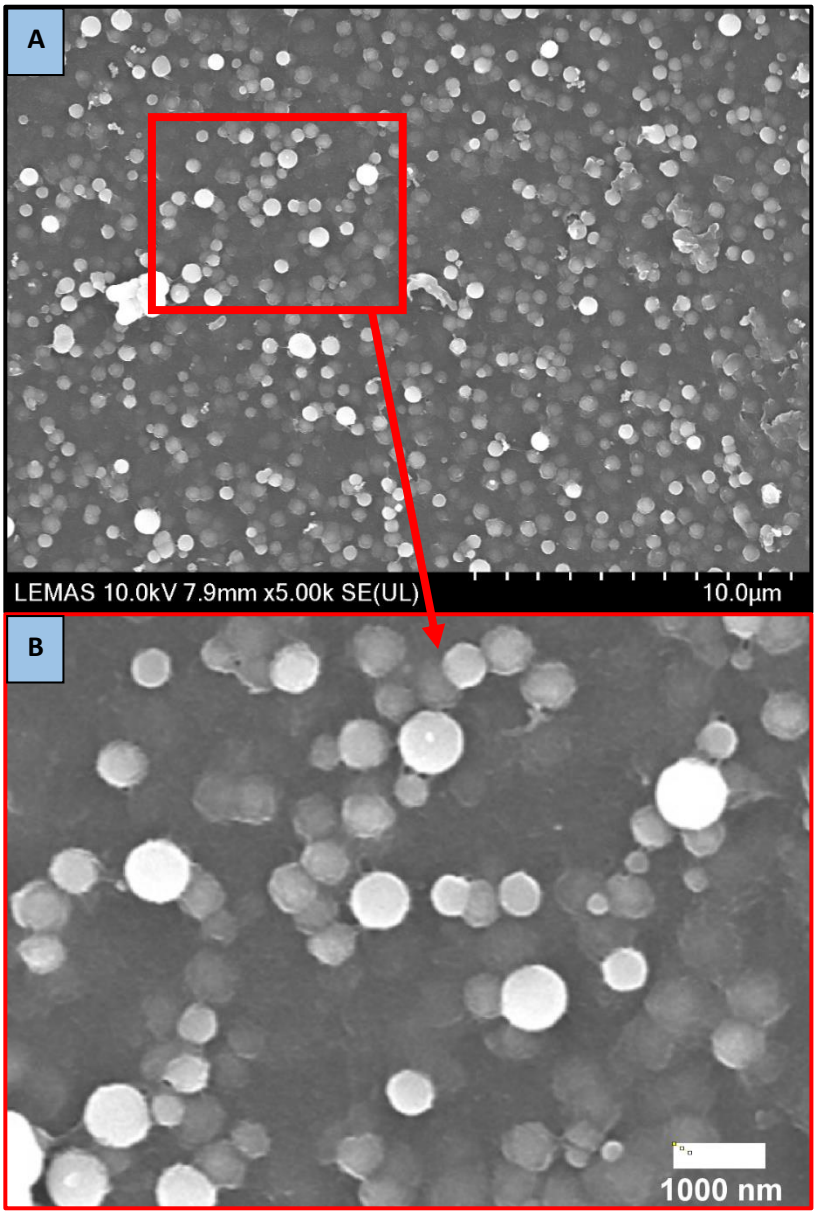
- CaP (25 mM HEPES)

Experimental Parameters:

- System: PS-DW-AGE
- Salt 1: 4.125 M $CaCl_2$
- Salt 2: 25 mM Na_2HPO_4
- Agarose: 1 wt % (SeaKem®)
- Applied potential: 180 V
- Temperature: 21 °C
- Buffer: 25 mM HEPES (pH 8.0)

Figure 4.44. Typical SEM images of CaP particles synthesised using 25 mM HEPES (pH 8.0). (A) Low magnification image of CaP particles and (B) higher magnification image of CaP particles. Red square indicates magnified area.

CaP particles synthesised using 25 mM Tris-HCl are shown in Figure 4.45 below. In this sample, there are several larger particles of the order of 500 nm or slightly larger. Particles here are more spherical than in the CaP HEPES sample, but appear more diverse in their size range which suggests greater modality.



Sample Name:

- CaP (25 mM Tris)

Experimental Parameters:

- System: PS-DW-AGE
- Salt 1: 4.125 M $CaCl_2$
- Salt 2: 25 mM Na_2HPO_4
- Agarose: 1 wt % (SeaKem®)
- Applied potential: 180 V
- Temperature: 21 °C
- Buffer: 25 mM Tris-HCl (pH 8.0)

Figure 4.45. Typical SEM images of CaP particles synthesised using 25 mM Tris-HCl (pH 8.0). (A) Low magnification image of CaP particles and (B) higher magnification image of CaP particles. Red square indicates magnified area.

CaP particles from both samples of buffer type were measured and plotted as histograms in Figure 4.46. There is a high degree of similarity between these histograms in terms of their relative primary and secondary modal peak separation and the width of their distribution. The CaP Tris sample displays primary and secondary modal peaks shifted toward smaller particle diameters compared to the CaP HEPES sample, but neither samples display sub-100 nm particles. The upper range of the CaP HEPES sample terminates abruptly at approximately 640 nm, indicating that a larger sample dataset may extend the range of this sample further. Meanwhile the CaP Tris sample continues to extend above 900 nm due to the presence of very large particles and some agglomerates.

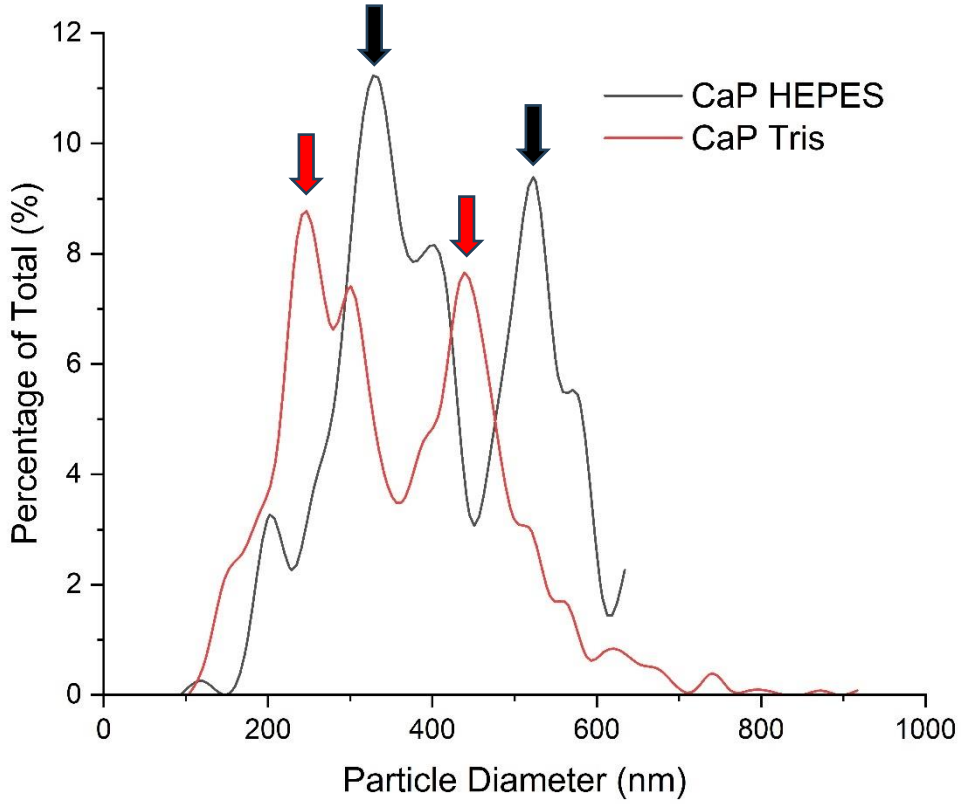


Figure 4.46. Histogram of CaP particle measurements from CaP HEPES and CaP Tris samples. Arrows indicate the primary and secondary (if applicable) modal peaks for samples of the same colour.

As previously mentioned, the separation between primary and secondary peaks is consistent between samples. The CaP Tris sample boasts a smaller primary and secondary peak of 247 nm and 440 nm respectively compared to 330 nm and 523 nm respectively for the CaP HEPES sample. Mean (± SD) values for both samples were calculated and are displayed in Figure 4.47. The CaP Tris sample has a slightly smaller mean of 345 nm ± 126 nm than the CaP HEPES sample

(390 nm ± 115 nm). Collectively, these results indicate that the use of 25 mM Tris-HCl (pH 8.0) facilitates the synthesis of smaller CaP particles in comparison to those synthesised using 25 mM HEPES (pH 8.0).

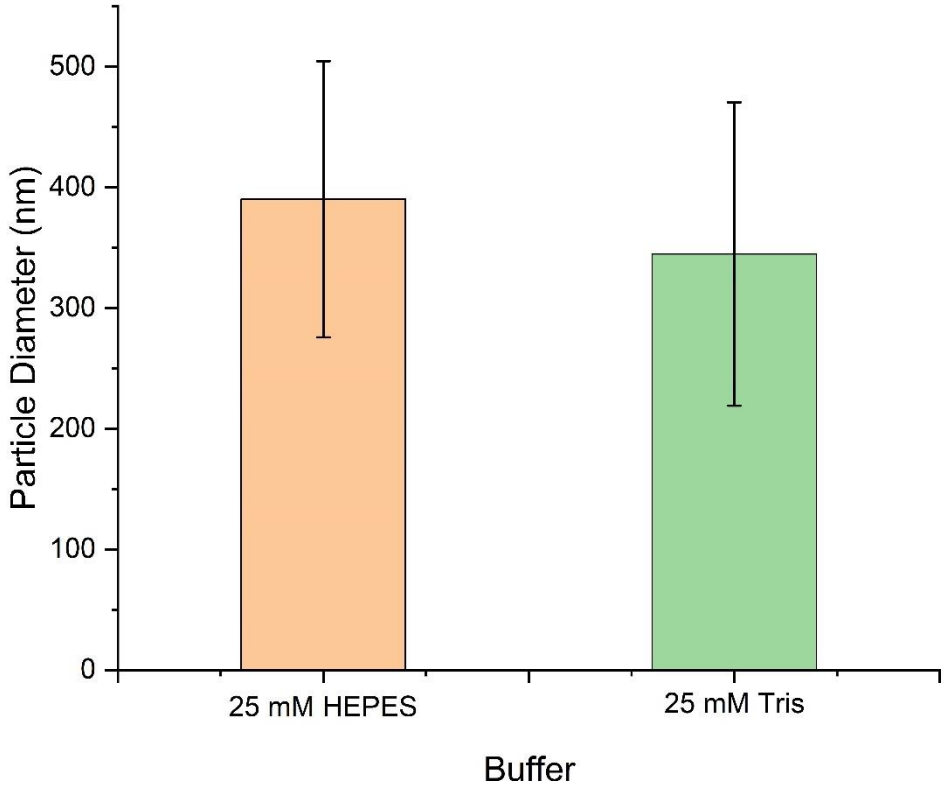


Figure 4.47. Mean (± SD) values of CaP particle diameters synthesised using either HEPES or Tris buffer.

It is interesting to note that the use of Tris-HCl buffer enabled a much faster precipitation of a CaP particle layer and a much larger current through the electrophoresis tank. This may be due to the greater conductivity of the Tris-HCl buffer compared to HEPES which facilitated a greater current through the electrophoresis tank. Faster CaP precipitation in Tris-HCl may therefore result from faster transportation and co-location of Ca^{2+} and $H_xPO_4^{x-3}$ ions within the agarose gel.

4.4.6 Particle Diameter and Combinative Parameters

Before an ideal subset was selected, tests were carried out using a select combination of parameters. In the first test set, the mean particle diameters from the 4.125 M $CaCl_2$ sample (Figure 4.8) and 3.75 M $MgCl_2$ sample (Figure 4.13) were plotted as 'unmodified' groups Figure 4.48 The 2 M $CaCl_2$ (Figure 4.9) and 1.8 M $MgCl_2$ samples (Figure 4.14), CaP 3 wt % agarose (Figure 4.22), and MgP 3 wt % agarose (Figure 4.25) samples were also plotted in Figure 4.48 to compare the effect of independent changes of salt and agarose concentrations with CaP and MgP particle diameters. Finally, the mean particle diameters of CaP particles synthesised using 2 M $CaCl_2$ and 3 wt % agarose, and MgP particles synthesised using 1.8 M $MgCl_2$ and 3 wt % agarose, are both plotted in Figure 4.48. Note that, for all samples plotted in Figure 4.48, a 180 V potential and 21 °C temperature was used.

From Figure 4.48, one can that CaP and MgP mean particle diameters are reduced by the independent use of a reduced salt concentration or increased agarose concentration, whilst the combinative use of these parameter changes reduces both mean particle diameters even further. For CaP particles, a reduction in salt concentration from the 4.125 M $CaCl_2$ in the

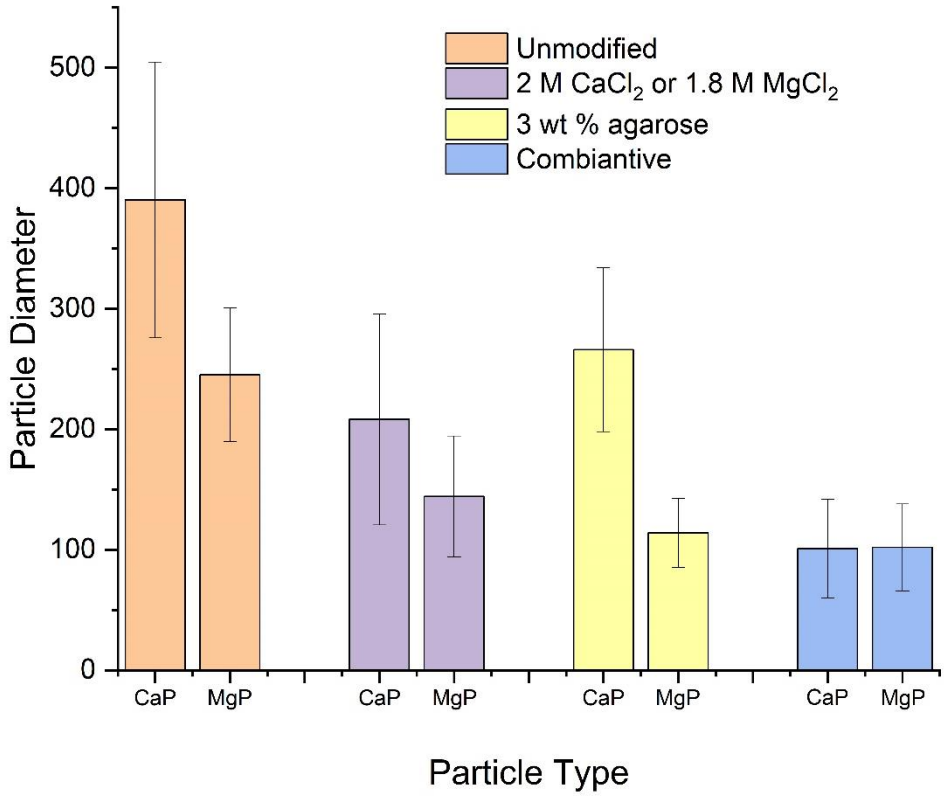


Figure 4.48. Mean (± SD) CaP and MgP particle diameters for unmodified, 2 M CaCl2, 1.8 M MgCl2, CaP 3 wt % agarose, MgP 3 wt %, and combinative samples. Error bars indicate standard deviation.

unmodified group to 2 M $CaCl_2$ demonstrates a greater reduction in mean particle diameter than increasing agarose wt % from 1 to 3 wt %. In contrast a greater reducing effect is observed for MgP particle diameters when increasing agarose concentration from 1 to 3 wt %. The combinative use of parameter changes was more substantial for CaP particles, whilst for MgP particles the use of combinative parameter changes had a more marginal effect due to the effectiveness of higher agarose wt % to reduce MgP particle diameters. Typical images of CaP particles synthesised at 2 M $CaCl_2$ and 3 wt % agarose and MgP particles synthesised at 1.8 $MgCl_2$ and 3 wt % agarose are shown in Figure 4.49 (A) and (C) respectively.

The effect of buffer type on particle diameter using these combinative parameter changes was also investigated. Figure 4.49 displays typical SEM images for CaP and MgP particles synthesised using 2 M $CaCl_2$ or 1.8 M $MgCl_2$ respectively, in 3 wt % agarose, using either HEPES or Tris-HCl buffer. Both CaP and MgP particles synthesised in Tris-HCl appear to have more regular morphologies than HEPES samples, as was found in Figure 4.45. Both CaP and MgP particles synthesised in Tris-HCl exhibit particles with diameters mostly within the range of 200 – 300 nm, in contrast to CaP and MgP particles synthesised in HEPES which are of the order of 100 nm.

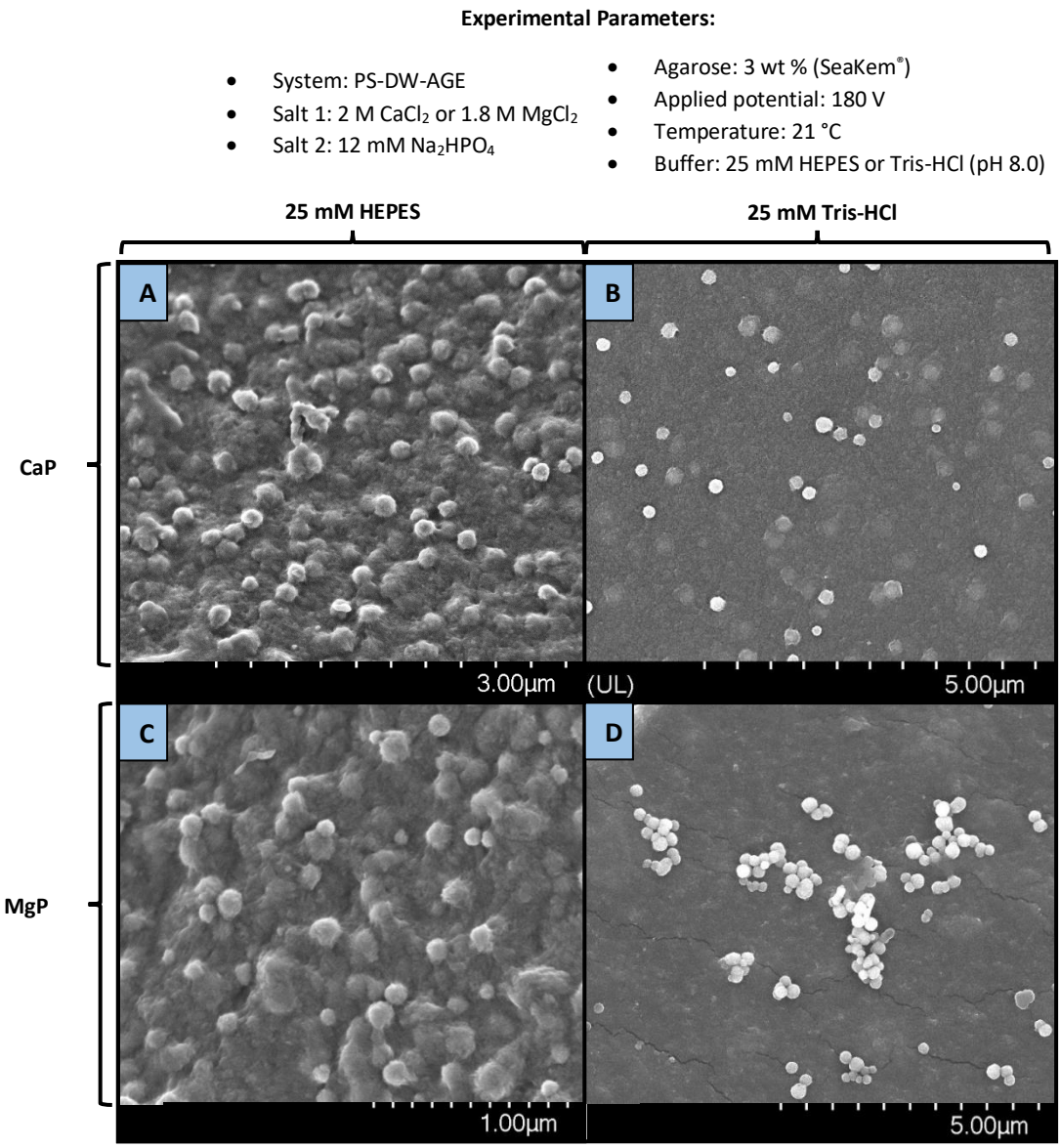


Figure 4.49. Typical SEM images of CaP and MgP particles produced using combinative parameter changes and different buffers. (A) CaP particles synthesised in 25 mM HEPES; (B) CaP particles synthesised in 25 mM Tris-HCl; (C) MgP particles synthesised in 25 mM HEPES; (D) MgP particles synthesised in 25 mM Tris-HCl.

Particles from each of the four samples were measured and plotted as histograms in Figure 4.50. There is a clear separation between samples synthesised using different buffers; where CaP and MgP HEPES samples have primary modal peaks close to 100 nm, compared to approximately 230 nm and 260 nm for the CaP and MgP Tris-HCl samples respectively. Both HEPES samples present size distributions that are mostly contained within the range of 50 – 200 nm, whilst Tris-HCl samples have a wider spread mostly contained within the range of 100 – 350 nm.

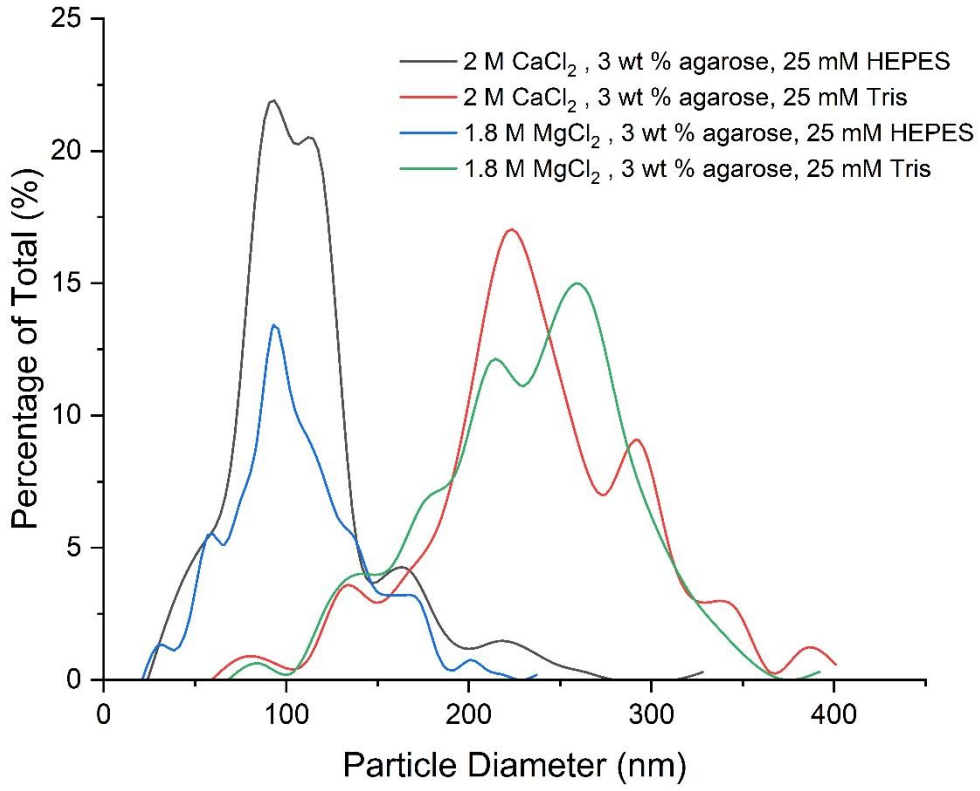


Figure 4.50. Histogram of CaP and MgP particle size measurements comparing combinative parameter changes in different buffers. Arrows indicate the primary and secondary (if applicable) modal peaks for samples of the same colour.

Mean particle diameters were calculated for all four samples and are plotted in Figure 4.51. Again, a clear separation between the HEPES and Tris-HCl samples can be seen. The HEPES samples both have mean diameters of around 100 nm whilst the Tris-HCl samples have mean particle diameters of around 225 nm.

This result is interesting, given that CaP particles synthesised in Tris-HCl were previously shown to be smaller than in HEPES buffer, which was thought to result from greater conductivity in Tris-HCl buffer.

This reduction of CaP and MgP particle diameters using HEPES buffer and combinative parameter changes could result from the Tris-HCl buffer size filtering particles from the zone of precipitation due to the greater current through the tank. Furthermore, precipitates in Tris-HCl buffer form at a much quicker rate than in HEPES buffer, hence particles are subject to electrophoretic transport for a longer period of time in Tris-HCl buffer. It is possible that this effect was not observed in Figure 4.47 due to the use of high salt concentrations that produce particles too large to be transported.

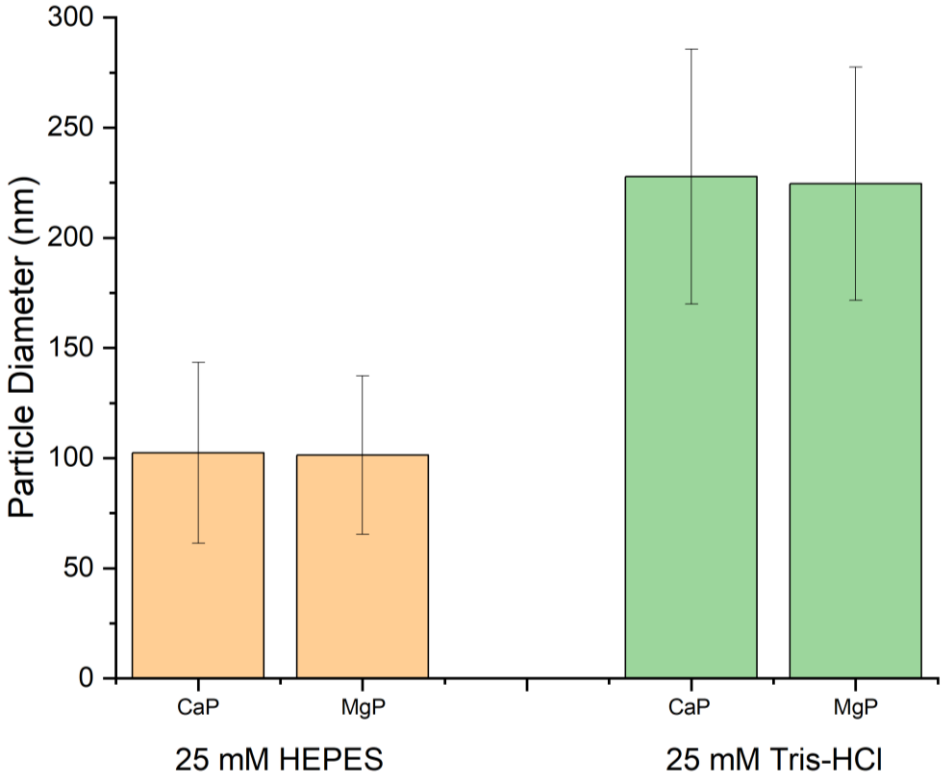


Figure 4.51. Mean diameters for CaP and MgP particles synthesised using combinative parameter changes* in either HEPES or Tris-HCl. *2 M CaCl2 or 1.8 MgCl2 and 3 wt % agarose.

Regardless of the mechanism by which this effect occurs, these results demonstrate that HEPES should be used in combination with other parameter changes, given the substantially lower mean diameters for CaP and MgP particles.

4.4.7 pDNA/PEI Layer Synthesis

Though pDNA/PEI complexes are not characterisable via SEM, a test was performed to determine whether a pDNA/PEI complex layer can be visualised in a gel slab using both the PS-DW-AGE and PS-CAGE systems. Figure 4.52 shows images of pDNA/PEI complex layers formed in the each system. The layers can be visualised more easily in the PS-DW-AGE system and measure 0.27 mm ± 0.05 mm (n = 3) and forms closer to the pDNA-loaded well. Comparatively, the pDNA/PEI layer formed in the gel cylinder using the PS-CAGE system is much fainter due to its depth below the surface of the gel, but appears to traverse the cross-section of the gel cylinder.

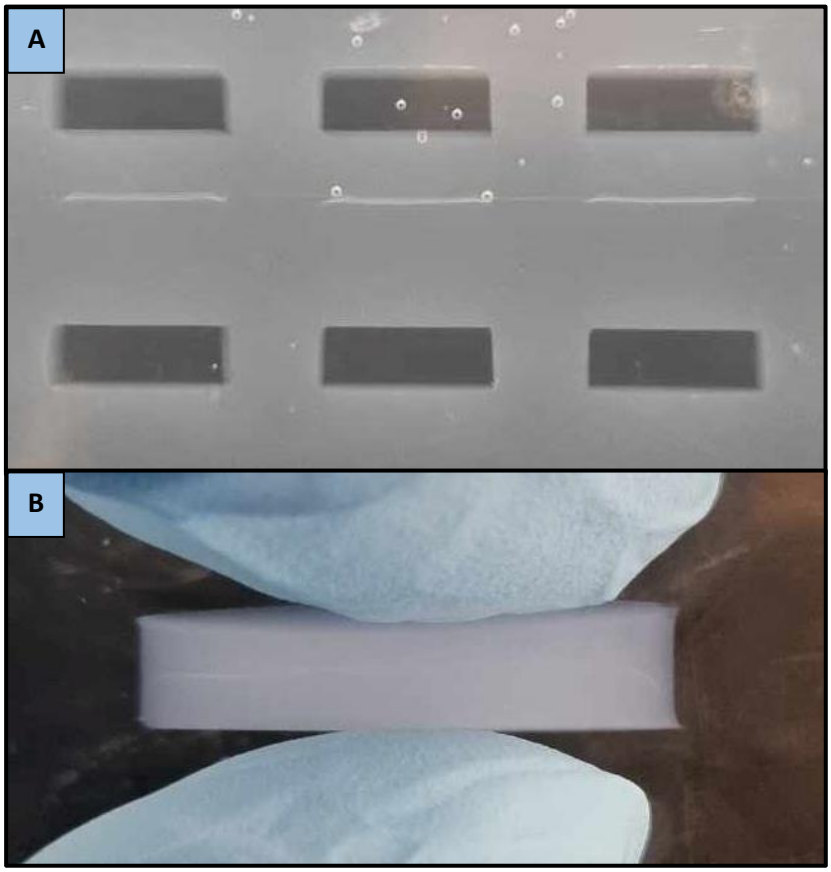


Figure 4.52. pDNA/PEI complexes formed in (A) the PS-DW-AGE system and (B) PS-CAGE system.

As previously discussed, pDNA/PEI complex diameters cannot be measured in this work. However, visualisation of pDNA/PEI complexation provides an indication that both systems can precipitate such complexes, despite their layer thickness being inadequate for a chondrogenic layer in a rabbit pre-clinical osteochondral defect model (~ 0.7 mm).

4.4.8 Particle Diameters in the PS-CAGE System

CaP and MgP particles were synthesised using the PS-CAGE system using either 2 M $CaCl_2$ or 1.8 M $MgCl_2$ and 1 wt % agarose. These samples were produced to compare the difference in particle sizes between the PS-DW-AGE and PS-CAGE systems using the same experimental

Experimental Parameters:

- System: PS-CAGE
- Salt 1: 2 M $CaCl_2$ or 1.8 M $MgCl_2$
- Salt 2: 12 mM Na_2HPO_4
- Agarose: 3 wt % (SeaKem®)
- Applied potential: 180 V
- Temperature: 21 °C
- Buffer: 25 mM HEPES

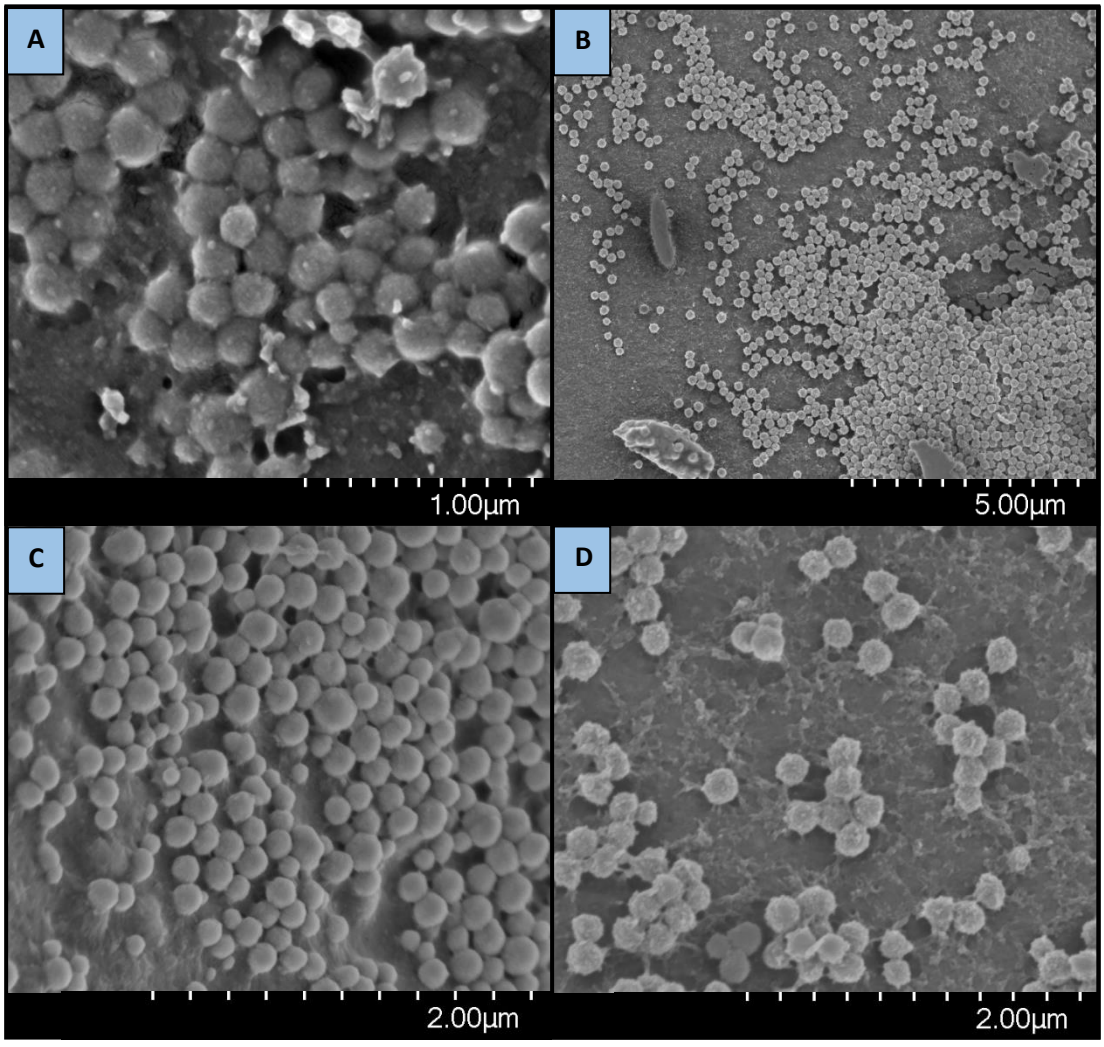


Figure 4.53. CaP and MgP particles synthesised via the PS-CAGE system. (A) and (B): CaP particles, (C) and (D) MgP particles.

parameters. Figure 4.53 shows typical SEM images of CaP and MgP particles synthesised using the PS-CAGE system. Both CaP and MgP particles are very similar with regard to their highly spherical morphology and their size. CaP particles Figure 4.53 (A) and (B) appear mostly to be of the order of 200 nm in diameter with some smaller (~ 50 nm) particles on the agarose fragment.

MgP particles (Figure 4.53 (C + D)) are also of the order of 200 nm with an even smaller subset of particles on the agarose fragment which are mostly 10 nm in diameter or smaller and spread across the agarose in thin projections.

Figure 4.54 shows the particle diameter histograms for the CaP and MgP particles synthesised via the PS-CAGE and PS-DW-AGE systems under the same parameter conditions. The CaP via PS-CAGE sample has a clear unimodal distribution with a single modal peak close to 200 nm, whilst the MgP via PS-CAGE sample has a primary peak close to 240 nm with a possible secondary peak at a lower diameter (as indicated by a red arrow). The PS-CAGE samples have primary peaks shifted toward larger particle diameters compared to the PS-DW-AGE samples but have distributions with stronger primary modal peaks and appear more unimodal in their distributions.

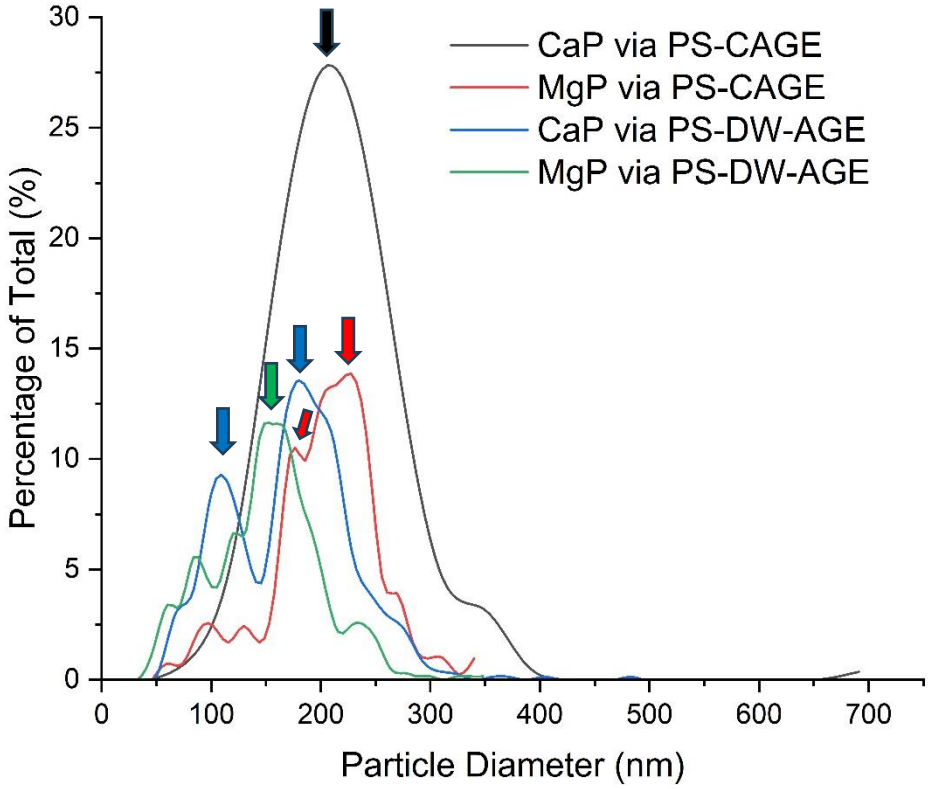


Figure 4.54. Histogram of CaP and MgP particle size measurements for samples synthesised using either the PS-CAGE and PS-DW-AGE systems.

Mean (± SD) particle diameters for CaP and MgP particles synthesised via the PS-CAGE and PS-DW-AGE systems were calculated and are plotted in Figure 4.55. The PS-CAGE system slightly reduces mean CaP particle diameters from 208 ± 88 nm to 198 ± 63 nm but there is an increase in mean MgP particle diameters from 144 ± 50 nm to 197 ± 49 nm. The SD for CaP particles is

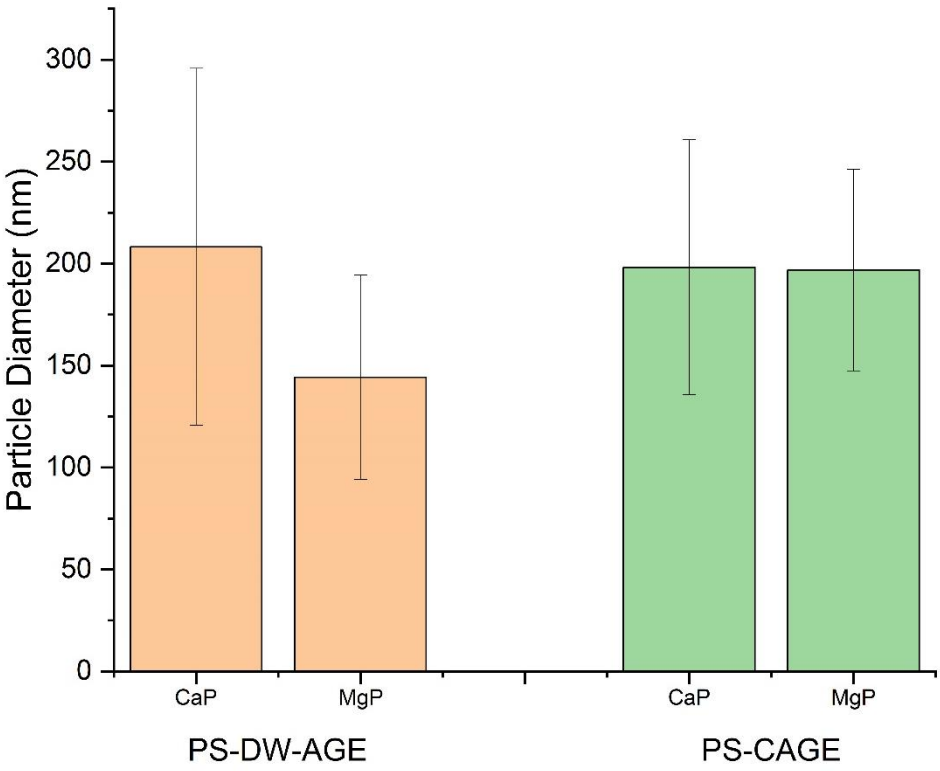


Figure 4.55. Mean particle diameters for CaP and MgP particles synthesised in the PS-DW-AGE and PS-CAGE systems.

reduced using the PS-CAGE system, whilst is remains consistent for MgP particles. These results show that the PS-CAGE system can synthesise CaP and MgP particles with size distributions that are more unimodal than the PS-DW-AGE system and with narrower size distributions. It is interesting that the mean MgP particle diameter is larger in the PS-CAGE system than in the PS-DW-AGE system, despite theoretically greater supersaturation maintained in the PS-CAGE system (according to computational calculations that assume supersaturation is proportional to mixing product). It is possible that the initial position of Mg^{2+} ions plays a role, where Mg^{2+} ions could take longer to be transported from the $MgCl_2$ loading gel than the $MgCl_2$. Though the 1 wt % agarose matrix of the loading gel is thought to have little impact of ion transport, the addition of OH^- ions (in the form of NaOH to adjust the pH of the loading gel) may introduce sufficient OH^--Mg^{2+}-OH^- interactions to reduce Mg^{2+} mobility. This would cause an ion band stretch at the loading gel-recipient gel interface and may sufficiently reduce supersaturation (and therefore nucleation rate) so as to increase MgP particle size.

4.4.9 Summary of Particle Diameter Investigations

Independently decreasing salt concentration and increasing agarose concentration was found to reduce mean CaP and MgP particle diameters, as well as primary modal diameters. However, the use of low (1 M $CaCl_2$ and 0.9 $MgCl_2$) salt concentrations has a more diminishing reduction on particle diameters. To maintain sufficient particle layer thickness for a pre-clinical osteochondral model, it would be sensible to use mid-range concentrations of 2 M $CaCl_2$ and 1.8 M $MgCl_2$ loaded opposite to 12 mM Na_2HPO_4. The Mg^{2+}-doped CaP sample (Figure 4.18), on the one hand, demonstrates that Mg^{2+} is able to substantially reduce CaP particle diameters from 390 ± 115 for the 4.125 M $CaCl_2$ sample to 216 ± 94 (Figure 4.21), but proportionally there is little change in the SD of the Mg^{2+}-doped CaP sample. This is theorised to arise from a binary population of CaP and MgP particles due to slower transport of Mg^{2+} ions. The clear overlap of both modal peaks with the primary modal peaks of 4.125 M $CaCl_2$ and 3.75 M $MgCl_2$ (Figure 4.19) further suggests the Mg^{2+}-doped CaP sample is a combination of these samples. To avoid potential amplification of this bimodal distribution, the use of Mg^{2+}-doping will be avoided in future experiments.

Agarose concentrations continue to reduce CaP and MgP particle diameters but – in contrast to salt concentration reduction – thinning of CaP or MgP particles was negligible with increasing agarose concentration. Whilst higher agarose concentrations would also enhance the compressive modulus of the hydrogel (and presumably the resultant cryogel), it is critical to consider that reducing the pore size of the resultant cryogel will eventually inhibit cellular infiltration (Murphy et al., 2010). As a compromise, a 4 wt % gel will be used given that a 5 wt % gel evokes marginally smaller mean particle diameters. Note that the use of 2 M $CaCl_2$ or 1.8 $MgCl_2$ with 3 wt % agarose gel was previously demonstrated to produce CaP and MgP particle diameters of 102 ± 41 nm and 101 ± 36 nm respectively in HEPES buffer (Figure 4.51), hence the use of a 4 wt % agarose should reduce this to the desired particle diameter range of < 100 nm.

Meanwhile synthesising CaP and MgP particles in NuSieve™ agarose resulted in smaller mean CaP and MgP particle diameters and primary modal peaks than in SeaKem® agarose. But as was discussed in Chapter 1, NuSieve™ is mechanically unsuitable for bone tissue engineering applications. However, the work here confirms that substantially smaller particles can be synthesised in NuSieve™ due to its (theoretically) smaller pore sizes. This brings evidence to the theory that pDNA/CaP and FBN-pDNA/CaP cryogels synthesised via the PS-SW-AGE approach had high transfection efficacies due (at least in part) to the presence of smaller pDNA-loaded particles.

Applied potentials of 60 V, 120 V, and 180 V had little impact on mean CaP particle diameters but there was evidence that 60 V and 180 V potentials produced multimodal particle size distributions compared to more unimodal distribution produced at 120 V. Furthermore, the 60 V potential resulted in a lower primary modal peak for CaP particles. It could be that a complex combination of reduced supersaturation at lower applied potential (due to ion diffusion) and particle size filtering at high applied potential is occurring within samples. Given that diffusion of ions is more restricted in the PS-CAGE system and particle transport will be more restricted due to the large cross-section of the particle layer, a 180 V applied potential should be utilised in the ideal subset of parameters.

Based on the results from Figure 4.43 it appears that mean CaP and MgP particle diameters have a complex relationship with temperature, as evidenced by a lower mean CaP diameter at 21 °C than at 4°C or 42 °C. Given the small sample sets and the absence of MgP paticles at 4 °C, it has not been possible to demonstrate a clear relationship between particle diameters and temperature in the PS-DW-AGE. Despite this, the temperature/pH control unit was able to sustain the desired temperature under all conditions. Therefore, a buffer temperature of 21 °C will be used in the ideal subset of parameters.

The use of Tris-HCl buffer slightly reduced the mean CaP particle diameter compared to CaP particles synthesised using HEPES, which is theorised to result from the greater high conductivity of the buffer and therefore more rapid transport and co-location of ions. This contrasts with the combinative use of mid-range salt and agarose concentrations to synthesise CaP and MgP particles. It was previously suggested that the reversal of this relationship could arise through particle size-filtering effects, where particles form much quicker in Tris-HCl buffer due to a greater current through the tank. Consequently, particles are subjected to an electric field strength for a longer period of time than in HEPES, where smaller particles are electrophoretically transported from the zone of precipitation. Hence excised gels contain a particle size population that is negatively skewed from its initial distribution. Regardless of mechanism, HEPES has been shown to produce smaller CaP and MgP species when combined with a combination of parameter changes and hence will be used in the ideal subset of parameters.

An interesting note is that the irregular morphologies and nodular appearance of particles synthesised using HEPES compared to Tris-HCl indicate particles synthesised via HEPES will have a greater surface-area-to-volume ratio. This is an important consideration for pDNA-loading and the dependence on surface-mediated transfection in-vitro, where larger particle surface areas

provide greater pDNA adsorption potential and greater metastability (provided surface energies remain constant in this comparison).

The combinative use of 2 M $CaCl_2$ and 1.8 M $MgCl_2$ with 3 wt % agarose gel demonstrated the ability to synthesise near-100 nm diameter particles through the compound reducing effect of a lower salt and higher agarose concentrations (than the unmodified control). This demonstrates that an ideal subset of parameters containing further parameter modulation should have a compound reducing effect on CaP and MgP particle diameters.

To summarise, the ideal subset of parameter conditions for synthesis of osteogenic-simulating particle layers in the PS-CAGE system is: either 2 M $CaCl_2$ or 1.8 $MgCl_2$, 4 wt % SeaKem® agarose, 25 mM HEPES buffer, a buffer temperature of 21 °C and an applied potential of 180 V.

4.4.10 Particle Synthesis in the PS-CAGE System Using an Ideal Subset of Parameter Conditions

The ideal subset of parameter conditions identified previously were utilised to produce PDA-coated cryogel groups for further particle analysis and *in-vitro* analysis. Powderisation of select samples revealed that PDA-CaP and PDA-pDNA/CaP groups demonstrated indistinguishable surface/particle properties. Furthermore, powdered PDA-MgP and PDA-pDNA/MgP samples had highly similar surfaces. PDA-pDNA/CaP and PDA-pDNA/MgP samples are shown in Figure 4.56 below. The PDA-pDNA/CaP sample exhibits a rough surface topography of nodules measuring between 40 – 80 nm, though isolated particles were absent from the surface. In a select area toward the top of the image, the nodule layer transitions to form a soft coating appearance. The PDA-pDNA/MgP sample displayed a small number of particles of the order of 150 nm in diameter, but the rest of the agarose fragment is coated in a sheet with the occasional particle growing out from the surface.

It seems that the compound reducing effects of PDA, pDNA, and the ideal subset of parameter conditions have indeed reduced CaP size further, but now particle measurements cannot be reliably made given the coated topography and absence of isolated particles. Despite this, it appears that the aim of reducing pDNA/CaP particle diameters below 100 nm has been achieved here.

Whilst the independent effects of PDA and pDNA on CaP particle size were previously established in Chapter 2 (both of which reducing mean CaP particle diameter), their effect on MgP was not investigated. It is interesting to now see that MgP particles can almost be

eliminated from the PDA-coated agarose surface. In both cases, the complete coating of agarose bodes well for transfection efficacy given the extremely large surface areas of pDNA/CaP and pDNA/MgP, but whether this will negatively impact cell attachment – and therefore cell viability – due to the occlusion of the PDA surface with require analysis.

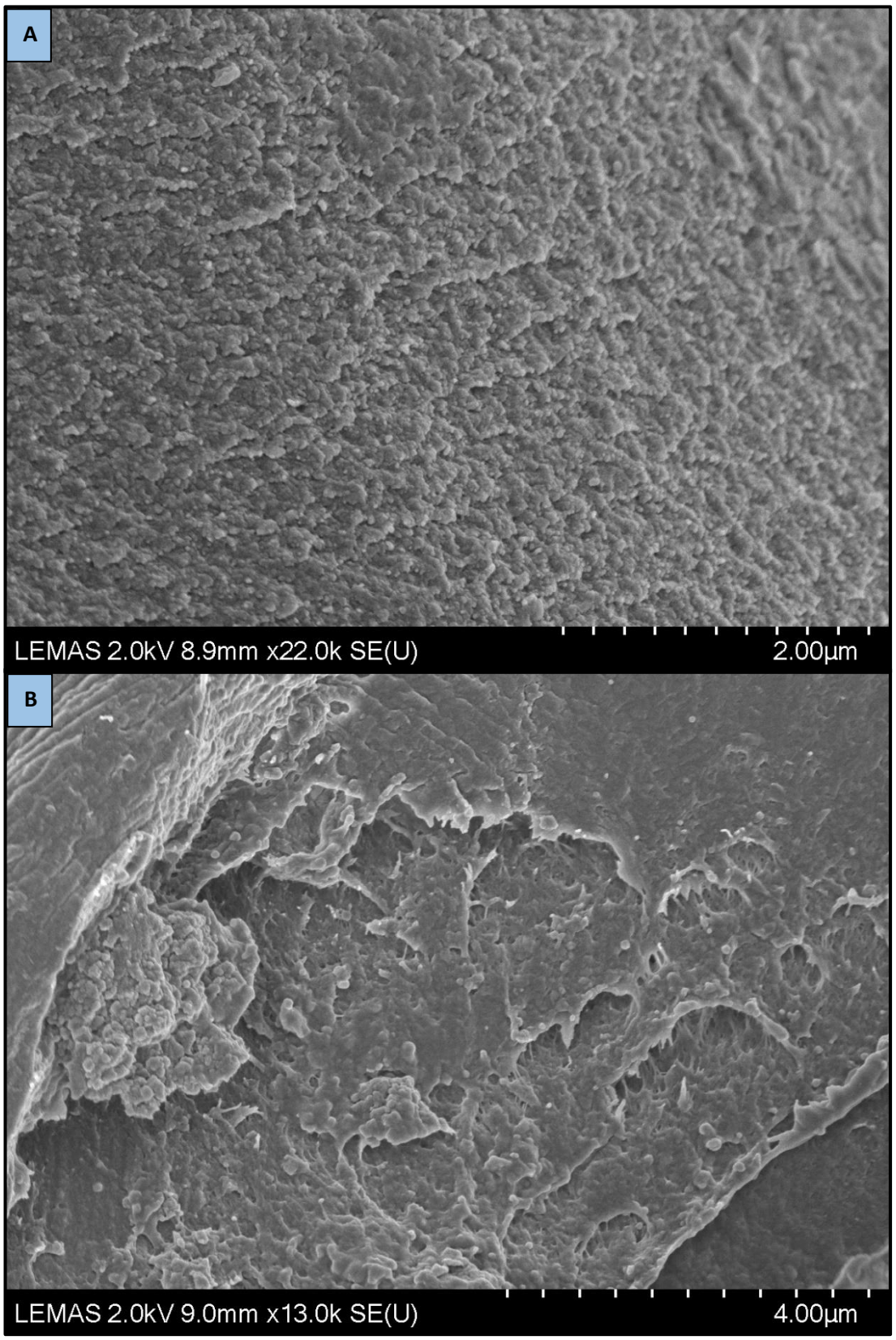


Figure 4.56. Surface topographies of: (A) the PDA-pDNA/CaP sample; and (B) the PDA-pDNA/MgP sample.

4.4.11 Hydrogel Appearance

Immediately after synthesis, PDA-pDNA/CaP and PDA-pDNA/MgP hydrogels were cut to size and imaged to determine layer thickness, as shown in Figure 4.57 below. The pDNA/CaP particle layer measured 2.54 ± 0.02 mm (n =6) whilst the pDNA/MgP layer measured 0.89 ± 0.14 mm (n = 6). It is interesting to note that whilst the pDNA/MgP layer is uniform, the pDNA/CaP layer appears as three separate regions: a thick brown layer (left side), a thin white layer (middle) and a mid-sized pale area (right side). This could be observation of a primary and secondary layers, as was previously seen in Figure 3.6. Images of cryogels demonstrate that both groups retain most of their initial volume and shape but tend to fray at edges.

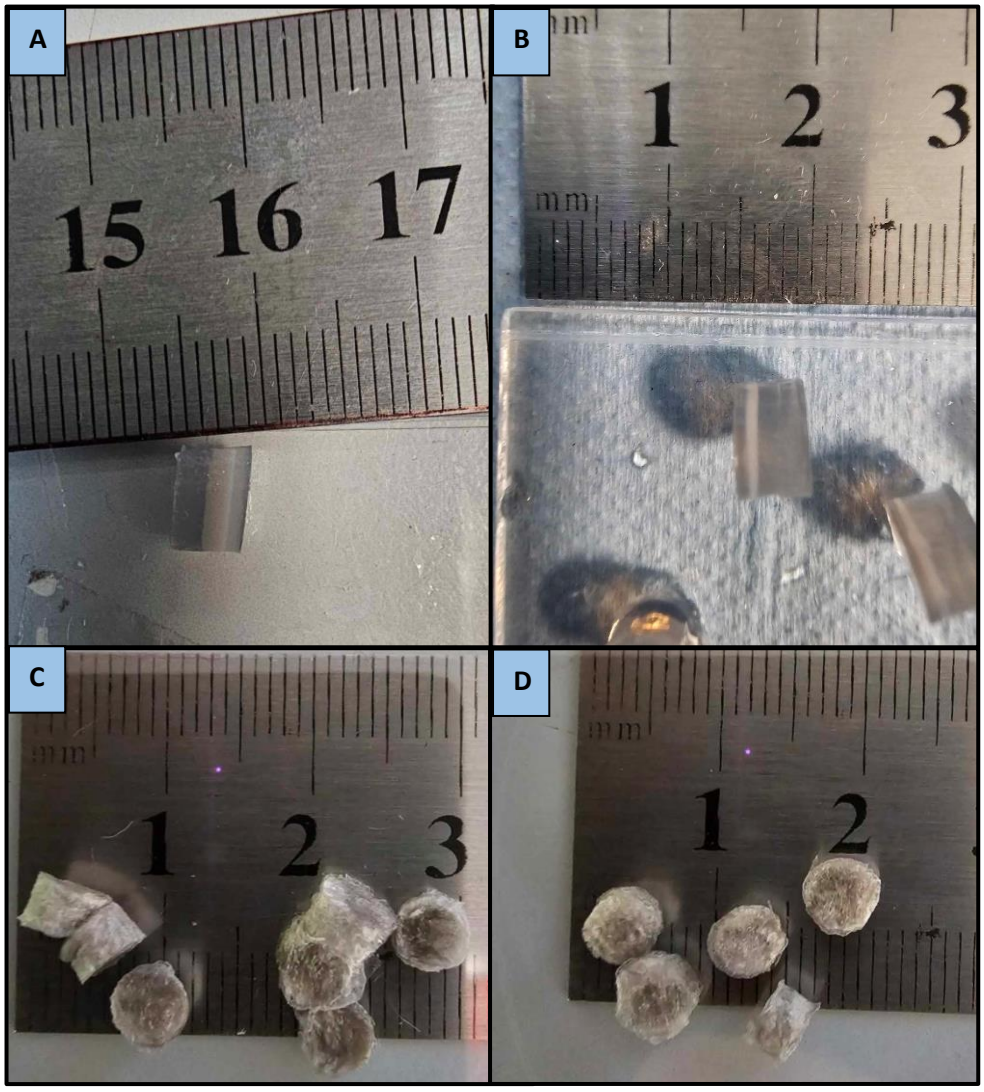


Figure 4.57. Images of hydrogels and cryogels. (A) pDNA/CaP hydrogel; (B) pDNA/MgP hydrogel; (C) pDNA/CaP cryogel; and (D) pDNA/MgP cryogel.

4.4.12 Cryogel Appearance

Cryogels were imaged after their first lyophilisation and prior to their sterilisation in 70 % EtOH. All cryogel groups were largely indistinguishable in terms of their overall size and shape with mildly frayed edges but retaining their cylindrical shape. A typical blank GAM is shown in Figure 4.58 (A) below, still measuring 5 mm in diameter after the first lyophilisation. Typical pDNA/CaP and pDNA/MgP GAMs (both prior to PEI soaking) have also retained their initial 5 mm in diameter, as shown in Figure 4.58 (B) and (C) respectively.

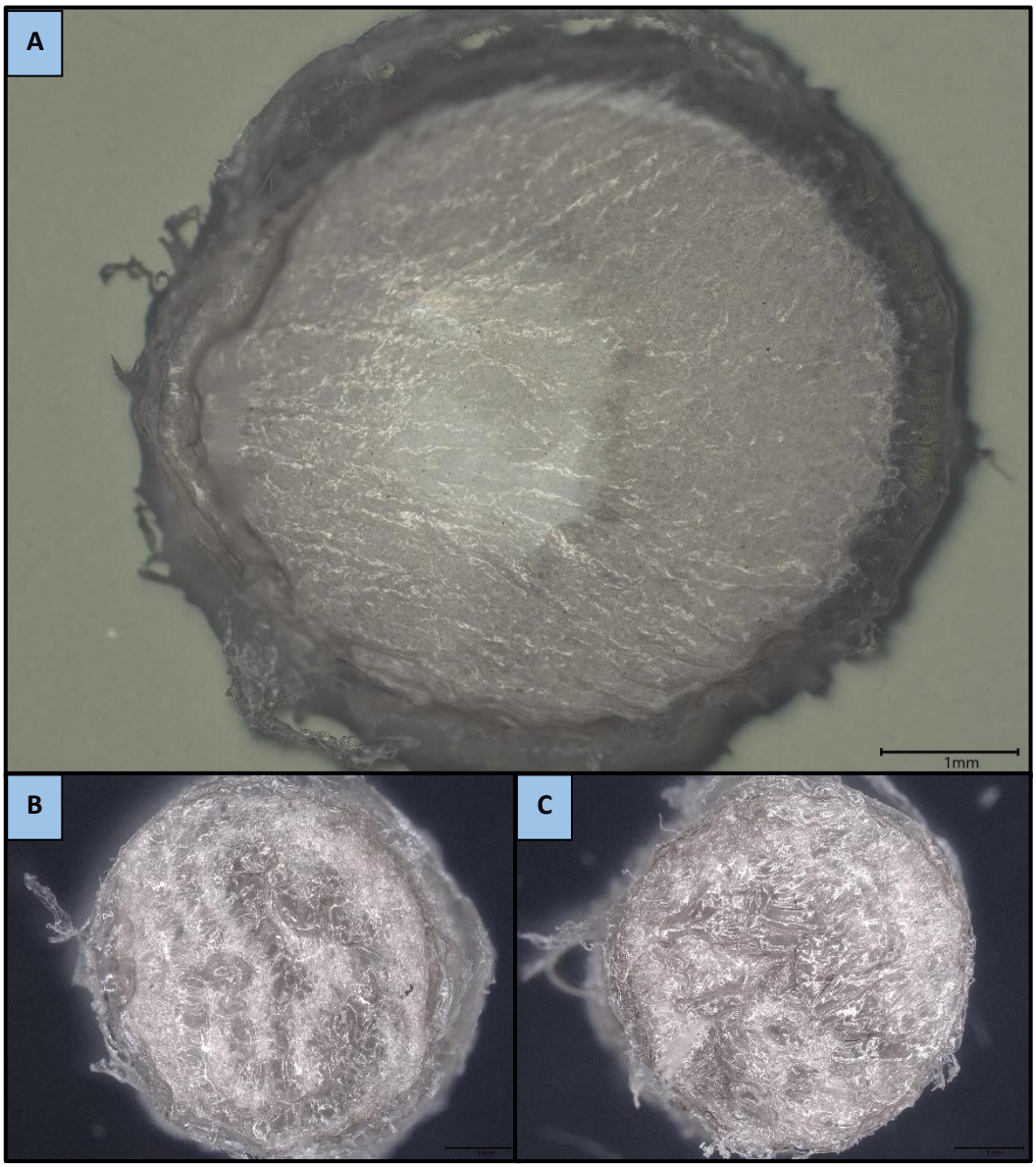


Figure 4.58. Digital microscopy images of (A) blank; (B) pDNA/CaP; and (C) pDNA/MGP cryogels.

Black spots – assumed to be PDA clusters - are easily noticeable in all cryogel groups at magnifications of 80x or higher. Figure 4.59 shows a higher magnification of a typical pDNA/MgP GAM with PDA clusters of the order of 2 – 10 μm in diameter. These PDA clusters did not appear to vary in density or size between cryogel groups.

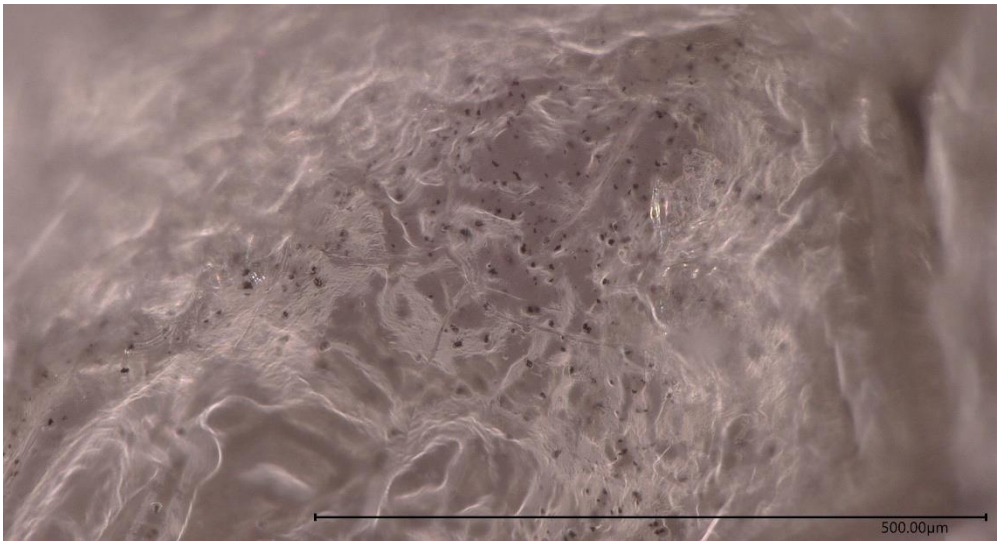


Figure 4.59. High magnification digital microscope image of a typical pDNA/MgP cryogel. Black clusters are approximately 2 - 10 μm in diameter.

When submerged in cell media, the pDNA/CaP and pDNA/MgP mineral layers seen in their hydrogel form can be observed more clearly. As shown in Figure 4.60, the pDNA/CaP cryogel again displays three layers that combined occupy more than half of the gel, whilst the pDNA/MgP cryogel has a far less intense layer of reduced thickness.

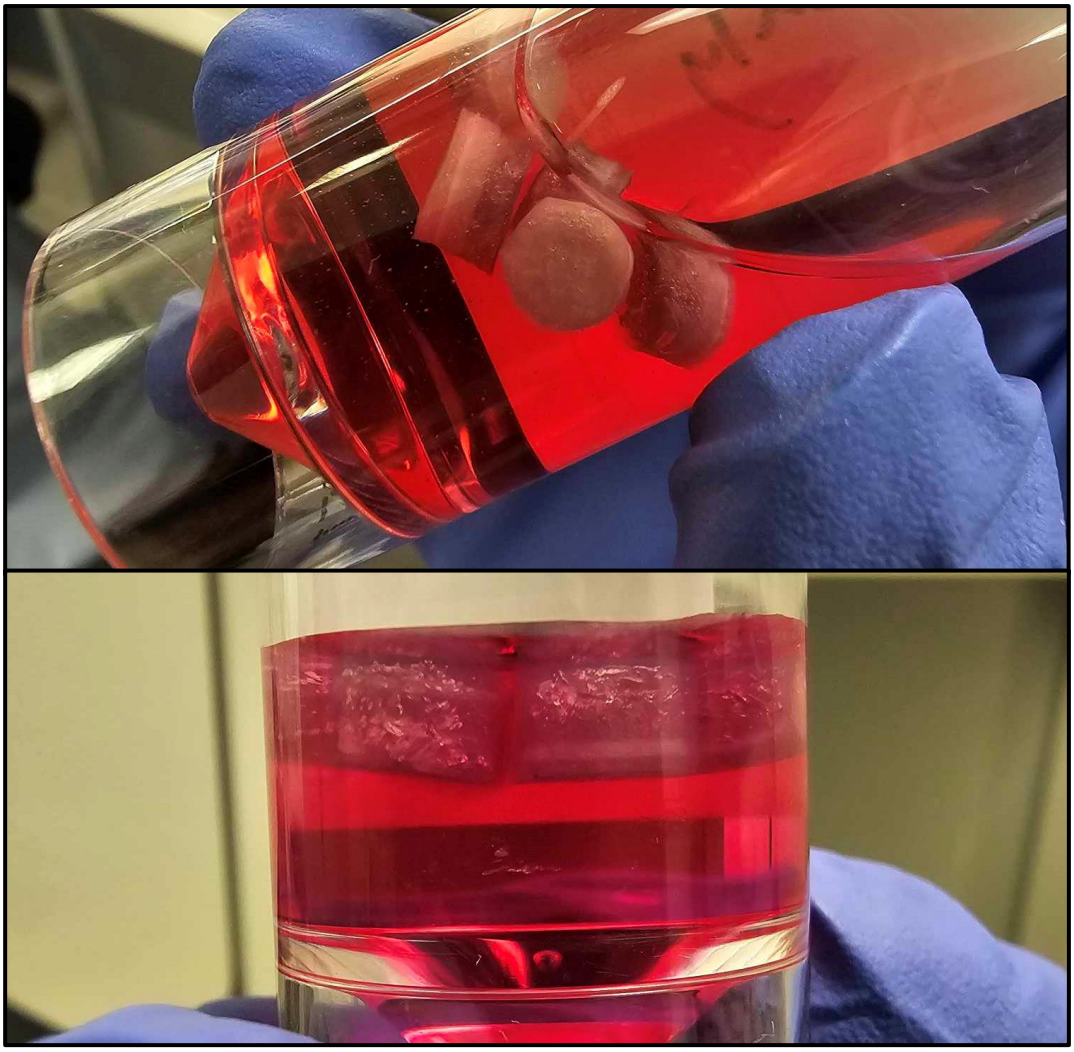


Figure 4.60. Appearance of cryogels when submerged in cell media. (Top) pDNA/CaP cryogels and (bottom) pDNA/MgP cryogels.

4.4.13 Cytotoxicity Assays

LDH assays were performed for control and cryogel groups to quantitatively assess cell viability. The blank cryogel group was used as a positive control to indicate 100 % cell viability, to which all other experimental groups were calibrated against. As shown in Figure 4.61, the pDNA group demonstrates the greatest cell viability at 65.4 ± 26.5 %, followed by PEI at 53.8 ± 7.5 % and the pDNA/PEI group at 50.3 ± 8.9 %. The CaP and MgP groups have comparable cell viabilities of 39.4 ± 7.4 % and 37.7 ± 7.1 % respectively. The lowest cell viabilities come from the pDNA/CaP/PEI and pDNA/MgP/PEI groups which have respective cell viabilities of 33.5 ± 6.6 % and 32.4 ± 9.1 %.

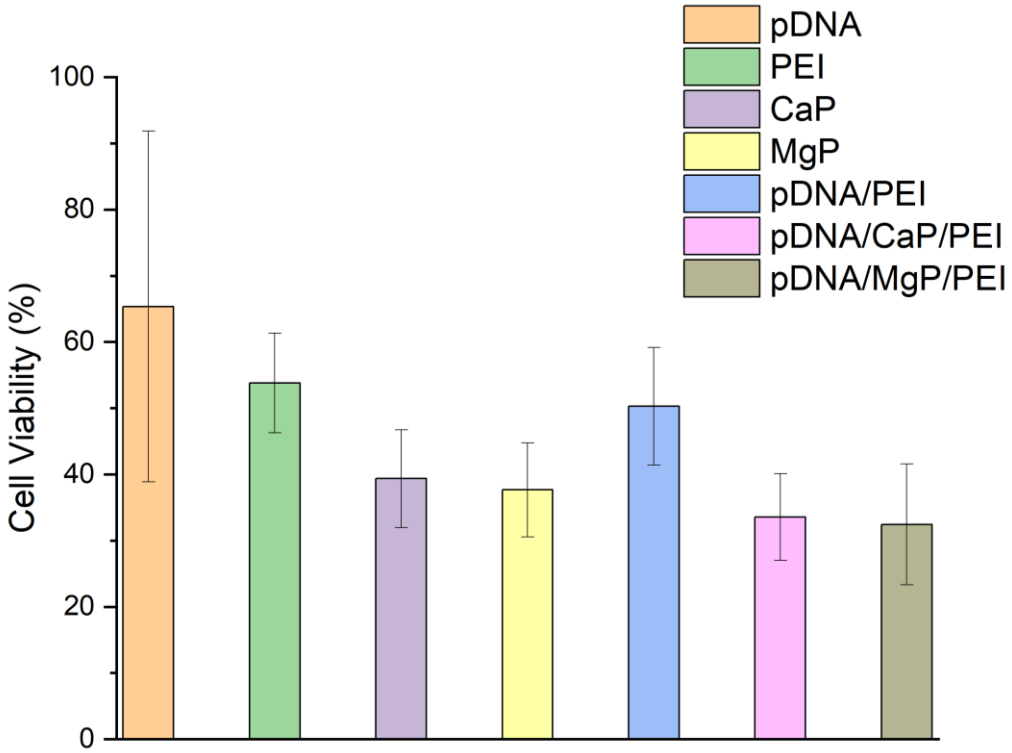


Figure 4.61. Cell viability as a percentage (%) of the blank cryogel control.

It is concerning that the pDNA group presented lower cell viability than the blank controls to which these groups are calibrated against. However, the large SD and large spread of data for the pDNA group suggest poor confidence in the mean and that these samples may have been poorly replicated. The slight difference in cell viability between the PEI and pDNA/PEI groups indicates the formation of pDNA/PEI complexes has negligible impact on free PEI concentration, which are attributed toward cell death in the PEI group.

There is also little difference between the CaP and MgP groups, indicating that neither particulate species is noticeably more toxic than the other. Similarly, there is only a slight difference between the pDNA/CaP/PEI and pDNA/MgP/PEI samples. It is interesting that the addition of PEI to the pDNA/CaP and pDNA/MgP groups only marginally reduced their cell viability, but this effect was also seen between the pDNA and PEI groups.

The lower cell viabilities of cryogels containing CaP or MgP particles could arise due to a severe occupation of PDA surfaces that was purposely employed to enhance cell attachment compared to the agarose surface. This is supported by greater cell viabilities in all cryogels that do not include CaP or MgP particles. Despite the large cell death occurring in most cryogel samples, there remains a large cell population within each sample well.

4.4.14 pDNA-encapsulation Efficiency

Prior to cryogel synthesis, pDNA gel loading cylinders were prepared by casting a 1 wt % agarose gel containing 0.1 µg uL^{-1} of pDNA to form a row of six pDNA loading gel cylinders. These were positioned adjacent a row of 6 gel cylinders comprised of PDA-coated 4 wt % agarose. pDNA release from the pDNA loading gels was first required to measure the release percentage of pDNA from loading gels after a 180 V had been applied for 18-minutes. The Picogreen™ assay showed that only 0.59 ± 0.03 % of the initial 125 µg of pDNA per gel cylinder was released from lyophilised pDNA loading gel cylinders, indicating that over 99% of pDNA (2.49 µg) was successfully ejected from the loading gel during electrophoresis. This assuming that pDNA has been loaded into the 4 wt % recipient gel and was not lost around the circumferential edge of the cylinder.

After their synthesis, cryogel groups were submerged in a buffer of 50 mM Tris-HCl + 150 mM EDTA (pH 8.0) and incubated for 4-days to measure pDNA release. Figure 4.62 below shows the pDNA release (µg) from cryogel groups which have all been calibrated against the blank cryogel control. The pDNA group displays a release of 0.4 ± 0.1 ug, which equates to 16.1 % release of the theoretical maximum 2.49 µg per cryogel. The PEI group demonstrates negligible pDNA

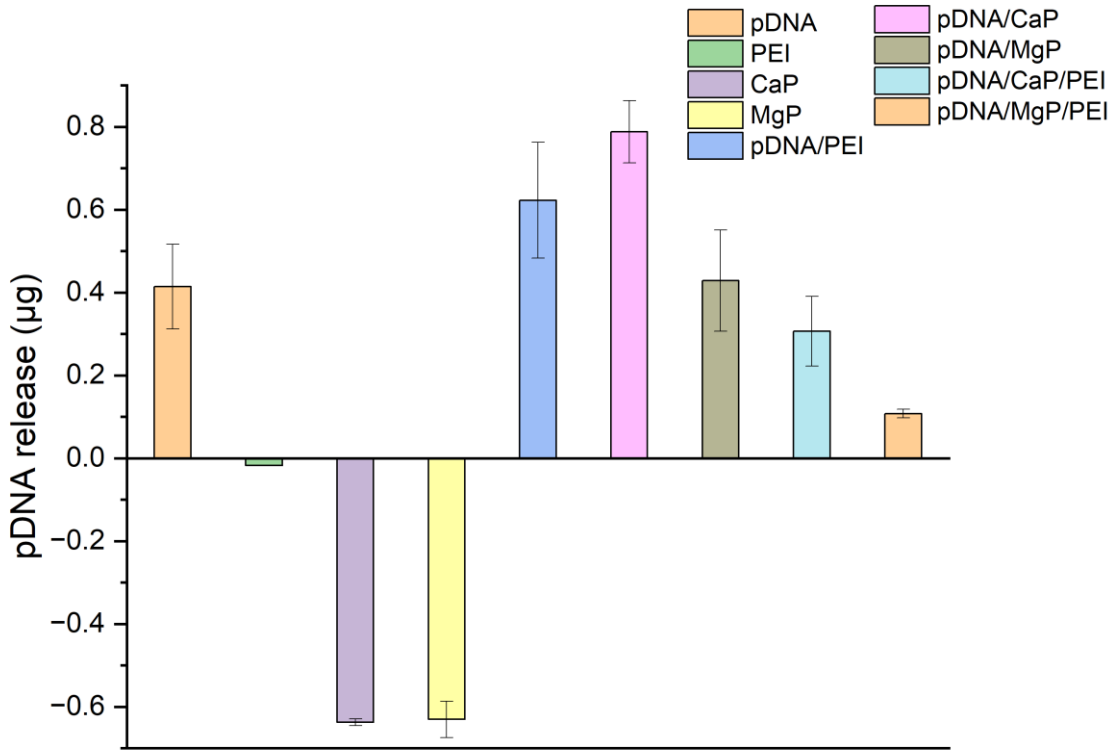


Figure 4.62. pDNA release from cryogel groups into decalcification buffer. Error bars indicate standard deviation.

release, whilst the CaP and MgP groups display negative pDNA release of over -0.6 μg, which may result from interference of Ca^{2+} and Mg^{2+} with the PicoGreen™ assay. Meanwhile, the pDNA/PEI group released 0.62 ± 0.14 μg of pDNA. The greatest pDNA release was from the pDNA/CaP group (0.79 ± 0.08 μg), which is far greater than that released by the pDNA/CaP/PEI cryogel. Similarly, the pDNA/MgP group released 0.43 ± 0.12 μg compared to a far lower release of 0.11 ± 0.01 μg for the pDNA/MgP/PEI group.

The greater release of pDNA from pDNA/CaP and pDNA/MgP compared to their PEI-soaked counterparts may be evidence that PEI is able to coat some particles in the cryogel and prevent the decalcification buffer from dissolving CaP surfaces. Meanwhile the greater release of pDNA in CaP-containing cryogels compared to MgP-containing cryogels may result from differences in particle layer thickness, where pDNA/CaP layers have been shown to be much thicker than pDNA/MgP layers.

4.4.15 Transfection Assays

Luciferase assays were performed to measure luciferase enzyme activity at 24-, 48-, and 72-hour time points. All measurements were calibrated against the blank control group to give a percentage luminescence of control and are displayed in Figure 4.63. All groups demonstrate less than 10 % luminescence of the blank control, with the CaP and MgP providing negative values. The pDNA group has percentage luminescence greater than 6 % for all time points, peaking at 9.1 ± 0.3 % at 72-hours. Despite no pDNA, the PEI group has a percentage luminescence greater than 3 % at all time points, though this is lower for each time point than the pDNA/PEI group which peaks at 8.6 ± 0.1 % at 48-hours. Note that MgP groups were excluded from this analysis due to contamination.

Luminescence values for pDNA/PEI and pDNA/CaP remain lower than 3 %. Meanwhile, pDNA/MgP and pDNA/CaP/PEI luminescence values generally increase with time to over 8 % at their respective maximum. Finally, the pDNA/MgP/PEI group displays luminescence of less than 3 % at all time points. There are several concerns with this data. Firstly, the PEI group displays

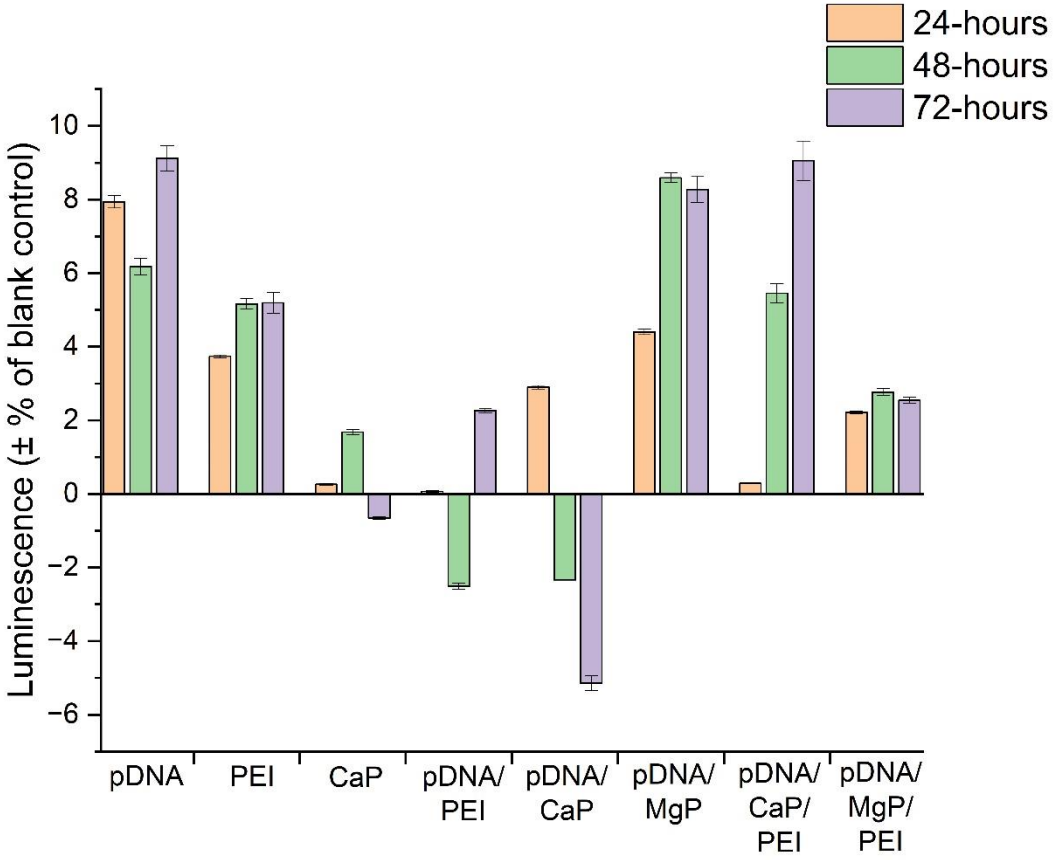


Figure 4.63. Luminescence (± % of blank control) for cryogel groups as a measure of transfection efficacy. Error bars indicate standard deviation.

luminescence above 5 % for two time-points. If this is background noise from some interaction with PEI and the assay, it could mean that pDNA/CaP/PEI and pDNA/MgP/PEI groups have even lower transfection efficacies than is observed here. If this is ignored, PEI appears to enhance transfection efficacy of pDNA/CaP cryogels but reduces the transfection efficacy of pDNA/MgP cryogels. As with the data from 2.4.7, it may be difficult to cleave any useful insights from this data given significant background signals from the PEI control and the fact that luminescence values are again contained within + 10 % of the blank control.

4.4.16 Fluorescence Microscopy

Figure 4.64 and Figure 4.65 display typical fluorescence images acquired by scanning laser confocal microscopy for all groups, which were each adjusted to + 40 % brightness and - 40 % contrast in ImageJ.

The blank group reveals the presence of cells scattered loosely about the cryogel cross section and limited green background fluorescence from the cryogel itself, where the central portion of the cryogel is not visible. The pDNA group reveals a similar disperse cell population to the blank control but with signs of GFP expression due to isolated and high intensity green spots that are identifiable despite strong background fluorescence from the cryogel. Large cell clusters are observed in the PEI group but with no isolated and intense green fluorescence. There is some green fluorescence co-located with the large cell cluster in the PEI group but this does not appear substantially more intense than the background fluorescence.

The CaP and MgP groups reveal contrasting cell concentrations; with CaP having a noticeably larger cell population. There is one area of strong green fluorescence in the CaP group which appears to be a portion of the cryogel with a high density of small pores and is therefore assumed to be background fluorescence. The MgP group has localised areas of green fluorescence, but these are not co-located with cells.

The confocal images for the pDNA/PEI, pDNA/CaP/PEI, and pDNA/MgP/PEI groups are shown in Figure 4.65. Whilst the pDNA/CaP/PEI and pDNA/MgP/PEI groups show a large number of cells in the images stained for DAPI, the pDNA/PEI group displays a comparatively smaller population. There is no indication of GFP expression in the pDNA/PEI group, whilst the pDNA/CaP/PEI and pDNA/MgP/PEI groups both display smaller, more discrete spots of green fluorescence co-located with cells in DAPI + GFP images.

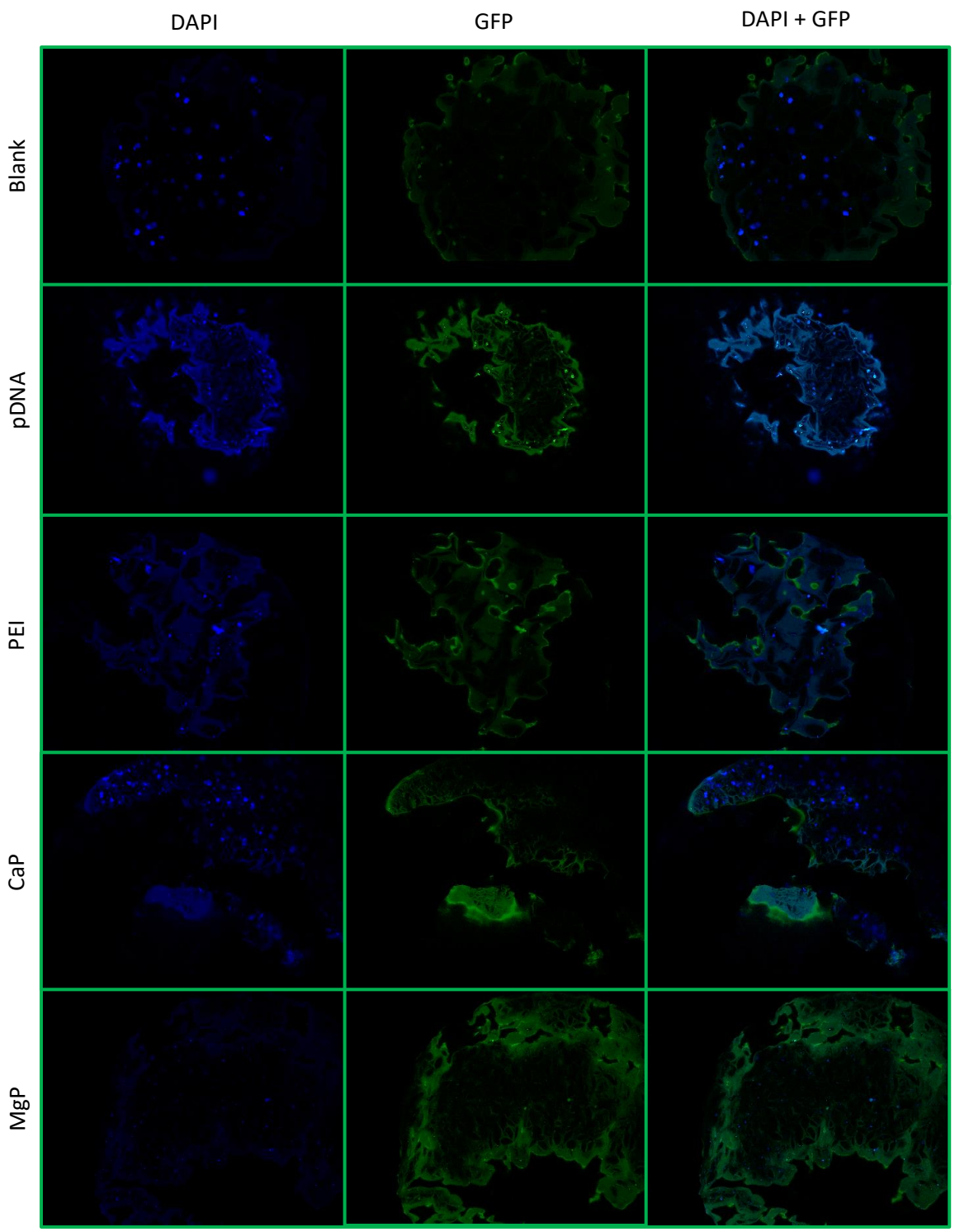


Figure 4.64. Fluorescence microscopy images of cryogel groups.

It should be noted that the blank, pDNA/PEI, and pDNA/CaP/PEI groups display mostly the outer edge of the cylindrical cryogel, whilst other groups do not fully display the cross-section of the cryogel. This is due to the microscope's small working distance and slight compression of the cryogel to obtain a focal plane within the bulk of the cryogel. The lens slightly compressing the

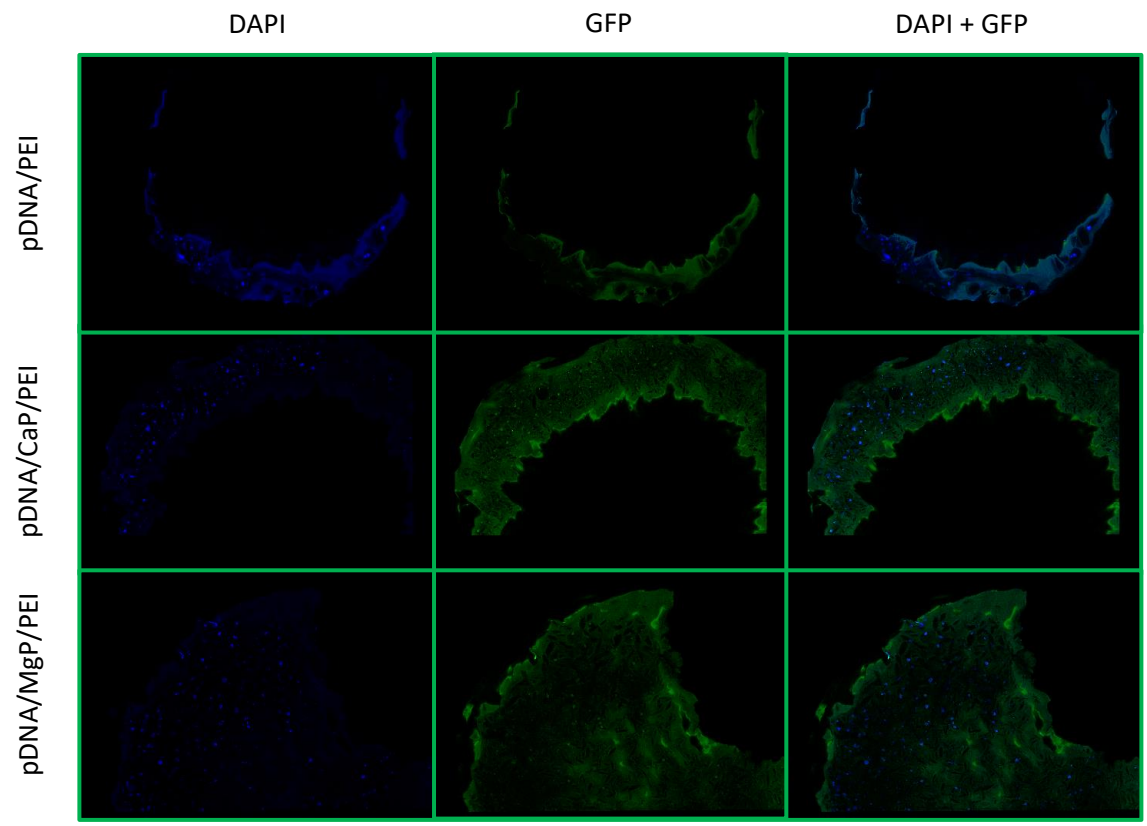


Figure 4.65. Fluorescence microscopy images of cryogel groups.

centre of cryogels will therefore push the cross-sectional centre below the focal plane. This reduces the resolved cross-sectional area of the cryogel to mostly outer areas.

Overall, all groups were able to demonstrate the presence of cells, and it appears that the pDNA, pDNA/CaP/CaP, and pDNA/MgP/PEI groups were able to produce evidence of GFP despite strong background fluorescence from the cryogel, whilst no evidence of GFP expression was evident in the pDNA/PEI group. The pDNA group produces the most obvious signs of GFP expression but this appears to be fluorescence from large cell clusters. Though less fluorescence is seen in the pDNA/CaP/PEI group (and even less in the pDNA/MgP/PEI group), the discrete spots of green fluorescence co-located with DAPI in these groups demonstrate more individual cell/cluster expression of GFP.

4.4.17 SEM analysis post-cell culture

A set of pDNA/CaP/PEI and pDNA/MgP/PEI cryogels were removed from cell media after a 24-hour incubation, washed with 70 % EtOH, lyophilised and prepared for SEM analysis. Typical SEM images of agarose surfaces from pDNA/CaP/PEI and pDNA/MgP/PEI cryogels are shown in Figure 4.66 and Figure 4.67 respectively. Both cryogels demonstrate a deviation from their appearance in Figure 4.56. Firstly, the nodular topography for the pDNA/CaP cryogel now displays sub-100 nm particles in clusters above the surface.

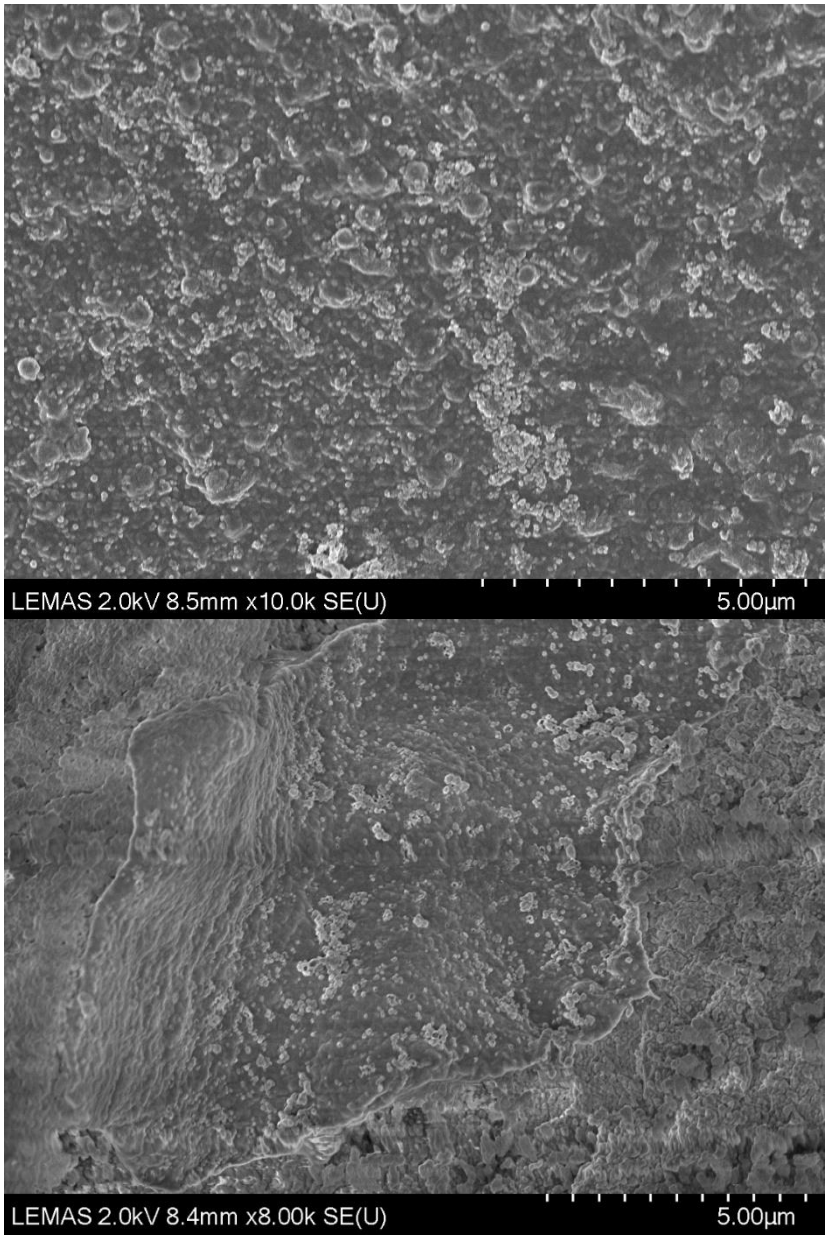


Figure 4.66. Typical SEM images of pDNA/CaP/PEI cryogels after a 24-hour incubation in cell media.

The pDNA/MgP sample now displays a surface containing sub-200 nm particles prior to incubation in cell media. However, many particles are buried beneath a surface coating, which could be PEI adsorbed onto the surface of the cryogel.

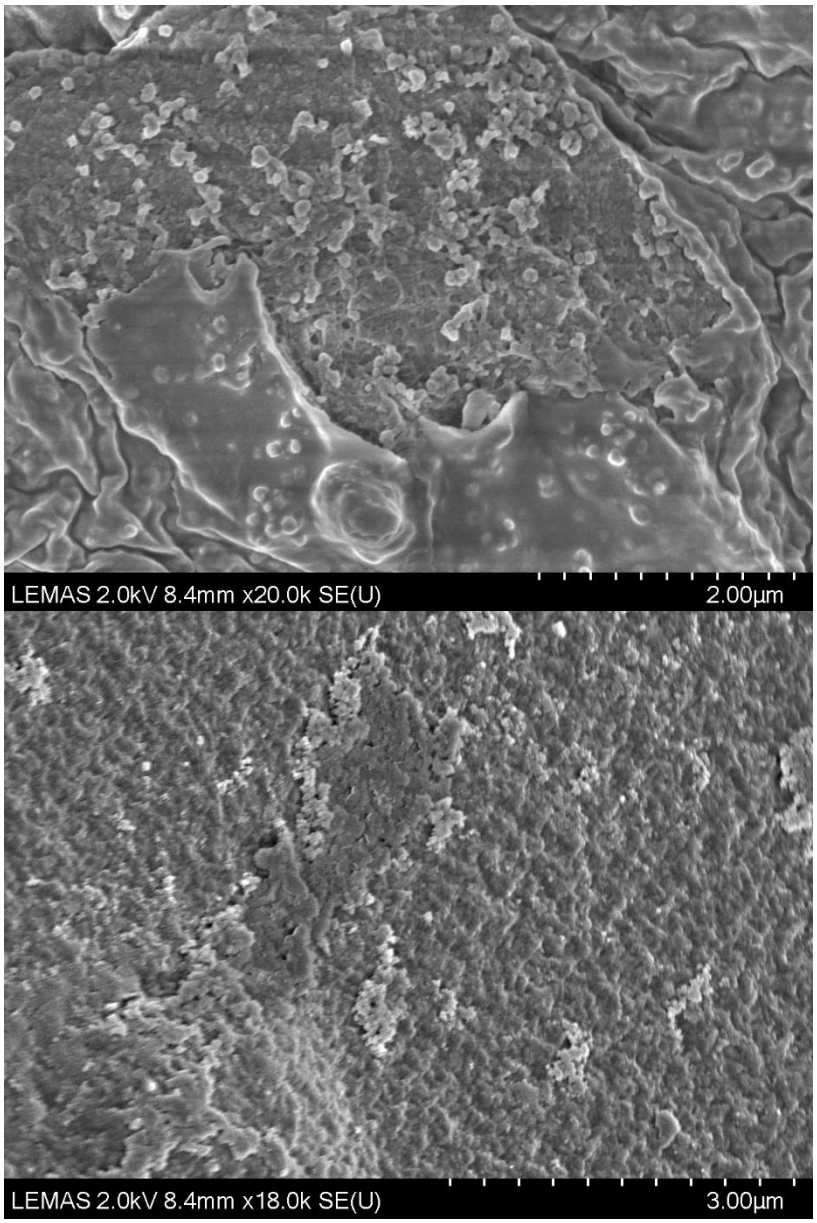


Figure 4.67. Typical SEM images of pDNA/CaP/PEI cryogels after a 24-hour incubation in cell media.

It is theorised that the change in surface topographies of these cryogels following incubation in cell media is due to the dissolution/transformation of primary particles/surfaces *in-vitro*.

4.5 Discussion

The PS-DW-AGE system, combined with an in-house built temperature/pH control unit has been used to observe the influence of experimental parameters with CaP and MgP particle diameters in an effort to identify an ideal subset of experimental parameter conditions for final cryogel fabrication via the PS-CAGE system.

4.5.1 PS-DW-AGE System

4.5.1.1 Salt Concentration

Reducing salt concentrations were found to reduce CaP and MgP particle diameters. This was interesting given higher salt concentrations provide greater supersaturation toward the desired species and therefore higher nucleation rates that produce smaller particles. It could be that, in the PS-DW-AGE system, an increasing salt concentration does not necessarily provide a greater supersaturation due to dynamic supersaturations created by the electric field. It would perhaps be useful to return to computational testing to model the relationship between salt concentration and supersaturation in porous gels. CaP particles were generally found to be larger than MgP under most experimental conditions, which is theorised to arise from the greater supersaturation toward CaP species than MgP species.

4.5.1.2 Agarose Concentration

Increasing agarose concentrations were found to reduce both CaP and MgP particle diameters, as was expected due to increase nanoconfining effects as pore size reduces with agarose concentration. It was also found that using NuSieve™ rather than SeaKem® agarose gel results in a large difference between particle sizes. Whilst NuSieve™ has already been discussed as being unsuitable for osteochondral tissue engineering applications due to its poor mechanical strength, these suggest that good transfection efficacies previously measured by our group may be in part due to these smaller particle sizes.

4.5.1.3 Applied Potential

The applied potential appeared to have a complex relationship with CaP particle size. This is theorised to result from a complex and highly dynamic zone of precipitation that is a product of the electric field profile. At low applied potentials, low supersaturations are produced due to slow ion transport, which should theoretically increase particle size via slower nucleation rates. In comparison, high applied potentials maintain high supersaturations due to more rapid ion transport, which should theoretically increase particle size via greater nucleation rates. However, higher potentials may induce a size filtering effect whereby newly formed particles are electrophoretically transported from the zone of precipitation and are therefore excluded from SEM measurements.

4.5.1.4 Combinative Parameters

Combinative use of parameter changes demonstrated that reduced salt concentrations and increased agarose concentrations harmonise to reduce CaP and MgP particles lower than their independent use. Surprisingly, these combinative changes were not enhanced by the use of Tris-HCl, which was previously found to slightly reduce CaP particle diameters. This was thought to occur via the previously discussed size-filtering effect, whereby the greater current through the electrophoresis tank when Tris-HCl was used (compared to HEPES) could electrophoretically transport particles away from the zone of precipitation.

4.5.2 Final Cryogel Synthesis in the PS-CAGE System

4.5.2.1 Hydrogel and Cryogel Appearance

An ideal subset of parameter conditions was selected and used for the synthesis of pDNA/CaP and pDNA/MgP particles in the production of final cryogels using the PS-CAGE system. Images of pDNA/CaP and pDNA/MgP hydrogels immediately post-synthesis demonstrated that both gels were of the size required for a pre-clinical rabbit osteochondral model. The pDNA/CaP gel demonstrated a pDNA/CaP layer measuring 2.54 ± 0.02 mm (n =6), which is approximately the size required for the osteogenic layer. However, the pDNA/MgP layer measured 0.89 ± 0.14 mm (n = 6) which is three-fold lower than the minimum thickness requirements for the osteogenic

layer. To produce a pDNA/MgP layer of adequate thickness, it will likely be necessary to increase salt concentrations to greater amounts and potentially increase agarose concentrations (which had negligible impact on layer thickness). However, this would reduce cell infiltration *in-vitro* even further.

4.5.2.2 pDNA encapsulation

pDNA encapsulation appeared to be greatest in the pDNA/CaP group, followed by the pDNA/PEI group, and then the pDNA/MgP group. As discussed, the larger layer thickness is likely the cause of greater pDNA encapsulation compared to MgP-based layers. Additions of PEI to pDNA/CaP and pDNA/MgP cryogels reduced pDNA release, which is theorised to result from either of PEI 'mopping up' unencapsulated or unabsorbed pDNA, and/or PEI forming protective shells around secondary particles.

4.5.2.3 Cytotoxicity

Cytotoxicity assays demonstrated that a low cell viability is prevalent amongst all cryogel groups compared to the blank control. Regardless, cell viabilities appear to be only slightly reduced when PEI is added to pDNA/CaP and pDNA/PEI cryogels. Similarly, the addition of PEI to the pDNA cryogel only slightly reduces cell viability compared to the PEI cryogel. Here it is thought that the complexation of pDNA with PEI results in a negligible decrease in PEI concentration (due to the use of a high N:P ratio of 10) and hence has negligible impact on cell viability.

4.5.2.4 Transfection

Transfection measured via luciferase assays proved ineffective at providing useful insight into potential transfection processes occurring within the cryogel. On the one hand, it is possible that there is simply insufficient cells penetrating into the cryogels. But, as was seen in fluorescence imaging, cells were found beneath the cryogel surfaces, though admittedly they were frequently clustered. Furthermore, fluorescence microscopy also demonstrated evidence of GFP production in the pDNA, pDNA/CaP/CaP, and pDNA/MgP/PEI groups despite strong background fluorescence from the cryogel itself.

It could be, then, that the luciferase assay is unsuitable for the cryogels tested in this work. Firstly, the PDA-coated surface or the cryogel network could be inhibiting the luciferase enzyme from diffusing into the surrounding supernatant. This could be possible given the intentional highly dynamic environment of the cryogel *in-vitro* where primary particles are dissolving and releasing ions and pDNAs into the surrounding environment. This mechanism would then allow for the formation of secondary particles in solution which could mobilise and blockade portions of the cryogel, or alternative secondary particles could form on pores themselves and prevent escape of molecular inhabitants.

Secondly, the release of PDA from agarose surfaces may be shielding luminescence measurements. Though gels underwent a rigorous wash cycle, it's plausible that PDA surfaces are fractured during lyophilisation (as observed in SEM analysis), hence rehydration of these cryogels in cell media releases PDA into the cell media and ultimately diminish luminescence measurements. Though PDA-blank controls were used to compensate for this change in cell media colour, sufficient PDA concentration could produce enough noise to preclude any luciferase released by these cryogels.

4.6 Conclusion

The PS-DW-AGE system was used to observe changes in CaP and MgP particle diameters in response to a range of experimental parameter conditions. This was done in the pursuit of obtaining an ideal subset of parameters to synthesise CaP and MgP particles below 100 nm diameters to increase surface areas of particles in cryogels, thereby enhancing their dissolution rate. This was theorised to result in greater nucleation rates of secondary particles *in-vitro* and hence reduce their diameter to enhance their transfection efficacy.

The combination of mid-range salt (2 M $CaCl_2$ or 1.8 M $MgCl_2$) and agarose concentrations was found to produce CaP and MgP particles that approached the desired 100 nm diameter region. Moving forward, the same salt concentrations were used but a higher agarose concentration of 4 wt % was used to reduce these diameters further. Alongside the use of room temperature conditions, a 180 V applied potential and HEPES buffer, these combined parameters formed the ideal subset of conditions to produce sub-100 nm CaP and MgP particles.

pDNA/CaP layers within cylindrical gels synthesised using these conditions in the PS-CAGE system were found to be of the appropriate size of an osteogenic layer for a GAM used in a pre-clinical rabbit osteochondral model. However, the pDNA/MgP layer proved three-fold smaller than the minimum thickness required. Meanwhile, pDNA/PEI layers were considerably smaller than the minimum thickness required for a chondrogenic layer.

pDNA encapsulation efficiency (measured by pDNA release) was found to be greatest in the pDNA/CaP cryogel – assumed to result from the thicker particle layer – was enhanced further by the inclusion of PEI. However, cell viabilities of all CaP- or MgP- encapsulating cryogels proved the worst of all groups. One possibility for this occurrence is the dissolution of embedded particles that release toxic concentrations of ions into surround cell media.

Whilst transfection assays again proved to be fairly inconclusive due to the high or negative background signals of control cryogels, fluorescence microscopy finally revealed evidence cells within cryogels and of transfection in pDNA, pDNA/CaP/PEI and pDNA/MgP/PEI cryogels.

5 Final Discussion

The PS-DW-AGE and PS-CAGE systems has demonstrated utility in synthesising pDNA/CaP and pDNA/MgP particles in layers within agarose hydrogels. Though these cryogels proved unsuccessful in transfecting C2C12 cells, the utility of these systems to synthesise metastable particles could be truly exploited for other osteogenic tissue engineering applications if they could only be extracted for characterisation and further functionalisation.

Despite no evidence of pMetLuc transfection using luminescence assays, pGFP transfection evidence provided by fluorescent microscopy in some groups uphold interest in GAMs fabricated using the PS-CAGE system for osteochondral tissue regeneration. However, further development of these GAMs must focus on their *in-vitro* testing to enhance transfection measurement sensitivity. For instance, using dynamic cell seeding to enhance cell infiltration and exposure to genetic payloads, in addition to developing more sensitive transfection assays. Using several alternative plasmids encoding for other luminescent enzymes or fluorescent proteins would ensure background signals from mineral particles and the agarose itself do not camouflage evidence of transfection.

Beyond transfection, one cannot ignore the capability of the PS-CAGE system to fabricate cylindrical GAMs embedded with uniform mineral-phosphate particle layers. Whilst cylindrically shaped biomaterials for osteochondral tissue regeneration are easily obtained in the laboratory, embedding them with discrete layers or gradients of genetic payloads is more complex. This often requires manufacturing processes such as 3D-printing, or simpler methods of mixing solutions at different rates to produce gradients. Whilst there are certainly reduced costs in using the PS-CAGE system compared to 3D-printing, one must also note the reduced complexity of PS-CAGE, reduced fabrication time, and the ability to synthesise genetic phosphate-mineral particles in-situ. This is opposed to encapsulating genetic payloads in ‘inks’ suitable for 3D-printing. Ultimately, the PS-CAGE system presents a one-step alternative to 3D-printing in fabricating osteochondral GAMs with layered genetic payloads. With further development of the loading regime, one could produce multi-layered or gradient GAMs using PS-CAGE to eliminate the need to bond layers together.

Though the PS-CAGE system has demonstrated the ability to synthesise layers of pDNA-loaded mineral-phosphate particles, the use of PEI to form pDNA/PEI complexes proved less successful.

Visually, a thin line provided evidence of complexation, but the layer's thickness was far too thin to be used as a chondrogenic layer in a pre-clinical osteochondral model. And, whilst SEM was appropriate for measuring phosphate-mineral particle diameters, the organic composition of pDNA/PEI complexes prevents the use of conventional SEM in measuring their diameters. Furthermore, the lyophilisation process – whilst not likely to effect phosphate-mineral particles – may be irreparably destroying the pDNA/PEI complex structure due to removal of H_2O molecules during sublimation. The PS-CAGE system may therefore only be suitable in producing GAMs with phosphate-mineral particles, unless a means of extracting particles for solution-based characterisation can be devised.

It is certainly of interest to extract CaP and pDNA/CaP particles, by some means, from cryogels so that particles can be resuspended in solution and characterised independent of the cryogel. Suspension in solution would facilitate more accurate determination of particle size would be measured via dynamic light scattering (DLS). In solution, dissolution of pDNA/CaP particles in acidic buffer could be conducted for subsequent characterisation in gel electrophoresis as a conventional means of investigating pDNA encapsulation efficiency. pDNA/CaP particles in solution could also be administered to cell monolayers to determine their transfection efficacy more accurately at different sizes. In significant amounts, extracted pDNA/CaP particles could also be prepared for XRD analysis in the absence of the amorphous agarose signal.

Given that PS-DW-AGE approaches are rare in the literature, there is a likewise scarcity of established methods to extract CaP-based particles from agarose hydrogels or cryogels. At a glance, one could simply continue to apply the electric field after the second 6-minute application to transport the CaP-based particles out of the agarose hydrogel. However, Kamitakahara et al. (2007) established that a continued application of the electric field resulted in a visual loss of the CaP precipitate and loss of particles through their transport. If electrophoretic transport of pDNA/CaP is possible, this could be one route for extraction.

Presently, there are four ways that show potential in releasing pDNA/mineral particles from agarose. These are: 1) electrophoretic removal *in-situ*; 2) enzymatic degradation of agarose post-synthesis; 3) thermal degradation of agarose post-synthesis; and 4) hydrogel melting in a salt solution. Electrophoretic removal *in-situ* is certainly the simplest of these routes given it requires no treatment of the agarose itself. In short, the applied potential would be sustained after the normal synthesis period to electrophoretically transport particles from the agarose into a collection medium, such as a semi-permeable membrane or – more simply - a pipette could be used to extract particles directly from solution. As simple as either of these routes appears,

one must keep in mind that sustained applied potentials reduce the visibility of CaP layers which is theorised to arise from particle dissolution and/or transport, where particle dissolution is of course undesirable. One must also acknowledge that only particles below a critical size (dependent on mean pore size) will be extracted from the agarose matrix due to Knudsen diffusion. For particle characterisation this is undesirable given the resultant particle population is not representative of that synthesised during PS-AGE, but as a pDNA/mineral synthesis route it size-filters particles below a critical size, further reducing particle size which is arguably beneficial for transfection efficacy.

Enzymatically degrading the agarose matrix has potential to allow for the separation of particles from agarose but will ultimately depend on the buffer required for the enzyme, as well as incubation time and temperature. According to it's protocol, one unit of β-agarase (Thermo Fisher Scientific Inc., USA) has the capacity to degrade 100 mg of low melting point agarose at 42 °C after a 30-minute incubation, using a buffer comprised of tris(hydroxymethyl)aminomethane (tris), an acidic conjugate of either borate, acetate, phosphate, HCl, and a small amount (1 – 2 mM) of EDTA. There are several immediate concerns over using β-agarase for pDNA/mineral particle extraction. Firstly, this protocol is supposedly only suitable for low melting point agarose, which Seakeam® is not. But if this is with regard to the incubation temperature at which high melting point agarose will begin to gel, one can simply melt the agarose and add heated buffer to reduce the concentration below the threshold required to remain liquid at 42 °C. Another concern in enzymatically digesting the agarose gel is the presence of EDTA in the buffer which is known to chelate divalent cations that would otherwise inhibit enzyme activity, but could simultaneously extract ions from particles embedded in the gel.

Thermal degradation of agarose is assumed to occur at temperatures greater than that required to degrade DNA and is therefore unsuitable for extraction of pDNA/mineral particles. Despite this, thermal degradation could still serve as a means of extracting non-pDNA particles into solution for functionalisation and/or characterisation. There would of course be further limitations with regard to retaining the initial crystallinity of minerals. Another complication is the temperature required to decompose agarose and reactant formed. Ouyang (2018) found that agar decomposes between 300 – 600 °C into a variety of organic compounds, namely furans and furfurals. If cryogels embedded with particles could be thermally degraded at sub-300 °C temperatures, and if the resultant organic compounds can be removed via washing in a suitable solvent, then resuspension of particulate species remains plausible using this route.

Agarose hydrogels embedded with particulate species could be re-melted and the resulting mixture centrifuged to pellet particles. However, the mixture will quickly form a gel if left to cool and heated mixtures are often unsuitable for centrifugation. Interestingly, dilution of the mixture below a critical concentration of agarose could be used to prevent re-gelling. Ichinose (2020) used surface tension measurements to identify this concentration threshold as approximately 0.3 wt % in an agarose-water system.

In all four extraction methods, a particle mixture can be obtained. Electrophoretic extraction in-situ would result simply in a buffered particle solution, whilst enzymatic degradation of agarose will result in a buffered solution of particles, enzymes and agarose debris (the latter assuming enzymes are not 100 % efficient). Thermal degradation would similarly result in a buffer-particle solution, though it would contain some impurities resulting from the thermal decomposition of agarose. Lastly, hydrogel melting in a salt solution would provide particles in a salt solution with 'solubilised agarose'. In the case of electrophoretic extraction, particles could be lightly pelleted using conventional centrifugation and resuspended at the desired concentration for characterisation or functionalisation. Meanwhile, the particle solutions from all other routes require a means of separating agarose and other impurities from the particles. Density gradient centrifugation is a relatively simple approach to separating the components of these solutions and is especially suitable here given the contrasting densities of the particle solutions. The approximate density of agarose is 1.6 gcm^{-3} (Laurent, 1967), whilst ACP (if similar to HAp) is 3.14 gcm^{-3} and MgP (if tri-MgP) is 2.16 gcm^{-3}.

Particle extraction of CaP and MgP particles would open a whole range of possible applications for the PS-DW-AGE and PS-CAGE systems, and crucially allow further investigations into the transfection capabilities of these particles. Nevertheless, in its current form, the PS-DW-AGE – any especially the PS-CAGE – have demonstrated the capacity to produce sub-100 nm particles that coat PDA-surfaces. There is perhaps further use for cryogels produced via these systems as more simply mineralised scaffolds rather than GAMs.

6 Appendix

Despite the damage, the target location stopped distorting after a few seconds of being under the electron beam and particles were still clearly visible on / below the agarose surface. Due to the low magnification used, no obvious co-location of calcium or phosphate signal is observed. Of course, high magnification could not be used because of the severe damage caused by the intense electron beam.

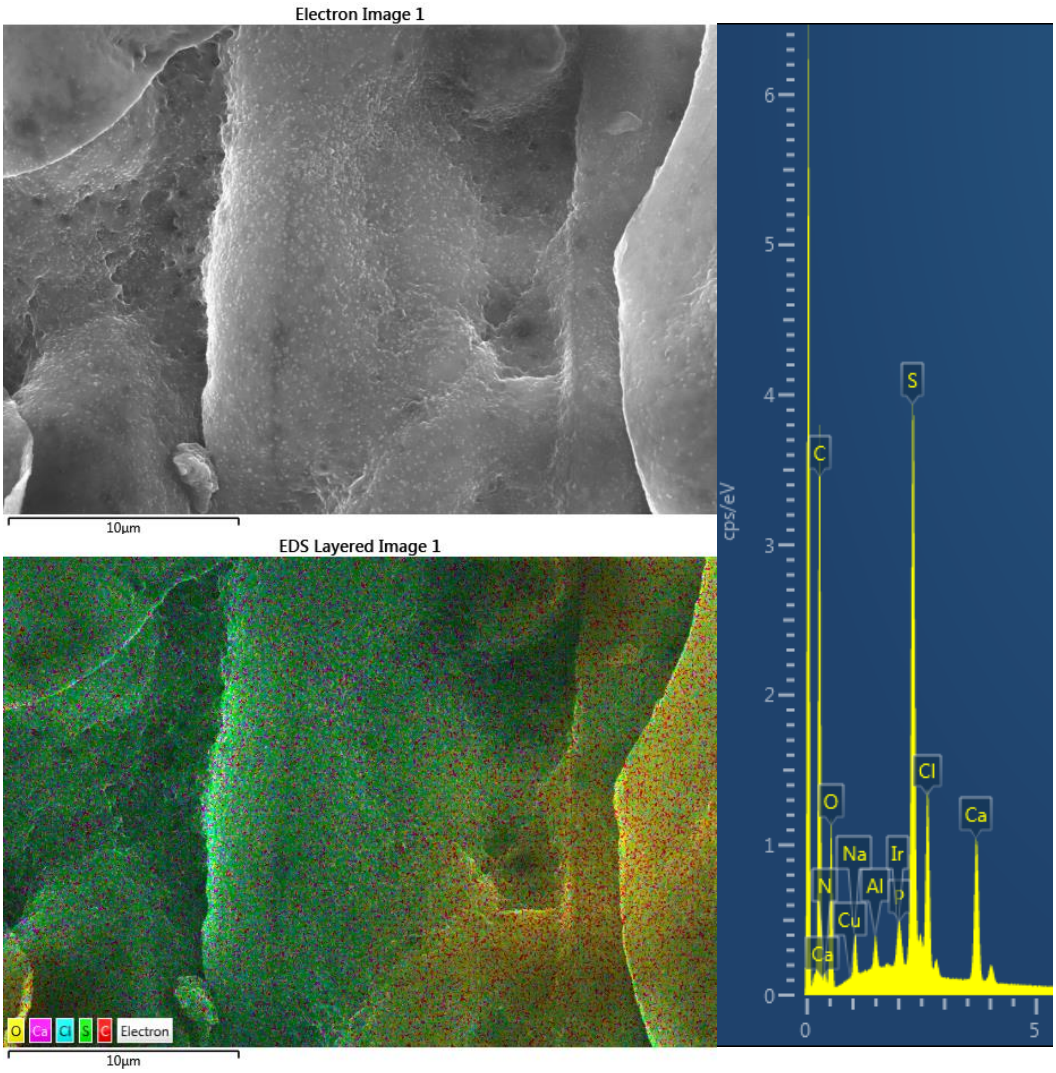


Figure 6.1. EDS map of an agarose fragment surface from a CaP cryogel sample. (A) SE image of target area; (B) EDS layered map and (C) EDS summary spectrum of detected elements.

The EDS spectrum in Figure 6.1 shows the presence of carbon, which will be from the carbon sticker, whilst the aluminium and copper signal will originate from the stub itself. Naturally, the

iridium signal is due to the iridium coating. Given the HEPES molecule boasts nitrogen and sulphur, and that the buffer contains Na_2HPO_4, nitrogen, sulphur and sodium signals are likely due to residual buffer crystals within the cryogel sample. Phosphorous signal could originate from either buffer crystals or CaP particles. Similarly, calcium signal could be produced by residual $CaCl_2$ loading solution or CaP particles. Chlorine signal will also result from residual $CaCl_2$. Oxygen signals will resonate from locations throughout the sample since it is a component of agarose, phosphate, and will be present in residual salt crystals. Oxygen will also be present in CaP particles due to their wet synthesis in the presence of H_2O. One must keep in mind that the depth at which characteristic x-rays originate can easily exceed that of SEs. X-rays produced at shallow depths and deep within the sample can therefore superimpose, making any identification of co-located calcium and phosphate signals difficult to visualise.

Figure 6.2 shows the EDS data for the pDNA/CaP cryogel sample. As with the CaP sample, the SE image shows the sensitivity of the agarose surface to high accelerating voltages. The agarose fragment initially had a mostly flat topography, but then bubbled rapidly during EDS data collection. Similar to the CaP sample, Carbon, Sulphur, Sodium, Aluminium, Iridium, and Chlorine signals are present. Calcium and Oxygen signals are present, but their co-location was not observed (Figure 6.1), whilst Phosphorous remains undetected.

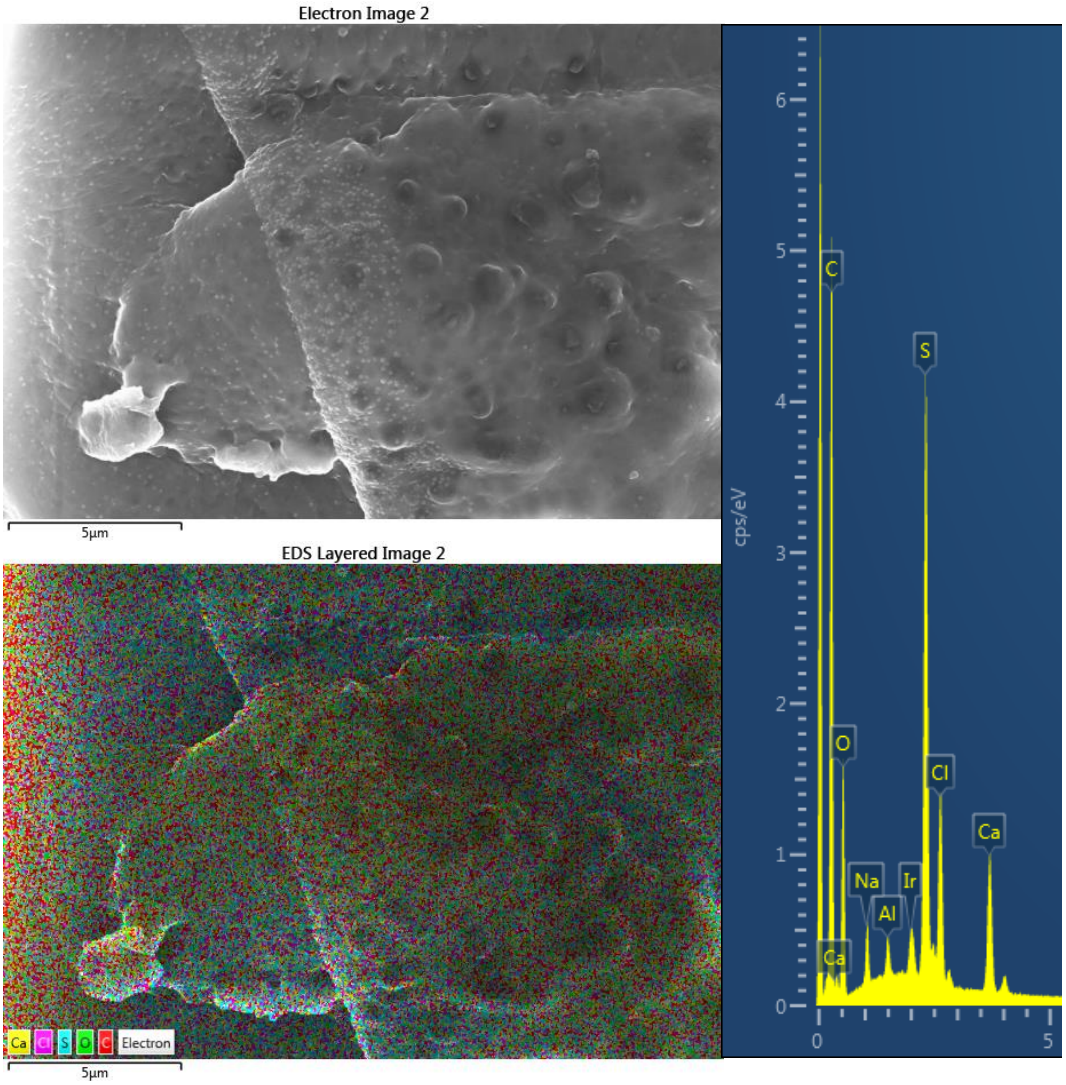


Figure 6.2. EDS map for pDNA/CaP cryogel sample. (A) SE image of target area; (B) EDS layered map and (C) EDS summary spectrum of detected elements.

Table 6.1. Gel tray design specifications.

Area	Specification Number	Description
Size	1.1.	The gel tray must have the same overall base dimensions as the existing gel tray (15 x 15 cm) to fit into the electrophoresis tank and hold a 130 mL agarose gel (6mm depth).
Size	1.1.	The gel tray must not exceed 160 cm total width to fit in the gel dam caster.
Size	2.1.	The height of the gel tray must not exceed 30 mm to allow the electrophoresis tank lid to sit on top of the tank.
Function	4.1.	Tray slots should fit 2mm thick combs with minimal clearance to restrict their movement in the x- and y-planes.
Function	5.1.	Tray slots should be spaced 9mm apart from centres
Function	6.1.	The tray should fit at least 10 combs
Durability	3.1.	The base and walls of the tray must be at least 4mm for adequate strength in adhesive joints
Material	8.1.	Tray base must be UV/Vis transparent to observe precipitate formation from the benchtop and for DNA stain visualisation in a UV gel imager
Material	9.1.	Tray material must be non-conductive and resistant to corrosion from salt solutions
Manufacture	10.1	+/- 0.05 mm tolerance for all dimensions

Table 6.2. Gel comb design specifications.

Area	Specification Number	Description
Size	1.1.	The width of the comb must not exceed 15 cm to fit into the gel tank
Size	1.2.	The thickness of the comb must be 2mm
Size	1.3.	The length of the teeth must be short enough to sit 2 mm from the gel tray base
Function	2.1.	The gel comb must have 16 teeth, each 6 mm thick, spaced 9 mm apart from centres (compatible with multichannel pipettes)
Function	2.2.	Both ends of the comb must have ledges that allow the comb to sit in the gel tray slots
Function	2.3.	Both ends of the comb should have grips to remove the comb from the gel by hand
Material	3.1.	The comb material needs to be rigid enough to resist bending under the pressures of the molten gel
Material	4.1.	Gel comb material should have low surface roughness
Material	4.2.	Material should be resistant to corrosion by salt solutions
Material	4.3.	Material should be a maximum working temperature over 100°c
Manufacture	5.1.	+/- 0.05 mm tolerance for all dimensions

The surface roughness and water contact angle of the gel comb material is a particularly important specification and is required to minimise the friction between the gel and comb when removing the comb. Extruded polyoxymethylene (acetal) is therefore an ideal choice of material due to its high contact angle with water that will reduce the surface tension between the gel and comb and reduce the pull-out force required post-casting. 3D printed materials are not an option given their surface roughness is often high and could therefore ‘grip’ gel surfaces. One difficulty in cutting from extruded sheet, rather than casting, is that the non-symmetrical design can strain the part and cause unwanted flexion. If this arises, the solution will be to induce stress relaxation by flattening the combs with a heavy weight and holding them at high temperature overnight, followed by slow cooling.

Table 6.3. Gel punch design specifications for the individual punch and piston components.

Area	Component	Specification Number	Description
Function	Punch	1.1.	Sharp cutting edges (≤ 0.5 mm) to prevent crushing samples
Function	Punch	1.2.	Retain samples after they have been sliced
Function	Piston	1.3.	Eject samples without altering their shape
Function	Piston	1.4.	Fit tightly within the shaft of the piston to trap water and create an almost air-tight seal above the trapped gel slice
Size	Punch	2.1.	Be large enough to be handled easily
Material	Punch + Piston	3.1.	Be made from 316 stainless steel to resist corrosion by salt solution and maintain sharp cutting edges
Manufacture	Punch + Piston	4.1.	+/- 0.05 mm tolerance for all dimensions

Table 6.4. Cutting mask design specifications.

Area	Specification Number	Description
Function	1.1.	Precisely position 16 square holes over a row of 16 particle layers for the gel punch to extract highly repeatable gels
Function	1.2.	Fit into the grooves of the well tray walls
Material	3.1.	Be made from 316 stainless steel to resist corrosion by salt solution and maintain sharp cutting edges
Manufacture	4.1.	+/- 0.05 mm tolerance for all dimensions

Table 6.5. Comb Riser Design Specifications.

Area	Specification Number	Description
Function	1.1.	Teeth should securely fit between the gel tray slots
Size	2.1.	Have a spine thin enough to snap by hand
Material /Manufacture	3.1.	Design features must be suitable for 3D printing
Manufacture	4.1.	+/- 0.1 mm tolerance for all dimensions

Unlike the gel tray and combs, the riser should not be in contact with molten gel. Combined with its size, the riser is ideally suited for manufacture on a benchtop 3D-printer. The riser will have a repeating pitch of 9 mm to fit between the slots of the gel tray. However, 3D-printing on a benchtop printer prevents low tolerances being used and hence the repeating 9 mm pitch is

likely to be misalign with the gel tray slots. The spine of the riser should therefore be thin enough to snap so that the riser can be used as segments.

Table 6.6. Specifications for the Gel Cylinder Cast.

Area	Specification Number	Description
Description	1.1.	A gel cast composed of a base, mould and lid, to cast cylindrical agarose gels.
Function	2.1.	The mould must have space for six, 22mm gels.
	2.2.	The mould should be smaller than 158mm to fit into the BioRad electrophoresis tank.
	2.3.	The lid should be flexible so it can be 'peeled' away, preventing gel cylinders being pulled out of the mould with a vacuum effect.
		The moulds must be able to connect to each other to prevent movement and misalignment of gels.
Material	3.1.	The materials for each component must have a maximum working temperature of at least 60°c.
	3.2.	Materials for all components must be watertight and leak proof at 60°c.
		The mould material must be non-conductive and salt-corrosion resistant.

Plastics are the most appropriate material choice for all components since they are non-conductive and resistant to salt-corrosion. Rather than casting, it would be much faster and cheaper to 3D-print the base and mould, whilst the lid can be made from thin acrylic sheet. 3D-printing would allow rapid prototyping and testing by hand to ensure the components function as intended, with the possibility of changing the design and reprinting in a short time if there are issues. VeroClear is a typical 3D-printing material that mimics polymethylmethacrylate (PMMA) that has a high enough working temperature for this application and can be printed with microporosity. Though not entirely waterproof without curation, VeroClear components should not leak solution under normal pressure when parts are at least a few millimetres thick. Retention of agarose in pores or gripping the part surface after use may be a problem though, so thorough cleaning is required between uses.

Table 6.7. Specifications of the raised electrode holders.

Area	Specification Number	Description
Description	1.1.	A pair of removable electrodes to fit onto the BioRad horizontal electrophoresis tank to provide a near-uniform electric field for gel cylinder.
Function	2.1.	Must be able to hook onto the walls of the electrophoresis tank and fit under the tank lid.
	2.2.	Must have banana plug connectors.
	2.3.	Any submerged platinum wire not inline with the centre of the gel must be covered with an electrical insulator.
	2.4.	The platinum wire must be taught enough not to sag significantly.
	2.5.	Air produced by redox reactions must be free to travel to the buffer surface.
	2.6.	Must not damage the standard platinum wire electrodes already in the electrophoresis tank.
Materials	3.1.	Both electrode wires must be platinum.
	3.2.	Supporting materials must be electrical insulators and resistant to salt-corrosion.
Safety	4.1.	The platinum wire-to-banana plug connection must be electrically insulated.

Acrylic is a suitable material to use as the electrode support material since it is salt-corrosion resistant, an electrical insulator, and can create multi-pieces components with chemical adhesives that would be rigid enough to keep the platinum wire in line with the gel cylinder centre.

Table 6.8. Heat exchanger and water loop specifications for the temperature/pH control unit.

Area	Specification	Description
Description	1.1.	A heat exchanger composed of Peltier modules thermally coupled to two water loops, absorbing thermal energy from one and donating thermal energy to the other.
Components	2.1.	The heat exchanger should be comprised of four, 60W Peltier modules.
	2.2.	Water blocks that are thermally coupled via a thermal compound to the Peltier modules should be used for water circulation and thermal energy exchange.
	2.3.	Fanned heat sinks will be thermally coupled to the top side of the hot water block for additional thermal energy extraction.
	2.4.	A small, high RPM fan should be used to provide additional thermal energy extraction from the fanned heat sinks.
	2.5.	
	2.6.	All components should be secured in a housing to maintain thermal coupling and thermally insulate cold components.
	2.7.	Tubing must be able to provide watertight fittings with all components in the water loops.
		Each of the two pumps must be able to pump ≥ 1 L/m.
Materials	3.1.	The water blocks should be made from a corrosion resistant material of high thermal conductivity.
	3.2.	The thermal compound should be malleable to enable maximum contact surface area between surfaces of different components.
	3.3.	The fanned heat sinks should be made from a material of high thermal conductivity.
	3.4.	The housing must be a rigid material to maintain a uniform pressure between the water blocks and Peltier modules.
Safety	4.1.	The housing must raise the heat exchanger off the ground with non-conductive materials to avoid contact with spillages or leaks.
	4.2.	The housing must be electrically grounded if metal.

Water blocks and fanned heat sinks are most commonly made from aluminium alloy due to the low cost of the material and for ease of milling. Aluminium also forms an oxide coating that inhibits corrosion when in contact with water. Copper heat sinks – which have a higher thermal conductivity than aluminium - are available but their much higher cost prohibits their use in this system, especially given that the heat sinks are only used as a secondary thermal extractor. Aluminium in the form of flat bar and angle bar can also be used for the housing since it will be far easier to machine than steel and has the necessary rigidity to maintain uniform pressure across the thermal couples.

Thermal compounds used to couple processors to heat sinks are ideally suited to couple the Peltier modules, water blocks and heat sinks together. Though thermal pads are easier to apply, thermal paste can fill in any gaps in imperfect surfaces such as machined aluminium for more efficient thermal transfer than pads.

Table 6.9. Design specifications for the electronic systems of the temperature/pH control unit.

Area	Specification	Description
Description	1.1.	An electronics system capable of measuring buffer temperatures, sending temperature data to an Arduino, then outputting on/off signals to a relay array controlling Peltier modules.
Components	2.1.	A printed circuit board (PCB) must be used for permanent, soldered connections.
	2.2.	Five digital and waterproof temperature sensors are required with ≥ 30 cm of wire length.
	2.3.	The relay module must be four-channel, 5V-powered and capable of at least 10A switching.
	2.4.	The Arduino must have enough digital ports for five sensors and four relay connections.
	2.5.	A DC power supply capable of supplying 5V and 12V, with at least 500 W total power output.
	2.6.	Three LCD screens are needed for temperature reading outputs
	2.7.	Two 12V water pumps are required, one for each loop, with a pumping rate ≥ 10L/min.
	2.8.	A 40 mm, high speed fan is required for the heat exchanger.
	2.9.	Four, 120 mm fans are needed: two to cool the radiator and two for the enclosure.
	2.10.	A voltmeter/ammeter must be used in parallel/series with each Peltier module to monitor power draw.
	2.11.	A USB male-to-female connection from the Arduino to the user interface to allow Arduino coding to be updated easily.
Safety	4.1.	All electrical connections from the DC power supply must be double insulated.
	4.2.	The voltage across and current through each Peltier module must be displayed on a screen to indicate any unsafe power draw.
	4.3.	Wiring responsible for carrying high currents i.e. for Peltier modules must have a redundancy of at least twice the maximum current of a module.
	4.4.	Apart from the Peltier modules and pumps, all electrical components must be kept separate from the water loops.

Table 6.10. Design Specifications of the enclosure.

Area	Specification Number	Description
Description	1.1.	An enclosure is required to encapsulate the heat exchanger, cold water pump, radiator, fans, and all other electronics system components, with an accessible user interface.
Function	2.1.	The front of the enclosure must have user-accessible controls to turn on/off the power supply, fans, pumps and Peltier modules.
	2.2.	The enclosure must have space for water reservoir 1 and provide an easily accessible fill port.
	2.3.	The enclosure must have space for fans to draw in air to be pumped into the enclosure.
	2.4.	Space for water loop tubing must be provided on one of the sides of the enclosure.
	2.5.	Have a 240mm radiator (suitable for 2 x 120mm fans) attached against an exhaust vent for the 'hot' water loop.
Size	3.1.	The base of the housing should not exceed 0.2 m^2 to fit on a laboratory benchtop.
Material	4.1.	The primary material should have a high toughness so it can be easily machined using non-CAM tools.
	4.2.	The primary material should be resistant to 70% EtOH so it can be cleaned in the laboratory.
Air Circulation	4.1.	The enclosure must provide sufficient air circulation to prevent the heat exchanger and radiator fans from over rotating due to a lack of air.
	4.2.	The housing should provide exhaust vents for the power unit, heat exchanger and radiator.
	4.3.	Air filtration should be used to limit dust build up on the inside of the housing.
Safety	5.1.	The enclosure material must be non-conductive to protect against shorting from uninsulated wiring.
	5.2.	The enclosure must separate the water loop and electronic components into two separate compartments to prevent water contacting electrical components in the event of a leak or malfunction.
	5.3.	The enclosure should make the internalised electrical components inaccessible without the use of a screwdriver.
	5.4.	Transparent materials should be used to allow immediate identification of leaks from water loops.

A good choice for the primary material of the enclosure if polycarbonate due to its good resistance to 70% EtOH, high toughness that makes it easy to machine with a low risk of damage during machining. Polycarbonate is also an electrical insulator which prevents the need for grounding as a safety feature in the event of a short.

The overall layout of the enclosure must separate the water loops from electronic components as a safety feature in the event of a leak or malfunction. For this reason, it would be appropriate to design the enclosure with two layers; the bottom layer holding the pump, reservoir, radiator, heat exchanger and fans, and the top layer holding the electronics systems (including the power supply). This will also reduce the benchtop space required for the temperature unit.

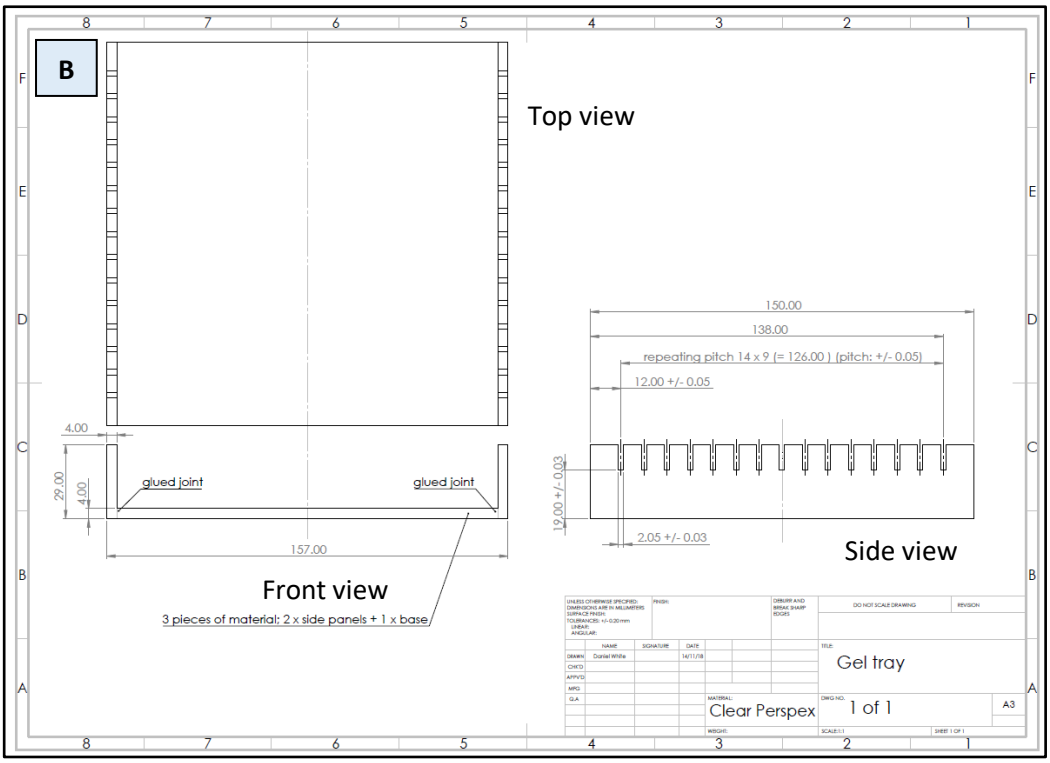


Figure 6.3. Orthographic drawing of the gel tray for the PS-DW-AGE system.

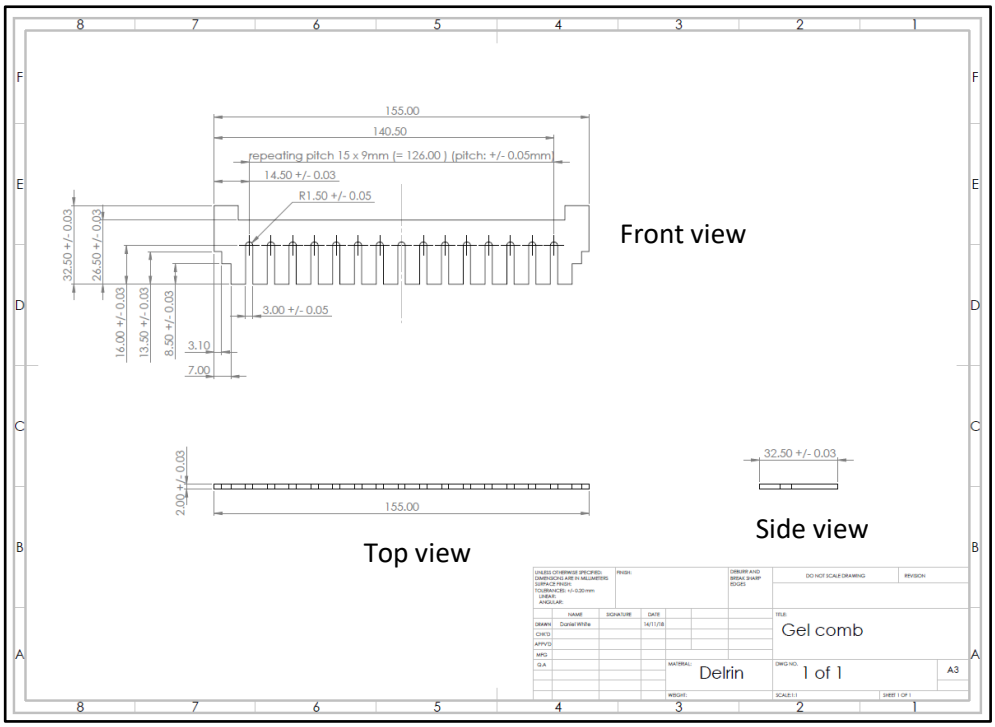


Figure 6.4. Orthographic drawing of a comb for the PS-DW-AGE system.

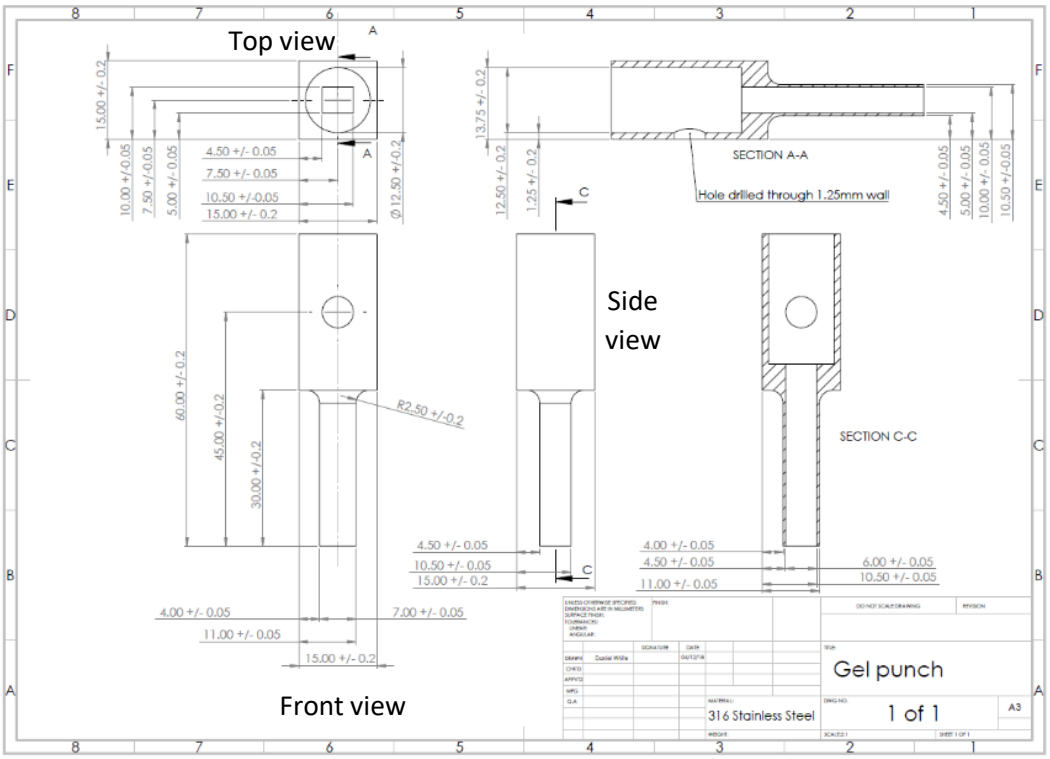


Figure 6.5. Orthographic drawing of the gel punch.

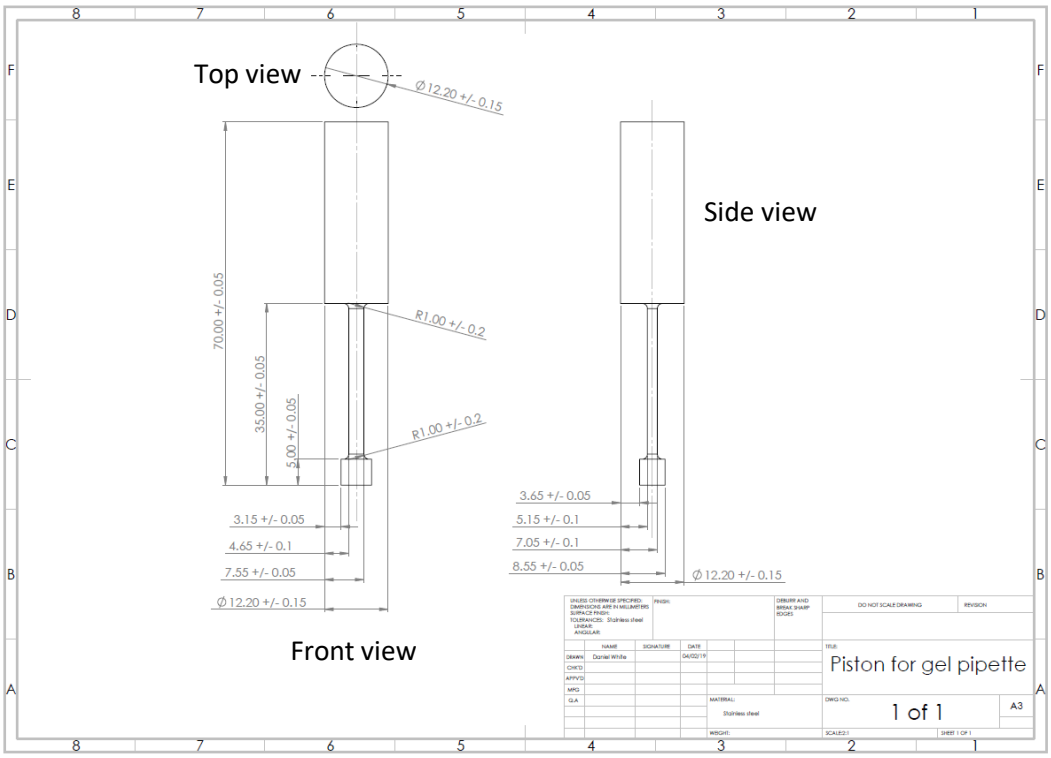


Figure 6.6. Orthographic drawing of the piston.

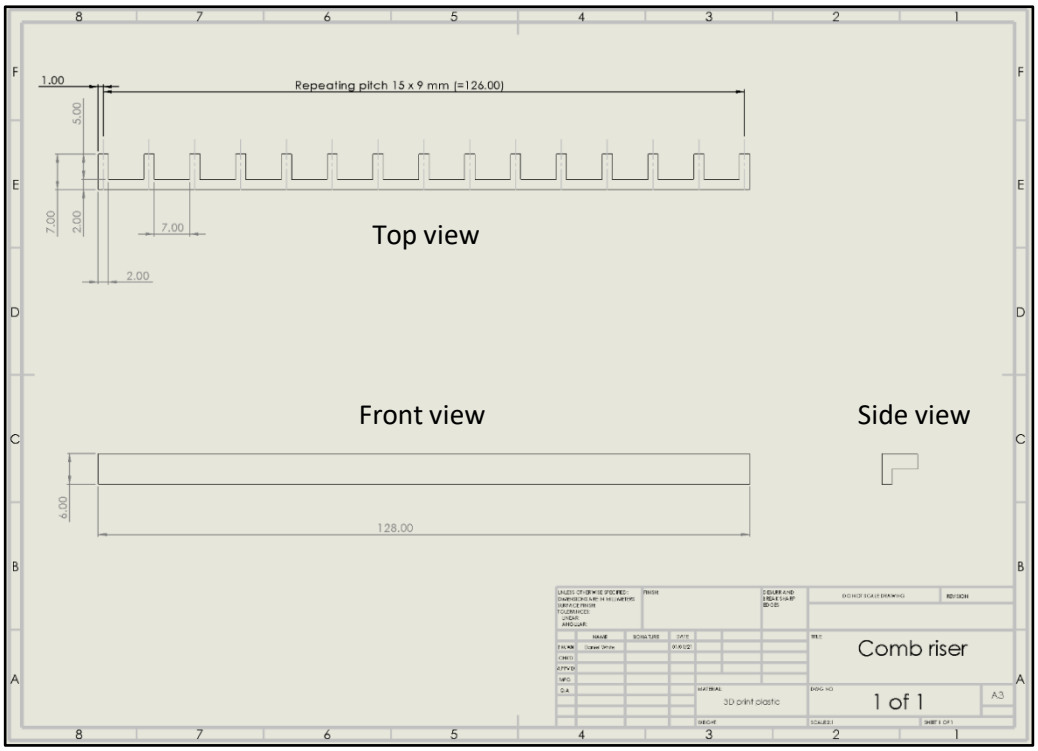


Figure 6.7. Orthographic drawing of the comb riser for the PS-DW-AGE system.

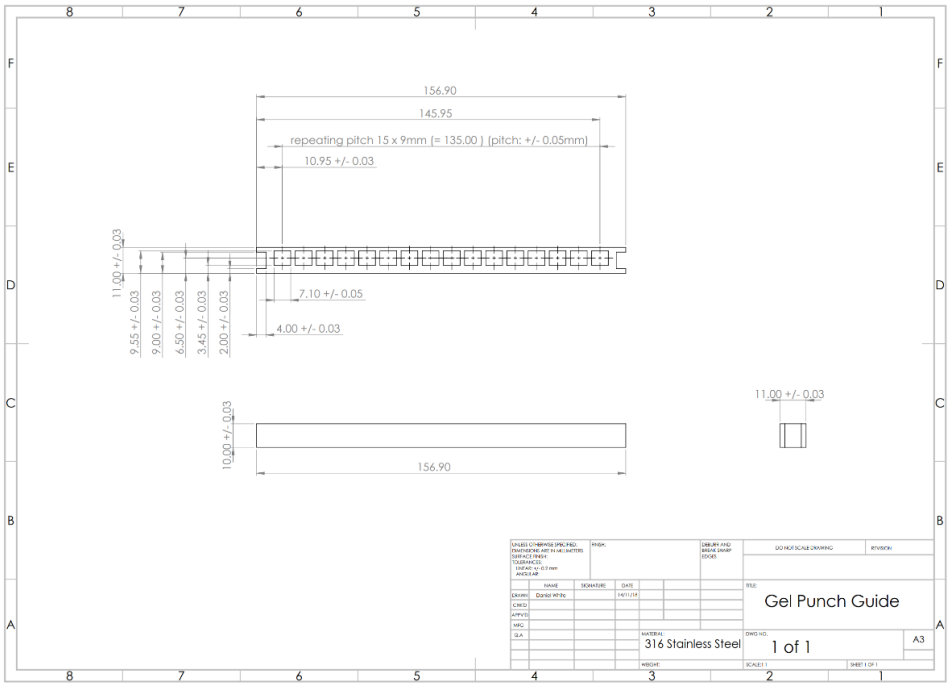


Figure 6.8. Orthographic drawing of the cutting mask for the PS-DW-AGE system.

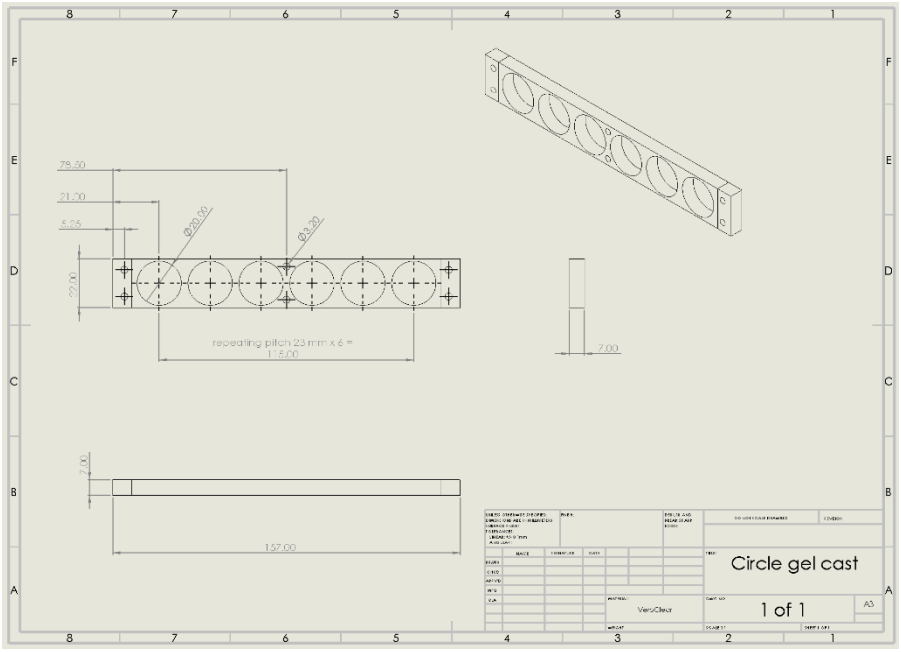


Figure 6.9. Orthographic drawing of the cylindrical gel cast for the PS-CAGE system.

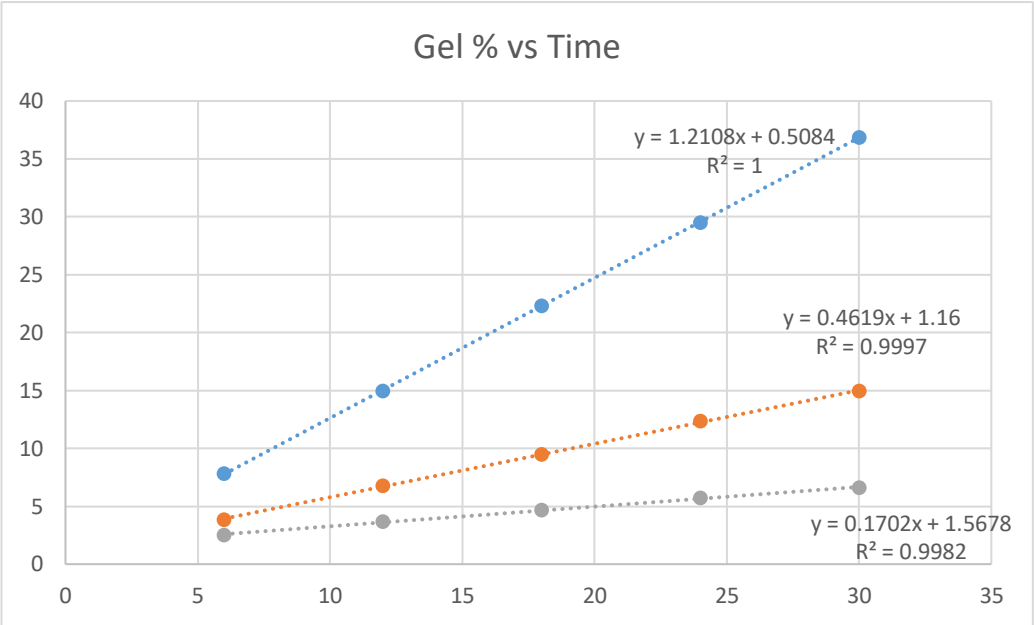


Figure 6.10. pDNA velocities in various SeaKem® agarose concentration plotted against time. Blue = 1 wt %; orange = 2 wt %; grey = 3 wt %.

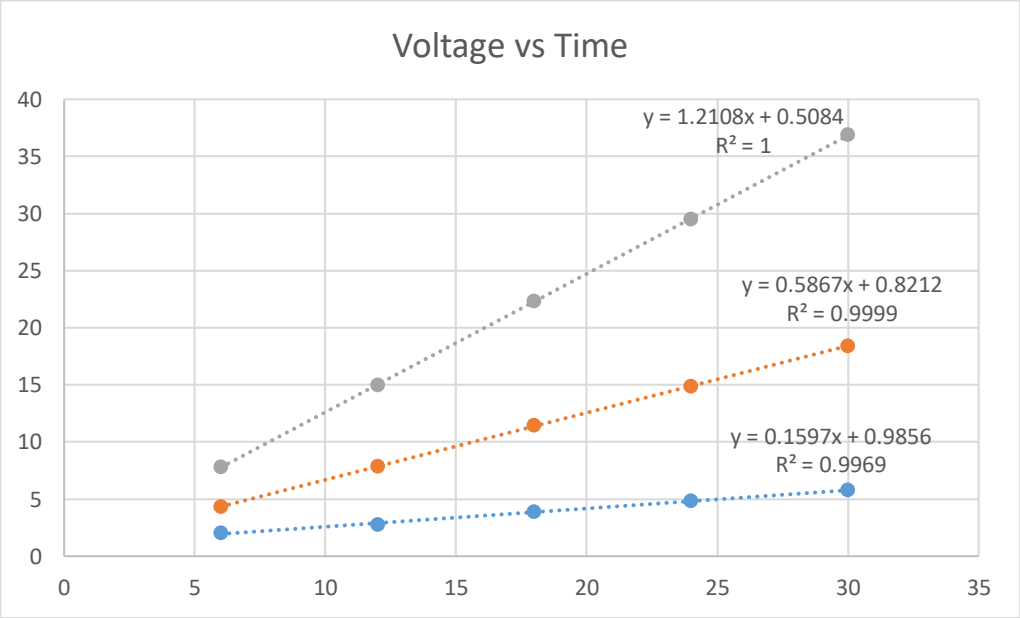


Figure 6.11. pDNA velocities in SeaKem® agarose at different applied potentials, plotted against time. Blue = 60 V; orange = 180 V; grey = 300 V

Bibliography

Electrochemical Crystal Growth.

AHERN, B. J., PARVIZI, J., BOSTON, R. & SCHAER, T. P. 2009. Preclinical animal models in single site cartilage defect testing: a systematic review. *Osteoarthritis Cartilage,* 17**,** 705-13.

AL-DOSARI, M. S. & GAO, X. 2009. Nonviral gene delivery: principle, limitations, and recent progress. *AAPS J,* 11**,** 671-81.

AL-GHOBASHY, M. A. 2014. Electrophoretic behavior of charge regulated zwitter ionic buffers in covalently and dynamically coated fused silica capillaries. *Bulletin of Faculty of Pharmacy, Cairo University,* 52**,** 71-78.

ANGULO-SHERMAN, A. & MERCADO-URIBE, H. 2014. Ionic transport in glycerol-water mixtures. *Ionics,* 21**,** 743-748.

ANNABI, N., NICHOL, J. W., ZHONG, X., JI, C., KOSHY, S., KHADEMHOSSEINI, A. & DEHGHANI, F. 2010. Controlling the porosity and microarchitecture of hydrogels for tissue engineering. *Tissue Engineering,* 16**,** 14.

ARCHER, D. G. & WANG, P. 1990. The dielectric constant of water and Debye-Hückel Limiting Law Slopes. *Journal of Physical and Chemical Reference Data,* 19**,** 41.

ARVIZO, R. R., MIRANDA, O. R., THOMPSON, M. A., PABELICK, C. M., BHATTACHARYA, R., ROBERTSON, J. D., ROTELLO, V. M., PRAKASH, Y. S. & MUKHERJEE, P. 2010. Effect of nanoparticle surface charge at the plasma membrane and beyond. *Nano Lett,* 10**,** 2543-8.

ATAOL, S., TEZCANER, A., DUYGULU, O., KESKIN, D. & MACHIN, N. E. 2015. Synthesis and characterization of nanosized calcium phosphates by flame spray pyrolysis, and their effect on osteogenic differentiation of stem cells. *Journal of Nanoparticle Research,* 17.

BAKAN, F. 2018. Gene Delivery by Hydroxyapatite and Calcium Phosphate Nanoparticles: A Review of Novel and Recent Applications. *Hydroxyapatite - Advances in Composite Nanomaterials, Biomedical Applications and Its Technological Facets.*

BAKAN, F., KARA, G., COKOL CAKMAK, M., COKOL, M. & DENKBAS, E. B. 2017. Synthesis and characterization of amino acid-functionalized calcium phosphate nanoparticles for siRNA delivery. *Colloids Surf B Biointerfaces,* 158**,** 175-181.

BAKER, A., SALTIK, M., LEHRMANN, H., KILLISCH, I., MAUTNER, V., LAMM, G., CHRISTOFORI, G. & COTTEN, M. 1997. Polyethylenimine (PEI) is a simple, inexpensive and effective reagent for condensing and linking plasmid DNA to adenovirus for geene delivery. *Gene Therapy,* 4**,** 10.

BAVYA DEVI, K., LALZAWMLIANA, V., SAIDIVYA, M., KUMAR, V., ROY, M. & KUMAR NANDI, S. 2022. Magnesium Phosphate Bioceramics for Bone Tissue Engineering. *Chem Rec,* 22**,** e202200136.

BHAKTA, G., MITRA, S. & MAITRA, A. 2005. DNA encapsulated magnesium and manganous phosphate nanoparticles: potential non-viral vectors for gene delivery. *Biomaterials,* 26**,** 2157-63.

BHAKTA, G., SHRIVASTAVA, A. & MAITRA, A. 2009. Magnesium phosphate nanoparticles can be efficiently used in vitro and in vivo as non-viral vectors for targeted gene delivery. *J Biomed Nanotechnol,* 5**,** 106-14.

BISHT, S., BHAKTA, G., MITRA, S. & MAITRA, A. 2005. pDNA loaded calcium phosphate nanoparticles: highly efficient non-viral vector for gene delivery. *Int J Pharm,* 288**,** 157-68.

BOFFA, A., SOLARO, L., POGGI, A., ANDRIOLO, L., REALE, D. & DI MARTINO, A. 2021. Multi-layer cell-free scaffolds for osteochondral defects of the knee: a systematic review and meta-analysis of clinical evidence. *J Exp Orthop,* 8**,** 56.

BOSE, S. & TARAFDER, S. 2012. Calcium phosphate ceramic systems in growth factor and drug delivery for bone tissue engineering: a review. *Acta Biomater,* 8**,** 1401-21.

CAI, Y., LIU, Y., YAN, W., HU, Q., TAO, J., ZHANG, M., SHI, Z. & TANG, R. 2007. Role of hydroxyapatite nanoparticle size in bone cell proliferation. *Journal of Materials Chemistry,* 17.

CANTAERT, B., BENIASH, E. & MELDRUM, F. C. 2013. Nanoscale confinement controls the crystallization of calcium phosphate: relevance to bone formation. *Chemistry,* 19**,** 14918-24.

CAO, X., DENG, W., WEI, Y., SU, W., YANG, Y., WEI, Y., YU, J. & XU, X. 2011. Encapsulation of plasmid DNA in calcium phosphate nanoparticles: stem cell uptake and gene transfer efficiency. *Int J Nanomedicine,* 6**,** 3335-49.

CHEN, D., ZHANG, P., LI, M., LI, C., LU, X., SUN, Y. & SUN, K. 2022. Hyaluronic acid-modified redox-sensitive hybrid nanocomplex loading with siRNA for non-small-cell lung carcinoma therapy. *Drug Deliv,* 29**,** 574-587.

CHEN, R., PYE, J. S., LI, J., LITTLE, C. B. & LI, J. J. 2023. Multiphasic scaffolds for the repair of osteochondral defects: Outcomes of preclinical studies. *Bioact Mater,* 27**,** 505-545.

CHEN, S. H., CHAO, A., TSAI, C. L., SUE, S. C., LIN, C. Y., LEE, Y. Z., HUNG, Y. L., CHAO, A. S., CHENG, A. J., WANG, H. S. & WANG, T. H. 2019. Utilization of HEPES for Enhancing Protein Transfection into Mammalian Cells. *Mol Ther Methods Clin Dev,* 13**,** 99-111.

CHENG, W., ZENG, X., CHEN, H., LI, Z., ZENG, W., MEI, L. & ZHAO, Y. 2019. Versatile Polydopamine Platforms: Synthesis and Promising Applications for Surface Modification and Advanced Nanomedicine. *ACS Nano,* 13**,** 8537-8565.

CHOW, L. C. & EANES, E. D. 2001. Solubility of calcium phosphates. *Octacalcium Phosphate*.

CHUPRUNOV, K., YUDIN, A., LEYBO, D., LYSOV, D., KOLESNIKOV, E., KUZNETSOV, D., GODYMCHUK, A. & MANDAL, A. R. 2020. Hydrothermal Synthesis Duration Influence on Calcium Phosphate and Hydroxyapatite Phase Composition. *Materials Science and Engineering,* 731.

COOK, J. L., HUNG, C. T., KUROKI, K., STOKER, A. M., COOK, C. R., PFEIFFER, F. M., SHERMAN, S. L. & STANNARD, J. P. 2014. Animal models of cartilage repair. *Bone Joint Research,* 3**,** 6.

DALTIN, A. L., BEAUFILS, S., ROUILLON, T., MILLET, P. & CHOPART, J. P. 2019. Calcium Phosphate Powder Synthesis by Out-of-Phase Pulsed Sonoelectrochemistry. *Ultrasonics Sonochemistry,* 58**,** 11.

DEL VALLE, L. J., BERTRAN, O., CHAVES, G., REVILLA-LOPEZ, G., RIVAS, M., CASAS, M. T., CASANOVAS, J., TURON, P., PUIGGALI, J. & ALEMAN, C. 2014. DNA adsorbed on hydroxyapatite surfaces. *J Mater Chem B,* 2**,** 6953-6966.

DINH, T. N., HOU, S., PARK, S., SHALEK, B. A. & JEONG, K. J. 2018. Gelatin Hydrogel Combined with Polydopamine Coating to Enhance Tissue Integration of Medical Implants. *ACS Biomater Sci Eng,* 4**,** 3471-3477.

DORDELMANN, G., KOZLOVA, D., KARCZEWSKI, S., LIZIO, R., KNAUER, S. & EPPLE, M. 2014. Calcium phosphate increases the encapsulation efficiency of hydrophilic drugs (proteins, nucleic acids) into poly(d,l-lactide-co-glycolide acid) nanoparticles for intracellular delivery. *J Mater Chem B,* 2**,** 7250-7259.

DOROZHKIN, S. V. 2010. Nanosized and nanocrystalline calcium orthophosphates. *Acta Biomater,* 6**,** 715-34.

DUFFUS, C., CAMP, P. J. & ALEXANDER, A. J. 2009. Spatial control of crystal nucleation in agarose gel. *Journal of the American Chemical Society Communications,* 131**,** 2.

EBRAHIMI, S., STEPHEN SIPAUT MOHD NASRI, C. & BIN ARSHAD, S. E. 2021. Hydrothermal synthesis of hydroxyapatite powders using Response Surface Methodology (RSM). *PLoS One,* 16**,** e0251009.

EL-SHERBINY, I. M. & YACOUB, M. H. 2013. Hydrogel scaffolds for tissue engineering: Progress and challenges. *Glob Cardiol Sci Pract,* 2013**,** 316-42.

FEICHTINGER, G. A., CHEN, R. & YANG, X. B. 2019. Novel, Multi-phasic Gene-Activated Matrices for Gradient-Based Multi Gene Delivery. University of Leeds, School of Dentistry.

FELL, N. L. A., LAWLESS, B. M., COX, S. C., COOKE, M. E., EISENSTEIN, N. M., SHEPHERD, D. E. T. & ESPINO, D. M. 2019. The role of subchondral bone, and its histomorphology, on the dynamic viscoelasticity of cartilage, bone and osteochondral cores. *Osteoarthritis Cartilage,* 27**,** 535-543.

FISCHER, D., BIEBER, T., LI, Y., ELSÄSSER, H.-P. & KISSEL, T. 1999. A non-viral vector for DNA delivery based on low molecular weight, branched polyethylenimine - effect of moleular weight on transfection efficacy and cytotoxicity.pdf>. *Pharmaceutical Research,* 16**,** 7.

GEULI, O., METOKI, N., ELIAZ, N. & MANDLER, D. 2016. Electrochemically Driven Hydroxyapatite Nanoparticles Coating of Medical Implants. *Advanced Functional Materials,* 26**,** 8003-8010.

GOLAFSHAN, N., VORNDRAN, E., ZAHARIEVSKI, S., BROMMER, H., KADUMUDI, F. B., DOLATSHAHI-PIROUZ, A., GBURECK, U., VAN WEEREN, R., CASTILHO, M. & MALDA, J. 2020. Tough magnesium phosphate-based 3D-printed implants induce bone regeneration in an equine defect model. *Biomaterials,* 261**,** 120302.

GRAHAM, F. L., EB, D. D. & A.J 1973. A new technique for the assay of infectivity of human adenovirus 5 DNA. *Virology,* 52**,** 12.

GRATTON, S. E. A., ROPP, P. A., POHLHAUS, P. D., LUFT, J. C., MADDEN, V. J., NAPIER, M. E. & DESIMONE, J. M. 2008. The effect of particle design on cellular internalisation pathways. *Proceedings of the National Academy of Sciences of the United States of America,* 105**,** 6.

GREGORY, T. M., MORENO, E. C., PATEL, J. M. & BROWN, W. E. 1974. Solubility of B-Ca3(PO4)2 in the system Ca(OH)2-H3PO4-H2O at 5, 15, 25, and 37 °C. *Journal of Research of the National Bureau of Standards - A. Physics and Chemistry,* 78A**,** 8.

GUO, L., WANG, L., YANG, R., FENG, R., LI, Z., ZHOU, X., DONG, Z., GHARTEY-KWANSAH, G., XU, M., NISHI, M., ZHANG, Q., ISAACS, W., MA, J. & XU, X. 2017. Optimizing conditions for calcium phosphate mediated transient transfection. *Saudi J Biol Sci,* 24**,** 622-629.

HAN, Y., WANG, X., DAI, H. & LI, S. 2012. Nanosize and Surface Charge Effects of Hydroxyapatite Nanoparticles on Red Blood Cell Suspensions. *ACS Applied Material Interfaces,* 4**,** 7.

HERWEIJER, H. & WOLFF, J. A. 2003. Progress and prospects: naked DNA gene transfer and therapy. *Gene Ther,* 10**,** 453-8.

HSU, J.-P., HUANG, C.-H. & TSENG, S. 2012. Gel electrophoresis: Importance of concentration-dependent permittivity and double-layer polarization. *Chemical Engineering Science,* 84**,** 574-579.

HU, Y., TANG, G., LIU, J., CHENG, W., YUE, Y., LI, J. & ZHANG, P. 2012. FGF receptor-mediated gene delivery using ligands coupled to PEI-beta-CyD. *J Biomed Biotechnol,* 2012**,** 989235.

HUNTER, G. K. & GOLDBERG, H. A. 1993. Nucleation of hydroxyapatite by bone sialoprotein. *Proceedings of the National Academy of Sciences of the United States of America,* 90**,** 4.

IBRAHEEM, D., ELAISSARI, A. & FESSI, H. 2014. Gene therapy and DNA delivery systems. *Int J Pharm,* 459**,** 70-83.

JOHNSSON, M. S. & NANCOLLAS, G. H. 1992. The role of brushite and octacalcium phosphate in apatite formation. *Critical Reviews in Oral Biology and Medicine,* 3**,** 22.

KABIR, W., DI BELLA, C., CHOONG, P. F. M. & O'CONNELL, C. D. 2021. Assessment of Native Human Articular Cartilage: A Biomechanical Protocol. *Cartilage,* 13**,** 427S-437S.

KALIA, P., VIZCAY-BARRENA, G., FAN, J. P., WARLEY, A., DI SILVIO, L. & HUANG, J. 2014. Nanohydroxyapatite shape and its potential role in bone formation: an analytical study. *J R Soc Interface,* 11**,** 20140004.

KAMITAKAHARA, M., KIMURA, K. & IOKU, K. 2012. Synthesis of nanosized porous hydroxyapatite granules in hydrogel by electrophoresis. *Colloids Surf B Biointerfaces,* 97**,** 236-9.

KAMITAKAHARA, M., OGATA, S., TANIHARA, M. & OHTSUKI, C. 2007. Control of Calcium Phosphate Precipitation in Hydrogel. *Key Engineering Materials,* 330-332**,** 79-82.

KAN, M., MINAMOTO, Y., SUNAMI, S., YAMANE, I. & UMEDA, M. 1982. The effects on cell adhesion of fibronectin and gelatin in a serum-free bovine serum albumin medium.pdf>. *Cell Structure and Function,* 7**,** 8.

KAZAKOVA, G., SAFRONOVA, T., GOLUBCHIKOV, D., SHEVTSOVA, O. & RAU, J. V. 2021. Resorbable Mg(2+)-Containing Phosphates for Bone Tissue Repair. *Materials (Basel),* 14.

KHAN, M. A., WU, V. M., GHOSH, S. & USKOKOVIC, V. 2016. Gene delivery using calcium phosphate nanoparticles: Optimization of the transfection process and the effects of citrate and poly(l-lysine) as additives. *J Colloid Interface Sci,* 471**,** 48-58.

KIMURA, K., KAMITAKAHARA, M., YOKOI, T. & IOKU, K. 2018. Formation Process of Hydroxyapatite Granules in Agarose Hydrogel by Electrophoresis. *Crystal Growth & Design,* 18**,** 1961-1966.

KOCK, N. B., VAN SUSANTE, J. L., BUMA, P., VAN KAMPEN, A. & VERDONSCHOT, N. 2006. Press-fit stability of an osteochondral autograft: Influence of different plug length and perfect depth alignment. *Acta Orthop,* 77**,** 422-8.

KOH, C. G., KANG, X., XIE, Y., FEI, Z., GUAN, J., YU, B., ZHANG, X. & LEE, L. J. 2009. Delivery of polyethylenimine-DNA complexes assembled in a microfluidics device. *Molecular Pharmaceutics,* 6**,** 10.

KOVTUN, A., HEUMANN, R. & EPPLE, M. 2009. Calcium phosphate nanoparticles for the transfection of cells. *Biomed Mater Eng,* 19**,** 241-7.

KU, S. H., RYU, J., HONG, S. K., LEE, H. & PARK, C. B. 2010. General functionalization route for cell adhesion on non-wetting surfaces. *Biomaterials,* 31**,** 2535-41.

KUROSAKI, T., KITAHARA, T., FUMOTO, S., NISHIDA, K., NAKAMURA, J., NIIDOME, T., KODAMA, Y., NAKAGAWA, H., TO, H. & SASAKI, H. 2009. Ternary complexes of pDNA, polyethylenimine, and gamma-polyglutamic acid for gene delivery systems. *Biomaterials,* 30**,** 2846-53.

KWAK, S., JANG, S., PARK, S., KANG, J., KIM, T. Y. & NAM, I. 2021. Synthesis of Au sponges based on agarose template. *Scripta Materialia,* 196.

KWON, S. G. & HYEON, T. 2011. Formation mechanisms of uniform nanocrystals via hot-injection and heat-up methods. *Small,* 7**,** 2685-702.

LANDI, E., LOGROSCINO, G., PROIETTI, L., TAMPIERI, A., SANDRI, M. & SPRIO, S. 2008. Biomimetic Mg-substituted hydroxyapatite: from synthesis to in vivo behaviour. *J Mater Sci Mater Med,* 19**,** 239-47.

LARSEN, M. J. & JENSEN, S. J. 1989. The hydroxyapatite solubility product of human dental enamel as a function of pH in the range 4.6 - 7.6 at 20 °C. *Archives of Oral Biology,* 34**,** 5.

LAURENTI, M., AL SUBAIE, A., ABDALLAH, M. N., CORTES, A. R., ACKERMAN, J. L., VALI, H., BASU, K., ZHANG, Y. L., MURSHED, M., STRANDMAN, S., ZHU, J., MAKHOUL, N., BARRALET, J. E. & TAMIMI, F. 2016. Two-Dimensional Magnesium Phosphate Nanosheets Form Highly Thixotropic Gels That Up-Regulate Bone Formation. *Nano Lett,* 16**,** 4779-87.

LEE, H., DELLATORE, S. M., MILLER, W. M. & MESSERSMITH, P. B. 2007. Mussel-inspired surface chemistry for multifunctional coatings. *Science,* 318**,** 426-30.

LEE, H., RHO, J. & MESSERSMITH, P. B. 2009. Facile Conjugation of Biomolecules onto Surfaces via Mussel Adhesive Protein Inspired Coatings. *Adv Mater,* 21**,** 431-434.

LEE, J.-H. & LEE, M.-J. 2012. Liposome-Mediated Cancer Gene Therapy: Clinical Trials and their Lessons to Stem Cell Therapy. *Bulletin of the Korean Chemical Society,* 33**,** 433-442.

LETT, J. A., SUNDARESWARI, M., RAVICHANDRAN, K., LATHA, M. B., SAGADEVAN, S. & BIN JOHAN, M. R. 2019. Tailoring the morphological features of sol-gel synthesized mesoporous hydroxyapatite using fatty acids as an organic modifier. *RSC Adv,* 9**,** 6228-6240.

LI, H., XIN, H. L., MULLER, D. A. & ESTROFF, L. A. 2009. Visualizing the 3D internal structure of calcite single crystals grown in agarose hydrogels. *Science,* 326**,** 1244-7.

LI, S. & HUANG, L. 2000. Nonviral gene therapy: promises and challenges. *Gene Therapy,* 7**,** 4.

LI, W., CHEN, L., HUANG, Z., WU, X., ZHANG, Y., HU, Q. & WANG, Y. 2011. The influence of cyclodextrin modification on cellular uptake and transfection efficiency of polyplexes. *Org Biomol Chem,* 9**,** 7799-806.

LIN, K., WU, C. & CHANG, J. 2014. Advances in synthesis of calcium phosphate crystals with controlled size and shape. *Acta Biomater,* 10**,** 4071-102.

LIU, S., DENG, Y., LIU, W., LI, Z., LI, L., ZHANG, R. & JIANG, Y. 2022. Chitosan hydrogel for controlled crystallization of loaded drug: Role of interplay of assembly processes. *Colloids and Surfaces A: Physicochemical and Engineering Aspects,* 644.

LIU, Y., WANG, T., HE, F., LIU, Q., ZHANG, D., XIANG, S., SU, S. & ZHANG, J. 2011. An efficient calcium phosphate nanoparticle-based nonviral vector for gene delivery. *Int J Nanomedicine,* 6**,** 721-7.

LONGO, P. A., KAVRAN, J. M., KIM, M. S. & LEAHY, D. J. 2013. Transient mammalian cell transfection with polyethylenimine (PEI). *Methods Enzymol,* 529**,** 227-40.

LÓPEZ-QUINTELA, M. A., TOJO, C., BLANCO, M. C., GARCíA RIO, L. & LEIS, J. R. 2004. Microemulsion dynamics and reactions in microemulsions. *Current Opinion in Colloid & Interface Science,* 9**,** 264-278.

LU, M., CHEN, H., YUAN, B., ZHOU, Y., MIN, L., XIAO, Z., ZHU, X., TU, C. & ZHANG, X. 2020. Electrochemical Deposition of Nanostructured Hydroxyapatite Coating on Titanium with Enhanced Early Stage Osteogenic Activity and Osseointegration. *Int J Nanomedicine,* 15**,** 6605-6618.

LUNDSTROM, K. 2018. Viral Vectors in Gene Therapy. *Diseases,* 6.

MAJDA, D., BHATTARAI, A., RIIKONEN, J., NAPRUSZEWSKA, B. D., ZIMOWSKA, M., MICHALIK-ZYM, A., TÖYRÄS, J. & LEHTO, V. P. 2017. New approach for determining cartilage pore size distribution: NaCl-thermoporometry. *Microporous and Mesoporous Materials,* 241**,** 238-245.

MALIK, M. A., WANI, M. Y. & HASHIM, M. A. 2012. Microemulsion method: A novel route to synthesize organic and inorganic nanomaterials. *Arabian Journal of Chemistry,* 5**,** 397-417.

MASOULEH, M. P., HOSSEINI, V., POURHAGHGOUY, M. & BAKHT, M. K. 2017. Calcium Phosphate Nanoparticles Cytocompatibility Versus Cytotoxicity: A Serendipitous Paradox. *Curr Pharm Des,* 23**,** 2930-2951.

MCDOWELL, H., GREGORY, T. M. & BROWN, W. E. 1977. Solubility of Ca5(PO4)3OH in the system Ca(OH)2-H3PO4-H2O at 5, 15, 25, and 37 °C. *Journal of Research of the National Bureau of Standards - A. Physics and Chemistry,* 81A**,** 9.

MELDRUM, F. C. & O'SHAUGHNESSY, C. 2020. Crystallization in Confinement. *Adv Mater,* 32**,** e2001068.

MILOVANOVIC, P., VUKOVIC, Z., ANTONIJEVIC, D., DJONIC, D., ZIVKOVIC, V., NIKOLIC, S. & DJURIC, M. 2017. Porotic paradox: distribution of cortical bone pore sizes at nano- and micro-levels in healthy vs. fragile human bone. *J Mater Sci Mater Med,* 28**,** 71.

MINOUEI, H., FATHI, M. H. & MERATIAN, M. 2012. Heat treatment of cobalt-base alloy surgical implants with hydroxyapatite-bioglass for surface bioactivation. *Iranian Journal of Materials Science and Engineering,* 9**,** 7.

MOLLERUP, J. M. & BREIL, M. P. 2015. Modeling the permittivity of electrolyte solutions. *AIChE Journal,* 61**,** 2854-2860.

MURARI, G., BOCK, N., ZHOU, H., YANG, L., LIEW, T., FOX, K. & TRAN, P. A. 2020. Effects of polydopamine coatings on nucleation modes of surface mineralization from simulated body fluid. *Sci Rep,* 10**,** 14982.

MURPHY, C. M., HAUGH, M. G. & O'BRIEN, F. J. 2010. The effect of mean pore size on cell attachment, proliferation and migration in collagen-glycosaminoglycan scaffolds for bone tissue engineering. *Biomaterials,* 31**,** 461-6.

NABIYOUNI, M., REN, Y. & BHADURI, S. B. 2015. Magnesium substitution in the structure of orthopedic nanoparticles: A comparison between amorphous magnesium phosphates, calcium magnesium phosphates, and hydroxyapatites. *Mater Sci Eng C Mater Biol Appl,* 52**,** 11-7.

NAM, H. Y., PARK, J. H., KIM, K., KWON, I. C. & JEONG, S. Y. 2009. Lipid-based emulsion system as non-viral gene carriers. *Arch Pharm Res,* 32**,** 639-46.

NARAYANAN, J., XIONG, J.-Y. & LIU, X.-Y. 2006. Determination of agarose gel pore size: Absorbance measurements vis a vis other techniques. *Journal of Physics: Conference Series,* 28**,** 83-86.

NAVARKHELE, V. V., AGRAWAL, R. S. & KURTADIKAR, M. L. 1998. Dielectric properties of electrolytic solutions. *Pramana - Journal of Physics,* 51**,** 8.

NEUHAUS, B., TOSUN, B., ROTAN, O., FREDE, A., WESTENDORF, A. M. & EPPLE, M. 2016. Nanoparticles as transfection agents: a comprehensive study with ten different cell lines. *RSC Advances,* 6**,** 18102-18112.

NEWMAN, C. M. & BETTINGER, T. 2007. Gene therapy progress and prospects: ultrasound for gene transfer. *Gene Ther,* 14**,** 465-75.

NOSEWICZ, T. L., REILINGH, M. L., VAN DIJK, C. N., DUDA, G. N. & SCHELL, H. 2012. Weightbearing ovine osteochondral defects heal with inadequate subchondral bone plate restoration: implications regarding osteochondral autograft harvesting. *Knee Surg Sports Traumatol Arthrosc,* 20**,** 1923-30.

OBERBEK, P., BOLEK, T., CHLANDA, A., HIRANO, S., KUSNIERUK, S., ROGOWSKA-TYLMAN, J., NECHYPORENKO, G., ZINCHENKO, V., SWIESZKOWSKI, W. & PUZYN, T. 2018. Characterization and influence of hydroxyapatite nanopowders on living cells. *Beilstein J Nanotechnol,* 9**,** 3079-3094.

OGRIS, M., STEINLEIN, P., KURSA, M., MECHTLER, K., KIRCHEIS, R. & WAGNER, E. 1998. The size of DNA/transferrin-PEI complexes is an important factor for gene expression in cultured cells. *Gene Therapy,* 5**,** 9.

OMEMA, U., KHALID, H. & CHAUDHRY, A. A. 2020. Magnesium-substituted hydroxyapatite. *Handbook of Ionic Substituted Hydroxyapatites.* Woodhead Publishing Series in Biomaterials.

ORRANTIA, E. & CHANG, P. L. 1990. Intracellular distribution of DNA internalized through calcium phosphate precipitation. *Experimental Cell Research,* 190**,** 5.

OSKUEE, R. K., DEHSHAHRI, A., SHIER, W. T. & RAMEZANI, M. 2009. Alkylcarboxylate grafting to polyethylenimine: a simple approach to producing a DNA nanocarrier with low toxicity. *J Gene Med,* 11**,** 921-32.

OYANE, A., WANG, X., SOGO, Y., ITO, A. & TSURUSHIMA, H. 2012. Calcium phosphate composite layers for surface-mediated gene transfer. *Acta Biomater,* 8**,** 2034-46.

PARKHURST, D. L. & APPELO, C. A. J. 2013. *Description of Input and Examples for PHREEQC Version 3 - A computer Program for Speciation, Batch Reaction, One-Dimensional*

Transport, and Inverse Geochemical Calculations, U.S. Department of The Interior, U.S. Geological Survey.

PEDRAZA, C. E., BASSETT, D. C., MCKEE, M. D., NELEA, V., GBURECK, U. & BARRALET, J. E. 2008. The importance of particle size and DNA condensation salt for calcium phosphate nanoparticle transfection. *Biomaterials,* 29**,** 9.

PERNODET, N., MAALOUM, M. & TINLAND, B. 1997. Pore size of agarose gels by atomic force microscopy. *Electrophoresis,* 18**,** 55-8.

PICULELL, L. & NILSSON, S. 1989. Anion-specific salt effects in aqueous agarose systems. 2. Nuclear spin relaxtion of ions in agarose gels and solutions. *Journal of Physical Chemistry,* 93**,** 10.

POURAN, B., RAOOF, A., DE WINTER, D. A. M., ARBABI, V., BLEYS, R., BEEKMAN, F. J., ZADPOOR, A. A., MALDA, J. & WEINANS, H. 2021. Topographic features of nano-pores within the osteochondral interface and their effects on transport properties -a 3D imaging and modeling study. *J Biomech,* 123**,** 110504.

PRAKASH, K. H., KUMAR, R., OOI, C. P., CHEANG, P. & KHOR, K. A. 2006. Apparent solubility of hydroxyapatite in aqueous medium and its influence on the morphology of nancrystallites with precipitation temperature. *Langmuir,* 22**,** 7.

PUJARI-PALMER, S., LU, X. & KARLSSON OTT, M. 2017. The Influence of Hydroxyapatite Nanoparticle Morphology on Embryonic Development in a Zebrafish Exposure Model. *Nanomaterials (Basel),* 7.

QIU, C., WU, Y., GUO, Q., SHI, Q., ZHANG, J., MENG, Y., XIA, F. & WANG, J. 2022. Preparation and application of calcium phosphate nanocarriers in drug delivery. *Mater Today Bio,* 17**,** 100501.

RACZ, G. J. & SOPER, R. J. 1968. Solubility of dimagnesium phosphate trihydrate and trimagnesium phosphate. *Canadian Hournal of Soil Science,* 48**,** 5.

RAMAMOORTH, M. & NARVEKAR, A. 2015. Non viral vectors in gene therapy- an overview. *J Clin Diagn Res,* 9**,** GE01-6.

RÄSÄNEN, T. & MESSNER, K. 1996. Regional variations of indentation stiffness and thickness of normal rabbit knee articular cartilage. *Journal of Biomedical Materials Research,* 31**,** 519-524.

REINER, J., WALTER, E. M. & KARBSTEIN, H. P. 2023. Assessment of droplet self-shaping and crystallization during temperature fluctuations exceeding the melting temperature of the dispersed phase. *Colloids and Surfaces A: Physicochemical and Engineering Aspects,* 656.

RODRIGUEZ, A., DEL, A. & ANGELES, M. 2013. Non-Viral Delivery Systems in Gene Therapy. *Gene Therapy - Tools and Potential Applications.*

ROEBUCK, B. D. & GOLDBLITH, S. A. 1975. Dielectric properties at microwave frequencies of agar gels. *Journal of Food Science,* 40**,** 4.

SABIN, J., ALATORRE-MEDA, M., MINONES, J., JR., DOMINGUEZ-ARCA, V. & PRIETO, G. 2022. New insights on the mechanism of polyethylenimine transfection and their implications on gene therapy and DNA vaccines. *Colloids Surf B Biointerfaces,* 210**,** 112219.

SADAT-SHOJAI, M., KHORASANI, M. T., DINPANAH-KHOSHDARGI, E. & JAMSHIDI, A. 2013. Synthesis methods for nanosized hydroxyapatite with diverse structures. *Acta Biomater,* 9**,** 7591-621.

SANG, Y., XIE, K., MU, Y., LEI, Y., ZHANG, B., XIONG, S., CHEN, Y. & QI, N. 2015. Salt ions and related parameters affect PEI-DNA particle size and transfection efficiency in Chinese hamster ovary cells. *Cytotechnology,* 67**,** 67-74.

SARKAR, K., BANERJEE, S. L., KUNDU, P. P., MADRAS, G. & CHATTERJEE, K. 2015. Biofunctionalized surface-modified silver nanoparticles for gene delivery. *J Mater Chem B,* 3**,** 5266-5276.

SARKARI, S., KHAJEHMOHAMMADI, M., DAVARI, N., LI, D. & YU, B. 2022. The effects of process parameters on polydopamine coatings employed in tissue engineering applications. *Front Bioeng Biotechnol,* 10**,** 1005413.

SHIN, J., PARK, J. K., KIM, G. W., NAM, I. & PARK, S. 2022a. Agarose Gel-Templating Synthesis of a 3D Wrinkled Graphene Architecture for Enhanced Supercapacitor Performance. *Micromachines (Basel),* 13.

SHIN, Y. S., JO, M. K., CHO, Y. S. & YANG, S. H. 2022b. Diffusion-Controlled Crystallization of Calcium Phosphate in a Hydrogel toward a Homogeneous Octacalcium Phosphate/Agarose Composite. *ACS Omega,* 7**,** 1173-1185.

SINGH, R. K., KIM, T. H., PATEL, K. D., KIM, J. J. & KIM, H. W. 2014. Development of biocompatible apatite nanorod-based drug-delivery system with in situ fluorescence imaging capacity. *J Mater Chem B,* 2**,** 2039-2050.

SINUSAITE, L., KAREIVA, A. & ZARKOV, A. 2021. Thermally Induced Crystallization and Phase Evolution of Amorphous Calcium Phosphate Substituted with Divalent Cations Having Different Sizes. *Crystal Growth & Design,* 21**,** 1242-1248.

SOKOLOVA, V. V., RADTKE, I., HEUMANN, R. & EPPLE, M. 2006. Effective transfection of cells with multi-shell calcium phosphate-DNA nanoparticles. *Biomaterials,* 27**,** 3147-53.

SON, S. & KIM, W. J. 2010. Biodegradable nanoparticles modified by branched polyethylenimine for plasmid DNA delivery. *Biomaterials,* 31**,** 133-43.

SOSA-ACOSTA, J. R., IRIARTE-MESA, C., ORTEGA, G. A. & DIAZ-GARCIA, A. M. 2020. DNA-Iron Oxide Nanoparticles Conjugates: Functional Magnetic Nanoplatforms in Biomedical Applications. *Top Curr Chem (Cham),* 378**,** 13.

SU, T., ZHANG, M., ZENG, Q., PAN, W., HUANG, Y., QIAN, Y., DONG, W., QI, X. & SHEN, J. 2021. Mussel-inspired agarose hydrogel scaffolds for skin tissue engineering. *Bioact Mater,* 6**,** 579-588.

SUN, I. & NEWMAN, J. 1970. The electrical conductivity of aqueous solutions of calcium chloride. *Lawrence Berkeley National Laboratory: Recent work*.

TABATA, M., SHIMODA, T., SUGIHARA, K., OGOMI, D., OHGUSHI, H. & AKASHI, M. 2005. Apatite formed on/in agarose gel as a bone-grafting material in the treatment of periodontal infrabony defect. *J Biomed Mater Res B Appl Biomater,* 75**,** 378-86.

TABATA, M., SHIMODA, T., SUGIHARA, K., OGOMI, D., SERIZAWA, T. & AKASHI, M. 2003. Osteoinductive and hemostatic properties of apatite formed on/in agarose gel as a bone-grafting material. *Osteoconductive and hemostatic properties of apatite***,** 9.

TAMURA, T. & SAKATA, T. 2003. Application of In vivo electroporation to cancer gene therapy. *Current Gene Therapy,* 3**,** 5.

TARN, M. D. & PAMME, N. 2014. Microfluidics. *Reference Module in Chemistry, Molecular Sciences and Chemical Engineering.*

TIAN, Y., YANG, D., WANG, Y. & JIANG, Z. 2013. Template-free synthesis of TiO2 microcages in agarose gels with improved photocatalytic activity. *Journal of Nanoparticle Research,* 15.

TRAN, D. T. 2016. Synthesis of porous ZnO based materials using an agarose gel template for H2S desulfurization. *RSC Advances,* 6**,** 1339-1345.

TSIKOURKITOUDI, V., KARLSSON, J., MERKL, P., LOH, E., HENRIQUES-NORMARK, B. & SOTIRIOU, G. A. 2020. Flame-Made Calcium Phosphate Nanoparticles with High Drug Loading for Delivery of Biologics. *Molecules,* 25.

UCHIDA, M., LI, X. W., MERTENS, P. & ALPAR, H. O. 2009. Transfection by particle bombardment: delivery of plasmid DNA into mammalian cells using gene gun. *Biochim Biophys Acta,* 1790**,** 754-64.

VELLIOS, E. E., JONES, K. J. & WILLIAMS, R. J. 2021. Osteochondral Autograft Transfer for Focal Cartilage Lesions of the Knee With Donor-Site Back-Fill Using Precut Osteochondral

Allograft Plugs and Micronized Extracellular Cartilage Augmentation. *Arthrosc Tech,* 10**,** e181-e192.

WANG, Y., MA, X., DING, C. & JIA, L. 2015. pH-responsive deoxyribonucleic acid capture/release by polydopamine functionalized magnetic nanoparticles. *Anal Chim Acta,* 862**,** 33-40.

WANG, Y., YANG, D., SHI, Y. & JIANG, Z. 2013. Bio-inspired synthesis of TiO2 hollow nanospheres in agarose gels. *Journal of Alloys and Compounds,* 560**,** 42-48.

WATANABE, J. & AKASHI, M. 2006. Novel biomineralisation for hydrogels: Electrophoresis approach accelerates hydroxyapatite formation in hydrogels. *Biomacromolecules,* 7**,** 4.

WATANABE, J., KASHII, M., HIRAO, M., OKA, K., SUGAMOTO, K., YOSHIKAWA, H. & AKASHI, M. 2007. Quick-forming hydroxyapatite/agarose gel composites induce bone regeneration. *J Biomed Mater Res A,* 83**,** 845-52.

WEI, M., RUYS, A. J., MILTHORPE, B. K. & SORRELL, C. C. 2005. Precipitation of Hydroxyapatite Nanoparticles: Effects of Precipitation Method on Electrophoretic Deposition. *Journal of Materials Science: Materials in Medicine,* 16**,** 6.

WEI, X. & MESSNER, K. 1999. Maturation-dependent durability of spontaneous cartilage repair in rabbit knee joint. *Journal of Biomedical Materials Research,* 46**,** 539-548.

WELZEL, T., RADTKE, I., MEYER-ZAIKA, W., HEUMANN, R. & EPPLE, M. 2004. Transfection of cells with custom-made calcium phosphate nanoparticles coated with DNA. *Journal of Materials Chemistry,* 14.

WENG, L. & ELLIOTT, G. D. 2014. Polymerization effect of electrolytes on hydrogen-bonding cryoprotectants: ion-dipole interactions between metal ions and glycerol. *J Phys Chem B,* 118**,** 14546-54.

WU, H., LI, Z., TANG, J., YANG, X., ZHOU, Y., GUO, B., WANG, L., ZHU, X., TU, C. & ZHANG, X. 2019. The in vitro and in vivo anti-melanoma effects of hydroxyapatite nanoparticles: influences of material factors. *Int J Nanomedicine,* 14**,** 1177-1191.

XUE, Q. & ZHANG, Q. 2019. Agar Hydrogel Template Synthesis of Mn(3)O(4) Nanoparticles through an Ion Diffusion Method Controlled by Ion Exchange Membrane and Electrochemical Performance. *Nanomaterials (Basel),* 9.

YANG, G., LV, F., WANG, B., LIU, L., YANG, Q. & WANG, S. 2012. Multifunctional non-viral delivery systems based on conjugated polymers. *Macromol Biosci,* 12**,** 1600-14.

YANG, X., LI, Y., LIU, X., ZHANG, R. & FENG, Q. 2018. In Vitro Uptake of Hydroxyapatite Nanoparticles and Their Effect on Osteogenic Differentiation of Human Mesenchymal Stem Cells. *Stem Cells Int,* 2018**,** 2036176.

YAO, C., TAI, Z., WANG, X., LIU, J., ZHU, Q., WU, X., ZHANG, L., ZHANG, W., TIAN, J., GAO, Y. & GAO, S. 2015. Reduction-responsive cross-linked stearyl peptide for effective delivery of plasmid DNA. *Int J Nanomedicine,* 10**,** 3403-16.

ZARIC, V., WELTIN, D., ERBACHER, P., REMY, J. S., BEHR, J. P. & STEPHAN, D. 2004. Effective polyethylenimine-mediated gene transfer into human endothelial cells. *J Gene Med,* 6**,** 176-84.

ZARRINTAJ, P., MANOUCHEHRI, S., AHMADI, Z., SAEB, M. R., URBANSKA, A. M., KAPLAN, D. L. & MOZAFARI, M. 2018. Agarose-based biomaterials for tissue engineering. *Carbohydr Polym,* 187**,** 66-84.

ZHANG, P. & RYAN, J. A. 1999. Transformation of Pb(II) from Cerrusite to Chloropyromorphite in the Presence of Hydroxyapatite under Varying Conditions of pH. *Environmental Science & Technology,* 33**,** 625-630.